UNIVERSITY OF BIRMINGHAM

Corrosion, Transport, and Deposition in Pressurised Water Nuclear Reactor Primary Coolant Systems

A thesis submitted to the University of Birmingham for the degree of

ENGINEERING DOCTORATE IN FORMULATION ENGINEERING

Jonathan J. Morrison

School of Chemical Engineering,
University of Birmingham
25th September 2014

Academic Supervisors:

Dr. Brian J. Connolly
Dr. Clive Ponton

School of Metallurgy and Materials
University of Birmingham

Industrial Supervisor:

Dr. Andy Banks

Rolls-Royce Plc.,
Derby

Abstract

Several unscheduled shut downs of the Cruas nuclear power plant in France have been caused by the deposition of corrosion products in flow broaches of the steam generator tube support sheets. The depositions are theorised to be the result of electrokinetically stimulated deposition.

In this work, a hot water loop to replicate these depositions in the laboratory was built, along with rigs to characterise supporting phenomena – the corrosion rate of stainless steel and the solubility of the corrosion products.

While the data obtained from the hot water loop did not provide conclusive proof of the existence or prevalence of the electrokinetically stimulated deposition mechanism, evidence of deposition caused by cavitation was found. In one case, the structure of the deposition appeared to match that of literature sources, suggesting that some amount of deposition in this experimental series was potentially a result of electrokinetically stimulated deposition.

The corrosion rate of stainless steel was measured at high temperatures in solutions of lithium hydroxide at various concentrations. Surface finish was found to have an effect on the corrosion rate, though the difference between mechanically ground surfaces with an order of magnitude difference in roughness was found to be minimal.

The solubility of the corrosion products formed was measured and found to be of similar order to that reported in the literature, however the minor alloying elements were found to leach from the surface in substantial quantites. Additional work is required to fully characterise this leaching process.

Acknowledgements

Firstly, I would like to thank the EPSRC, the University of Birmingham, and Rolls-Royce Ltd. for supporting and funding this project. Additionally, I wish to thank the Worshipful Company of Tinplate Workers, specifically Bev Page, for travel assistance to the Nuclear Plant Chemistry Conferences in Quebec 2010, and Paris 2012.

I thank the Department of Metallurgy and Materials for hosting the laboratory facilities required for the project.

I would also like to thank my academic supervisors Dr. Brian Connolly and Dr. Clive Ponton, and my industrial supervisor Dr. Andy Banks, for their help, guidance and inexhaustible patience. Further, I would like to thank my EngD programme manager, Dr. Richard Greenwood, for his generous support in all variety of matters.

Further to those already mentioned, I would like extend my thanks to the following people for their support in a multitude of areas: from the University of Birmingham, Dr. Chris Cooper, Prof. Martin Freer, Dr. Steve Baker, Dr. Gillian Kingston, Mr. Jeff Sutton, Mr. Andy Bradshaw, Ms. Avril Rogers, Mr. Geoff Dolman, and Mr. Warren Hay. From the University of Surrey, Dr. Steve Hinder and Prof. John Watts. From Kratos Analytical, Dr. Helen Brannon. From Roll-Royce plc, Dr. Richard Wain, Dr. Lara-Jane Pegg, Dr. Andrew Powell and Mr. Sam Parry.

Finally, I wish to thank my family for their ever present love and support, throughout this project. Without the six of you, I would not have been able to do this.

Glossary of Terms

AAS	Atomic Absorption Spectroscopy
ABWR	Advanced Boiling Water Reactor
AC	Alternating Current
AGR	Advanced Gas Reactor
AIM	Argon Ion Milling
ALARP	As Low As Reasonably Practicable
AOA	Axial Offset Anomaly
ASTM	American Society of Testing and Materials
BOA	Boron Offset Anomoly
BUR	Build-up Rate
BWR	Boiling Water Reactor
CAD	Computer Aided Design
CANDU	Canadian Deuterium Uranium Reactor
ccp	Cubic Close Packed
CIPS	CRUD Induced Power Shift
CRUD	Chalk River Unidentified Deposit
.csv	"Comma Separated Value" File
dP	Differential Pressure
ECP	Electrochemical Corrosion Potential
EDL	Electrical Double Layer
EDX	Energy Dispersive X-ray Spectroscopy
EPRI	Electric Power Reseach Institiute

FAAS	Flame Atomic Absorption Spectroscopy
FAC	Flow Accelerated Corrosion
FEG	Field Emission Gun
FIB	Focussed Ion Beam
FID	Flow Induced Deposition
fcc	Face-Centred Cubic
GC	Gas Chromatography
GCR	Gas Cooled Reactor
GFAAS	Graphite Furnace Atomic Absorption Spectroscopy
GIXRD	Grazing Incident X-ray Diffraction
Grafoil	A material composed of laminated graphite
GW	Gigawatts ($1x10^9$ J/s)
GWe	Gigawatts Electrical
Heavy Water	Deuterium enriched water (D_2O)
HPLC	High Performance Liquid Chromatography
HWC	Hydrogen Water Chemistry
Hydrothermal Water	Liquid water at high temperature.
ICP-MS	Inductively Coupled Plasma Mass Spectroscopy
ID	Inner Diameter
IEP	Isoelectric Point
IHL	Inner Helmholtz Layer
IHP	Inner Helmhotlz Plane
IGSCC	Intergranular Stress Corrosion Cracking

LWR	Light Water Reactor
Light Water	Water containing hydrogen's most abundant isotope (H_2O)
MCM	Mixed Conduction Model
MIC	Microbiologically Influenced Corrosion
MULTEQ	Multiple Equilibrium (EPRI proprietary software)
NHE	Normal Hydrogen Electrode (see SHE)
NNL	National Nuclear Laboratories
NPP	Nuclear Power Plant
OD	Outer Diameter
OHL	Outer Helmholtz Layer
OHP	Outer Helmholtz Plane
PDM	Point Defect Model
PEEK	Polyether-ether-ketone
PID	Proportional Integral Differential
ppb	Parts Per Billion; equal to $\mu g.kg^{-1}$
ppm	Parts Per Million; equal to $mg.kg^{-1}$
PV	Process Value
PWR	Pressurised Water Reactor
PWSCC	Primary Water Stress Corrosion Cracking
PZC	Point of Zero Charge
RCS	Reactor Coolant System
SCC	Stress Corrosion Cracking

SEM	Scanning Electron Microscopy
SG	Steam Generator
SHE	Standard Hydrogen Electrode
SS	Stainless Steel
SP	Set Point, sometimes called the Set Value (SV)
SV	Set Value, more often referred to as Set Point (SP)
TEM	Transmission Electron Microscopy
TGSCC	Transgranular Stress Corrosion Cracking
TSP	Tube Support Plate
VVER	Vodo-Vodyanoi Energetichesky Reactor
WDX	Wave Dispersive X-ray Spectroscopy
XRD	X-ray Diffraction
XPS	X-ray Photoelectron Spectroscopy
YSZ	Yttria-Stabilised Zirconia
ZRA	Zero Resistance Ammeter

Table of Contents

1 Introduction

1.1 Project Background

Pressurised Water Reactors (PWRs), such as the Sizewell B power station in the UK, are enormously complicated thermodynamic heat engines. Nuclear fission of uranium-235 fuel produces fast neutrons, which are moderated into thermal neutrons by the coolant water. Thermal neutrons are responsible for maintaining the criticality of the nuclear reaction, and for heating coolant water, that is held under high pressure to maintain a liquid state. The heat in the primary coolant is transferred to a secondary coolant loop where steam is raised to drive a conventional steam turbine.

PWR power plants consist of almost 100 km of pipe, about 65% of which is less than 50 mm in diameter, and approximately 15,000 valves and several large forgings [1]. Much of the small diameter tubing is used in the steam generators, an example of which can be seen in Figure 1.1 The vast majority of these components are metal alloys designed and specified to provide the best performance for specific tasks, be that mechanical hardness for bearing type components, strength to withstand the high pressure, or corrosion resistance for service in the hostile environment of the coolant circuits.

The alloys used in nuclear plants for their corrosion resistance are largely nickel base alloys, with Alloy 690 being the grade most used for steam generator (SG) tubing applications, and stainless steels of various grades (see Figure 1.2). Alloy 690 has been found to be resistant to stress corrosion cracking (SCC) [2], a problem that has appeared in almost every other material used for SG tubing. It should be noted that SCC mechanisms account for 39.6% of all corrosion issues on plant (see Figure 1.3). However, stainless steels are often retained for other components in the plant due to their mix of excellent general corrosion resistance, comparatively low cost, and wide availability.

Construction of a new generation of nuclear reactors for the UK is expected to begin in 2015. This follows a recent interest across the world for new nuclear plants to meet rising electricity demand while maintaining low carbon emissions [3,4]. For these plants to operate safely for their designed lifetime and possibly beyond, it is crucial that materials performance issues seen on current generation II and III reactors be identified, and preferably mitigated, to provide operational guidance and experience to the new generation III+ reactors.

As part of this effort, computational modeling of nuclear power plants is becoming an invaluable tool. While computers were available and quite wide spread during the design and construction of the last generation of reactors, exponential improvements in computing power and scientific modelling software provide a unique advantage that was not previously available.

To this end, many companies, consultancies and institutes are in the process of developing computer models of their plant designs, which seek to model the fluid dynamics, chemical and radiological environment, and mechanical integrity of the system given various input parameters. Notable examples of computer models developed to predict conditions in plant include the BOA (Boron Offset Anomoly) code [5] and MULTEQ (MULTiple EQuilibrium), both of which were developed by the Electric Power Research Institiute (EPRI) [6].

For computer models to accurately represent reality, it is important that the fundamental mechanisms being used in the calculations be well-characterised and empirical measurements provided. Arguably, one of the most important parameters to plant chemistry/materials interaction models is the environmental degradation mechanism of plant materials (which are dominated by stress corrosion cracking and flow assisted corrosion, (see Figure 1.3).

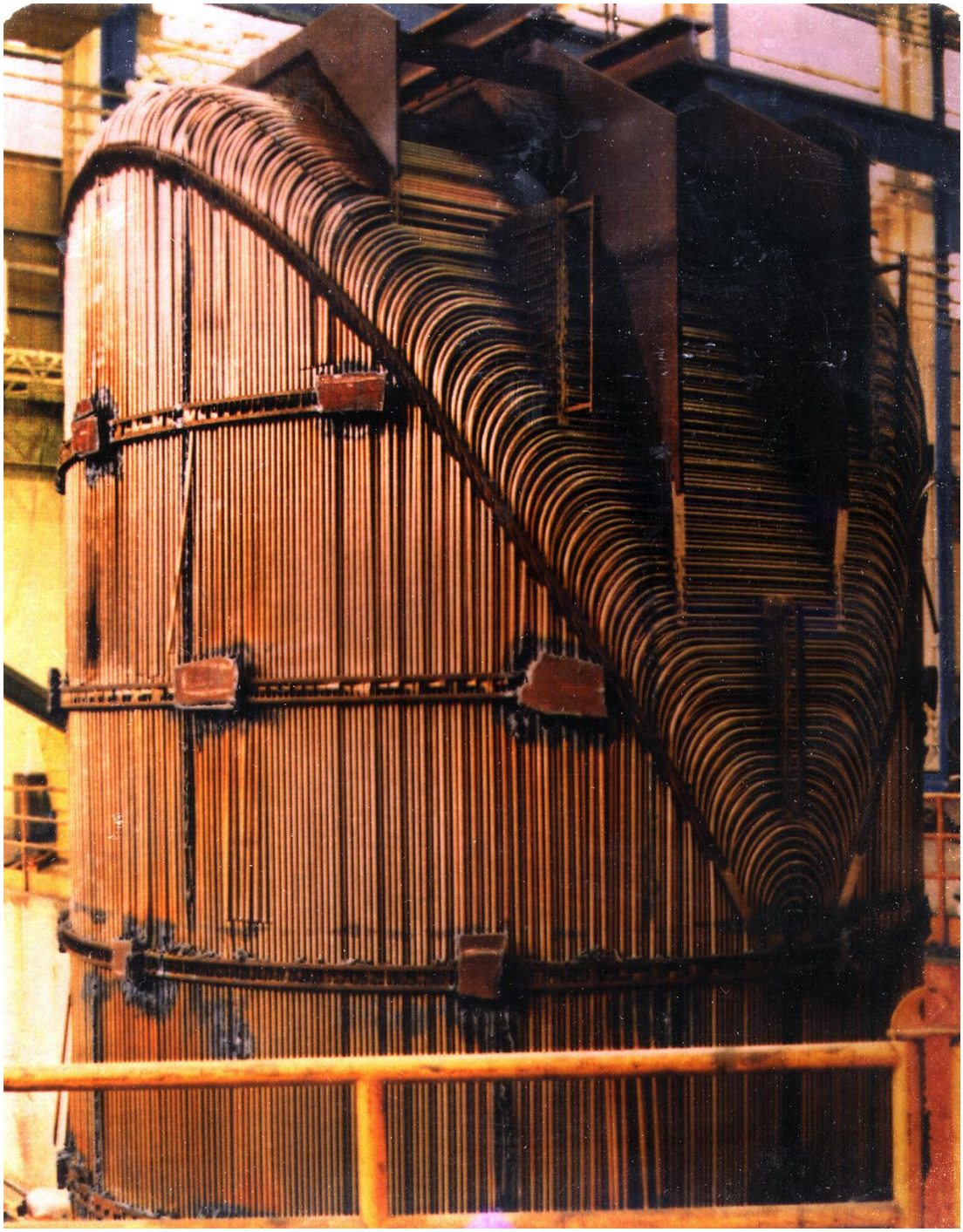

Figure 1.1 - The internal tubing structure of a nuclear steam generator during decommissioning. The steam generator accounts for nearly 75% of total surface area within the core. For scale, the outer diameter of the tube bundle seen here is approximately 3 meters [7]. Image courtesy of the United States Nuclear Regulatory Commission [8].

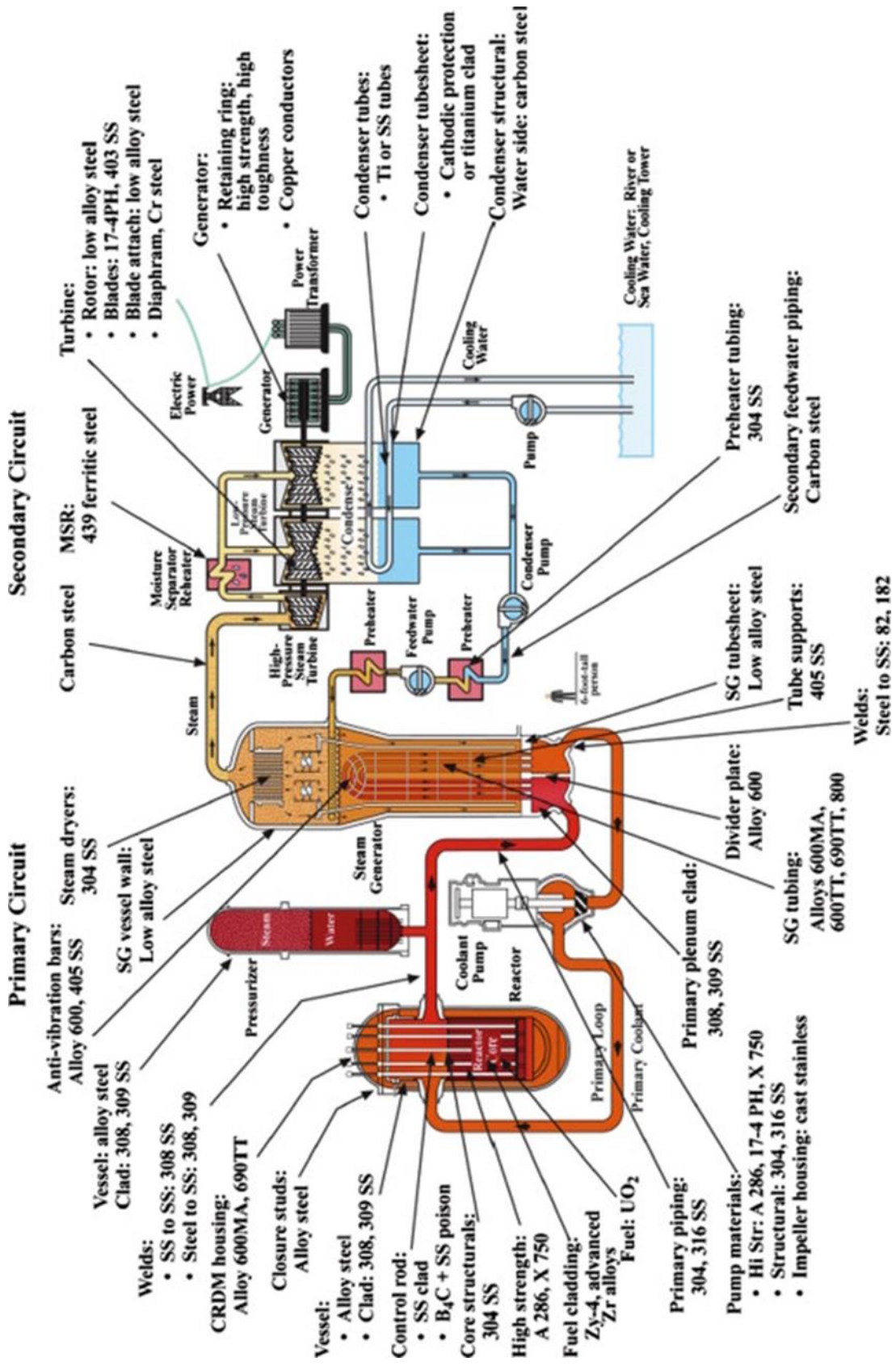

Figure 1.2 - This diagram shows where particular materials are used in a generic PWR power plant. Image taken from [9]

One aspect that is particularly important to the industry in terms of environmental degradation of plant materials is a phenomenon known as CRUD. The corrosion products that have been dissolved by the coolant water (see Figure 1.4), can eventually find themselves deposited at certain locations in the core, in so-called CRUD deposits. CRUD is an umbrella term for any metal oxide deposit, and the word itself is both an acronym, standing for "Chalk River Unidentified Deposit", and a description.

The mechanisms of materials corrosion and the equilibrium solubility of the metal oxides produced associated with CRUD deposition are complex, being heavily dependent on system chemistry and temperature. Empirical inputs to existing models are essential to ensure accuracy of prediction and understanding of second order mechanisms.

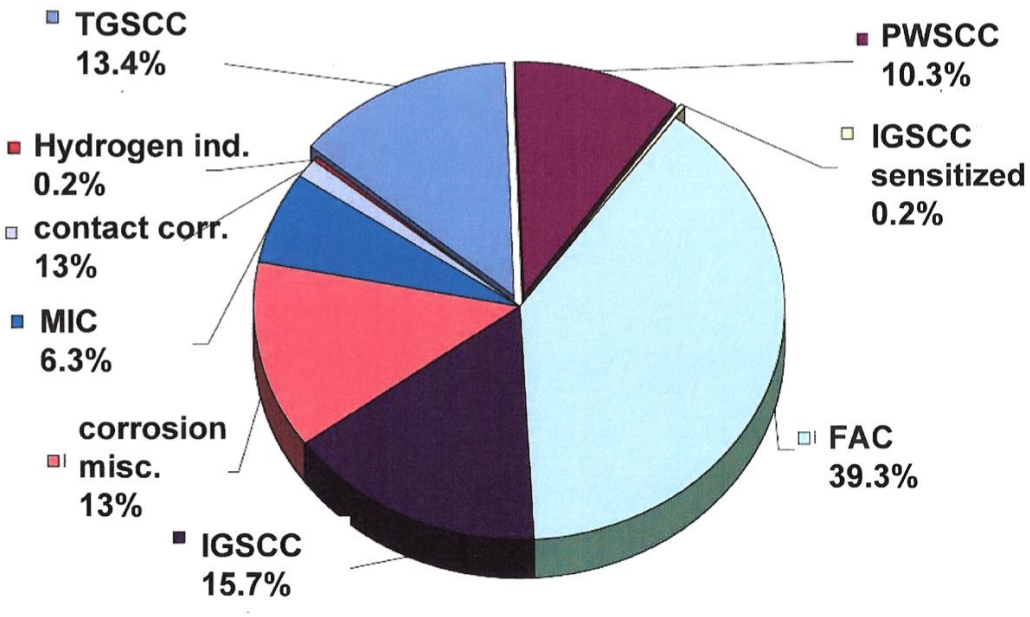

Figure 1.3 - A breakdown of the magnitude of current corrosion issues affecting nuclear power station coolant circuits [10]. The largest single proportion of problems is currently Flow Accelerated Corrosion (FAC), while Stress Corrosion Cracking (SCC) modes (which include Trans-Granular (TGSCC), Inter-Granular (IGSCC) and Primary Water (PWSCC)) account for the largest number of issues between them. General corrosion and contact based corrosion provide 26% between them, with Microbial Induce Corrosion (MIC) causes a small proportion, generally on the condenser side of the coolant system. Finally, hydrogen induced cracking events, which can result in component failure are quite rare.

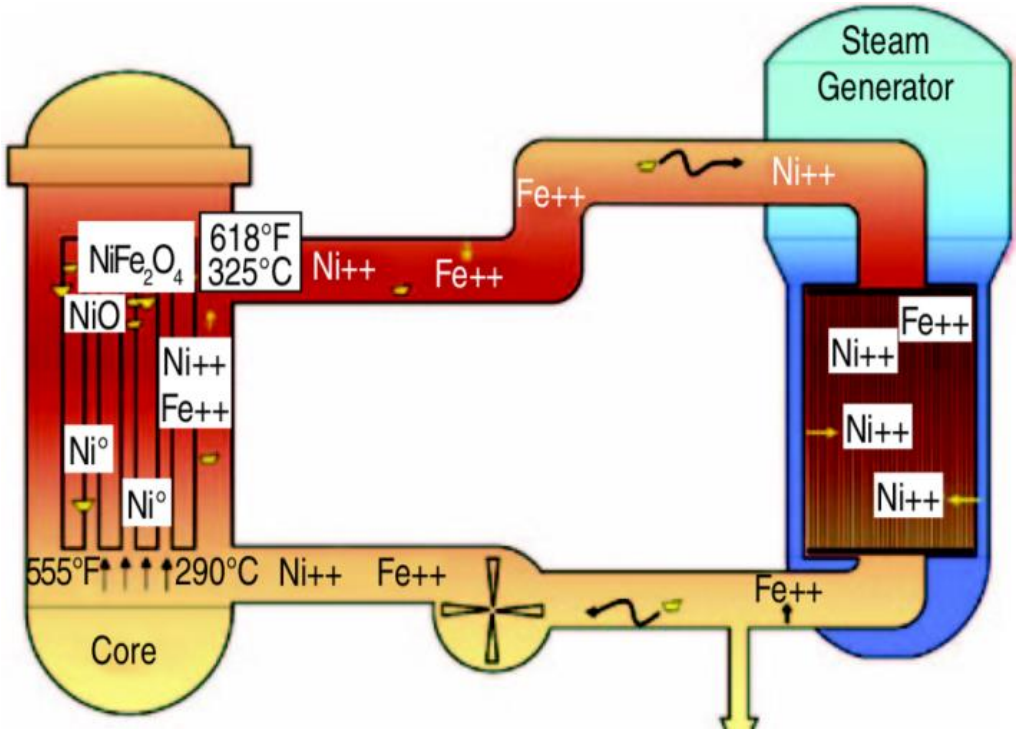

Figure 1.4 - A sketch of the primary coolant circuit. Corrosion is an inevitable consequence of operations in high temperature aqueous conditions, and the ions generated by corrosion are governed by the materials of construction. In the image above, iron and nickel ions are shown being produced and deposited at various locations around the reactor. Image from Deshon *et al.* [5].

1.2 Industrial Problem/Business Case

An ongoing issue seen on many PWR power plants, related to the CRUD phenomena, is that of Flow Induced Deposition (FID) of soluble corrosion products at the mouth of a flow restriction. The term flow restriction covers any type of change of hydraulic geometry. This can be an orifice plate in a flow meter, the broach holes of a tube support plate (see Figure 1.5) or the hydraulic diameter decrease associated with primary coolant entering SG tubing. Such deposition reduces the overall heat transfer efficiency of the plant, disrupts flow uniformity (which can also effect heat transfer efficiency), cause blockages in vital apparatus and subsequent component ruptures, and can provide a porous structure in which aggressively corrosive chemicals and radioactive species (such as cobalt-60, or Co-60) can accumulate. The accumulation of corrosive chemicals (an example is illustrated in Figure 1.6) can lead to accelerated localised corrosion, and ultimately to early component failure,

while the accumulation of active nuclei outside of the bio-shield can lead to increased radiation doses for plant workers.

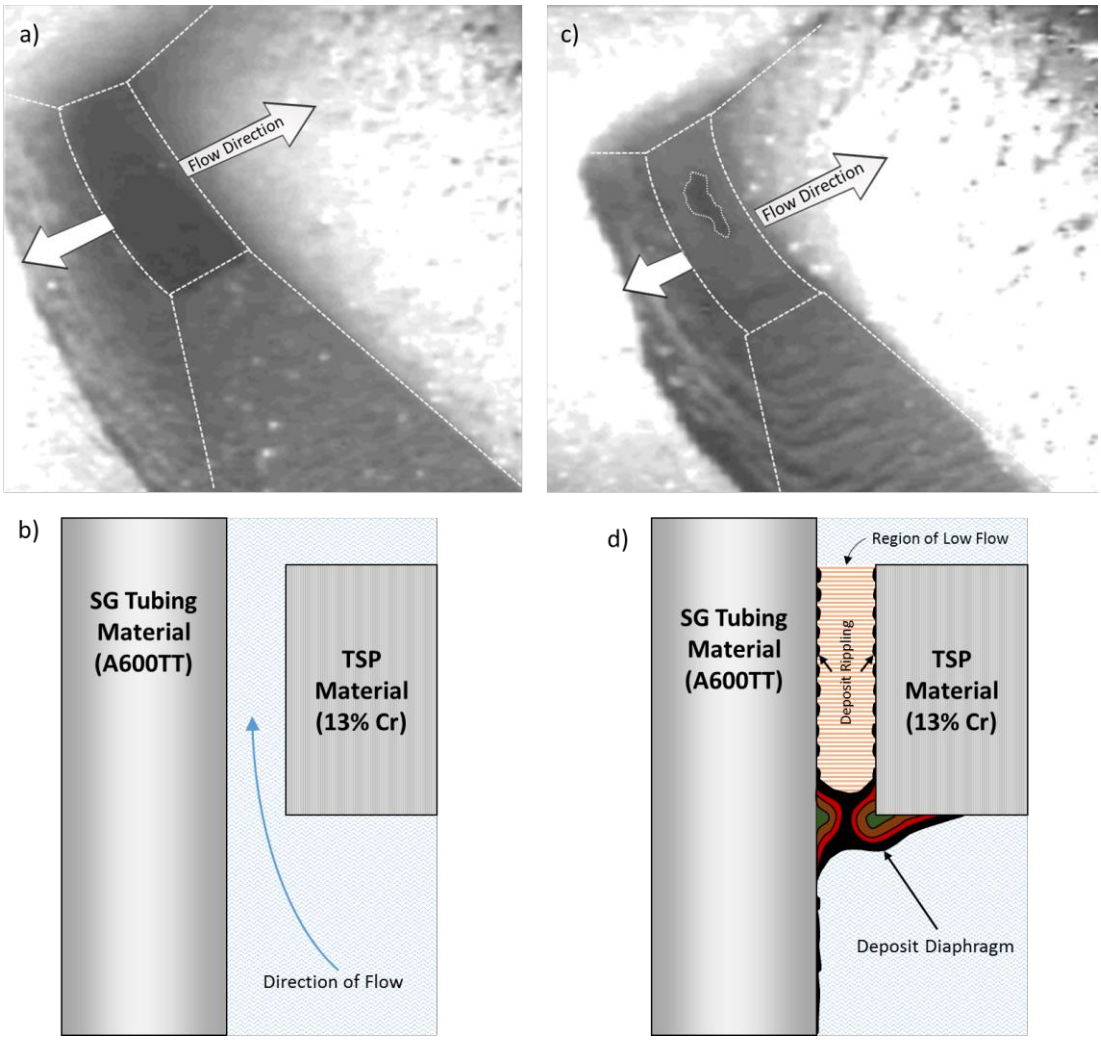

Figure 1.5 – Flow assisted deposition in the broach hole of a tube support plate (TSP) in a steam generator. The width of each broach is approximately 25 mm. Image a) shows the normal operational condition; no deposition and a clear broach hole – image b) shows this schematically. In image c) the entrance to the broach hole has been occluded by deposition with only a small portion remaining unblocked - image d) shows this schematically. Images a) and c) taken from [11] and anotated, images b) and d) are redrawn from those provide by Dr. Pierre Combrade [12].

FID is generally known to occur when reactor coolant chemistry strays outside of its normal specification. However, it has also been seen to occur even when the reactor is operating within its specified limits.

It cannot be overemphasized that it is clearly of importance to determine the controlling mechanism causal to this deposit formation for both safety and efficiency reasons. It should also be noted that it is also valuable to quantify

the fundamental variables at play. Such quantification could be used as inputs into a whole-plant model, which itself could be used to inform upon best practices and operational parameters for next generation nuclear power plants.

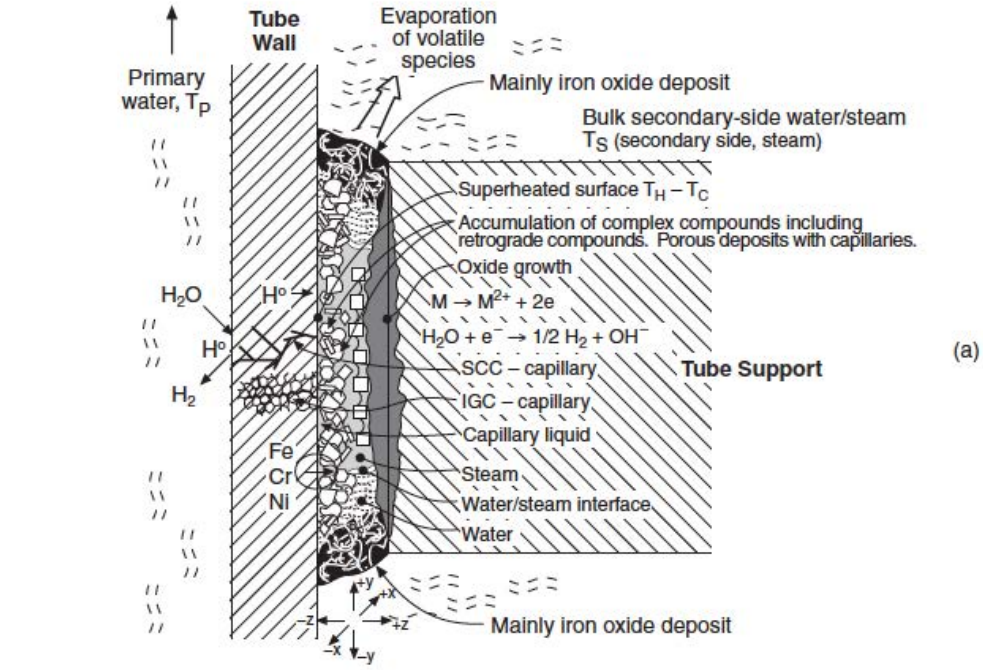

Cl	(Cl^-, HCl)	B, Ti, Zn	(inhibitors)	
SO_x	(retrograde compounds plus $S^{6+} \rightarrow S^{4+} \rightarrow S^{2+} \rightarrow S^0 \rightarrow S^{2-}$)	O_2	(O_2, H_2O, compounds)	
SiO_x	(SiO_2, complex compounds)	H_2	(H_2, H^+, H^0)	
AlO_x	(Al_2O_3, complex compounds)	N_2H_4	(N_2H_4, NH_3, N_2)	(b)
Cu	(Cu^0, Cu^{2+}, CuO)	C	(CO_3^{2-}, organic)	
Pb	(Pb^0, $PbO_x^{\pm y}$)	N	(NO_x, organic)	
Na, Ca, Mg	(complex compounds)	Fe, Cr, Ni	(Fe^{2+}, Cr^{3+}, Ni^{2+}, complex compounds)	
Na_2HPO_4	(retrograde compounds plus H_3PO_4)			

Figure 1.6 - A schematic diagram of a deposit within a heat transfer crevice of a tube support plate (a). Chemical species responsible for the accelerated localised corrosion and cracking of underlying metallic components can accumulate in these locations - such chemicals are listed in (b). Image taken from [7].

1.3 Project Objective

In response to this problem, the University of Birmingham was commissioned by Rolls-Royce Marine Power Operations to build facilities to study CRUD deposition at fluid flow restrictions.

This EngD program's primary objective has been the design and construction of research facilities and associated apparatus to reproduce morphology, and elucidate mechanisms, causal to deposition at restrictions in flow. All

apparatus within the facility was purpose-built to accurately represent the conditions found in a PWR's primary coolant circuit.

To meet this primary objective, a system was designed and built to study CRUD deposition at tube geometries of similar scale to those found on plant, while operating at temperatures, pressures and flow velocities comparable to those of the reactor coolant system.

As the deposition phenomena is a product of several mechanisms (*i.e.*, corrosion and corrosion release rate of primary piping system, and solubility of metal oxide corrosion products), it was seen as prudent to investigate these as secondary objectives. Firstly, the corrosion of wetted materials in the plant provides the source term of metal ions that make up the CRUD deposits. A bespoke system was designed and built to characterise material corrosion rates in simulated PWR primary coolant conditions, with the intention of determining the corrosion kinetics of 316L stainless steel, as well as the fraction of oxidised material released to the coolant depending on the specific chemistry. Secondly, the metal oxides formed by corrosion are sparingly soluble in the coolant. Ions released into the coolant are the source of the CRUD deposits. For this study, a second bespoke system was designed and built which could reach the temperatures and pressures of primary coolant. Samples of a metal oxide of interest could be placed inside the system, and the concentration of metal ions in the outlet water could be measured as a function of specific simulated coolant chemistry.

In summary, the program of work within this EngD project seeks to (1) provide facilities for the measurement of fundamental quantitative data associated with CRUD deposition at flow restrictions, (2) the rate of corrosion and of corrosion release, and (3) the solubility of metal oxides of interest. All of this characterisation could be used as empirical inputs into existing plant computer models to refine accuracy of prediction. Indeed, the ultimate goal of a group

of projects, sponsored by Rolls-Royce and NNL (National Nuclear Laboratories), is to use these empirical inputs to develop a whole-plant model. As a final aspect to this thesis, a preliminary computer model of deposition in a flow restriction has been developed.

2 Literature Review

2.1 General Introduction

The life cycle of a corrosion product in a nuclear reactor coolant system can be split into three distinct sections; the corrosion of a material, the solubility of the corrosion product in the aqueous coolant, and the deposition of the corrosion product within the reactor (assuming it is not removed by the coolant purification system). The rates of corrosion and deposition will be governed by the particular conditions of the hydrothermal system, as will the equilibrium solubility level of the corrosion product.

This review seeks to cover the current state of the knowledge in these areas, with specific interest in the equipment and methods used to study the phenomena. The chemical environment of a PWRs primary coolant circuit is fundamental to this thesis, and a brief explanation of guideline chemistry conditions for the primary coolant can be found in section 2.2.

Deposition at any location throughout the reactor coolant system (RCS) is an undesirable occurrence. Deposition impedes heat transfer at the fuel rods and in the steam generators, disrupts flow uniformity, can incorporate large quantities of activated nuclei into its structure (compared with a usual corrosion film), and has been seen to be the cause of vibrational fatigue of steam generator materials [5,7,13–15]. Each deposit is formed through a different mechanism dependent on the conditions present at a particular locality within the RCS; however the mechanism of interest to this thesis is that of electrokinetically stimulated deposition, a type of flow induced deposition behaviour. This phenomenon has been studied by a very limited number of research groups [16–27]. Section 2.3 seeks to consolidate the information regarding this deposition mechanism.

The corrosion of stainless steels is a well-documented topic at ambient conditions, in salt water environments and in chemical industry uses. However stainless steels have only been given limited attention with regards to their long term use in nuclear power stations [28–31], possibly due to the expense and effort required to perform such testing [32]. It is known that the application of particular surface finishes to reactor surfaces can vastly reduce the amount of corrosion that any given component will undergo. Examples of this are processes such as mechanical polishing, electropolishing, and thermal annealing, which reduce the general corrosion [28,31,33–36]. Reducing the corrosion of a component limits the volume of the metal oxide present on the surface, which also restricts the quantity of radioactive nuclei, most notably Co-60, that can become incorporated into the film oxide film elsewhere in the coolant loop [32]. The incorporation of Co-60 and other active nuclei into the oxide films is a major safety concern, and so utilities seek to reduce it wherever reasonable and economically viable [32,37–39]. Section 2.4 will outline the current knowledge of stainless steel corrosion under PWR primary coolant conditions, as well as the effects of electropolishing on the corrosion rate of the material and the composition of the oxide film.

The solubility of corrosion products in reactor coolant is of fundamental importance to understanding the quantity of soluble material available for deposition on wetted RCS surfaces, and the amount of material available for neutron activation [40–42], as discussed in Section 2.2. Research to determine a metal oxide's solubility as a function of the coolant conditions has been on-going since the invention of the light water reactor (LWR) for power generation [40,42–61]. Even before this, the formation of magnetite was of interest to geologists [62–65] and early LWR chemical control was based on geological findings. While the minima in solubility of several metal oxides have been determined, work is still on-going to improve the available data and to match

thermodynamic models to data. As modelers have discovered, it is often the case that model predictions and published data are not always in agreement [61,66]. Section 2.5 will outline the current state of the literature regarding the measurement of metal oxide solubility in reactor coolant.

2.2 Chemical Environment of PWR Primary Coolant

Pressurised water nuclear reactors maintain a tightly controlled chemical environment in both primary and secondary coolant circuits [14,38,67]. The temperature, pH, ion concentration, dissolved gas concentration, and numerous other parameters are measured constantly in order to ensure that the reactor is operating within an acceptable chemical region. This emphasis on stringent chemical control is due to the danger posed by straying outside specified limits; irreparable damage can quickly be inflicted upon the reactor were the chemistry of the coolant allowed to wander too far beyond the control guidelines.

In a PWR, light water (*i.e.*, H_2O) is used as primary reactor coolant for two central purposes [68]:

1) Moderation of fast neutrons into thermal neutrons, which allows the reactor to maintain criticality.
2) To act as the heat transfer medium, moving energy from the core to the steam generator, where steam is raised and used to drive a conventional steam turbine.

In general, primary side coolant is at a temperature between 275˚C and 325˚C depending on its location within the coolant cycle; the coldest location will be at the inlet to the coolant pump (which is normally situated in the cold leg), and the hottest location will be at the surface of the fuel rods. The temperature difference between coolant at the fuel rod surface and in the cold leg of the RCS

will produce two slightly different chemical environments, differing in pH and corrosion product solubility levels [38,68].

The coolant water is treated with great care before it is put into the RCS. It is first run through numerous ion exchange systems to remove dissolved ions, then thoroughly degassed to remove all traces of dissolved oxygen. The gas content of the system is then corrected using hydrogen gas (which is used to scavenge any residual oxygen during critically, to adjust the electrochemical corrosion potential (ECP), and suppress the formation of oxidising radiolysis products), before being chemically treated with pH modifying chemicals [41].

However, water has several undesirable effects which must be accounted for by modifying the overall chemistry of the system. The most fundamental requirements of the water chemistry can be related to material compatibility and minimisation of the radiation field. The chemistry must meet the following criteria [38]:

- Mitigate or avoid the radiolysis of the aqueous solvent.
- Minimise or avoid the deposition of CRUD on fuel elements.
- Maintain the integrity of the fuel elements, and not compromise material/coolant compatibility.
- Maintain the integrity of all primary coolant system components (*i.e.*, tubing/piping/RPV), by producing a compatible corrosion environment.
- Minimise and control the radiation field at a level that is As Low As Reasonably Practicable (ALARP).

While these fundamental requirements make the use of water seem like a questionable choice, water's ability to act as a solvent, moderator and heat transfer medium compensates for this. Treatment chemicals, such as inorganic bases like lithium hydroxide (used on PWRs) and potassium hydroxide (used on Russian originating Vodo-Vodyanoi Energetichesky Reactor or VVERs) are soluble in water across a wide range of temperatures [38]. Water's polarity falls

with increasing temperature and it becomes capable of acting as a solvent for a very large number of chemicals, even allowing miscible solutions of non-polar organic compounds to become possible, though such chemicals are not used as PWR primary coolant [42].

The concept of the "correct" pH of the RCS can normally be drawn back to the first attempts to measure magnetite's solubility in water by Sweeton and Baes in 1969 and 1970 [14,38,47,48], who presented the solubility equation as:

$$1/3\, Fe_3O_{4\,(s)} + (2-b)H^+ + 1/3\, H_{2\,(g)} \leftrightarrows Fe(OH)_b^{(2-b)+} + (4/3-b)H_2O$$

Equation 2.1

Where 'b' a coeffiecent determined by the number of complexing hydroxide groups associated with the Fe^{2+} solvated ion. The equation involves the reduction of the Fe^{3+} ions in magnetite to Fe^{2+} in solution. The equilibrium implies that the soluble iron is heavily suppressed by the presence of a vast concentration of water; increasing the concentration of H^+ ions or dissolved H_2 will increase the solubility.

It was determined, through both experimental measurement [45,48,52,53,58] and thermodynamic calculation [42,47,53], that magnetite's minimum solubility in water at 300 °C exists at pH_T 6.9, which requires 2.2 ppm of LiOH to be added to the water. Operating at this pH would reduce the total inventory of iron available for deposition on fuel elements, which also has a secondary impact on the integrity of the fuel cladding and minimising the radiation field. However, the contribution of iron to the total radiation field is small compared to that of nickel, which can be transmuted into radioactive Co-60 when exposed to the high neutron flux in the core. Work has been performed to determine the minimum solubility of nickel ferrite under coolant conditions, the findings of which have been that nickel ferrite's minimum solubility exists at pH_T 7.4 [52,54,59,69,70].

The general guidance for LiOH is a maximum of 2.2 ppm. This is to avoid corrosion of Zircaloy, which begins at approximately 5 ppm, and avoids cracking behaviour in nickel base alloys, especially Alloy 600, which is observed to start at ~4.25 ppm LiOH (see Figure 2.1) [14,38].

Boron is known to be an excellent moderator, and so boric acid (enriched with Boron-10) is added to PWR water as chemical shim to control fuel reactivity uniformity, as well as operating temperature. At the beginning of a fuel cycle, reactivity must be suppressed so high concentrations of boric acid are injected. After the fuel has partially burned during the cycle, the boric acid concentration level is reduced to maintain a 100% power output. While boric acid is not used to control the pH (due to its nature as a weak Brønsted–Lowry acid), it does have an effect on the overall system pH, especially at start up where high concentrations are necessary. As this can significantly lower the pH of the system, increased quantities of LiOH are needed to bring the pH back to pH_T ~6.9. During the cycle, the boric acid and LiOH levels are reduced until a LiOH concentration of 2.2 ppm is reached, after which the reduction in boric acid allows the pH_T to rise to ~7.2 - 7.4. Plant operators can use curves such as those produced by the Electric Power Research Institute (EPRI) (see Figure 2.2) to adjust concentrations appropriately [14].

The ideal concentration of Li for use in PWR primary coolant has not been precisely defined and there are numerous programs ongoing to study the effects of increased Li concentrations (to pursue reduced radiation fields), despite the known issues of Zircaloy corrosion and nickel base alloy cracking. However, there appears to be a worldwide upward trend in Li concentrations, the effects of such programs will be seen in the near future [14,38]. This is perhaps a result of an increase in the number of plants using 'high-duty' fuel cycles, which require increased boric acid concentrations to maintain reactivity

uniformity and thus higher Li concentrations to maintain the pH_T between 6.9 – 7.4 [71].

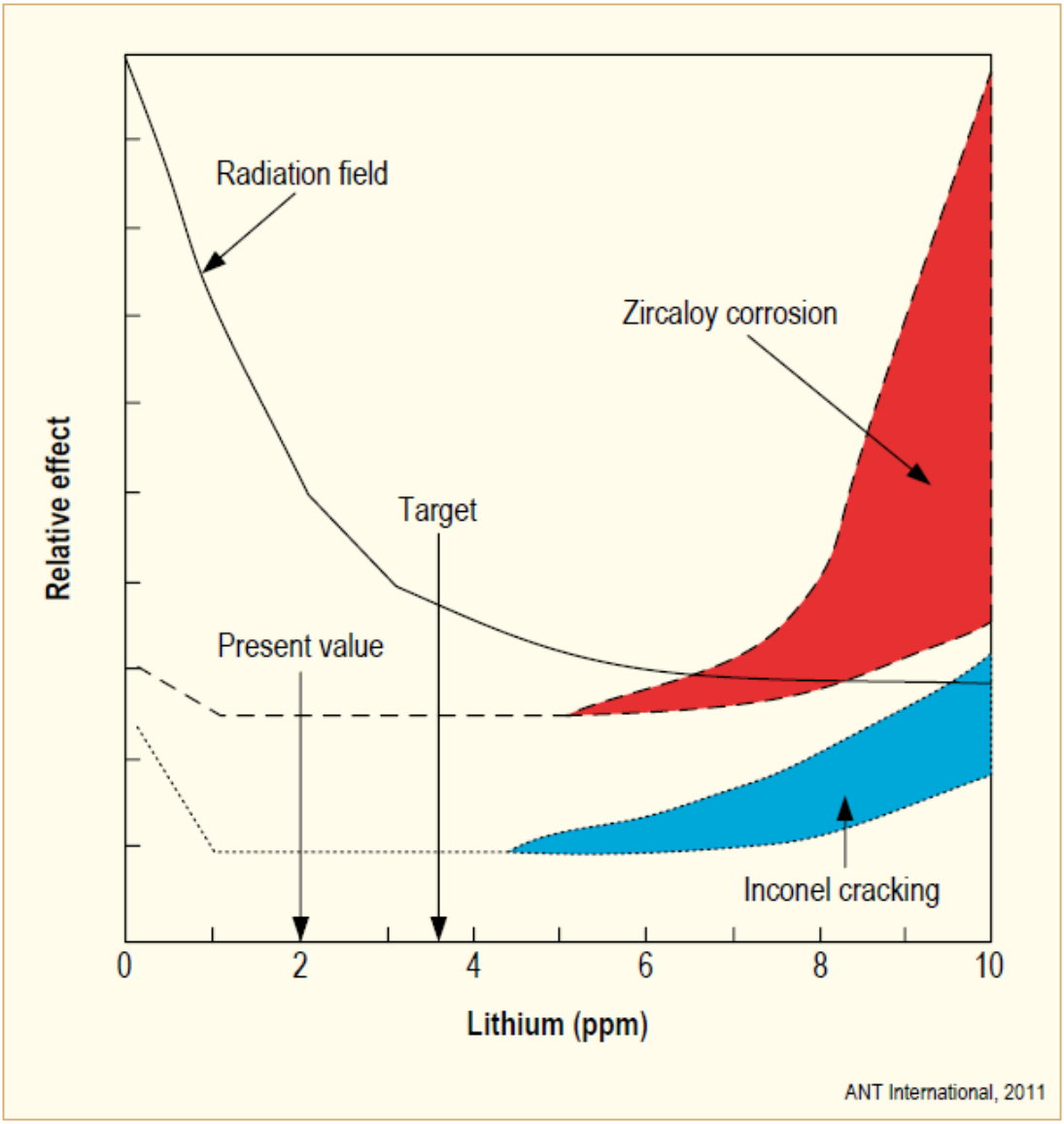

Figure 2.1 - Curves for the onset of Zircaloy corrosion and Inconel (nickel base alloy) cracking. The vertical axis represents a qualitative effect of a particular phenomenon and does not provide any quantitative information. The arrows denoting 'Present' and 'Target' indicate the points where the guidelines for LiOH concentration are at present, and the optimisation target for the radiation field, where nickel base alloy cracking and Zircaloy corrosion have not been accelerated. It should be noted that the increase in Li concentration is directly related to the decrease in radiation field. Image taken from Advance Nuclear Technologies (ANT) International, LCC8 – Special Topic Report [38]

High-duty plants are those in which power output has been uprated by allowing the increase of fuel burn-up rate; this increases the total energy output of each rod and due to the temperature increase the upper section of the rod may experience subcooled nucleate boiling. Subcooled nucleate boiling occurs

when the local temperature exceeds to the saturation temperature of the coolant fluid, allowing it form vapor bubbles at nucleation sites. These bubbles grow to a critical size at which point they are detached and carried into the subcooled bulk fluid, where they condense and transfer heat to the fluid [72].

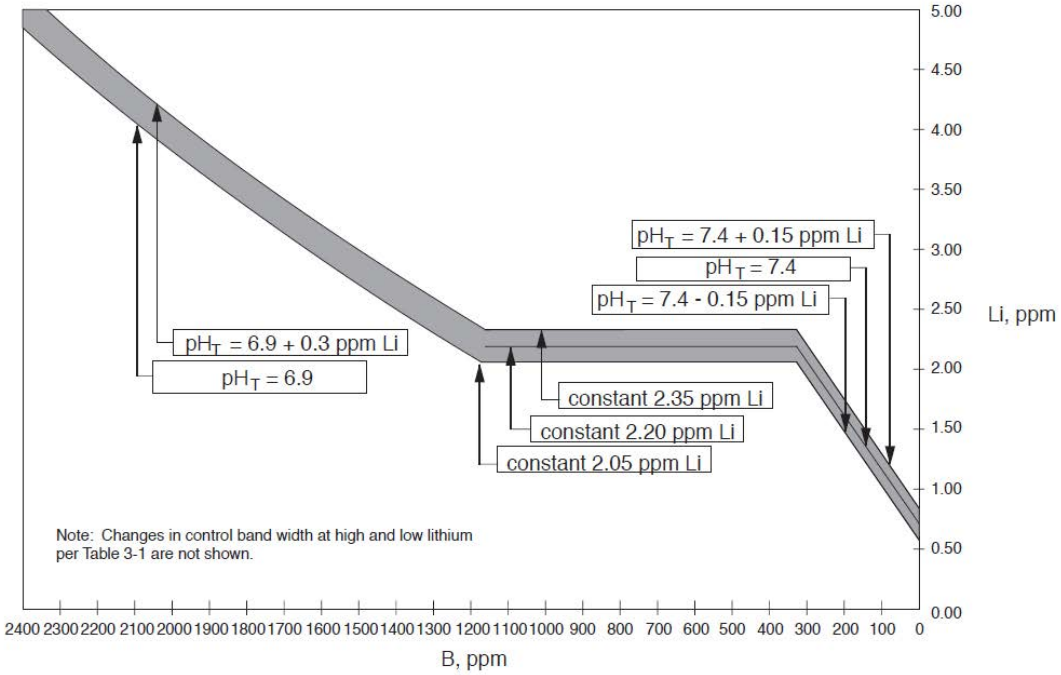

Figure 2.2 - A curve for the pH of the system at a temperature of 300 °C, dependant on the concentrations of Li and B. Image taken from [14].

This boiling is advantageous, improving heat transfer efficiency, but also introduces difficulties associated with fuel cladding deposition and axial offset anomaly (AOA) [5,15,73]. AOA is a phenomena brought about by deposits formed on fuel rods due to boiling. These deposits can contain quantities of boron (derived from the boric acid added to control reactivity) that will decrease the local fission rate and thus decrease the power output of the fuel [74]. The decision to uprate a plant is driven by economic considerations, but regulators and vendors will also have a large part to play [75].

Hydrogen gas is added to coolant as a means to maintain the system in a reducing environment. Small additions of hydrogen, less than 15 cc.kg^{-1}, have been calculated to scavenge residual oxygen left over from the preparation of coolant when the plant is critical, and to also suppress the products of

radiolysis reactions which are oxidising species. These include the highly oxidising radicals $OH^{\cdot}$, $H^{\cdot}$, and HO_2, and the hydrogen peroxide molecule H_2O_2 [14,76].

Initial guidelines recommend the use of 25-50 $cc.kg^{-1}$ [77], however evidence was published that some mill-annealed alloy 600 was susceptible to stress corrosion cracking initiation in high temperature water [14]. In the late 1980's and early 1990's, guidelines were tightened to a recommended concentration band of 25-35 $cc.kg^{-1}$ after several tests showed an inverse proportionality between hydrogen concentration and time-to-cracking in nickel base alloys [78–80]. More recently, extensive statistical analysis of the cracking phenomena was performed, which concluded that there was no significant effect of dissolved hydrogen in the range of 25-50 $cc.kg^{-1}$ on the primary water stress corrosion cracking (PWSCC) initiation times of alloy 600 and this is now the range used in the operational guidelines [81–84].

The suppression of oxidising agents is directly linked to the systems ECP. The ECP of the system is measured as the potential different between a component in the RCS and a reference electrode, the result of which is compared to the normal hydrogen electrode (NHE). Negative values of ECP (wrt the NHE) indicate a reducing environment, which is the type of environment that is requried for operatioin of the primary coolant circuit; movement of the potential in a positive direction indicates that the enviroment is becoming increasly oxidising and action to correct these conditions should be taken. The ECP is very sensitive to small quantities of oxygen or oxidising agents and research has been performed to determine the efficacy of online monitoring in PWR primary circuits [85–88].

Currently, guidelines recommend the use of 25-50 $cc.kg^{-1}$ [14], however there are ongoing programs in the USA studying the benefits of high dissolved

hydrogen concentrations, and in Japan to study the effects of low dissolved hydrogen concentrations [38].

There are other newer chemistry systems being used, the most common of these is the addition of depleted zinc to nuclear power plants; it has been found to mitigate stress corrosion cracking, and to reduce radiation field build up, however this particular chemistry regime is beyond the scope of this thesis.

In summary, the chemistry conditions of a PWRs primary coolant circuit is a aqueous solution of at least Li, B and H_2, which is carefully maintained within a very tight band during the course of a fuel cycle. Programs exist to study the effects of changing these variables outside of their current guideline limits.

2.3 **Corrosion Related Deposition**

Deposition of corrosion products in the RCS is a phenomenon of interest to the nuclear industry as, in the short term, deposition can greatly impact upon heat transfer efficiency, which in turn limits the profitability of a given power plant. In the medium and long term there are several other undesirable effects induced by the formation of a deposit, including flow uniformity loss, incorporation of radioactive species (most notably Co-60), and concentration of aggressively corrosive chemicals close to construction material walls (see Figure 1.6).

Between 2004 and 2006, units 1 and 4 of EDF's Cruas nuclear power plant (NPP) experienced primary to secondary coolant leaks, leading to shut down of these units on three separate occasions [18]. The reason for these shutdowns was attributed to the deposition of material within the tube support plate (TSP) broach holes which caused an increase in flow velocity through the broach hole, leading to flow-induced vibration (FIV) and eventually to fatigue cracking of the tube.

Of particular interest to this project is the type of deposition seen on the units of the Cruas plant, where deposition is seen to occur at restrictions in the flow path (see Figure 1.5). Depositions that occur in these locations are hypothesized to be the result of a charge imbalance at the electrical double layer (EDL) – the interfacial layer between the surface of the solid material and the bulk fluid. This type of deposition has been under research since it was first put forward as a possible mechanism by Robertson in 1986 [89], which explained later in section 2.3.6.

2.3.1 Locations

2.3.1.1 Fuel Cladding

The fuel cladding is often found to be coated with a CRUD deposit when fuel assemblies are extracted from the core. The appearance of these deposits depends on the duty of the plant in which they are found. As previously mentioned in section 2.2, there is a general trend for uprating of PWR power plants. The uprating results in improved power output but can also result in deposition of material on the fuel rods due to sub-nucleate boiling [75].

2.3.1.2 Instrumentation

Due to the importance of the coolant to the longevity and safe operation of the reactor, there is a vast array of instrumentation and ancillary monitoring equipment associated with the core. Of particular note to this project is deposition in orifice type flow meters.

These flow meters are simply a plate into which a precisely sized hole has been drilled. The differential pressure (dP) between the two sides of the plate is measured and, using Benoulli's equation, the flow rate of the water can be calculated. Deviation in the differential pressure is proportional to the flow rate, but as the calculation requires precise knowledge of the orifice geometry, any deviation in the diameter can cause spurious flow rate measurement. Deposition within the restriction reduces the hydrodynamic diameter and increases the velocity and turbulence within the restriction.

2.3.1.3 Steam Generators

The steam generator of a PWR is a chemically complex system on both primary and secondary sides. Deposition in the secondary side has been observed on several different occasions, and attributed to steam formation. While this may be the case further toward the top of the steam generator, lower down the

secondary coolant is still at low enough temperature that the pressure keeps it from boiling, so deposition in these locations cannot be explained by an evaporation-deposition mechanism alone.

A wide range of steam generator designs exist, however only the design used for French PWR's has been given any particular attention in literature – this design uses a quatrefoil broach hole TSP design (see Figure 2.3).

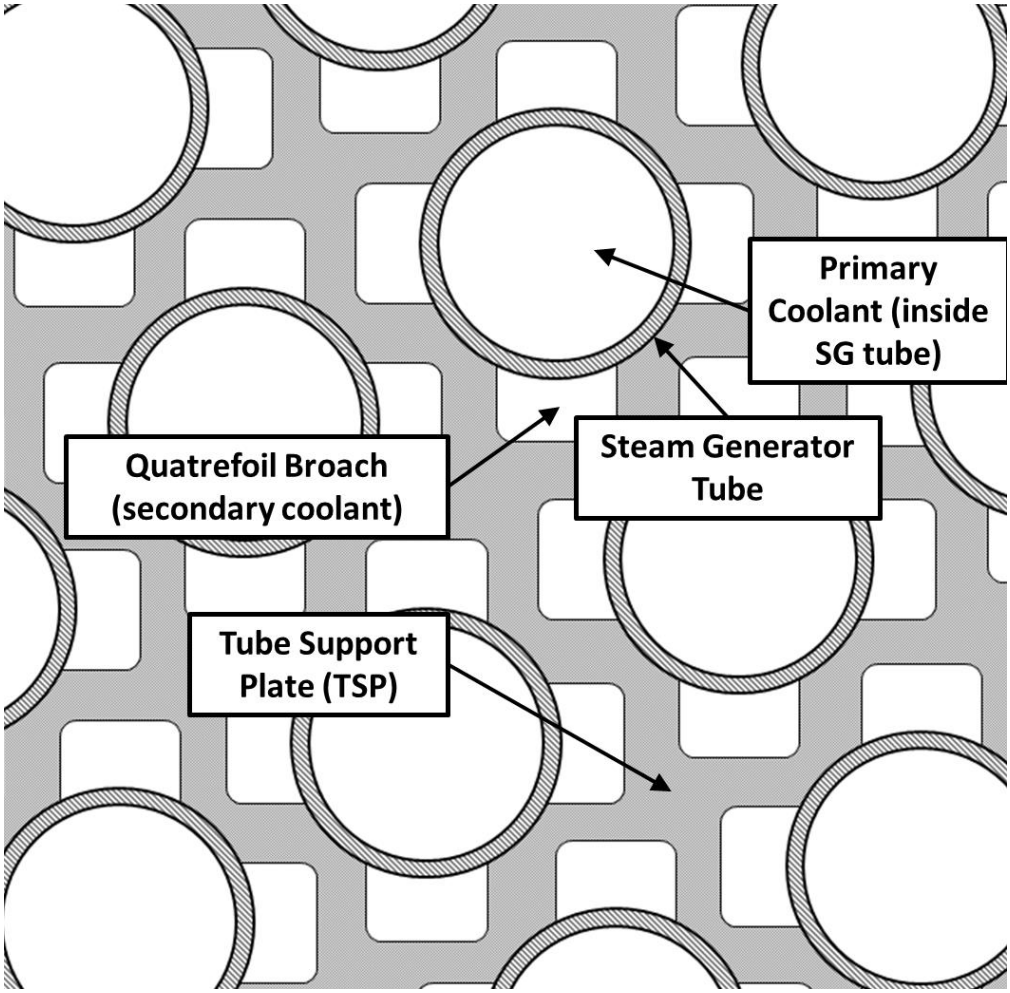

Figure 2.3 - A schematic diagram of a steam generator TSP with quatrefoil broach holes allowing the flow through of secondary coolant. Image by the author.

Other designs include the "egg crate" type, where tubes are held in place by plates of metal crossing in diagonal paths, and drilled plate type TSPs, where the broach holes are simply holes drilled to have a large diameter than the SG tube. No reports of deposition specifically related to these designs have been reported in the literature.

2.3.2 Consequences of Deposition

2.3.2.1 Offset Anomaly/CRUD Induced Power Shift

Axial offset anomaly (AOA), or CRUD induced power shift (CIPS), is a phenomenon that occurs due to evaporation-deposition of material on the fuel cladding. As the deposits can incorporate boron (derived from the boric acid added to the primary water as a neutron poison) into the structure, the neutron flux of the fuel, and thus the output of the fuel rod in the locality of the deposit, is suppressed. This leads to a reduced power output from the plant overall unless something is done to mitigate the power loss [32].

As AOA/CIPS is a result of a boiling deposition mechanism, it does not have a direct bearing on the flow enhanced deposition of material and will not be further discussed.

2.3.2.2 Acceleration of Localised Corrosion

Deposits have been shown to accelerate localised corrosion and are often found to be present at the site of a component failure. This is due to the deposit concentrating aggressively corrosive species in very close proximity to the wall of a pipe or pressure vessel; the pH modifying chemicals used as water treatment (such as lithium hydroxide, boric acid or ammonia and hydrazine which are used in some PWR secondary coolant systems) do not pose a risk to construction materials when used in low concentrations, however in high concentrations and high temperatures they are capable of corroding many alloys used in plant [90]. A plant must be regularly inspected to ensure that this type of corrosion does not compromise the system's pressure integrity.

2.3.2.3 Out-of-Core Radiation Fields

Deposits are capable of incorporating many different materials into their structure, one of great concern to operators is the incorporation of Co-60, a

radioactive nuclei with a half-life of 5.271 years, which emits a pair of high energy gamma rays (1.17 and 1.33 MeV) [91]. Co-60 is a major contributor to plant worker radiation dose as it is able to incorporate itself into practically any deposit and oxide layer in the core. Due to the small volume of oxide layers, Co-60 incorporation is generally considered to be low enough to satisfy the ALARP principle; deposits, however, are of significantly greater volume and incorporation of Co-60 can be orders of magnitude greater, exposing workers to much larger doses.

Monitoring of personal exposure helps to prevent any single worker from receiving an excessive dose, however some parts of the core must be attended manually, and so preventing the build-up of Co-60 containing deposits outside of the core is of great importance.

2.3.3 **Deposited Material**

Material deposited around the primary circuit is a combination of corroded materials which have crystallised at a location in the reactor due to a change in a parameter related to their solubility. This parameter is often temperature – the coolant's ability to hold material in solution changes significantly as a function of temperature (discussed in section 2.5) and as a nuclear reactor generates electrical energy by creating a temperature gradient, a change in material solubility is inevitable. Other mechanisms behind deposition are colloidal crystallisation, where particulate matter agglomerates into large particles which eventually adhere to the wall or sediment out to form sludge [23,92], and "flow enhanced deposition", which is believed to be a result of charge imbalance in the electrical double layer and occurs at sudden changes in the flow geometry [18,19,21,22,89,93].

Regardless of the mechanism, the deposits tend to contain the same elements, derived from the corrosion of construction materials, the most common being

iron and nickel, which form deposits of magnetite (Fe_3O_4) and non-stoichiometric nickel ferrite ($(Ni_nFe_{1-n})Fe_2O_4$) [18,19].

Due to the sheer volume of a deposit (ranging from a few hundred microns to several centimeters in the case of sludge), they are able to incorporate large quantities of radioactive nuclei (*i.e.*, Co-60) making their presence in operator-accessible areas of the reactor a special cause for concern. Fortunately, large sludge deposits generally occur in the RPV, which is heavily bio-shielded, and in the secondary side of the steam generator. The deposits that do occur in operator-accessible areas generally appear as tube-scale deposits [94].

2.3.4 Electrokinetically Stimulated Deposition in Nuclear Reactors

Of greatest interest to this project are the deposits formed at the entrance to a flow restriction under conditions of hot shut down, a condition where the fission reaction is halted by insertion of control rods, but the temperature of the system is held at a reasonably high level by decay heat of the fuel and the heat input of the primary coolant pumps. These deposits are widely attributed to the electrokinetically stimulated deposition mechanism, however this can be more generally described as being of a flow induced deposition mechanism. This type of deposit occurrence has been observed on plant, and an extensive research program is being conducted by the French vendor, AREVA [18]. While the deposits appear to be forming mainly in the secondary side of the plant in question, it is entirely possible that similar deposits are appearing within the primary side and work under primary coolant simulating conditions has shown such eventualities to be possible [19,26,27].

These deposits appear at the entrance and along the length of a flow path, as a series of very small ridges; a photograph of a clear TSP broach can be seen in Figure 1.5 a) and the deposit formed in the same broach can be seen in Figure

1.5 c). In the photographs, the flow would be entering at the far end of the channel and exiting at the broach at the top. The entrance to the broach is almost blocked by the deposited material, while the insides of the broach and the tube have received a covering of ridge deposits. The deposit will reduce flow through this section of tube just based on the entrance blockage, but even without the blockage, the deposits ridge structure acts as a series of small diaphragms which significantly increases the differential pressure across this particular broach [18]. The result is that this deposit has the potential to render this particular channel useless in terms of heat transfer efficiency. Figure 1.5 d) presents a sketch of the blockage and the rippled deposit along the annulus of the broach from a cross section perspective.

2.3.5 General Interfacial Electrochemistry

The mechanism of interest to this project is the proposed electrokinetically simulated deposition mechanism. In this mechanism, an imbalance in the electrical continuity at the wall caused by a disturbance in the fluid flow must be balanced by drawing an electrical current from the wall. In order to satisfy charge neutrality, an anodic reaction occurs resulting in the deposition of magnetite through the oxidation of dissolved Fe^{2+} ions (see Equation 2.1). As this reaction creates an anode for the deposition, a cathodic reaction takes place at another location to provide electrical neutrality. The reaction can be the reverse of Equation 2.1, or another reaction such as the formation of H_2 from H^+ ions, or that of disolved oxygen and water to from hydroxide ions [89]. To correctly describe such a phenomenon, which is described in further detail in section 2.3.6, an understanding of interfacial electrochemistry is required.

2.3.5.1 The Electrical Double Layer

The EDL is an interfacial region formed in a fluid which is in contact with a solid. The layer forms as a means to reach charge neutrality between the

material and the fluid, as the solid is normally charged at the surface. In order to balance the charge of the wall with an equal and opposite charge in the fluid, a layer of charged ions forms [95–97].

Several models for the structure of the double layer have been put forward, each building on the previous model's shortcomings. The first model, suggested by Helmholtz in 1879 [98], simply consisted of a rigid double layer structure where the electrode's charge is countered by equal and opposite charges adsorbed directly upon the electrode wall (see Figure 2.4).

Such a structure is clearly analogous to a parallel plate capacitor, and the capacitance of the layer can be described by:

$$\frac{\partial \sigma}{\partial V} = C_{d,H} = \frac{\varepsilon_r \varepsilon_0}{x_H}$$

Equation 2.2

Where $\boldsymbol{\varepsilon_r}$ is the relative permittivity, $\boldsymbol{\varepsilon_0}$ is the permittivity of free space, and $\boldsymbol{x_H}$ is the spacing between the "plates". The differential capacitance is the derivative of stored charge density, $\boldsymbol{\sigma}$, and $\boldsymbol{V}$ is the voltage drop across the "plates", [96,97,99].

As shown by c) in Figure 2.4, the Helmholtz model predicts that the differential capacitance is constant with varied potential. The validity of each of the preceding models can be judged on its ability to correctly describe the differential capacitance, as well as predict the point of zero charge (PZC), denoted $\boldsymbol{E_z}$. As can be seen from the predicted differential capacitance in Figure 2.4, and the measured differential capacitances in Figure 2.5, the Helmholtz model is a over simplification of reality.

Helmholtz Model

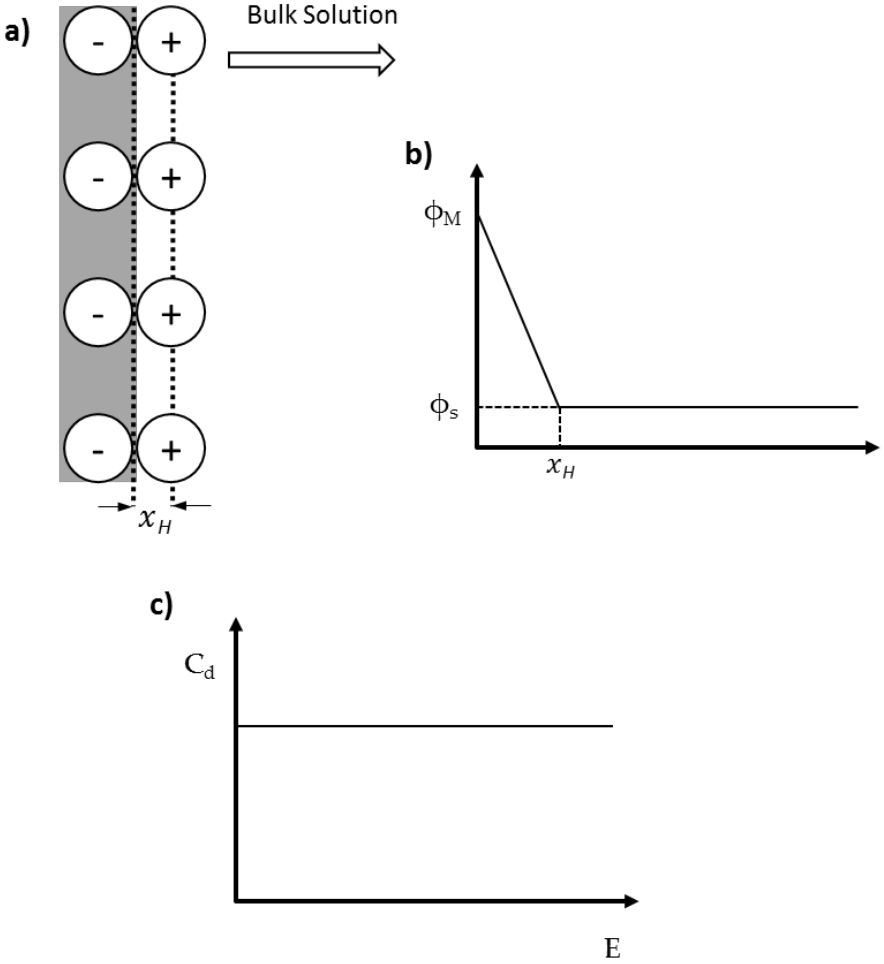

Figure 2.4 - The Helmholtz model of the electrical double layer. The electrode (carrying a negative charge) is balanced by the adsorbed ionic charges. The electrostatic potential drop across this layer is linear, reaching the same value as that of the bulk solution at distance x_H from the electrode wall. Image adapted from [99] and [97].

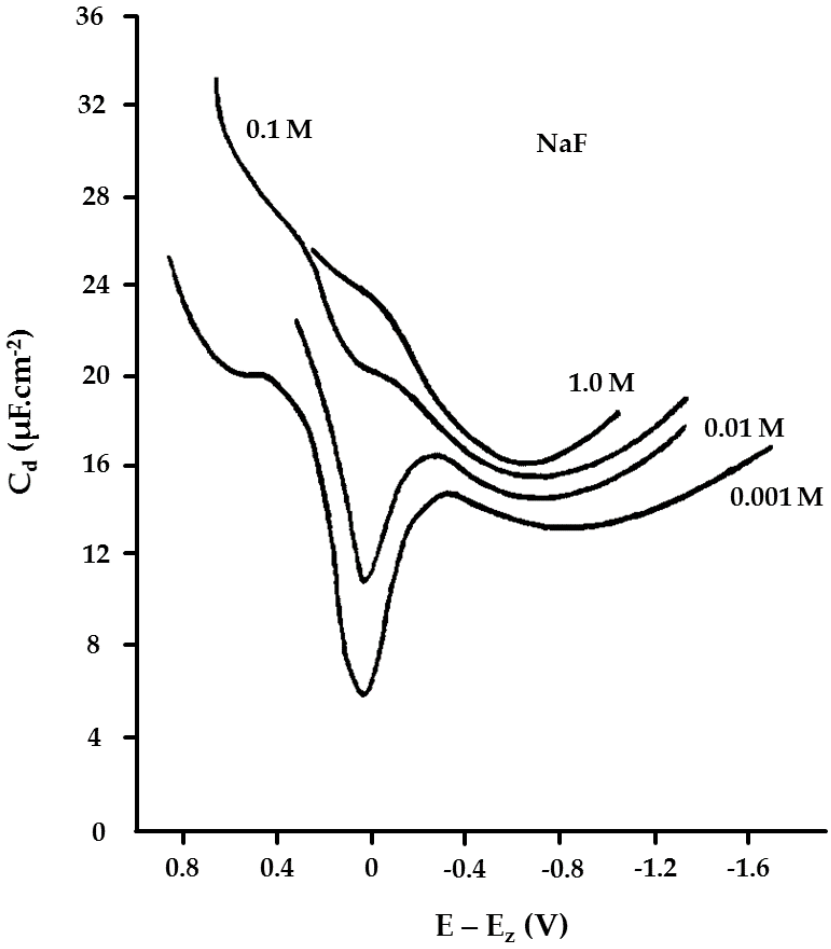

Figure 2.5 - Variation in differential capacitance with potential of sodium fluoride solutions in contact with mercury at 25 °C, as described by Grahame. The behaviour of real systems is clearly not simple to describe. Image taken from [100].

Further to the incorrect predictions of differential capacitance, the Helmholtz model does not take into account the any effects of bulk electrolyte concentration, nor does it account of any interactions that occur beyond the first layer of absorbed ions [97].

In order to overcome these deficiencies, a model was suggested independently by both Gouy and Chapman [101] which took into account the ability of dissolved ions to move freely through solution, as well as the tendency to accumulate in close proximity to an opposite charge. Their model consisted entirely of a diffuse layer (see Figure 2.6, image a), where the concentration of ions was highest close to the metal surface and gradually diminishing with

distance from wall, until the concentration was equal to that of the bulk solution [101].

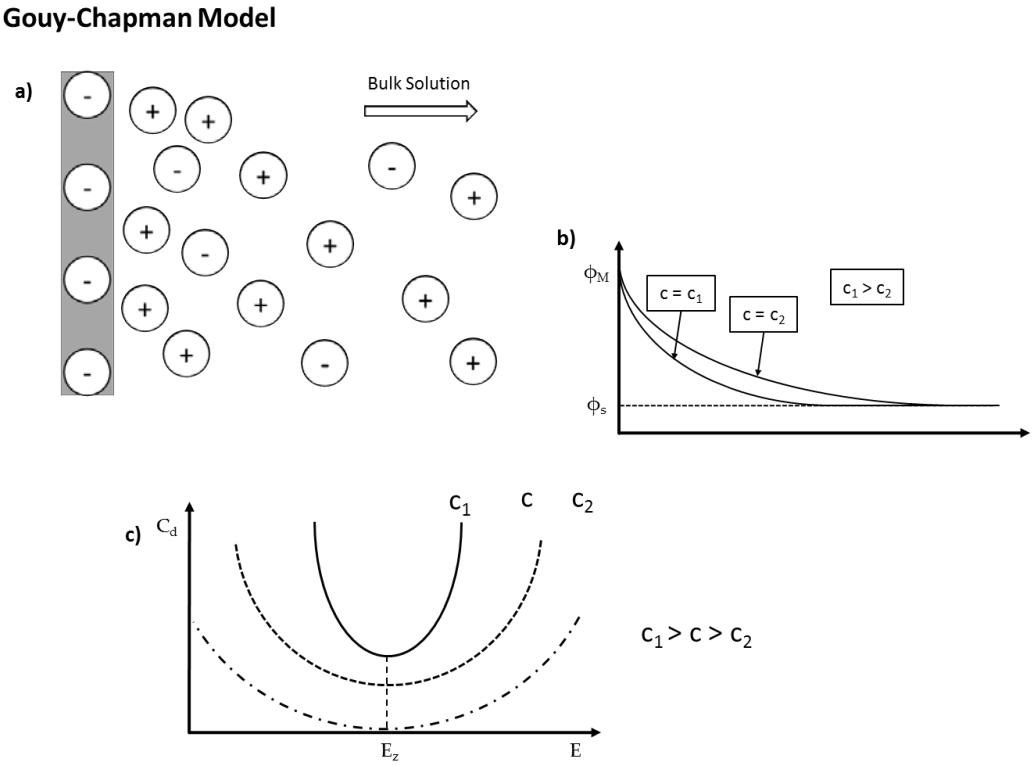

Figure 2.6 - The Gouy-Chapman model of the electrical double layer. This model uses a purely diffuse layer to balance the surface and solution charges, and can better describe the interaction of the surface with solution further from the wall than a single layer, and also takes into account the bulk electrolyte concentration, as seen in b), the sketched plot of electrostatic potential vs distance from wall. Image adapted from [99], [97] and [96].

The models prediction of differential capacitance is an improvement over that of the Helmholtz model, the U-shaped curves close to the PZC are reminiscent of the curves shown in Figure 2.5, however this similarity only exists for low concentration electrolytes within the PZC region [96,97].

A further model was suggest by Stern in 1924, which combined both the Helmholtz and the Gouy-Chapman model into a single structure. A sketch of the Stern Model can be seen in Figure 2.7. As in the Helmholtz model, a portion of the electrostatic potential drop is linear across the region of adsorbed ions; once past this layer, the potential falls as a smooth curve across the diffuse layer, eventually falling to the same value as the bulk solution potential.

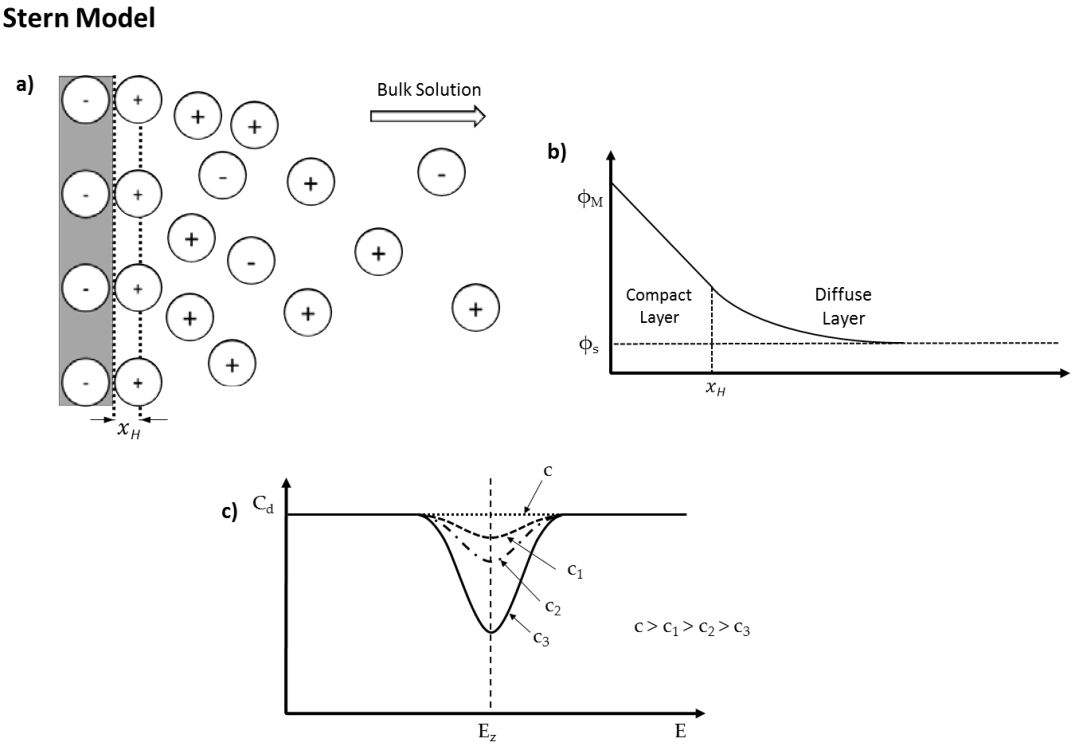

Figure 2.7 - The Stern model of the electrical double layer, combining the Helmholtz and Gouy-Chapman models. Image adapted from [99], [97] and [96].

Stern's modification to the Gouy-Chapman model resulted in a different predicted C_d, seen in c) of Figure 2.7. The layers can be treated as a pair of capacitors, C_H for the Helmholtz compact layer and C_{GC} for the Gouy-Chapman diffuse layer, which are connected in series. The differential capacitance is the sum of the reciprocals of the capacitances of these two layers:

$$\frac{1}{C_d} = \frac{1}{C_H} + \frac{1}{C_{GC}}$$

Equation 2.3

As a consequence of the reciprocal function, the smaller of the two component capacitances is responsible for the majority of the differential capacitance. This combination creates the profile shown in c) of Figure 2.7, which shows the U-shaped drop near the PZC, while outside of this region the capacitance is independent of potential. The profile accounts for the general features of low concentration solutions, seen in Figure 2.4

While Stern had corrected previous models to account for adsorbed ions, it was Grahame [100] who is credited with adding the concept of specifically absorbed ions to the double layer model and for developing a model with three distinct regions. Specifically adsorbed ions are those which have lost their hydration sheath (the water molecules which have attached themselves to the ion due to dipolar attraction) and advanced into direct contact with the metal wall. Specifically adsorbed ions can have the same or opposite charge as the electrode and are bonded strongly to the surface.

The three regions described by Grahame can be seen in Figure 2.8. These are the inner Helmholtz plane (IHP), which is the plane passing through the centre of the specifically adsorbed ions, the outer Helmholtz plane (OHP), which passes through the centre of the solvated, non-specifically adsorbed ions, and finally the diffuse layer which is bounded by the OHP and the bulk solution.

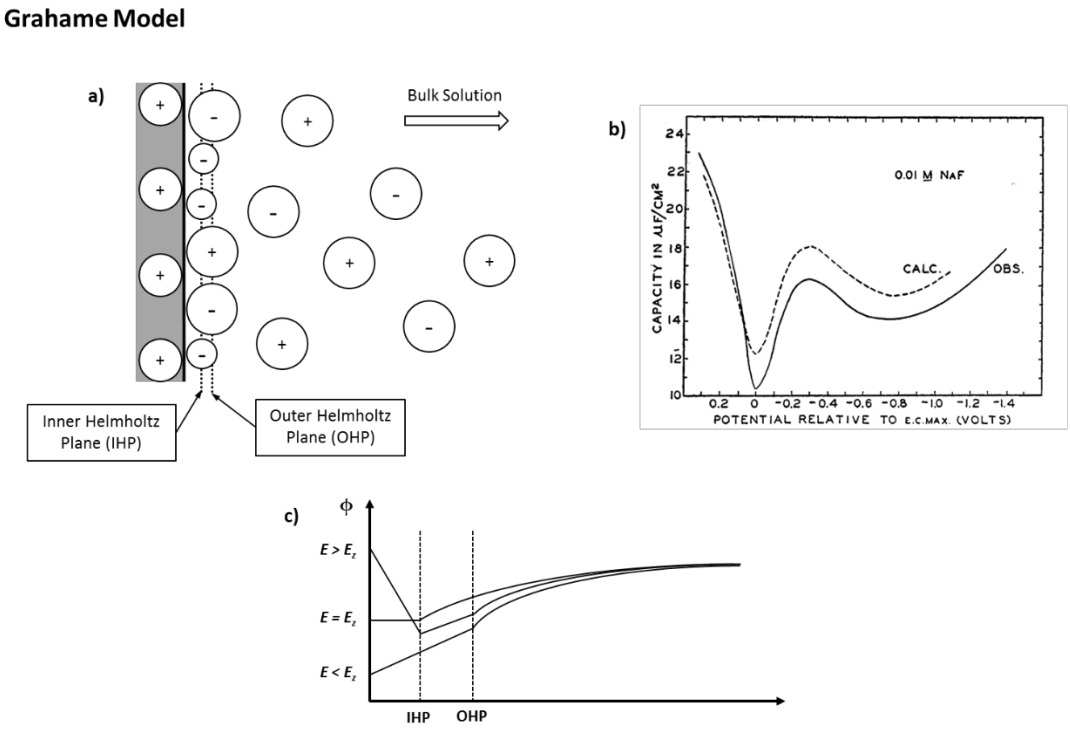

Figure 2.8 - The Grahame model of the electrical double layer. The graph shown in b) shows the capacitance of a low concentration NaF solution in contact with a liquid mercury electrode alongside the calculated value [100]. **Image adapted from** [97].

Grahame's prediction of differential capacitance, shown in b) of Figure 2.8, fits remarkably well with actual observed capacitances at a liquid mercury electrode in contact with a low concentration solution of sodium fluoride.

The most recent version of the double layer is that put forward by Bockris, Davanthan and Müller (see Figure 2.9) [95,97]. The model is qualitatively the same as the Grahame model, the calculated differential capacitance of which is the same as that calculated for the Grahame model (see Figure 2.9 (b)) [97].

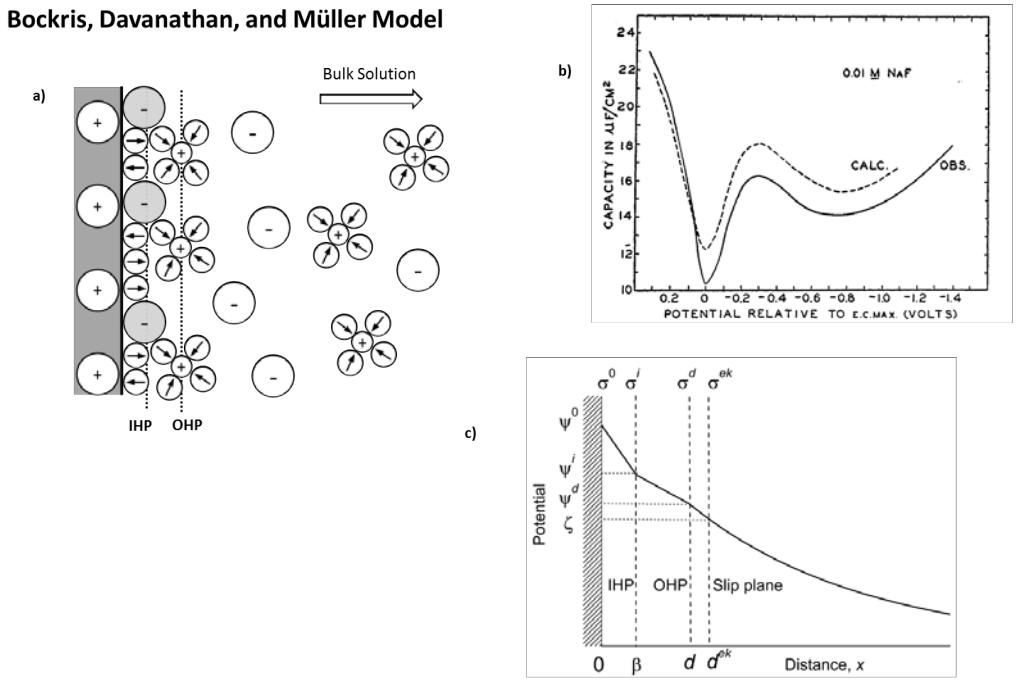

Figure 2.9 – Schematic diagrams of the various properties of the Bockris-Davanathan-Müller Electrical Double Layer model. Part a) shows the schematic of particle arrangement at the electrode surface, b) shows the differential capacitance curve of a liquid mercury electrode in contact with low concentration sodium fluoride compared to the calculated capacitance curve, and c) shows the variation of potential between the electrode surface and the bulk solution. Image adapted from [95–97,100,102]

In the Grahame model, and by extension the Bockris, Devanathan and Muller model, the characteristic length scale of the EDL is described by the Debye-Hückel length, $\boldsymbol{\kappa^{-1}}$ which is given by:

$$\kappa^{-1} = \left(\frac{\varepsilon_r \varepsilon_0 k_B T}{2 N_A e^2 I}\right)^{1/2}$$

Equation 2.4

Where $\boldsymbol{\varepsilon_r}$ is the relative permittivity of the electrolyte, $\boldsymbol{\varepsilon_0}$ is the permittivity of free space, $\boldsymbol{k_B}$ is Boltzmann's constant, $\boldsymbol{T}$ is the absolute temperature, $\boldsymbol{N_A}$ is Avogadro's constant, $\boldsymbol{e}$ is the elementary charge, and $\boldsymbol{I}$ is the ionic strength of the electrolyte, given by:

$$I = \frac{1}{2}\sum_{i=1}^{n} c_i z_i^2$$

Equation 2.5

Where $\boldsymbol{c_i}$ is the molar concentration of ion $\boldsymbol{i}$, and $\boldsymbol{z_i}$ is the integer charge number of the ion.

The Debye–Hückel length is a term found in the linearized Poisson-Boltzmann equation, which describes the distribution of electrical potential in a direction normal to a charged surface:

$$\nabla^2\phi(r) = \left(\sum_{i=1}^{n} \frac{c_i q_i^2}{\varepsilon_r \varepsilon_0 k_B T}\right)\phi(r) - \frac{1}{\varepsilon_r \varepsilon_0}\sum_{j=1}^{n} c_i q_i$$

Equation 2.6

The first bracketed term on the right hand side of the equation can be dimensionally analysed to find that it is the reciprocal of square meters, assuming SI units are used. This is the foundation of the Debye-Hückel length, described by Equation 2.4.

It should be noted that the Debye-Hückel length is not the absolute thickness of the electrical double layer – rather it describes the distance from the OHP at which the potential has dropped by a factor e^{-1} of it's total change into the bulk [103,104].

The potential difference between the wall and the IHP, and the IHP and OHP vary in a linear fashion: in the case of Figure 2.10, the potential falls from a positive value at the wall due to the negative ions which make up the stagnant layer. The potential across the diffuse layer varies in an exponential manner,

changing from the potential at the OHP to that of the bulk solution according to the equation:

$$\psi_x = \psi_0 e^{-\kappa x}$$

Equation 2.7

Where $\boldsymbol{\psi_x}$ is the potential at a given distance away from the OHP, $\boldsymbol{\psi_0}$ is the potential at the OHP, $\boldsymbol{\kappa}$ is the reciprocal of the Debye-Hückel length and $\boldsymbol{x}$ is distance from the OHP (see Figure 2.10). As the Debye-Hückel length varies with ionic strength and temperature, the potential drop across the layer is also affected.

An important consequence of the Bockris-Davanathan-Müller model is that the slip plane, the plane at which particles cease to be rigidly held by adsorption to the electrode wall, is not necessarily coincident with the OHP. The implications of this are mainly for colloidal systems, where the radius of the particle measured by electrokinetic means (such as electrophoresis, or electro-acoustics) will include the distance between the wall and the slip plane. The approximation of the OHP being equal to the slip plane is still a useful approximation in the case of extremely large electrodes. If one makes the assumption that the slip plane is coincident with the OHP, $\boldsymbol{\psi_0}$ in Equation 2.7 can be replaced with $\boldsymbol{\zeta}$, the ζ-potential, which is discussed in section 2.3.5.2.

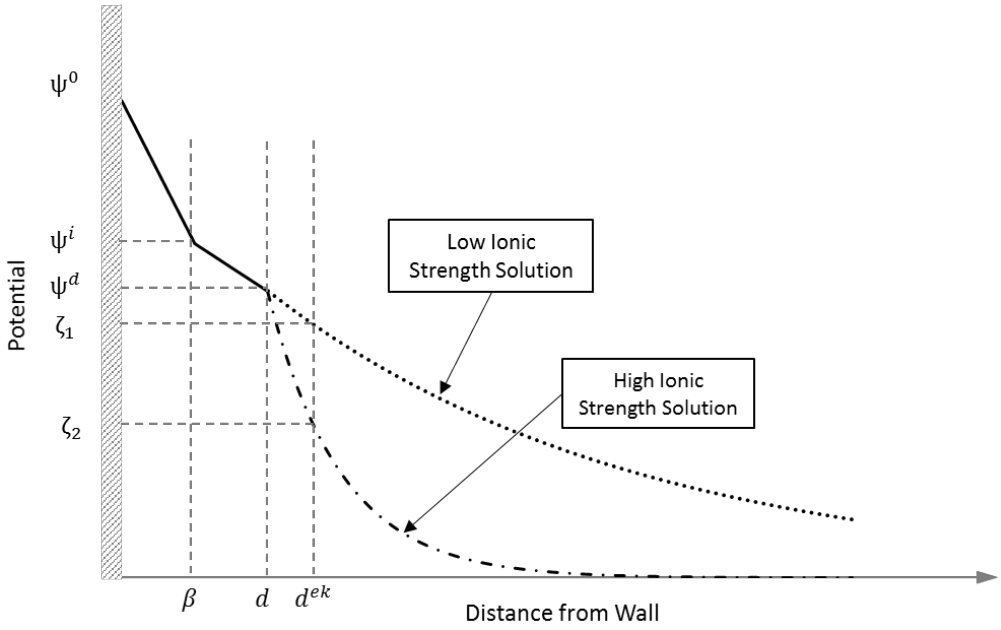

Figure 2.10 – A sketch of the potential variation across the electrical double layer. The potential between the surface and IHP, as well as the IHP and the OHP varies linearly, and then exponentially in the diffuse layer (between the OHP and the bulk solution). Image adapted from [102].

2.3.5.2 Zeta Potential

The zeta (ζ) potential is defined as the difference in potential between the shear plane and the bulk fluid. The shear plane is the plane at which particles near to the wall of an electrode cease to be held immobile, and can be made to flow given sufficient impetus. The ζ-potential is a function of the net electrical charge bounded by the electrode surface and the shear plane – effectively the sum of all charge held immobile on the electrode wall [95,97,99,102].

The ζ-potential should not be confused with the surface potential, denoted $\boldsymbol{\psi_0}$ in Figure 2.10, which cannot be directly measured for solid electrodes. As such, ζ-potential is sometimes the only method by which a researcher can characterise the charge of the EDL.

The ζ-potential must be calculated from various electrokinetic phenomena. The four most basic electrokinetic phenomena are:

- **Electrophoresis;** the motion of colloidal particles through a fluid which is at rest with respect to the particle in response to the application of a

uniform electric field [102,105,106]. Electrostatic attraction draws the particle toward one pole of the electric field, while retardation forces (from viscous stress of the oppositely charged double layer, and friction from the fluid) slow the colloids progress. The velocity of the particle in the fluid can be related to the electric field by:

$$v_e = \frac{\varepsilon_r \varepsilon_0 \zeta}{\eta} E$$

Equation 2.8

Where $\boldsymbol{\varepsilon_r}$ and $\boldsymbol{\varepsilon_0}$ are the relative permittivity and permittivity of free space respectively, $\boldsymbol{\zeta}$ is the ζ potential, $\boldsymbol{\eta}$ is the dynamic viscosity, and E is the applied electric field. Smoluchowski's equation for electrophoretic mobility [107], $\boldsymbol{u_e}$, is simply the velocity divided by the electric field:

$$u_e = \frac{v_e}{E}$$

Equation 2.9

- **Electro-osmosis;** the opposite of electrophoresis, in that fluid is compelled to move through a charged capillary channel or porous membrane by the application of a uniform electric field. The equation describing the motion of the liquid at a large distance from the double layer that causes the motion is the same as Equation 2.8, but with the sign reversed [102,105]:

$$v_{eo} = -\frac{\varepsilon_r \varepsilon_0 \zeta}{\eta} E$$

Equation 2.10

- **Sedimentation Potential;** the potential created by sedimenting particulate matter where a dipole moment is set up as the EDL lags behind a particle which is descending through a solution under gravity.
- **Streaming Current and Potential;** when a differential pressure (in the equations, $\Delta \boldsymbol{P}$) is applied to an electrolyte in a capillary with charged

walls of length $\boldsymbol{L}$ and radius, $\boldsymbol{a}$, a current named the streaming current, $\boldsymbol{I_{str}}$, is generated by the motion of the excess charge in the EDL [102,105]:

$$I_{str} = -\frac{\varepsilon_r \varepsilon_0 a^2}{\eta} \frac{\Delta p}{L} \zeta$$

Equation 2.11

The streaming current can be observed by connecting the extreme ends of the capillary through a low resistance circuit, such as a Zero Resistance Ammeter (ZRA).

However, if they are instead connected via a high resistance circuit (such as a voltmeter), charge accumulate can occur and a potential difference between the ends of the capillary will appear, named the steaming potential, $\boldsymbol{U_{str}}$. The streaming potential gives rise to a conduction current, $\boldsymbol{I_c}$:

$$I_C = K_L a^2 \frac{U_{str}}{L}$$

Equation 2.12

Where $\boldsymbol{K_L}$ is the conductivity of the dispersion medium. The streaming potential is calculated from the condition of equality between the streaming current and the conduction current, thus no net current:

$$\frac{U_{str}}{\Delta p} = \frac{\varepsilon_r \varepsilon_0 \zeta}{\eta K_L}$$

Equation 2.13

Of all phenomena, only streaming current and potential can be used for flowing systems, as the other phenomena require that the system be at rest until an electric field is applied, or that the system is allowed to induce its own field [102].

The ζ-potential of any given system is dependent upon the pH of the electrolyte in which the double layer exists. The point at which the double layer exhibits

a zero ζ-potential, or neutral net charge in the double layer has been interchangeably named the point of zero charge (PZC) and the isoelectric point (IEP). The two are slightly different, however the distinction is often ignored.

The IEP is the point at which the ζ-potential (charge at the shear plane) is zero. At this point electrokinetic phenomena, such as electrophoretic motion of particles, will simply not occur. The PZC differs from this in that it only describes systems where the surface potential-determining ions are the products of the dissociation of water (H^+/OH^-) [95]. This means that there will be no other specifically absorbed ions at the surface to influence the charge within the double layer. The PZC is effectively the IEP in the absence of any absorbed ions, beyond those which determine the pH of the system. The PZC of magnetite has been measured as $pH_{23\,°C}$ 6.2 and $pH_{235\,°C}$ 6.1 - 8.4 by Jayaweera *et al.* [108,109].

2.3.5.3 **Streaming Current**

As discussed in section 2.3.5.2, streaming current is the current generated by the motion of excess charge present in the EDL, compelled to move the application of an external differential pressure. The differential pressure induces a velocity in the fluid and for fully developed laminar flow regimes the velocity profile is a parabola (as show in Figure 2.11).

In the near-wall region, the flow profile can be approximated to a linear curve, originating at zero due to high viscous drag forces which lessen with distance away from the wall. The drop in potential, and thus the change in ion density across this region (the diffuse layer of the EDL), can be approximated with decaying exponential curve, as described by Equation 2.7 (see in Figure 2.12). Qualitatively, the region where streaming current is carried can be shown by multiplying the ion density with the simplified velocity profile to produce the curve seen in Figure 2.13.

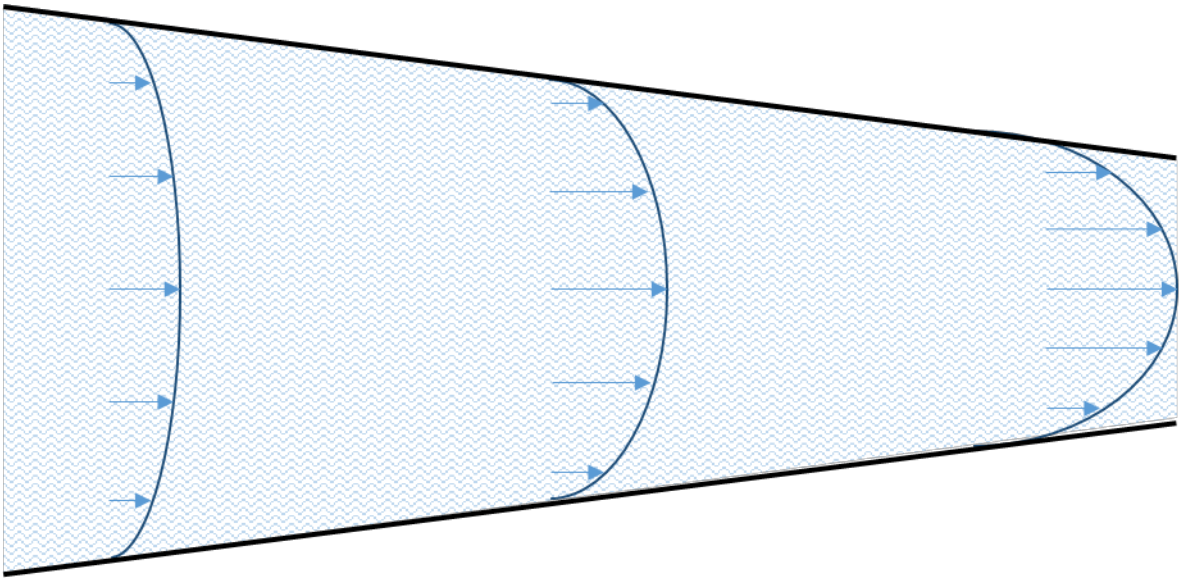

Figure 2.11 – Two dimensional velocity profile of an accelerating fluid as a function of distance from the wall in a tube. Average velocity increases along the length of the tube as the radius decreases.

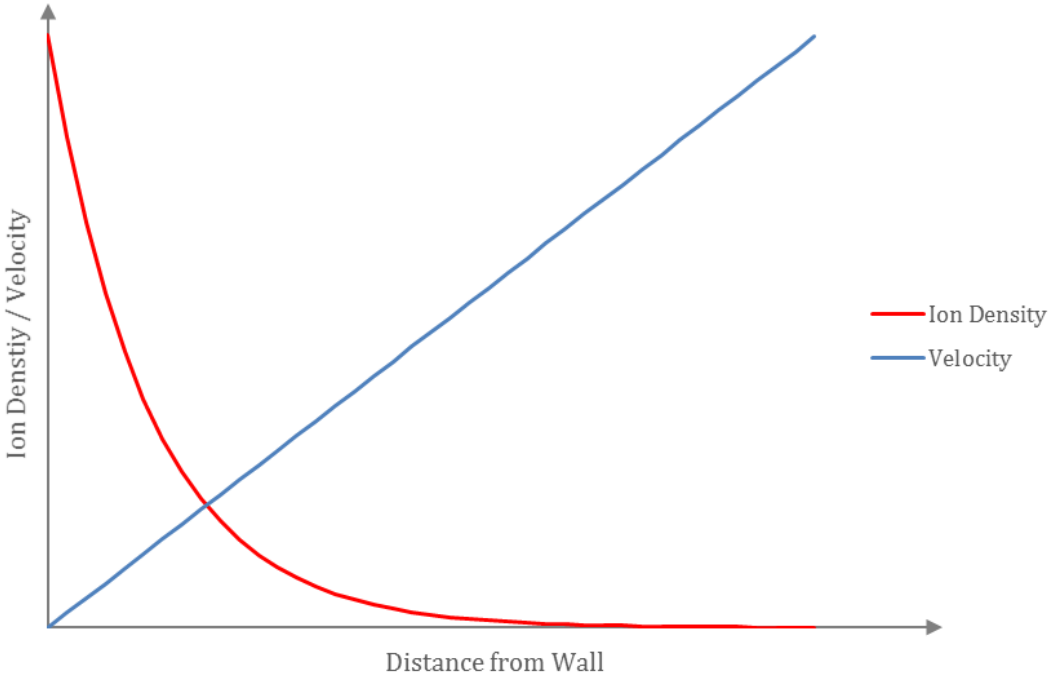

Figure 2.12 – Qualitative curves representing the drop of ion density from the level at the wall to that of the bulk solution, and the velocity gradient across the diffuse layer. The velocity profile is based on the simplification that the near-wall velocity can be approximated to a linear curve, while the ion density decay is based on the drop in potential across the diffuse layer of the EDL, described by Equation 2.7.

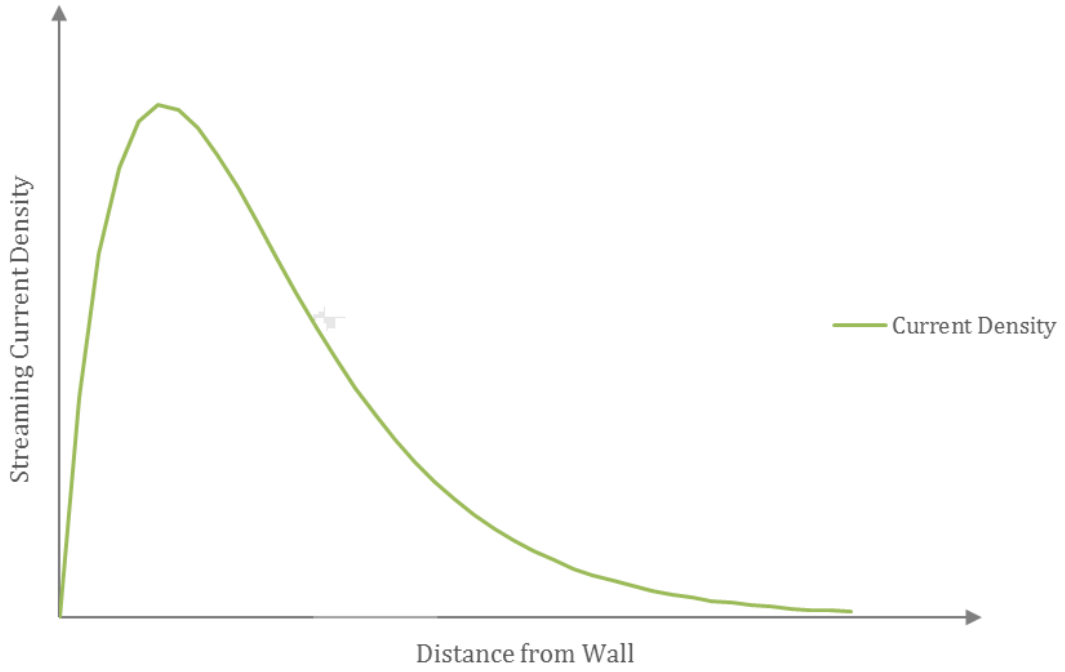

Figure 2.13 - Streaming current density at a short distance from the wall. The current density is the product of the velocity gradient, which rises linearly away from the wall, and the ion density which fall exponentially with distance from the wall.

2.3.6 Electrokinetic Deposition Formation Mechanism

The mechanism by which deposits form due to the action of electrokinetic streaming current is far from fully solved, however several mechanisms have been put forward which provided consistent predictions for deposition under given conditions. The first attempt to provide a model for conditions similar to nuclear reactor coolant was made by Robertson [89]. Robertson's work was later used by Woolsey *et al.* [24] and Morris *et al.* [25] as a theoretical basis for their experiments. More recently, Brun *et al.* [18], Guillodo *el. al.* [19,21,23] and Barale *et al.* [20,22] at AREVA have studied deposition on an array of materials at various chemistries, temperatures and flow rates. The work of all of these authors has been used by McGurk [17] to build upon the mechanism suggested by Robertson. Most recently, Scenini *et al.* [27] have studied deposition in micro flow channels, using electrochemical techniques to characterise and quantify the deposition behaviour.

McGurk's theoretical work is based directly on Robertson's, however McGurk works toward an expression for the wall and conduction currents, denoted $\boldsymbol{i_w}$ and $\boldsymbol{i_f}$ in McGurk's work and $\boldsymbol{j_y}$ for both in Robertson's work. These currents are responsible for the electrochemical reactions which result in deposition.

McGurk begins by defining the ion density in the diffuse layer, $\boldsymbol{\rho}$, with distance from the surface $\boldsymbol{y}$ as:

$$\rho = -\varepsilon_r \varepsilon_0 \kappa^2 \varphi_0 e^{-\kappa y}$$

Equation 2.14

The Debye-Hückel parameter, $\boldsymbol{\kappa}$, is the reciprocal Debye-Hückel length, defined in Equation 2.4. McGurk states that for small values of $\boldsymbol{\kappa}$, the type that would be produced by a thick double layer found in low conductivity water, the difference between ζ-potential and wall potential $\boldsymbol{\psi}$ should be small enough to ignore [17,110].

The streaming current in a cylindrical tube can be obtained from:

$$I_s = 2\pi \int_0^a r.u(r).\rho(r).dr$$

Equation 2.15

Where $\boldsymbol{a}$ is the hydrodynamic radius, $\boldsymbol{r}$ is radial distance from the tube's central axis, and $\boldsymbol{u(r)}$ is the velocity of the water. In turbulent flow conditions, the variation in velocity with distance from wall can be described by:

$$u \cong \left(\frac{du}{dy}\right)_{y=0} y$$

Equation 2.16

Where $\left(\frac{\boldsymbol{du}}{\boldsymbol{dy}}\right)_{\boldsymbol{0}}$ is the velocity gradient at the wall. This equation is valid for situations where the diffuse layer thickness is smaller than the laminar sublayer thickness, which is the case for the experiments used in McGurk's work.

Substitution of Equations 2.14 and 2.16 into Equation 2.15, intergrating for the condition $\boldsymbol{\kappa\alpha \gg 1}$, and replacing $\boldsymbol{\psi_0}$ with $\boldsymbol{\zeta}$ (as Eqaution 2.16 is measured from the slip plane), yields:

$$I_s = -2\pi a \varepsilon_r \varepsilon_0 \zeta \left(\frac{du}{dy}\right)_0$$

Equation 2.17

Assuming linear shear rate in the locale of the double layer, velocity gradient can be obtained from:

$$\left(\frac{du}{dy}\right)_0 = \frac{f}{2}\frac{u^2}{\nu}$$

Equation 2.18

Where $\boldsymbol{u}$ is the flow velocity, $\boldsymbol{\nu}$, is the kinematic viscosity of the fluid, and $\boldsymbol{f}$ is the friction factor, which varies with Reynolds number, according to:

$$\frac{f}{2} = \frac{0.023}{Re^{0.2}}$$

Equation 2.19

Reynolds number (for Re between 30,000 and 1,000,000) in a cylindrical tube is given by:

$$Re = \frac{2au}{\nu}$$

Equation 2.20

Substituting Equation 2.18, Equation 2.19 and Equation 2.20 into Equation 2.17 produces the following formula for streaming current:

$$I_s = -0.046\pi \left(\frac{\nu}{2a}\right)^{\frac{1}{5}} \left(\frac{a}{\nu}\right) \varepsilon_r \varepsilon_0 \zeta u^{\frac{9}{5}}$$

Equation 2.21

Equation 2.21 states that any change in fluid velocity, such as would occur at a flow restriction, will cause a change in $\boldsymbol{I_s}$ in the flow direction, $\boldsymbol{x}$. As stated by Robertson [89], any change in the $\boldsymbol{I_s}$ in the direction of flow will draw a current

normal to the wall in order to satisfy the electrical continuity equation, $\boldsymbol{\nabla . i = 0}$. McGurk related the continuity equation and the changes in streaming current to the flow in a cylindrical tube by [17]:

$$i_w - i_f = \frac{1}{2\pi a}\frac{\partial I_s}{\partial x}$$

Equation 2.22

Where $\boldsymbol{i_w}$ is the wall current density, generated by the transfer of electrons between the conducting wall and the solution, and $\boldsymbol{i_f}$ is the conduction current density produced by the difference in potential between anodic and cathodic locations in the solution (see Figure 2.14). In McGurk's work, the conduction currents are largely ignored in favour of the wall current, as low conductivity solutions make the fluid currents negligibly small in comparison to the dominant wall currents.

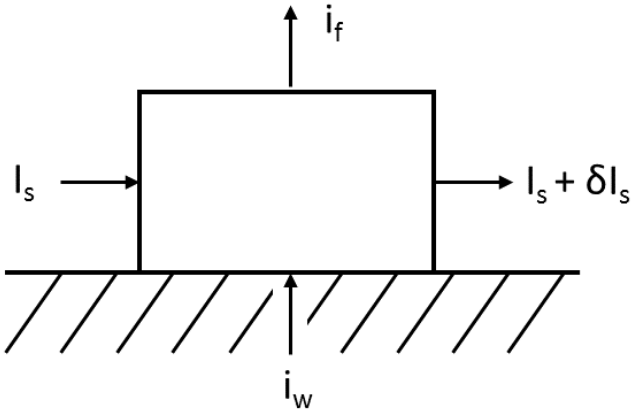

Figure 2.14 - Sketch of the streaming current flows within an example box of accelerating fluid. In order to retain electrical continuity, the wall current, i_w, is drawn. The fluid current, i_f, is ignored due to the low conductivity of the fluid compared with that of the metal electrode. Image adapted from [17,89].

Anodic reactions that can be driven by wall currents are exemplified by the corrosion of iron and the precipitation of magnetite:

$$Fe \leftrightharpoons Fe^{2+} + 2e^-$$

Equation 2.23

$$3Fe^{2+} + 4H_2O \leftrightharpoons Fe_3O_4 + 8H^+ + 2e^-$$

Equation 2.24

An example of a cathodic reaction is the evolution of hydrogen:

$$2H^+ + 2e^- \leftrightharpoons H_2$$

Equation 2.25[110]

The corrosion potential in a PWR primary circuit, which is equal to the hydrogen electrode potential, is given by the following reaction:

$$E_H = -\frac{RT}{2F}\ln(10)\left[\log\frac{V_{H_2}}{22414} - \log K_{H_2} + 2\,pH\right]$$

Equation 2.26

Where $\boldsymbol{V_{H_2}}$ is the concentration of H_2 in solution (in $cm^3{}_{(STP)}.kg^{-1}$), $\boldsymbol{K_{H_2}}$ is the equilibrium constant for the partition of hydrogen between the gaseous and liquid phases and $\boldsymbol{pH}$ is the negative logarithm of hydrogen ion activity. $\boldsymbol{K_{H_2}}$ can be calculated from:

$$\log K_{H_2} = \frac{2089.83}{T} - 45.335 + 14.241\log T$$

Equation 2.27

The corrosion potential is a measurement of the difference between the potential of the metal and the potential of the solution, all compared to the normal hydrogen electrode (NHE). Making the assumption that the difference between ζ-potential and wall potential $\boldsymbol{\psi_0}$ is negligibly small, the ζ-potential can be related to the NHE by:

$$\zeta = \zeta_0 + E_H - E_H^0$$

Equation 2.28

Where $\boldsymbol{\zeta_0}$ is the value of $\boldsymbol{\zeta}$ when $\boldsymbol{E_H = E_H^0}$; in actuality, $\boldsymbol{\zeta_0}$ is measured under the conditions of $\boldsymbol{V_{H_2}}$ and $\boldsymbol{pH}$ corresponding to a calculated value of $\boldsymbol{E_H^0}$, which itself is calculated from Equation 2.26. Using the calculated value of $\boldsymbol{E_H^0}$, $\boldsymbol{\zeta}$ can be calculated from Equation 2.28 for given values of $\boldsymbol{V_{H_2}}$ and $\boldsymbol{pH}$ [17].

The ζ-potential of metal oxides found in a reactor is governed by the pH of the system and specifically by the acid-base reactions which occur at the interface between oxide and fluid:

$$-SOH + H^+ \rightarrow -SOH_2^+$$

Equation 2.29

$$-SOH + OH^- \rightarrow -SO^- + H_2O$$

Equation 2.30

From Equation 2.29 and Equation 2.30, it can be seen that an acid reaction with surface hydroxides (-SOH) will result in a more positively charged surface. Conversely, a basic reaction will result in a more negatively charged surface. Assuming that only H^+/OH^- are the surface potential determining ions, the pH at which the positive and negative surface charge is equal is the PZC (as discussed in secion 2.3.5.2) [95,111]. With knowledge of the PZC, one can define the sign of ζ-potential sign – for $pH<pH_{PZC}$, (acidic system, more positively charged surface) $\zeta>0$, while $pH>pH_{PZC}$ (basic system, more negatively charged) $\zeta>0$. McGurk claims that the metal oxide films covering the surfaces of stainless steels and nickel base alloys are both thin and conductive, meaning that the ζ-potential of such surfaces is governed by the underlying metal rather than the surface film [17,110,112].

Returning to the anodic and cathodic reactions which can be driven by the electrokinetic wall currents, McGurk states that magnetite deposition from solution can occur via anodic wall currents only when $\boldsymbol{i_w} > 0$ or when $\boldsymbol{\partial I_s/\partial x} > 0$. In regions of acceleration, (or points of fluid attachment, where flow impinges on the wall), this will occur when $\boldsymbol{I_s} > 0$, or when $\boldsymbol{\zeta} < 0$. Conversely, in regions deceleration (points of separation, where flow detaches from the wall) the conditions for deposition are met when $\boldsymbol{I_s} < 0$, or $\boldsymbol{\zeta} > 0$.

The theory as it has been shown thus far [17,89,110] suggests that electrokinetic deposition under nominal PWR primary coolant conditions should not occur,

as deposition is a response to a positive ζ-potential in regions of acceleration. McGurk claims that, normal PWR primary coolant conditions are found to produce a negative ζ-potential, preventing deposition across regions of acceleration [17].

Experiments which have observed deposition under simulated PWR coolant conditions have seen deposition at points of hydrodynamic separation. At these locations, the parameters for deposition are reversed, requiring a negative ζ-potential [18,19]. McGurk's recalculation of the ζ-potentials seen in these articles shows that they are consistent with the presented theory.

Experiments in boiler conditions [24,25] were found to be controlled mainly by mass transfer. However, when the flow rate was halved, the lack of any deposition at all suggested that deposition under these conditions is more than simple mass transfer

In a similar vein to McGurk's work, AREVA's research group has attempted to provide a mechanism to explain the annular rippled deposits that had been seen both in plant (Cruas NPP) [18], on their test loop 'EMILIE' [18–23] (see Figure 2.17) and even before this, in work done by Woolsey *et al.* [24] and Morris *et al.* [25].

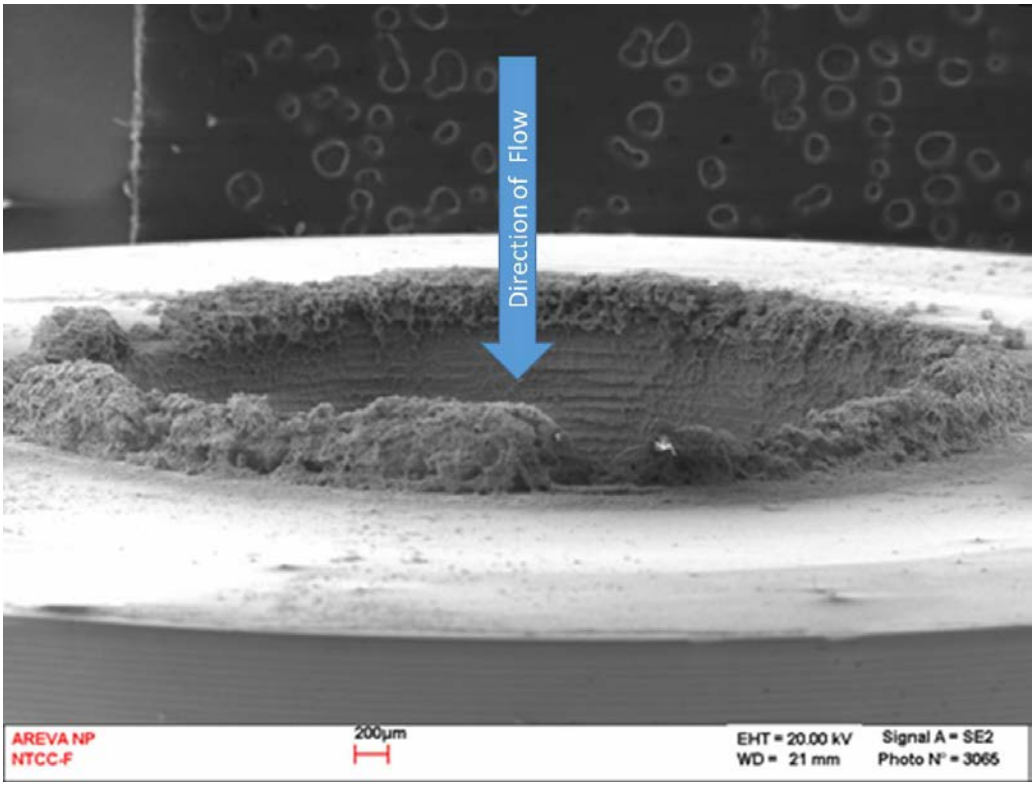

Figure 2.15 – Deposition formed at the mouth of an Alloy 600 flow restriction, 6 mm in diameter. The annulus of the restriction can also be seen to be covered by deposit, and a cross section is shown in Figure 2.16. Image taken from [11].

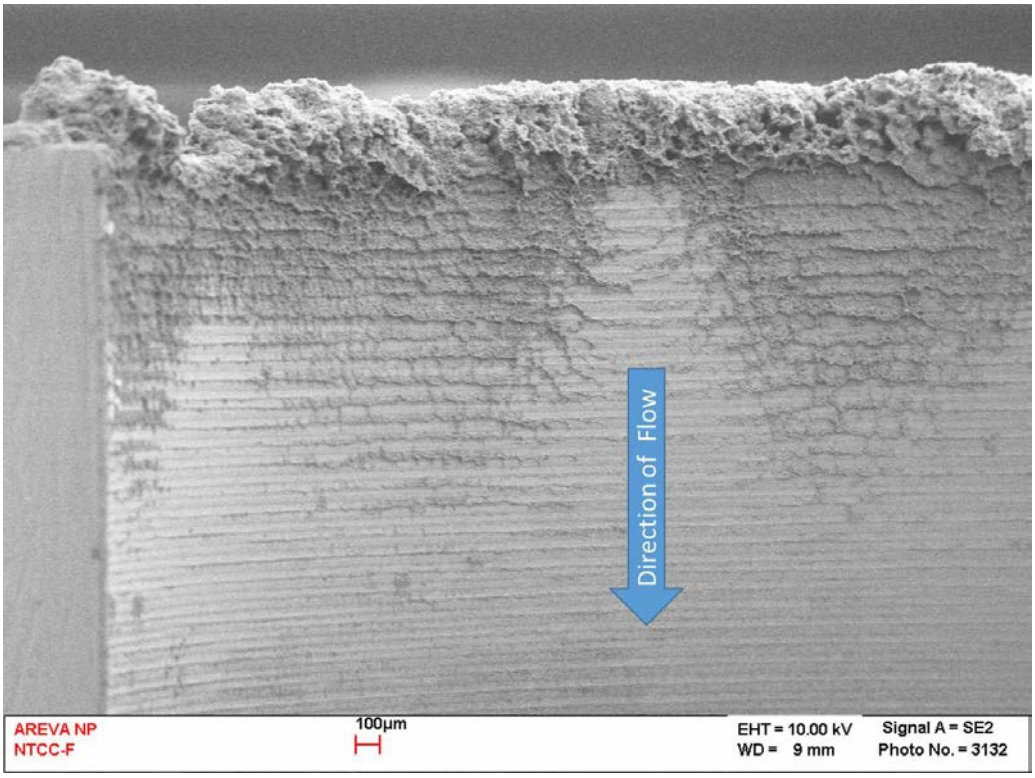

Figure 2.16 – The deposition within a 6 mm radius flow restriction of an Alloy 600. The pseudo-periodic deposition along the length of the restriction is normal to the direction of flow. Image taken from [11]

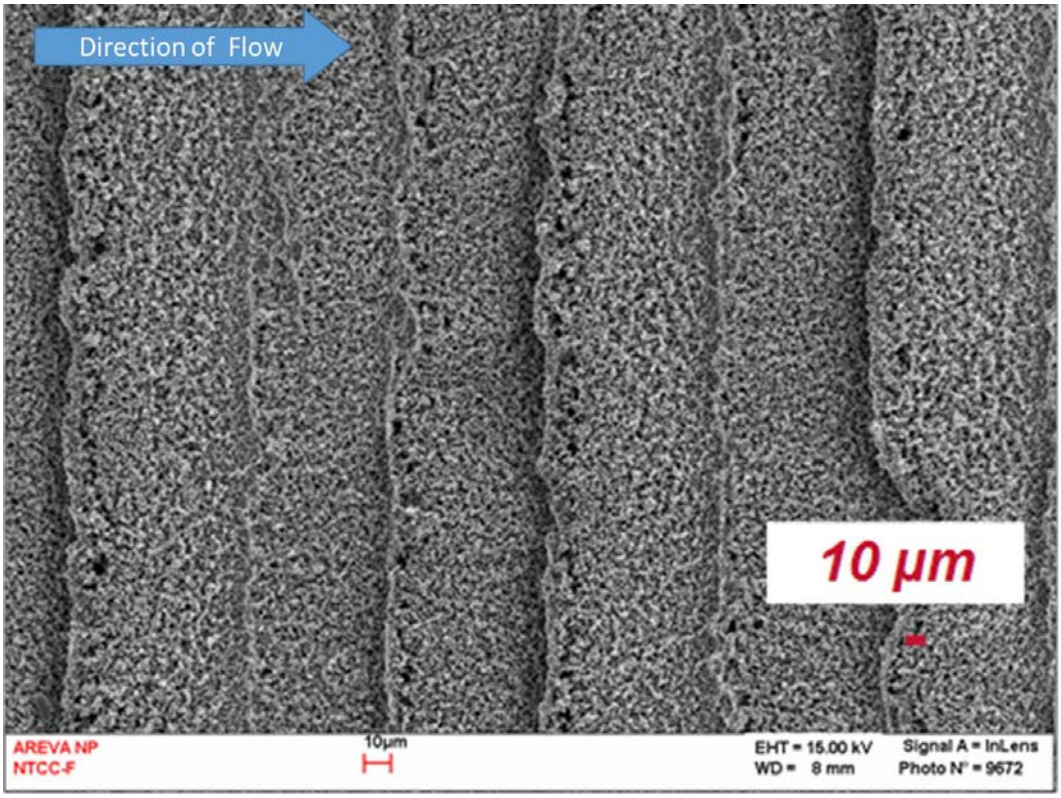

Figure 2.17 - Pseudo periodic deposition seen on nickel base alloy flow restrictions. Image taken from [11].

A mechanism was proposed by Guillodo *et al.* [19], shown schematically in Figure 2.18, in which the deposition was initiated at the entrance of the restriction by a streaming current loop. It was proposed that the formation of the initial deposit disturbs the flow enough to form another flow singularity and thus a second current loop, forming another deposit which again disturbs the flow, resulting in a propagation of annular deposits along the length of the restriction.

This mechanism is consistent with Robertson's and McGurk's, where areas of flow disturbance, be they regions of acceleration or deceleration, are the locus of the deposition.

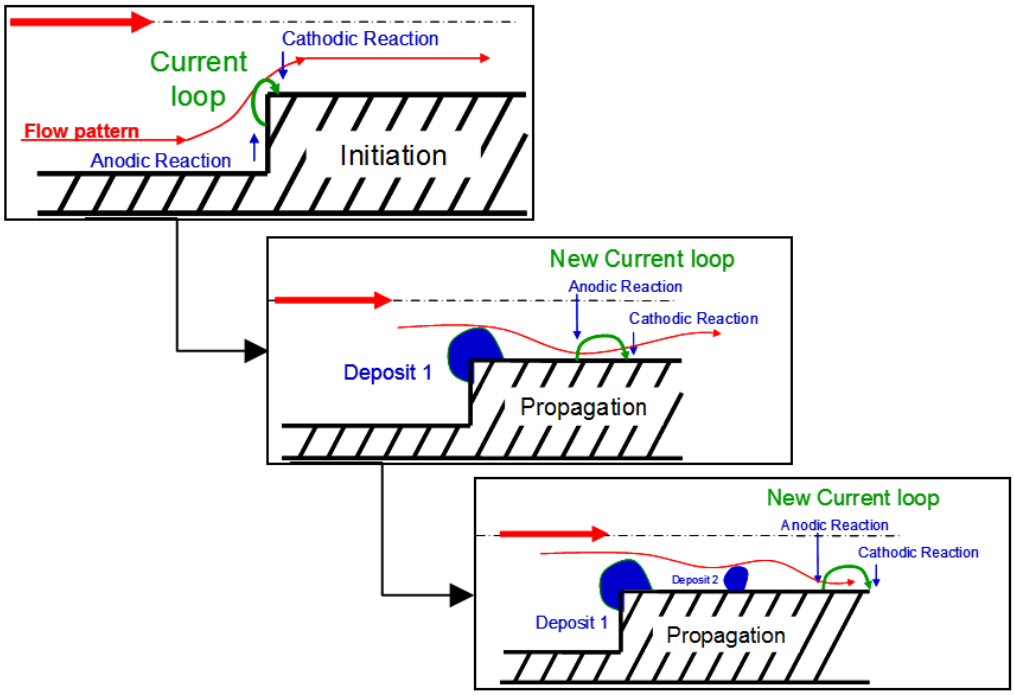

Figure 2.18 - The proposed mechanism of deposit propagation along the annulus of a flow restriction [19].

2.3.6.1 Conditions of Occurrence

There is very little published work detailing the conditions of deposit formation beyond the publications of Woolsey *et al.* [24], Morris *et al.* [25], the AREVA research group [18–23], and those of Scenini *et al.* [26,27].

Woolsey *et al.* observed deposition on nickel base alloy samples for temperatures between 149.4 °C and 246.5 °C, at approximately $pH_{25\,°C}$ of 9, modified by NH_3 in fully deoxygenated water; the rate of deposition was reported to be dependent on the dissolved iron concentration. It was found that even small quantities of dissolved oxygen could suppress the deposition [24].

A similar study performed by Morris and Woolsey [25] used a full scale steam generator rig facility to study deposition on the inlet side at two orifices. Tests were carried out at 160 °C, with $pH_{25°C}$ initially controlled at 9.4 by adding 10 parts per billion (ppb) hydrazine. During the test runs, the pH was changed to pH 8.8 immediately following an initial period at 9.4, or to pH 8.6 stepwise over

a period of time. The conclusion of this study was that the effect of oxygen and iron concentration on deposition was not clearly defined. Instead, the effect of variable pH was a more dominant controlling factor [25]. The deposition is described as being most heavily concentrated at the entrance to the orifice, though the author observes that this is the point of maximum mass transfer.

In contrast, the AREVA research group put the mechanism down to the surface charge of reactor materials, which is controlled by the H^+/H_2 equilibrium. By varying the pH and dissolved H_2 concentration throughout an experimental program, a critical potential above which deposition would occur was established for nickel base Alloys 600 and Alloy 690 [19,20], a martensitic stainless steel Z10C13 [22] and AISI 410 ferritic stainless steel [23] (see Figure 2.23).

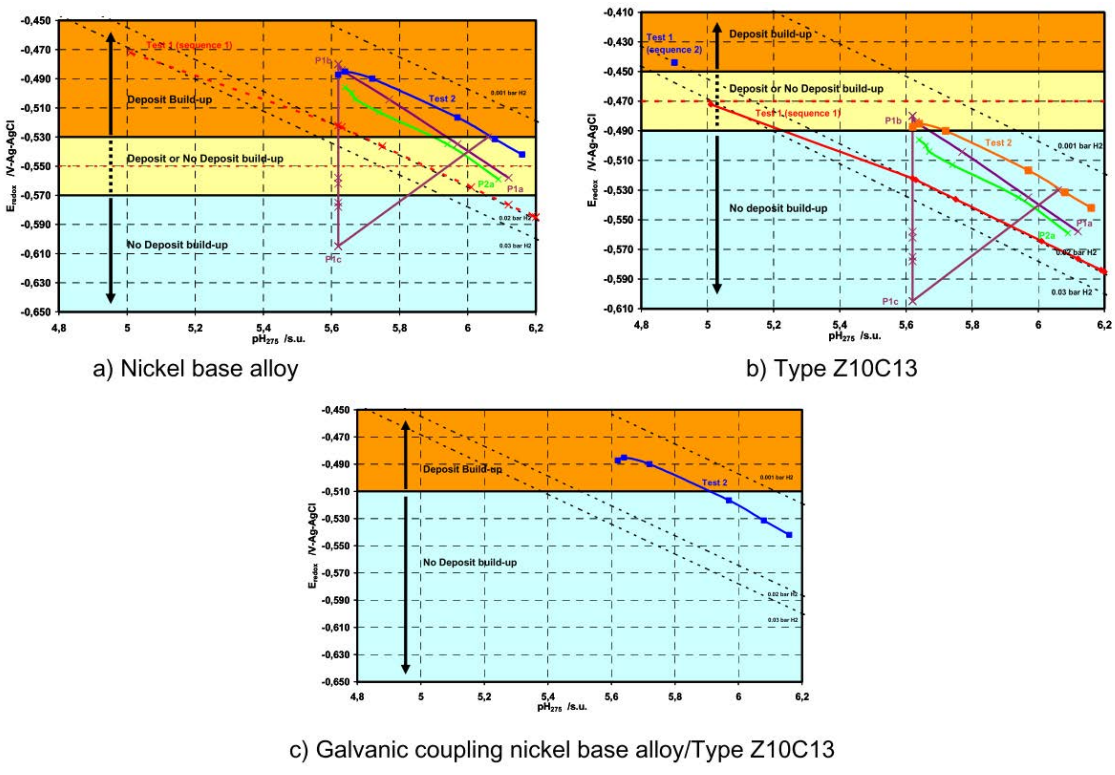

Figure 2.19 - Potential/pH diagrams for Nickel base alloys, martensitic stainless steel Z10C13, and feritic stainless steel AISI410. Regions where deposition is known to occur are denoted by orange, intermediate deposition regions by yellow, and deposit free conditions by blue [23].

Recently, researchers at the University of Manchester have studied the deposition phenomena using orifices with an internal diameter <1 mm [26,27]

(see section 2.3.7.3). Results for their deposition experiments found that deposition occurred in the micro-orifices in question and occurred under the conditions used in previous work. The build-up rate (BUR) of CRUD at orifices was calculated for a range of experimental conditions and found to be between 1 – 6 $\mu m.hr^{-1}$.

However, contrary to previous published work, it was found that increasing dissolved hydrogen concentration in high purity water experiments increased the build-up rate. Additionally, no correlation between flow velocity and build-up rate was identified, though the authors of the work observe that change in velocity is brought about by the changing of orifice size, which may have obscured this effect as the available area for deposition is dramatically reduced [27]. This result is in agreement the conclusion of Brun *et al.* [18] who also did not observe any dependence of deposition on velocity, however it is surprising given the streaming current dependence on shear rate, which is dependent on bulk velocity (see section 2.3.6).

2.3.7 Reproduction of Plant Deposits at Laboratory Scale

2.3.7.1 Central Electricity Generating Board (Woolsey *et al.* and Morris and Woolsey)

Woolsey *et al.* were active in this area of research during the late 1980's and 1990's [24,113,114]. The work described uses a high velocity, high temperature loop built largely from 316 stainless steel components, capable of operating at temperatures of up to 350 °C and at pressures of 217.8 bar. The circuit consists of four flow routes; two for testing purposes and two for clean-up and chemistry control.

During testing, the system was at a temperature of 160 °C on the inlet side, increasing to 482 °C on the outlet side, simulating the temperature gradient within a boiler.

Each of the flow channels were fitted with test sections like those shown in Figure 2.20. Each cell contained three flow restrictions, machined from Alloy 600, with inner diameters ranging in size between 2.5 and 3.6 mm [24]. At the highest flow rates listed, this system is capable of reaching a flow velocity of ~50 $m.s^{-1}$ inside a 2.5 mm test piece.

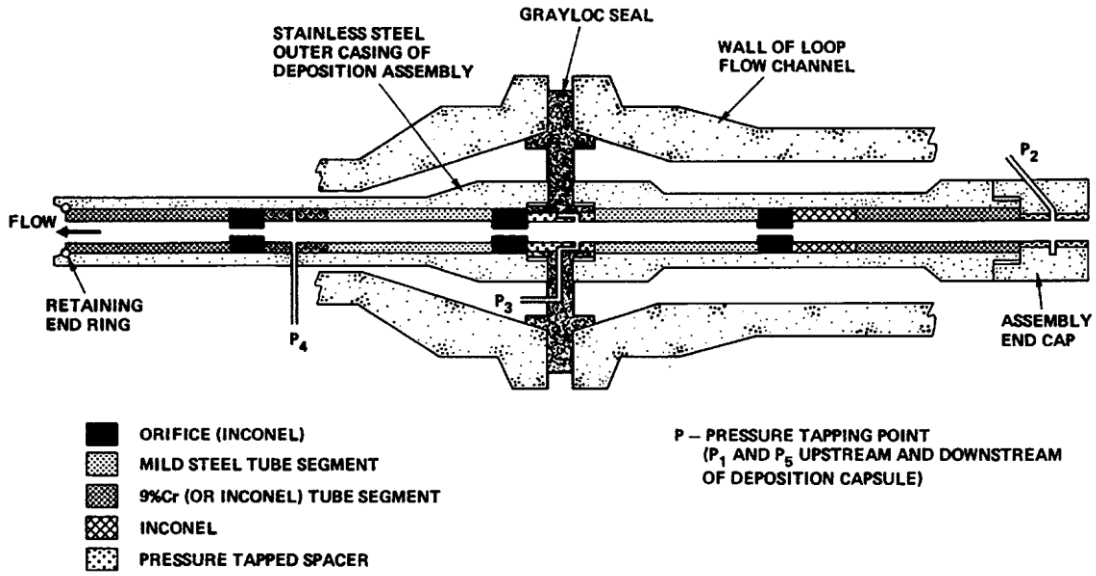

Figure 2.20 - The test section as used by Woolsey *et al.* to study deposition of soluble corrosion products on Alloy 600 flow restrictions. Image adapted from [24]

Morris and Woolsey [25] performed similar tests using the plant scale Wythenshawe boiler rig facility. Few technical details are provided by the authors beyond the test conditions of the two experiments run and the design of the orifice test pieces.

2.3.7.2 AREVA (The EMILIE Water Loop)

The EMILIE loop is a test loop designed and built by a research group at AREVA [18]. A line diagram of the first version of EMILIE is shown in Figure 2.21. Its purpose was originally to replicate the deposition seen on TSP's, shown in Figure 1.5, and early studies showed similar results to those seen by Woolsey *et al.*

Throughout all design iterations, the system used the same test geometries; an 11 mm lead up, followed by a 6 mm restriction. The flow velocity through the restriction was controlled between 8 – 12 $m.s^{-1}$.

The first iteration of EMILIE (Figure 2.21) consisted of 3 separate loops;

1) A pump bypass loop, which allowed the pump to be operated at a single speed – flow rate was controlled by a valve an outlet line.
2) The test loop into which test sections could be fitted.
3) A chemistry control loop in which a 12 L autoclave was used to inject new chemistry with an 18 L autoclave as a system pressuriser [18].

The pump recirculation line also possesses a cooler, presumably to prevent the water from exceeding the maximum temperature capabilities of the pump; two 9 kW heaters are present upstream of the pump which provide the heat to the system.

Each sample is electrically isolated from the rig, and the differential pressure across each is logged. Flow rate is measured using a venturi flow meter and orifice flow meter in series with each other – any deposition on the orifice flow meter can be monitored by observing the difference in flow rate readings between the two meters.

The system was further expanded to include high temperature ζ-potential measurement equipment as part of a fouth loop within the system, shown in Figure 2.22. The measurement of ζ-potential using the EMILIE loop is discussed in section 2.3.8.1.

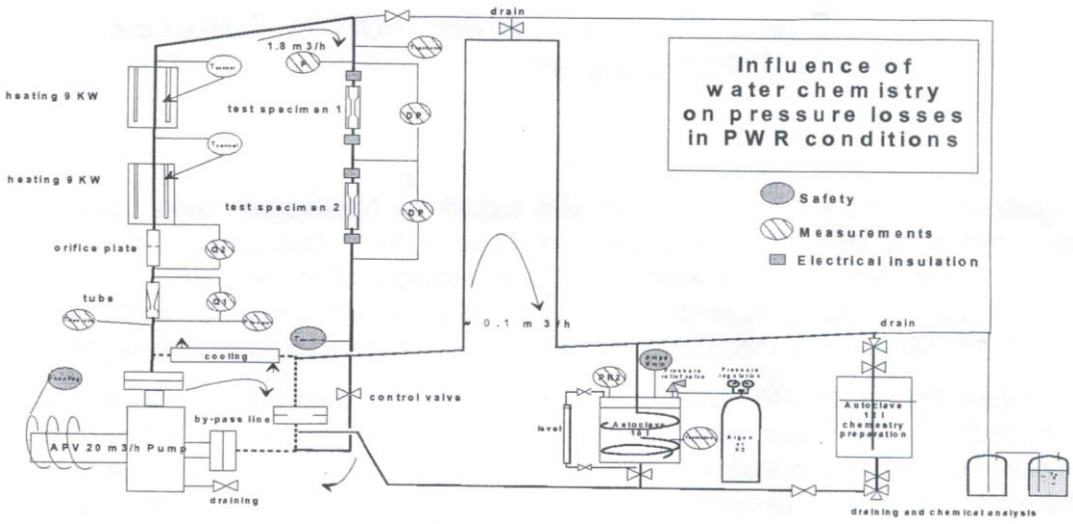

Figure 2.21 - A line diagram showing the design of the first version of the EMILIE loop [18].

It also appears that there has been an overhaul of some of the more fundamental components. The pump recirculation loop is now fitted with a 12 kW heater, which suggests that the pump was either replaced or found to be capable of high temperature operation. An additional 2.7 kW heater is present on the test section loop, perhaps providing a final temperature increase to the water coming from the pump recirculation loop. The pressure vessels used for the chemistry control system have been replaced with larger vessels, possibly due to the increased system volume brought on by the installation of the high temperature zeta potential loop.

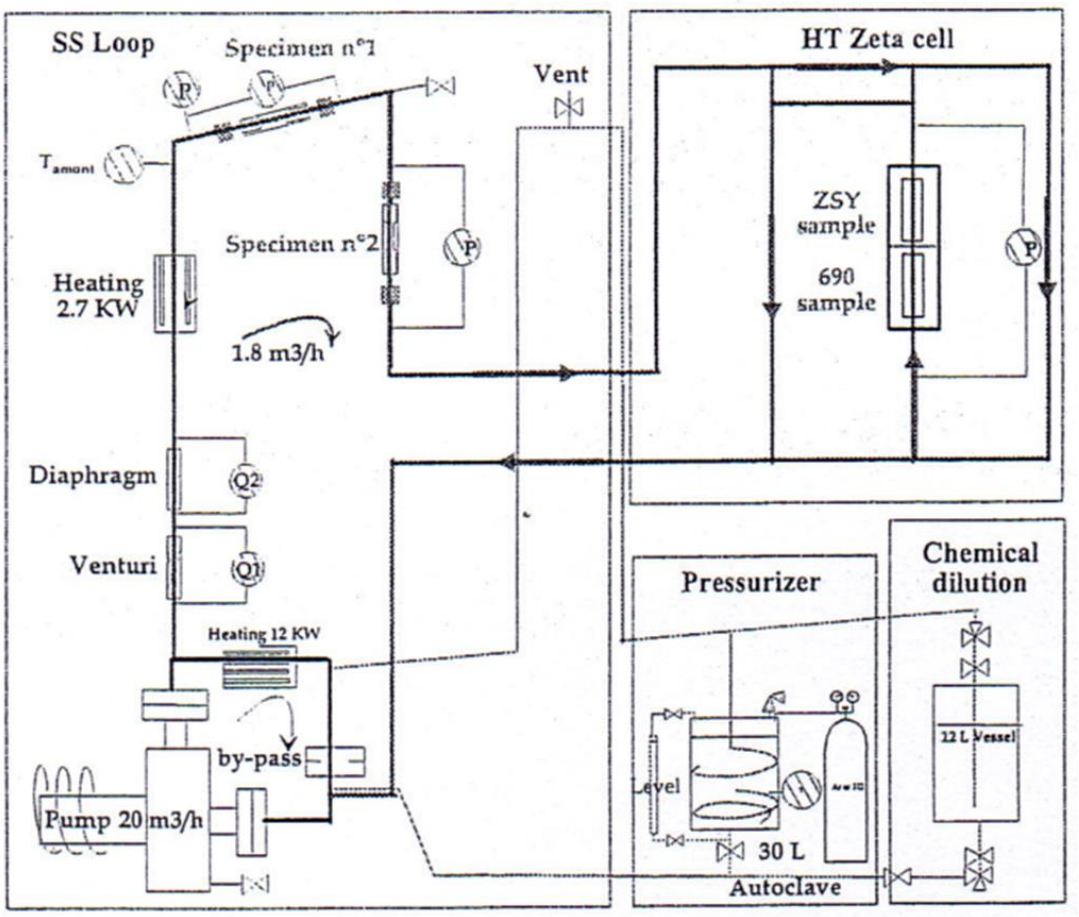

Figure 2.22 - The second reported design of the EMILIE loop. The most obvious improvement to the system is the inclusion of the high temperature zeta potential cell. Other improvements include a larger pressure vessel used in the chemistry control loop [19].

The most recent iteration of the EMILIE loop is shown in Figure 2.23 and Figure 2.24; the system now includes an extensive chemistry control system. The control loop now consists of a 100 L autoclave, sensors for measurement of pH, dissolved H_2 and O_2, and conductivity, as well as piston pumps to provide high pressure dosing of pH control chemicals.

Two versions of the system are shown, as it is used for both deposition studies and high temperature ζ-potential studies (discussed further in section 2.3.8.1). Photographs of this version of the system can be seen in Figure 2.25 and Figure 2.26.

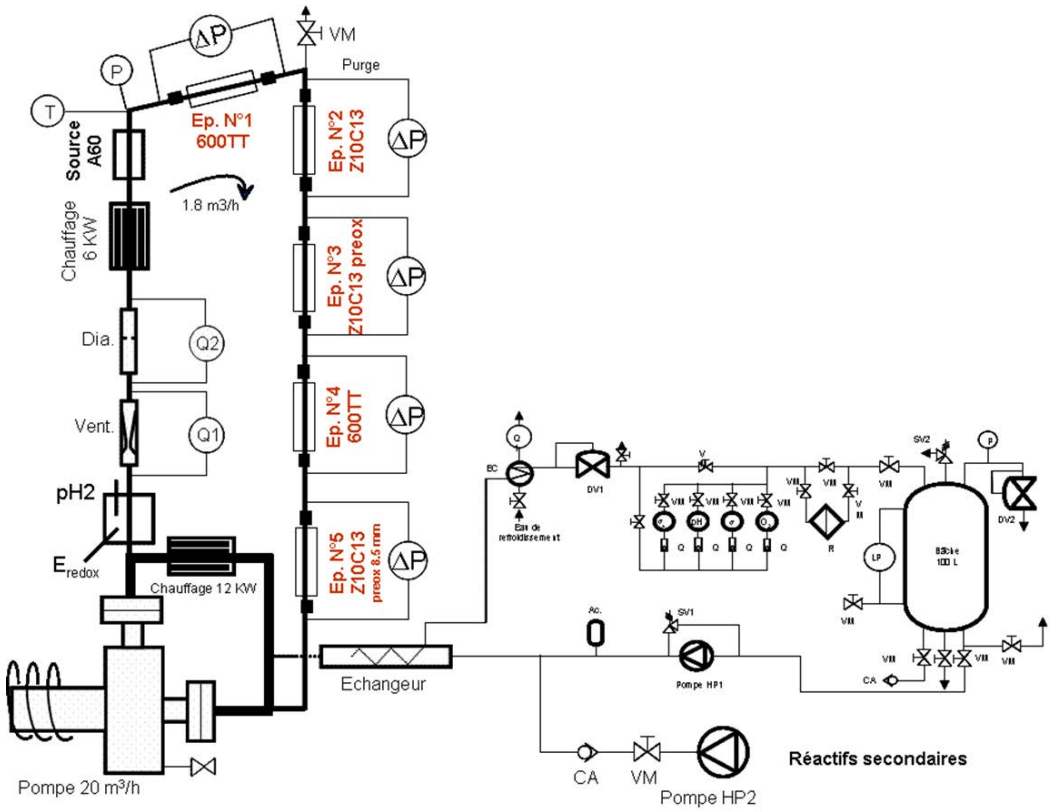

Figure 2.23 - Most recent version of the EMILIE loop set up for deposition studies on five sample sections [22].

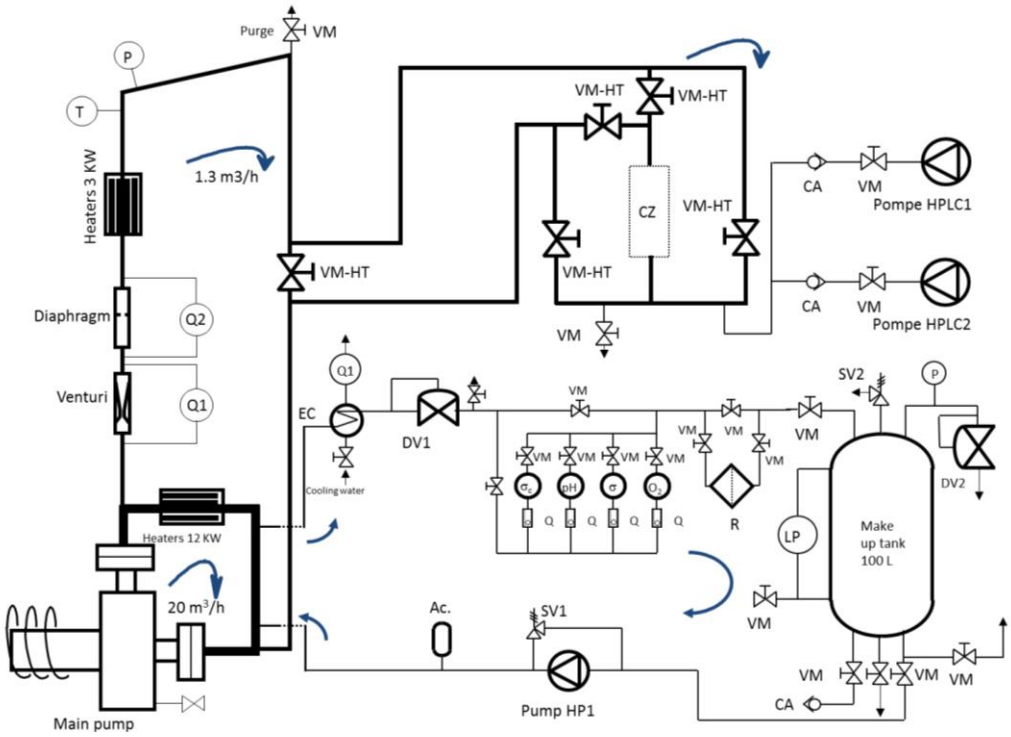

Figure 2.24 - The most version of the EMILIE loop, set up for zeta-potential studies [21].

Figure 2.25 - The EMILIE Loop. Image courtesy of Pierre Combrade [12].

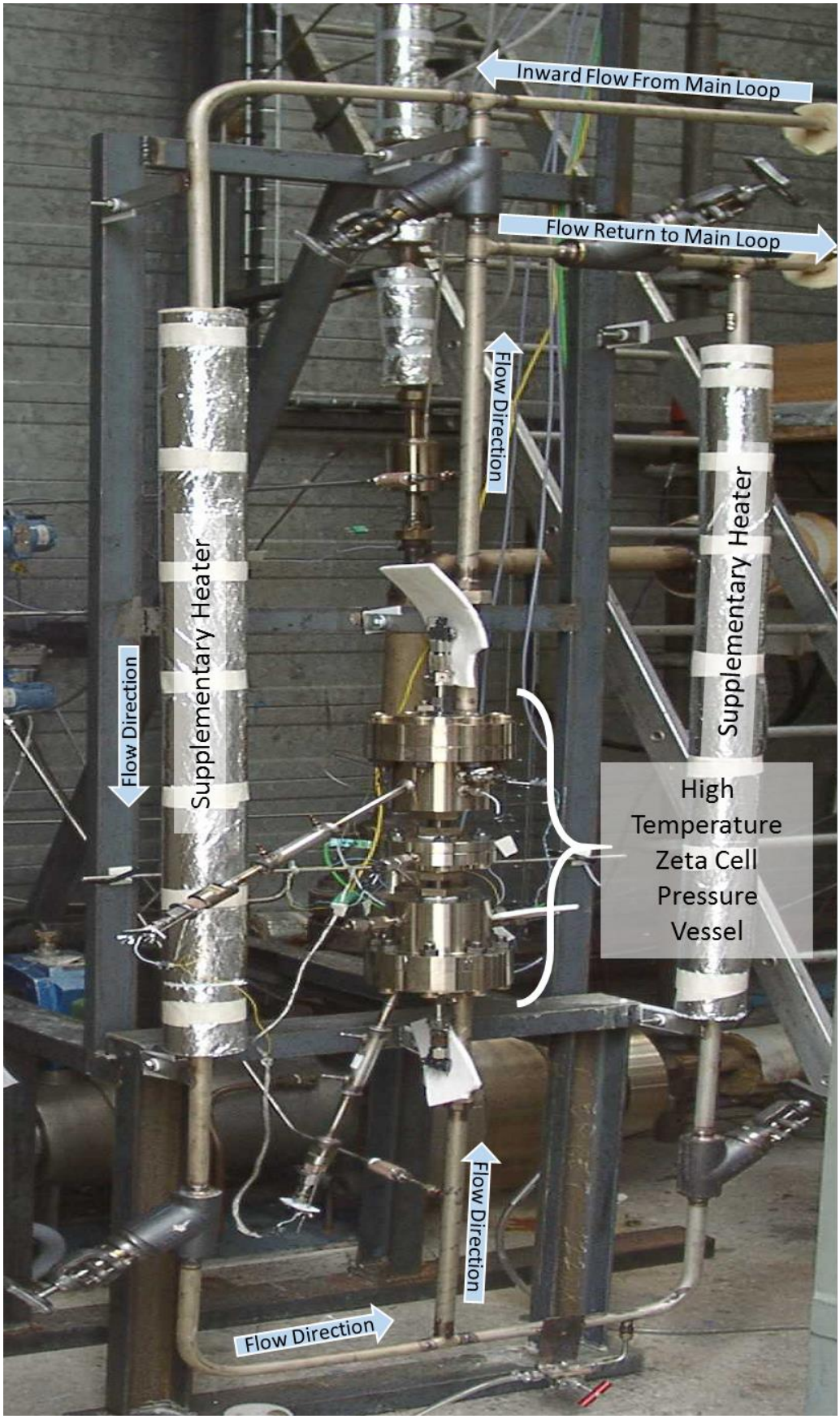

Figure 2.26 - The high temperature zeta potential cell, fitted to the EMILIE Loop, one of the secondary loops listed in Figure 2.22.

2.3.7.3 Deposition in Micro-Orifices and Electrochemcial Observations

Work performed at the University of Manchester has been heavily focused upon the electrochemical aspects of the deposition mechanism, as it applies to so-called micro-orifices [26,27]. Instead of generating high volumetric flow rates to replicate deposition on a plant-scale test piece, the micro-orifice method allows for very high flow velocities with small flow rates.

Several tests have been carried out with this type of set up, including simple deposition at an orifice [26,27] mapping of the electrochemical potential through the annulus of a test piece and deriving a build-up rate of deposited magnetite [93,115]. Experiments performed by this group are discussed in section 2.3.8.2.

2.3.8 Measurement of Electrokinetic Behaviour

2.3.8.1 Steaming Current Measurement

The only recorded attempt to measure streaming current at high temperature and pressure, and representative scale, was made by the AREVA group using an additional loop that was fitted the EMILIE loop [19,21] (see Figure 2.26). The test system used in the additional loop is shown schematically in Figure 2.27.

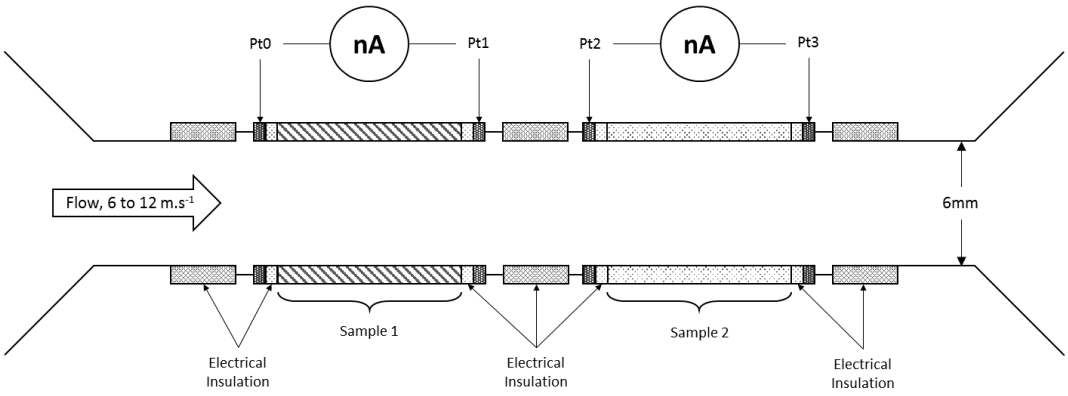

Figure 2.27 - The high temperature, high pressure streaming current cell used on the EMILIE loop. Two low resistance ammeters, connected to platinum electrodes, are used to collect streaming current readings across two different samples. Image adapted from [19].

Two metal substrate samples could be fitted into the locations labeled sample 1 and sample 2, and streaming current measurements were made using a zero resistance ammeter (ZRA) capable of reading nanoamps.

The equipment was shown to be able to reproducibly measure the streaming current on the system as a function of velocity to the power of 7/4 (see Figure 2.28). The researchers applied the following relationship for the calculation of ζ-potential:

$$\zeta = \frac{16}{0.316}\mu.\frac{\rho.2.R^{1/4}}{\mu}\frac{1}{\varepsilon_0\varepsilon_r R\rho}.\frac{1}{v^{7/4}}$$

Equation 2.31

Where $\boldsymbol{\mu}$ is the dynamic viscosity of the fluid, $\boldsymbol{\rho}$ is the fluid density, $\boldsymbol{R}$ is the hydrodynamic radius, $\boldsymbol{\varepsilon_0}$ and $\boldsymbol{\varepsilon_r}$ are the permittivity of free space and the relative permittivity of the fluid respectively, and $\boldsymbol{v}$ is the fluid velocity. Under pH 5.4, 290°C water, and a variable concentration of dissolved H_2 (four concentrations, 30, 50, 60 and 110 $cm^3.kg^{-1}$), the zeta potential of the Alloy 690 test section was found to vary between 56 and 60 mV, and between -75 and -120 mV for a Yttria-Stabilised Zirconia (YSZ) surface.

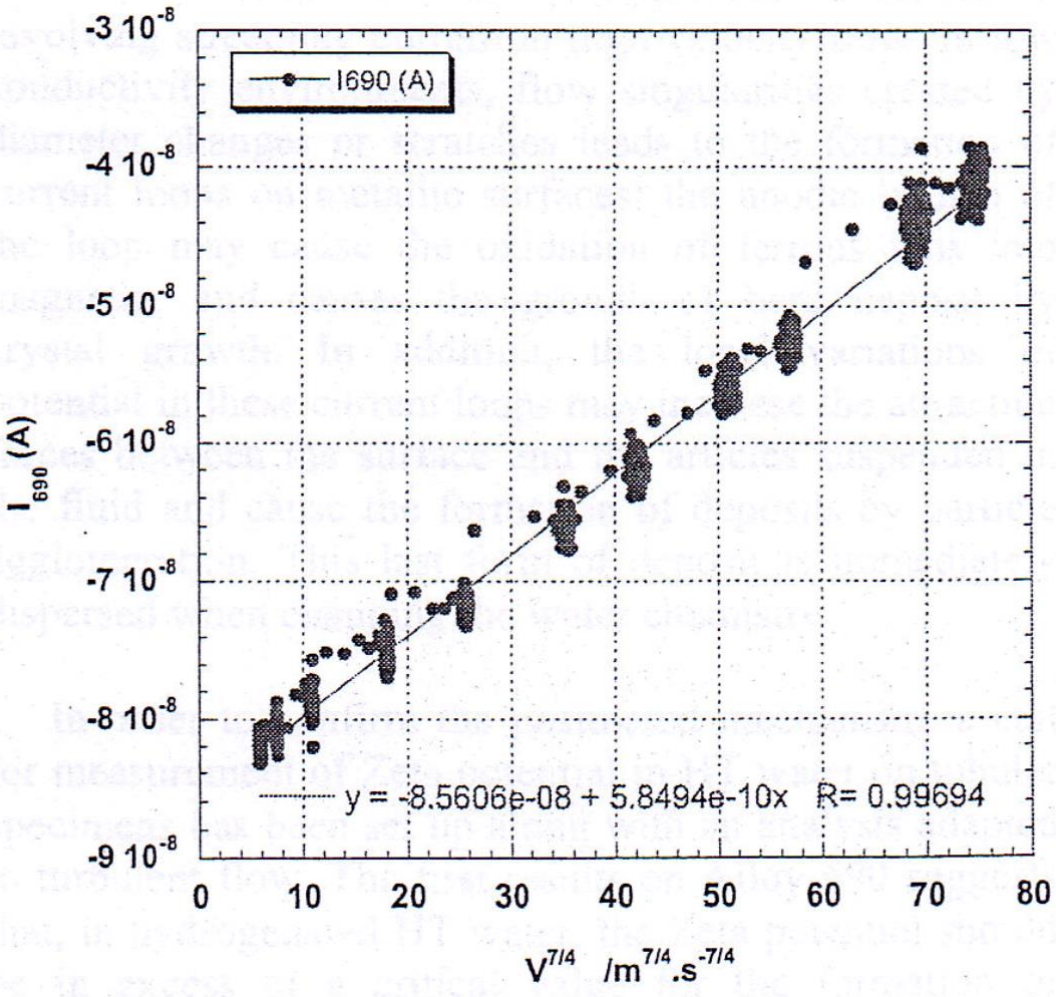

Figure 2.28 - Variation of streaming current with increasing velocity to the power 7/4, across an Alloy 690 surface. Image taken from [19].

2.3.8.2 Electrochemical Characterisation

Further to the deposition rate characterisation work performed by the research group at the Scenini *et al.*, two areas of electrochemical study were also followed. These were:

1) Mapping of the polarization across the solution/surface interface at the transition from wide radius to small internal diameter.
2) Measurement of the equilibrium deposition rate of oxide at a surface in static conditions, due to polarization by an external potentiostat.

Part one of this work made use of a travelling reference electrode, which consisted of a platinum wire inside a sealed oxidised zirconium sheathe, into

which two 300 μm windows were bored on opposite sides of the sheathe. The entire assembly could be moved axially through a 2 mm ID, 304L stainless steel working electrode, allowing the mapping of the potential at any location within the orifice. An image of the travelling electrode can be seen in Figure 2.29.

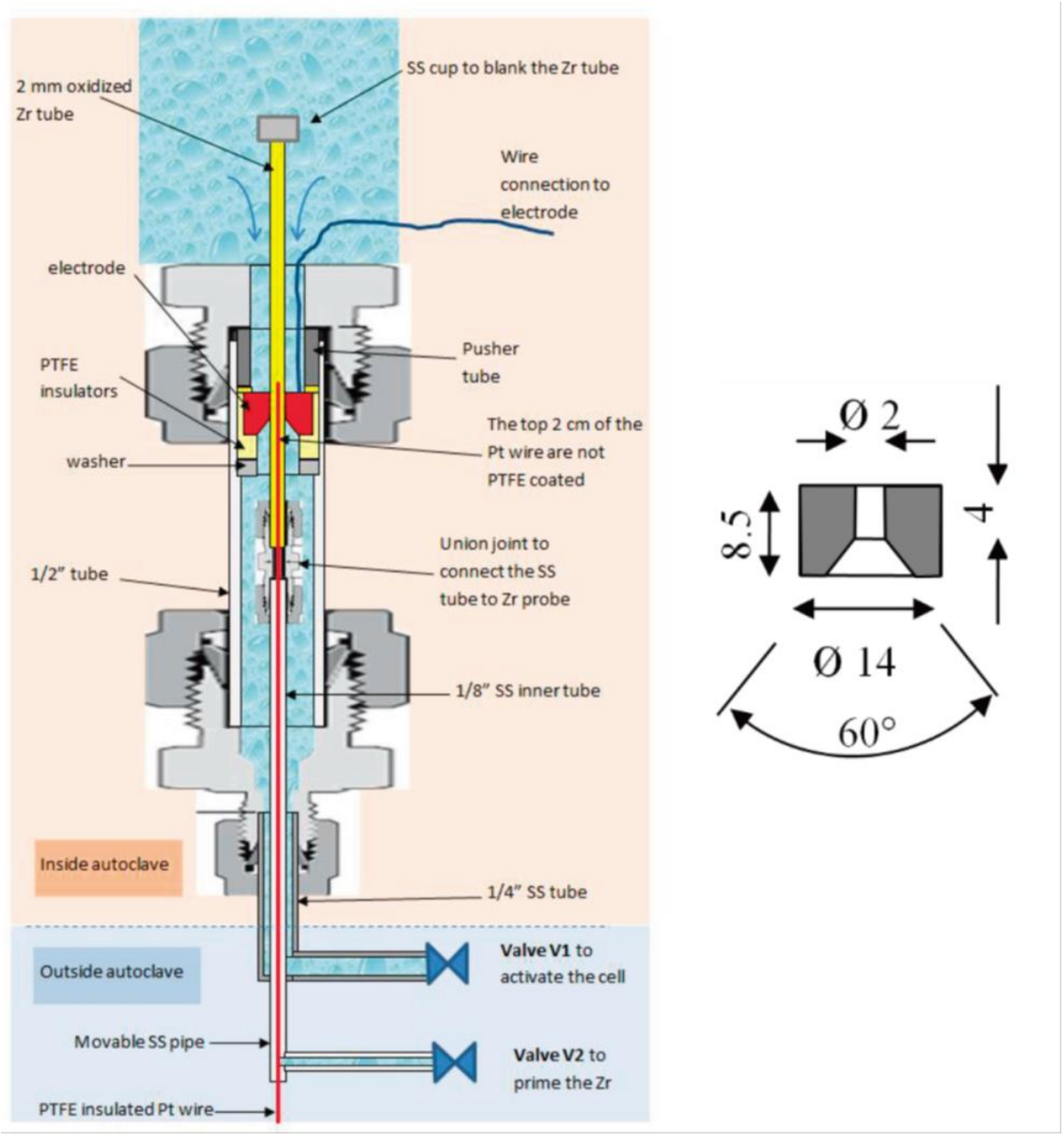

Figure 2.29 - The travelling electrode system used by researchers at the University of Manchester for mapping of potential through the annulus of a 2mm orifice. The orifice itself is coloured red in the left hand image, and geometry of the orifice is detailed in the on the right hand side. Image taken from [115].

During high temperature testing, it was found that reproducible curves could be obtained for potential. The probe was translated through the annulus of the

orifice in a stepwise fashion, moving 0.25 mm at each step, with a dwell time of 30 seconds at each location. The resulting plot (see Figure 2.30) shows the presence of two anodic peaks, corresponding to approximately 1 mm inside the orifice, and 1 mm beyond the beginning of the flared section of the orifice. The presence of these pronounced negative potentials is consistent with the expected anodic wall currents, which are believed to be responsible for the deposition.

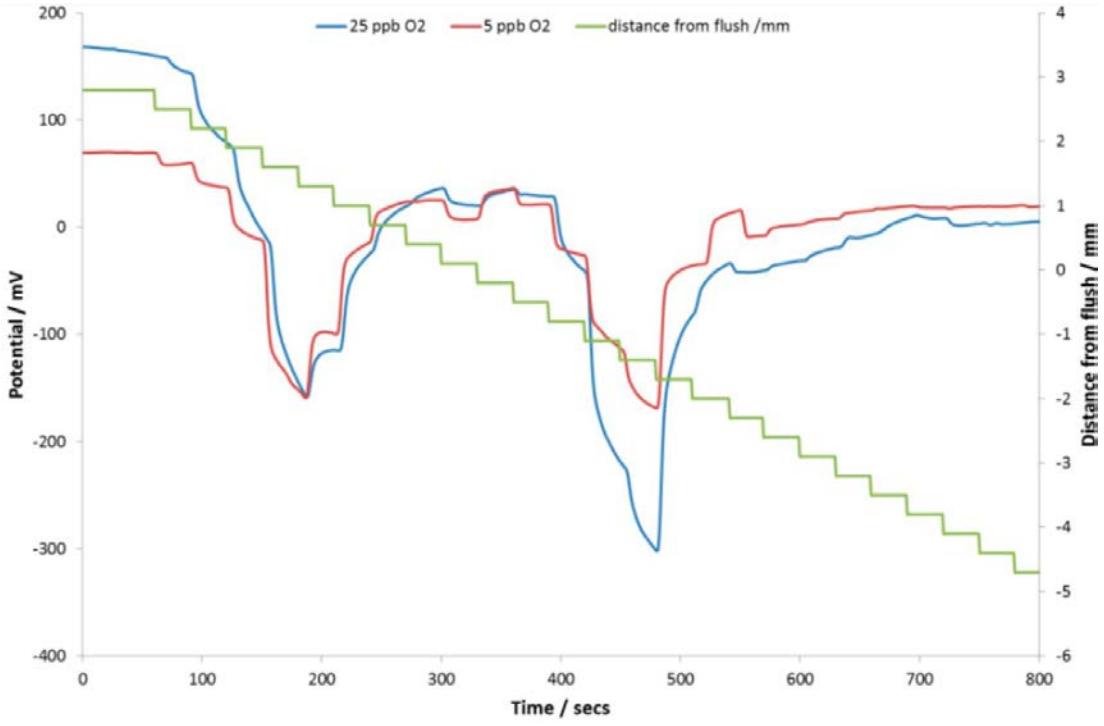

Figure 2.30 - The measured variation in electrode potential relative the traveling Pt reference electrode. The red and blue potential curves show the electrode potential (with respect to the Pt reference electrode) for dissolved oxygen concentrations of 5 and 25 ppb. The green curve represents the motion of the working electrode window as it was stepped through the restriction – 0 mm marks the point at which the electrode is flush with the top of the restriction, shown in Figure 2.29. Image taken from [115]

The second part of this work focused on the electrokinetic deposition mechanism's stipulation that the wall currents must be able support Faradaic reactions occurring at the wall, provide spatial separation of the anodic and cathodic ends of the current loop and allow for the oxidation of Fe^{2+} to Fe^{3+} ions (see section 2.3.6). The test performed was intended to artificially simulate the type of electrochemical current distribution that is seen at a location of flow

acceleration, while decoupling the deposition from the effect of flow, and determine the build-up rate of metal oxides under such conditions.

This was done by anodically polarizing a plate of 304L stainless steel while at temperature and under a no forced-convection flow (*i.e.*, flow would entirely be due to thermal convection). A cylindrical cathode near the surface was used to create an uneven current distribution across the surface. The lack of a reference electrode for this system meant that the polarization potential had to be calculated from the applied cell potential. A drawing of the concept is shown in Figure 2.31.

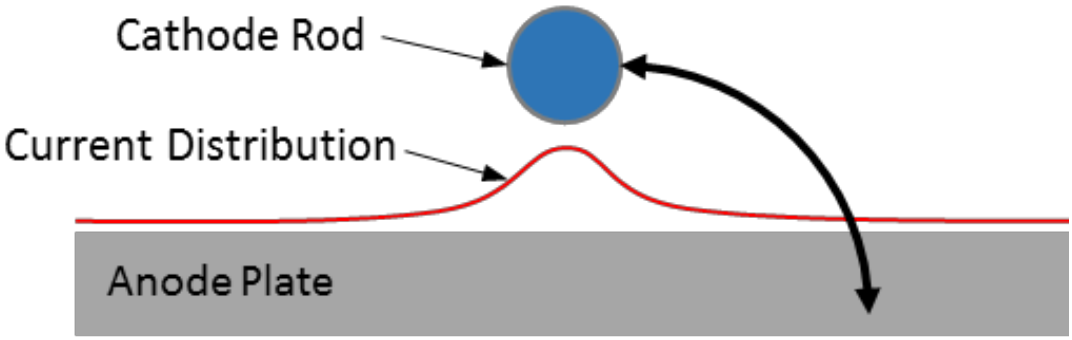

Figure 2.31 - A sketch of the artificial polarization experimental set up. An anodically polarized plate is held in close proximity to a cylindrical cathode, producing a non-linear current distribution. Image redrawn from [27].

It was observed that this polarization method created three distinct regions, where the optical appearance of the oxide was significantly different (see Figure 2.32), simply labeled "The Black Region", "Region 2" and "Region 3".

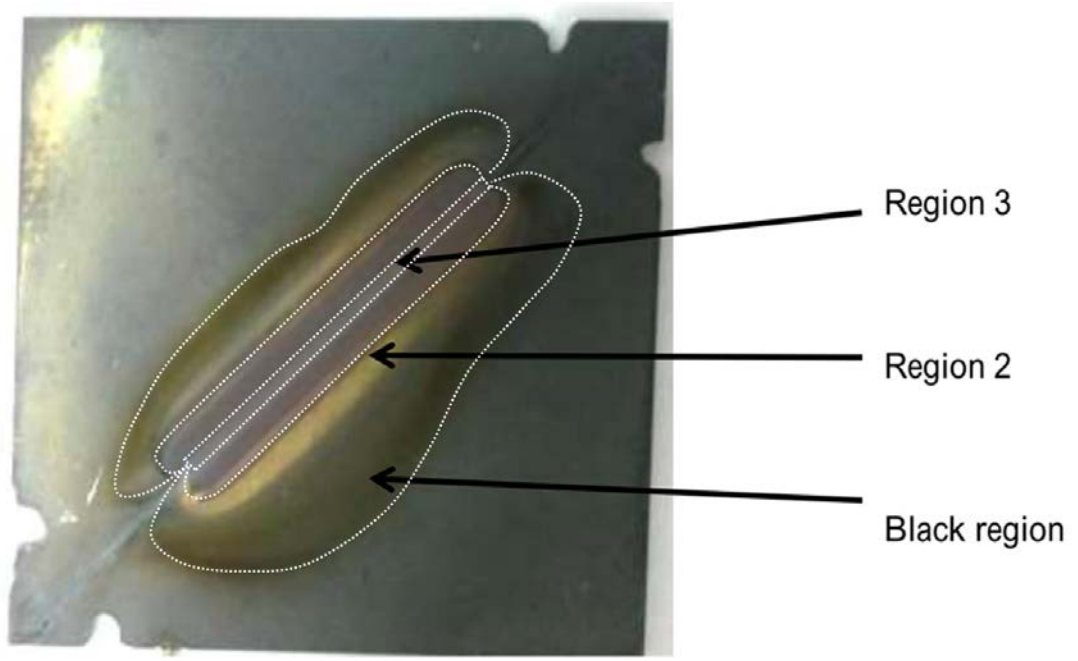

Figure 2.32 - Image of the flat plate, anodically polarized sample, upon which three regions of interest have been specified. The areas have been annotated with white boundary lines for clarity [27].

Region 3, the area of supposed highest current density was found to consist exclusively of small (<2 μm) crystals, while regions 2 and the "black region" were quite similar, with a near-continuous coverage of small (< 100nm) crystallites interspersed with larger particles (1 – 5 μm). Finally, the BUR calculated by this method was found to be ~30 $nm.hr^{-1}$, significantly different from the BUR of 1 – 6 $\mu m.hr^{-1}$ calculated for experiments where the mass of deposition was calculated from actual deposits formed on micro-orifices. The difference is believed to be a result of poor mass transport within the static experiment, compared to that of the flowing experiments, which reduces the presence of dissolved ions for the deposition process and limits oxide formation to the few ions in the locale and those derived from the alloy. However it is noted that increasing the ionic strength of the electrolyte would reduce the size of the EDL, and thus the relative magnitude of the electrokinetic phenomena at work, leading to potentially inconclusive results [27].

2.3.9 Summary of Electrokinetically Stimulated Deposition

The mechanism of electrokinetically stimulated deposition has been discussed alongside evidence of its occurrence in simulated primary and secondary coolant. The mechanism set forward by Robertson [16] and built upon by McGurk [17] provides a theoretical foundation.

Evidence put forward by Woolsey *et al.* [24] and Morris and Woolsey [25] has shown the production of deposition at flow restrictions is possible under boiler chemistry conditions, and that flow induced deposition is not completely controlled by mass transfer, suggesting a contribution from electrokinetically stimulated deposition is possible. It was also found that very low levels of oxygen in the feed water could inhibit deposition.

Measurements performed by the AREVA research group show that the electrochemical potential of the system is a major factor in the deposition mechanism [18–23]. Upon reanalysis of these results, McGurk [17] identified that the ζ-potential value is reliant upon the electrochemical potential of the system.

Work performed by the research group at the University of Manchester [26,27] has shown the presence of variable electrochemical potential in the annulus of an orifice consistent with the anodic wall currents, which are believed to be responsible for driving deposition reactions at the surface. Further to this, a series of tests using various sized micro-orifices has been used to calculate the build-up rate of deposit on the surface under given chemical conditions [27].

2.4 Corrosion Kinetics of Stainless Steels in High Temperature Water

The corrosion kinetics of stainless steel in high temperature water conditions is an area of great interest for the nuclear industry. The rate of deterioration of coolant facing materials is a critical factor in reactor design, and while many materials can ultimately fail through material cracking, the oxidation and formation of the passive layer on the surface is still of primary interest. In modern reactors, nickel based alloys have become widely used due to their excellent resistance to general corrosion and especially to stress corrosion cracking (SCC) mechanisms that have plagued other materials, however stainless steels have remained in service due to their excellent balance of corrosion resistance and cost.

Stainless steels are well known for their capacity to form a passivating oxide layer on their surface, which protects the underlying metal from rapid oxidation [116–118]. In atmospheric conditions the passivation layer consist of chromia (Cr_2O_3) and is on the order of a few nanometers thick [117]. In high temperature water conditions, such as those found in a reactor coolant system chromia is not thermodynamically stable [119,120] and instead a double layer consisting of an iron rich outer layer consisting of non-stoichiometric magnetite (Fe_3O_4) and nickel ferrite ($NiFe_2O_4$), and an chromium rich inner layer consisting of non-stoichiometric chromite ($FeCr_2O_4$) [31,90,119,120]. Each layer grows through a different mechanism; the inner layer grows through a solid state diffusion mechanism, which the outer layer grows through a dissolution/redeposition mechanism [29,90,119]. This is discussed further in section 2.4.2.

While the chemical composition of the passive film is well characterised and consistent across most variations of high temperature reactor coolant, the rate of film formation is only partially dependent on the material itself. The coolant facing surface condition prior to exposure has been seen to have an enormous

effect on the rate of film formation due to many factors such as changes in surface chemistry, physical roughness, removal of metallic inclusions, and relaxation of residual surface strain [28,31,36,90,121,122].

There are numerous methods of surface finishing intended to improve a surfaces performance in a given environment; of interest to this work are mechanical and electrochemical polishing. Electrochemical polishing, more often referred to as electropolishing, is a process which preferentially removes the peaks of outstanding scratches on the surface of a metal, reducing the roughness of the surface. The advantages of electropolishing over other techniques (such as mechanical polishing) is that the electropolished materials corrode substantially slower, and the oxide films grow in a more compact manner [28,31]. The consequences of this are that there is a reduced inventory of dissolved metal ions in the coolant, and more importantly from a safety perspective, the smaller volume of the oxide layer reduces the total quantities of dangerous radioactive nuclei (such as Co-60) that can become incorporated into the structure of the layer.

2.4.1 **Physical Metallurgy of Austenitic Stainless Steel**

Stainless steel is an iron-chromium based corrosion resistant alloy used in virtually every modern industry, with an expanding list of grades based on different alloying elements in varying proportions. Different grades are used in different industries; some grades will find extensive in civil engineering, where high strength is required in conjunction with reasonable corrosion resistance, while other grades find use in marine construction, where resistance to corrosion under salt water and high humidity conditions is the critical requirement. Stainless steels' resistance to corrosion stretches across a wide range of conditions, and the various alloy grades have inevitably found use in both fossil fired and nuclear power stations.

There are three traditionally recognized types of single-phase stainless steel, based on the crystal phase adopted by the bulk of the material: ferritic, martensitic, and austenitic. Another two classes of stainless steel exist; duplex stainless steels and precipitation hardening stainless steels. Due to the corrosion resistance of austentic grades of stainless steel they are widely used in coolant-facing applications in nuclear reactors and will be discussed below. The other classes have no bearing on this work and will not be discussed any further.

Austenitic stainless steels are those whose bulk phase is a face-centered cubic structure. This particular phase is can be produced in pure iron or low alloy steel, however it is only stable while the material is above 910 °C [123,124] so the structure much be stabilised through the addition of nickel, a so-called 'austenite stabilizer' [123–125]. Austenitic stainless steels exhibit a superior corrosion resistance to both ferritic and martensitic stainless steels, can be easily machined and can strengthened through work-hardening. The steels used in nuclear reactors for coolant facing materials are exclusively austenitic stainless steels, and so this literature review will focus on this particular class of material from here on in.[117,126–130].

The formation of the protective chromium oxide passivation layer is a product of stainless steels comparatively high chromium content; by specification, any truly 'stainless' steel must contain an approximate minimum of 10.5% chromium [117]. However, with chromium content below 12% the steel can activate in acid solutions with a wide range of potentials. If a reduced chromium content appears at the grain boundaries, despite a higher level in the base solid solution the metal is liable to be intergranularly attacked [131,132], thus it is normally found that stainless steels in contact with highly corrosive environments are specified with a minimum of 12-13% Cr . While increases in the chromium content often show improvement to the corrosion resistance,

very few alloy grades contain greater than 30% Cr, due to the brittleness of such alloys [130]. The absolute minimum 10.5% Cr content allows the formation of the Cr_2O_3 layer at the metal surface, which is able to self-heal if damaged through reaction of chromium and atmospheric oxygen or water.

This work is focused on the corrosion behaviour of grade 316L stainless steel; a low carbon austenitic stainless steel with the following composition specification:

Table 2.1 - The composition of grade 316L stainless steel [117].

Element	Concentration
Iron	Balance (61.64 - 72.00 %)
Chromium	16.00 – 18.00 %
Nickel	10.00 – 14.00 %
Molybdenum	2.00 – 3.00 %
Manganese	2.00 % Max
Silicon	0.75 % Max
Phosphorus	0.45 % Max
Nitrogen	0.10 % Max
Sulphur	0.03 % Max
Carbon	0.03 % Max

Grade 316L stainless steel is widely used, and total production of type 316L is second only in production the ubiquitous grade 304 [117]. Grade 304 and 316L differ slightly in their nickel and chromium contents, but the major difference is the addition of molybdenum to 316L. Molybdenum-bearing stainless steels are generally more resistant to localised corrosion, and also possess greater mechanical strength at elevated temperature.

2.4.2 Corrosion Mechanisms of Stainless Steel under Primary PWR Coolant Conditions

Stainless steels owe their excellent corrosion resistance to the thin layer of Cr_2O_3 on the surface of the metal. This layer is on the order of nanometres thick, containing no pores (which further increases the corrosion resistance as water

and air can only access the underlying metal by diffusion along grain boundaries), and is formed spontaneously on contact with oxygen making it self-repairing [29,119,133].

In liquid water above ~150 °C, the oxide film takes a significantly different form, a duplex layer type structure. The outer layer of this duplex layer is a mixed spinel of magnetite (Fe_3O_4) and nickel ferrite ($NiFe_2O_4$), while the inner layer retains something of its chromium rich origins as Cr_2O_3, forming non-stoichiometric iron chromite ($FeCr_2O_4$) [28–31,35,36,90,119,121,122,133–151].

The inner, iron chromite, layer is formed by the solid state growth mechanism, closely related to the reaction that forms Cr_2O_3 under atmospheric conditions [119]. The inner layer is described by various researchers as being either poorly crystallised [136], or amorphous [145], and the composition to be non-stoichiometric with a thickness of between 50 – 200 nm [29,90,145]. Oxides of an amorphous nature contain point defects, rather than two or three dimensional defects such as grain boundaries which can act as transport channels for ions in the alloy [29,152]. Point defects limit the transport of ions through the layer, which explains the corrosion resistance of the chromium-rich inner layer [29,152,153].

The outer layer is formed by the dissolution of metal ions in the coolant, the partial mixing of the corrosion products from the local surface with those from elsewhere, followed by precipitation at the surface due to localised saturation of the corrosion product in the coolant, forming the coarse crystals which make up the outer layer [29,90,154,155]. While the outer layer has little to do with corrosion protection, in a nuclear reactor the outer layer and its constituents are responsible for much of the radiation field outside of the core. The outer layer may also provide some protection to the inner layer by preventing the direct chemical attack of oxidising species, which might result in transpassive corrosion and dissolution of the inner layer [156].

The formation of the oxide layer has been modelled through the use of the Point Defect Model (PDM) [157–161] and the Mixed Conduction Model (MCM) [154–156]. In both of these models, the growth of the inner layer proceeds via a series of reactions which describe generation of normal cation positions, injection of oxygen vacancies at the alloy/film interface, transport of vacancies through the alloy and film via a diffusion/migration mechanism, and finally their consumption at the film/electrolyte interface [156]. The outer layer is modelled in by considering the production of cation vacancies at the film/electrolyte interface and their transport through the film to the alloy/film interface where they are consumed [156]. The released cations are those which redeposit on the surface to form the outer layer. The simplified reaction pathways used for the MCM are shown in Figure 2.33, and the model has been shown to accurately describe the composition of oxide layers formed, based on the reaction parameters [156].

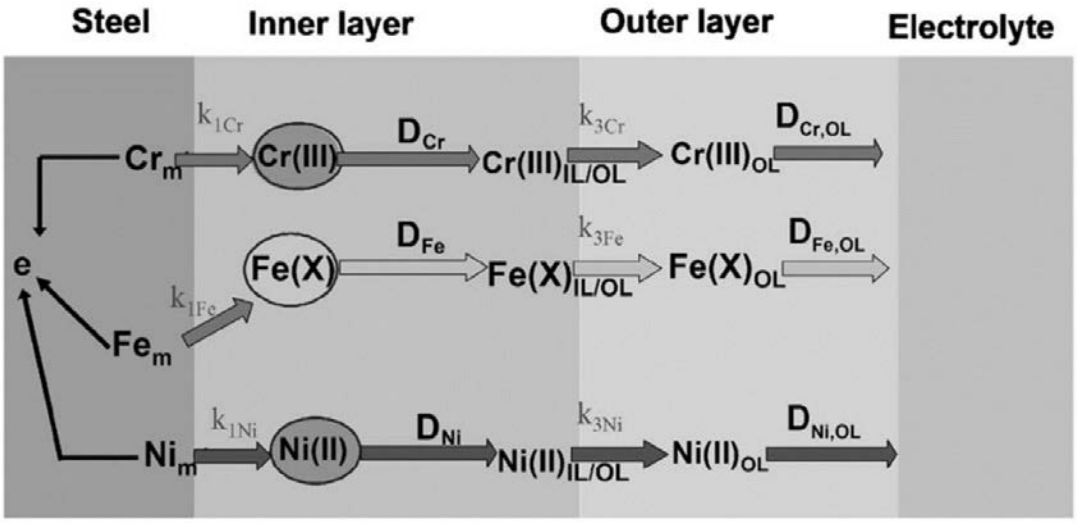

Figure 2.33 - The simplified reaction pathways for stainless steel according to the Mixed-Conduction-Model. Image taken from [156].

2.4.2.1 Corrosion Kinetics

The growth of the oxide layer can proceed in a way described by several different oxide growth laws. The most common of these are the linear,

parabolic, and logarithmic rate laws, which are drawn demonstrated schematically in Figure 2.34.

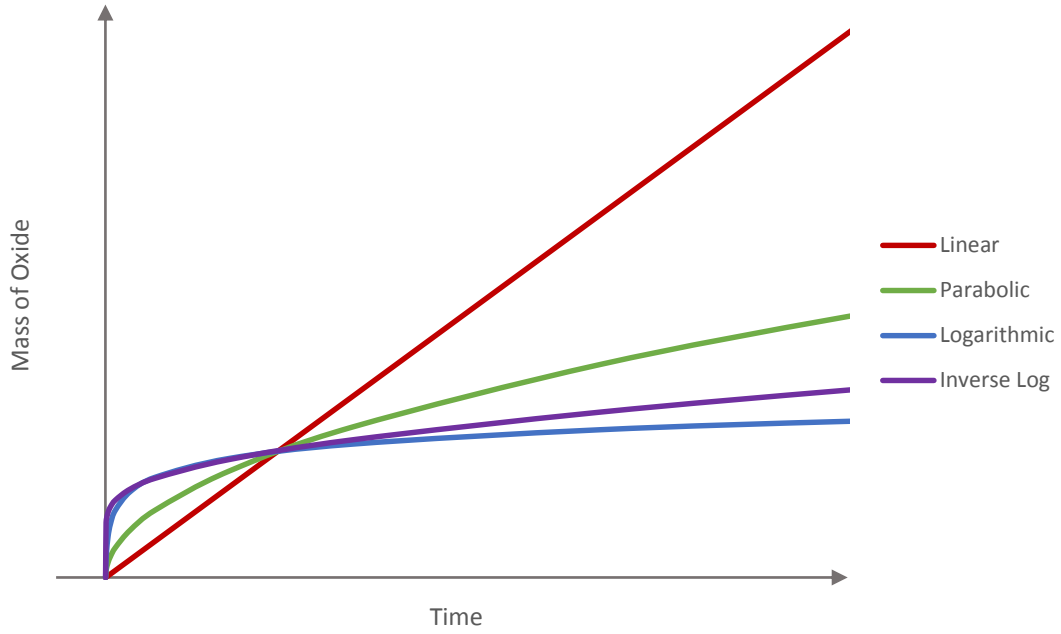

Figure 2.34 - Schematic drawing of the variation of oxide mass with time according to the linear, parabolic, logarithmic and inverse logarithmic rate laws.

Linear corrosion kinetics occur in circumstances where either metal is being dissolved into the corrosive media, or where an adherent oxide is formed which is not protective; under such conditions the metal is eventually entirely consumed [162]. When the mass of oxidised alloy ($\boldsymbol{W_l}$) is plotted against time, kinetics are described by the general formula:

$$W_l = k_l . t$$

Equation 2.32

where $\boldsymbol{k_l}$ is the linear corrosion rate constant and $\boldsymbol{t}$ is time. These conditions are not descriptive of the behaviour of coolant loop alloys, which are specified (along with the chemistry of the system) to form protective oxide films; as such linear corrosion kinetics can be ignored for the purposes of this review.

Parabolic corrosion kinetics are observed in systems where the rate of corrosion is limited by the diffusion of either the metal species or oxidising agent [119]

and is derived from Fick's law of corrosion [162,163], derived for high temperature oxidation conditions by Wagner [164]. The kinetics are described by the general formula:

$$W_p^2 = k_p . t$$

Equation 2.33

where $\boldsymbol{W_p}$ is the mass of alloy oxidised, and $\boldsymbol{k_p}$ is the parabolic corrosion rate constant. The parabolic corrosion rate is directly related to the diffusion processes through:

$$k_p = 2 . D . A . c$$

Equation 2.34

Where $\boldsymbol{D}$ and $\boldsymbol{c}$ are the diffusion coefficient and concentration difference of the rate limiting species respectively, and $\boldsymbol{A}$ is the proportion of cross sectional area available for diffusion [119,133]. Parabolic kinetics describe the formation of the oxide in a uniform layer across a surface [162,163].

Finally, logarithmic (and inverse logarithmic) kinetics describe the very rapid formation of the protective oxide in islands across the surface, which quickly join together into a continuous layer, limiting further corrosion. The logarithmic law is based on the assumption that the rate limiting step is adsorption of the oxidising agent to the metal surface [162]. In gases, oxygen molecules striking the surface either rebound or adsorb onto the surface. Adsorbed molecules react to form metal oxides, which form in the islands previously mentioned. Even when a continuous oxide layer is formed, the adsorbed oxygen will still withdraw electrons from the oxide lattice, creating a strong electric field across the oxide [162,165]. The electric field, coupled with the quantum mechanical tunnelling of electrons across the oxide film, can increase the rate of migration of mobile ionic species. While the oxide film is thin, the rate of migration is high, however as the film thickens the field strength is reduced; above 100 nm, quantum tunnelling of electrons across the

film is also greatly reduced [162,165]. Consequently, the reaction rates fall to very low levels, limiting the file thickness.

The logarithmic corrosion rate is described by the general formula:

$$W_{log} = k_{log}.\log(t + t_0) + A$$

Equation 2.35

Where $\boldsymbol{W_{log}}$ is the mass of alloy oxidised, $\boldsymbol{k_{log}}$ is the logarithmic corrosion constant, and $\boldsymbol{t_0}$ and $\boldsymbol{A}$ are constants; all constants are temperature dependent. The progression of oxide formation can be seen in Figure 2.34.

The inverse logarithmic rate law general formula is:

$$^1/_{W_{il}} = B - k_{il}.log.t$$

Equation 2.36

Where $\boldsymbol{W_{il}}$ is the mass of alloy oxidised, $\boldsymbol{k_{il}}$ the inverse logarithmic rate constant and B is a temperature dependant constant. The progression of inverse log kinetics, which are similar to logarithmic kinetics but presenting a more prolonged continuation of corrosion, can be seen schematically in Figure 2.34.

Researchers working on this area of corrosion rate have observed the corrosion rates of stainless steel generally follow a parabolic, or close to parabolic, rate law [28,31,90,119]. In circumstances where thin films have been formed over a short period of time researchers have fitted their data to a cubic power [166,167], which represent an intermediate between parabolic and inverse logarithmic kinetics [90]. The cubic law can be seen as a combination of the parabolic and inverse logarithmic corrosion law, where the initial rapid corrosion follows the inverse log law but changes to the parabolic law as time continues [163]. Depending on the time resolution of a data set, it can be difficult to determine exactly what point the changeover occurs, cubic kinetics can be used to describe the overall situation.

2.4.3 Relevant Metal Surface Finishing Methods

2.4.3.1 Mechanically Finished Surface Treatments

There is an extensive list of mechanical finishing methods, and an exhaustive review is beyond the scope of this document. Of interest to this review are grinding and polishing, two closely related metal finishing procedures.

Grinding is generally defined as the process of removing small quantities of a metal's surface using hard abrasive materials, which leaves small uniform scratches on a sample. The grinding process introduces cold work into the surface of the material, improving the strength and hardness characteristics of the metal surface, and removes small imperfections in the surface such as pits and large scratches. When used to remove metallic inclusions in the surface which could establish local galvanic couples, or by reducing the total surface area of the exposed material, grinding can impart some resistance to corrosion [121].

Polishing of a metal is closely related to the grinding, as it is the continuation of the grinding technique but with ever-finer abrasive until the grinding scratches left by the abrasive media are no longer visible to the naked eye. This will give a dull but reflective surface, which can be made brighter by buffing, a technique, which uses loose abrasive particles on the wheel rather than the static, glued-in-place abrasives used for polishing. Both techniques produce a particular distribution of roughness levels on a surface and are believed to impart improved corrosion resistance, however this assumption has been recently challenged for high temperature applications [36].

2.4.3.2 Electropolished Surfaces

Electropolishing (also called Electrolytic Polishing) is the removal of material from a surface by use of an electrical current and a corrosive electrolyte bath. The work piece is attached to the cathode (+ve) of a power supply, and the

anode (-ve) is connected to a polishing implement, which can take many possible forms, for instance a wand or a plate held at constant distance from the work piece.

Electropolishing preferentially removes material at sharp features and surface discontinuities, the final surface will be close to being perfectly smooth, as this condition would be the point where surface charge density is uniform at all locations.

The electropolishing process can be used on many metals and while it is often used to produce an aesthetically pleasing appearance on structural components, it can be used as a metallographic preparation method [168] and to passivate stainless steels [169].

2.4.4 Methods used for the Study of Corrosion Rates and Metal Oxide Film Morphologies of Stainless Steels under PWR Coolant Conditions

The corrosion of reactor relevant metals in simulated coolant has been studied since before the introduction of water cooled nuclear power plants and in this time, the experimental methods of measuring the corrosion rate and studying the corrosion film formed have changed significantly in practically every respect. This section collates the methods used to study corrosion rate and film morphology in environments that are chemically similar to those of the primary RCS of a PWR.

The first method discussed is the gas collection tube method described in section 2.4.4.1, where measurements of the quantity of hydrogen gas produced during the corrosion of a stainless steel test piece were made during a prolonged test. Other methods directly analysed coupons of material exposed to conditions of interest by either destructive or nondestructive means; these are described in section 2.4.4.2 where a high velocity flowing loop was used to

create hydrodynamic as well as chemical conditions of interest, and in section 2.4.4.3 where low flow rate systems were used to create the chemical environment of interest for a period of 10,000 hours for some of the longest term tests carried out.

2.4.4.1 Gas Collection Tube

The gas collection tube method, used by Warzee *et al.* [121], makes use of the reaction of metals with highly pure, oxygen-free water to produce hydrogen gas which is able to diffuse through metals.

The capsules used in the study were made by taking cylinders of the material of interest, and sealing them with caps which were electron beam welded to the ends of the tube. A filling tube present in one cap was used to fill the capsule with high purity, oxygen-free water before being pinched off and spot welded to seal. A schematic of such a capsule can be seen in Figure 2.35. These finished capsules were placed in a gas collection rig, which was made of Pyrex glass. The capsules were then individually heated by electric furnace.

By virtue of hydrogen's ability to diffuse through thin metal walls, the gas could move from within the sealed capsule to the glass collection rig. The gases present in the glass rig were periodically swept into a gas chromatograph which was used to determine the total volume of hydrogen present from which the corrosion rate of the material was calculated. Test duration was generally 1,000 hours. No information is given as to the capability of this method after this time; it is likely that with careful operation this method could continue to give corrosion information for a longer period. However, it should be noted that due to the enclosed nature of the system, the chemistry of the water in the capsule will change as the components of the stainless steel form their various metal oxides.

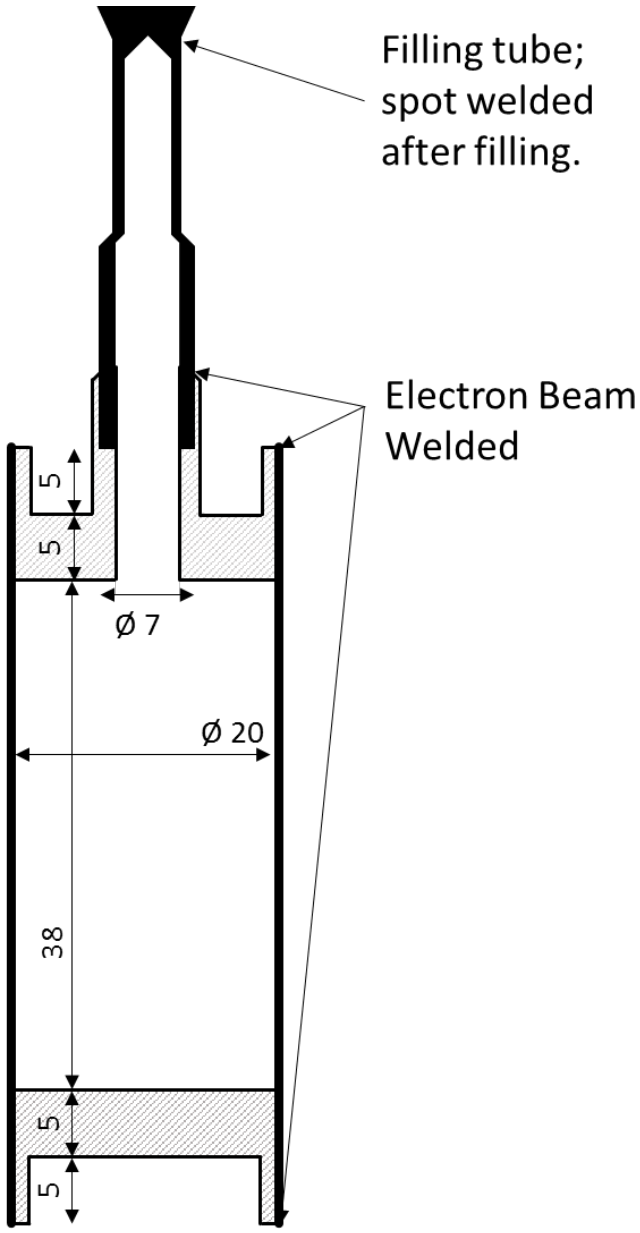

Figure 2.35 - A hydrogen diffusion capsule, as used by Warzee *et al.* for determination of corrosion rates. Image redrawn from [121].

2.4.4.2 High Velocity Flowing Rig

Measurements of corrosion rate and film morphology were made by Lister *et al.* using a rig designed to produce high flow velocities across test coupons inserted into the rig [145].

The system described by Lister *et al.* moved prepared feed water (lithiated and saturated with hydrogen at room temperature) through a heated 1 litre 304 stainless steel autoclave filled with carbon steel and Alloy 600 turnings. These

turnings were used to ensure that the water was entirely saturated with corrosion products before reaching the first sample.

After the first sample, the water would pass through a zirconium oxide bed to remove the corrosion products before the water contacted the second sample, after which the water passed out of the system. It should be noted that the system was composed entirely of Zircaloy-2 and titanium between the zirconium oxide bed, until shortly after the second coupon chamber; this was to prevent pick up of any corrosion products from the materials of construction before the water came into contact with the second coupon.

In contrast to the system used by Warzee *et al.,* this flowing system afforded Lister's research group excellent control of the system chemistry, which can be assumed to be constant as it is refreshed so quickly; the system's flow rate is quoted as being between 17.5 and 17.7 $ml.s^{-1}$ (1050 – 1062 $ml.min^{-1}$). A diagram of the system can be seen in Figure 2.36.

It should be noted that while this rig design could potentially have produced data for long-term tests, the system was only designed to hold 2 coupons for a time of 168 hours. This decision appears to have been made so that the focus of the experiment was on studying the morphology of the oxide and developing a mathematical model of the oxide formation, rather than producing definitive data for the corrosion rate of the materials.

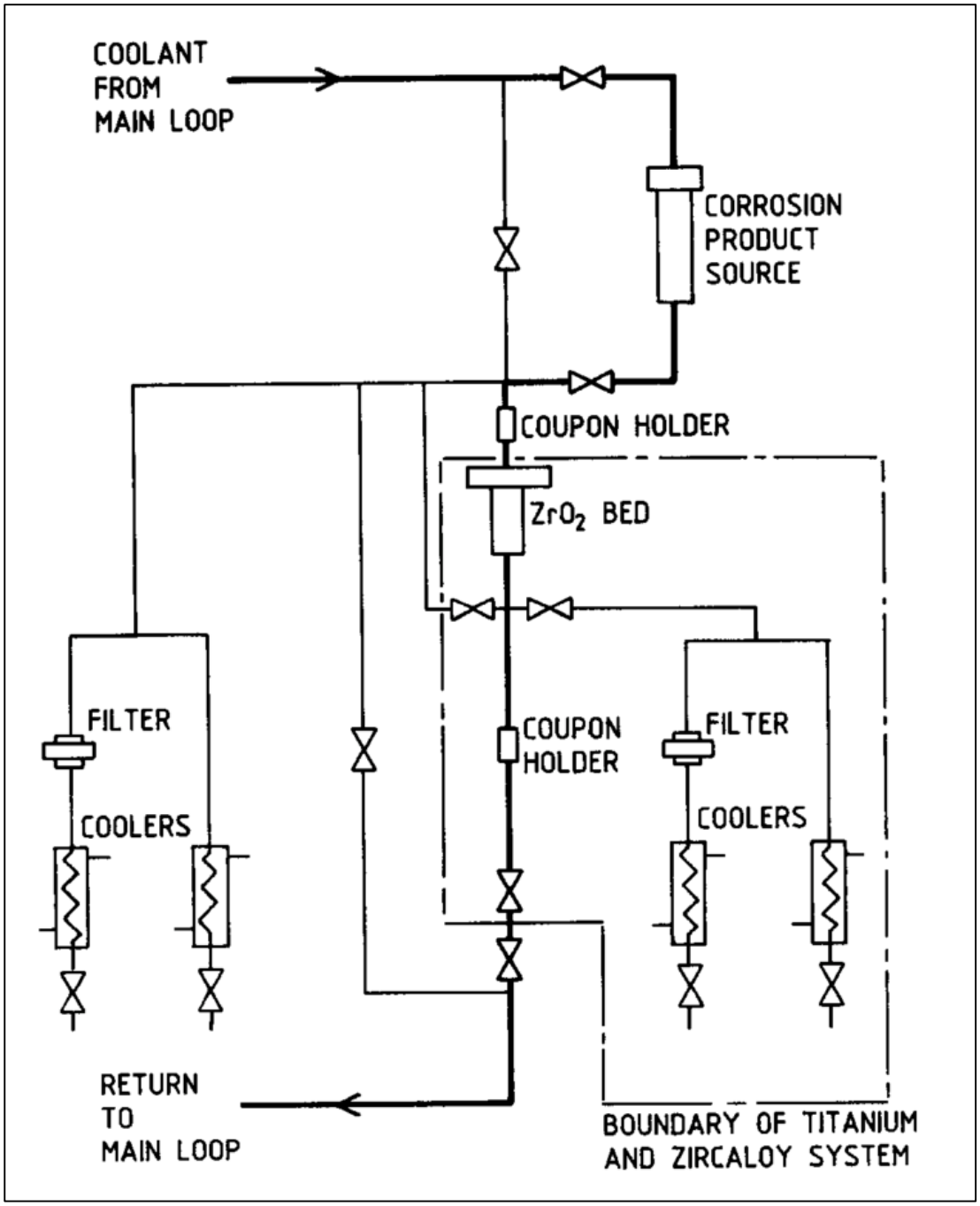

Figure 2.36 - The high flow rate corrosion loop, as used by Lister *et al.* [90].

2.4.4.3 Flowing Autoclave System

The first attempt to produce long-term exposure data was performed by Ziemniak *et al.* [28,31], who made use of a flowing autoclave type system. These tests appear to be the only set that have been performed for greater than 2,000 hours, stretching up to 10,000 hours for each of the two tests reported for 304L stainless steel [28,31], alongside tests of nickel alloys [170].

The system is possibly the most simple of the types reviewed here; it consists of a single batch type autoclave made from type 347 stainless steel, which was connected to a high pressure, low flow rate pump.

Deionized water was prepared in the feed tanks by sparging with hydrogen gas to reach a dissolved hydrogen concentration of 45 $scm^3.kg^{-1}$ (4.2 ppm), and by adding enough ammonia to reach a $pH_{(260\,°C)}$ of 6.70, the exact amount added was not reported, nor is the pH of the water prior to the additions.

Once prepared, the feed water is moved from the holding tanks to the autoclave by a pump, at a flow rate of 10 $ml.min^{-1}$, where it was heated to 260 °C. Test samples of 304L stainless steel, polished on one side with diamond grit paste to a mirror finish (0.15 μm arithmetic average roughness) in the first test [31], and electropolished after this treatment for the second test [28], were mounted inside the autoclave vessel in sets that were to be removed after time periods of 1,000, 2,000, 5,000, 8,000 and 10,000 hours. After one set of samples had been removed, another set would be inserted to take its place in the autoclave and maintain a constant corroding surface area.

Samples were analysed using gravimetric descaling analysis, scanning electron microscopy and energy dispersive X-ray spectroscopy (SEM-EDX), X-ray photoelectron spectroscopy with argon ion milling (XPS-AIM) and grazing incident X-ray diffraction (GIXRD).

This test system appears to have been built to ensure that chemistry is kept as constant as possible, however the flow rate was significantly lower than that reported by Lister *et al.* [90]. Other corrosion investigations conducted by this group include the studies of Alloy 600 and 690 [33,171]. The results of this work are presented in section 2.4.1.

2.4.5 Recent Studies

Recently, Cissé *et al.* [36] have studied the effect of significantly different surface finishes on the corrosion mechanism of 304 stainless steel and make the claim that the corrosion film of a polished piece of stainless steel will have a thicker oxide layer formed at the surface than a similar specimen with a mechanically ground surface would have. This is based on the concept of the recrystallized area beneath the surface; that is, the region beneath the surface where the grain size is significantly smaller than the grain sizes found in the bulk metal. Using Transmission Electron Microscopy (TEM), Cissé *et al.* were able to successfully show a difference between the recrystallized area in a polished sample and in a mechanically ground sample. The polished metal possessed a thin recrystallized area, while the ground sample had a significantly thicker region. The impact of this observation is that the rate of ion diffusion is directly related to the length of the diffusion path along grain boundaries; a larger recrystallized area presents a much longer diffusion pathway for ions (assuming that their diffusion follows a random-walk), resulting in a thinner oxide layer on the surface of metals finished by grinding than samples finished by polishing. A schematic of this concept can be seen in Figure 2.37.

2.4.1 Review of Published Corrosion Rates

The medium term corrosion rate of grade 304 stainless steel has been studied by Warzee *et al.* [121,136] and Ziemniak *et al.*. [28,31]. Other studies have studied corrosion of stainless steel in PWR-type environments, however, most are focused on studying the microstructure of the oxide films formed over a few hundred hours, largely ignoring the corrosion rate over a realistic time scale [30,35,122,150,151].

4

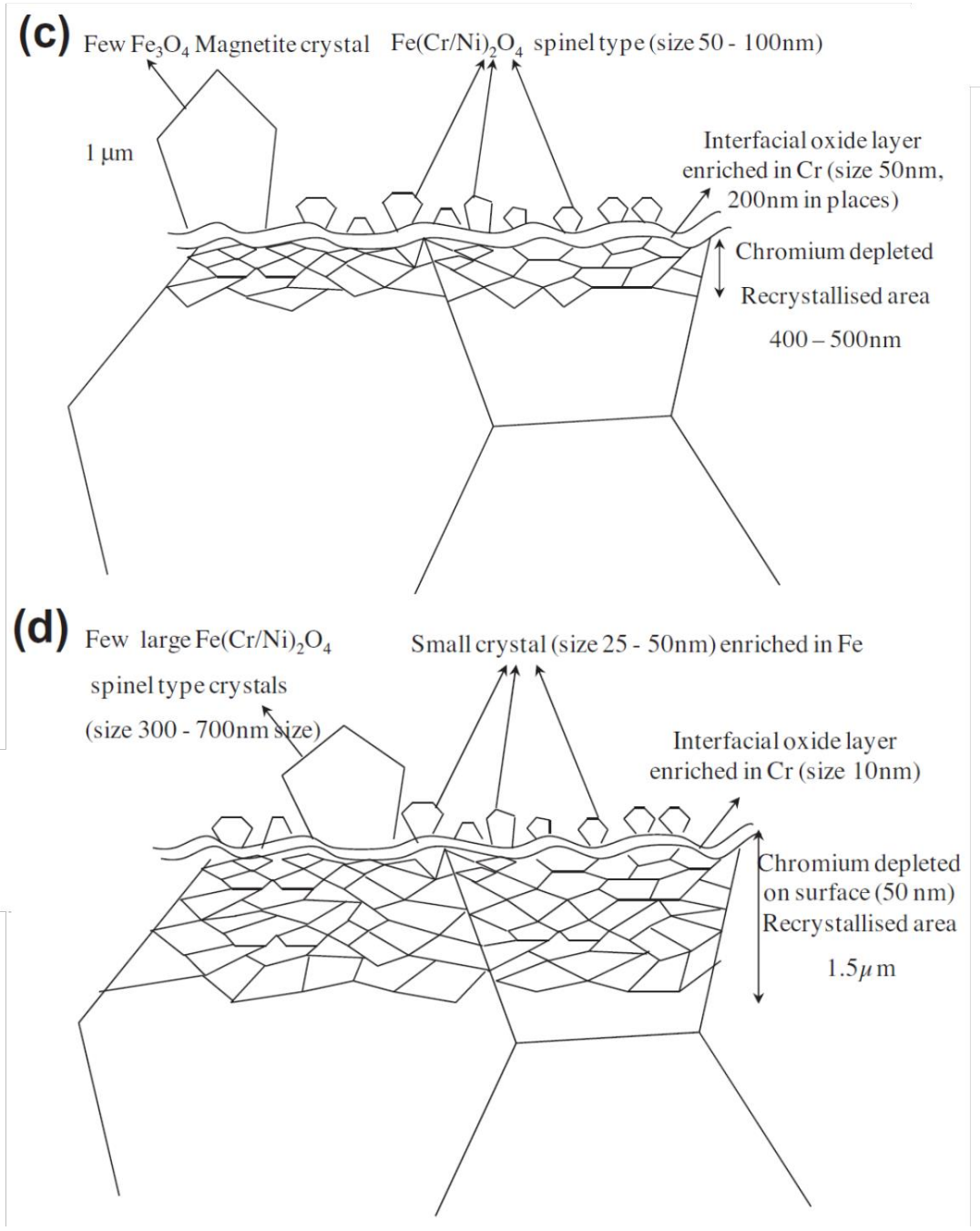

Figure 2.37 - The recrystallization areas of a polished sample (c) and a ground sample (d), along with approximate orders of magnitude for the size of various regions of the oxide layers. Image taken from [36].

For experiments in pure water at 300 °C, Warzee *et al.* give their corrosion kinetics as being linear, with a rate constant of 0.008 $mg.dm^{-2}.hr^{-1}$ for machined samples, and 0.003 $mg.dm^{-2}.hr^{-1}$ for their electropolished samples. The data

from their work is plotted in Figure 2.38, and it can be seen that the shape of the curve is not well described by linear kinetics.

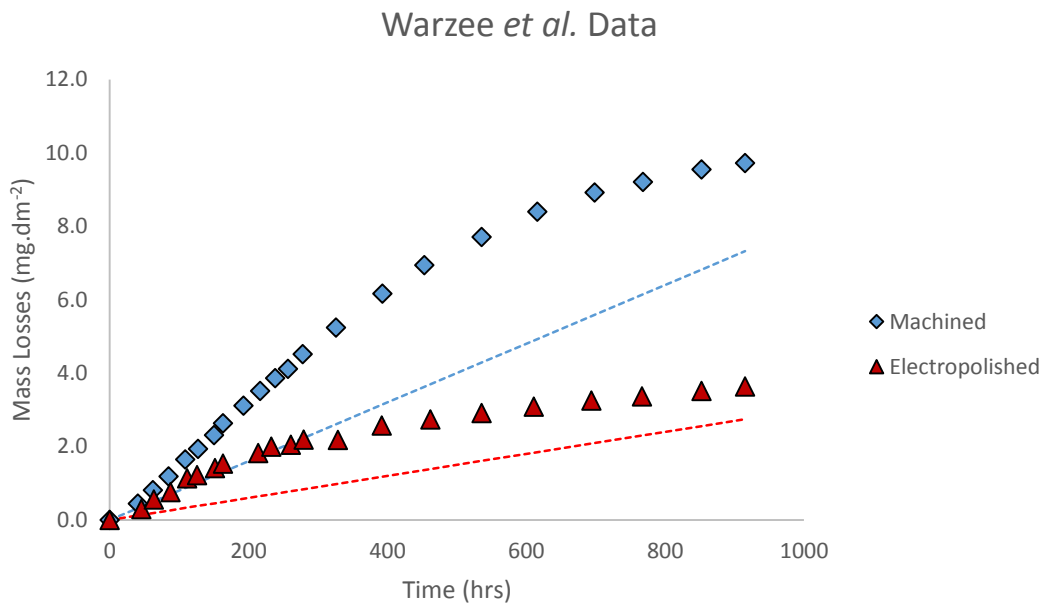

Figure 2.38 - Data of Warzee *et al.* in pure water at 300 °C [121]. **The dotted lines drawn on represent the curve calculated from the stated corrosion rates of 0.008 mg.dm^{-2}.hr^{-1} for machined samples and 0.003 mg.dm^{-2}.hr^{-1} for electropolished samples.**

If the data is plotted against the parabolic and logarithmic kinetics described in section 2.4.2.1, an improved fit can be obtained. In Figure 2.39, the data is plotted against the square root of time, and reasonable fits are found, giving a parabolic corrosion rate constant (k_p) of 0.2968 mg.dm^{-2}.hr$^{-1/2}$ for machined surfaces and 0.1216 mg.dm^{-2}.hr$^{-1/2}$ for electropolished surfaces. The fit is not perfect, however it is an improvement over the linear fit initially put forward. In Figure 2.40, the data is plotted against the logarithm of t+1, however the fit from this process is not an improvement on linear kinetics originally quoted by Warzee.

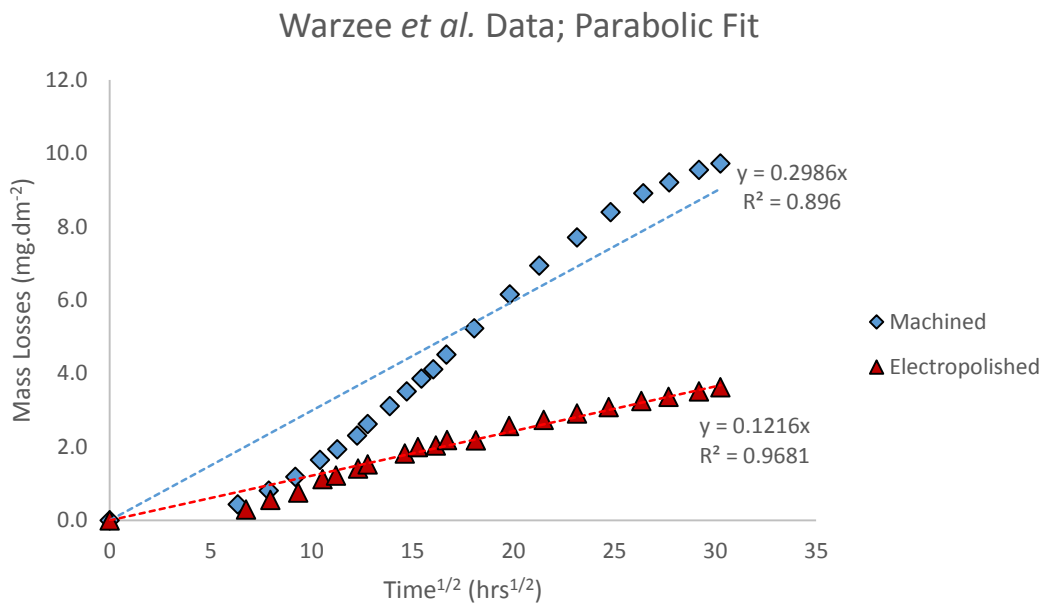

Figure 2.39 - Warzee *et al.* data [121], plotted as a function of square route of time for parabolic kinetics. The gradient of the fit line is the parabolic corrosion constant k_p. This model improves the fit over the suggested linear kinetics.

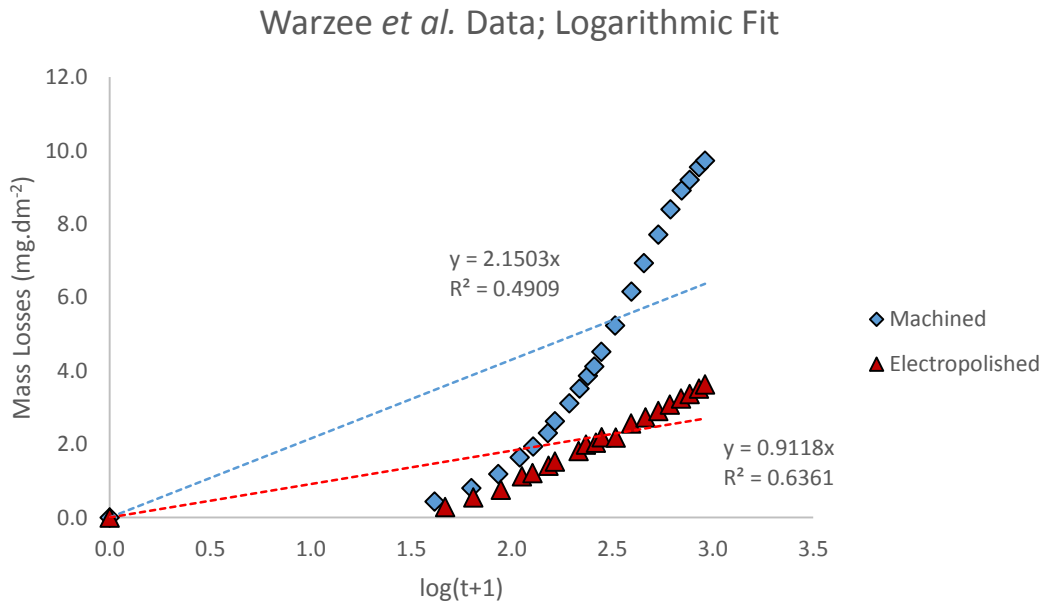

Figure 2.40 – Warzee *et al.* data [121], plotted against the logarithm of (t+1). The calculated fits for logarithmic kinetics are not an improvement over the linear kinetics originally states by Warzee,

In the work of Ziemniak *et al.* [28,31] the corrosion kinetics are reported to be parabolic in nature, and the rate of corrosion described by Equation 2.33 in section 2.4.2.1. By obtaining the parabolic corrosion coeffiecent (k_p) of a material, it is possible to compare it directly to other literature results.

Ziemniak *et al.* present k_p data directly deduced from gravimetric analysis and XPS-AIM data, giving the parabolic corrosion constant as 1.16 ± 0.054 mg.dm^{-2}.hr$^{-1/2}$ for mechanically polished samples, and 0.336 ± 0.117 mg.dm^{-2}.hr$^{-1/2}$ for electropolished samples. This data can be seen plotted in Figure 2.41.

It is clear that the two data sets are widely different, however it is likely to be a function of the differing exposure conditions; Warzee's experiments were performed in high purity water at 300°C, while Ziemniak's were performed at 260°C, $pH_{260°C}$ 6.7, and [H_2] of 45 scc.kg^{-1}. There is a common theme between the two data sets in that the electropolished samples performed better than the mechanically finished surfaces by approximately a factor of 3 (3.1 for Warzee, 3.5 for Ziemniak).

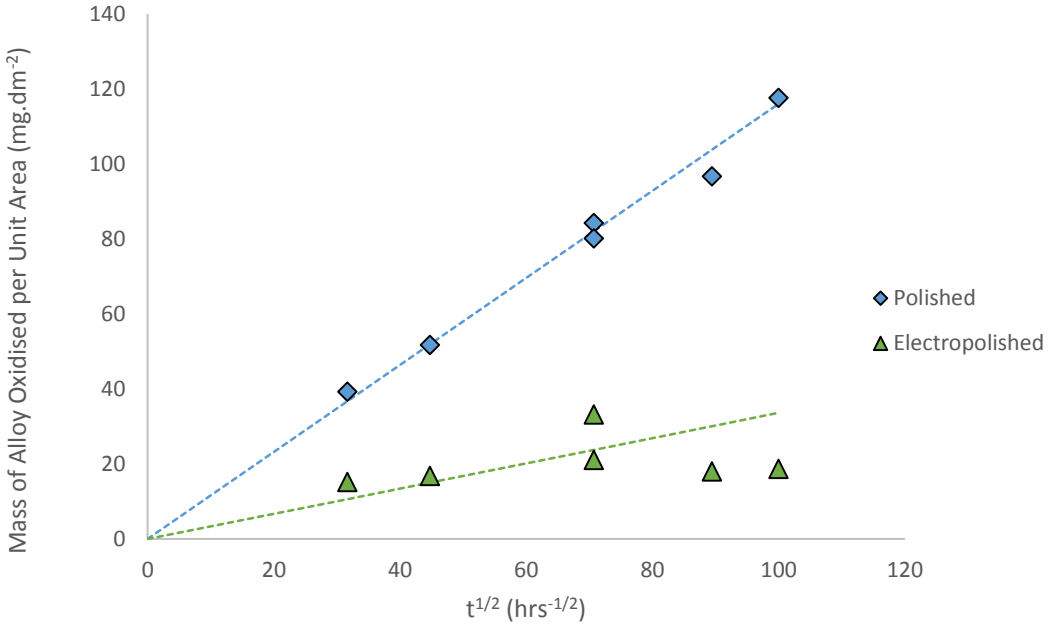

Figure 2.41 - Corrosion data from the work of Ziemniak *et al.* for both mechanically polished and electropolished corrosion specimens (plotted against the square root of time) exposed to water at 260 °C, modified to pH_T of 6.7, with 45 cc.kg^{-1} dissolved hydrogen. Data reproduced from [28,31].

2.4.2 Summary of Corrosion Rates and Release Rates

While a plethora of information regarding the short and medium term (100 – 1,000 hours) growth of oxide films exists [29,90,121,134,135,139,140,143,145,148–151], there is little data in the way of

corrosion rate determination over what could be described as medium to long term (1,000 – 10,000 hours) [28,31,33,171]. While such time scales are still much shorter that that the total life of a reactor, they can provide an excellent basis for corrosion rate prediction. The corrosion rate and the release rate of a material under certain conditions is an important variable for computer modeling of the RCS [5,15,32].

2.5 Metal Oxides and Metal Oxide Solubility of Stainless Steels in High Temperature Water

As discussed in section 2.2, the chemical environment of a PWR's coolant circuit is tightly controlled at an operational $pH_{300\,°C}$ of 7.4. This pH was chosen in a deliberate effort to minimise the total inventory of dissolved metal ions, derived from the formation of the oxide films formed on coolant-facing materials, present in the coolant. The solubility of metal oxides, especially magnetite (Fe_3O_4), have received a great deal of attention in the context of nuclear power coolant chemistry development, however the results produced by researchers have often been contradictory or widely dissimilar. More recent publications have begun to produce consistent results between different research groups, however there is still considerable variation in the available data.

The solubility of metal oxides in aqueous environments is dependent upon both temperature and pH, and so it must be noted here that the definition of pH is such that the scale changes quite significantly with increasing temperature, due to the changing self-ionization constant of water [172].

The benefits of the tight chemistry control are related to the corrosion protection of plant materials, prevention of deposit formation, and radiation field reduction. As discussed in section 2.4, coolant facing metals are protected from rapid corrosion by the formation of a passive metal oxide layer. The

oxides formed are highly insoluble in mildly alkaline aqueous conditions at operational temperature. By controlling pH, and thus the inventory of dissolved material present in the coolant, operators can reduce the quantity of material available for deposition at any location in the plant. One of the most problematic type of deposition that can form in the primary loop is fuel rod deposition, where deposited ions are exposed to the intense neutron flux of the core. The result of this type of deposition can be the activation of nuclei into species such as Co-60.

2.5.1 Corrosion Products of 316L Stainless Steel

2.5.1.1 Magnetite (Fe_3O_4)

Magnetite, Fe_3O_4, (systematic name - Iron (II, III) Oxide) is the main corrosion product of stainless steels under the conditions found in a PWR primary coolant loop [28,31,119,151]. It is a sparingly soluble metal oxide, and represents the extreme case in terms of iron purity for mixed metal oxide spinels.

2.5.1.2 Nickel Ferrite ($NiFe_2O_4$)

Nickel accounts for between 10 and 14% of type 316L stainless steels content, and is often found to be present in the outer layer of oxide films on stainless steel surfaces [28,31,151]. Assuming that a mixed oxide consisting of only nickel and iron were found, it would exist in the form of $(Fe_{1-x}\ Ni_x)\ Fe_2O_4$, also known as non-stoichiometric nickel ferrite.

2.5.1.3 Chromite ($FeCr_2O_4$)

Chromium accounts for 16 to 18% of 316L stainless steels alloy content and much of the alloy's corrosion resistance is attributed to this element. In combination with iron under PWR primary coolant conditions, it will form the oxide Chromite, $FeCr_2O_4$.

Chromite is a normal spinel, a crystal structure where the oxygen ions exist in a face-centered cubic structure which creates a pair of octahedral and one tetrahedral interstitial site per unit cell. In normal spinels, the 2+ ions occupy $1/8^{th}$ of the tetrahedral sites while the 3+ ions occupy half of the octahedral types. Conversely, both magnetite and nickel ferrite are belong to the inverse spinels, where all of the 2+ ions and half of the 3+ ions occupy the octahedral sites while the remaining 3+ ions occupy tetrahedral interstitial sites [173]. The difference in structure means that chromite is immiscible with magnetite and nickel ferrite in solid solution, forcing them to exist in distinct spatial locations [28,31].

2.5.1.4 Mixed Metal Oxides of Fe, Ni and Cr

The cases discussed in the above sections (*i.e.*, Sections 2.5.1.1, 2.5.1.2, and 2.5.1.3) are stoichiometrically pure. As both nickel and chromium are present in the alloy, they are also present in the oxides formed by corrosion. The metal oxide layer consists of a duplex layer; the inner layer is a chromium rich layer, while the outer layer is rich in iron [28,31,35,90,119,140,143,150,151].

The formula for the inner and outer layer composition were determined by Ziemniak *et al.*, where the composition of the inner (chromium rich) and outer layer (iron rich) were given as $(Ni_{0.2}\ Fe_{0.8})\ (Cr_{0.7}\ Fe_{0.3})_2\ O_4$, and $(Ni_{0.2}\ Fe_{0.8})\ (Fe_{0.95}\ Cr_{0.05})_2\ O_4$ respectively [28,31].

2.5.2 Solubility of Metal Oxides in PWR Coolant

Ionic salts, such as the metal oxides discussed in section 2.5.1, are held together by strong ionic bonds between ions of opposite charge. In order for an ion to become dissolved in an aqueous media, the bonds in the ionic crystal must be broken and the hydrogen bonding network of water must become disrupted to allow the dissolved ion to become associated with water molecules. Ionic salts which are 'soluble' are more stable when associated with water molecules than when they are in an ordered crystal structure; *i.e.*, it is more energetically

favourable to exist in solution that in a solid crystal. Conversely, 'insoluble' (or 'sparingly soluble') salts are those where the crystal lattice is more energetically favourable, ions are found in solution due to a heavily weighted equilibrium reaction which favours the solid lattice [173].

2.5.2.1 Production and Dissolution of Magnetite

Magnetite, and other reactor relevant oxides discussed in section 2.5.1, are generally considered to be insoluble in water. This cause of this insolubility (or stability in solid state) has been determined by measurement of the bond lengths in the structure of magnetite to be 1.88 Å for the iron (III)/oxygen bond, and 2.03 Å for the iron (II)/oxygen bond [40].

It is useful to consider first to generation of magnetite from an iron hydroxide solution, as discussed by Bohnsack [40], before contemplating the dissolution and solubility, as previous authors have attributed the solubility behaviour to the normally irreversible Schikorr reaction.

At low temperature, the formation of magnetite requires the presence of both ferrous (Fe^{2+}) and ferric (Fe^{3+}) ions in solution. This is problematic, as any dissolved ferric ions will rapidly condense from solution to form a hydrated oxide [40,174]. In order to provide the required two thirds of metal ions for the magnetite, a redox step must take place to oxidise ferrous ions into ferric ion. However, below 100 °C, this step is blocked due to the requirement that a special steric configuration be present to allow the simultaneous formation of molecular hydrogen during the redox reaction. In low temperature environments, this difficulty is overcome through a different reaction pathway; ferrous hydroxide is partially oxidised by small amounts of molecular oxygen, which undergo a polycondensation reaction to form lepidocrocite (γFeOOH). In combination with the remaining ferrous hydroxide, the γFeOOH precipitates magnetite:

$$\gamma FeOOH + Fe(OH)_2 \rightarrow H_2Fe_3O_5 \rightarrow Fe_3O_4 + H_2O$$

Equation 2.37

Above 150 °C, the production of magnetite through the condensation of ferrous hydroxide and oxidation by water, without the need for molecular oxygen is possible, though this process only becomes spontaneous above 200 °C, where steric configurations for the reaction are favourable [174]. The reaction, better known as the Schikorr reaction [175] is a two-step process, where the condensation step (Equation 2.38) and the oxidation step (Equation 2.39) occur simultaneously:

$$Fe(OH)^+ + Fe(OH)_2 \rightarrow Fe^+OFeOH + H_2O \rightarrow (FeO)_n + H^+$$

Equation 2.38

$$3FeO + H_2O \rightarrow Fe_3O_4 + H_2$$

Equation 2.39

The spontaneity of the Schikorr reaction also suggests resistance to the reverse reaction. The redox reaction, shown in Equation 2.39, is essentially irreversible due to the required steric configuration for the reaction to occur; that is to say, redox reaction forms a hydrogen molecule which is highly mobile and unlikely to return to the surface for a reverse reaction to occur. Bohnsack [40] postulates that the dissolution mechanism instead follows the reverse of Equation 2.37 (the production of magnetite through the condensation of γFeOOH and $Fe(OH)_2$).

2.5.3 Experimental Determination of Metal Oxide Concentration in High Temperature Water

2.5.3.1 Preparation of Solubilised Metal Oxide in High Temperature, pH Controlled Water

The solubility of magnetite in aqueous systems at elevated temperature has been an area of interest to geologists before the introduction of water cooled

nuclear power plants, however few studies from the time are directly relevant as newer studies with greater accuracy and more accurate analysis methods has superseded them.

Experimental methods used for the preparation of soluble metal oxide solutions have evolved significantly since these experiments were first carried out. This section brings together the experimental methods used during tests where the system chemistry was close to primary side PWR coolant.

2.5.3.1.1 Static Bomb/Autoclave type systems

Static bombs are the simplest form of pressure vessel available; they normally consist of a container with either one or two ports located at each end of the vessel. The bomb is normally filled with the reactants in question and pressurised, with or without heat.

There are numerous possible difficulties with this method; the system's chemistry is not constant during the experiment, rapid decompression of the sample is likely to cause phase changes of the fluid, leading to inaccuracies in the final data, there is a limit to the volume of sample that can be taken, and the lack of agitation means that diffusion and thermal convection are the only means by which the fluid can reach equilibrium with the solid metal oxide.

Such systems were used in the mid-20th century to determine the solubility of magnetite by experimenters such as Holser & Schneer [45] who, to their credit, did everything within their power to reduce the possibility of contamination and re-precipitation, in order to collect a representative sample. Their experiments were however limited by the analysis technology of the time, and many of the samples relevant to the conditions found in a PWR contained such low levels of iron they have been listed as below the detection limit.

Similarly, Helz [49] used static bomb type systems for his experiments. He describes the use of a series of 1.1 litre stainless steel vessels used for lower

temperature tests (150 – 275 °C) with baked-on Teflon liners to control corrosion of the vessel. Higher temperature tests (275 – 500 °C) were performed using smaller vessels of 0.5 litre volume, made from Vascojet 1000, a high strength steel; these vessels were not Teflon lined due to Teflon's thermal decomposition at temperatures above ~280 °C, instead the systems were allowed to oxidise to produce a magnetite passivation layer.

Each vessel was loaded with synthetic magnetite (and other solid phases being studied), evacuated overnight in a furnace, and then charged with the aqueous chemistry of interest. The vessels could accommodate the addition of other gases such as H_2 and CO_2. Once all components were present in the system, it would be sealed and placed in a furnace at the chosen temperature.

2.5.3.1.2 **Stirred Autoclave**

A stirred or mechanically agitated autoclave is a relatively simple system, requiring the experimenter to fill the vessel with the sample and the test solution, heat to the desired temperature and sample. Such systems are prone to the same problems as the static bomb type autoclave systems discussed in section 2.5.3.2.1, with the exception that the system is now agitated mechanically, providing forced convection of the fluid in a predictable pattern.

These limitations were accepted by Styrikovich *et al.* [50] in their experimental work. They made use of a 12Cr1MoV steel autoclave lined with titanium to prevent construction materials from interfering with the final analysis, and mounted the autoclave in a frame which allowed it to swing at 45 ° to vertical, with a period of 1 minute (see Figure 2.42).

While this method overcame the agitation and equilibrium hurdle, the sampling method used (pressurised expulsion) was still likely to cause spurious results.

2.5.3.1.3 **Flowing Autoclave/Plug Flow Systems**

Plug-flow type systems represent the state of the art for performing solubility measurements of metal oxides during both short and long term experiments. The development of this system type solved the problems of constant water chemistry, the condition of the extracted sample, sample volume and time resolution. During a long term test, an experimenter could take representative samples of water which could show a change in the equilibrium solubility of a particular metal oxide, something that could not be done with any previous method as discussed here.

This method has been used extensively since it was first introduced by Sweeton & Baes [48] (see Figure 2.43). The system they used consisted of an atmosphere controlled feed water tank feeding a high pressure diaphragm pump set up. The flow was driven by oil from a piston pump, using a pressure relief valve to control the pressure developed by the diaphragm pump, and thus control the system flow rate. Flow rate was measured using a mercury manometer.

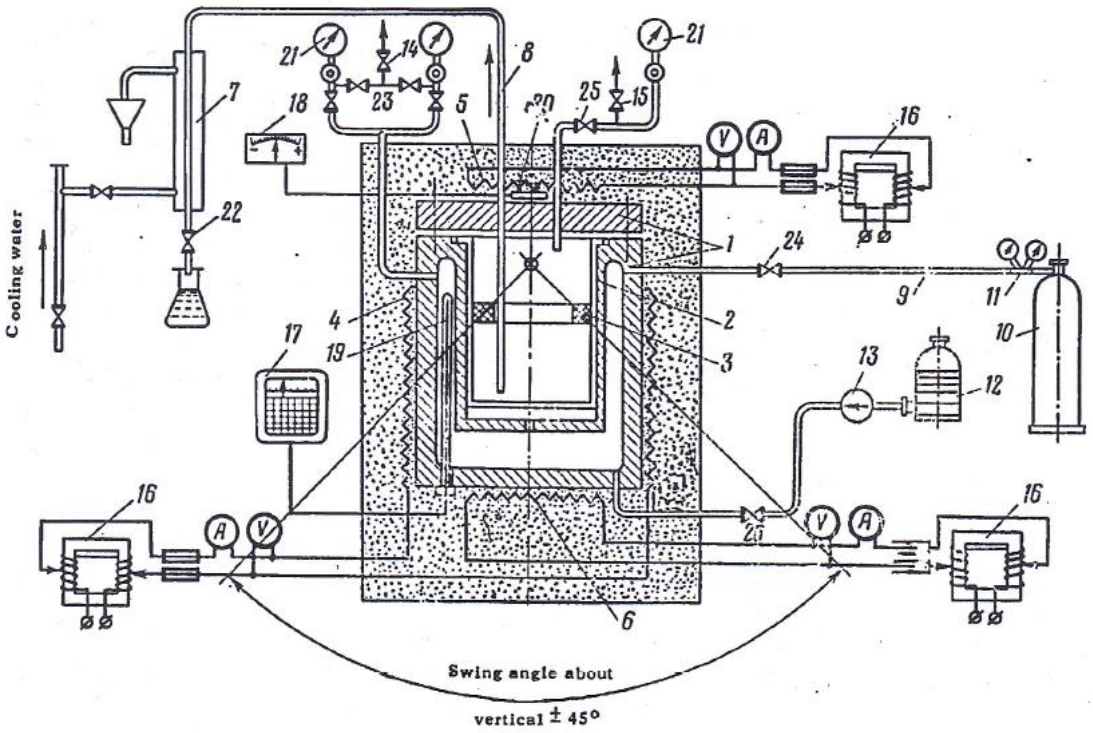

FIG. 1. Experimental apparatus for studying the solubility of iron corrosion products in water at high temperature, in a reducing medium.

1 – body of autoclave; *2* – experimental chamber; *3* – packing with magnetite; *4* – main electrical heater; *5* – auxiliary electrical heater (bottom); *6* – auxiliary electrical heater (top); *7* – condenser; *8* – sampling tube; *9* – pressure relieving tube; *10* – cylinder of argon; *11* – pressure reducing valve; *12* – bottle with distillate; *13* – makeup pump; *14, 15* – air vents; *16* – variable ratio transformer; *17* – electronic potentiometric recorder; *18* – zero galvanometer; *19* – thermocouple; *20* – differential thermocouple; *21* – pressure gauge; *22-26* – valves.

Figure 2.42 - The autoclave system used by Styrikovich *et al.* to measure the solubility of magnetite in hydrothermal conditions. Image taken from [176].

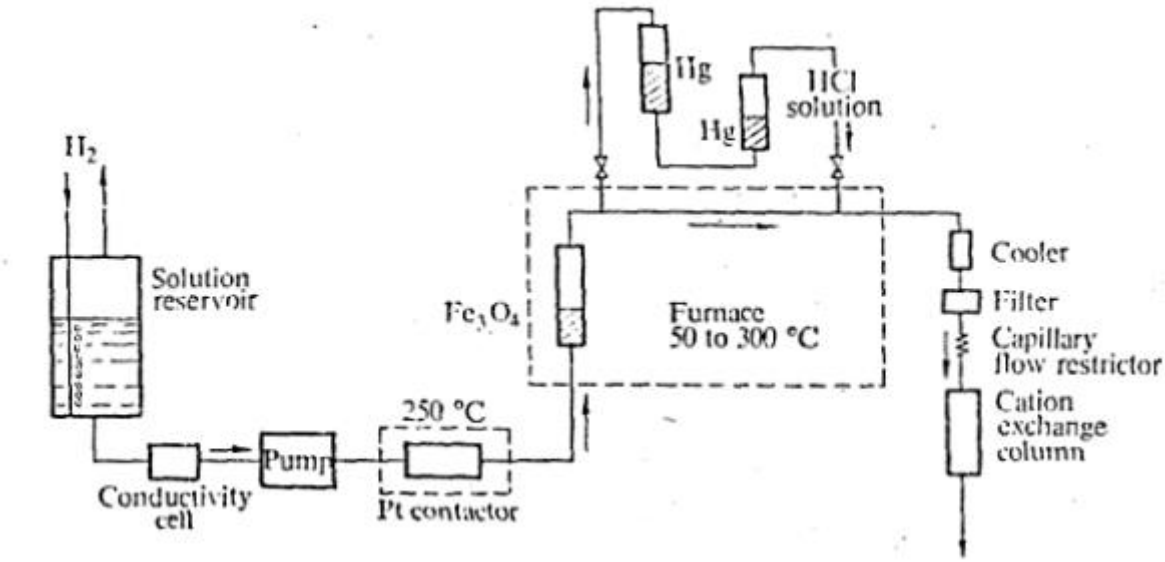

Figure 2.43 - The system used by Sweeton and Baes for measurement of the solubility of magnetite at temperatures up to 300 °C [48].

The pump fed water into the pipe system built from platinum capillary tubing, copper and gold plated stainless steel vessels in high temperature regions, and glass in low temperature/pressure regions. A platinum contactor, consisting of 6 layers of platinum gauze separated by copper spacers, was used to catalyze a reaction between dissolved H_2 and O_2. Sampling was performed using an ion exchange column, fitted after a length of capillary tube which was used to regulate system pressure.

Following Sweeton and Baes' work, Kanert *et al*. [177] produced a more simplified system, where the flow was directly controlled by the feed of a metering pump. Test solution was pumped into a small titanium test cell where a sample of radioactive magnetite and a sample of isotopically stable magnetite were placed one after the other, respectively. The solubility was calculated by measuring the level of radioactivity transferred from the active magnetite to the inactive magnetite through use of a NaI(T1) crystal scintillator, and comparing the detected levels to standards. The apparatus can be seen in Figure 2.44 and Figure 2.45.

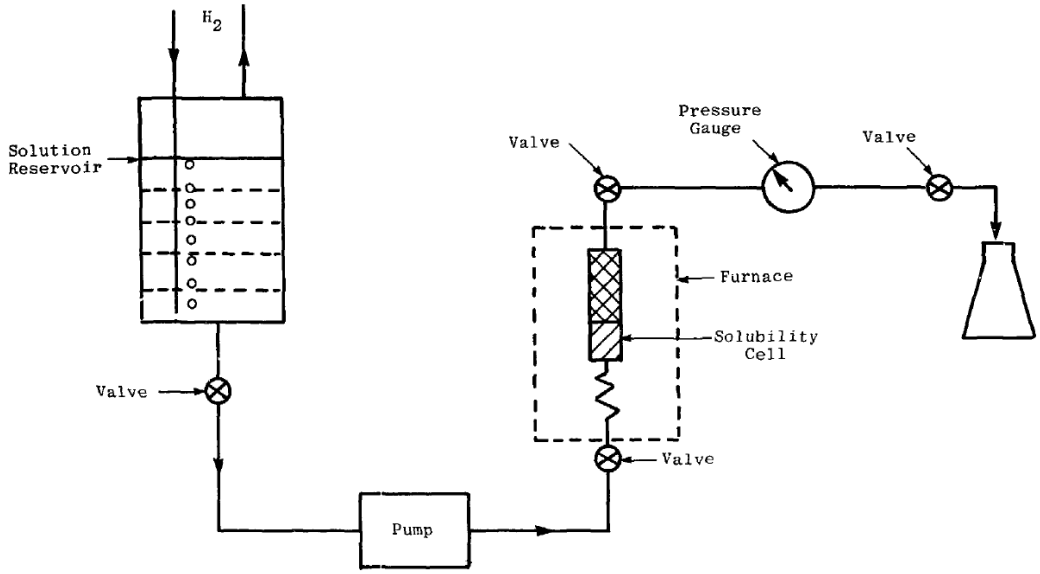

Figure 2.44 - The flowing rig set up used by Kanert *et al.*, which was reduced the complexity of the system used by Sweeton and Baes, and followed a different experimental method to analyse the solubility of magnetite. Image taken from [177]

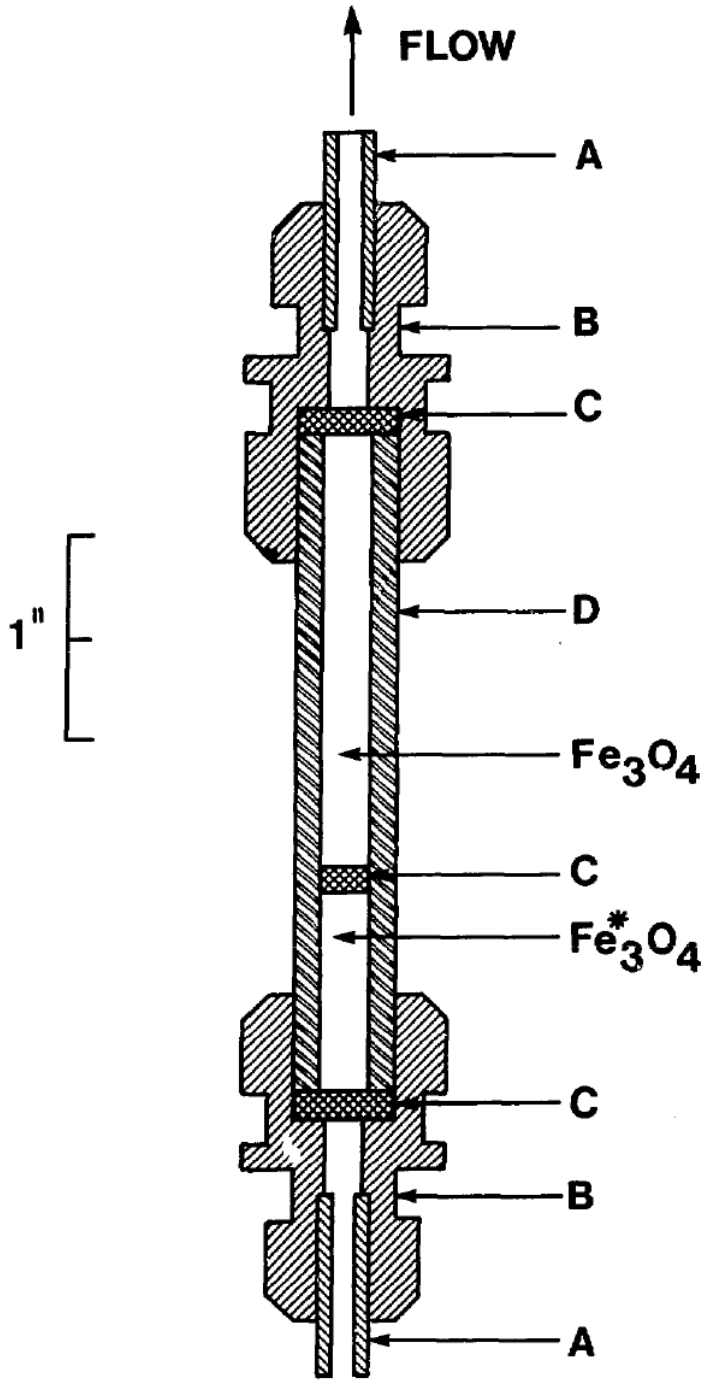

Figure 1: The solubility cell. A, stainless steel tubing; B, 0.5 in to 0.25 in. Swagelok reducing union; C, titanium frit; D, titanium tube. The asterisk denotes Fe^{59}-labelled magnetite.

Figure 2.45 - The sample cell as used by Kanert *et al.*, where activated magnetite and non-acitvated magnetite were contained within a single cell as a means to measure magnetite solubility. Image taken from [177].

A system similar to that of Sweeton and Baes in terms of method, but Kanert *et al*. in terms of simplicity, was used by Tremaine & LeBlanc to study the solubility of magnetite solubility [53] and of nickel oxide [52] at temperatures up to 300 °C. The system followed the same principle of forcing pressurised water through a packed bed of magnetite powder and collecting the sample in a ion exchange column, however the system differed in that it was constructed entirely from titanium components (except for the pump, where stainless steel and oxidised zirconium were unavoidable). Flow rate was controlled by the pump and no online provision for measurement was made beyond this; flow rate could have been calculated from the mass of water in the drain however this is not explicitly stated to be the case. A diagram of the system can be seen in Figure 2.46.

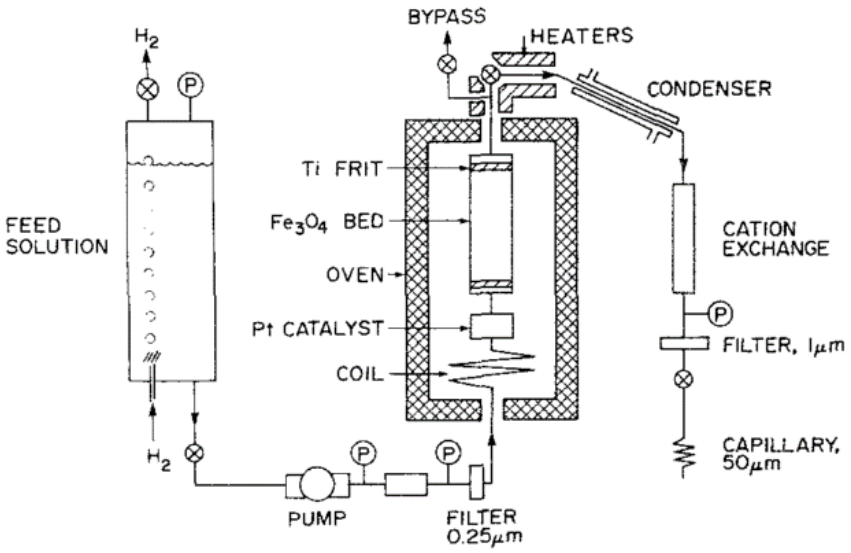

Figure 2.46 - The system used by Tremaine and LeBlanc for the study of metal oxide solubility [52,53].

The systems used by Ziemniak *et al.* [54,55,57,59] for measuring the solubility of various metal oxides consists of a pair of identical stainless steel autoclaves linked together, with all high temperature components and sampling tubes lined with platinum. One of the autoclaves was designated as the preheater autoclave and the other as the magnetite column, both housed in a heating jacket; the preheater autoclave provided enough residence time for the feed

water to reach temperature and then fed the water into the bottom of the magnetite column.

Flow is provided by a high pressure pump, controlled at a flow rate of 5.5 $cm^3.min^{-1}$ and feed water is stored and conditioned in a pair of pressurised tanks, which could be alternately removed and refilled during the test without disrupting the feed water supply to the system. In a similar fashion to Tremaine & LeBlanc's system, Ziemniak *et al.* used a constant flow system where the system flowed at all times, only redirecting flow when a sample was taken. A diagram of the system can be seen in Figure 2.47.

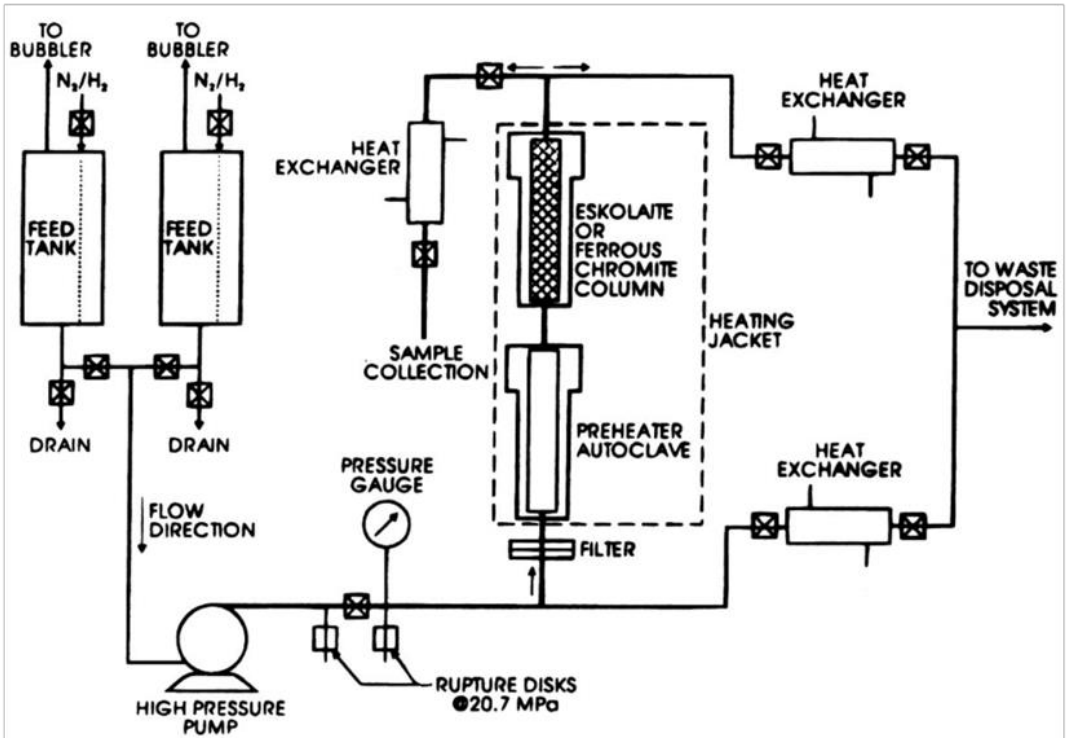

Figure 2.47 - The system used by Ziemniak *et al.* for the measurement of various metal oxides; in the image above the system is set up to use chromium containing material, however the test apparatus is identical across the series of solubility tests [54,55,57–59]. **Image taken from** [58].

The most modern system reported so far has been that used by a collaborative group headed by Wesolowski [42] at the Oak Ridge National Laboratory, Tennessee. The system draws heavily on the designs previously discussed, as well as the designs of groups performing kinetic studies at ambient temperatures [178], and groups producing metal oxide nanoparticles in

supercritical water [179,180], who have designed plug-flow reactors of their own.

Wesolowski *et al.* [42] constructed a system of pressure vessels machined from titanium and zircalloy, with screw end caps sealed with gold gaskets. Gold frits were used to hold the metal oxide powder in place within the column. All other high temperature capillary tubing used was made from a platinum-rhodium alloy, while lower temperature areas made use of PEEK capillary tubing.

Flow to the system is provided by a High Performance Liquid Chromatography (HPLC) pump capable of producing flows of between 0.01 – 5.00 $cm^3.min^{-1}$, fitted with a titanium pump head ensuring the incoming feed water was only in contact with inert materials. Feed water was stored and conditioned in a pressurised reservoir. The system's pressure was maintained by use of a large drain reservoir filled with N_2 gas, and regulated by a back pressure regulator above the reservoir, releasing the gas to maintain the pressure.

The column and heat exchanger were wrapped in an aluminium heater block, and the entire assembly situated in a furnace. Using both the coarse temperature control of the furnace and the secondary controller from the aluminium heater block, temperature accuracy of ±0.2 °C were possible. A diagram can be seen in Figure 2.48, along with annotations by the group.

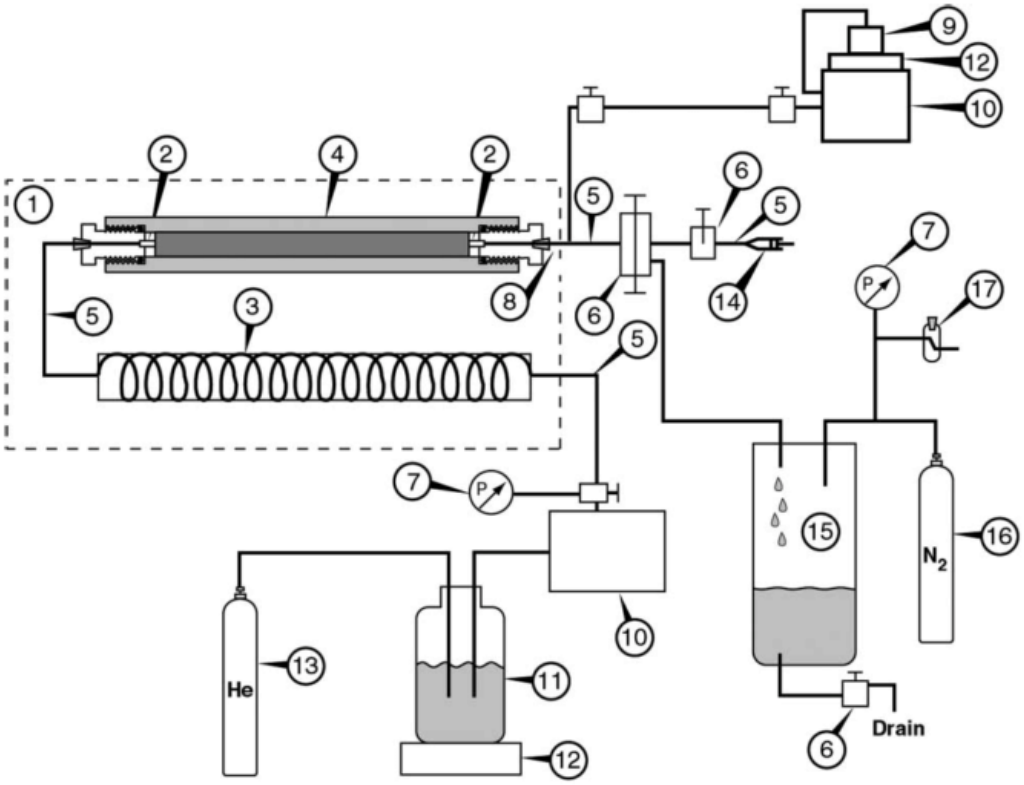

Fig. 14.9. Schematic of plug-flow solubility apparatus currently in use at Oak Ridge National Laboratory: (1) aluminum block within electrical resistance furnace; (2) Au–Pt outlet filter; (3) Pt-capillary heat exchanger; (4) titanium or zircalloy pressure vessel; (5) Pt-capillary inlet–outlet tubing; (6) titanium flow control and sampling valves; (7) pressure transducer; (8) Pt mixing tee at experimental p and T; (9) strong acid or base reservoir; (10) HPLC pump with titanium pressure head; (11) feed solution reservoir; (12) top-loading balance to calibrate fluid delivery rate; (13) He, H_2, O_2, N_2, *etc*. pre-saturating gas; (14) sample container; (15) outlet solution reservoir; (16) high pressure N_2 tank to provide backpressure; (17) backpressure regulators.

Figure 2.48 - The Oak Ridge National Laboratory metal oxide solubility system, as reported by Wesolowski *et al.* [42]

2.5.3.2 Sampling Methods

2.5.3.2.1 Direct Extraction by Pressurised Expulsion

The simplest way to extract solution from a pressurised system is to simply open a valve and allow the system pressure to discharge some of the fluid.

In experiments below 300 °C, Helz [49] made use of a simple stainless steel tube which was evacuated and attached to the main pressure vessel. The sample was taken into the tube, then immediately expelled from the vessel into a sample flask; this produced samples of between 3 and 4 grams.

Styrikovich *et al.* [50] used a similar method to Helz, but with a missing step - discharging the sample directly into the sample flask without the intermediate pressurised tube, though no information is given about acidification of the sample to avoid precipitation.

2.5.3.2.2 **Quenched Cold Extraction**

Holser & Schneer [45] describe a significantly different procedure to deal with the issue of iron precipitation. The vessels in use were quenched in water at the end of the test to rapidly cool them, after which a hole would be punched in the top seals through which four samples were extracted by pipette. They make the assumption that any precipitated iron would be in the form of suspended colloidal iron and would therefore be dispersed in the solution and be detected alongside any iron which is actually dissolved in the solution being analysed.

2.5.3.2.3 **Ion Exchange**

Ion exchangers use a high surface area, organic polymer resin packed column to remove certain ions from a solution, while releasing other ions which were previously coordinated in the resin structure.

This process can be exploited to remove particular ions from a flowing stream and has been used by both Sweeton & Baes [48], and Tremaine & LeBlanc [53] to remove soluble iron ions from a known volume of saturated solution as it leaves the system. Iron ions were removed from the ion exchange resin using aliquots of hydrochloric acid, which were then analysed for their ion content.

This sampling method has an advantage as it provides an accurate number for the average amount of iron in a unit volume of test solution with low error, due to the large volumes of water passed through. However it cannot be used to study momentary changes in iron solubility with time.

2.5.3.2.4 Collection from Constant Flow

The constant collection of outward flowing solution is probably the simplest method of collecting samples for analysis, however it was not used until comparatively recently due to the limitations and availability of analysis techniques able to detect iron concentrations at levels in the low ppb range. Before this point samples needed to be concentrated, or contain a large amount of iron in a small volume (see section 2.5.3.2.3).

Constant collection simply requires that the test solution draining from the system be collected in a clean environment to prevent external contaminants entering the sample. While Ziemniak *et al.* simply took samples directly into polystyrene auto-sampler vials containing concentrated nitric acid [53–55,57,59], extended provision for cleanliness is made by Wesolowski *et al.* [42]; samples from their system can be taken in a class 100 clean-room environment if necessary.

2.5.4 Review of Published Magnetite Solubility Data

Within published literature on the topic of magnetite solubility, there is a great deal of variation in results as can be seen in Figure 2.49. This chart shown presents the solubility ranges across three orders of magnitude, and showing little agreement between any of the individual sets. There is a trend in almost all of these sets, where a local minima solubility is experienced between $pH_{25\,°C}$ 9 and 11, but the location of this minima varies heavily between data sets. As the chart was published using measured data obtained before 1987.

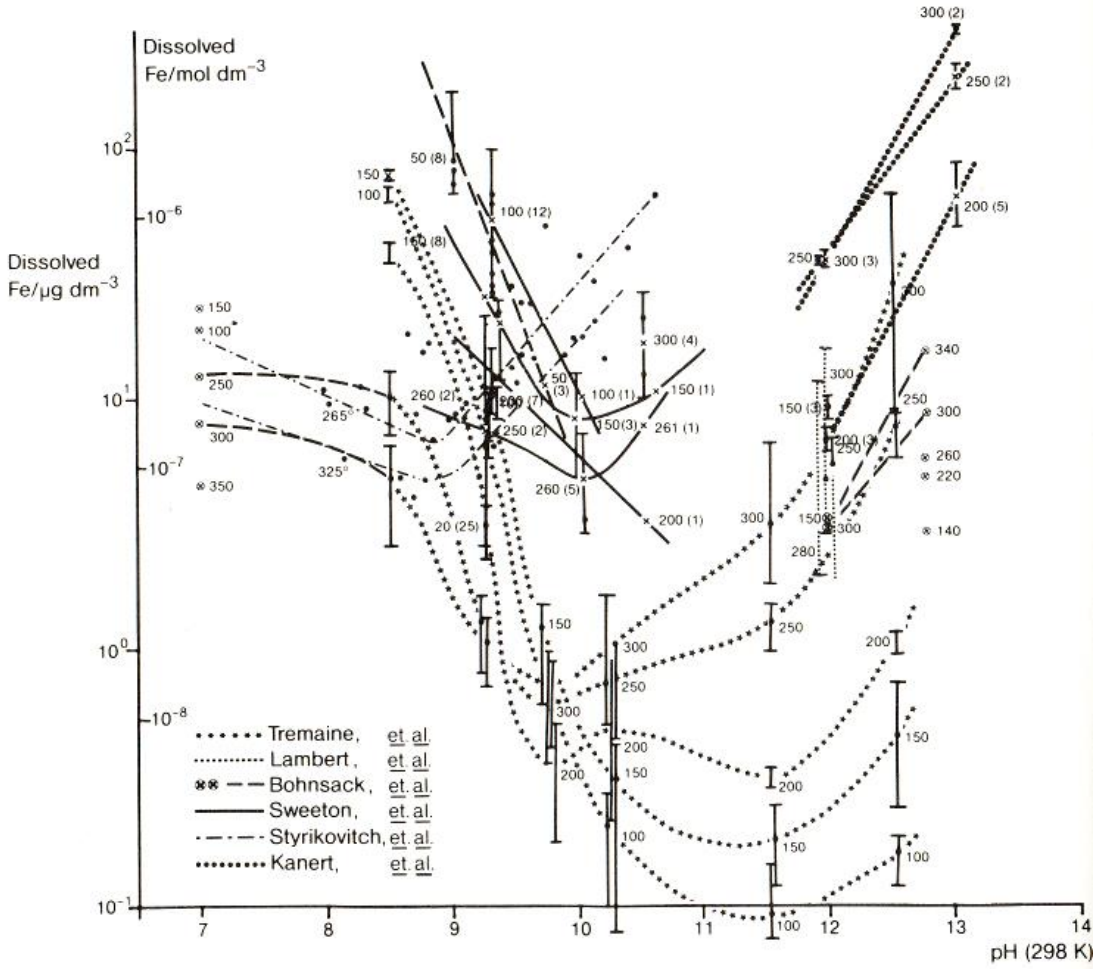

Figure 2.49 – Literature data for measured magnetite solubility at temperatures between 100 – 350 °C, as a function of the $pH_{25\,°C}$ of the aqueous solvent. The chart shows no clear agreement between the data sets beyond local trends and minima, however these are spread across orders of magnitude in both the pH_{298K} and measured solubility. The image is taken from [40], it lists data taken from [48,53,176,177,181,182]

To clarify the information in the chart above, some of the data (from available papers) have been replotted individually in Figure 2.50, Figure 2.51 and Figure 2.52. More recent data from Ziemniak *et al.* [57], not covered in Bohnsack's review [40], have been plotted in Figure 2.53. The region of interest to this project is elevated pH level between 9 and 11, and temperatures between 200 and 300 °C, so the data has been reproduced in the region of these parameters, though extending beyond the limits to provide a complete picture of the trends. In some cases, the results within a single temperature and pH set are spread widely across an order of magnitude, so for clarity these data have been sorted into bins and averaged, with error bars based on the standard deviation of the

bin. The data here is taken only from papers which used flowing autoclave or plug flow type systems, described in section 0.

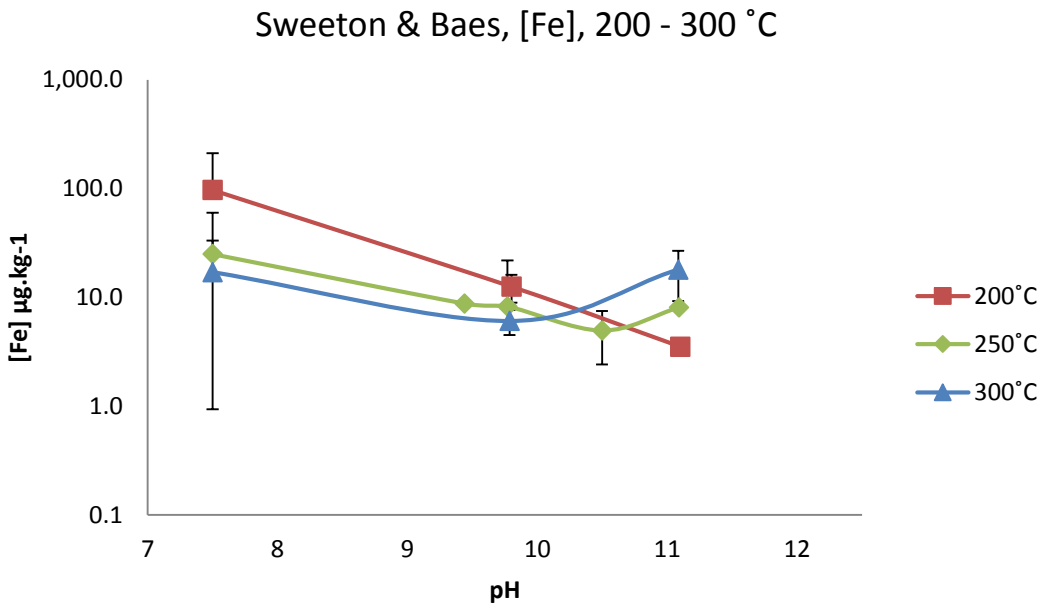

Figure 2.50 - Data published by Sweeton and Baes [48] for the solubility of magnetite between pH$_{25^\circ C}$ 7 and 11, for T = 200, 250, and 300˚C. Connecting lines for illustration purposes only.

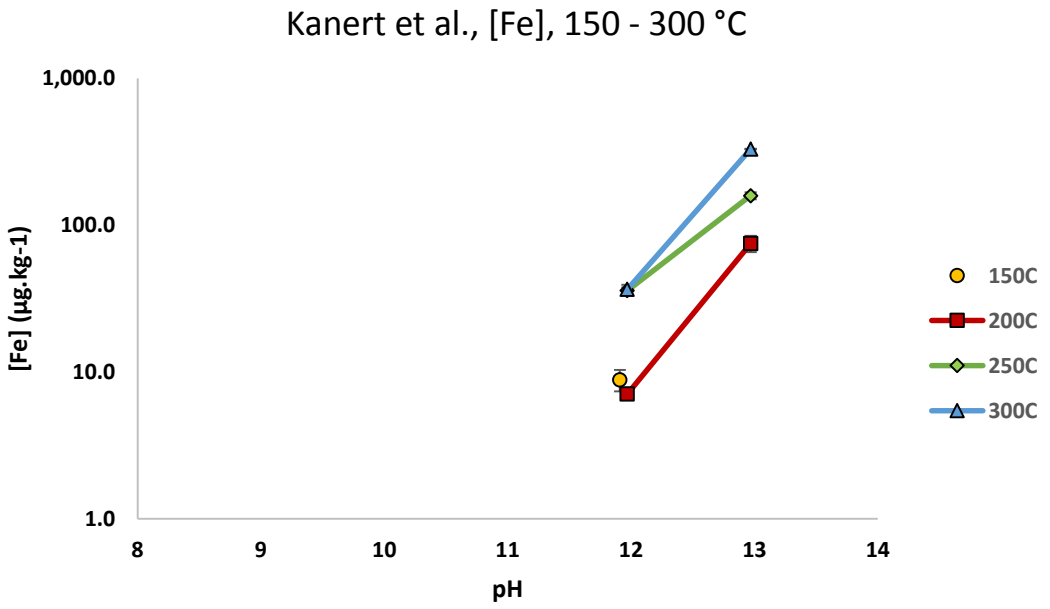

Figure 2.51 - Data published by Kanert *et al.* [177] for the solubility of magnetite at pH$_{25^\circ C}$ of 11.91 and 12.97 between temperatures of 150 and 300C. Connecting lines for illustration purposes only.

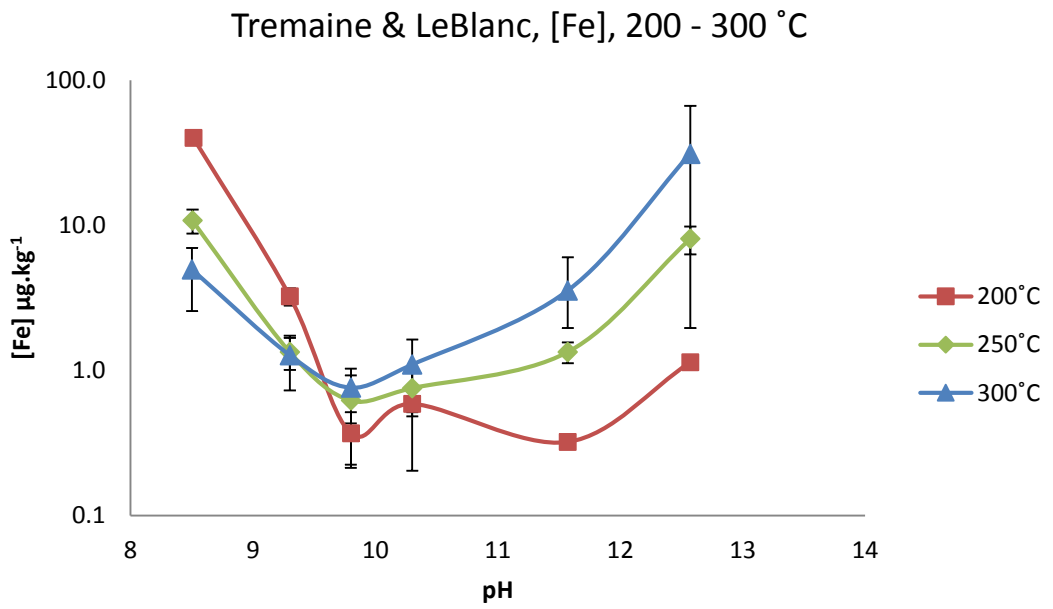

Figure 2.52 - Data published by Tremaine and LeBlanc [53] for the solubility of magnetite between $pH_{25^\circ C}$ 8 and 12, for T = 200, 250, and 300˚C. Connecting lines for illustration purposes only.

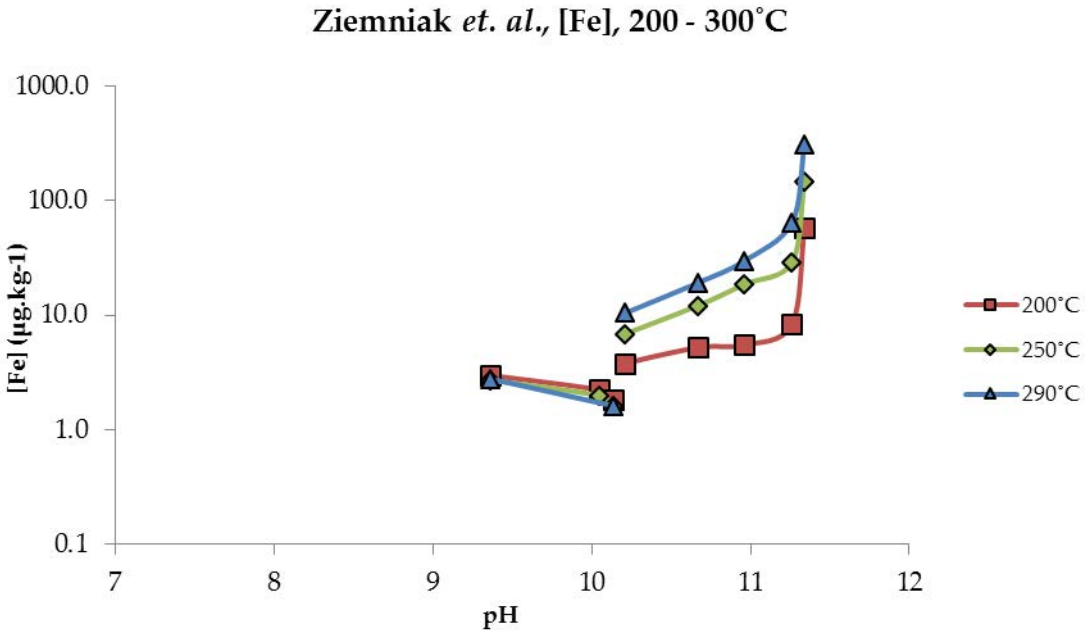

Figure 2.53 - Data published by Ziemniak, Jones and Combs [57], for the solubility of magnetite between pH 9 and 11.5, for T = 200, 250, and 290˚C. Modification of pH was done using Ammonium Hydroxide and Sodium Phosphate. Connecting lines for illustration purposes only.

Data produced by Sweeton & Baes [47,48] (see Figure 2.50) is close to the chemistry conditions of interest, however the results are high compared with those of similar conditions present by Tremaine & Leblanc [53] (see Figure 2.52), possibly due to the use of less accurate analytical equipment.

Finally results from Ziemniak *et al.* are presented in Figure 2.53, however results are significantly different from those of both Sweeton & Baes and Tremaine & Leblanc due to the chemistry used for the tests.

As can be seen from the data sets, a solubility minima is expected for magnetite between $pH_{25\,^{\circ}C}$ 9 – 10.

2.5.4.1 Discussion of Literature Data

Measurement of magnetite's equilibrium solubility in mildly alkaline solution is clearly a difficult proposition, and subject to wide variation as a result of several reasons. These have been discussed by the authors as a means to explain the variation between data sets.

The degree of crystallinity of the magnetite has a great effect on the dissolution of the material. As the dissolution of the magnetite is a surface reaction, the properties of the solid at the interface are important and these properties are determined by the lattice energy, the free energy of the surface, the formation of a solid solution and the degree of hydration of the surface. Lattice energy is a substance specific quantity, and is essentially an estimate of bond strength between the various ions in a crystal [183].

The free energy of an ionic crystal surface is surface specific, and increases with increasing surface area, as well as in the presence of dislocations in the crystal surface [40,42,48,53,57]. This essentially suggests that very small crystallites (those of diameter of <0.1 μm), which have a greater specific surface area than larger crystals, and are rapidly formed from solution, can be substantially more soluble than larger well-formed crystals [53]. In circumstances where a bed of magnetite beads was exposed to high temperature water for an extended period of time, solubility was seen to fall with time (see Figure 2.54), suggesting that the smallest crystals, which were not fully hydrated and dissolved but also

not detectable are being either washed away from the larger must fully crystalized structures [53,181].

The suspended matter has been discussed by researchers in practical terms. Attempts to eliminate suspended matter through use of filtration has been able to reduce, but not fully avoid scatter [48–50,176]. Sweeton and Baes [48] discuss the issue, and conclude that the filtered material is previously dissolved matter that should be included in the final solubility level which is presumably the reason for their comparably higher solubility results. Tremaine and LeBlanc's [53] experiments found that increased throughput of solution over time lead to considerably less wide scatter and significantly lower values for solubility. The lowest values obtained by experiment can be considered to be the most accurate, as it is reasonable to assume that higher numbers can be contaminated by undissolved suspended crystallites, while lower numbers cannot [40,181].

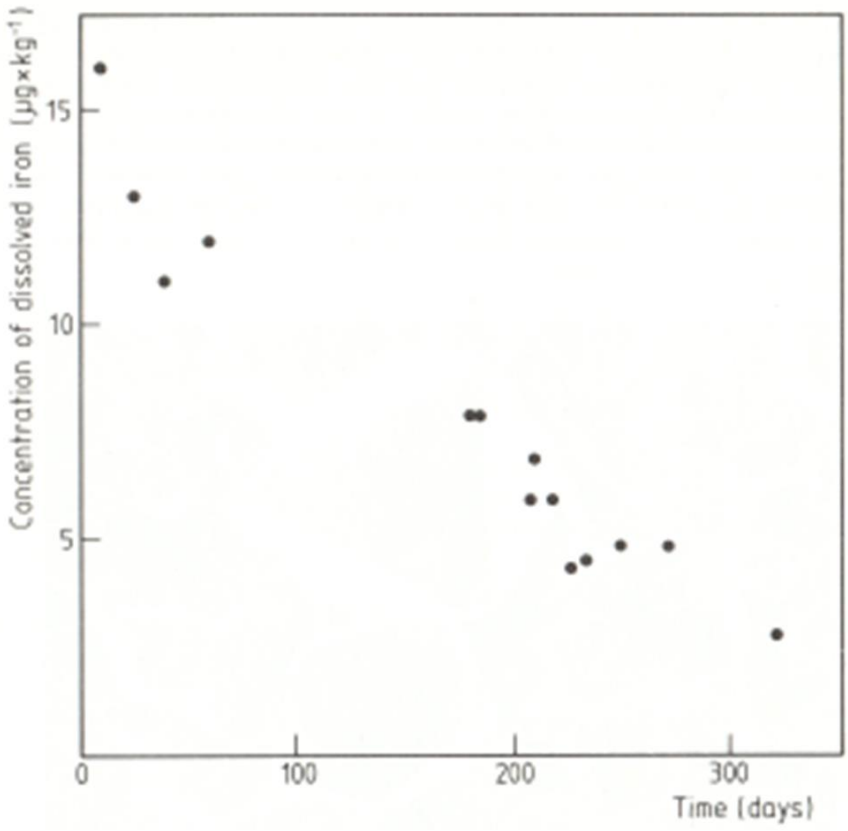

Figure 2.54 – The variation in measured magnetite solubility with time, as observed by Lambert *et al.*, [181]. Similar trends were observed and commented on by Tremaine and Leblanc [53]. Figure taken from [40].

Finally, the analysis method used for the study is of importance. In most studies, detection limits have been too high to determine the solubility of magnetite in a aqueous solution [45,49]. Sweeton and Baes [48] and Tremaine and LeBlanc [53] avoided this difficulty by using ion exchange resins to concentration the dissolved iron from large volumes of water prior to analysis, however this allowed for only a limited number of samples from each experiment, and could not be used to resolve the solubility change over short periods of time (as too small a volume of water would have passed through the exchange to provide detectable amounts of iron). In later work, more advanced techniques had become available, and Ziemniak *et al.* [57], measured iron concentrations in effluent taken from their flowing autoclave apparatus using Graphite Furnace Atomic Absorption Spectroscopy (GFAAS), which provided a detection limit below the equilibrium solubility. In measuring the solubility in unmodified samples of solution, Ziemniak *et al.* were able to very accurately detect concentration, but lost the ability to differentiate between the oxidation states of the dissolved ions.

2.5.5 Summary of Metal Oxide Solubility in PWR Coolant

The solubility of magnetite, among other metal oxides produced by the corrosion of plant relevant materials, has been studied by numerous research groups over an extended period of time for various chemical conditions [16,40,42–45,47–60,62,64,69,184–186]. Experimental methods have improved with time, from basic batch autoclave systems through to inert surfaced plug flow rigs. Concurrently, trace element analysis has greatly improved, making it possible to determine concentration of elements at values lower than 1 ppb [187,188].

Work is on-going to determine the solubility of metal oxides under the range of conditions present in an RCS with the intention of improving the predictive accuracy of models currently in use [61,66].

3 Scope of Work

The primary aim of the work presented in the thesis is to provide fundamental rate and equilibrium data associated with CRUD deposition for computational modelling of the primary coolant system of PWR type nuclear reactors. In order to do so, this project's primary focus has been on the design, construction and preliminary operation of research apparatus for the study of:

1) Corrosion product deposition at restrictions in flow, under simulated reactor coolant conditions
2) Corrosion kinetics of materials under simulated reactor coolant conditions.
3) Solubility of metal oxides in simulated reactor coolant.

Finally, a computational fluid dynamics model of the deposition environment was produced and has been used to provide supplementary information for the experiments performed for 1).

The experimental procedure / results section of this thesis is split into four parts associated with the topics above. The structure for the remainder of this dissertation is presented as follows:

- **Chapters 4: Section A -** Flow Assisted, Electrokinetically Stimulated Deposition
- **Chapter 5: Section B -** Corrosion Kinetics of 316L Stainless Steel in High Temperature Water
- **Chapters 6: Section C -** Metal Oxide Solubility in High Temperature Water
- **Chapters 7: Section D -** Finite Element Modeling of Flow Assisted Deposition

3.1 Flow Assisted, Electrokinetically Stimulated Deposition

No available apparatus existed which could be used to simulate the deposition of dissolved corrosion products at the entrance to a flow restriction, and experience of construction, operation and maintenance such laboratory flow loops was no longer easily available in the UK. Design of the loop was undertaken through consultation with Dr. Pierre Combrade, who has previously been involved with the construction of the EMILIE loop at AREVA, upon which the University of Birmingham loop is based. Due to complexity of design, and complications with construction through an external pressure-engineering firm, the hot loop was delivered 2 years later than originally planned. Details of the design and construction of the University of Birmingham hot loop system can be found in Appendix A and details the results of initial trial test runs can be found in section 4.2.

3.2 Corrosion Kinetics of 316L Stainless Steel in High Temperature Water

3.2.1 Preliminary Corrosion Kinetics and Oxide Film Morphology Studies

Initial experiments were carried out using an existing, refurbished and recertified batch-type autoclave. The refurbishment included the installation of a 316L stainless steel liner inside the Hasteloy C-276 autoclave vessel, the machining of a new lid in 316L stainless steel, and replacement of all other wetted components with 316L stainless steel. Refurbishment plans are presented in 5.1. The experiments carried out were short-term tests lasting 300 hours, and using XPS-AIM for film characterisation. The test matrix is presented below:

Table 3.1 - Tabulated experimental conditions and the appropriate experiment number.

pH	Temperature		
	200˚C	250˚C	300˚C
9.5	1	2	3
10.5	4	5	6

In each experiment, two surface conditions were tested and the results of these are presented in 5.2. While the tests returned valuable information concerning the oxide film formation across temperatures and pressures, the rates of formation were based only on a single data point and thus are not necessarily accurate to the level desired by the customer.

3.2.2 Extended Corrosion Kinetics Studies

In order to obtain more accurate corrosion kinetics for 316L stainless steel, a bespoke test rig was designed and built. The rig is capable of holding 48 coupons in four cells, each of which can be removed from the rig without disturbing the others cells. The design and construction of this rig (presented in section 5.4) took a considerable period of time, and only a limited number of results were obtained, for $pH_{T=25\,^{\circ}C}$ 9, 10 and 11, at a temperature of 300 ˚C, during the first proof-of-concept experiments, which are presented in section 5.5.

3.3 Metal Oxide Solubility in High Temperature Water

3.3.1 Preliminary Metal Oxide Solubility Studies

The solubility of metal oxides was initially studied using the same refurbished autoclave, described for use in the preliminary corrosion kinetics experiments (see Section 3.2.1 above), fitted with a pair of small gauge porosity cages in which powdered metal oxide, in this case magnetite, could be placed to act as the soluble iron source 6.1). Graphite Furnace Atomic Absorption

Spectroscopy (GFAAS) was used to determine the concentration of material is samples of fluid taken from the experiments. It was found that the experimental technique and the GFAAS analysis were inadequate to accurately determine the solubility of metal oxides, and so a new approach was taken.

3.3.2 Extended Metal Oxide Solubility Studies

Design and construction of a bespoke test rig for metal oxide solubility is detailed in section 6.4. The system implemented during this stage of the project was a stainless steel system intended as a proof-of-concept design before an inert materials rig was built.

During the proof-of-concept testing, it was found that the stainless steel tube materials within the rig could be used as the source of soluble metal oxides, in place of using a metal oxide powder. Results of these tests are detailed in section 6.5.

3.4 Finite Element Modeling of Flow Assisted Deposition

A computational fluid dynamics model to describe CRUD deposition within the 11 mm to 6 mm diameter flow restriction has been developed with the assistance of a modeling consultancy firm using the COMSOL Multiphysics finite element modeling package. The model is an extension on simple models, which were used to extract fluid dynamic information; these models are described in section 7.1.

The deposition model was specified to make use of the 'moving mesh' function available in COMSOL, to simulate the growth of a deposit when the local shear rate maximum exceeds a predetermined limit. During each iteration, the model calculates the shear rate along the boundaries and moves the mesh by a set amount, growing the deposit incrementally with each subsequent time step. Results of parametric sweeps performed using the deposition model are presented in section 7.2.

3.5 **Summary**

The primary aim of this EngD project was the development of research apparatus, designed specifically to provide fundamental kinetics and equilibrium information, which can be used in the construction of full-plant computer models. Such models require extensive libraries of data that cover possible materials, chemistries, and the interactions between them. This project is directed toward providing data about the corrosion of an austenitic stainless steel, the solubility of the metal oxides produced by corrosion, and the deposition of the solubilized metal oxide at restrictions in flow. Additionally, the preliminary version of a finite element model of the deposition process has been built, using the COMSOL Multiphysics, and has been used, in the first instance, to study the effects of various parameters on the shear rate at the entrance to a flow restriction.

4 Section A: Flow Assisted Electrokinetically Stimulated Deposition – Experimental

In order to study the deposition seen in restrictions in flow in the RCS, the type discussed in section 2.3, it is necessary to have a system capable of replicating the hydrodynamic and chemical conditions found within the RCS. The University of Birmingham Hot Loop was designed based on the need to produce high velocity flow in a flow restriction with a high-pressure drop.

Previous work, performed at AREVA from 2002 onward [18–23] used a recirculating hot water loop, designated "EMILIE", for deposition experiments.

The loop consisted of a high flow rate pump that provided flow to a set of test cells placed sequentially before being returned to the pump. Later versions of EMILIE were upgraded to possess a chemistry control system (operated by automated feedback loops), and a streaming current measurement cell. As EMILIE is the only known existing example of a hot water loop, much of the design of the University of Birmingham hot loop is based on information published about the EMILIE system.

Details of the design, construction and operation of the University of Birmingham hot loop can be found in Appendix A.

4.1 Methodology

Set up and operation of the Hot Loop is an intricate process that was performed with caution and attention to detail in order to achieve the correct conditions for the experiment. The methodology of operation changed as experience was gained from each experiment.

Essentially the process of operation consists of cleaning the loop as extensively as possible using large volumes of rinse water and inline filtration prior to charging it with test solution. Test solution was carefully prepared and

degassed with oxygen-free nitrogen in a clean stainless steel tank, before being moved to the loop using gas back pressure. When the loop was filled with test water and gas dead-volume had been eliminated, heating was applied using an autoclave and two top-up heaters and flow was provided by the regenerative turbine pump. During the test, temperature, flow rate and dP across the test cell were data logged continuously. At the end of the test, the test cell was isolated from the rest of the rig and the fluid expelled by opening a pneumatic valve into a vessel, keeping the test specimen dry while the system cooled.

The methodology presented is that with which the best possible conditions within the hot loop were achieved.

4.1.1 Test Piece Preparation

Test pieces were machined from 25 mm OD 316L stainless steel round bar stock, the composition of which is shown in Table 4.1. The test pieces were 60 mm in length 18 mm OD. Initially the test pieces were drilled and the inside edge was chamfered with a counter-sink to remove burrs (shown schematically in Figure 4.1). This was not ideal, as it introduced an unexpected face to the system. For the final test in the series (run 5), the specimen was cut with extra length, the outside diameter turned down to 18 mm in a lathe, the restriction drilled and chamfered, before finally turning the face of the restriction in a lathe to make the final length 60 mm and produce a sharp corner. Burrs were avoided by using very small cuts during the last few passes with the lathe. The test piece is shown schematically in Figure 4.2.

Table 4.1 – Composition of 316L stainless steel bar stock used for the machining of the test specimens.

Fe	Cr	Ni	Mo	Mn	Si	C	P	S
Bal.	17.1%	10.8%	2.5%	0.91%	0.32%	0.058%	0.031%	0.015%

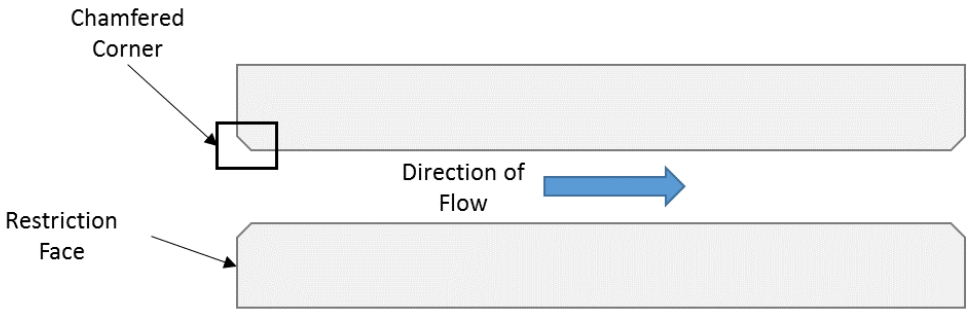

Figure 4.1 - A sketch of the cross section of the test piece used for runs 1 and 2. The corner of the restriction was chamfered during machining to remove burrs, leaving a 45 ° angled face at the entrance to the restriction annulus.

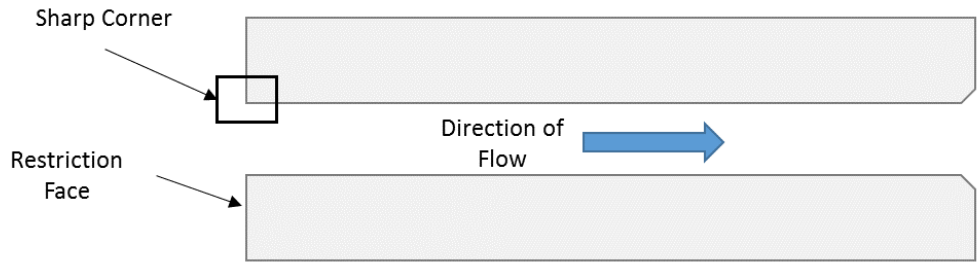

Figure 4.2 – A sketch of the cross section of the test piece used for run 5. The chamfer has been removed by turning down the face in a lathe, leaving a sharp corner at the entrance to the restriction annulus.

4.1.2 Pre-run cleaning

The deposition process is sensitive to contaminants due to the electrokinetic nature of the phenomenon; as ionic strength increases the size of the double layer is suppressed. As ionic strength will have a direct impact on conductivity, the conductivity of the water must be kept as low as possible.

The hot loop effluent water has often been seen to contain a large amount of extraneous materaial, which was later confirmed to be graphite by Raman spectroscopy and EDX analysis. The most likely source of this graphite was the in-line autoclaves main sealing ring; when compressed the graphite ring would be extruded and flakes of the material would be entrained in the fluid

flow and carried around the loop. Removing the material by simply rinsing the hot loop proved unsuccessful, so an inline water filter was purchased with removable filter cartridges with 1 μm pores.

After being cleaned with inline filtration, the loop would be rinsed through to remove any contaminated water remaining in the loop, and to ensure that any water traps (such as the pump) were flushed to contain only clean ultrapure water.

4.1.3 Test Solution Preparation

As deposition was expected to occur in low conductivity environments, addition of pH modifiers was expected to quickly suppress the formation; nonetheless, great care was exercised when preparing test solutions. All experiments were performed in either ultrapure water or dilute LiOH solutions.

Test solution was made up in a thoroughly cleaned 15 L stainless steel feed tank. Ultrapure water was added to this tank and the total mass was measured by a platform balance. The water was then sparged with nitrogen gas at a rate of ~20 $ml.min^{-1}$ for no less than 30 hours. The dissolved oxygen remaining in the feed water was measured using the American Society of Testing and Materials (ASTM) Standard D5543-09, for the measurement of low levels of dissolved oxygen [189].

Briefly, the methods requires that an ampoule containing an oxygen sensitive indicator under vacuum is submerged in a steady flow of the water being tests. The tip of the ampoule is broken off, allowing the vacuum to draw water into the ampoule to mix with the indicator. The presence of oxygen changes the colour of the indicator to reddish-violet hue, the intensity of which is proportional to the concentration of oxygen [190]. The ampoule is immediately compared to a colour scale which allows for estimation of oxygen concentration.

In tests using pH modified water, the required volume of LiOH stock solution was added to the water ahead of degassing. The prepared water would be charged to the loop under pressure of nitrogen; the loop having been purged with nitrogen gas to exclude oxygen from the gas volume. Care was taken to ensure that dead end tubes were also filled with water rather than gas.

For tests involving dissolved hydrogen gas, a different approach was used. Due to the pressures at which the hot loop operates and the fact that the system's pressure is controlled using cold gas pressure, it was necessary to use a mixture of 0.5% H_2 in 99.5% N_2 gas at a pressure of 105 bar to achieve the target hydrogen concentration of 10 cm^3/kg; this had the side effect of dissolving ~1500 $cm^3.kg^{-1}$ of N_2 into the water, however the gas is not expected to have any effect on the chemical behaviour of the system, and using pure hydrogen gas instead would give a H_2 concentration of ~1850 $cm^3.kg^{-1}$.

For these experiments, water was sparged in batches of ~2.5 kg in the pressuriser autoclave for ~5 hours at a pressure of 105 bar. The conditioned solution would be transfer to the hot loop using the pressure in the autoclave. Dissolved gas will immediately begin to come out of the solution during the transfer, but the hot loop tubing was pressurised to 105 bar after the transfer in order to maintain the return to the correct dissolved gas concentration while the next batch was sparged. In a similar manner to the non-hydrogen tests, care was taken to ensure that dead end tubes were also filled with water rather than gas.

4.1.4 **Temperature Ramp**

The hot loop was heated by four separate heating elements; a twin 3 kW heating element around the autoclave, and three 1.5 kW mineral band heaters fitted to the length of tube running up to the pump. Alone, the autoclave was able to

heat the system to 230 °C, while the top up heaters alone were capable of only ~222 °C.

A Eurotherm PID (proportional integral differential) temperature controller controlled the temperature within ±1 °C. The top up heaters were not controlled by any feedback mechanisms. Instead, they were simply set to a value of between 500 and 650 °C, depending on the target temperature.

4.1.5 Pump Power

The flow rate of solution inside the loop was directly dependent on the power setting of the regenerative turbine pump. No type of feedback system was installed to control the pumps power as a function of temperature; instead the power of the pump was manually increased until the target flow rate was achieved.

Flow rate was largely dependent on temperature. It was found that as temperature increased, the maximum flow rate of the pump was able to reach would fall, and at 300 °C the flow rate was limited to ~18.6 $L.min^{-1}$, however, corrected for effect of temperature on fluid density, this gave a mean fluid velocity in the restriction of 15.4 $m. s^{-1}$.

4.1.6 Data Logging

An RS-232 serial outlet connection to a computer was used to data log seven of the displayed process values (PV) from the hot loops main panel. These included two solution temperature readouts (the temperature just before entering the flow meter, and just after exiting the test cell), the temperature of one of the top-up heaters, the flow rate of the system, the dP across the cell, the pump power, and the pressure of the system when under vacuum.

The software used for data logging was Eurotherm's proprietary "OPC Scope", designed to work specifically with Eurotherm controllers. A template

spreadsheet file was made in Microsoft Excel to collate the data and produce an understandable interpretation of the data as the test progressed.

4.1.7 Blowdown Sequence

At the end of the test, the blowdown sequence was activated to remove water in the test section in a bid to prevent dissolution of any deposit that may have formed. The blowdown sequence was automatically controlled; upon initiation, the pump would be stopped, two pneumatic globe values around the test section would close, and a third would open the test section to the low pressure dump vessel (see Figure 9.9). The heaters were deactivated manually, and the system left to cool fully before the test section was removed.

4.1.8 Analysis Methods

4.1.8.1 Differential Pressure Measurements

Differential pressure was used as the primary method for detecting deposition while the experiment was in progress. As discussed in section 4.1.6, the information was logged by computer with a refresh rate of 30 secs. The data were processed from the raw output, and the results are shown in section 4.2.1

4.1.8.2 SEM/EDX Analysis

Imaging and EDX analysis of the test pieces was performed using a Jeol 7000 field emission SEM, fitted with an Oxford Instruments Inca EDX spectrometer. All images were taken using the secondary electron detection mode at a beam energy of 20 kV and a working distance of 10 mm. Similarly, all EDX analysis was performed using a beam energy of 20 kV and a workin distance of 10 mm. Results of these studies can be found in section 4.2.2.

4.1.8.3 Raman Spectroscopy

Raman spectroscopy was used as a means to analyse the material removed by the 1 μm inline filter from rinse water during pre-test cleaning. A Renishaw

inVia Confocal Raman Microscope was used for this study and the results can be found in section 4.2.3.

4.2 Results

The aim of the work described in the previous chapter and detailed here is to replicate the flow-induced deposition behaviour seen on plant, as discussed in section 2.3. Tests were carried out in high purity water, and additions of reagent grade LiOH when required.

The test restrictions were all machined from 316L stainless steel round bar stock, with a 6 mm (±0.1 mm) drilled hole through the central axis. Data logging recorded the water temperature a short distance past the test cell, the dP across the cell, flow rate and pump power.

Experiments detailed in the literature [18–27] have observed deposition by measuring the increase in dP across the test cell at constant flow rate. In the experiments presented here, dP observation did not directly yield variations consistent with deposition. However, it was noted that the dP across the test cell would remain constant as the system flow rate declined, so it was necessary consider both variables simultaneously.

Several tests were carried out using the Hot Loop, the conditions of which are presented in Table 4.2.

Table 4.2 – Table of all experiments performed using the University of Birmingham Hot Loop.

Run No.	Temperature (°C)	[LiOH] ($mg.kg^{-1}$)	[H2] ($cc.kg^{-1}$ STP)	Flow Rate ($kg.min^{-1}$)		Velocity in Restriction ($m.s^{-1}$)	
				Part 1	Part 2	Part 1	Part 2
1	227.2 ±1.6	0.1	0	16.62 ±0.10	16.94 ±0.03	14.18 ±0.08	14.47 ±0.02
2	300.7 ±0.3	0	0	13.12 ±0.27	12.75 ±0.02	15.25 ±0.31	14.82 ±0.49
3	299.7 ±0.5	0	0	12.93 ±0.02		15.04 ±0.28	
4	276.6 ±0.9	0	10	15.42 ±0.02		15.85 ±0.01	
5	222.3 ±0.7	0.25	3.5	18.42 ±0.40		15.75 ±0.34	

4.2.1 Differential Pressure Measurements

Differential pressure is the primary means by which deposition behaviour was expected to be observed. The inclusion of flow rate on the graphs is to account for a short coming of the hot loop; there is no feedback loop controlling the pump to maintain a constant flow rate, rather, the pump is set to a certain percent power. As a result, should a deposit begin to form, the dP would remain approximately constant (or rising slightly), while the flow rate falls. Literature researchers have seen that the deposition does not continue indefinitely in the range of chemistries investigated even with constant flow rate [18,19,24]; given these observations, it is likely that any fall in flow rate experienced in this experimental series will level off eventually as deposition ceases.

It must be borne in mind that the flow rate is affected by the system temperature, and to a lesser extent by overall pressure, through the change in density (see Figure 4.3). The effect of temperature on dP appears to be an approximately linear relationship with a negative gradient, so one can expect dP to fall as temperature rises (see Figure 4.4).

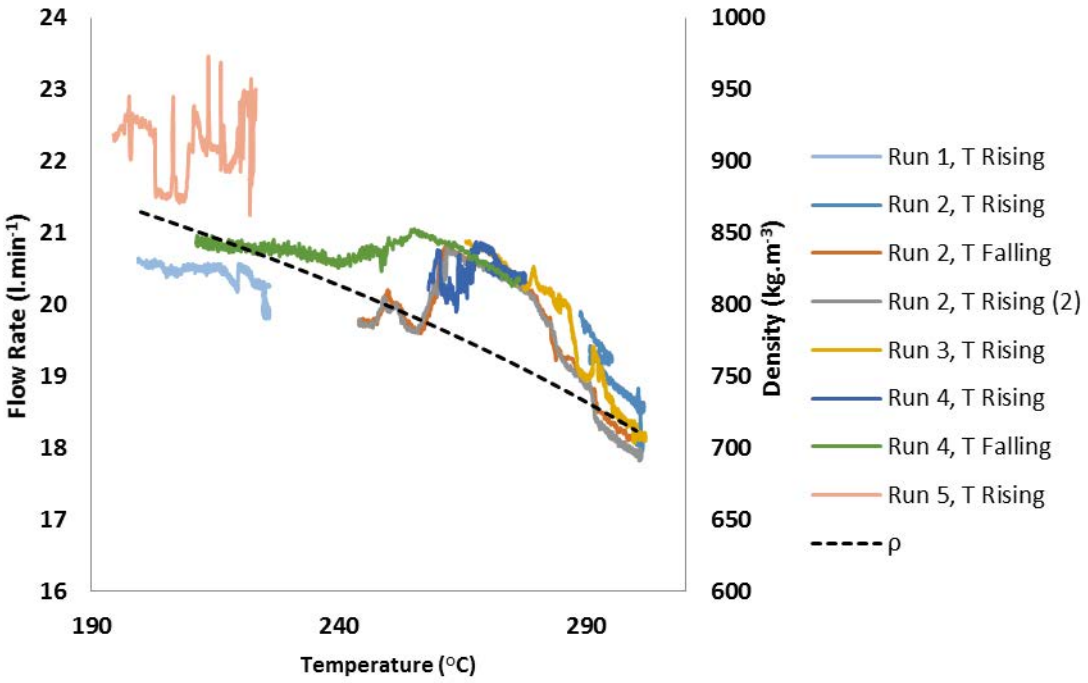

Figure 4.3 - The relationship between flow rate and temperature, with the density of water at the vapour pressure of water for each temperature. The relationship between temperature and flow rate due to density variation is clearly a dominant effect, however the flow rate variation is clearly not based solely on density.

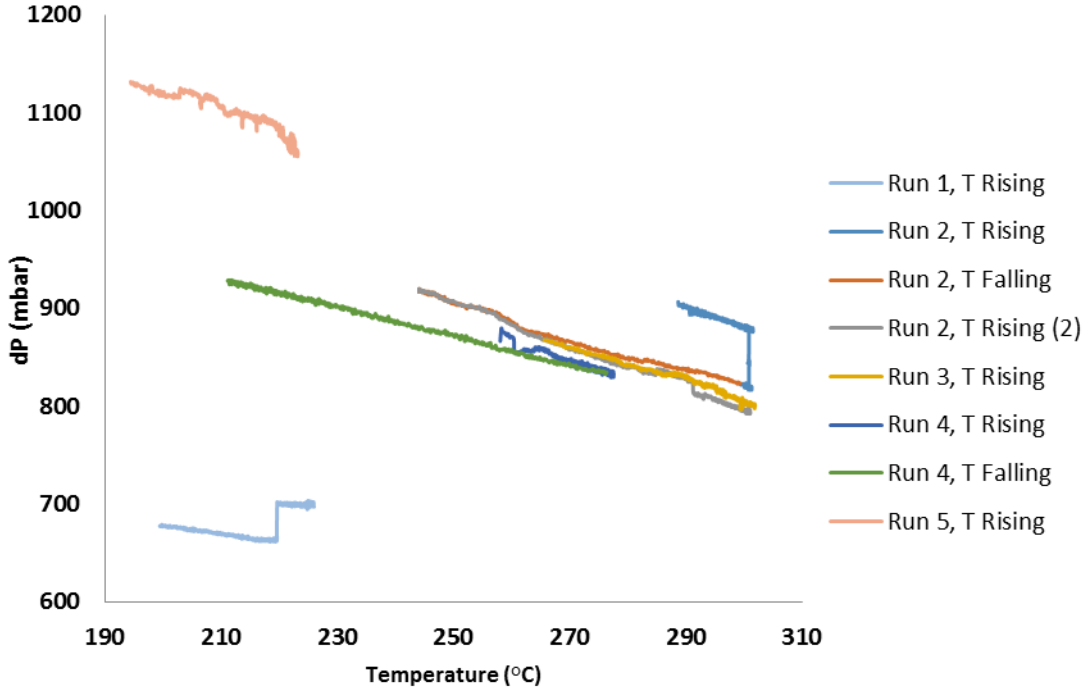

Figure 4.4 - The relationship between temperature and dP, which is a consistent approximately-linear negative gradient. The curves here are for rising and falling temperatures; in some cases no data is available for falling temperature as the blowdown sequence deactivates the pump. Falling temperature data was obtained from situations where heaters had failed during the test, leaving the pump running.

The differential pressure as a function of flow rate at experimental temperature is plotted in Figure 4.5. It can be seen that there is considerable discrepancy between the data sets and no immediately obvious trends. When the data is plotted as a function of mass flow rate (correcting the volumetric flow rate for the density of the fluid), as in Figure 4.6, trends in the data become more apparent. It is clear that higher temperature conditions result in a decrease in maximum flow rate at a given differential pressure. The behaviour visible in the run 5 data is potentially due to the presence of transient deposits forming in the restriction, repeatedly causing the flow rate to fall and the dP to rise before falling back toward the higher flow rate, lower dP condition. This behaviour is discussed more extensively later.

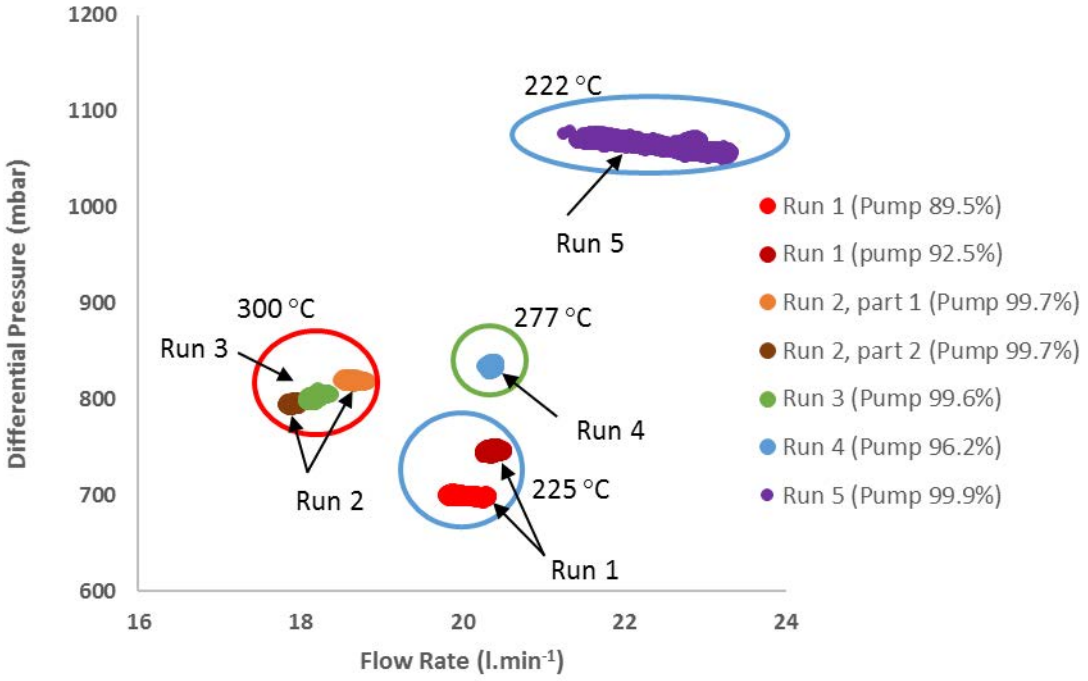

Figure 4.5 - The relationship between velocity and dP for all tests at test temperature. Tests at 222 °C and 225 °C were both performed at high pump power levels, though run 5 was performed without the inline autoclave, reducing the total head loss and affording a higher flow rate.

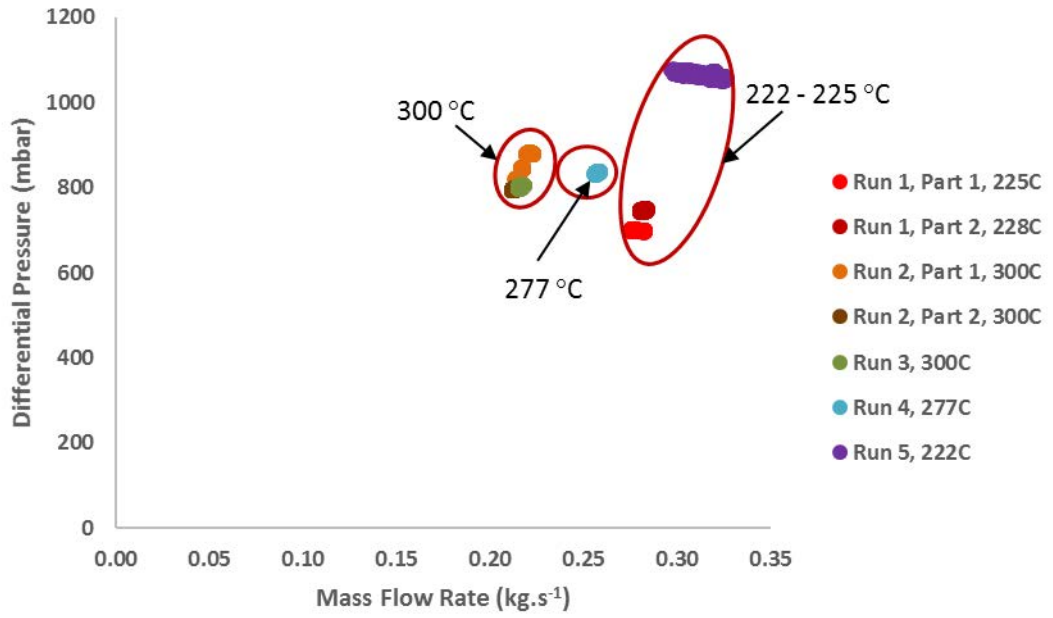

Figure 4.6 – Differential pressure plotted as a function of mass flow rate. The trend between the increasing dP and flow rate can be seen far more clearly when the changing density of the fluid is taken into account.

Figure 4.7 presents the data from Run 1 (227 °C, 0.1 mg.kg^{-1} LiOH, ~14.18 to 14.47 m.s^{-1}, see Table 4.2). At the beginning of the test, 'part 1', the expected behaviour for both flow rate and dP in the presence of a growing deposit appears to be occurring – flow rate is falling and appears to be leveling off, while dP is rising slightly. In 'part 2' of the experiment the pump power was increased to full, however this appears to have had the effect of removing any deposit which may have formed – flow rate is generally rising, while dP remains constant. This increase in power was to return the flow rate back to the original level. During 'part 2' a temporary heating power loss induced wide variation in dP and flow rate, which have been excluded for clarity.

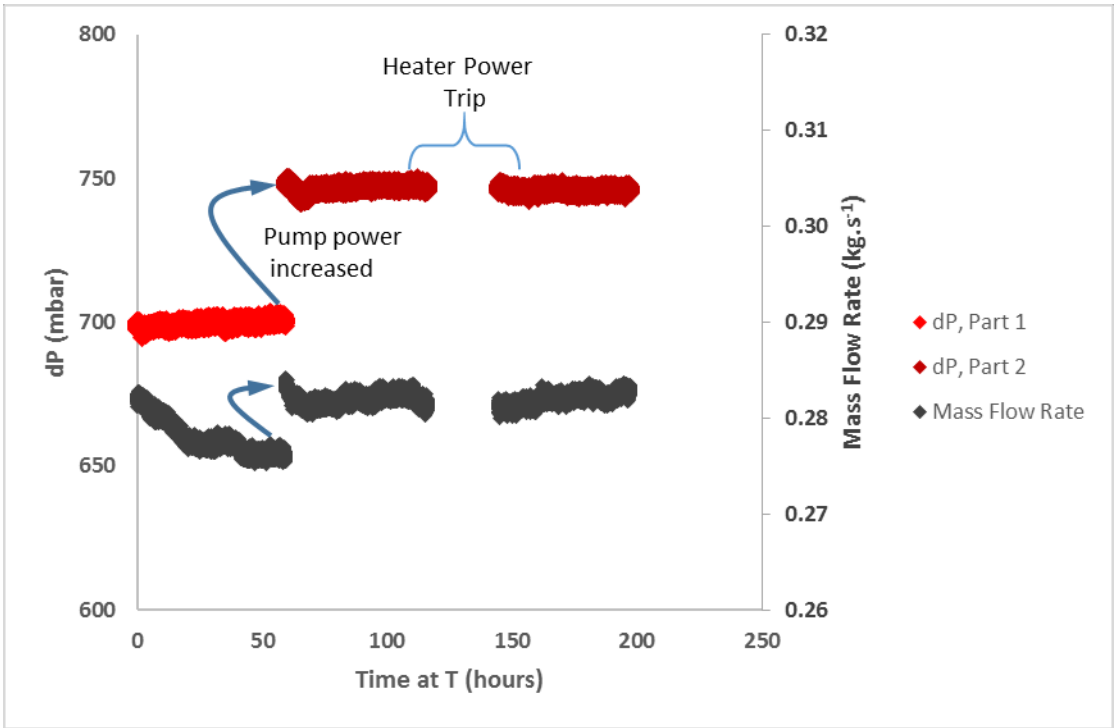

Figure 4.7 – Run 1 dP vs time. Two curves are presented - part 1 shows the dP when the pump was held at 88.5% while part 2 shows the dP when the pump was held at 92.5%. The gap in the middle of the part 2 data series is due to a heater trip which caused wide variation in dP and flow rate, and has been excluded for clarity.

Run 2 (300.7 °C, 0.0 mg.kg^{-1} LiOH, 14.28 – 15.25 m.s^{-1}, see Table 4.2) 'part 1' (see Figure 4.8) is comprised of three segments where there are large drops in both dP and flow rate simultaneously. A small fall in flow rate alongside a small rise in dP midway through the first segment of 'part 1' is indicative of deposition, however this is coupled with instability in the flow rate (a sharp rise in the middle of the segment). The following segments of 'part 1' both show dP losses coincident with flow rate losses, behaviour indicative of a blockage elsewhere in the system. In 'part 2' both dP and flow rate are constant and stable. Between part 1 and 2, a heater power trip occurred, causing variation in dP and flow rate; the data has been excluded for clarity.

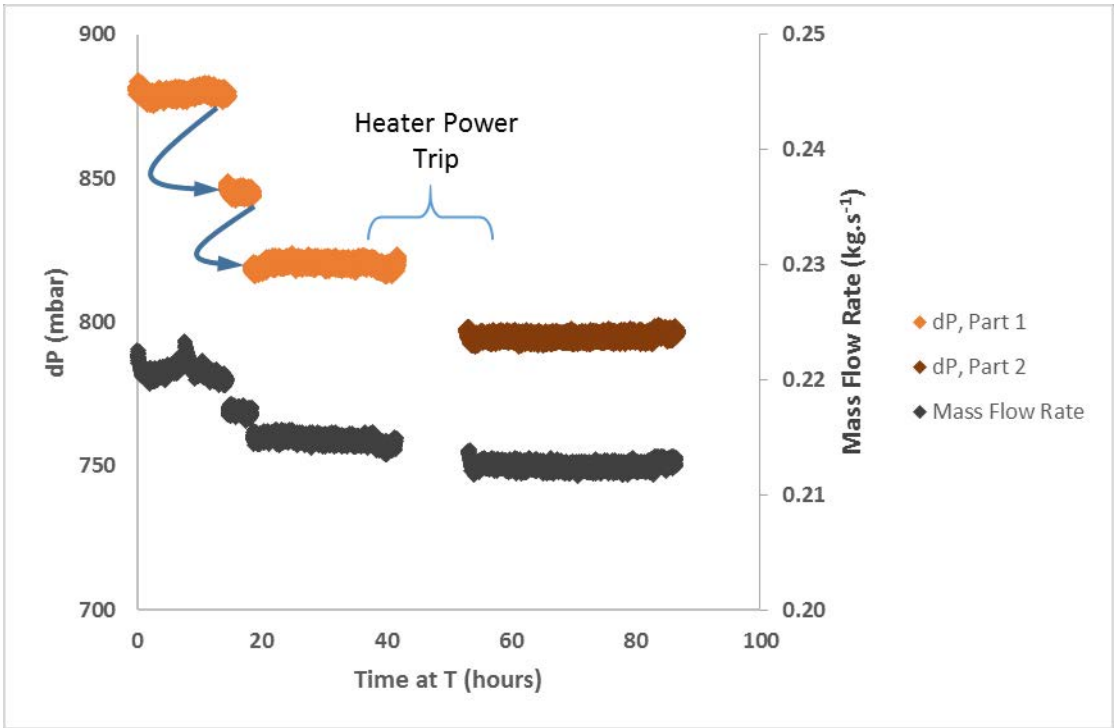

Figure 4.8 - Run 2 dP vs time. Two curves are drawn for this graph - a heater power trip occurred at approximately 41 hours, and temperature was restored at approximately 53 hours. The gap in the part 1 and part 2 data series is due to a heater trip which caused wide variation in dP and flow rate; the data has been excluded for clarity.

Run 3 (299.7 °C, 0.0 mg.kg^{-1} LiOH, 15.04 m.s^{-1}, see Table 4.2) dP data (see Figure 4.9) shows very little evidence of any type of deposit – a slight decrease in flow rate coupled with the constant dP is visible; this cannot be attributed to a variation in temperature as the decay in flow rate is accompanied by almost stable temperature as can be seen in Figure 4.10. Regardless, the flow rate variation is very small, and the test was only able to run for ~47 hours before a large leakage was discovered and the test was shutdown.

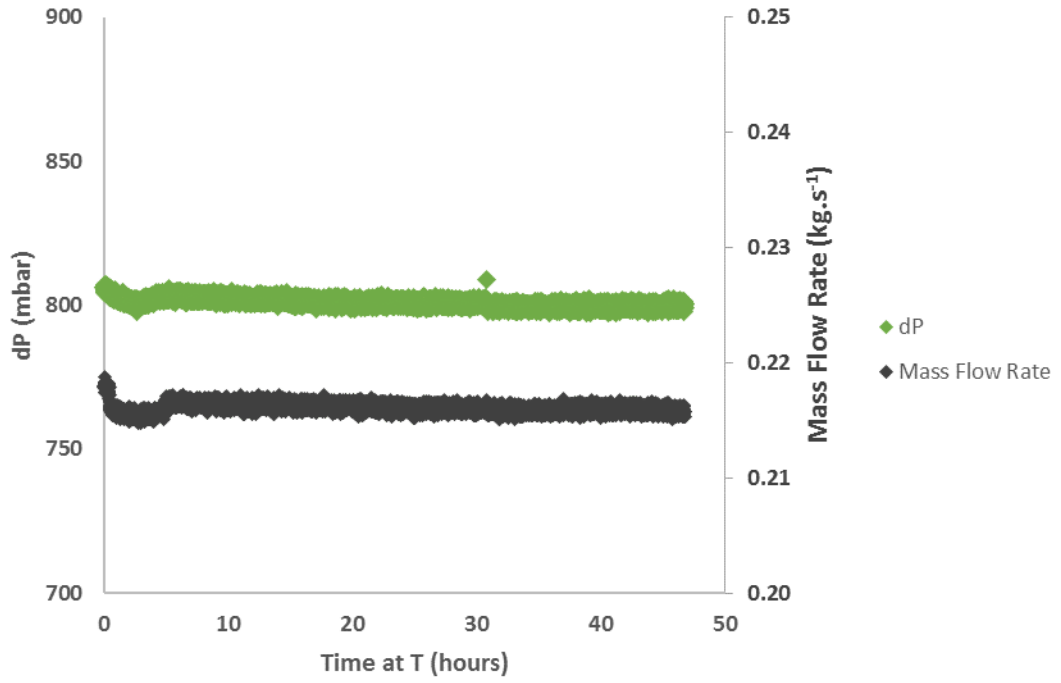

Figure 4.9 - Run 3 dP vs time. This test lasted for ~47 hours before a large steam leak was discovered, and the system shut down.

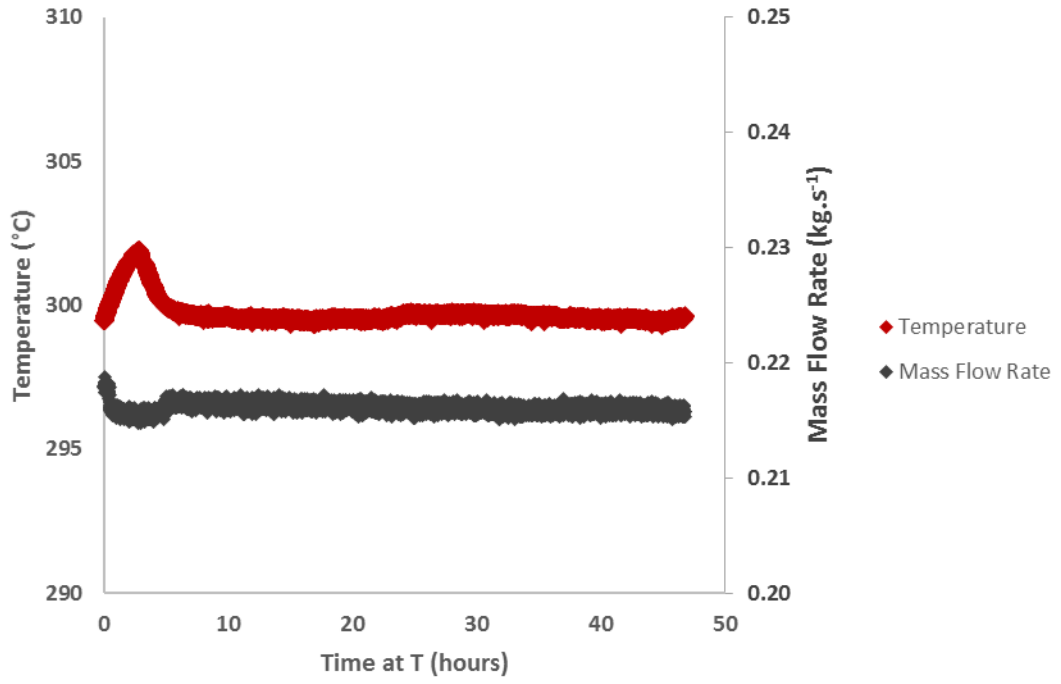

Figure 4.10 - Run 3 temperature and flow rate vs time. The slight decay in flow rate is plotted against the temperature of the system.

Run 4 (276.6 °C, 0.0 mg.kg^{-1} LiOH, 15.85 m.s^{-1}, see Table 4.2) was only run for ~5.5 hours at temperature due to a sudden failure of the inline autoclave heaters. Mass flow rate and dP of the experiment are shown in Figure 4.23 The target temperature of the system for this test had been 275 °C, however it can be seen in Figure 4.12 that the temperature overshoots the set point by approximately 3 °C before the heaters fail (see Figure 4.12). During the time above the set point temperature, a very slight decline in the dP and flow rate can be seen however this is likely due to the steadily rising temperature rather than a deposit forming (see Figure 4.12 and Figure 4.13); the expected rise in flow rate is also absent.

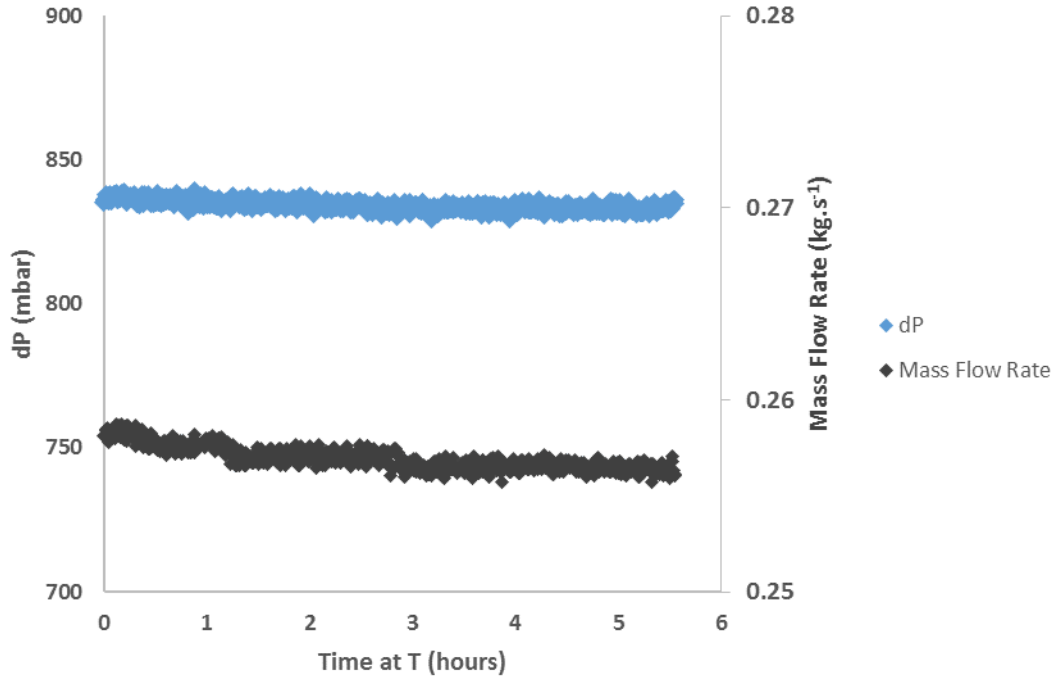

Figure 4.11 - Run 4, dP vs Time. This particular test was only able to run for a very short period of time due to a failure of the inline autoclave's heaters.

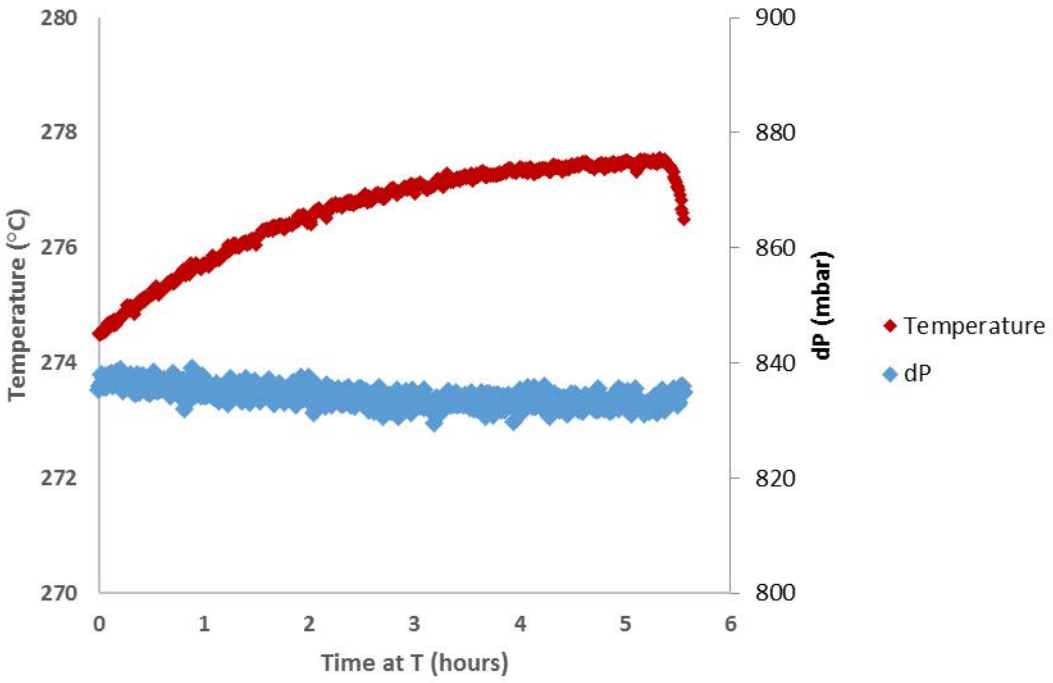

Figure 4.12 - Run 4, dP and temperature vs time at temperature.

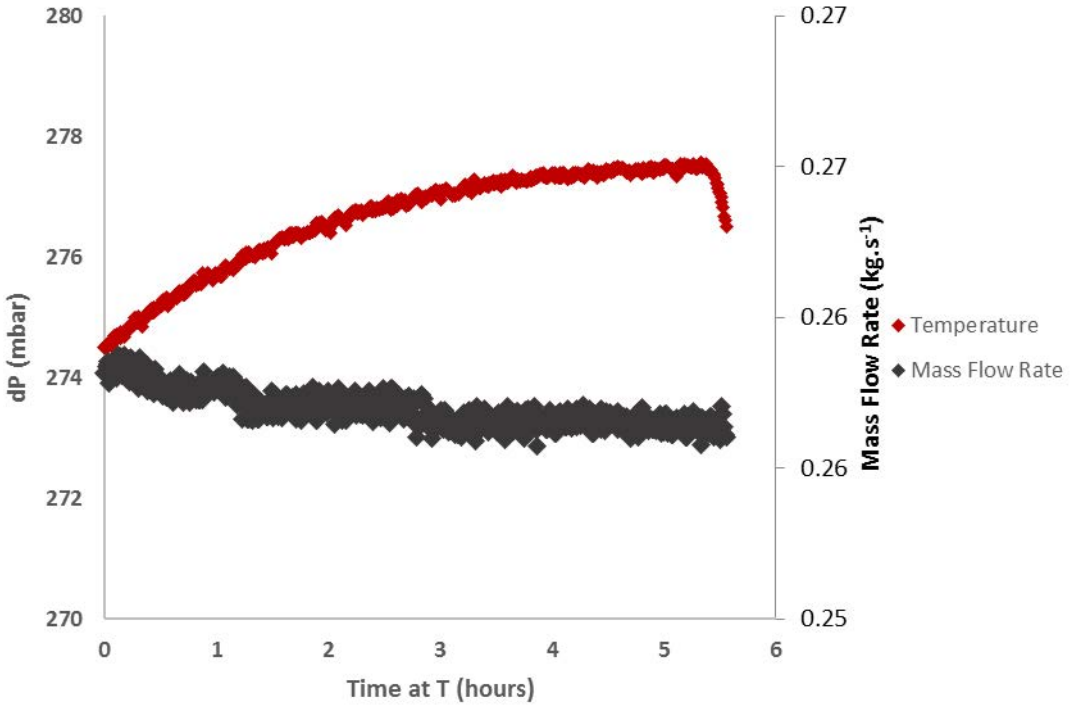

Figure 4.13 - Run 4, temperature and flow rate vs time.

The behaviour of all variables during run 5 (222.3 °C, 0.25 mg.kg^{-1} LiOH, 15.75 m.s^{-1}, see Table 4.2) is markedly different from that of the other tests, however it should be noted that run 5 is the first test in which the heater autoclave had

been removed from the flow loop. This increased the maximum flow rate of the pump, but introduced temperature instability of ~±2 ° C, and limited maximum temperature to ~222 ° C. The heater autoclave was removed after the heaters had failed during the previous test.

Initially, the flow rate and dP are relatively steady with a single perturbation caused by a loss of pressure due to incorrect operation of the gas cylinder/back pressure regulation couple (see Figure 4.14). Once corrected the flow rate stabilised to a constant value, and the dP declined slightly over the course of ~24 hours. After ~48 hours online, there was a sudden jump in dP across the cell accompanied with a drop in flow rate. The system continued to oscillate with the daily temperature variation (see Figure 4.15), however there are numerous rapid drops in dP followed by equally rapid rises which are not explained by the temperature variation. These were measured by two independent differential pressure sensors, which indicates that the variation is no the result of improper operation of a single instrument.

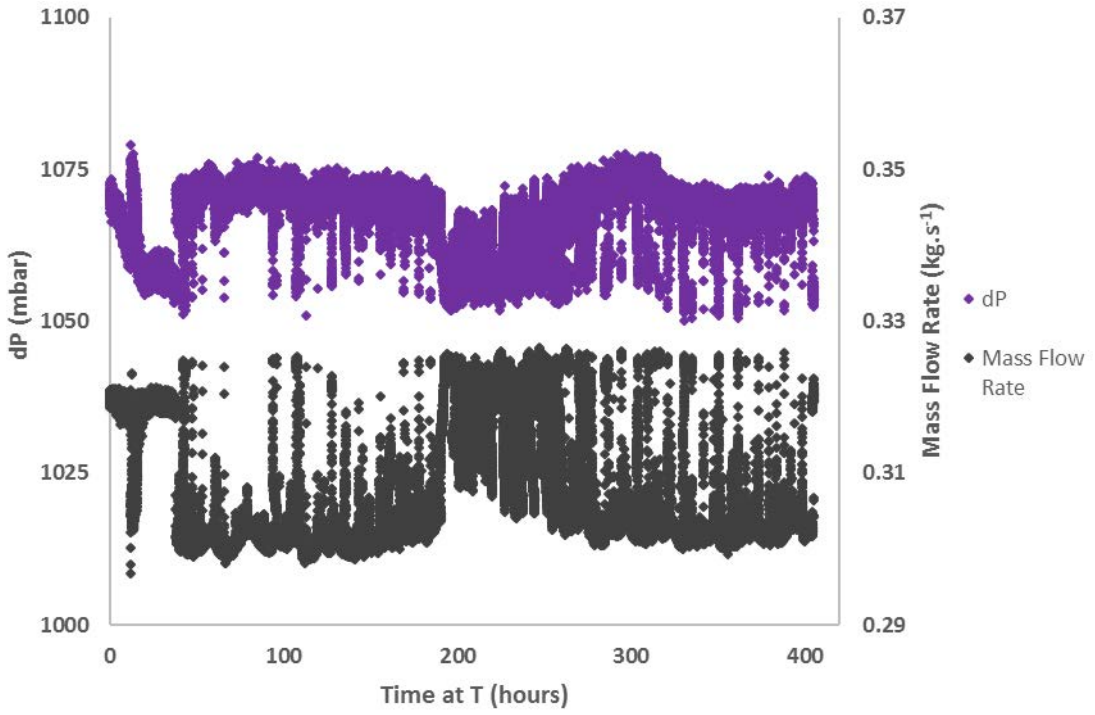

Figure 4.14 - Run 5, dP and flow rate vs time at temperature.

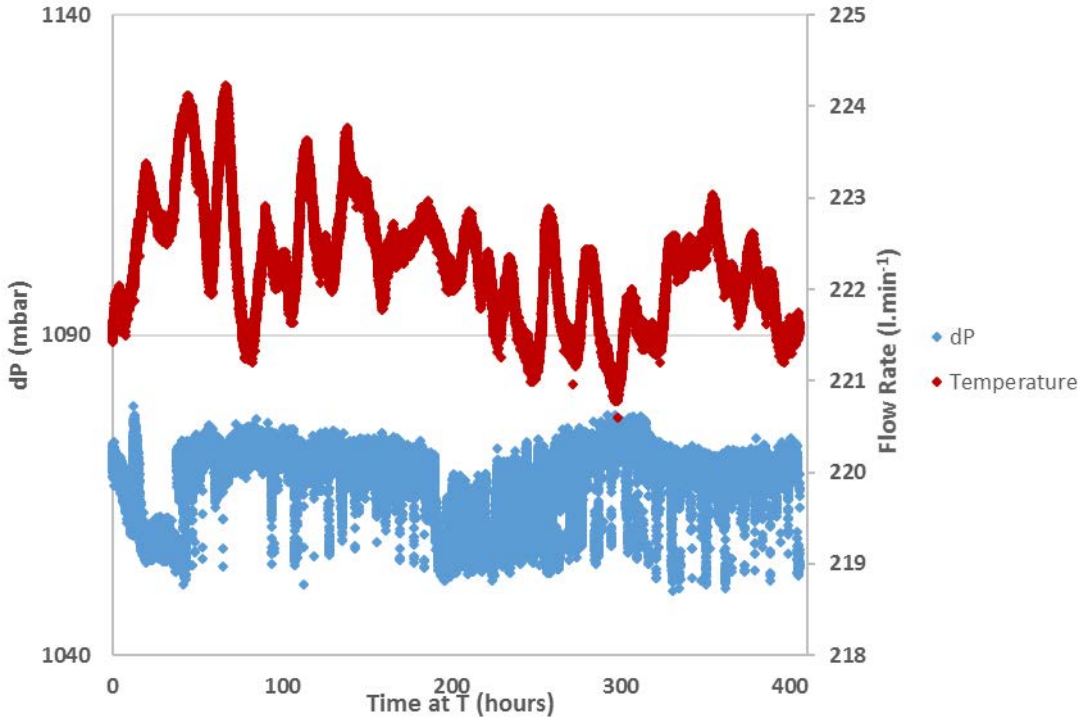

Figure 4.15 - Run 5, variation in temperature and dP as a function of time online.

4.2.2 SEM Imaging

Images of the test section face, where deposition was expected to occur, are presented below. Runs 1, 2 and 5 were studied; runs 3 and 4 were excluded due to the brevity of the tests.

SEM images of the run 1 test piece (~227 °C, 0.1 mg.kg^{-1} LiOH, 14.2 – 14.4 m.s^{-1}) shows the presence of a distinctly different material at the corner between the restriction face and the chamfer face (images shown in Figure 4.16 and Figure 4.17, EDX composition maps shown in Figure 4.18), and the chamfer face and the restriction annulus (images shown in Figure 4.19, Figure 4.20 and Figure 4.21). These are both points of fluid detachment, which is not a location where electrokinetic deposition is expected to occur, so it is likely that a different deposition process is responsible. The difference in deposition morphology between the chamfer face and the annulus corner is potentially a consequence of the flow regimes produced by the boundary geometry.

What is of greatest interest, is the lack of iron in the deposited material. Instead, the dominant element present is antimony, with only small additions from other elements. The blockage phenomena seen in literature has not fully manifested in this test, and only a small deposit has been grown, measuring approximately 35 μm in height.

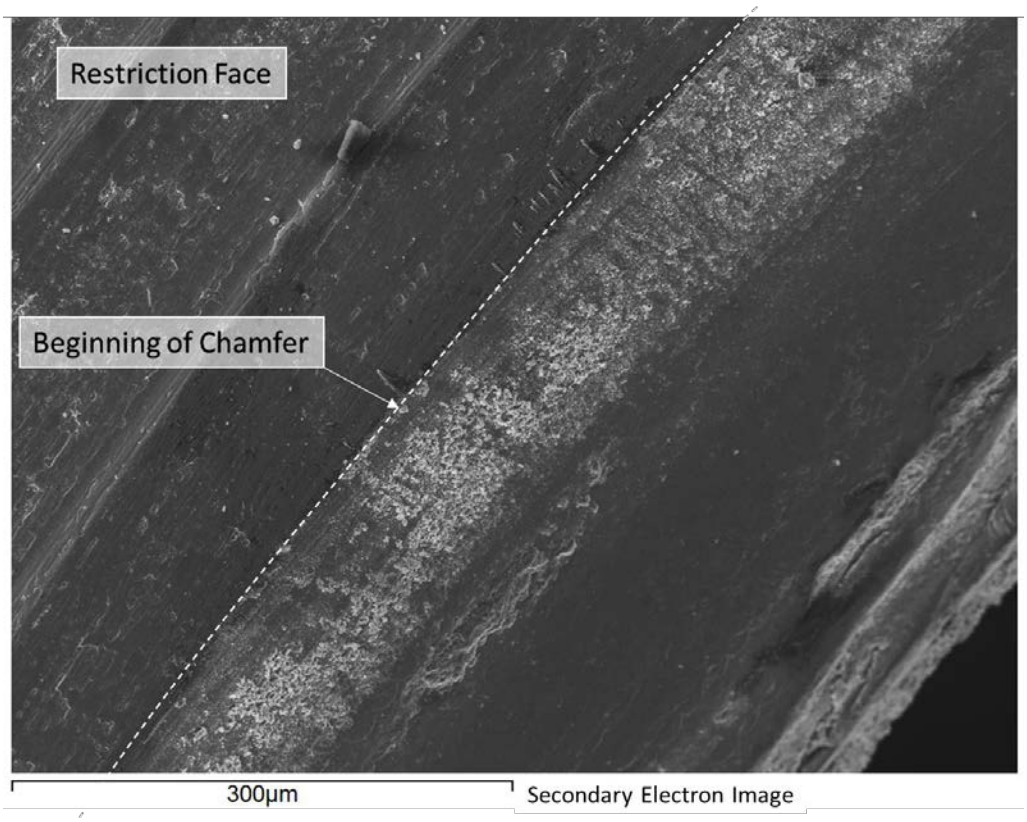

Figure 4.16 – Run 1 test piece: SEM of the corner between the restriction face and the chamfered face (a schematic of this is shown Figure 4.1). Images taken in secondary electron detection mode, with a beam energy of 20 kV at a working distance of 10 mm.

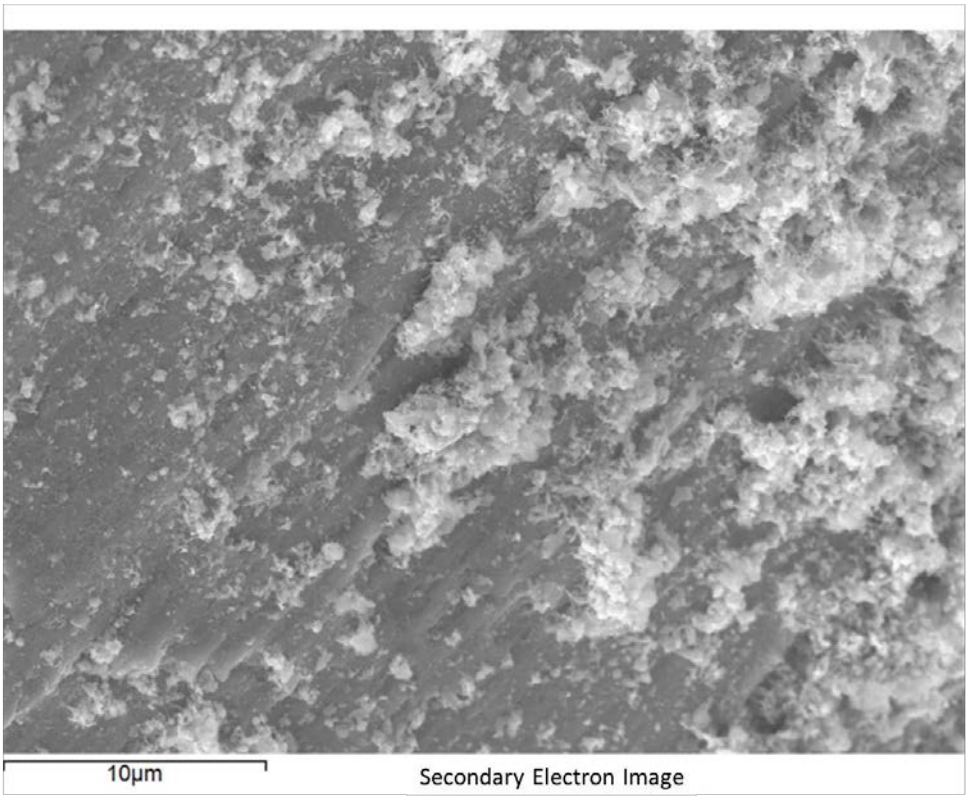

Figure 4.17 – Run 1 test piece: higher magnification image of the lighter shaded material seen in Figure 4.16. Images taken in secondary electron detection mode, with a beam energy of 20 kV at a working distance of 10 mm.

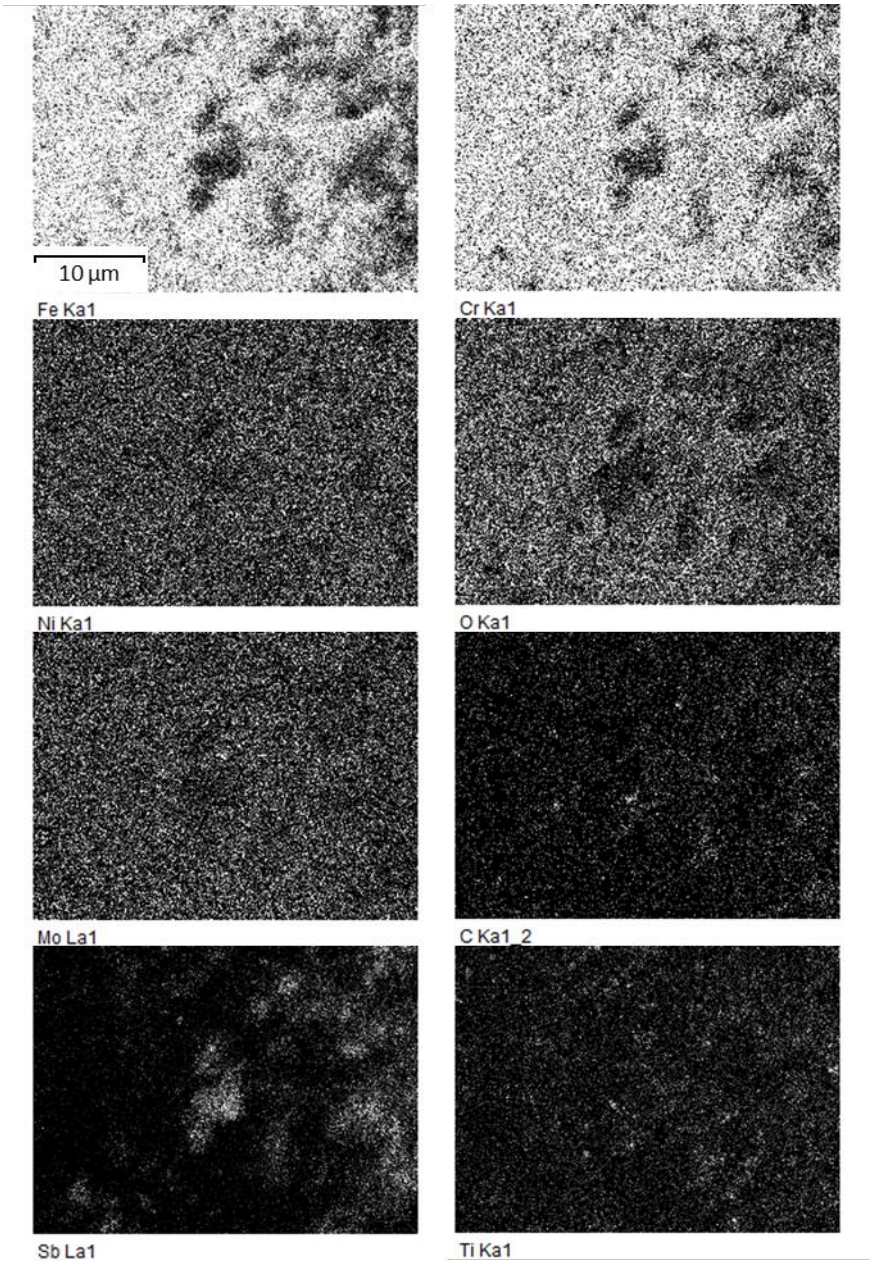

Figure 4.18 – Run 1 test piece: EDX composition maps of the site of interest, show in Figure 4.17. The deposited material appears to be composed largely of antimony, while being devoid of iron and chromium.

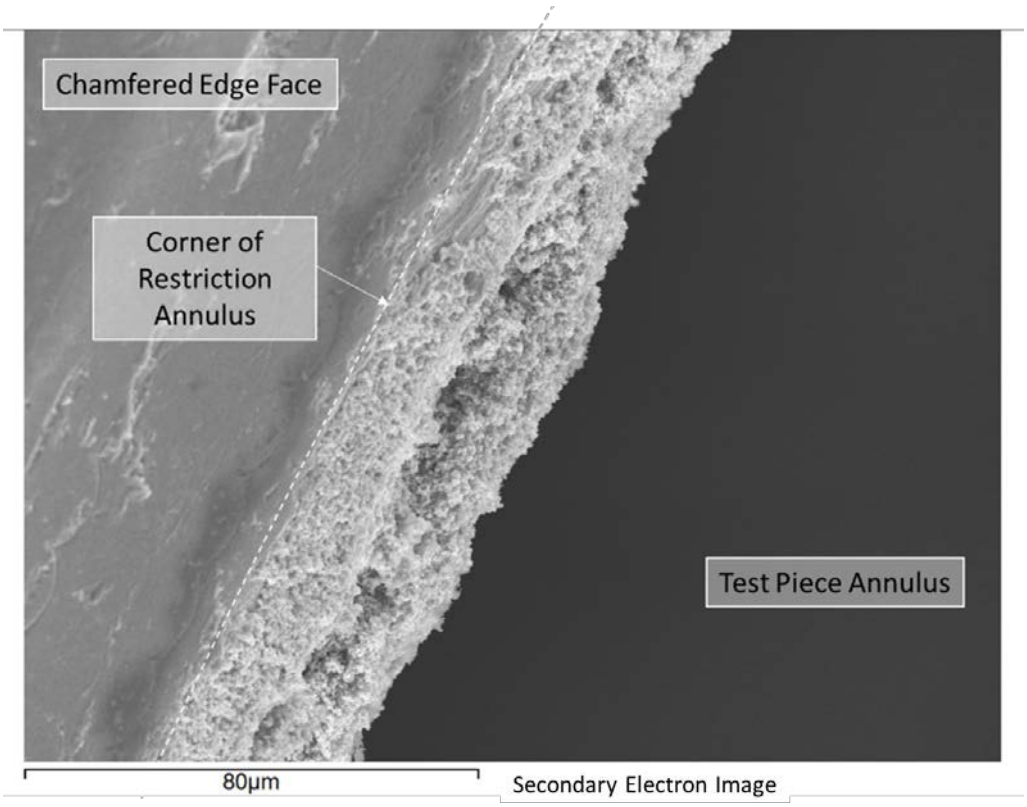

Figure 4.19 – Run 1 test piece: deposition at the entrance to the annulus of the test piece. Images taken in secondary electron detection mode, with a beam energy of 20 kV at a working distance of 10 mm.

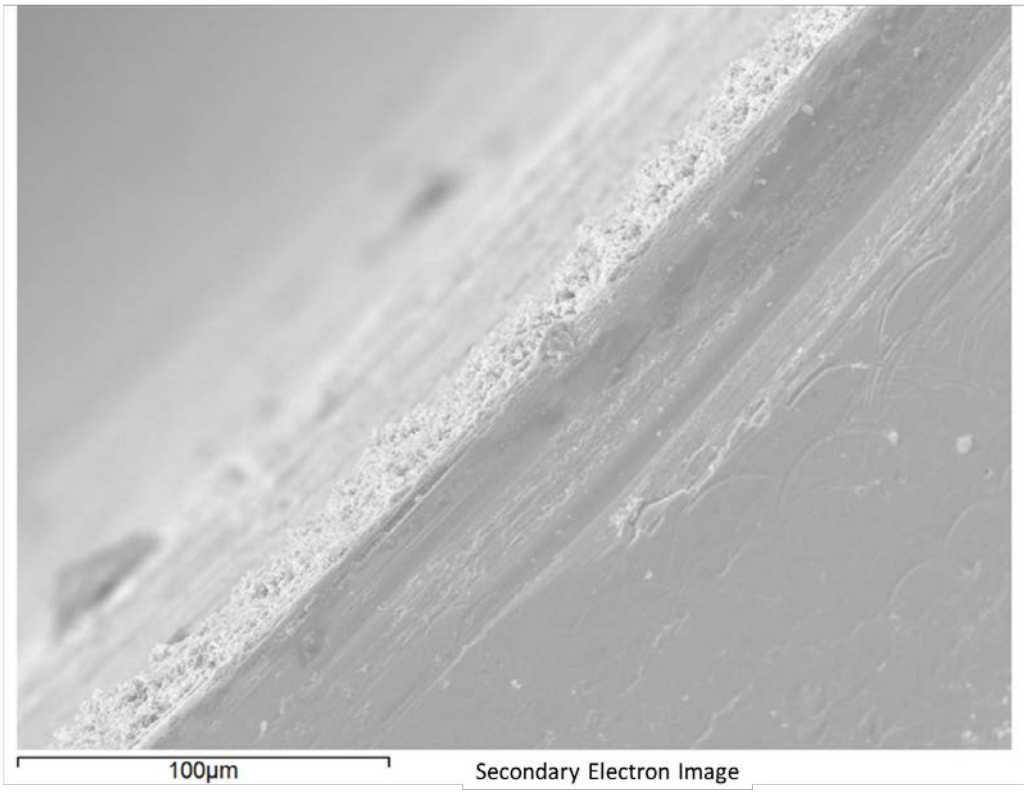

Figure 4.20 – Run 1 test piece: deposition at the entrance to the annulus of the test piece. Images taken in secondary electron detection mode, with a beam energy of 20 kV at a working distance of 10 mm.

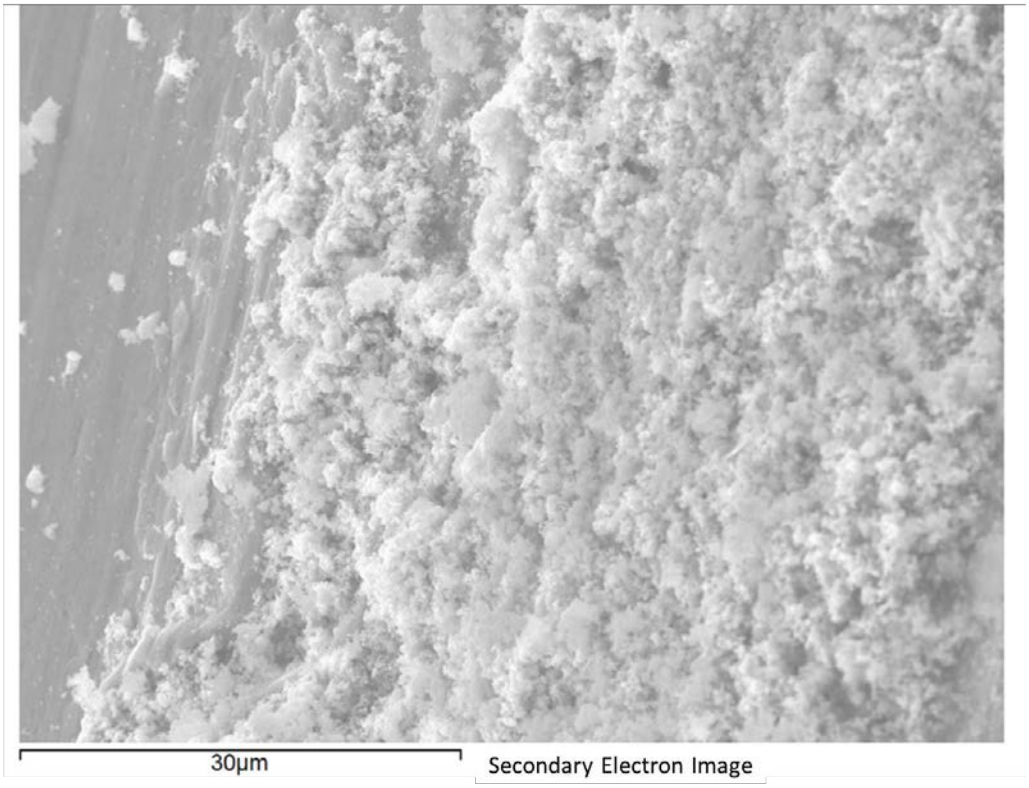

Figure 4.21 - Higher magnification image of the deposition seen at the entrance to the restriction annulus, shown in Figure 4.20. Images taken in secondary electron detection mode, with a beam energy of 20 kV at a working distance of 10 mm.

Deposition seen on the run 2 (300 °C, 0.0 mg.kg^{-1} LiOH, 14.9 – 15.3 m.s^{-1}) test piece is significantly different in morphology to that of run 1; deposition in run 1 has a powder-like appearance, while deposition of run 2 appears to have a sharply defined crystalline structure (see Figure 4.22). EDX analysis of the deposition confirmed the presence of antimony in the deposits as the dominant element, which also contained a significant amount of copper. In contrast to the depositions in run 1, iron as found to be present, but in very small quantities (see Figure 4.23).

The tendril-like morphology of these deposits is consistent at all sites of occurrence around the test piece (see Figure 4.24, Figure 4.25 and Figure 4.26). The structure is similar to the morphology seen on the EMILIE loop for tests

performed under secondary chemistry conditions, using an Alloy 600 test piece (see Figure 4.27) [12].

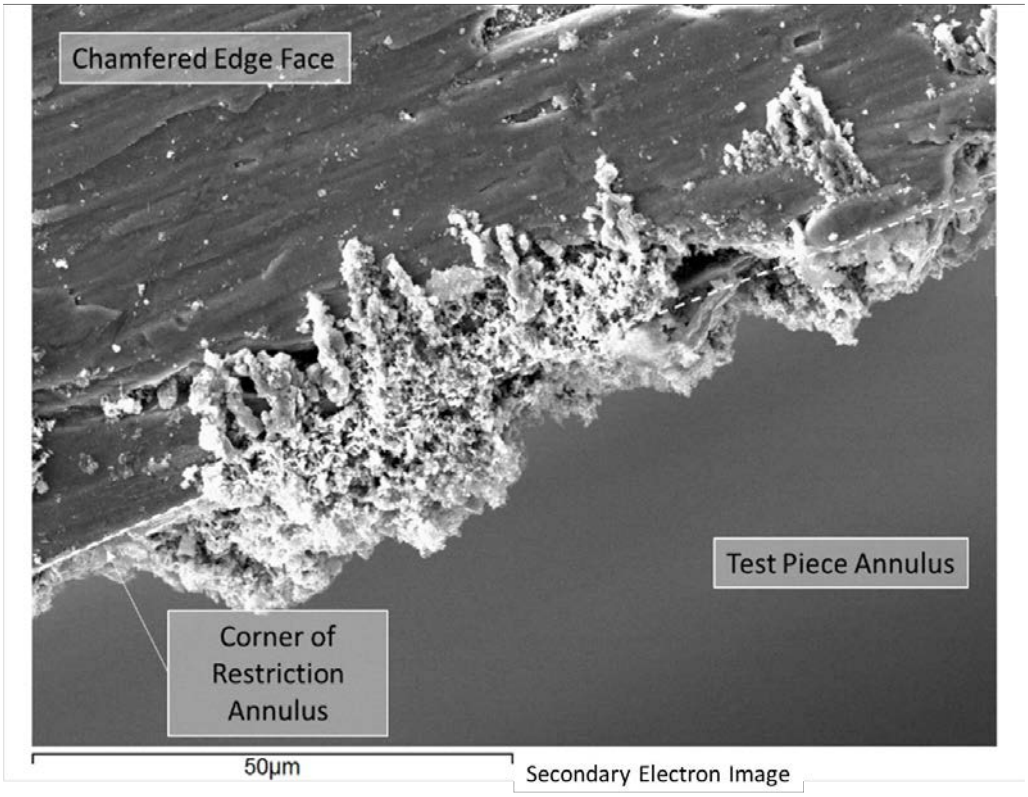

Figure 4.22 – Run 2 test piece: deposition at the entrance to the annulus of the test piece of run 2. The tendril-like appendages of the deposit are a common feature across other deposition sites. Images taken in secondary electron detection mode, with a beam energy of 20 kV at a working distance of 10 mm.

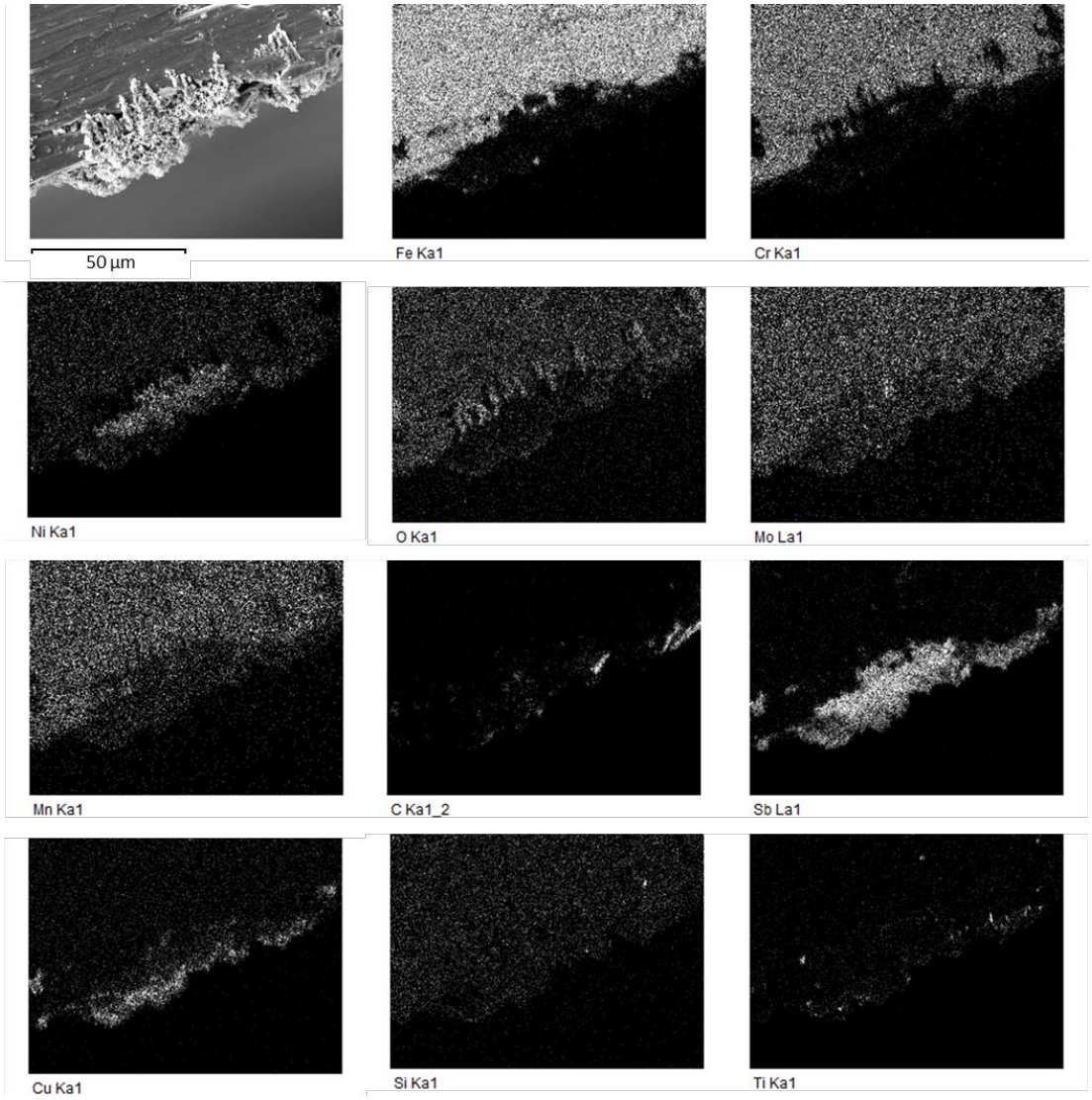

Figure 4.23 – EDX composition maps of the site of interest, show in Figure 4.22. The deposited material appears to be composed largely of antimony, nickel and copper, with small additions from other elements, suggesting that the deposit are not formed from the expected mechanism, which would produce magnetite deposits.

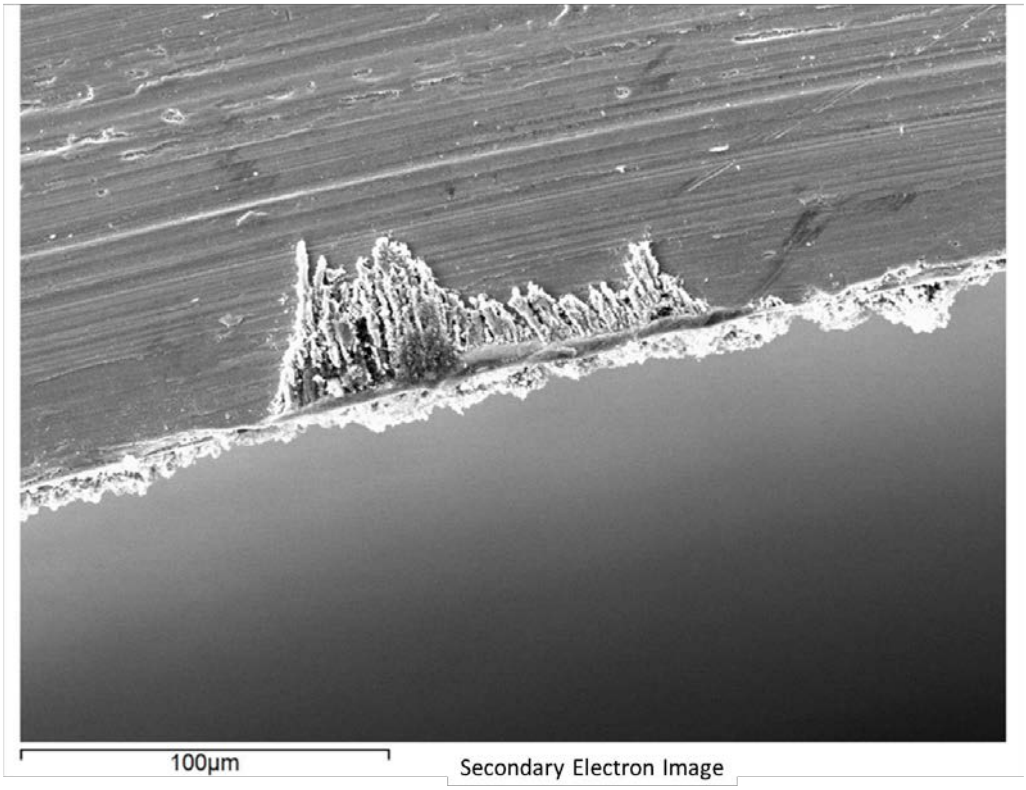

Figure 4.24 – Run 2 test piece: deposition at another location. Images taken in secondary electron detection mode, with a beam energy of 20 kV at a working distance of 10 mm.

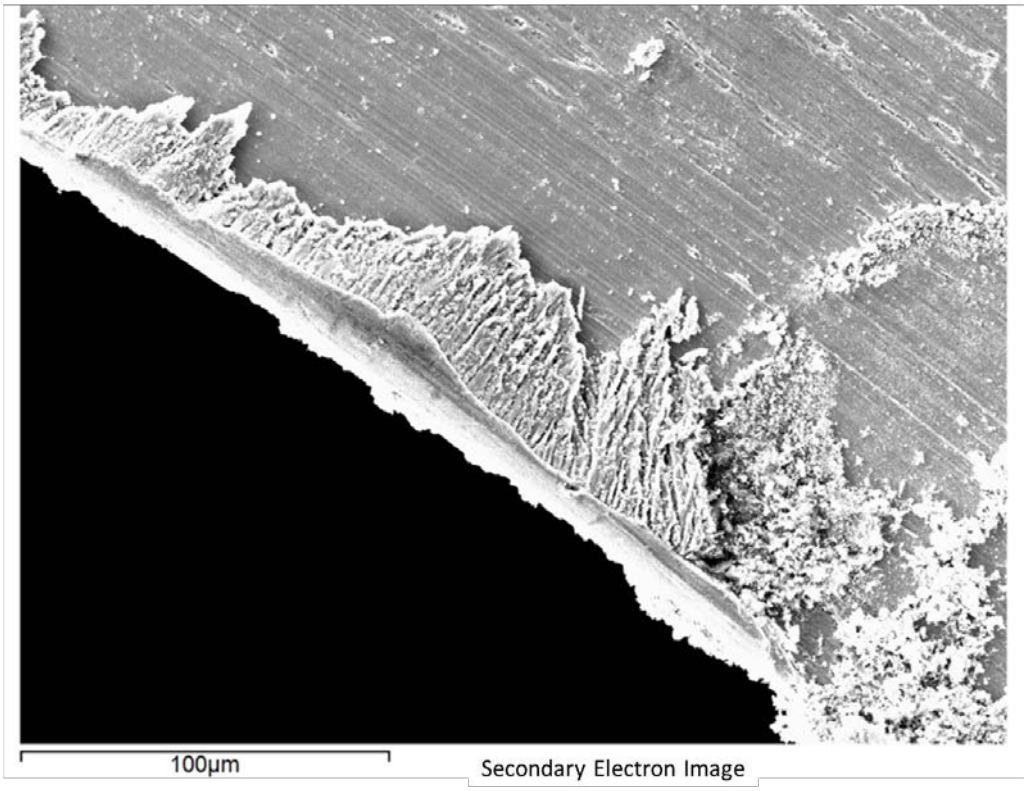

Figure 4.25 - Run 2 test piece: deposition on the restriction annulus entrance. Images taken in secondary electron detection mode, with a beam energy of 20 kV at a working distance of 10 mm.

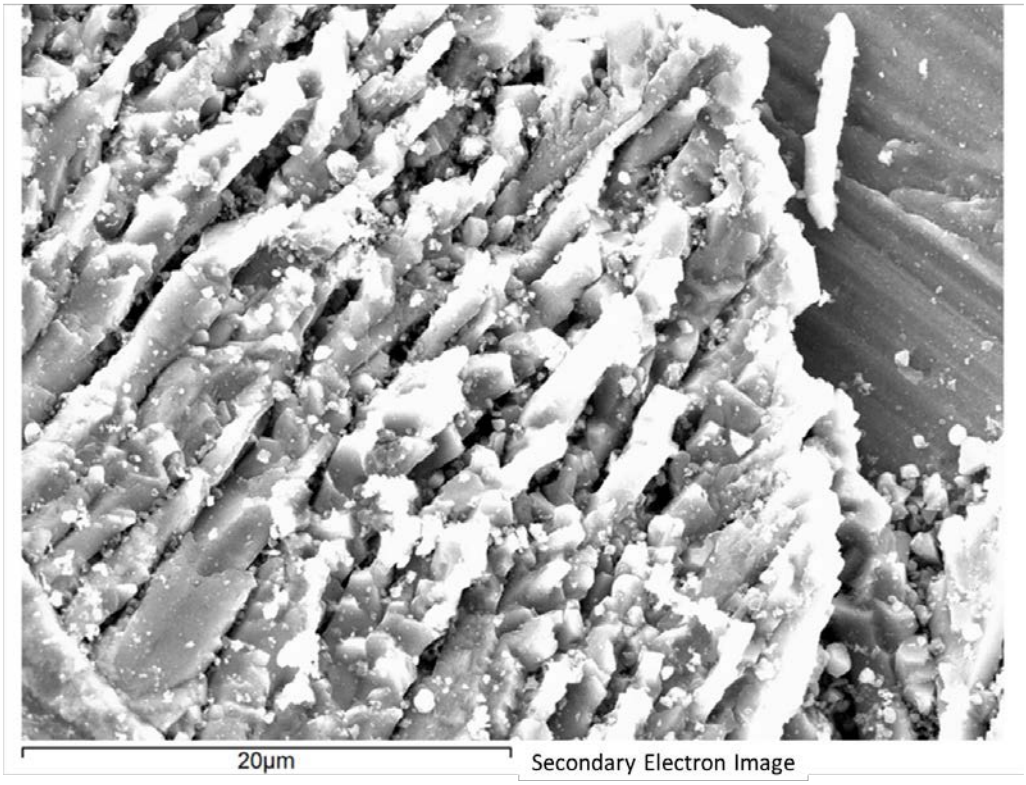

Figure 4.26 – Run 2 test piece: a higher magnification image of the deposition seen in Figure 4.25. The deposition morphology shows striking similarity to that seen in some runs from the EMILIE loop [12], shown in Figure 4.27. Images taken in secondary electron detection mode, with a beam energy of 20 kV at a working distance of 10 mm.

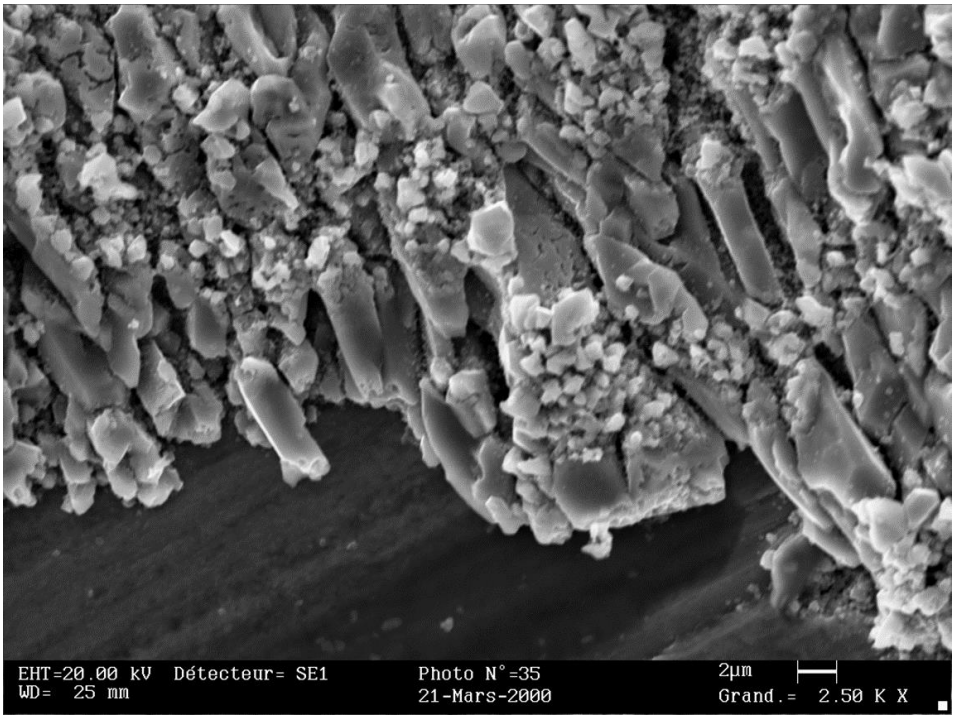

Figure 4.27 - A high magnification image of the deposition of material on an Alloy 600 sample in the EMILIE loop [12]. The magnification in this image is identical to that of Figure 4.26.

The deposition observed on the test piece of run 5 (~222 °C, 0.25 mg.kg^{-1} LiOH, 3.5 cc.kg^{-1} H_2, 15.8 m.s^{-1}) was found to be significantly different from that of runs 1 and 2 (see Table 4.2 for experimental details); where runs 1 and 2 showed a sprinkling of matter distributed across the surface of the chamfer and some on the inside edge of the restriction entrance, run 5 deposition exhibited large walls of material flush with the face of the test piece. This may be due the change in flow regime, instigated by the difference in test piece geometry – the face of the test piece was carefully turned down to ensure that it met the annulus at a 90° angle, rather than over a chamfered face.

The walls of deposition, which appear to have grown flush with the face of the test piece, and normal to the wall of the annulus (see Figure 4.28, 4.41, 4.42 and 4.43), which is similar to, but not exactly what is suggested by the electrokinetic deposition theory (see section 2.3.6) [17,89]. The deposits grow only on the inside of the restriction face, not from the point of fluid attachment (*i.e.*, the face of the restriction) as is expected. Again, it is likely that another deposition mechanism is dominant.

While morphologically different from the depositions of run 1 and 2, the structures seen in run 5 are chemically similar. In both areas of interest (see Figure 4.28 and Figure 4.31), composition maps showed the dominant element in the deposit to be antimony, with minor additions from other elements (see Figures 4.44 and 4.45). Similar to run 1, no iron was found in these deposits.

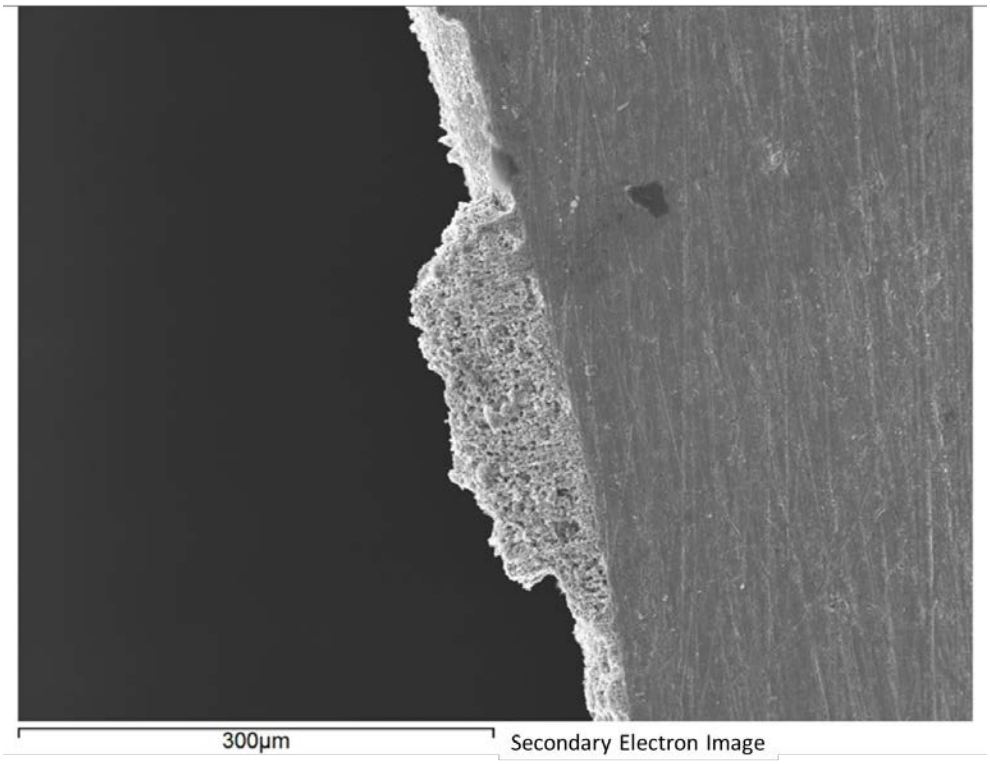

Figure 4.28 - Deposition at the entrance to the annulus of the test piece of run 5. This test piece has a sharp corner, rather than a chamfered face with a 45 ° turn. Images taken in secondary electron detection mode, with a beam energy of 20 kV at a working distance of 10 mm.

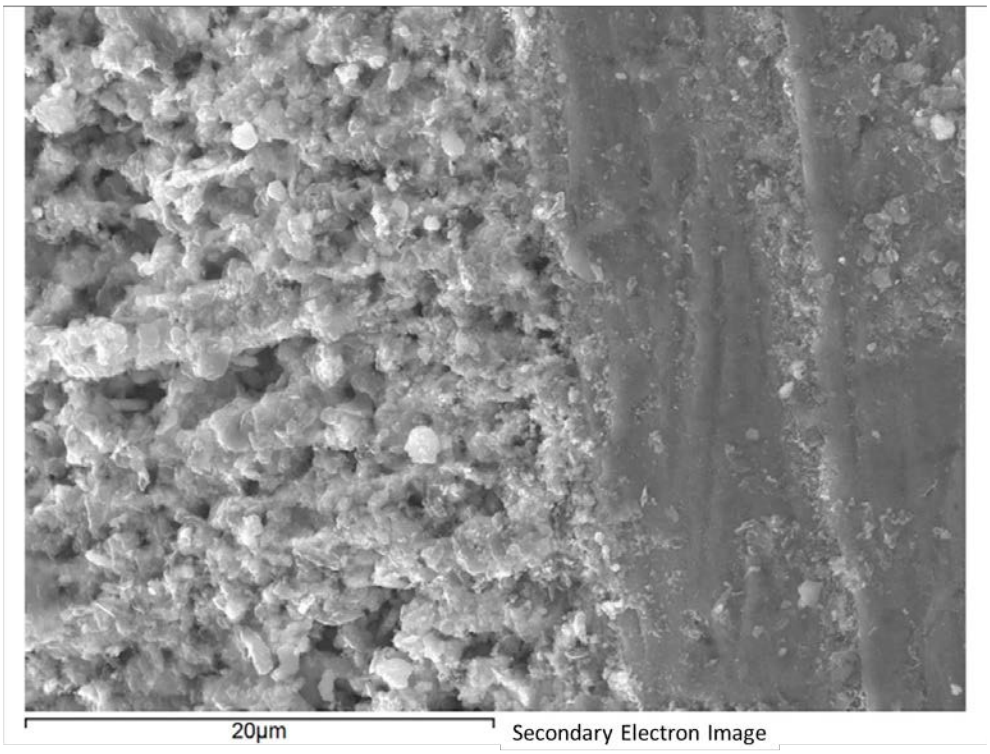

Figure 4.29 - Higher magnification image of the corner of the restriction, showing the interface between the deposit and the wall. Images taken in secondary electron detection mode, with a beam energy of 20 kV at a working distance of 10 mm.

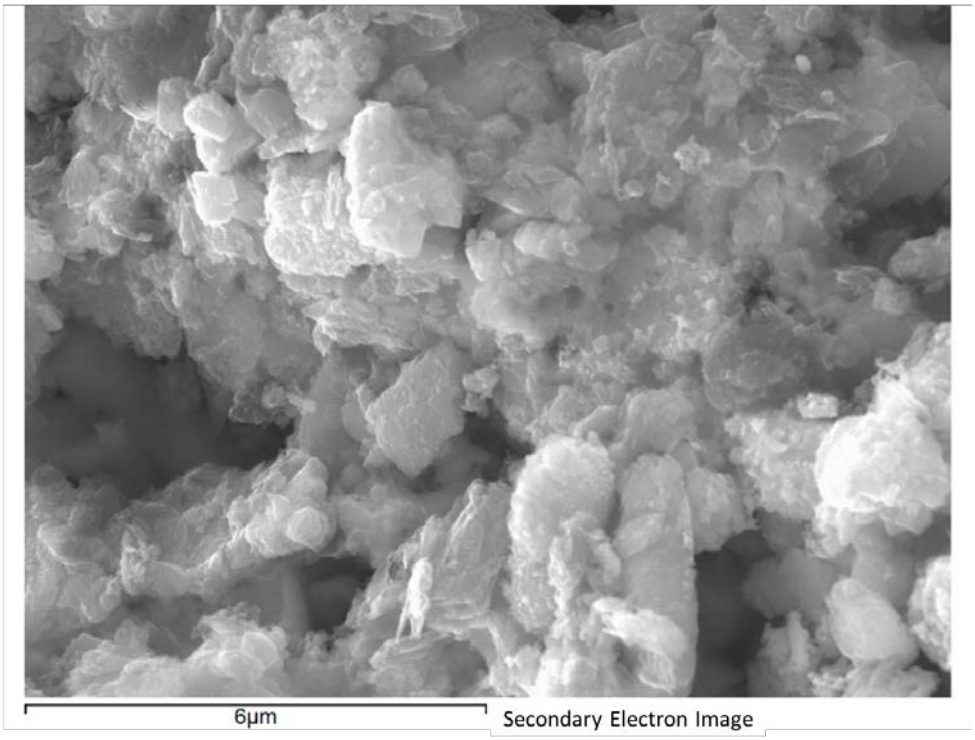

Figure 4.30 - A high magnification image of the microstructure of the deposition shown in Figure 4.29. Images taken in secondary electron detection mode, with a beam energy of 20 kV at a working distance of 10 mm.

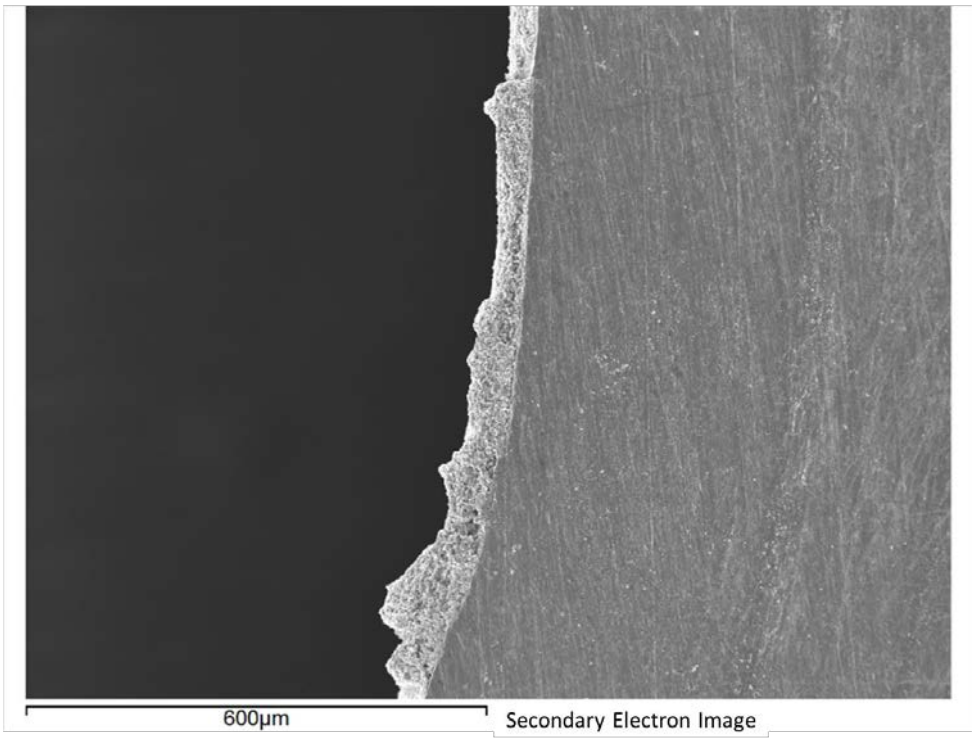

Figure 4.31 – Deposition at the entrance to the annulus of the test piece of run 5. The deposit shown here is the largest one found across all test pieces studied, stretching approximately 800 µm end to end, and approximately 100 µm in height at the tallest point. Images taken in secondary electron detection mode, with a beam energy of 20 kV at a working distance of 10 mm.

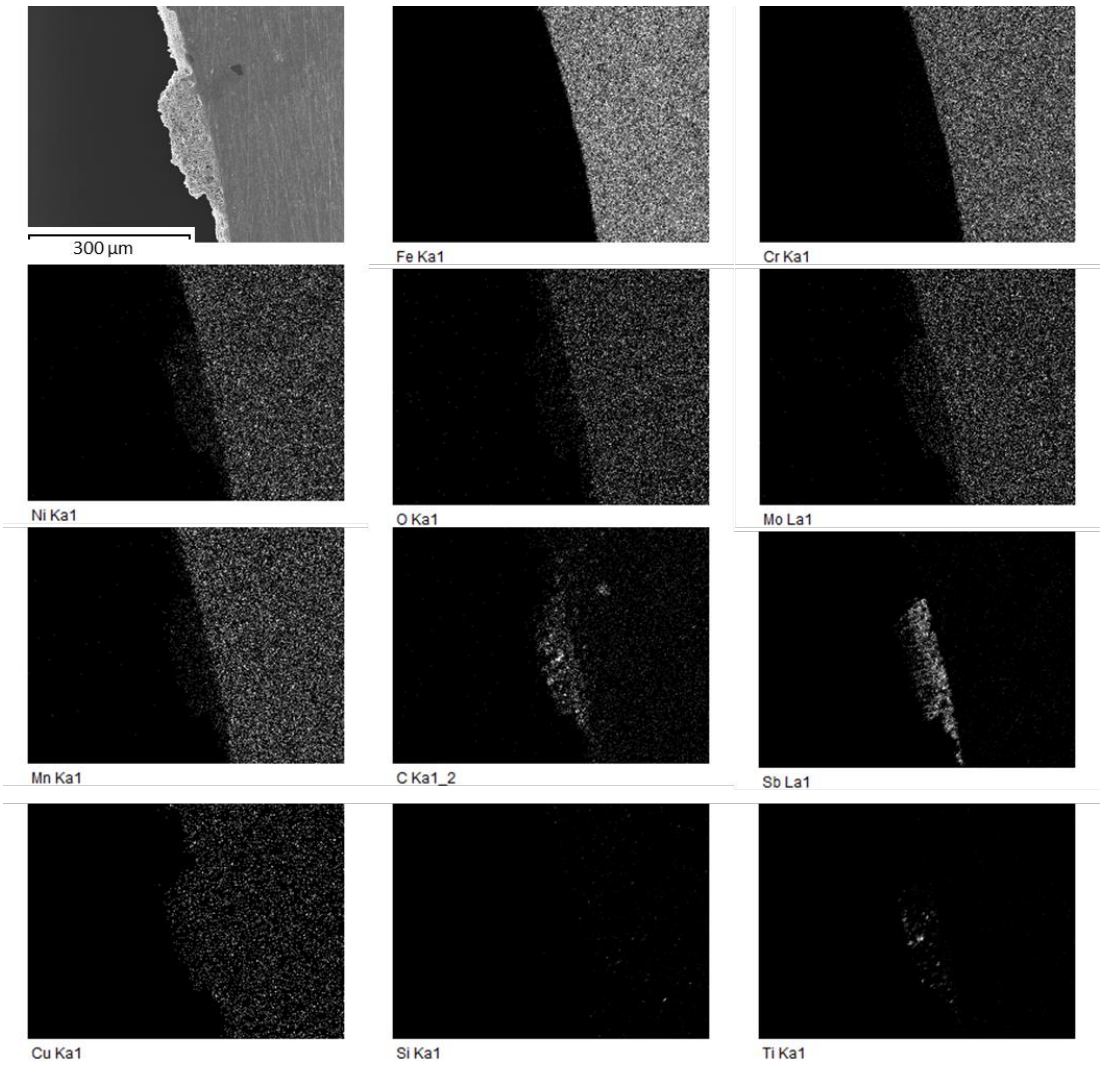

Figure 4.32 – EDX composition maps of the site of interest, show in Figure 4.28. The deposited material appears to be composed largely of antimony and carbon, with small additions from other elements shown, with the notable exception of iron. Copper appears to be a surface contaminant in this analysis rather than a specifically included component of the deposit.

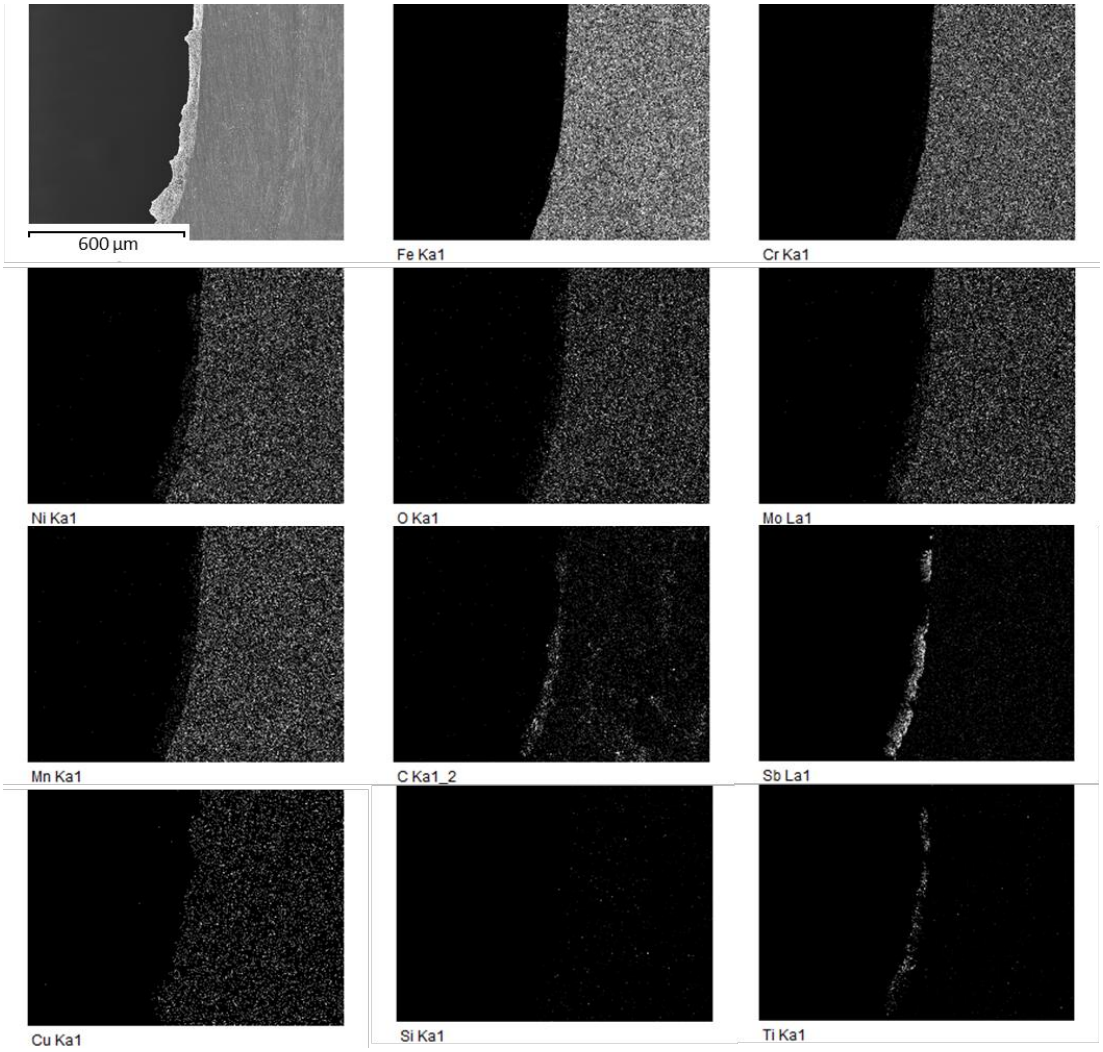

Figure 4.33 – EDX composition maps of the site of interest, show in Figure 4.31. Similar to the analysis of the deposition shown in Figure 4.32, the deposit appears to be composed largely of antimony and carbon, with small additions from other elements shown. No iron is observed in this deposit.

4.2.3 Raman Spectroscopy

After every run, the water from test was found to be heavily ladened with a black particulate material. The hot loop was cleaned using a 1 µm water filter, and the black particulate material collected by the filter was analysed using which was identified to be graphite by Raman spectroscopy (see Figure 4.34). The filters are made from polypropylene, and thus some of the bands expected for graphite were obscured, however the main G-band at 1582 cm^{-1} (sp^2 bond stretching mode in graphite sheets) and the G'-band at ~2720 cm^{-1} (second vibrational mode of the G-band stretching mode) were both observed [191]. The sp^3 vibrational band at 1620 cm^{-1} is also observed, which is indicates the

presence of some sp^3 character (tetrahedral bonding) to the graphite bonding structure [191].

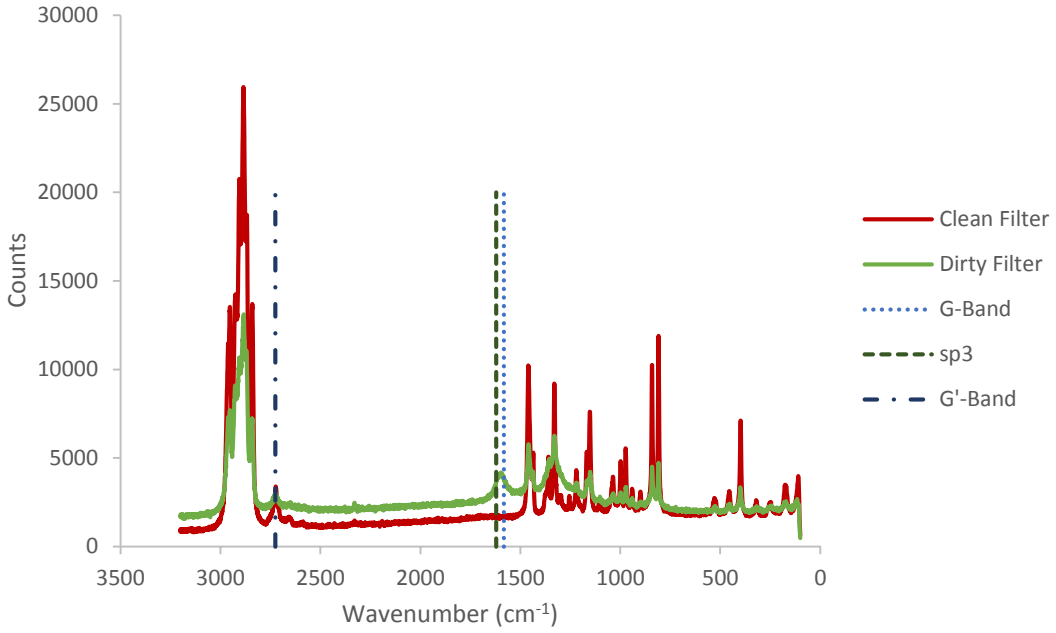

Figure 4.34 – Raman spectra of a clean polypropylene filter and one soiled by a cleaning run. The presence of the peak at the highlighted location indicates the presence of graphite on the soiled filter amongst the other possible forms of carbon. The various stretching and vibrational peaks of graphite are noted on the plot [191].

4.3 Discussion of Section A

4.3.1 Differential Pressure Measurements

Differential pressure measurement during testing produced data to suggest the presence of deposition occurring during some of the runs, however none of the data sets showed trends indicative of electrokinetic deposition. Such trends, as seen in the literature [18] involve a gentle increase in differential pressure with time as the deposition builds. Due a shortcoming in the hot loop, electrokinetic deposition (which would increase the head loss across the test cell) would manifest as a loss of flow rate at the pump and a steady dP across the cell; no feedback system was installed to automatically adjust the flow rate. This trend was not observed in any of the experiments.

Only run 5 showed any significant deviation in differential pressure and flow rate observed. This experiment was different from runs 1 – 4 in several ways. First, and most significant, was the removal of the heating autoclave from the flow path, which removed some of the pressure drop in the system and increased the maximum flow rate in the loop markedly, as shown in Figure 4.6. The autoclave was removed from the system after a heater failure, and the system temperature for this run was provided entirely by the top-up heaters and the pump. The average temperature for the experiment was 222.3 ±0.7 °C, though this was prone to fluctuations of a daily frequency as the temperature of the room changed during the day and night, as can be seen in Figure 4.15. Secondly, a large amount of dissolved gas was present in the system, primarily as a means to dissolve hydrogen gas into the water for the test, as discussed in section 4.1.3. The level of hydrogen was 3.5 $cc.kg^{-1}$, however since the gas mix contained 0.5% H_2 in 99.5% N_2, the water also contained ~1500 $cc.kg^{-1}$ of N_2 which was not expected to have any chemical effect on the deposition process. Finally, the test piece used in this experiment was more carefully machined to ensure a sharp corner at the inlet.

During run 5 significant deviation in both flow rate and differential pressure are observed, but the deviations are transient in nature (see Figure 4.15), appearing as spikes which rapidly disappear. The same pattern is seen independently by both the flow meter and test cell differential pressure meters, indicating that the variations are not a result of instrumental failure.

Given that deposition is observed in the SEM micrographs of this test piece (see section 4.2.2), it is reasonable to assume that the variation in the dP and flow rate are a result of deposition forming rapidly in the mouth of the test piece, before being physically broken away from the surface by the flow. Such deposition is not similar to the hard deposits seen in electrokinetic deposition,

where deposits form slowly over time and appear to be resistance to the hydrodynamic force of the flow.

It is more likely that these depositions are a result of 'flashing' at the test piece, a mechanism similar to the deposition process associated with sub-cooled nucleate boiling, where the fluid is converted to a gas phase and deposits dissolved ions at the location where the phase change occurred. This is reasonable, due to the presence of an enormous quantity of gas dissolved in the liquid and as the flow rate is this experiment was higher than previous tests. Within the test restriction is a region of low pressure associated with the point of maximum flow velocity, the 'Vena Contracta'. As flow rate increases, the relative pressure at this location will fall. A diagram of the flow region is shown in Figure 4.35. It is possible that the high flow rate and dissolved gas content in the system were high enough during run 5 that the region of low pressure permitted for the presence of a two phase fluid – dissolved gas bubbles suspended in the test solution.

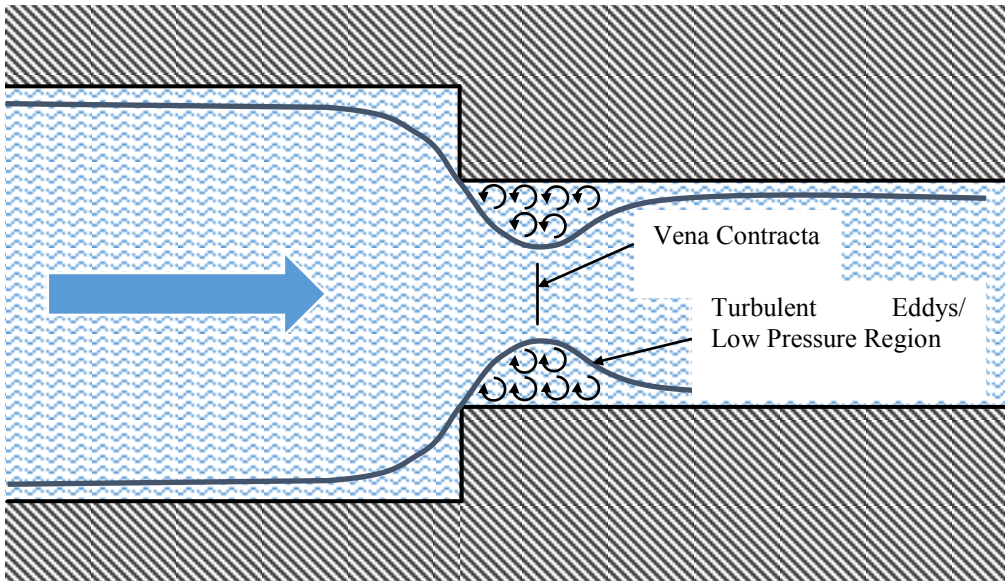

Figure 4.35 - Diagram of the fluid flow pattern within the flow restriction. The vena contractor is the point of maximum flow rate and coincides with the region of lowest pressure at the wall. It is inside this region that the flashing deposition mechanism takes place.

This mechanism explains the rapid formation kinetics, as the build-up rate would be limited only by the rate at which solid material could be transported to the deposition location, however the size of the deposit is limited. At a critical size the deposit appears to become unable to resist the force of the flow, and is sheared from the surface, which is observed as a sudden rise in system flow rate and fall in dP across the test cell.

4.3.2 SEM/EDX Analysis

SEM imaging of test pieces from runs 1, 2 and 5 revealed the presence of deposits at the entrance to the restriction, however EDX spectroscopy has shown the depositions to be composed largely of antimony rather than magnetite, as was initially expected.

Deposition on the run 1 test piece (exposed to 0.1 ppm [LiOH] at ~227 °C) was quite sparse and present in two discrete locations, the leading edge of the counter-sunk restriction and the inside edge of the restriction annulus (see Figure 4.16 and Figure 4.19). The deposit is powdery and granular, and does not extend away from the surface by more than a few tens of microns, so it is not surprising that the differential pressure data (see Figure 4.7) shows no deviation. The deposit appears to be composed of antimony, as Figure 4.18 shows, and is conspicuously devoid of oxygen.

The two locations where deposition is visible are regions where flashing would be expected to occur, though the small quantity of dissolved gas in the test water is probably responsible for limiting the amount of deposit formed – lower dissolved gas levels mean that very high flow rates would be required to generate a region of pressure low enough to cause dissolved gas to leave solution.

Test pieces from run 2 (exposed to high purity water at 300 °C) exhibits a deposit of very different morphology. Instead of the powder-like scattering

seen on the run 1 test piece, the deposition is columnar is structure (see Figure 4.26), very similar to the structure of depositions seen by the AREVA research group (see Figure 4.27) [12]. However, the deposition formed on the run 2 test piece is composed of antimony, as shown by EDX spectroscopy in Figure 4.23, while that seen by AREVA was characterised as magnetite. In similar fashion to the result composition of the run 1 test piece, the deposit lacks a significant quantity of oxygen, suggesting that the deposit is metallic. The deposits are clearly more extensive than those seen on the run 1 test piece, but are still small enough in extent not to disturb the flow rate or differential pressure.

Finally, the imaging of the run 5 test piece (exposed to 0.25 ppm [LiOH] solution at ~222 °C, and with high volumes of dissolved gases present) shows large and extensive deposits around the edge of the annulus entrance, as seen in Figure 4.28 and Figure 4.31. These depositions are far larger than anything seen in runs 1 or 2 yet they appear to be granular in structure similar to run 1, rather than columnar crystals seen in run 2; it is possible that the structure of the deposit under these conditions is dependent on temperature, though this data does not provide clear indication of how.

The deposits stand approximately 100 μm from the surface at their highest point, which is tall enough to have an effect on flow rate and dP which is of similar size to that seen by Brun *et al.* [18], who saw head loss variations of up to 50 %.

The deposit present on the run 5 test piece was again found to consist largely of antimony, with the absence of a significant oxygen peak, making identification of the phase structure difficult.

4.3.3 Raman Spectroscopy

Raman spectroscopy was carried out on sectioned pieces of the in-line polypropylene filters with were used to extract particulate matter from the hot loop during cleaning in between tests.

The technique successfully shows the presence of graphite, which has been used in place of polytetrafluoroethylene (PTFE) for all compressible sealing materials. Locations of use include gaskets for the autoclave heads, spiral wound gaskets for the test cell flanges, needle valve packing, and sealing gaskets for the pump; it has been seen on regular occasion that compressing the grafoil gasket on the hot loop autoclaves results in gasket splitting slightly under the applied force. The presence of the graphite particles in the test solution offers an explanation for the source of the antimony from which the deposits are composed – in high pressure applications, carbon seals are often doped with antimony to improve the mechanical qualities of the seal [192].

If small flakes of graphite are being pulled around in the hot loop flow, it stands to reason that they are homogenized into small particles in the pump, whereupon the antimony used to dope the seals is also released into the fluid.

4.4 Conclusions for Section A

This experimental programme set out to build a water loop capable of reproducing depositions seen in plant and experimentally in the work of Brun *et al.* [18] and Guillodo *et al*. [11,19–21], however the experimental series has been unable to produce deposits which can be shown to conclusively the result of electrokinetically stimulated deposition.

The deposits formed in these appear to have been caused by an alternative mechanism 'flashing', where high flow rates coupled with high dissolved gas concentrations permit a two phase fluid to exist in low pressure regions inside the flow restriction. The occurrence of this mechanism appears to be supported

by the production of large deposits when dissolved gas levels were high, as evidenced in the results of run 5 (see Figure 4.14, Figure 4.28 and Figure 4.31), compared to the small dusting of deposition were seen on the test piece of run 1 (see Figure 4.7, Figure 4.16 and Figure 4.19) which was performed under similar conditions.

The deposition seen in run 2 were significantly different in morphology from those of run 1 and 5, and strikingly similar to results of deposition seen in the EMILIE loop [12]. This implies that either the deposition in run 2 is at least partially the result of electrokinetically stimulate deposition, or the results seen in the EMILIE loop were partially the result of flashing. Considering the presence of structured columnar crystallites rather than the granular material seen in run 1 and 5, it seems unlikely that the deposits are the result of flashing, and given that the location of the deposition is on the face of the restriction (a point of fluid attachment) it is possible that this is one example of electrokinetically simulated deposition.

The composition of the depositions on all samples has been found to be largely antimony, though the exact composition has not been fully analysed; this would require a technique more accurate and comprehensive than EDX. The EDX spectra found there to be very little oxygen present in the depositions, suggesting that the deposits are not antimony oxides, and while the small quantity of oxygen suggests a metallic deposit it is possible that the structure made be something else. Antimony is a soluble species, and thus must exist as either an oxide or hydroxyl species in solution [193], so deposition of a metallic species would require than the dissolved ion be reduced. Without further analysis of these deposits using a more comprehensive technique (such as TEM), it is difficult to speculate on what may have cause them to become deposited.

This programme has shown that a high temperature, high pressure and high flow rate loop can be successfully operated to produce deposition in environments similar to those of a PWR primary coolant circuit, however the deposition mechanism demonstrated was one not initially expected and has been shown to dominate deposition type across the range of tested conditions. To bring the loop into a condition capable of studying electrokinetically stimulated deposition, there are several equipment improvements and experimental changes recommended in section 9.1.1.

5 Section B: Corrosion Kinetics of 316L Stainless Steel in High Temperature Water

This chapter details the development of the Corrosion Kinetics of 316L Stainless Steel procedure. Preliminary experiments were carried out as a means to gather experience of operating high-pressure, high temperature equipment for corrosion purposes, and to assess the suitability of available analytical equipment while gathering the baseline sets of results. This work is described in section 5.1.

The design, construction, and initial operation of the purpose-built corrosion rate rig, as well as analytical methods are described in section 5.2. Experimental results for each program are presented in sections 5.2 (preliminary work) and 5.5 (improved work).

5.1 Preliminary Experimental Work

5.1.1 Preliminary Experimental Equipment

5.1.1.1 Autoclave

Out of use pressure equipment was available within the University however the systems were not fully certified and were in need of refurbishment. The vessel selected for this work was a ~3 L batch type, Hastelloy C-276 autoclave, which was refurbished, fitted with a 316L stainless steel liner and head, before being fully recertified for use up to 300 °C and 155 bar. This reduced the total vessel volume to ~2.6 litres.

In the experiments performed, two sample coupons (each of a different surface finish) were to be exposed to high temperature, high pressure water. The samples were hung from an alumina bar and separated from each other using small sections of alumina tubing, threaded over the support bar. All clamping

apparatus had to be cut to precise sizes to fit within the autoclave. In order to fit all of these parts into the autoclave, the stirrer shaft was removed. A diagram of the autoclave configuration can be seen in Figure 5.1.

5.1.1.2 Coupons

Coupons of stainless steel were machined from 316L stainless steel bar stock, composition shown in Table 5.1. Coupons were first cut to approximate size, before being milled down to size and to remove a slight camber in the bar. The samples were 40x25x5 mm^3 in dimensions, with a 5 mm hole drilled at one end, centered 5 mm from the top edge and 12.5 mm from the either side. An example can be seen in Figure 5.2.

Table 5.1 - Composition of stainless steel used for the preliminary experiment sample coupons.

Fe	Cr	Ni	Mo	Mn	Si	C	P	S
Bal.	16.3%	10.3%	2.1%	0.84%	0.34%	0.061%	0.023%	0.013%

The coupons were mechanically ground to 400 grit using silicon carbide grinding papers. Half of these samples were electropolished in accordance with ASTM Standard B912 – 02 [169] by Anopol Ltd., giving two surface conditions for initial investigations. Electropolishing of the coupons was performed in a constantly circulating tank containing a 50/50 vol/vol solution of sulphuric acid (96% by weight) and orthophosphoric acid (85% by weight), at a temperature of 75 °C for a period of 4 mins, at a current density of ~0.15 $A.cm^{-2}$.

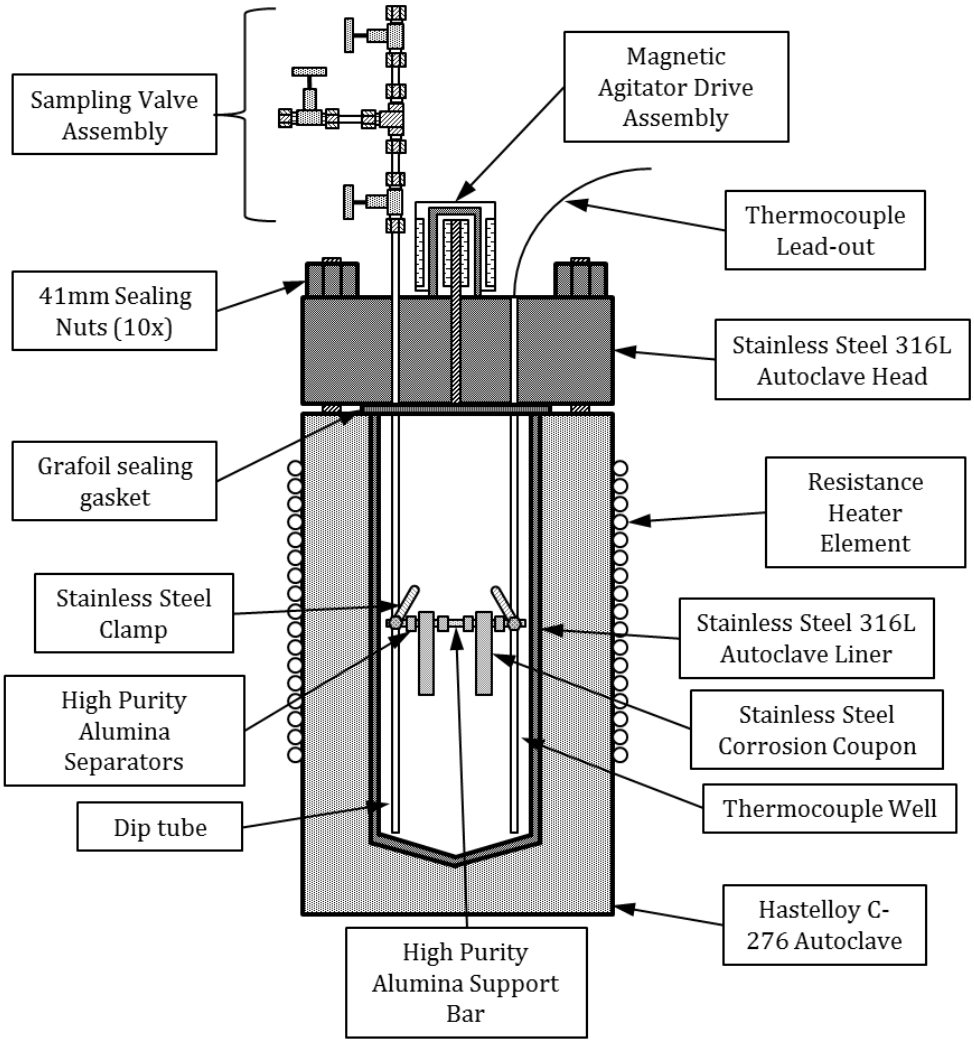

Figure 5.1 - A schematic of a batch type autoclave used for metal oxide solubility experiments.

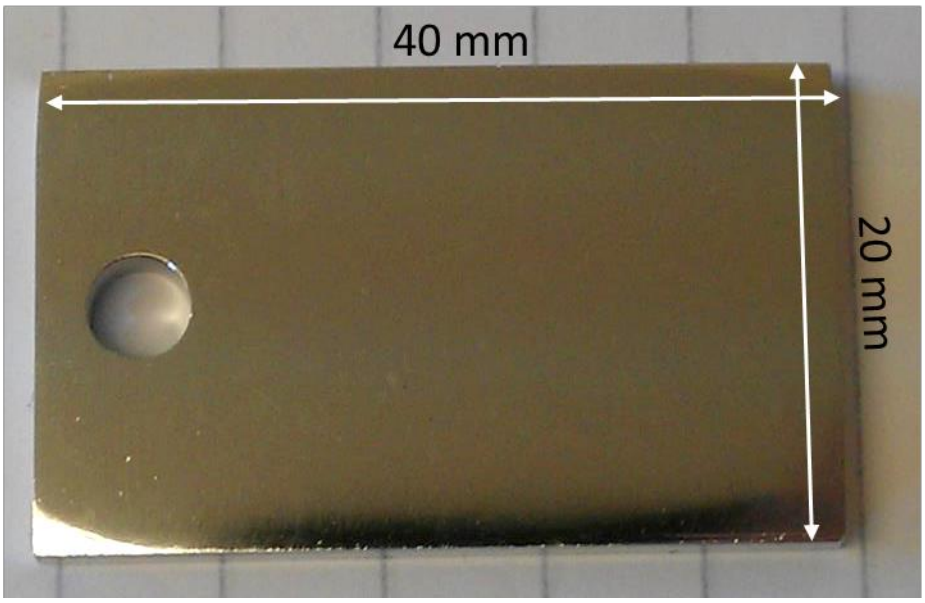

Figure 5.2 - A photograph of a coupon used for preliminary testing.

5.1.2 Methodology

In all situations, the autoclave was cleaned down using ethanol absolute and high purity water prior to installing samples – the samples were also cleaned using ethanol absolute in an ultrasonic bath.

Samples were installed as shown in Figure 5.1 and the autoclave was closed to a predefined torque which prevented leakage. This was tested by charging the vessel with 100 bar of N_2 gas for a period of 24 hours.

Test solution was prepared by taking 3 litres of high purity water and adjusting the pH to the desired point using reagent grade LiOH. The water was sparged with N_2 gas for 1 hour at a flow rate of 50 $ml.min^{-1}$ before being transferred to the autoclave.

The heaters were activated and the vessel brought to temperature; the experiment time was started upon reaching temperature.

Further details of the methodology can be found in Appendix B, section B.1.

5.1.3 Analysis Methods

5.1.3.1 SEM

Oxide film morphology was imaged using Scanning Electron Microscopy. All imaged were taken using a Hitachi S4500 Field Emission Gun (FEG) SEM, with a beam energy of 20 kV at a working distance of 10 mm in secondary electron detection mode. Images can be found in section 5.2.1.

5.1.3.2 X-Ray Photoelectron Spectroscopy and Argon Ion Milling (XPS-AIM)

Oxide film thickness and composition as a function of depth were studied using XPS-AIM, through the University of Surrey, by Dr. Steven Hinder. Results of depth profiling was further processed to extract information about the presence of iron and chromium oxides using target factor analysis software;

this was performed by Dr. Hinder on behalf of this project and can be found in section 5.2.2.

5.1.3.3 Confocal Microscopy

XPS-AIM uses an argon ion gun to sputter material away from a location of a surface to build composition depth profiles, however the depth of sputtering is not measured by the spectrometer. Confocal Microscopy was used to estimate the depth of the sputter crater on several samples, after which the average sputter rate as calculated and applied to all samples. Images and calculations can be found in section 5.2.3.

5.2 Preliminary Experimental Results

5.2.1 SEM Imaging

SEM was used to image the samples after exposure to observe the structure of the surface for comparison with literature results. Control samples were studied imaged after surface finishing Figure 5.3 which shows the clear and difference between mechanically ground and electropolished surfaces. The electropolishing process has removed the grinding scratches and left the surface smooth; it is even possible to observe the some of the grains at the surface in image (d) of Figure 5.3.

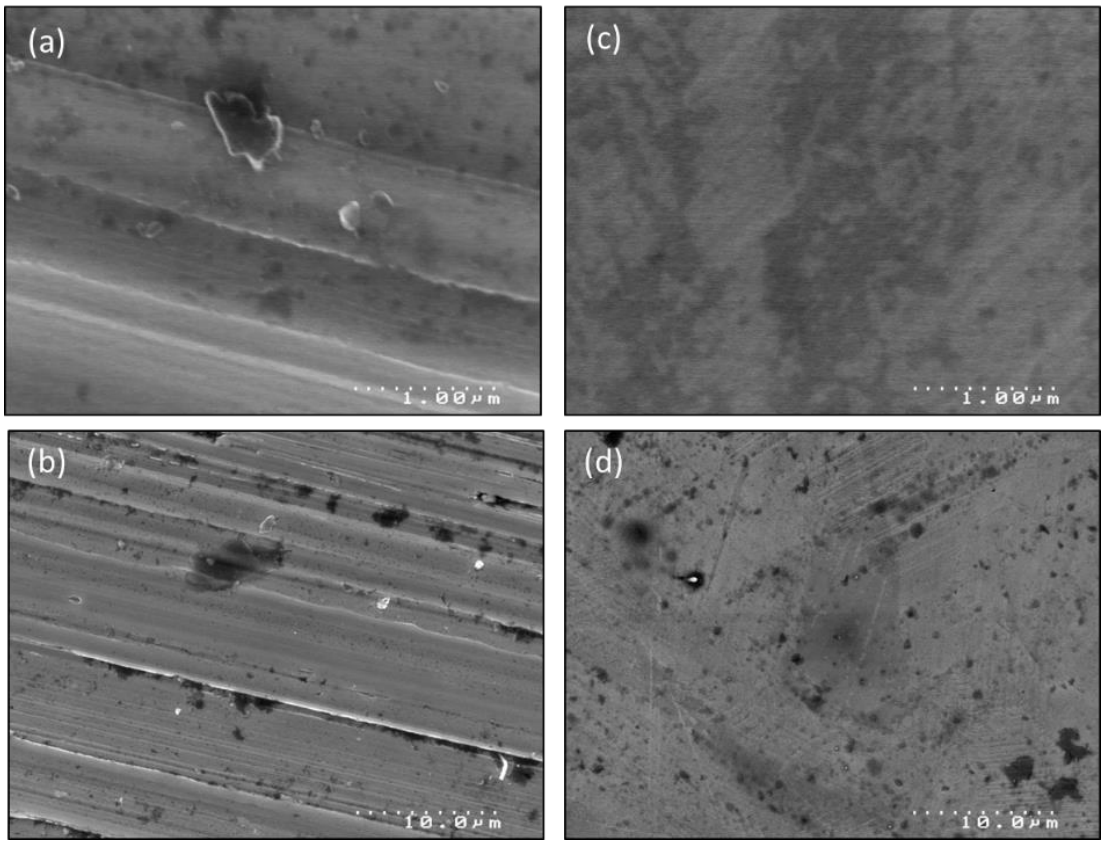

Figure 5.3 - SEM images of mechanically finished samples (a) and (b), and electropolished (c) and (d). Images taken in secondary electron detection mode, with a beam energy of 20 kV at a working distance of 10 mm.

Figure 5.4 shows images of samples after exposure to pH 9.5 water at 250 °C for 300 hours. It is clear that the electropolished samples have been afforded a significantly improved resistance to corrosion that the mechanically polished samples. The visible crystals on the surface of the samples belong to the iron rich, non-stoichiometric magnetite/nickel ferrite outer layer of the oxide film; on the mechanically polished surface, shown in (a) and (b), the outer layer has almost entirely covered the observed area with small crystals, while the electropolished surface, shown in (c) and (d), is only sparsely covered with crystals. The crystals in (c) and (d) also appear to have formed preferentially in straight lines, possibly due to the presence of scratches that were not fully removed by the electropolishing process. Ziemniak *et al.* [28,31] also observed the formation of lines of crystals and suggested that they were formed on the boundaries of grains which were obscured by the crystals, however it seems

unlikely that this is the case for the surfaces shown in Figure 5.4, due to the proximity of lines with common direction in some areas – such grains would need to be very small and all point in the same direction.

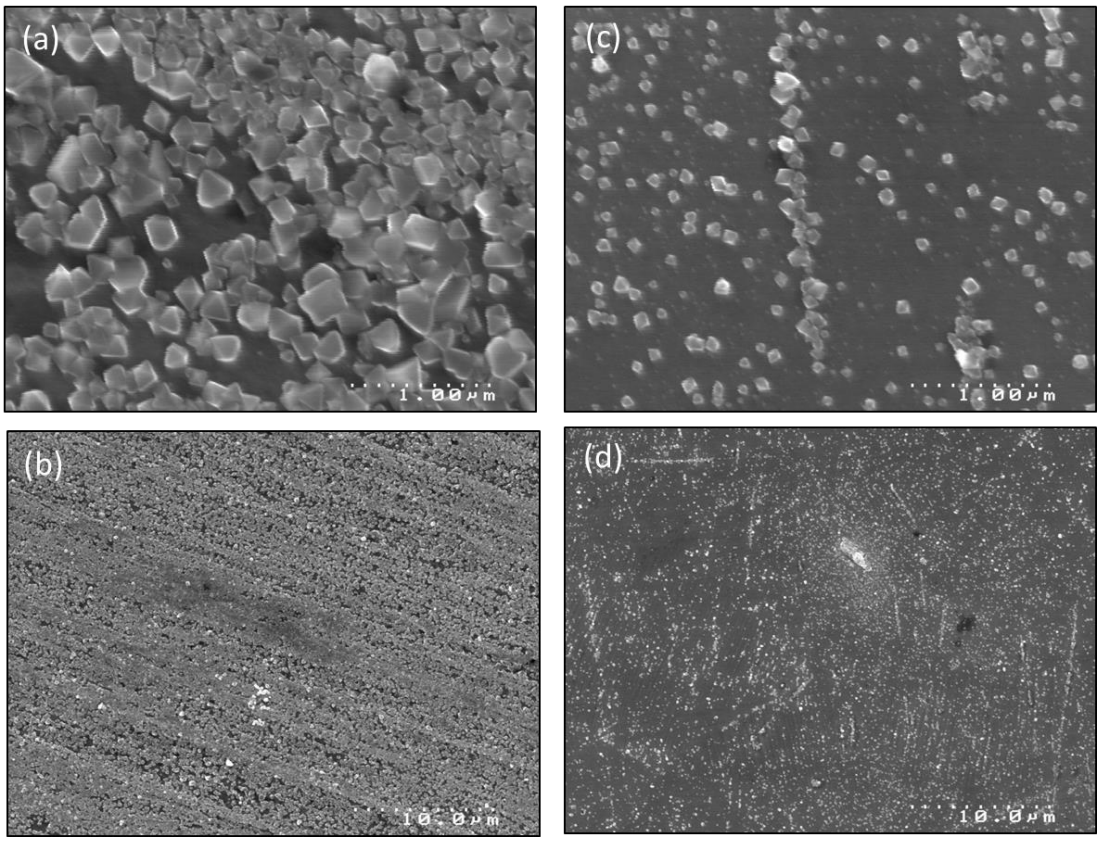

Figure 5.4 - SEM images of samples exposed to pH 9.5 water at 250 °C for 300 hours. Images (a) and (b) were mechanically ground prior to exposure, while images (c) and (d) were electropolished. Images taken in secondary electron detection mode, with a beam energy of 20 kV at a working distance of 10 mm.

The tendency to form small straight line clusters of metal oxides on the electropolished surface could instead be due to the presence of slip systems at the surface of the material [124,194]. Slip planes within a crystal would produce nucleation sites at the surface in the form of surface defects, where the formation of oxide crystals would be more favourable than at a flat surface (see Figure 5.5).

A slip system can occur in metals where dislocations in the crystal lattice allow reasonably low externally applied forces to cause the passage of one crystal plane over another. In metals where cold work has been applied (such as the

P120 grit ground samples in this experiment), numerous dislocations have been introduced to the surface, which strengthens the material, due to the fact that the motion of one dislocation will hinder the motion of another dislocation [124]. Slip systems are most easily produced when there are few obstacles along the slip plane, and by cold working the surface such obstacles have been artificially inserted. However, electropolishing removes the cold worked layer at the surface, removing the majority of the dislocations and allowing slip systems to form more easily. This explains why such oxide crystal lines are only visible on the electropolished surfaces in Figure 5.4, however if they were to form on the grit ground surface they would have been obscured by the extensive outer oxide film coverage.

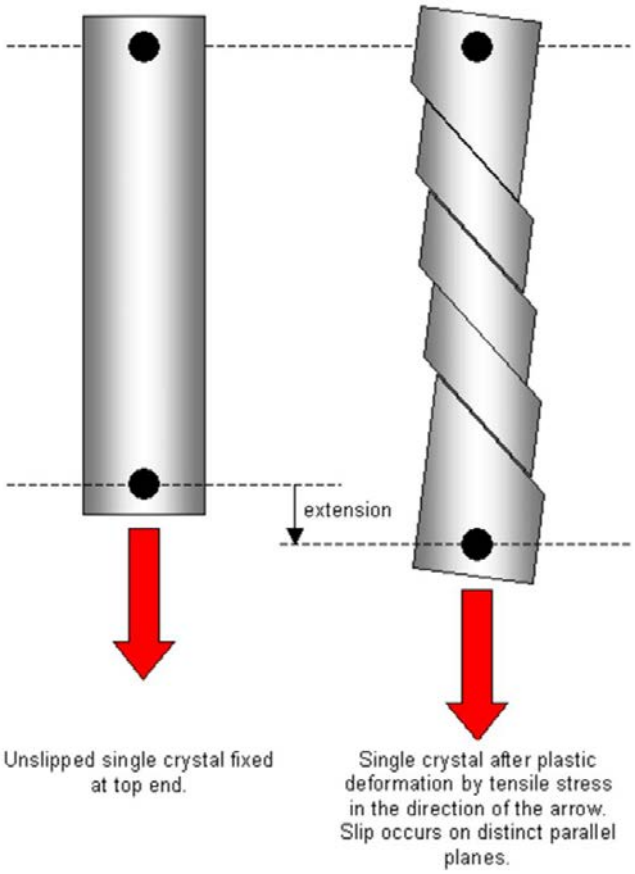

Figure 5.5 – Diagram of slip systems in a single crystal. In the left hand image, the crystal has not been subjected to any extension forces, however in the right hand image, the crystal has experienced extension and slip systems within the crystal have activated. The resulting exposure of a slip plane could act as nucleation sites for outer layer oxides, as seen in Figure 5.4. Image taken from [194].

5.2.2 XPS-AIM

XPS-AIM has been used to produce elemental depth profiles of the specimens. Confocal microscopy was used to estimate the depth of the sputter crater, results of which can be found in section 5.2.3.

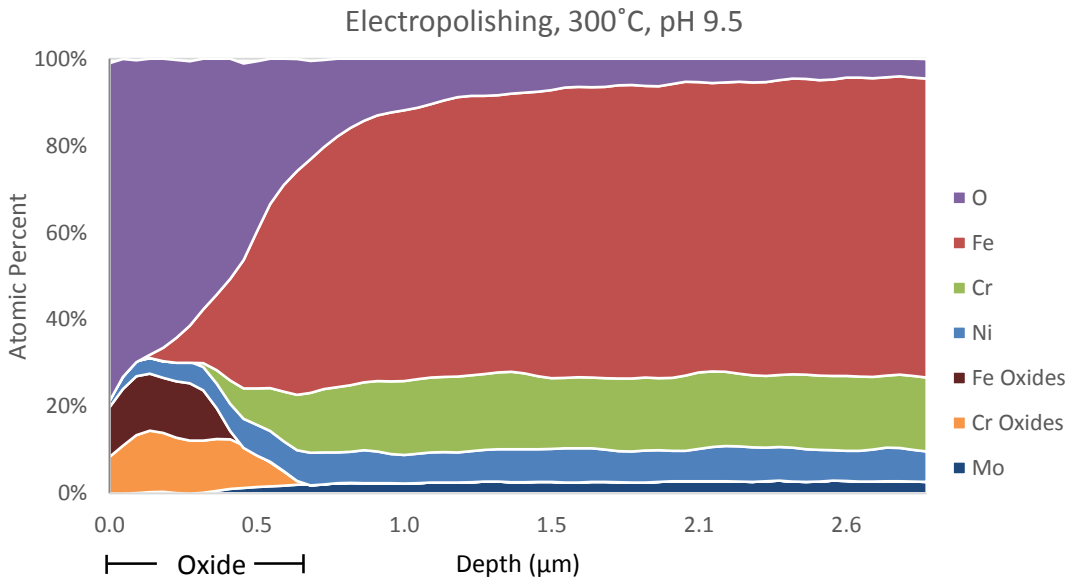

Figure 5.6 - The elemental depth profile of the electropolished coupon exposed to pH 9.5 water at 200 °C. The data in this graph has been normalised to 100%, however it excludes carbon contamination at the surface

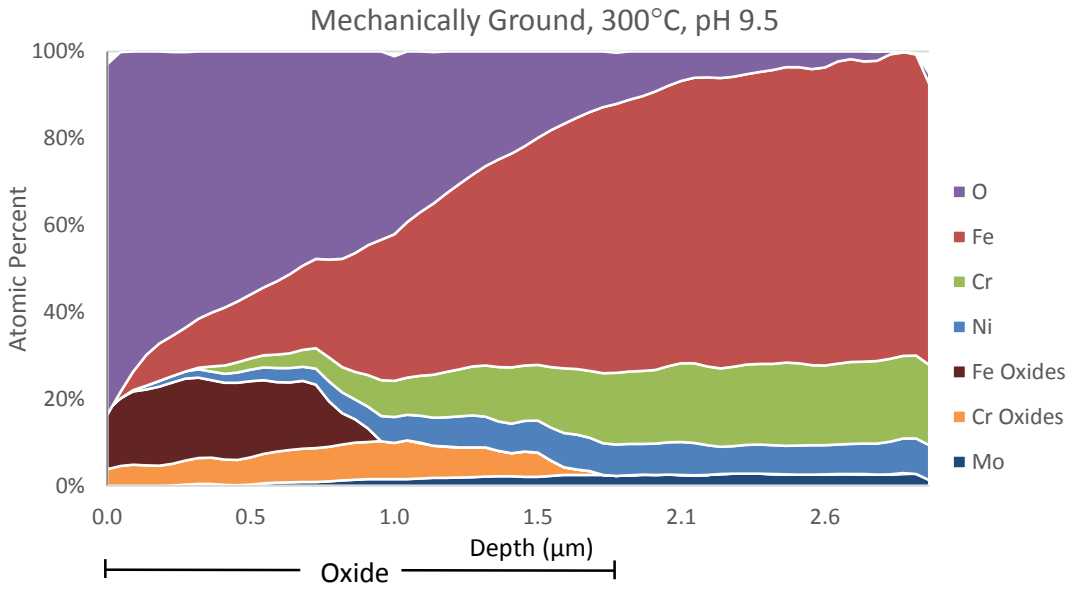

Figure 5.7 - The elemental depth profile of the mechanically ground coupon, exposed to pH 9.5 water at 200C.

Figure 5.6 shows the elemental depth profile of an electropolished sample exposed to pH 9.5 water at 300 °C, while Figure 5.7 shows the elemental depth profile of a mechanically ground sample exposed to the same conditions. As XPS is able to distinguish between elemental metal and oxidised species, it is possible to see the region where the duplex layer exists (shown in Figure 5.6 and Figure 5.7 as dark red and orange areas), and the depth to which oxygen has penetrated into the surface. The oxygen present in the surface presents a concern, as it is present at a greater depth than the metal oxides is expected to be associated with; this is discussed further in section 5.6. From the depth and volume of oxide regions in Figure 5.6 and Figure 5.7, it can clearly be seen that the extent of corrosion is greater for the mechanically ground sample than the electropolished sample.

In order to determine corrosion rates the following arithmatic is used (which is discussed further in 5.4.3.2.1:

$$W_p = W_i - (W_f - W_{dl})$$

Equation 5.1

The mass of oxidised material per unit area ($\boldsymbol{W_p}$) was calculated from atom percent given by XPS and the diameter of the X-ray spot (80 μm), and from the rate of etching calculated from confocal microscope estimation (see section 5.2.3). With a known depth of sputter and area of analysis, the mass of oxidised material was then determined by analytical integration of the curves of iron and chromium oxides. This mass was taken to be ($\boldsymbol{W_{dl}}$), and $\boldsymbol{W_p}$ was calculated from the initial and final coupon masses, $\boldsymbol{W_i}$ and $\boldsymbol{W_f}$ respectively.

Errors in this estimation process are determined based on the variation in the sputter rate (depth of sputter crater divided by total sputter time) determined using confocal microscopy measurements and estimated variation in X-ray beam spot size. The estimated sputter rate based on confocal microscopy is 4.66×10^{-9} m.min^{-1} and from this the estimated volumetric sputter rate is 2.34

$\pm 0.89 \times 10^{-17}$ $m^3.min^{-1}$. Further, a 1 % standard error was placed on all XPS composition measurements, however this is dwarfed by the error determined for the volumetric sputter rate. Propagated through the calculation for mass of retained oxide, the error remains as a percentage at ~38 %.

Based on literature data for corrosion laws at work (see section 2.4.2.1), parabolic corrosion behaviour is often observed. If this is assumed to be the case in for this experimental work, the parabolic corrosion rate constant ($\boldsymbol{k_p}$) can be calculated using Equation 2.33. The calculated values of mass of alloy oxidised and the associated parabolic corrosion rate constant are presented in Table 5.2.

Table 5.2 - Tabulated Kp values, calculated from total mass of corroded material. The final experiments (pH 10.72, 300 °C) were cut short at 136 hours due to a heater fault.

$pH_{25°C}$	T (°C)	Surface Finish	t (hours)	$t^{1/2}$	Mass of Alloy Corroded, W_p ($mg\ alloy.dm^{-2}$)	Parabolic Corrosion Rate, K_p ($mg\ alloy.dm^{-2}.hr^{-1/2}$)
9.6	200	MG	306.5	17.51	1.39	0.079
	200	EP	306.5	17.51	0.58	0.033
9.63	250	MG	340.5	18.45	3.26	0.177
	250	EP	340.5	18.45	0.94	0.051
9.37	300	MG	301.8	17.37	2.44	0.141
	300	EP	301.8	17.37	0.90	0.052
10.49	200	MG	327	18.08	3.38	0.187
	200	EP	327	18.08	2.58	0.143
10.69	250	MG	305.3	17.47	4.05	0.232
	250	EP	300.3	17.33	0.62	0.036
10.72	300	MP	135.7	11.65	2.10	0.180
	300	EP	135.7	11.65	0.80	0.069

The mass of each metal oxide category (iron oxide/chromium oxide) has been plotted against temperature for each surface condition in

Figure 5.8 and Figure 5.9 for samples exposed to $pH_{25\,°C}$ ~9.5, and in Figure 5.10 and Figure 5.11 for samples exposed to $pH_{25\,°C}$ ~10.5. It is known that the chromium rich inner layer is responsible for corrosion resistance [28,31,32],

however electropolished samples show consistently lower quantities of chromium oxide than the mechanically ground samples, and yet still possess lower corrosion rates overall (see Figure 5.12).

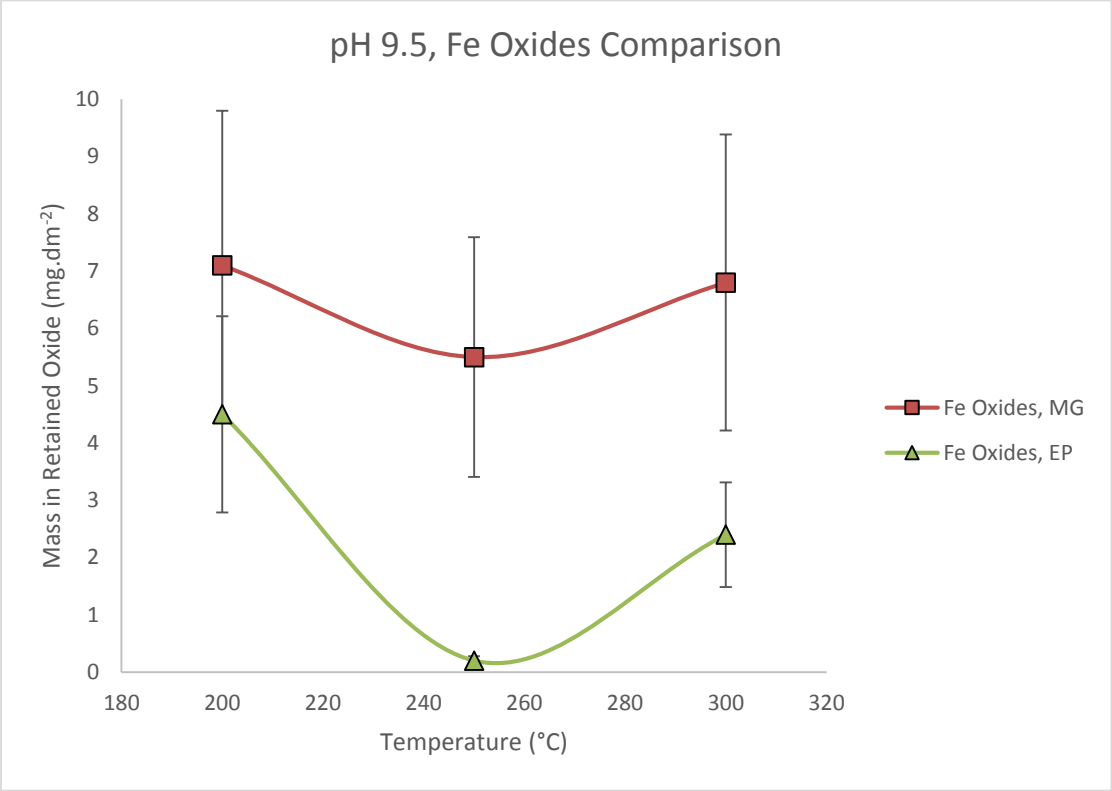

Figure 5.8 - The masses of iron oxides in the retained oxide film of mechanically ground and electropolished surfaces at various temperatures in pH ~9.5 water.

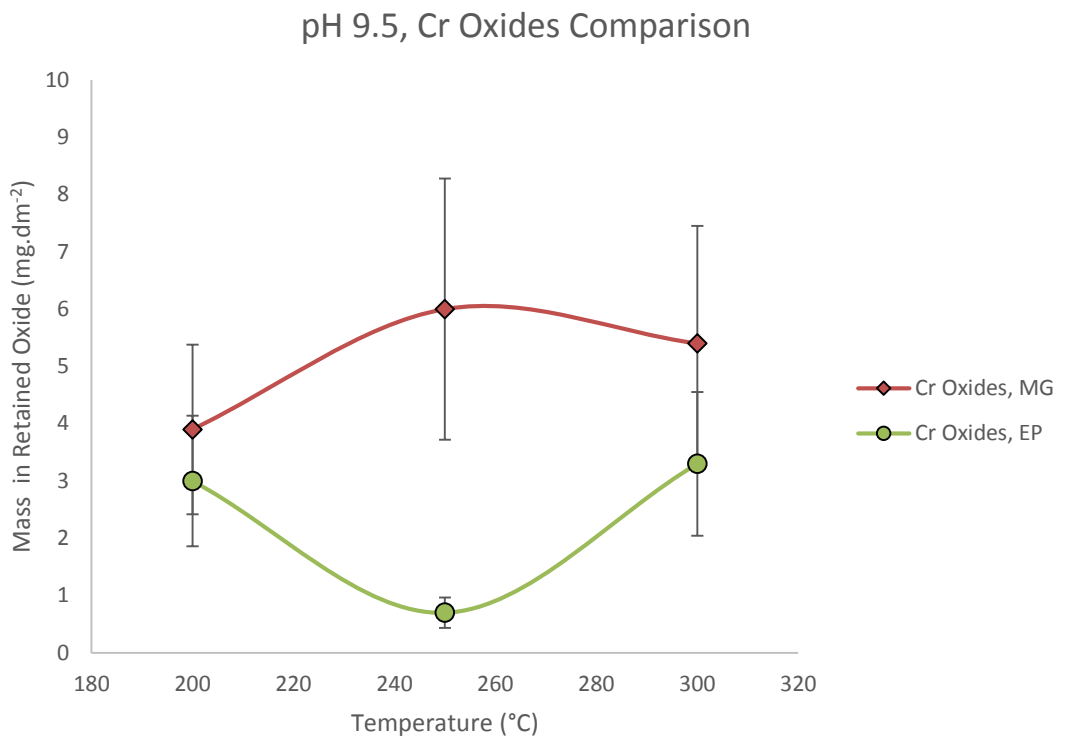

Figure 5.9 – The mass of chromium oxides in the in the retained oxide film of mechanically ground and electropolished surfaces at various temperatures in pH ~9.5 water.

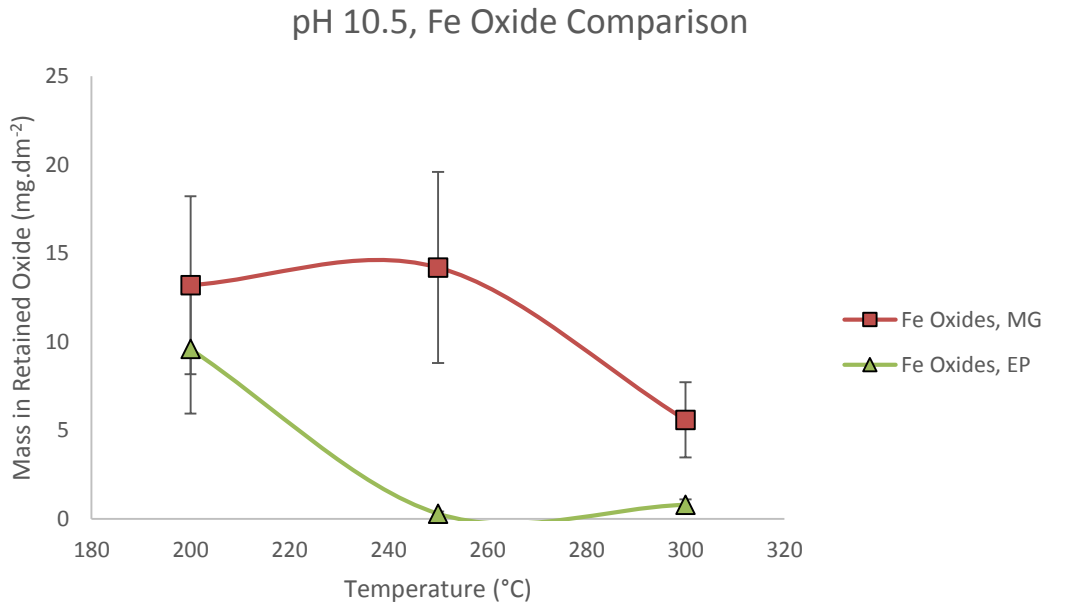

Figure 5.10 – The mass of iron oxides in the retained oxide film of mechanically ground and electropolished surfaces at various temperature in pH ~10.5 water.

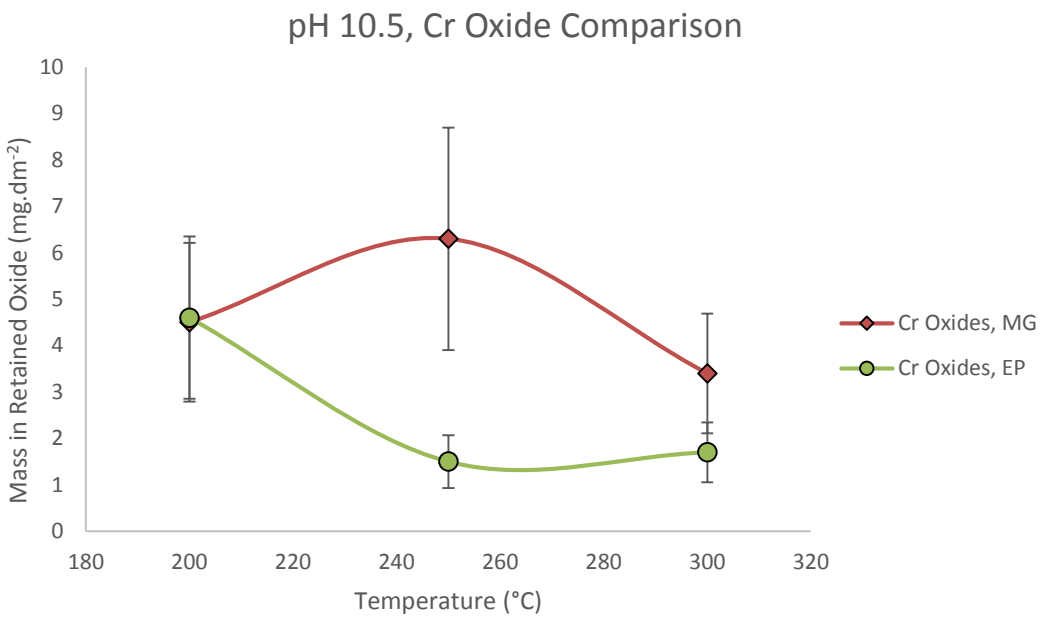

Figure 5.11 - The volumes of chromium oxides in the retained oxide film for mechanically ground and electropolished surfaces at various temperatures in pH ~10.5 water.

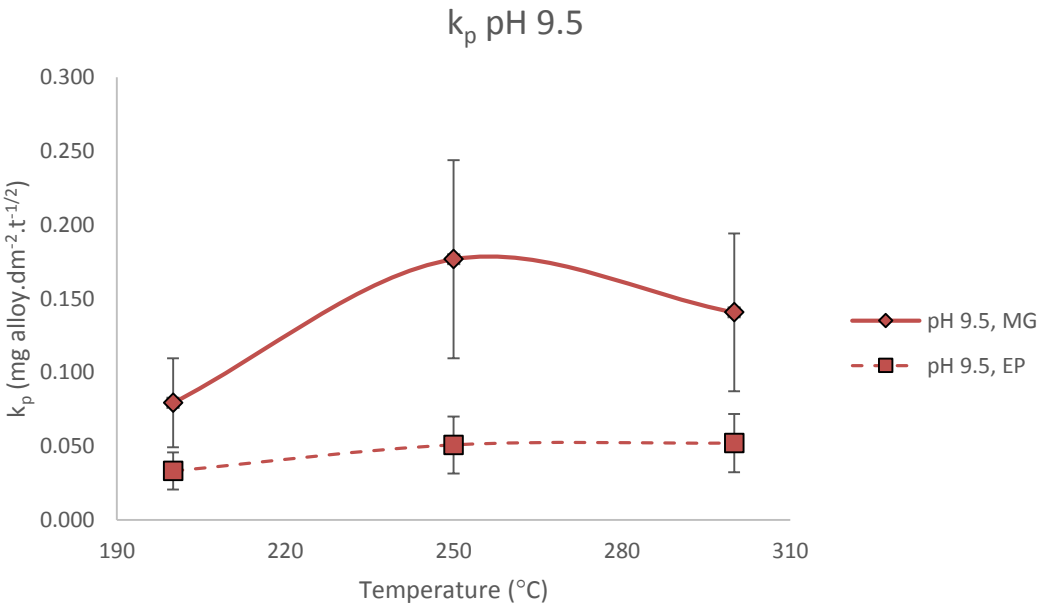

Figure 5.12 - Comparison of the corrosion rate constants, assuming parabolic kinetics, of electropolished and mechanically ground samples at pH 9.5 as a function of temperature.

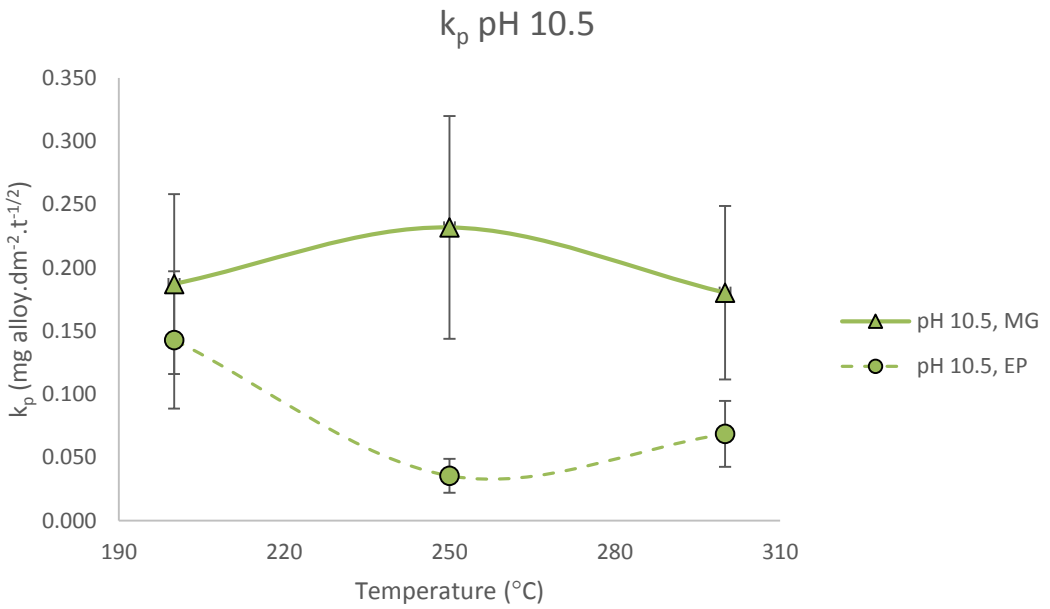

Figure 5.13 - Comparison of corrosion rate constants, assuming parabolic kinetics, of mechanically finished and electropolished samples in pH 10.5 water as a function of temperature.

The estimated parabolic corrosion rate of each condition are plotted in Figure 5.12 and Figure 5.13. While improvement is seen in the corrosion resistance of all electropolished over mechanically ground samples, the greatest improvement in resistance is seen at a temperature of 250 °C for both pH 9.5 and 10.5.

5.2.3 Confocal Microscopy

Confocal microscopy has been employed to measure the depth of the milling crater produced during argon ion milling for XPS depth profiling.

The samples used for this work were electropolished samples as the smooth surfaces would make measurement of the crater depth easier compared to the use of the ground samples which were geometrically complex. Examples of the images used for the analysis are shown in Figure 5.14 and Figure 5.15 (electropolished specimen pH 10.5, 200 °C), and Figure 5.16 and Figure 5.17 (electropolished specimen pH 9.5, 200 °C).

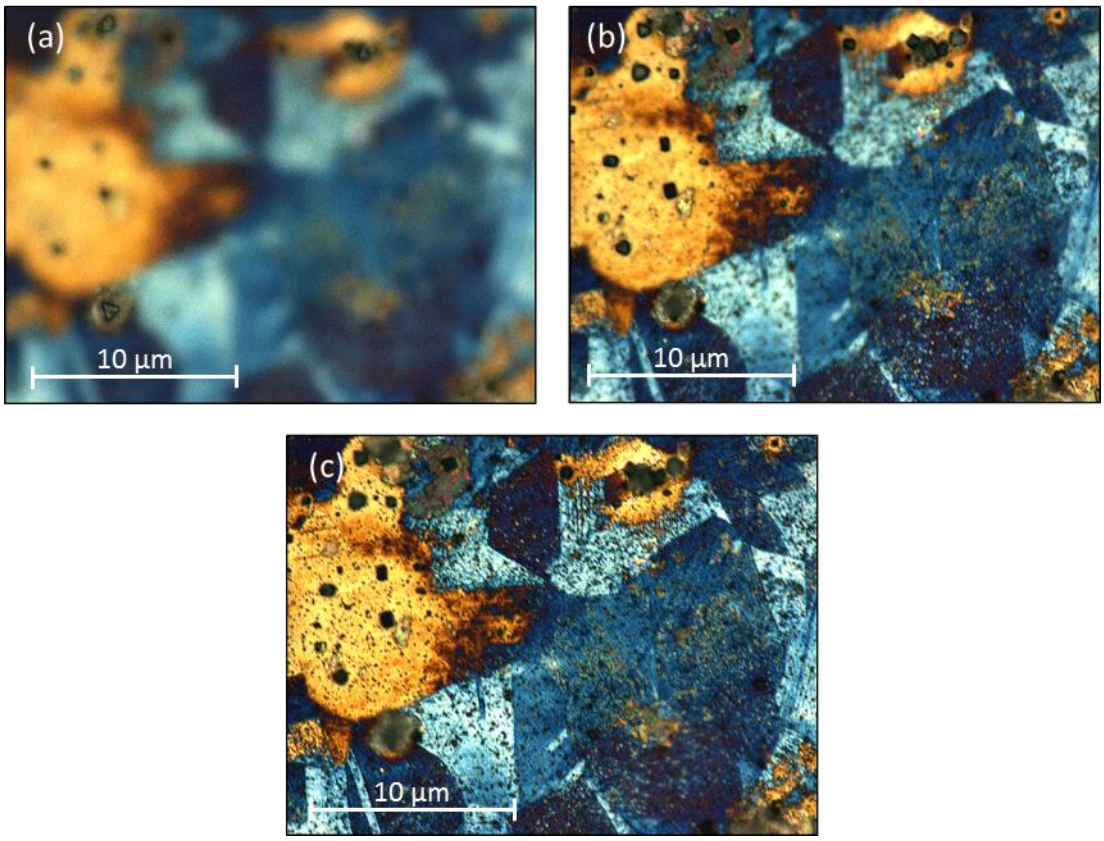

Figure 5.14 - The image shown are taken outside of the sputter crater. They show: (a) the focal points at the highest point of an outer layer crystal (2012.70 µm), (b) highest point on the surface (2015.00 µm), and (c) lowest point on the surface outside of the sputter crater of specimen (2016.11 µm). Average relative height is 2014.60 µm.

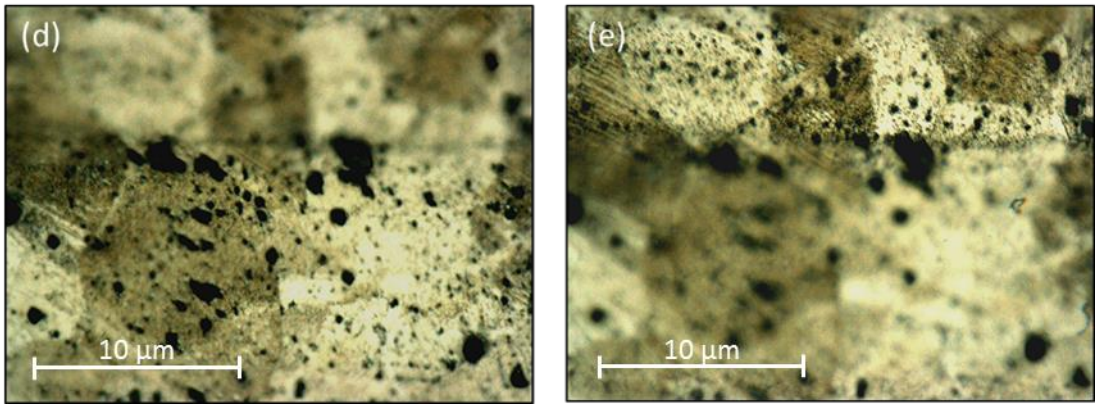

Figure 5.15 - The focal points at the (d) highest (2016.00 µm) and (e) lowest (2019.35 µm) levels inside the sputter crater of specimen EP, pH 10.5, 200 °C. Average relative height is 2017.68 µm.

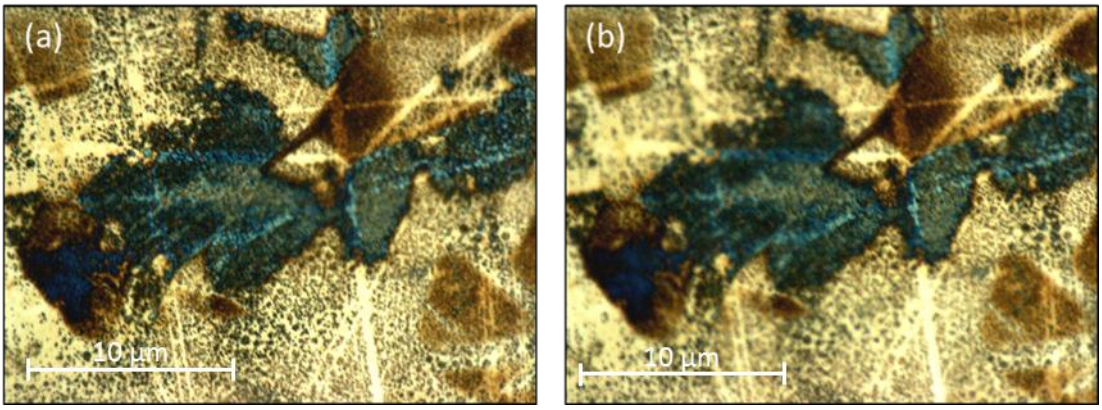

Figure 5.16 - The focal points at the (a) highest (2015.85 µm) and (b) lowest (2017.08 µm) levels outside the sputter crater of the EP specimen, pH 9.5, 200 °C. Average relative height is 2016.47 µm.

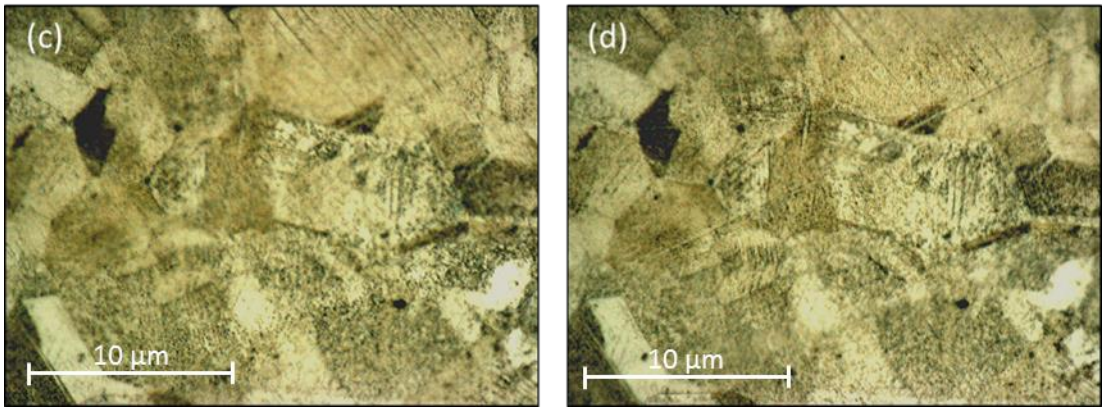

Figure 5.17 - The focal points at the (c) highest (2018.41 µm) and (d) lowest (2019.85 µm) levels inside the sputter crater of specimen EP, pH 9.5, 200 °C. Average relative height is 2019.13 µm.

The microscope was set to use a single focal plane and the sample was moved upward into the focal plane. As locations on the surface came into focus, it was possible to assign heights relative to each other. The highest point outside of the sputter crater and the lowest point inside the crater were averaged and the difference taken as the depth of the crater. The measurements of height were made electronically using the microscope's calibrated sample table; the reported height is the position of the sample table, not the absolute value of depth within or outside of the sputter crater.

The average level outside and inside the crater were found to be 3.08 µm and 2.67 µm for samples EP, pH 10.5, 200 °C and EP, pH 9.5, 200 °C respectively. When this depth is divided by the number of etch levels recorded by the XPS spectrometer, an average sputter rate of 4.66 $nm.min^{-1}$ was determined.

5.3 **Discussion of Preliminary Work**

Preliminary work in this section has focused on developing the capability to expose samples of material to high temperature, high pressure environments and estimate the corrosion rate based on data from XPS-AIM analysis. While the method has provided some useful results, the method is fundamentally flawed for the observation of medium-long term corrosion kinetics without a number of changes.

SEM imaging of the surfaces showed the extent to which the corrosion of the surface had progressed, based on the formation of a continuous outer layer film on the ground samples, and a very sparse coverage of the electropolished samples. The ordered nature of crystal formation on the surface of the electropolished sample suggested the presence of numerous slip system in the surface, a result of the low dislocation density of the surface after the electropolishing treatment.

XPS-AIM analysis was used to make single-point estimates of corrosion rate, based on the assumption of parabolic rate kinetics, an assumption based on the experience from the literature. The results of this were able to show a difference in the corrosion rates due to temperature, surface finish, and pH. A feature of note in the XPS data is the presence of a substantial quantity of oxygen at a greater depth than the metal oxides with which is expected to be associated. In Figure 5.6, the metal oxides are in a confined to a region between the surface and approximately 0.7 μm into the sample, while the oxygen is still present at a concentration of ~20 at% at this same depth. While it diminishes with increasing depth it does not fully disappear. Similarly, in Figure 5.7 the oxygen level ~10 at% at 1.7 μm where the metal oxide film ends, falling to near 0 at% toward the bottom of the sputter crater. The oxygen is not associated with any other element present in the metal (*i.e.*, a metal oxide or a surface adherent carbon-oxygen compound).

The source of the additional oxygen is not well understood, but it is possible that it is a contaminant gas within the vacuum chamber of the XPS. Oxygen gas is known to adsorb on to surfaces, and in order to operate at high vacuum, systems such as XPS vacuum chambers must be 'baked-out' periodically while under vacuum - it is possible procedure had not been performed prior to analysis and the introduction of large samples, recently exposed to water and atmosphere exacerbated the issue.

Another possibility is that the lithium hydroxide used to modify the pH of the test solution is present on the surface of the sample after it was removed from the autoclave – possibly deposited on the surface during cooling of the autoclave, the associated drop in density meaning that the water level fell below the samples, leaving LiOH on the sample surface. This also explains why the oxygen does not appear to be associated with any other element, as XPS has a low sensitivity for lithium, and the only lithium peak (the Li1s) is obscured by the iron Fe3p peak components.

Confocal microscopy was used to make estimates of the depth of the sputter crater created by the argon ion milling during XPS depth profiling. The technique proved successful, though error propagation calculation yielded a percent error of 38 % due to the use of this method.

5.3.1 **Limitations**

The preliminary experiments were found to have a number of limitations that restricted the amount of useful data that could be extracted from them. The limitations which were considered most important to address were:

i. Inability to extract accurate corrosion rate data – only XPS was used to study the extent of corrosion on samples.
ii. Small number of samples and few variables.

iii. No time dependent sample removal – the corrosion kinetics are assumed to be parabolic and so require that samples be removed after set periods of time for analysis.

iv. Chemistry alters during the test – as the autoclave is a batch type system, the test solution present in the vessel is not refreshed and changes the test.

v. No soluble hydrogen gas control.

It was decided that a new system needed to be developed to address the problems listed above, the design and construction of which is described in the next section.

5.4 Design Criteria/Experimental Requirements for Improved Corrosion Rate System

The design and construction of the corrosion rate rig systems required significant forethought regarding the conditions that needed to be created. The criteria are described in detail throughout this section.

5.4.1 Experimental Conditions Criteria

5.4.1.1 Chemistry

The chemistry of the system needed to be reliably constant. Early on, it was identified that there were two methods for maintaining the chemistry at a known level; constant corrective dosing with pH modifying lithium hydroxide, or simply constantly refreshing with new feed water. The constant flow of new feed water was quickly established as being the most cost effective option.

Feed water pH was controlled using lithium hydroxide (reagent grade powder, ≥98%), purchased from Sigma Aldrich. Solutions of 0.25, 2.5 and 25 ppm LiOH equate to approximately pH 9, 10 and 11 respectively.

5.4.1.2 **Temperature**

The system needed to be capable of reaching up to 300 °C with a good degree of accuracy across all cells simultaneously. It was decided that the cells should all be in the same heated compartment, as the heating medium (air) would be of equal temperature throughout the chamber.

The chamber also needed to be capable of holding the cells in place as the tubing would otherwise be unsupported.

5.4.1.3 **Time**

The conditions being studied in this experiment are designed to simulate the conditions of the coolant found in the RCS, conditions that are specifically designed to slow the corrosion of plant materials. As well as the slow progress of corrosion, one must remember that the RCS is in operation for in excess of 40 years (~350,000 hours) so exposures covering a few hundred hours do not necessarily give meaningful data for the life of the plant.

It is clearly necessary to expose test materials for long periods of time. To the best of the authors knowledge, the longest term tests of this type published in literature exposed samples for 10,000 hours (~417 days), which is still only a fraction of the RCS's overall life span. However, the tests were able to demonstrate a parabolic corrosion trend over this time period [28,31]. Other work has demonstrated near-parabolic behaviour (*i.e.*, $time^{0.44}$, rather than $time^{0.5}$) over a period of 168 hours [90], as well as cubic behaviour in specific some circumstances [166].

Due to time constraints on this project, the experiments performed will act as proof of concept for longer term experiments to be performed in the future. An experimental time of 1,000 hours was choosen, with coupons being removed for examination after 250 hours exposure.

5.4.1.4 Test Coupons

Test coupons used in this experiment needed to have a large surface area to mass ratio, be made from 316L stainless steel, and be made in large quantities relatively quickly. An example taken from the literature is the coupons used by Ziemniak *et al.*, which were described as being 4 in. x ¾ in. x 0.032 in. (101.6 mm x 19.05 mm x 0.81 mm) [28,31].

5.4.2 Experimental Rig

The experimental rig was designed and built to meet the stipulations of section 5.4.1. It consists of multiple removable cells and a large reservoir of pH modified water for extended test time. A schematic of the rig can be found in Figure 5.18; further details of its design and construction can be found in Appendix B, section B.2.

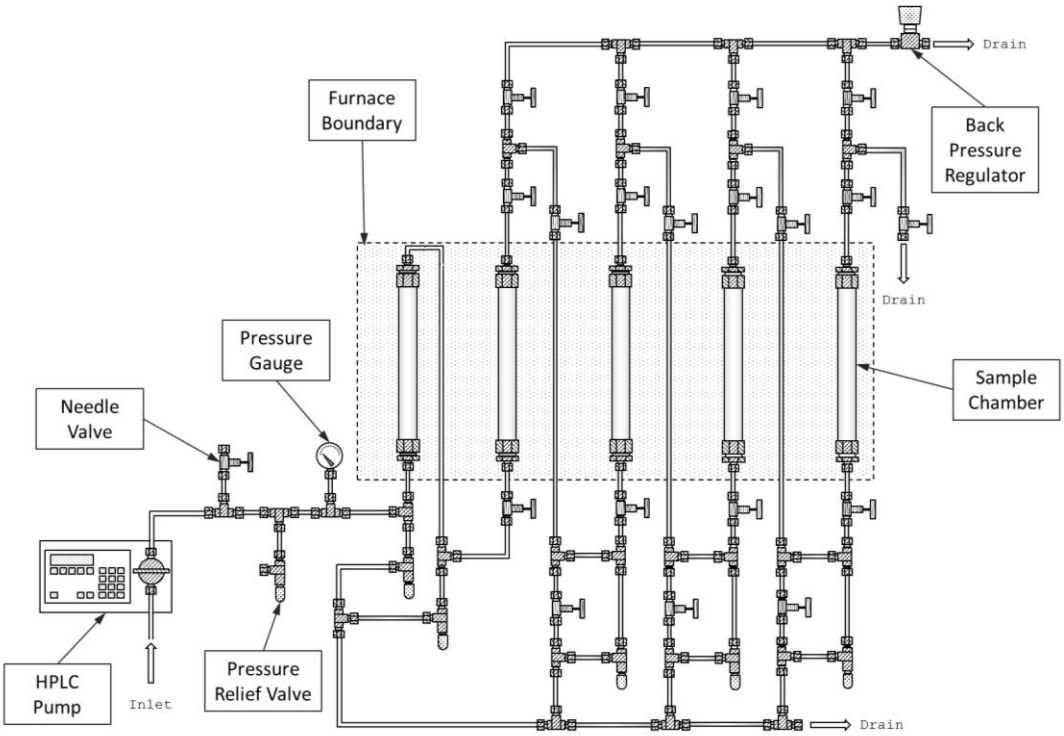

Figure 5.18 - Finalised design of the Corrosion Kinetic rig.

5.4.2.1 Materials and Ancillary Apparatus

5.4.2.1.1 Test Coupons

The test coupons used were cut from a single sheet of 1 mm thick 316L stainless steel (composition shown in Table 5.3) and machined to a final dimension of 100 mm x 18 mm x 1 mm, giving an ideal volume of 1.8×10^{-6} m^3 and surface area of 3.836×10^{-3} m^2.

Table 5.3 - Composition of 316L stainless steel used for test coupons in the rig based experiments.

Fe	Cr	Ni	Mo	Mn	Si	C	P	S
Bal.	16.9	10.6	2.8%	0.91%	0.39%	0.056%	0.018%	0.015%

The finishes used on the samples were applied using silicon carbide grinding paper. Samples were ground to a 120 and 1200 grit, using successively finer grit paper when polishing to 1200 grit. Once ground, samples were washed carefully in acetone and high purity water, and stored in a desiccator prior to use in the experiment.

It had been intended that coupon be ground before being electropolished by an external service, however the dimensions of the coupons made it difficult to find a company able to perform the electropolishing on the number required. Section 9.1.2 builds on possible ways to prepare electropolished samples on a large scale.

When installed into the rig, the samples were supported within the test cells upon sections of high purity alumina tube. These were 19 mm OD, 10 mm deep with an 8 mm hole in the center. Each of the rings was ground using a 3 mm diameter diamond-grinding tool to produce parallel channels in the top and bottom of the ring (see Figure 5.19).

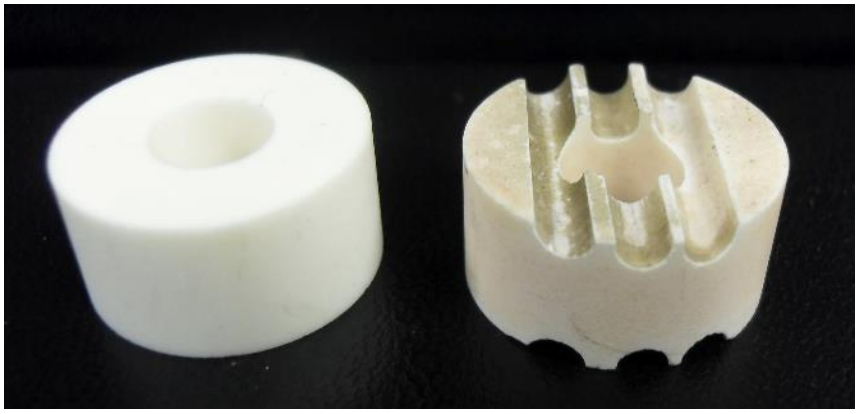

Figure 5.19 - Alumina separators, before (left) and after (right) preparation. The prepared ring (right) has also been used for a test, which has discoloured the ceramic.

5.4.3 Bespoke Corrosion Kinetics Rig Experimental Methodology

5.4.3.1 Methodology

Feed water was prepared by adjusting the pH the feed water and degassing this water by sparging with N_2 gas for a period of ~400 hours (2 hours per kilo of water).

Samples were loaded into the tubes, which were then installed into the rig. Once the rig was fully constructed, it was leak tested by pressurising with 100 bar of nitrogen gas and leaving for a period of 24 hours.

When ready to begin the test, the system was filled with water using the pump which pressurised the system to the set point of the outlet BPR. The oven was set to the target temperature and once this was achieved the experiment time was started.

Sample cells were removed from the system at certain time points and the samples were analysed by various methods described further in this section.

Further detail on the set up and operation of Appendix B, section B.2.3.

5.4.3.2 **Analysis**

5.4.3.2.1 **Gravimetric Descaling Analysis**

Gravimetric analysis was performed using a modification of the two-step descaling method designated C.7.4, described in ASTM standard G1-03 [195]. This method is similar to the method used by Ziemniak *et al.* [28,31] which was itself was a modification of a process taken from the now obsolete ASTM standard G1-67 [196].

Prior to the descaling process, the dried samples were weighed accurately using a calibrated five decimal place balance. The chemical descaling was performed by placing samples in a solution of 200 g sodium hydroxide and 30 g potassium permanganate made up to 1000 ml using reagent water, for 10 minutes at 90 °C. A water bath was used to provide heating. The samples were then removed from the step one solution, washed with high purity water to remove residual step one liquid, and placed into the step two solution, which was composed of 100 g ammonium citrate dibasic, $(HOC(CO_2H)(CH_2CO_2NH_4)_2$ made up to 1000 ml using high purity water, and heated for a further 10 minutes at 90 °C. The ASTM standard test requires that each step in the descale process last for 15 minutes [195], however this was found to remove excessive quantities of oxide in each step.

The samples were then rinsed with high purity water and hot air dried before being weighed using a calibrated five decimal place balance and the mass recorded. The descaling step was then repeated.

The mass loss of the sample after each descaling run was plotted against the number of cycles it had undergone, resulting in two approximately linear segments; one segment representing the oxide film removal, the other the chemical attack of the base metal. Lines of best fit were applied to the two segments, the first of which is for the oxide film (line AB in the plot shown in

Figure 5.20). This line was set to intercept the y-axis at $y = x = 0$. The second line (line BC in the plot shown in Figure 5.20) represents the attack on the base metal. The equations of the lines were used to calculate position of point B, which is the total mass of the oxide film that was present on the sample, by simultaneous equations. This is done for each coupon data set individually.

The mass of the retained oxide ($\boldsymbol{W_{dl}}$) is subtracted from the mass of the sample after exposure ($\boldsymbol{W_f}$) to give the mass of the alloy untouched by corrosion ($\boldsymbol{W_b}$). $\boldsymbol{W_b}$ is subtracted from the mass of the coupon prior to exposure ($\boldsymbol{W_i}$) to give the total mass of corroded alloy ($\boldsymbol{W_p}$), both retained and released:

$$W_b = W_f - W_{dl}$$

Equation 5.2

$$W_p = W_i - W_b$$

Equation 5.3

By comparing the $\boldsymbol{W_p}$ value to a function of time, a corrosion constant can be determined. The formulae used by Ziemniak et al. [28,31,171], and Orr *et al.* [33] was simplified to the following:

$$\boldsymbol{W_p}(mg\ alloy.dm^{-2}) = \boldsymbol{k_p}(mg\ alloy.dm^{-2}.hrs^{-1/2}).\boldsymbol{t}(hrs)^{1/2}$$

Equation 5.4

Where $\boldsymbol{k_p}$ is the parabolic rate constant, and $\boldsymbol{t}$ is time in hours. As $\boldsymbol{W_p}$ and $\boldsymbol{t}$ are both measureable quantities, $\boldsymbol{k_p}$ is calculated as the gradient of the line where $y = W$ and $x = t^{1/2}$.

A plot of fitted data from the Ziemniak *et al.* papers which focused on the corrosion of 304 stainless steel at 260°C, $pH_{260°C}$ 6.70, and [H_2] at 45 cc.kg^{-1} is shown in section 2.4.1.

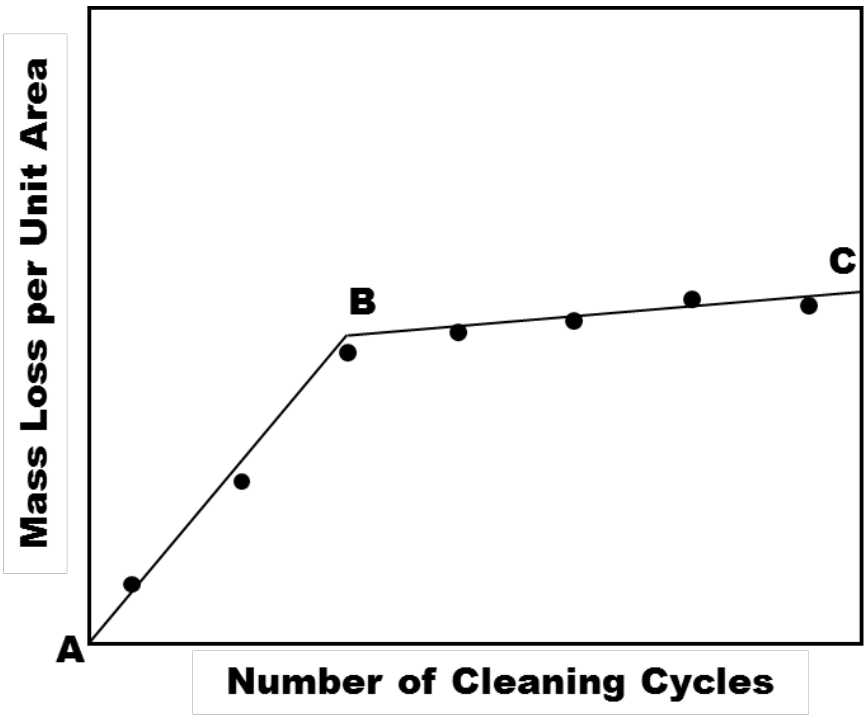

Figure 5.20 - A mock graph of descaling a sample over several cycles. The line 'AB' shows the removal of the oxide scale, while line 'BC' shows the attack on the base metal. At the intercept between the two lines is taken to be the total mass of oxide removed from the surface. Image redrawn from ASTM Standard G1-03: Standard Practise for Preparing, Cleaning, and Evaluating Corrosion Test Specimens [195]. Descaling graphs produced in this work can be seen in section 5.5.1.

In Ziemniak's work [28,31], the fraction of released material, *i.e.* material that has been corroded but dissolved by the fluid, is shown to be a very small quantity. This was done by comparing the measured mass of retained oxide at the surface, to the theoretical mass of oxidised material assuming that none had been dissolved. This is done by calculating the mass of oxygen in the material by multiplying the mass of the alloy corroded ($\boldsymbol{W_p}$) by the fraction of oxygen in magnetite, which is found to be 27.6%. In Ziemniak's work, the mass fraction used was 0.387, which is approximately the mass fraction of oxygen in magnetite divided by the mass fraction of iron in the stainless steel. The calculation defined for this work is as follows:

$$W_{po} = 1.387 \times W_p$$

Equation 5.5

$$W_{ro} = W_{po} - W_{dl}$$

Equation 5.6

Where $\boldsymbol{W_{po}}$ is the theoretical mass of metal oxide were none released to solution (the "zero release condition"), and $\boldsymbol{W_{ro}}$ is the mass of metal oxide released to the solution. To convert mass of metal oxide to mass of alloy released ($\boldsymbol{W_r}$):

$$W_r = W_{ro} - (0.387 \times W_{ro})$$

Equation 5.7

This method makes the assumption that the oxide released to the water was entirely magnetite, which is a reasonable assumption due to the low solubility of chromium oxides [58,61] (see section 6.5.1).

The first set of chemical descalings were carried out (points for coupons from rig 1, 1000 hours and 750 hours, 120 grit) using a descaling time of 15 minutes for each step. However, it was found that the oxide films were being removed too quickly, giving only two descaling data points which representing the oxide layer on the mass loss vs descale cycle graph. As this was a problem that had been considered prior carrying out the process, the first descaling runs were carried out on the coupons that had been exposed for the longest periods of time, and thus had the thickest oxide layers. The time of exposure to each of the two solutions was reduced to 10 minutes in each solution, with the intention of increasing the resolution in the oxide film region.

5.4.3.2.2 SEM-EDX

Cross sectional analysis of the final time point of the corrosion rate experiments were performed. Samples were cut with no lubricant using a low speed diamond saw, before mounting in Epofix resin. The samples were then polished using 0.25 μm diamond grit paste, and sputter coated with gold prior to SEM analysis.

SEM imaging and EDX spectroscopic analysis were performed at the University of Birmingham, with the assistance of Dr. Mary Taylor, using a Jeol

7000F microscope and fitted with an Oxford Instrument EDX module. Imaging was performed using secondary electron detection mode, at a beam energy of 20 kV and working distance of 10 mm; EDX spectroscopy was also performed at a beam energy of 20 kV and a working distance of 10 mm. Under these conditions and based on the ideal density of magnetite, the interaction was estimated to approximately 1.0 μm in depth using the CASINO trajectory simulation tool [197].

5.4.3.2.3 **XPS-AIM**

XPS-AIM depth profiling analysis was performed for a select number of samples taken from the first experiment performed. Analysis was performed through Kratos Analytical Designs Ltd, by Dr. Helen Brannon. Target factor analysis to identify oxidation states was also performed by Dr. Brannon on behalf of this project.

Survey scans were performed initially, as a means to identify elements and oxidation states, and to determine possible crystal structure based on target factor analysis models. Initial survey scans of the surface were performed over a rectangular area 700 x 300 μm^2, at a pass energy of 160 eV.

Composition depth profiles of the samples were produced using an argon ion etching gun, using monoatomic argon (as opposed to argon clusters) accelerated by a 5 kV electric field. Rather than calculating sputter depth from average crater depth using confocal microscopy (as seen in section 5.2.3), the etch rate was estimated from a Ta_2O_5 standard to be 3.315 $nm.min^{-1}$. The Ta_2O_5 standard was used as its density is similar to that of stainless steel [198].

5.5 **Corrosion Rate Rig Experimental Results**

Three experiments were performed using the bespoke corrosion kinetics rig. The commissioning tests (experiment 1, rig 1 and experiment 1, rig 2) were performed at 2.5 ppm LiOH, and 300°C for 1000 hours, with four time points.

A further two tests were performed within the time frame of this project; test 2, rig 1 was performed at 0.25 ppm LiOH and test 2, rig 2 was performed at 25 ppm LiOH. Both tests lasted for 922 hours with two time points in each.

Table 5.4 - Table of experiments performed using the Corrosion Kinetics Rigs.

Exp Number	Rig		T	[LiOH] ($\mu g.kg^{-1}$)	Calculated pH_T=25˚C		Time (hrs)	Time Points (hrs)
1	1		300˚C	2.50	10		1,000	288, 500, 788, 1004
	2		300˚C	2.50	10		1,000	288, 500, 788, 1004
2	1		300˚C	0.25	9		500	588, 922
	2		300˚C	25.00	11		500	588, 922

5.5.1 Gravimetric Descaling

The total mass of corroded material was calculated for each individual sample by chemical descaling; the method of this process is discussed in section 5.4.3.2.1.

The mass of retained oxide film is calculated from each coupon, and using the arithmetic provided in Equations 5.2 and 5.3, the total mass of corroded alloy ($\boldsymbol{W_p}$) is calculated.

Initially, it has been assumed that parabolic corrosion rates would be observed (based on literature evidence of similar systems) and the fact that the oxide films exhibit a reasonably thick oxide film, as shown in section 5.5.2 (see Equation 5.3).

To reflect this, the average value of $\boldsymbol{W_p}$ for each time point and surface finish is plotted against the square root of time in hours; the gradient of this line is the parabolic corrosion rate, $\boldsymbol{k_p}$. Errors are based on the standard deviation of each data set. The collated data for each test and rig is presented in Figures 5.29, 5.30, 5.31, and 5.32.

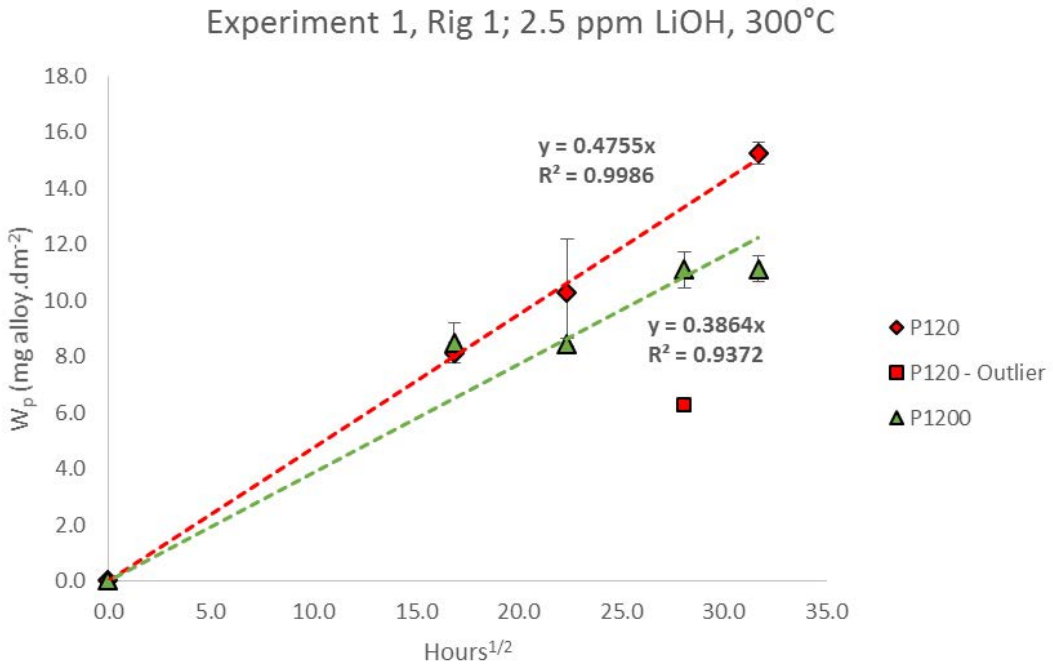

Figure 5.21 – Experiment 1, rig 1 (2.5 ppm LiOH, 300 °C), total mass of corroded alloy vs square root of time. A single outlier has been identified; it is believed to have been produced during an incorrectly carried out descaling procedure.

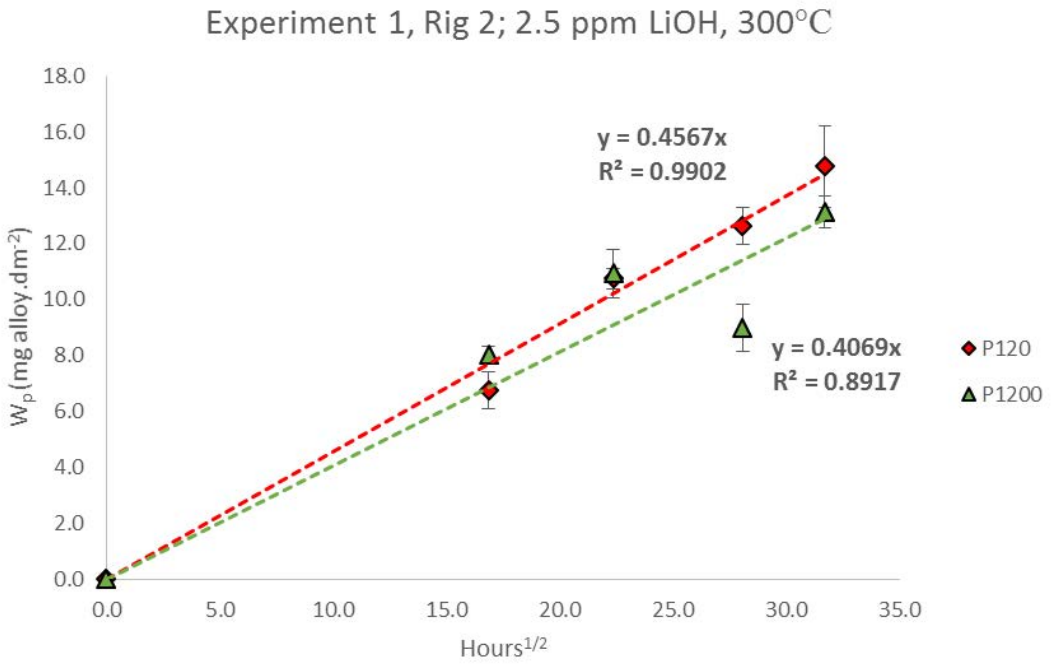

Figure 5.22 – Experiment 1, rig 2 (2.5 ppm LiOH, 300 °C); total mass of corroded alloy vs square root of time

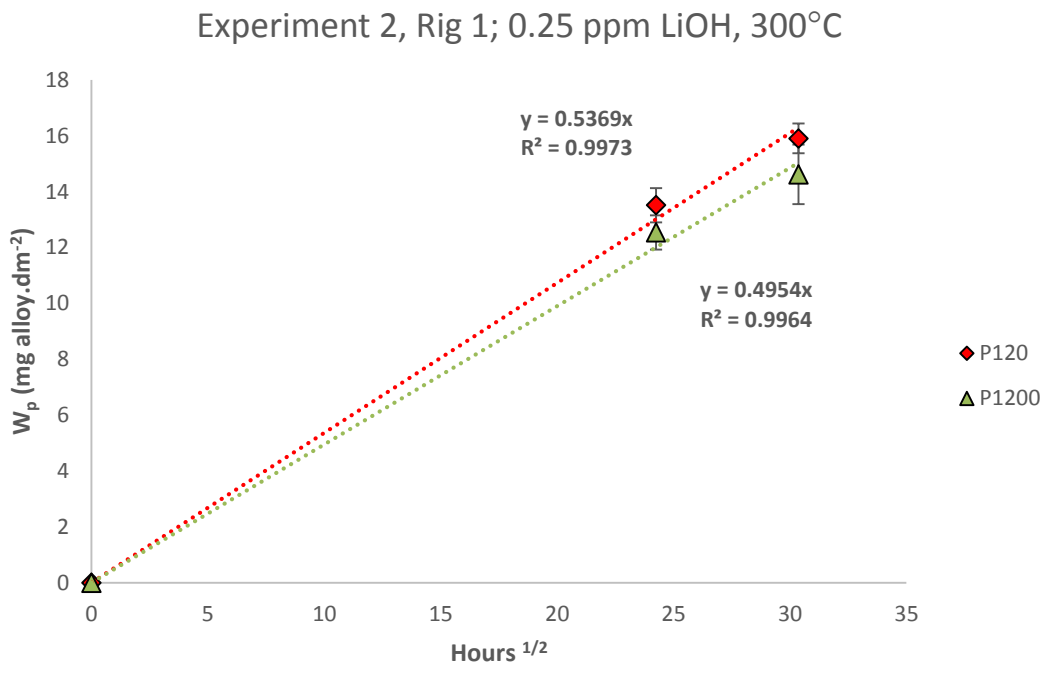

Figure 5.23 - Experiment 2, rig 1 (0.25 ppm LiOH, 300 °C); total mass of corroded alloy vs square root of time.

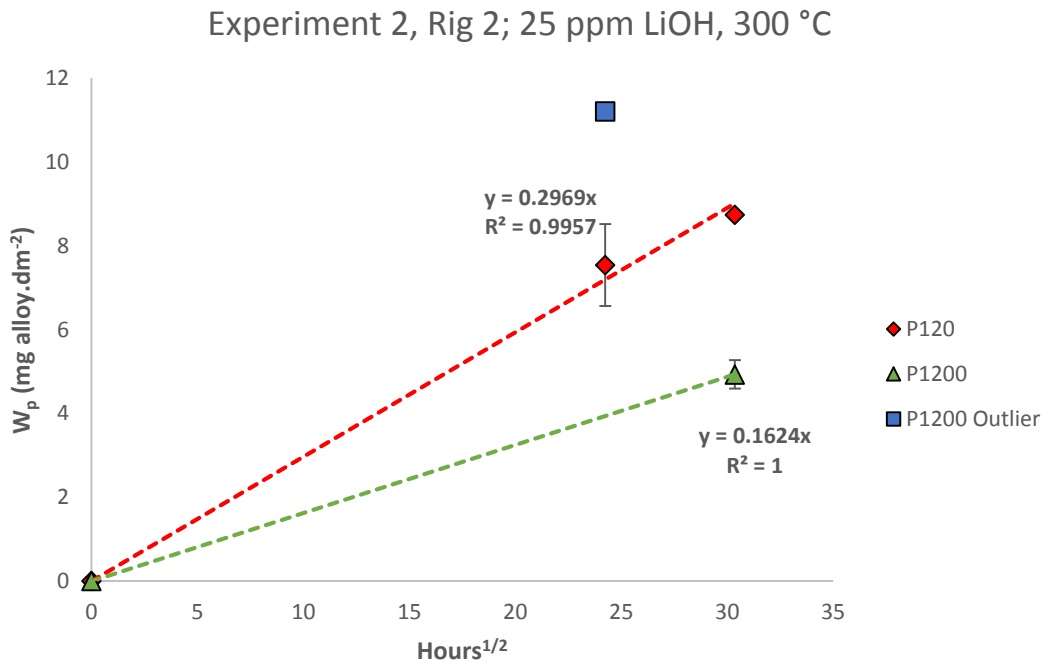

Figure 5.24 - Experiment 2, rig 2 (25.0 ppm LiOH, 300 °C); total mass of corroded alloy vs square root of time. The P1200 outlier result was due to an incorrect calibration of the balance which was only discovered after the analysis was complete. This outlier has been discounted from the overall result, but presented here for completeness.

For the majority of the results, this assumption of parabolic kinetics provides a reasonable description. However, in the case of P1200 ground sample in experiment 1, (see Figure 5.21 and Figure 5.22) a parabolic trend does not appear to hold particularly well. If the data for all P1200 samples in experiment 1 is plotted assuming logarithmic kinetics, an improved fit for the data is obtained, as can be seen in Figure 5.25. However, logarithmic kinetics do not describe the corrosion of the P120 samples, which are plotted in Figure 5.26, where the fit is considerably worse than that obtained for the parabolic kinetics (Figure 5.21 and Figure 5.22).

The difference between kinetics law which provides the best fit for the data is surprising, given that many literature sources have observed parabolic, or near-parabolic, kinetics. Without additional data from time points beyond 1,000 hours it is difficult to assert that the logarithmic kinetics are correct, and describe the corrosion for a significant period of time, or that parabolic kinetics will become dominant given sufficient time. This is discussed further in section 5.6.

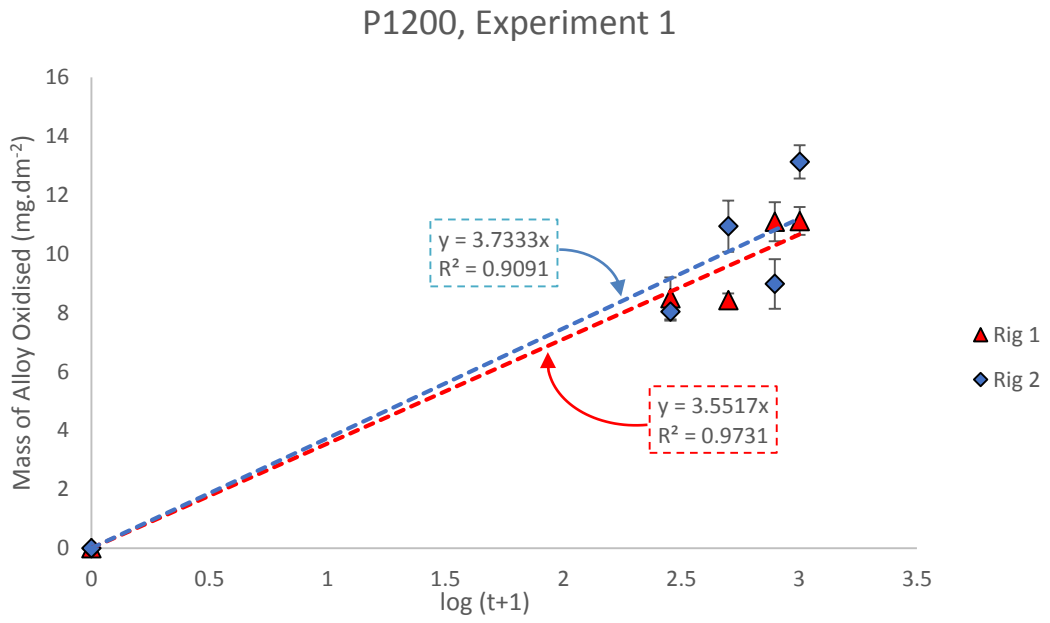

Figure 5.25 – Mass of alloy oxidised for all P1200 samples in experiment one compared with the logarithm of time. The fits are found to be an improvement over those of the parabolic fit.

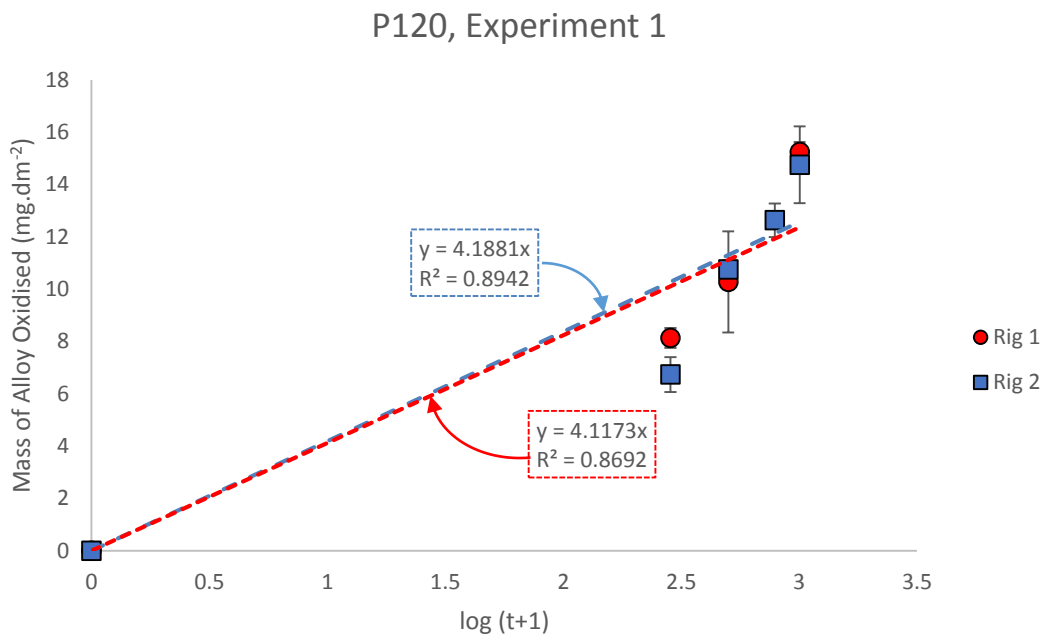

Figure 5.26 - Mass of alloy oxidised for all P120 samples in experiment 1 compared with the logarithm of tim. The fits are obviously poor compared with those of the parabolic kinetics assumption. A single trend line is show as this line is identical for both data sets.

Given the small volume of data from experiment 2, it is difficult to have any certainty that the chosen kinetics law is correct. This is made more difficult by the presence of an outlier in the dataset of P1200 for experiment 2, rig 2, as seen in Figure 5.24. This outlier was the result of a fault in the automatic calibration system of the balance. This is normally an automatic process, however the balance was found to be faulty shortly after the descaling was performed, invalidating the result set. The balance was repaired before any other results were obtained.

Parabolic corrosion kinetics have been chosen for experiment 2 data, in an attempt to draw comparison between data sets, however these are by no means confirmed and further work should be conducted to confirm the relationships. The corrosion kinetics are listed in Table 5.5.

Table 5.5 - Tabulated parabolic corrosion rates. The coefficients of the P1200 samples for experiment 1 have been highlighted to indicate that a better fit is given by the use of logarithmic kinetics in Table 5.8.

Exp Number	Rig		T	[LiOH] ($\mu g.kg^{-1}$)	Calculated pH_T=25˚C		Kp	
							120grit	1200grit
1	1		300˚C	2.5	10		0.4755	0.3864
	2		300˚C	2.5	10		0.4567	0.4069
2	1		300˚C	0.25	9		0.5369	0.4954
	2		300˚C	25.0	11		0.2969	0.1624

Table 5.6 - Tabulated logarithmic kinetic coefficients for theP1200 samples from experiment 1. The rate law is described by Equation 2.35.

Exp Number	Rig		T	[LiOH] ($\mu g.kg^{-1}$)	Calculated pH_T=25˚C		K_{log}	t_0	A
1	1		300˚C	2.5	10		3.5517	1	0
	2		300˚C	2.5	10		3.7333	1	0

The descaling data shows that there is a small, but measureable improvement in corrosion resistance for coupons polished to a higher finish, *i.e.* P1200, than those not so well finished. The direct comparison between the two surfaces is made slightly more complex by the different kinetics trends exhibited by each data set, however the fitting of the data allows for calculation of idealised values which can illustrate the improvement.

The corrosion masses observed, and the rates derived from them, are consistent with those of Warzee [121] (see Figure 2.38), whose data fitted a parabolic law profile and showed the corrosion rate of 304 stainless steel in pure water at 300 °C to be ~0.298 $mg.dm^{-2}.hr^{-1/2}$ for mechanically polished samples.

Furthermore, plotting the parabolic corrosion rate coefficient for P120 samples as a function of LiOH concentration (see Figure 5.27) reveals a downward trend. This this may be a local minimum rate, *i.e.*, the corrosion rate may increase should LiOH concentration be increased further. This is based on the solubility trends of the protective oxide film, discussed in section 2.5, where it is shown that there is a very rapid rise in solubility of passive film oxides as pH

increases. In high pH conditions, the film which would otherwise protect the underlying metal is dissolved away. The resulting corrosion kinetics would likely be linear, as the alloy would be afforded no protection from the highly corrosive test solution.

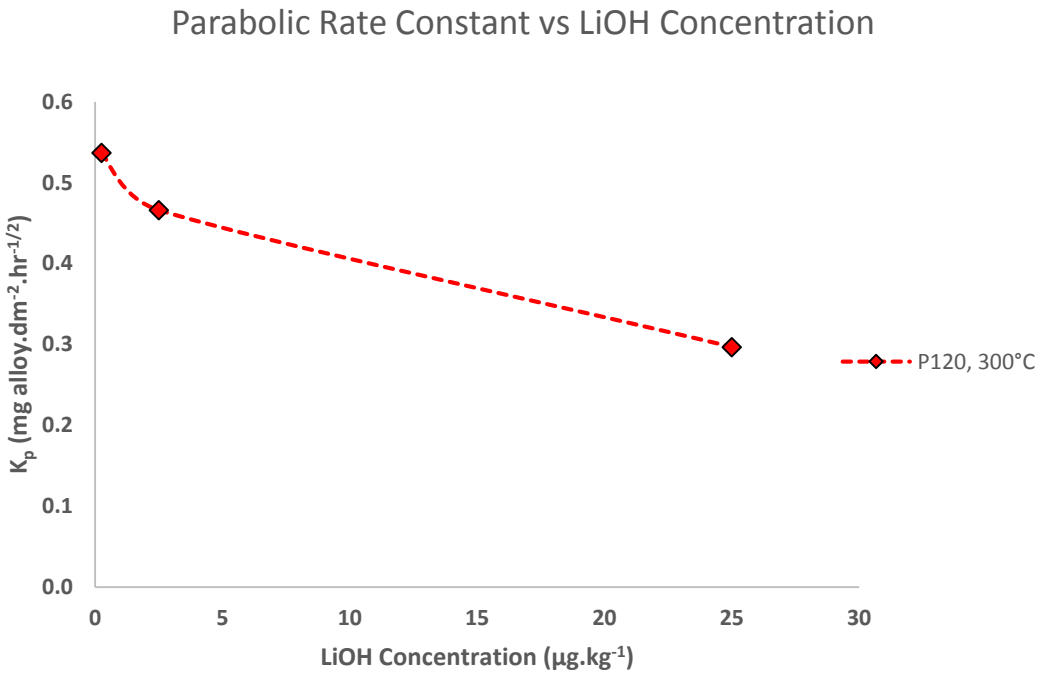

Figure 5.27 – Collated parabolic corrosion rate constants plotted as a function LiOH concentration. There appears to be a negative relationship between increased LiOH concentration and corrosion rate.

The calculation of release rates for these experiments has proved unsuccessful. Release rate can be defined as the mass of indigenous material lost to solution. Equation 5.7 details the arithmetic used to determine the mass of released material ($\boldsymbol{W_r}$), however it was found that the mass of material removed by descaling was consistently greater than the theoretical mass determined for the zero release condition. The variable $\boldsymbol{W_r}$ has been plotted against square root of time in Figures 5.36, 5.37, 5.38 and 5.39; it can be seen that there is no consistent trend.

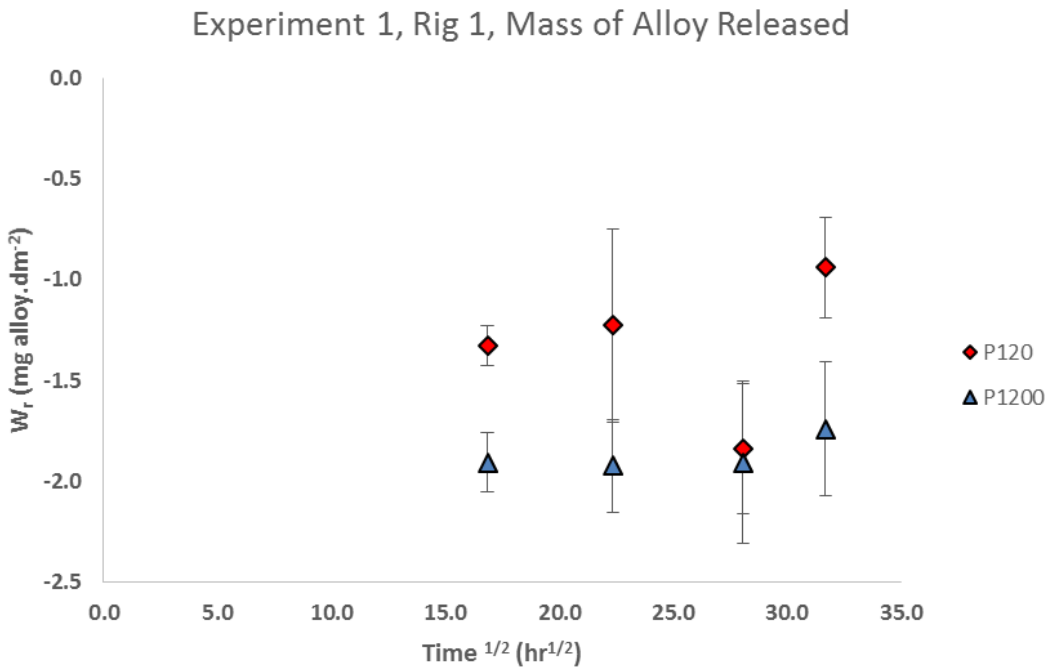

Figure 5.28 - Mass of released alloy for samples in rig 1 during experiment 1; 2.5 ppm LiOH at 300 °C

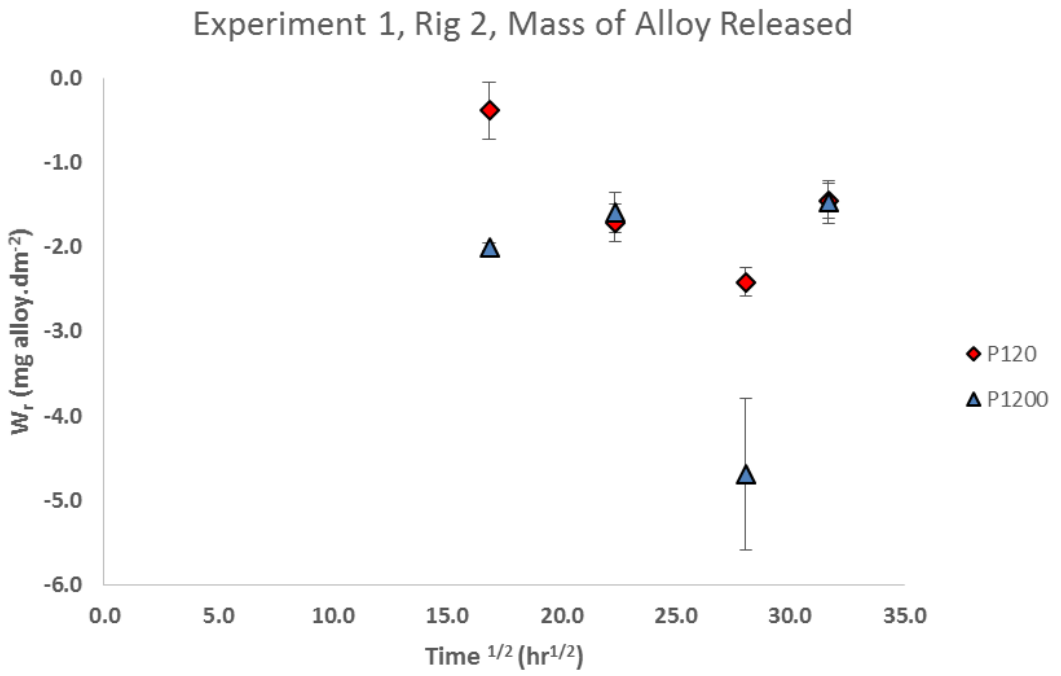

Figure 5.29 - Mass of released alloy for samples in rig 2 during experiment 1: 2.5 ppm LiOH at 300 °C

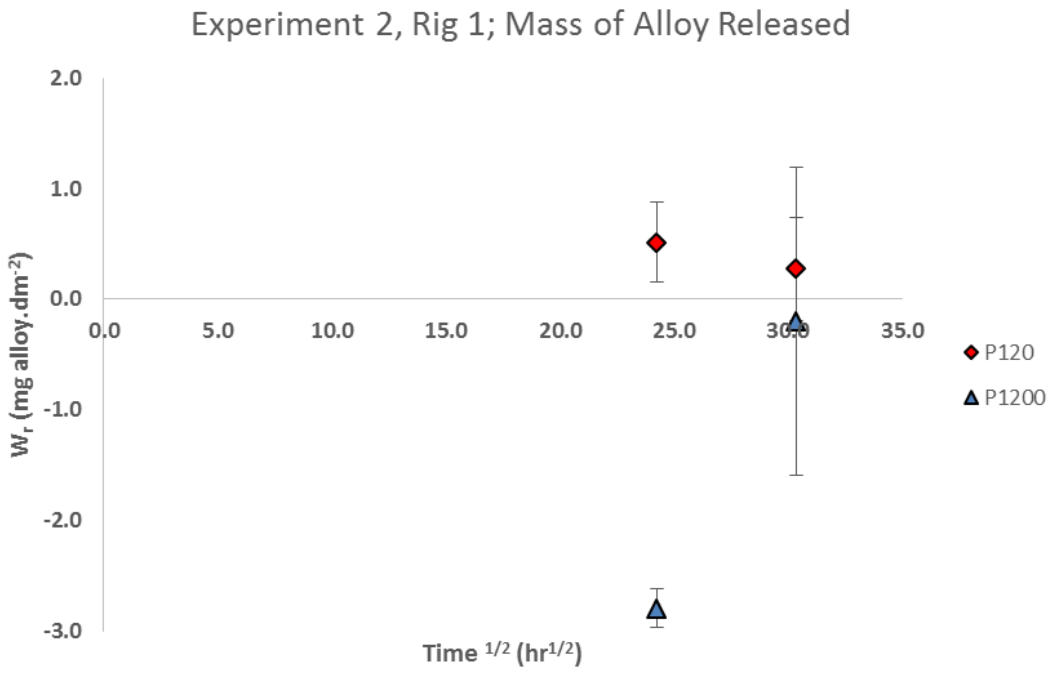

Figure 5.30 - Mass of released alloy for samples in rig 1 during experiment 2; 0.25 ppm LiOH at 300 °C

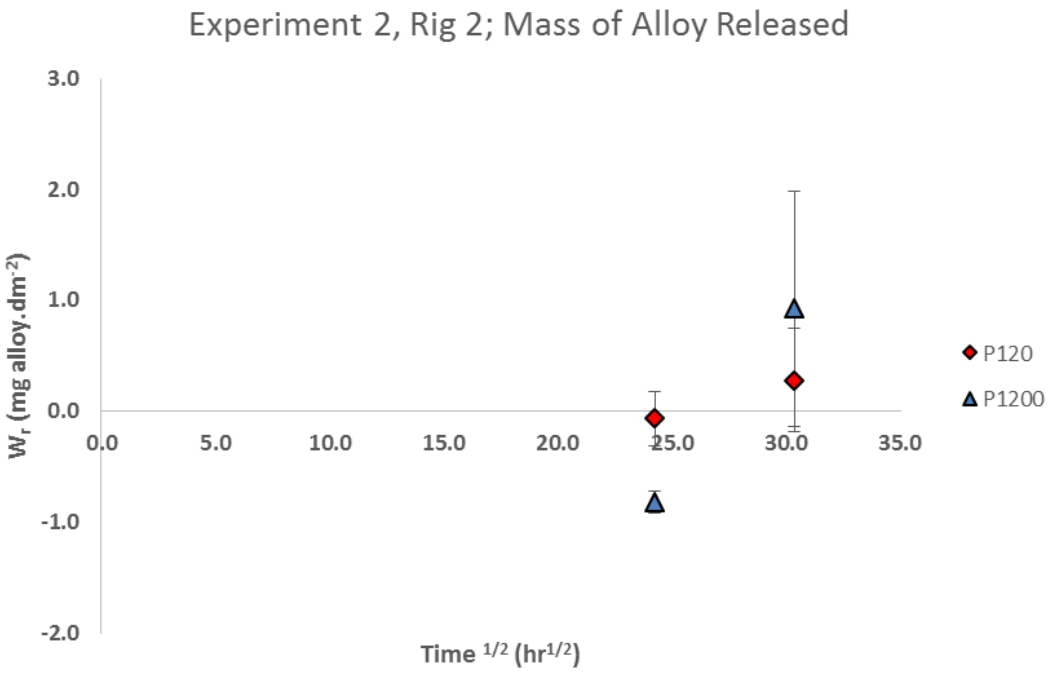

Figure 5.31 - Mass of released alloy for samples in rig 2 during experiment 2; 25 ppm LiOH at 300 °C

Two possible explanations for this exist; either the descaling mass loss ($\boldsymbol{W_{dl}}$) is being systematically underestimated, or a mechanism exists whereby non-indigenous metal oxides are being deposited on the coupons (*i.e.*, metal oxides formed by corrosion of the rig materials). This second mechanism is possible

due to the fall in metal oxide solubility with rising temperature [53]. As the test solution is warmed from ambient temperature to 300 °C, it will corrode and dissolve material from the tubing of the rig. As the temperature rises to its final value, the solution is now super saturated with metal oxides which precipitate on surfaces around the rig, including the coupons.

It is unclear which of these explanations is correct, however this issue has rendered calculation of corrosion release rates impossible by this method.

5.5.2 **SEM-EDX**

The oxide films of the samples exposed for the ~1,000 hours were observed in cross section, as described in section 5.4.3.2.2.

Secondary electron images of the cross sections are shown in Figures 5.39, 5.41, 5.43, 5.45, 5.47, 5.49, 5.51 and 5.53. These images were taken in pairs, one of an outer layer crystal and one with no crystal. Accompanying these images is the EDX composition line scan; in images of the outer layer crystal the scan line transited the crystal. Line scans were taken in semi-quantitative mode as microscope availablility was too limited to produce a full set of quantitative scans. The line scans have been re-plotted for greater clarity in Figures 5.40, 5.42, 5.44, 5.46, 5.48, 5.50, 5.52 and 5.54.

In all cases where the scan transits an outer layer crystal (Figures 5.39, 5.43, 5.47 and 5.52) a clear enrichment is visible. This plateaus as the scan approaches the region where the inner oxide film is expected to be and begins to rise toward a stable value as the scan moves into the bulk of the unlying metal. The point of highest chromium to iron ratio has been included in each EDX re-plot graph as a vertical black dotted line and in the graphs for outer layer crystals, this coincides with exactly the location expected for the chromium-enriched inner film. In the case of Figure 5.44 this demarcation is difficult to see as the outer layer crystals on this sample were particularly small.

In the cases of scans without the presence of an outer layer crystal (those seen in Figures 5.41, 5.45, 5.49 and 5.53) it is difficult to draw any instant conclusions as the compositions simply rise toward stable values. The re-plotted EDX data (see Figures 5.42, 5.46. 5.50 and 5.54) includes the point of highest chromium to iron ratio and this lines-up with the expected location of the inner layer – i.e., at the surface of the metal.

There is some uncertainty surrounding these results due to the interaction volume of the electron beam; this has been estimated to be approximately 1.1 μm in diameter at its widest point. As a result of this it is not possible to conclusively characterise the oxide films developed on these materials.

Notably, there is an apparent absence of nickel in the outer layer crystals of these samples; literature data suggests that austenitc stainless steels for nickel ferrite crystals at the surface under high temperature, high pH and hydrogenated water conditions [28,31]. Given the lack of dissolved hydrogen in this experiment, it is possible that nickel ferrite forms as a result of the presence of hydrogen. However, given the variabliltiy and semi-quantitiative nature of the EDX data, it is possible that nickel was not detected as in too low a concentration.

Further work using more precise methods such as TEM and Wave Dispersive X-ray Spectroscopy (WDX) would be needed to provide quantitative composition data.

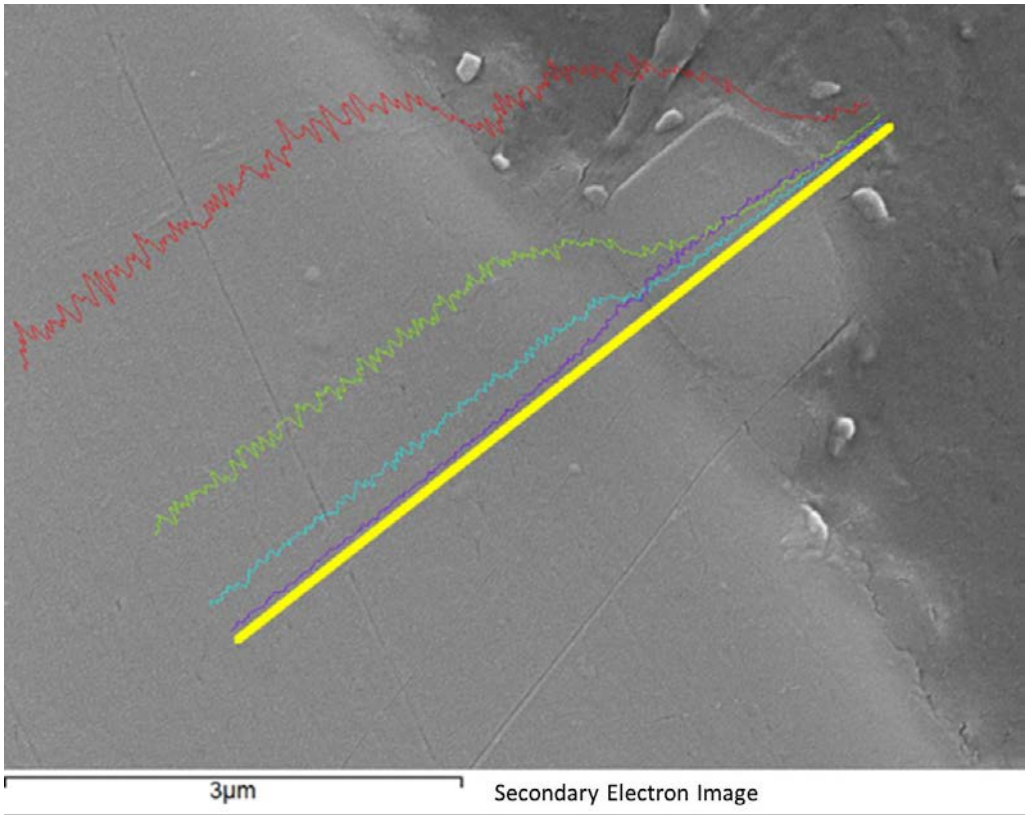

Figure 5.32 - SEM image of a P120 grit finished specimen, removed from rig 1 after 1,000 hours' exposure, with the EDX line scan location superimposed. Images taken in secondary electron detection mode, with a beam energy of 20 kV at a working distance of 10 mm.

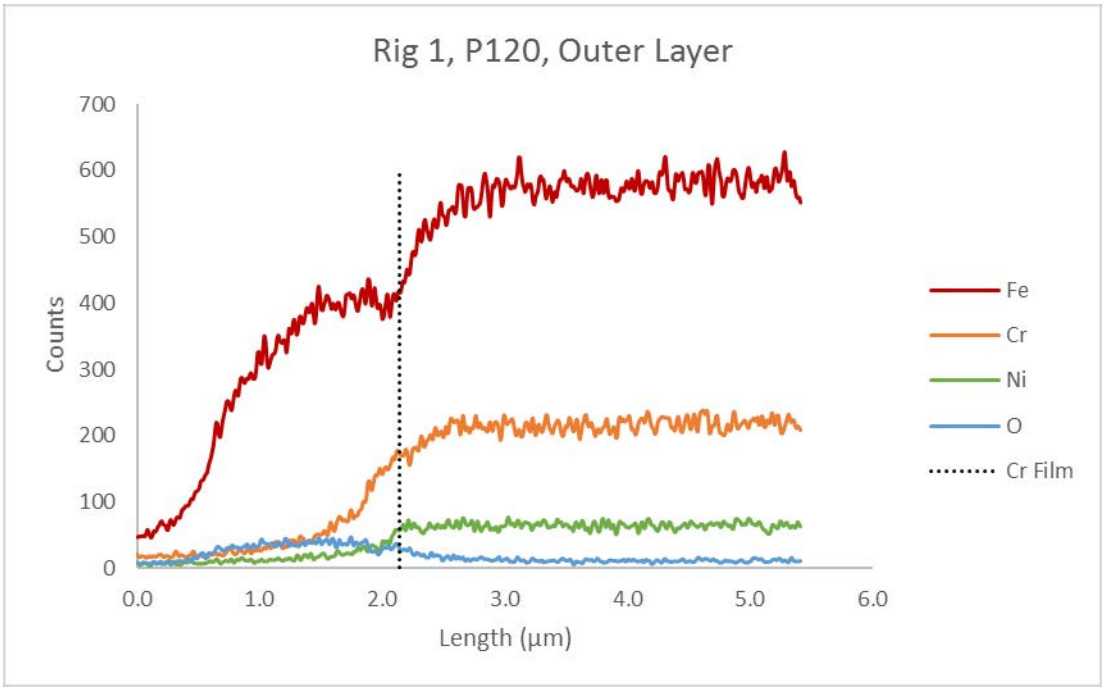

Figure 5.33 – EDX data from the line scan shown in Figure 5.32.

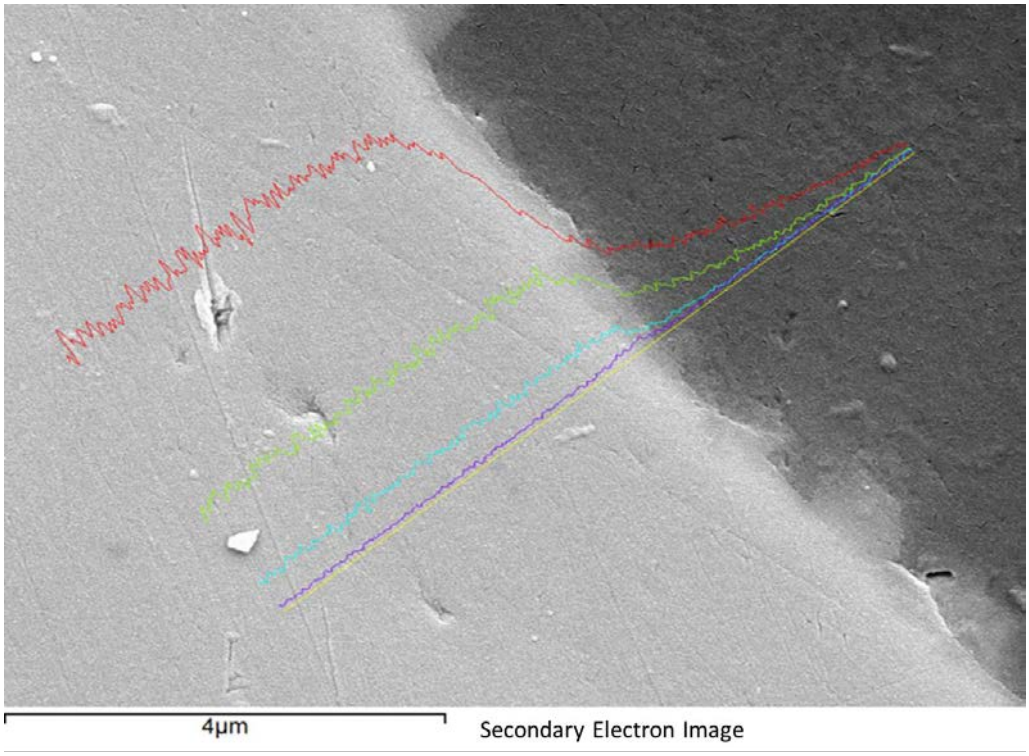

Figure 5.34 - SEM image for the cross section of a P120 grit finished specimen, removed from rig 1 after 1,000 hours' exposure, with the EDX line scan location superimposed. Images taken in secondary electron detection mode, with a beam energy of 20 kV at a working distance of 10 mm.

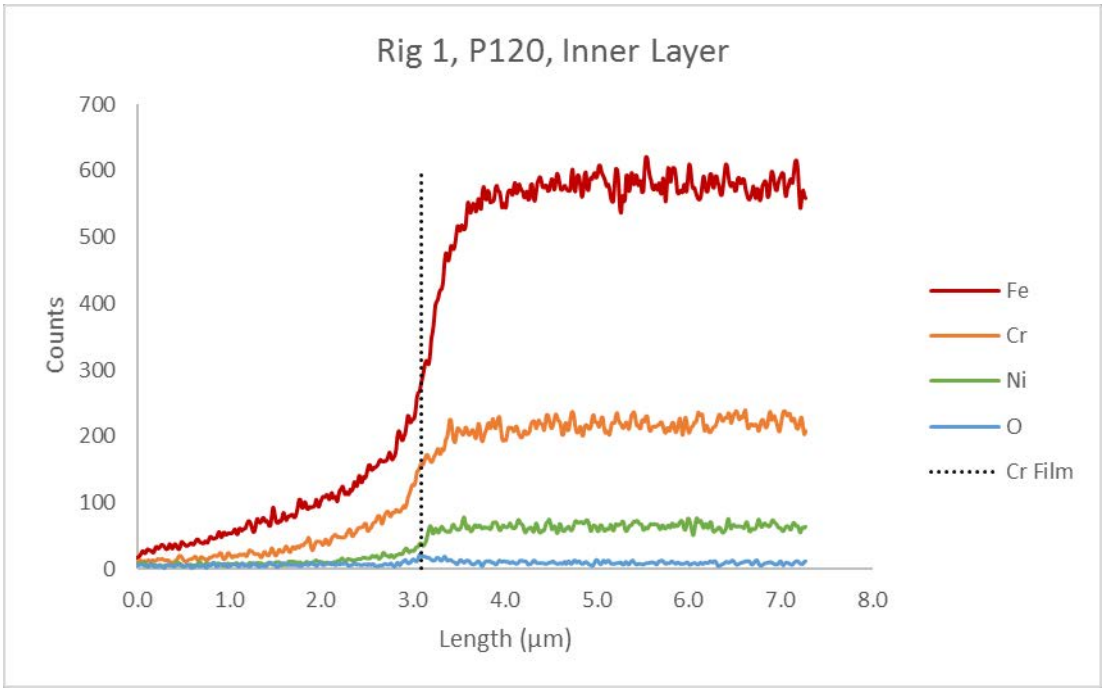

Figure 5.35 - EDX data from the line scan shown in Figure 5.34.

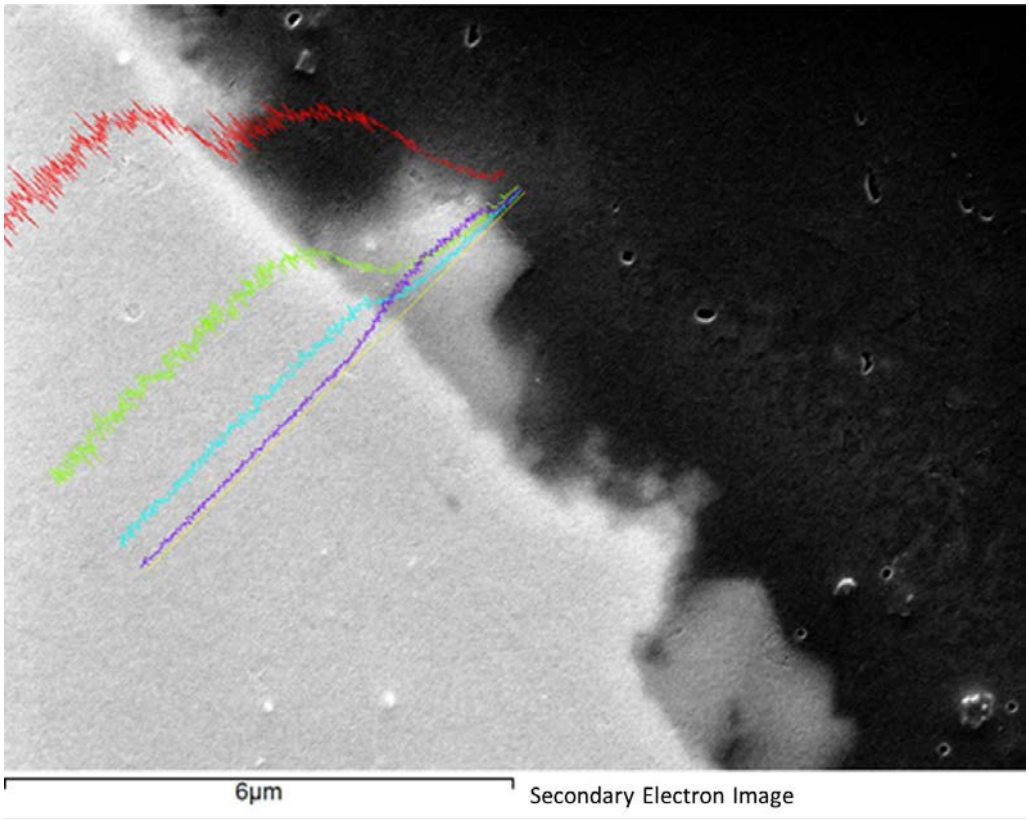

Figure 5.36 - SEM image for the cross section of a P120 grit finished specimen, removed from rig 2 after 1,000 hours' exposure, with the EDX line scan location superimposed. Images taken in secondary electron detection mode, with a beam energy of 20 kV at a working distance of 10 mm.

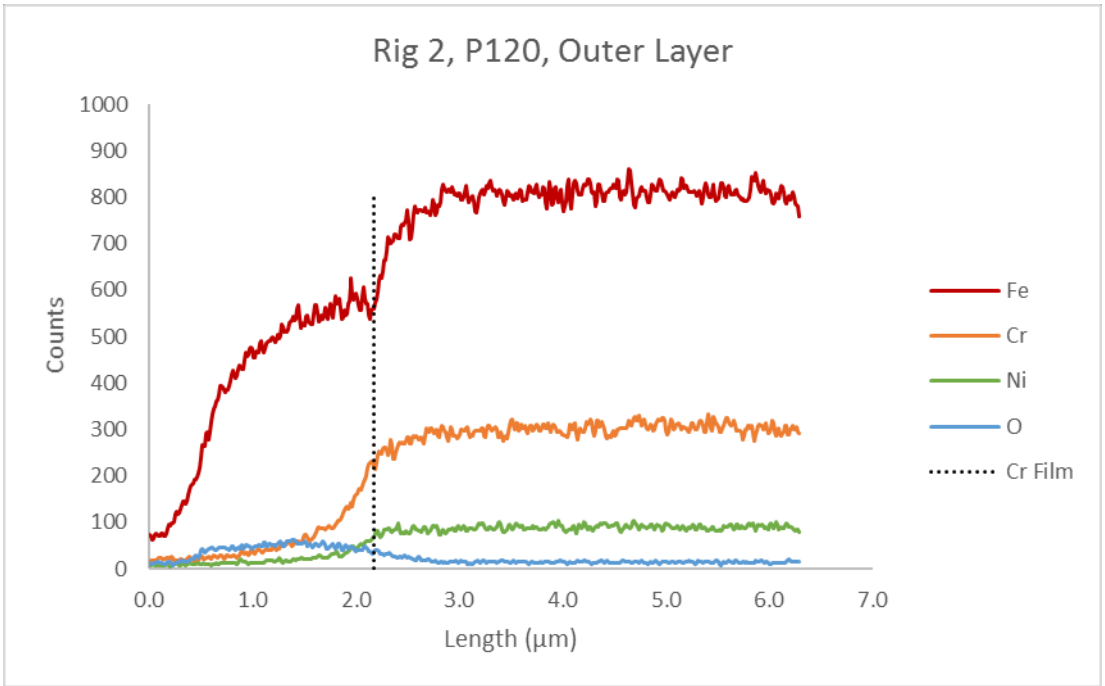

Figure 5.37 - EDX data from the line scan shown in Figure 5.36.

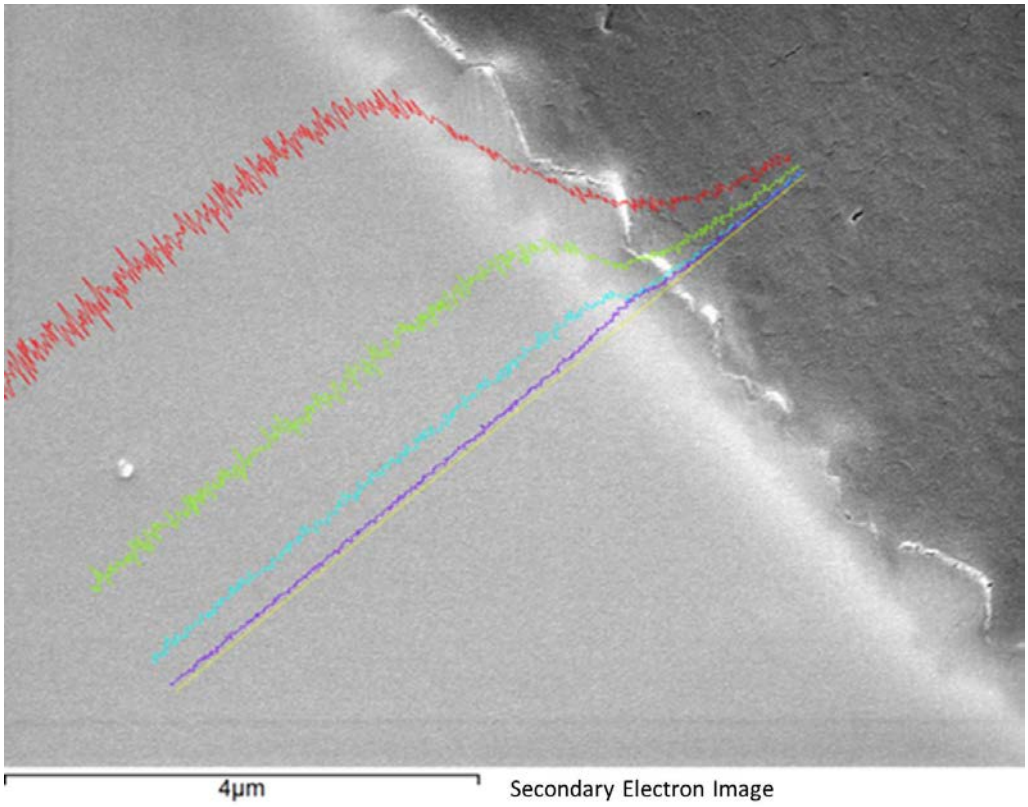

Figure 5.38 - SEM image for the cross section of a P120 grit finished specimen, removed from rig 2 after 1,000 hours exposure, with the EDX line scan of the location superimposed. The EDX line runs through the inner layer, avoiding large outer layer crystals. Images taken in secondary electron detection mode, with a beam energy of 20 kV at a working distance of 10 mm.

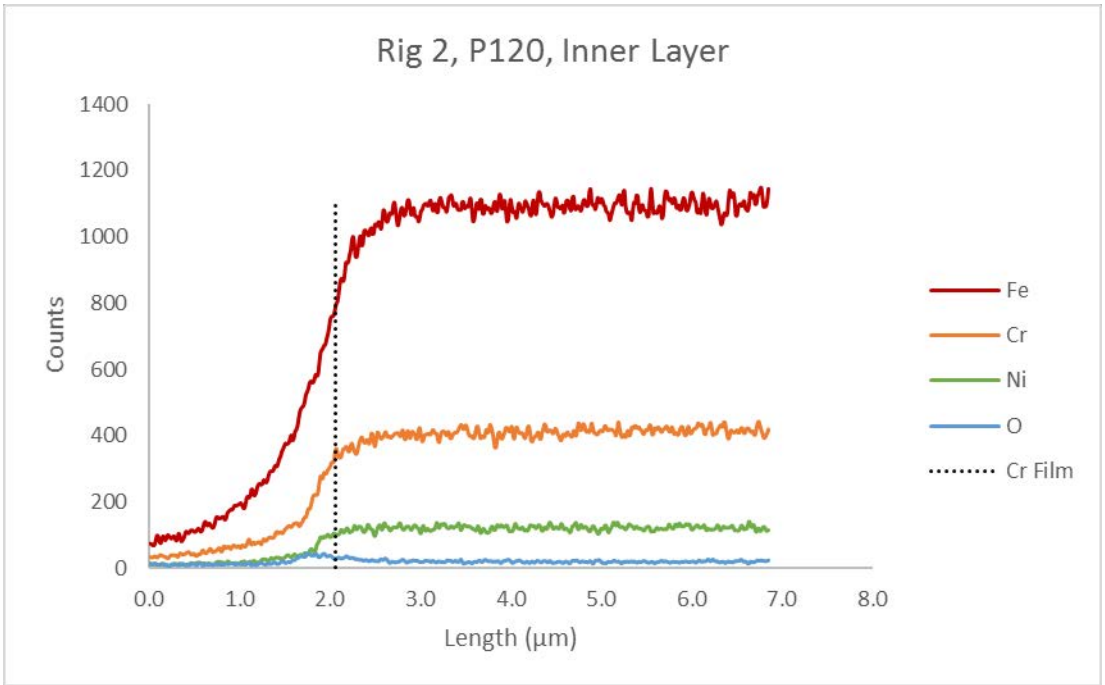

Figure 5.39 - EDX data from the line scan shown in Figure 5.38.

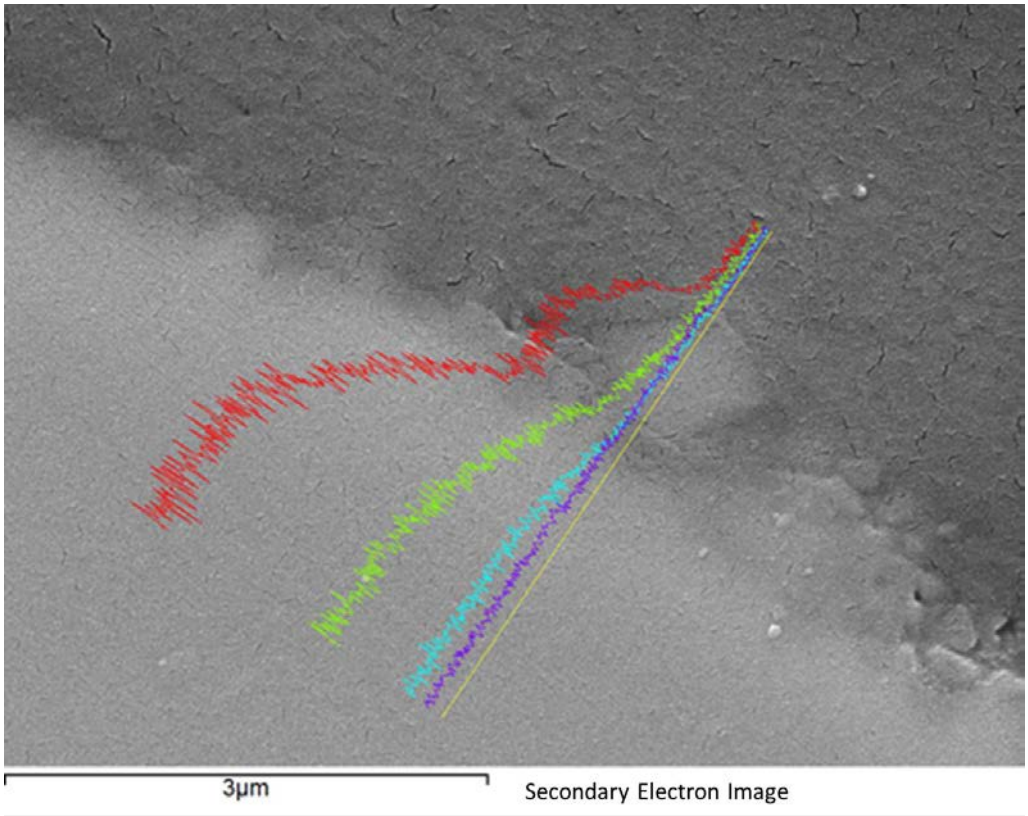

Figure 5.40 - SEM image for the cross section of a P1200 grit finished specimen, removed from rig 1 after 1,000 hours exposure, with the EDX line scan of the location superimposed. Images taken in secondary electron detection mode, with a beam energy of 20 kV at a working distance of 10 mm.

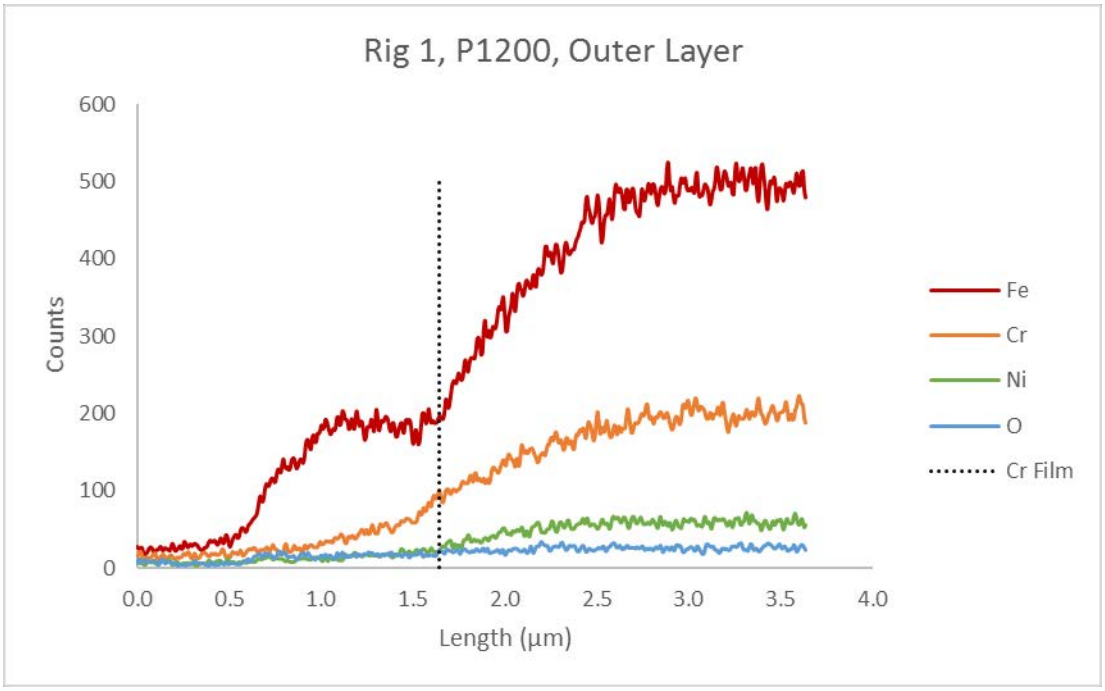

Figure 5.41 - EDX data from the line scan shown in Figure 5.40.

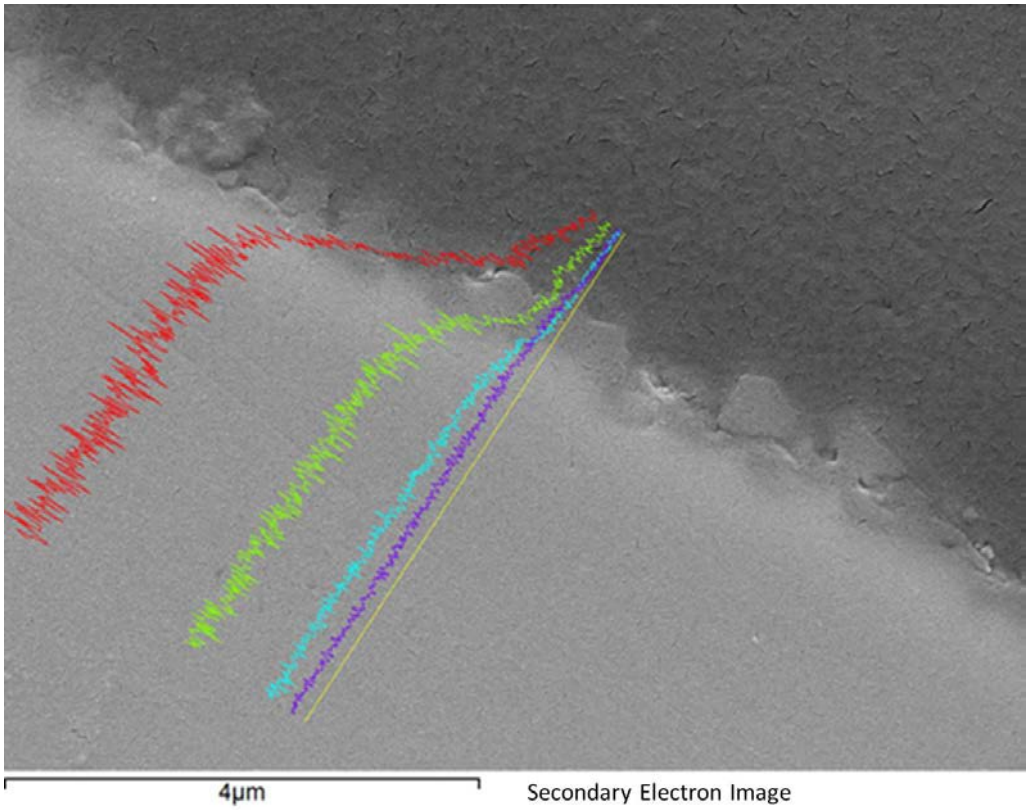

Figure 5.42 - SEM image for the cross section of a P1200 grit finished specimen, removed from rig 1 after 1,000 hours' exposure, with the EDX line scan of the location superimposed. Images taken in secondary electron detection mode, with a beam energy of 20 kV at a working distance of 10 mm.

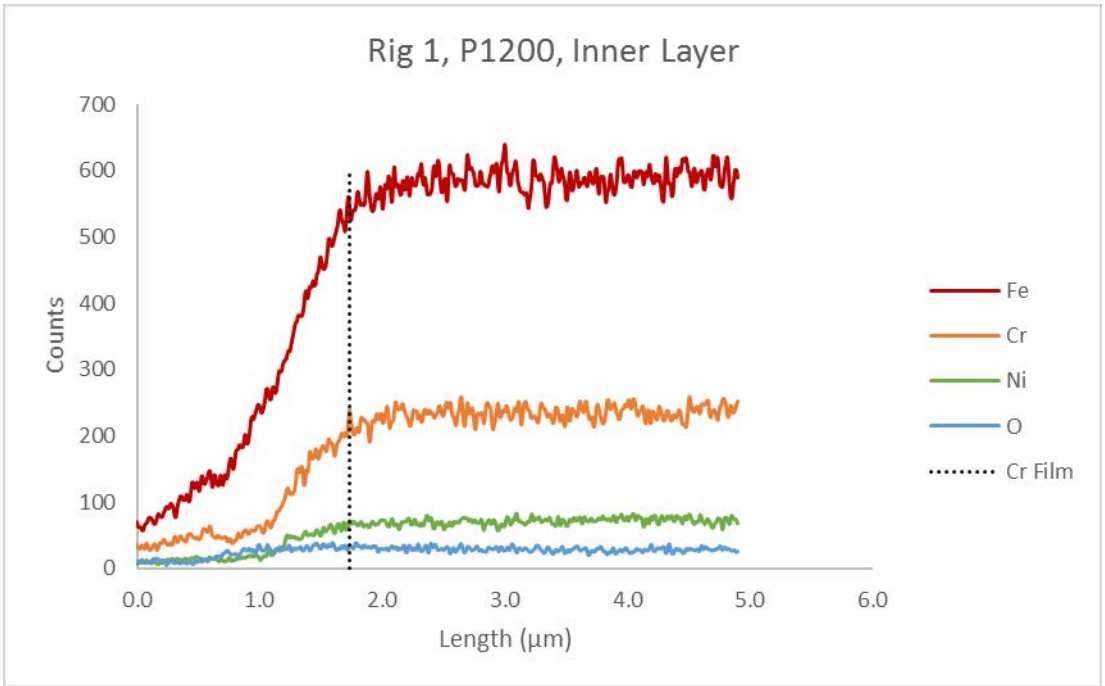

Figure 5.43 - EDX data from the line scan shown in Figure 5.42.

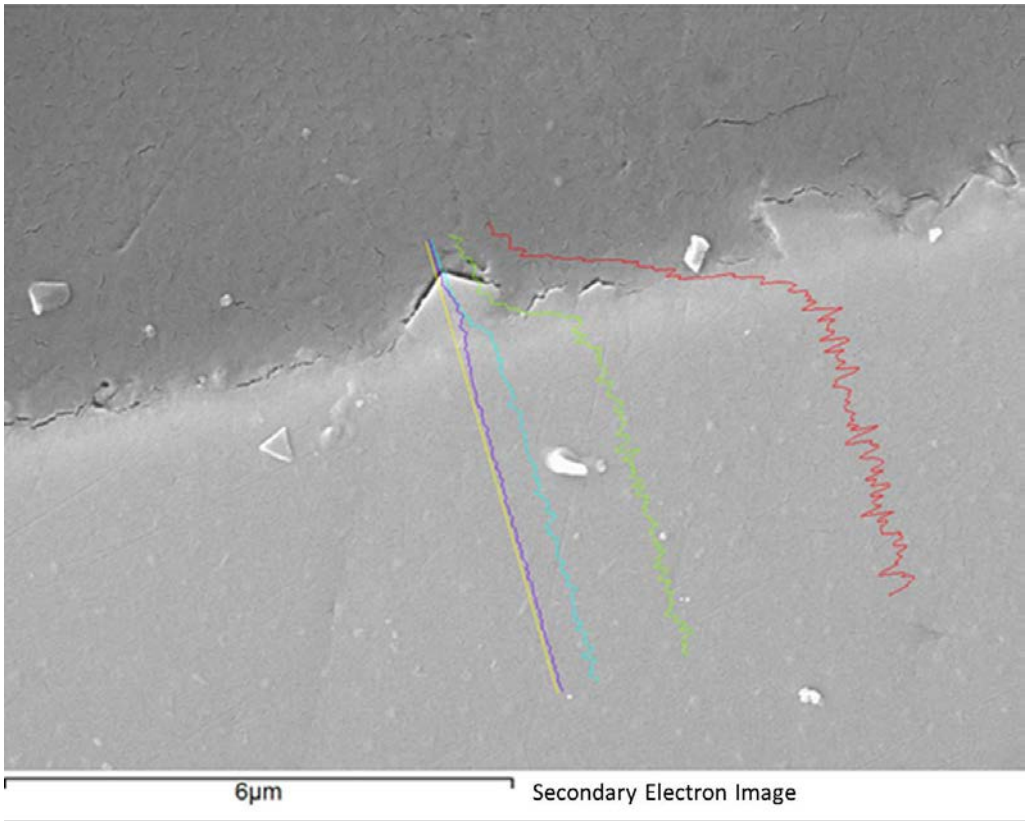

Figure 5.44 - SEM image for the cross section of a P1200 grit finished specimen, removed from rig 2 after 1,000 hours exposure, with the EDX line scan of the location superimposed. Images taken in secondary electron detection mode, with a beam energy of 20 kV at a working distance of 10 mm.

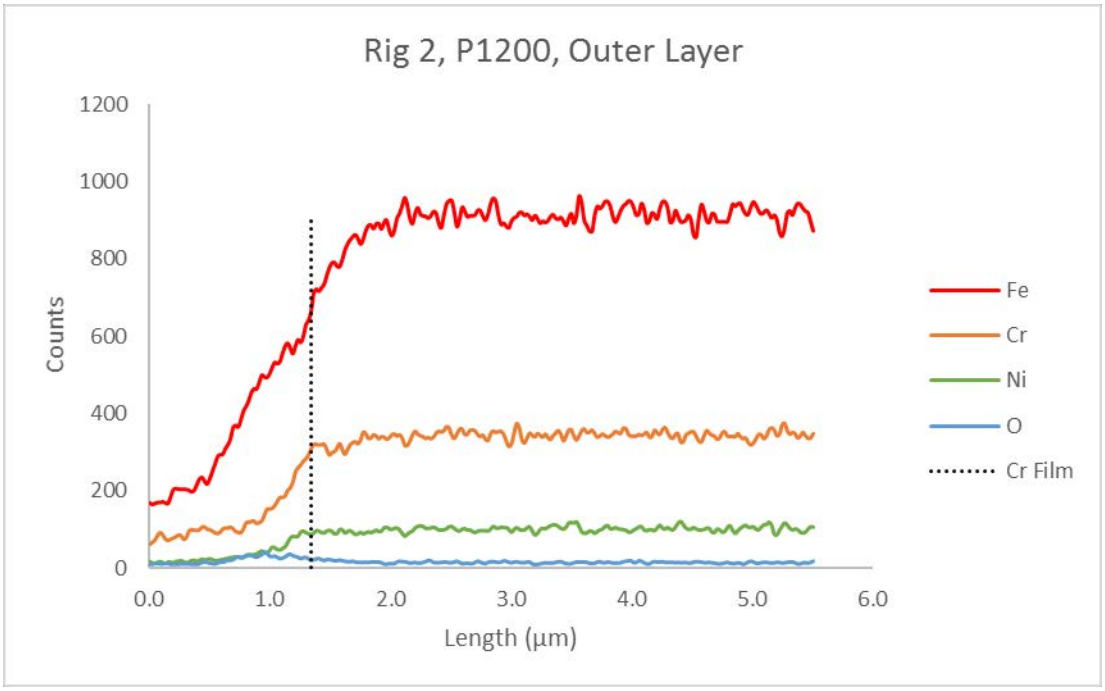

Figure 5.45 - EDX data from the line scan shown in Figure 5.44.

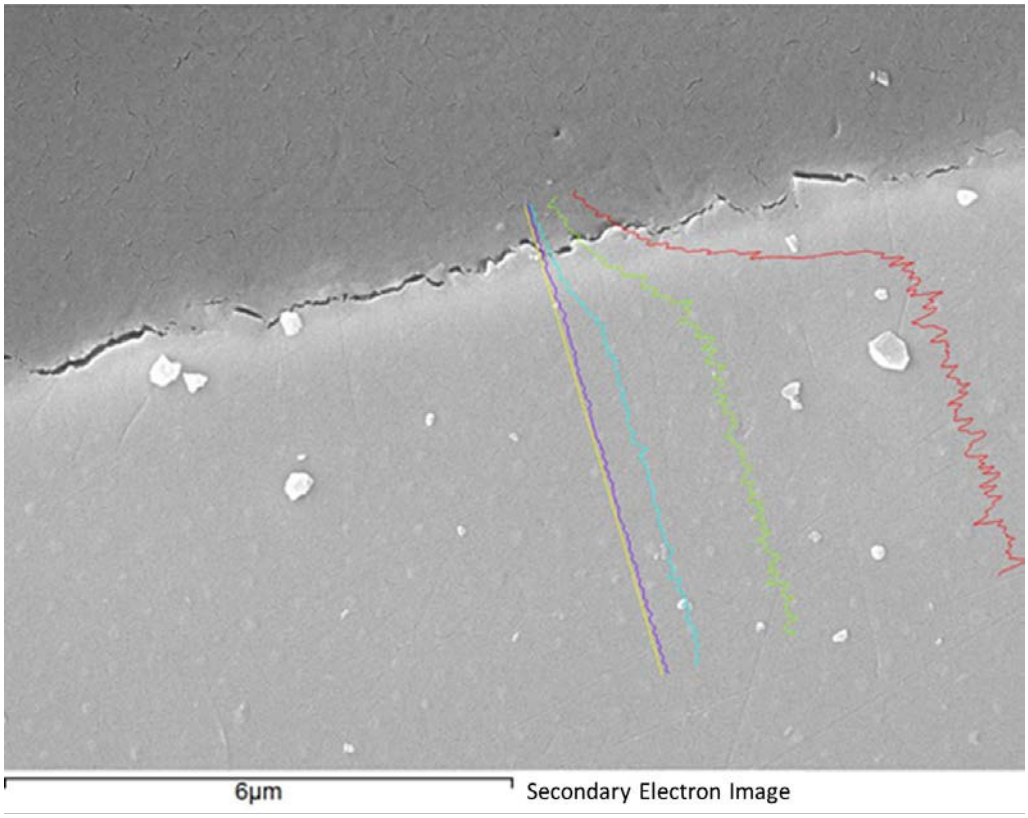

Figure 5.46 - SEM image for the cross section of a P1200 grit finished specimen, removed from rig 2 after 1,000 hours' exposure, with the EDX line scan of the location superimposed. Images taken in secondary electron detection mode, with a beam energy of 20 kV at a working distance of 10 mm.

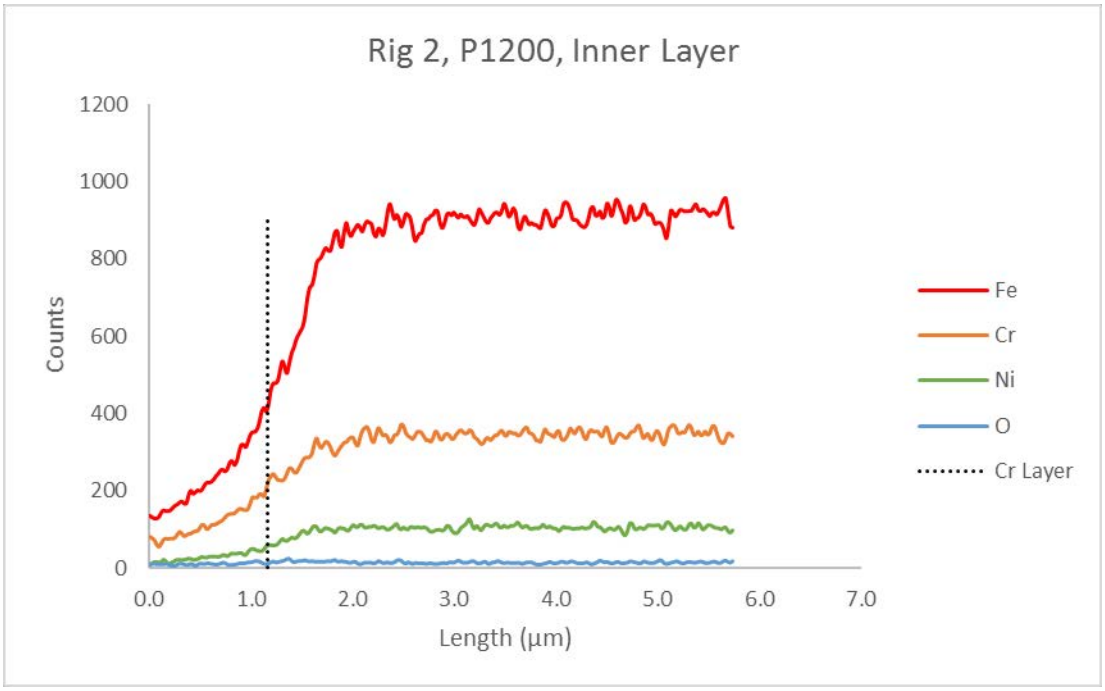

Figure 5.47 - EDX Data of 2-D-1200 inner layer Figure 5.46.

Table 5.7 – Point of highest chromium to iron ratio.

Sample Code	Layer	Highest Cr/Fe Ratio Position (µm)
1-D-120	Inner	3.09
	Outer	2.14
2-D-120	Inner	2.06
	Outer	2.17
1-D-1200	Inner	1.73
	Outer	1.64
2-D-1200	Inner	1.17
	Outer	1.34

5.5.3 XPS-AIM

XPS surface chemistry and composition depth profiles were performed using a Kratos Analytical AXIS Supra spectrometer. The four 1,000 hour exposed specimens from corrosion experiment 1 were put forward for testing as these were considered to be of most interest. The analysis process began with survey scans to determine the surface chemistry prior to etching, followed background correction and peak fitting to determine elements and speciation, and finally depth profiling of the sample using argon ion. As an extension of the depth profiling, surface chemistry studies and composition maps of the etch crater were produced.

5.5.3.1 Survey Scans and Oxidation State Identification

Survey scan spectra have been interpreted for elemental composition, which is tabulated in Table 5.8. As the surfaces are heavily contaminated with carbon, ratios of iron, chromium and oxygen were included for cross sample comparability (nickel is excluded as the analysis found only trace quantities).

Interestingly, samples finished to P120 grit exhibited smaller Fe:Cr ratios than P1200 grit samples. The Rig 1, P1200 sample shows inconsistently high oxygen

content; however this may be a result of surface contamination and not just the metal oxide oxygen content.

Table 5.8 - Elemental composition of the sample surfaces prior to depth profiling.

	Element							
	Ni	Fe	Cr	O	C	Al	Mo	N
Rig 1, P120	Trace	5.07	1.9	26.9	57	8.4	0.0	-
Rig 1, P1200	Trace	8.9	1.8	44.5	31.3	12.1	0.0	1.3
Rig 2, P120	Trace	7.8	2.8	38.8	40.3	8.5	0.0	1.8
Rig 2, P1200	Trace	9.7	3.0	41.6	33.6	11.5	0.0	0.6

Peak fitting of iron, nickel, chromium, oxygen and carbon were performed identifying oxidation states – the sum of these peaks creates the "model" curve, which is fitted to the measured spectra along with appropriately applied background correction. This provides quantitative information regarding the quantity of each species present.

In Figure 5.48, peak fitting for iron oxides based on and Fe^{3+} and Fe^{2+} finds a ratio of 1.71:1 for Fe^{3+}/Fe^{2+}, which is close to the reported values for pure magnetite [199].

Figure 5.49 shows the peak fitting for peaks in the region of nickel metal and nickel oxides binding energies. As can be seen in the spectrum, no nickel oxides were found. While literature findings have suggested that nickel ferrite should be present in the outer oxide layer of 304L stainless steel [28,31,150], some work focussed on 316L stainless steel has found pure magnetite rather than nickel ferrite/magnetite [122].

Figure 5.50 shows the peak for Cr^{3+} which is easy to identify as a single oxidation state. This is the correct oxidation state for the presence of chromite ($FeCr_2O_4$), however XPS along cannot conclusively confirm this structure.

Finally, surface contaminants oxygen (Figure 5.60) and carbon (Figure 5.61) have been observed and species identified. The bulk of the oxygen found in the surface samples is a result of its presence in the metal oxides upon the

surface, with a small contribution from carbonyl and carboxyl organic contaminants. Carbon is present mostly as simple hydrocarbon chains, with a small quantity of oxygen bearing functional groups.

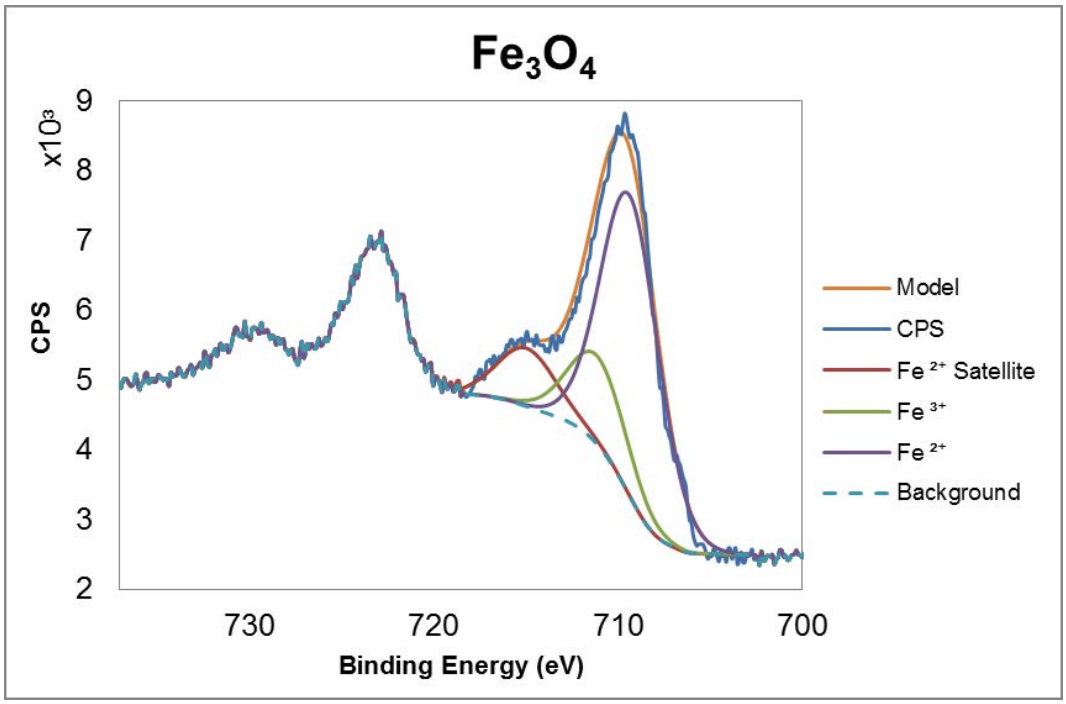

Figure 5.48 - Surface chemistry peaks in the region of nickel species binding energies. The measured ratio of Fe^{3+} / Fe^{2+} is 1.71 : 1, close to the reported magnetite value (1.84:1) [199].

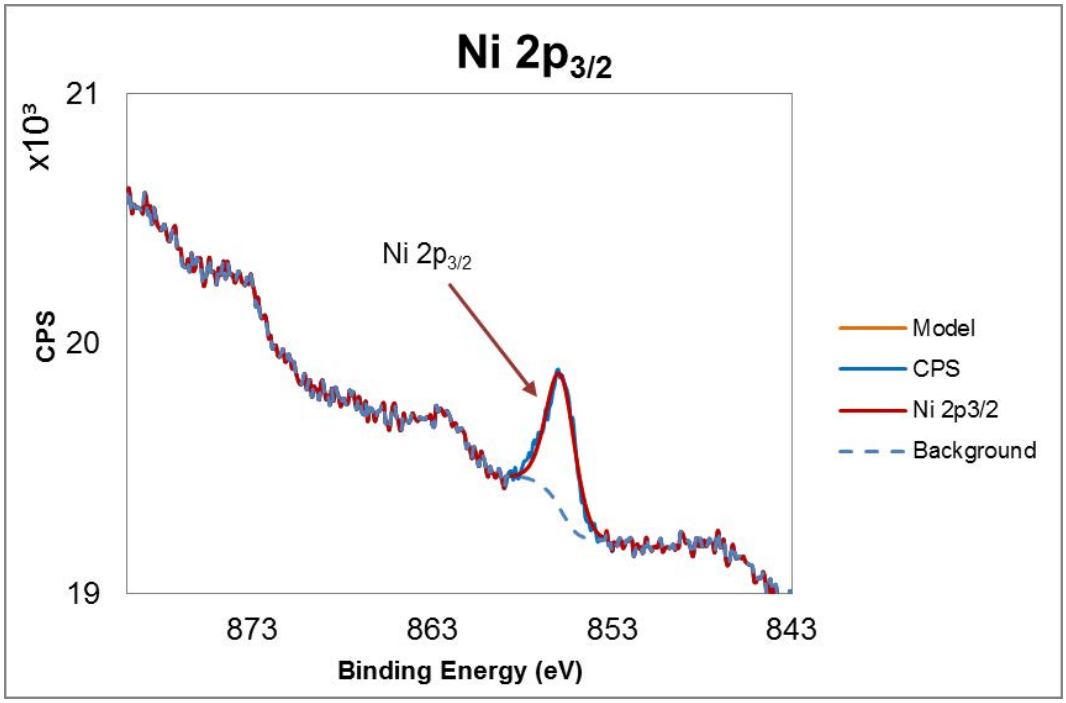

Figure 5.49 - Surface chemistry peaks in the region of nickel species binding energies. Only nickel metal was observed - no nickel oxide states were found in the surface oxides.

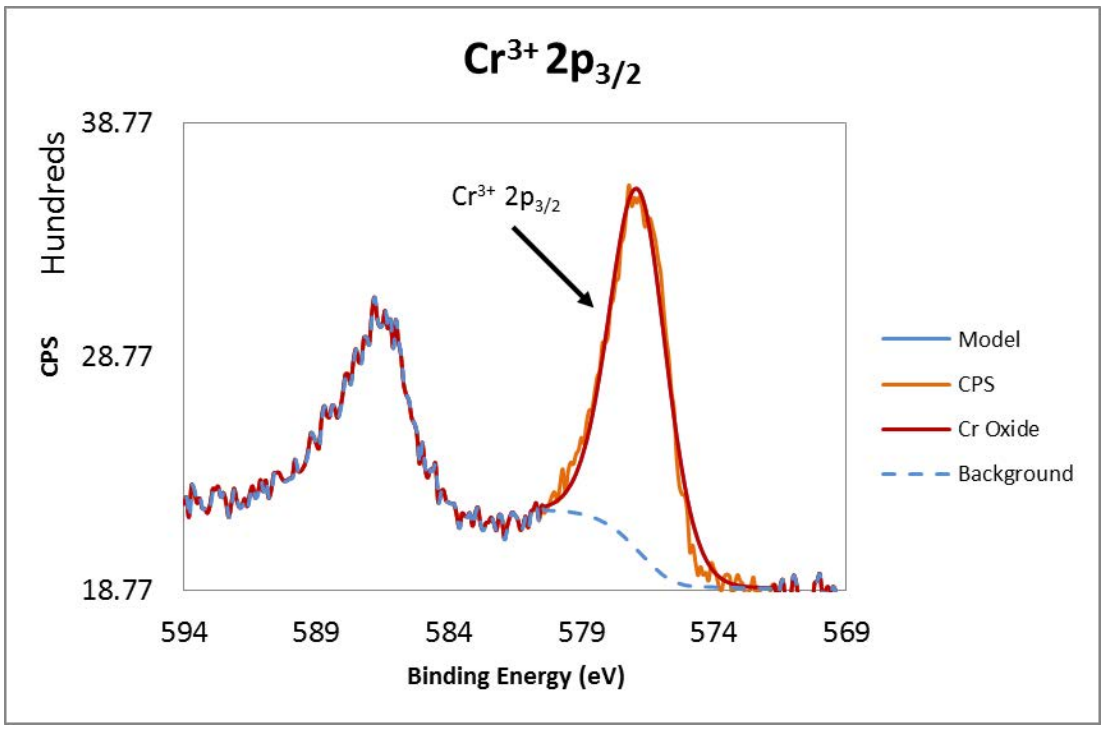

Figure 5.50 – Surface chemistry peaks in the region of chromium species binding energies. The presence of Cr^{3+} is convincingly confirmed, requiring no further species added to the model curve to fit the measured peak.

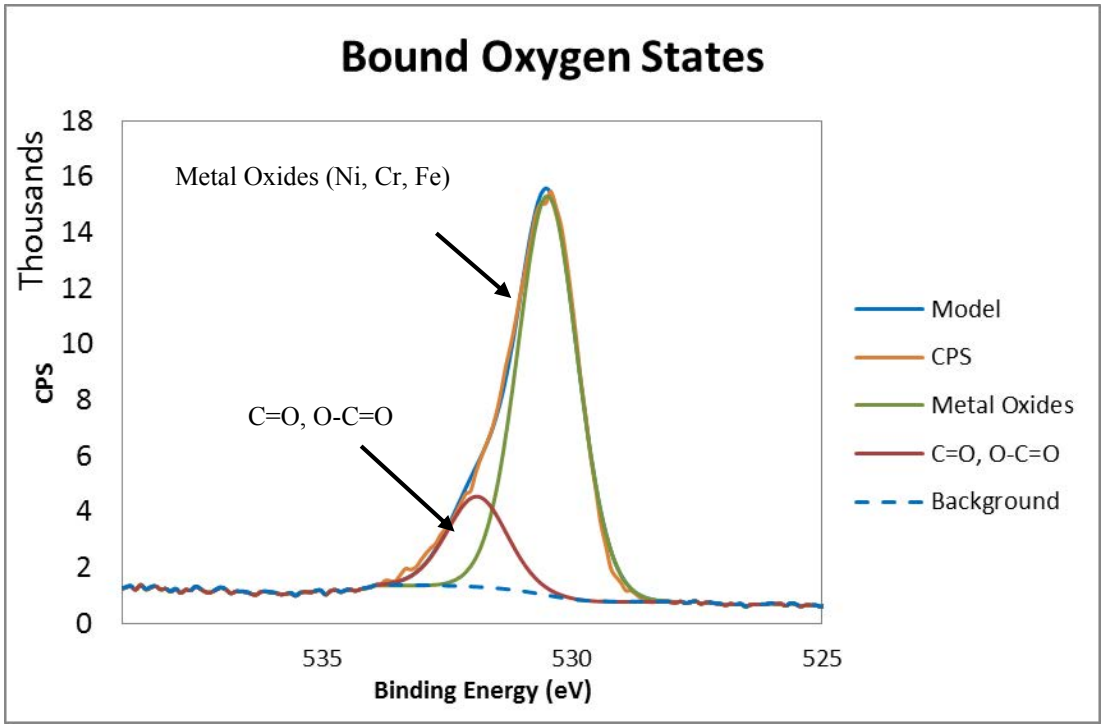

Figure 5.51 – Surface chemistry peaks in the region of oxygen species binding energies. The largest proportion of oxygen found at the surface was a result of the metal oxides, however oxygen bearing carbon molecules provide a small but significant contribution.

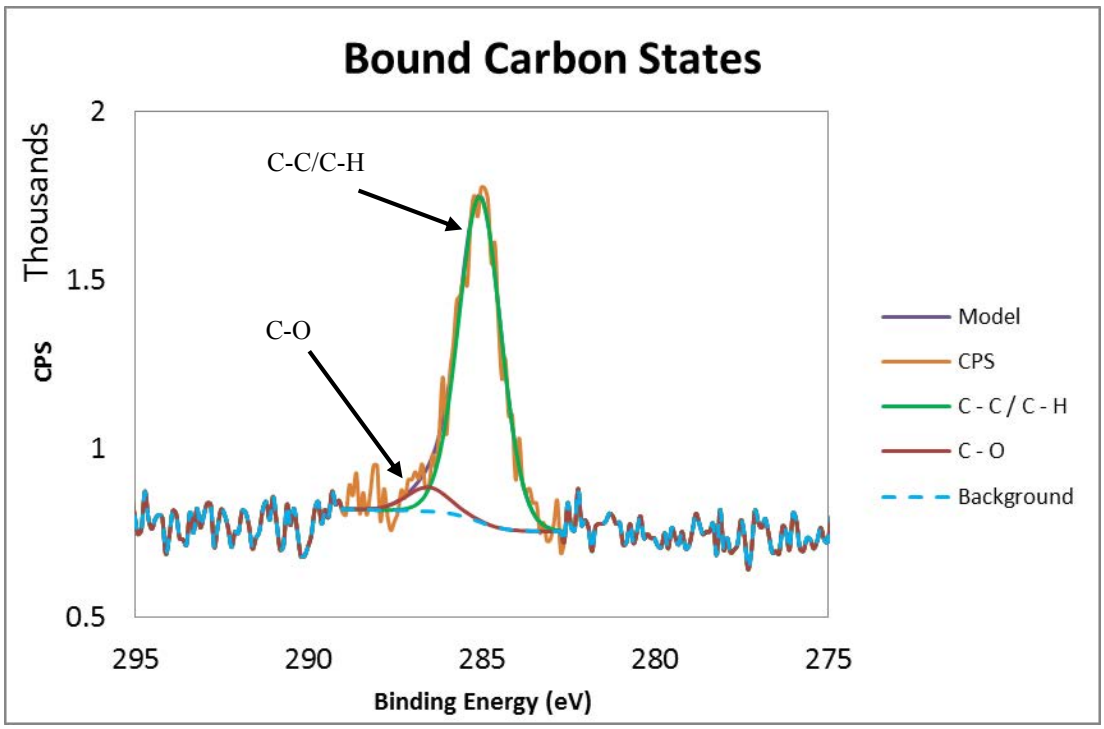

Figure 5.52 – Surface chemistry peaks in the region of carbon species binding energies. The majority of the carbon found at the surface was in the form of simple hydrocarbon chains, accompanied by oxygen bearing organic functional groups.

5.5.3.2 Composition Depth Profiling

Depth profiling of the samples was performed, however due to time constraints, limited spectrometer access time and the thickness of the oxide films, it was not possible to etch the samples to the point where the oxide film was fully penetrated. This is shown by the presence of iron and chromium oxides throughout each of the depth profiles. There appears to be little difference between each of the surface finishes – both finishes follow the same initially high oxide concentration (compared to the metallic element content at the surface), before etching begins to remove the thinner areas of each layer and expose the under lying base metal. Given enough time (on the order of a further 10 hours of etching time for each sample), the oxide would be fully etched away, leaving just the composition profile of the alloy (as seen in previous XPS depth profiles where the oxide layer was significantly thinner), however this point was not reached.

The appearance of metal oxides alongside the un-oxidised alloy is due to the uneven distribution of the oxides across the surface – this can be seen in any of the SEM images in section 5.5.2. As the etching progresses, thinner areas of the oxide will be fully removed, exposing the alloy below, while thicker areas (especially outer layer magnetite crystals) will take significantly longer to be removed, resulting in the simultaneous appearance of oxide and alloy in the depth profile. A sketch of this concept is seen in Figure 5.57.

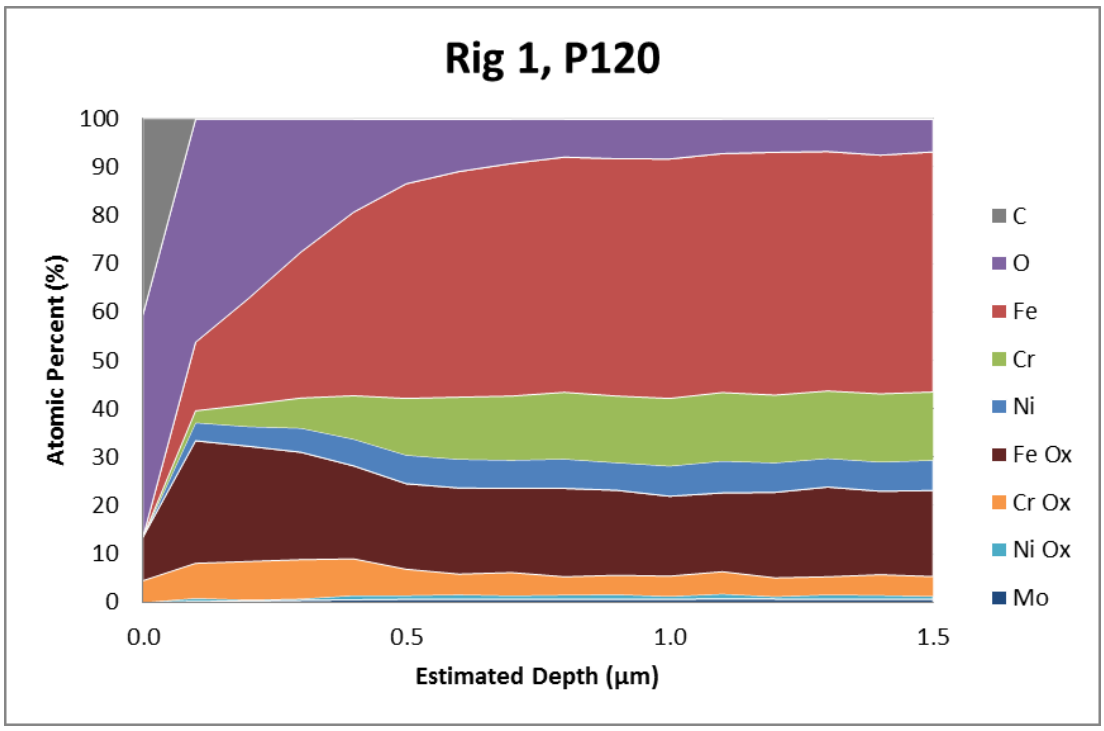

Figure 5.53 –Elemental depth profile of the P120 grit coupon extracted from rig 1 after 1,000 hours exposure.

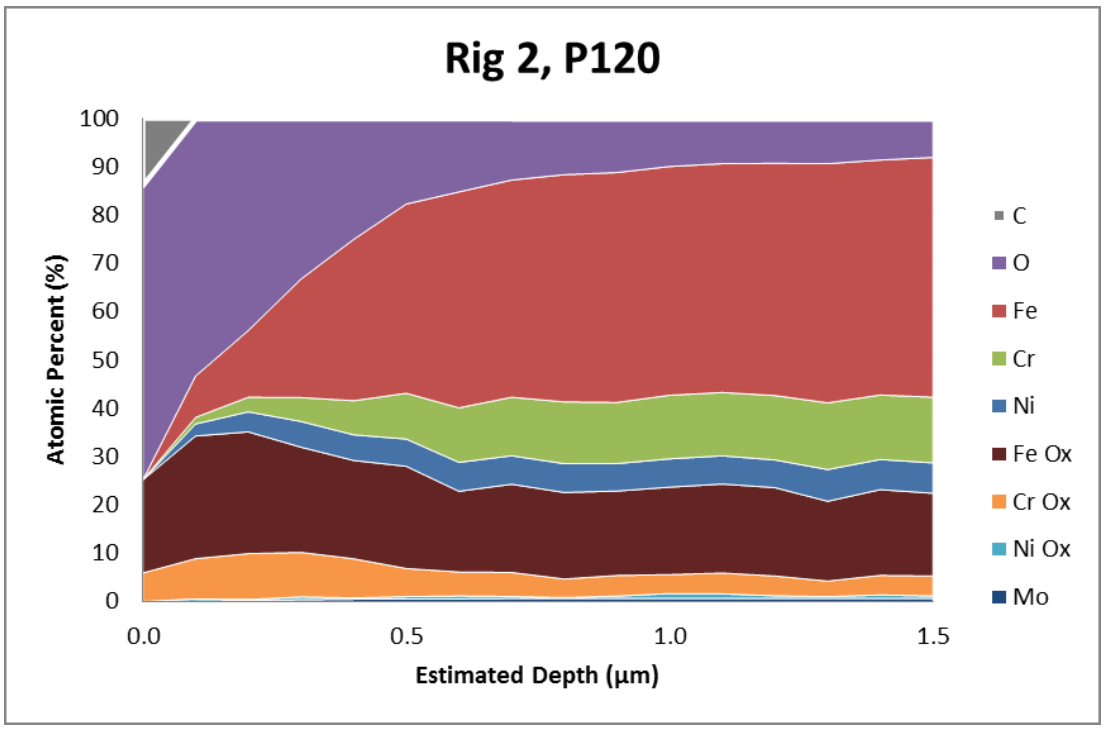

Figure 5.54 - Elemental depth profile of the P120 grit coupon extracted from rig 2 after 1,000 hours exposure.

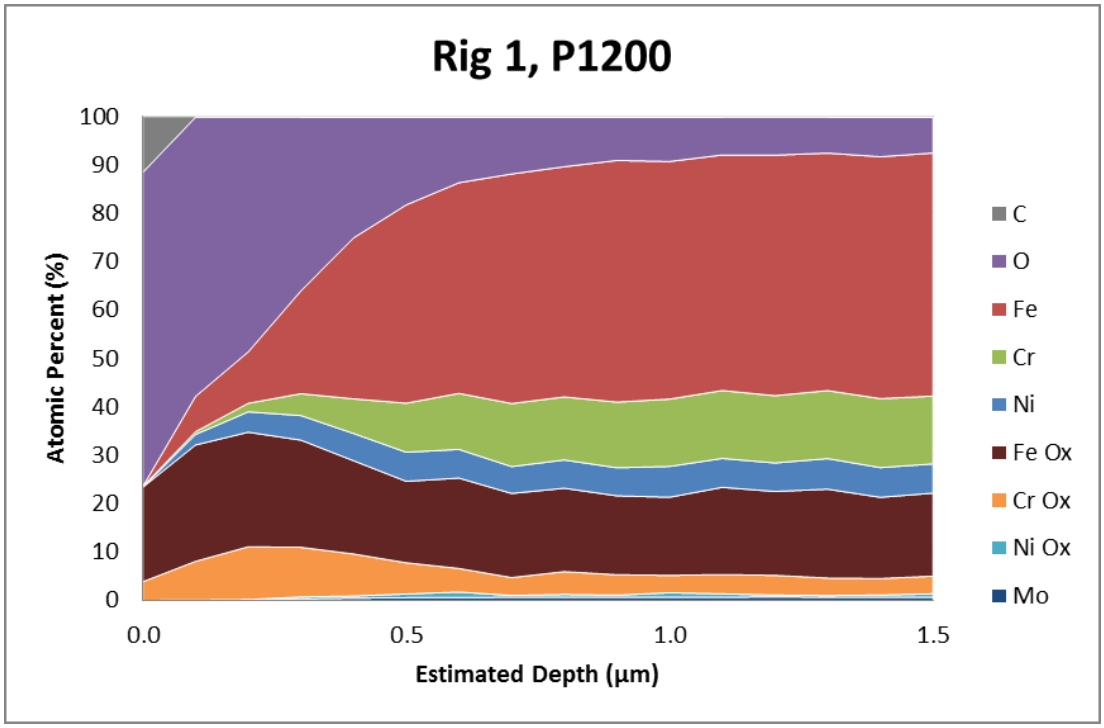

Figure 5.55 - Elemental depth profile of the P1200 grit coupon extracted from rig 1 after 1,000 hours exposure.

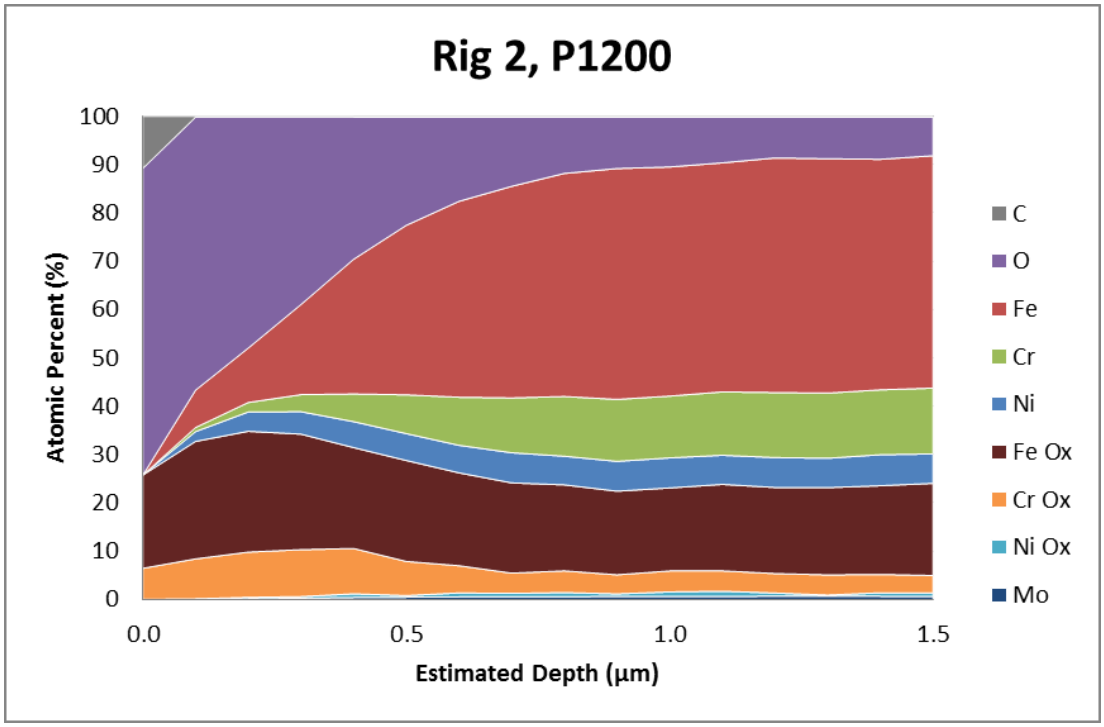

Figure 5.56 - Elemental depth profile of the P1200 grit coupon extracted from rig 2 after 1,000 hours exposure.

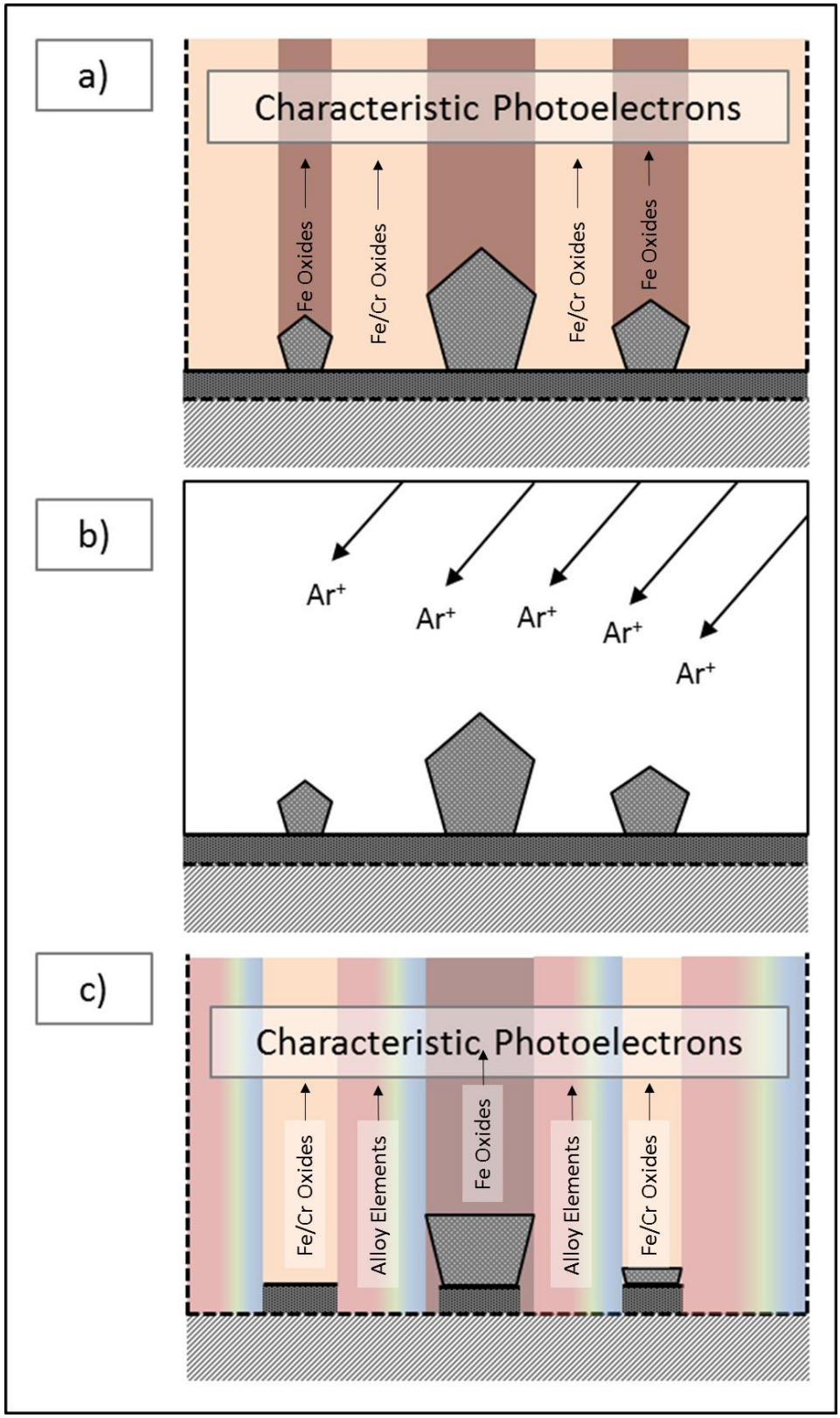

Figure 5.57 - Sketch of the sputter process and the difficulty involved in correctly identifying each layers content. When the surface is first studied, as in a), characteristics from both the inner and outer oxide layer are observed as the outer layer does not fully obscure the inner layer. Sputtering, as in b), using argon ions etches away the material at the surface, producing a surface like that shown in c). At this point, etching has not fully removed the oxides, and the resulting spectrum contains peaks for the inner and outer oxide layers, as well as those of the base metal.

5.5.3.3 **Elemental Surface Mapping**

After depth profiling of the P1200 sample from rig 2, the crater left by the argon etching was reanalysed using a surface chemistry mapping technique. The map is stitched together from one hundred 30 x 30 μm^2 squares. The images show the presence of the major alloy elements and their oxides (see Figure 5.58, Figure 5.59 and Figure 5.60), minor alloy elements (see Figure 5.63), as well as oxygen and carbon (see Figure 5.64 and Figure 5.65).

The maps here show analytically the view the spectrometer has of the etch crater after etching through approximately 1.5 μm of material. As has been shown in Figure 5.57, the surface of the sample after etching will not necessarily be devoid of oxides due to the lack of uniformity. This is shown well by Figure 5.58 and Figure 5.59, where it can be seen that the metallic iron concentration at the surface is high within the crater and low outside. However the difference in concentration of iron oxides (Figure 5.59) between the crater and the rest of the sample is not so well defined indicating that the concentration has not been significantly reduced by the etching, which is consistent with the samples depth profile (see Figure 5.56). The difference between chromium metal (Figure 5.60) and chromium oxides (Figure 5.61) is similar. No nickel oxides were discovered at the surface, and concentrations in the depth profiles are extremely low, so only a map of nickel metal is presented (Figure 5.62). Oxygen concentration (Figure 5.64) is clearly reduced in the etch crater, but is still present in sufficient quantities to support the metal oxides.

The maps of molybdenum (Figure 5.63) and carbon (Figure 5.65) surface concentrations lack contrast and however this is a product of the low concentration of the element in all regions.

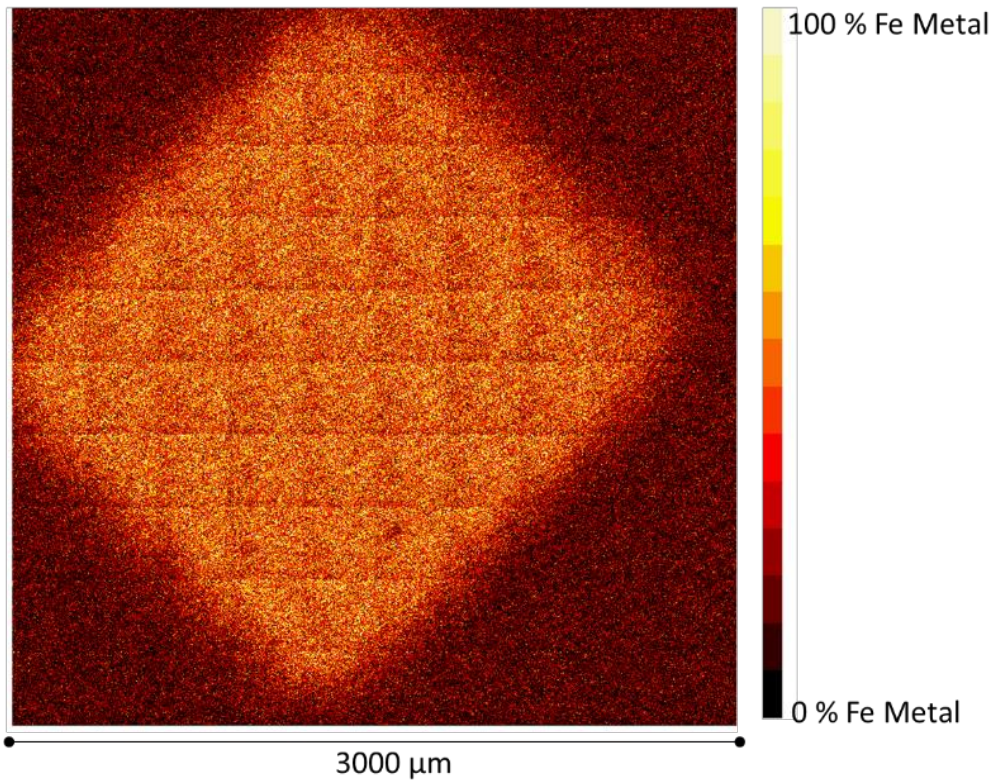

Figure 5.58 - Stitched XPS imaging of the etch crater. This image shows only the presence of metallic iron.

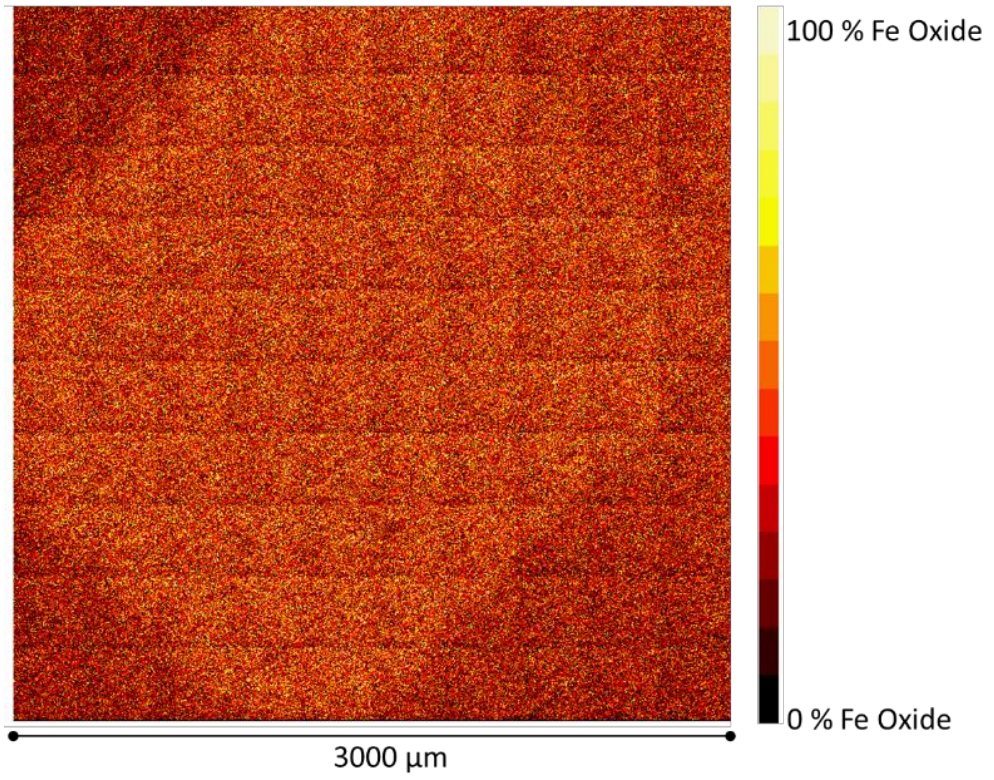

Figure 5.59 - Stitched XPS imaging of the etch crater. This image shows only the presence of iron oxides (both Fe2+ and Fe3+ are presented together.

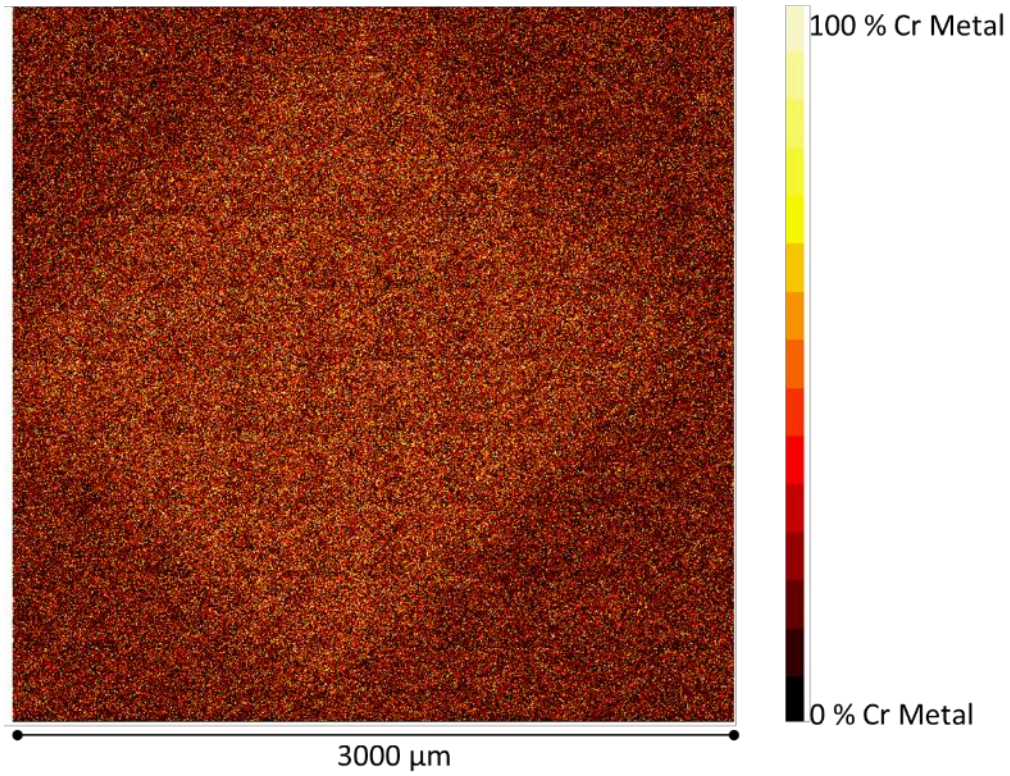

Figure 5.60 - Stitched XPS imaging of the etch crater. This image shows only the presence of metallic chromium.

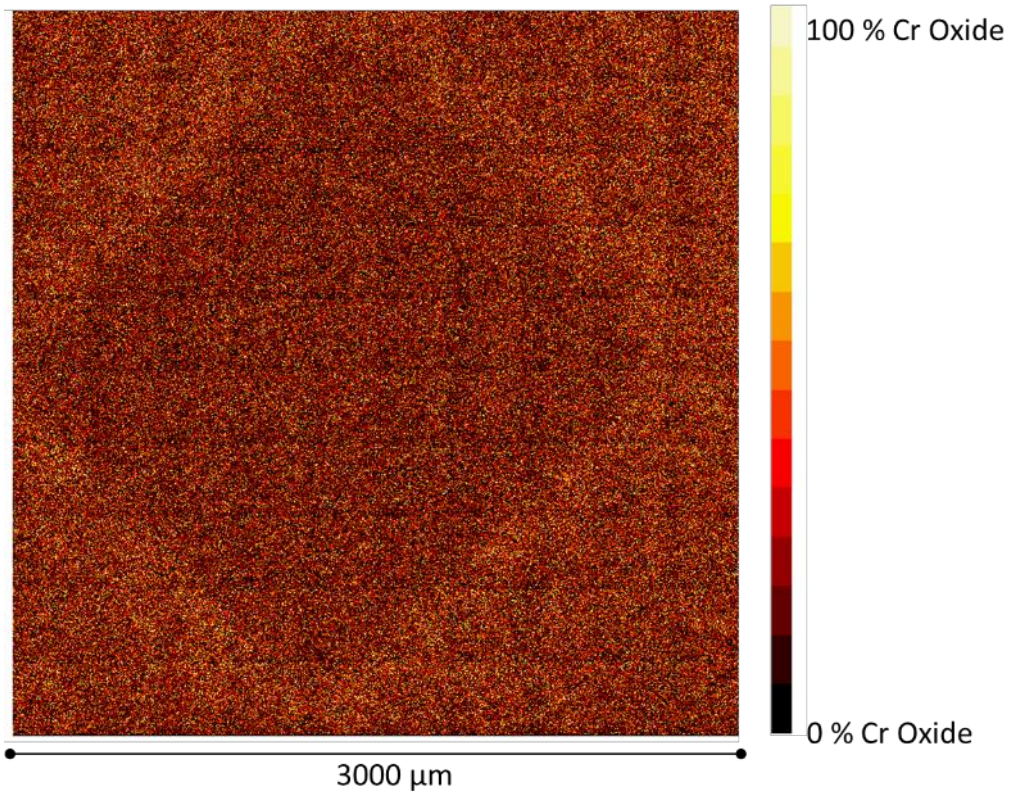

Figure 5.61 - Stitched XPS imaging of the etch crater. This image shows only the presence of chromium oxide, specifically $Cr^{3+<-}$ as this is the only oxidation state present.

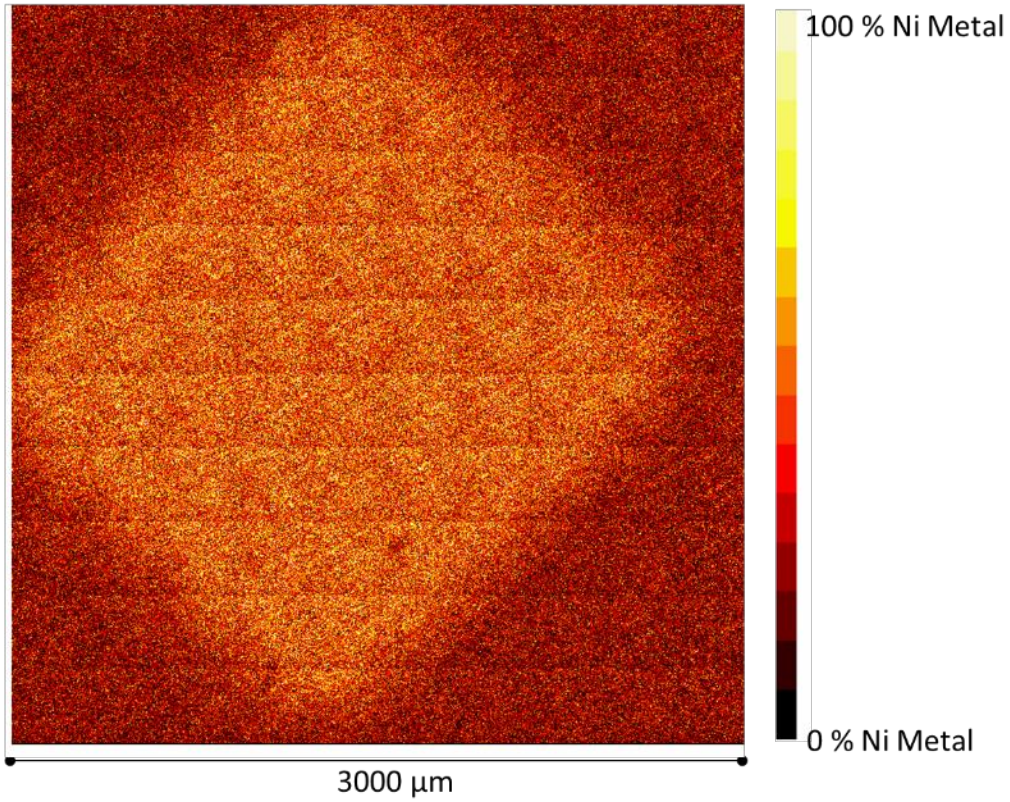

Figure 5.62 - Stitched XPS imaging of the etch crater. This image shows only the presence of metallic nickel.

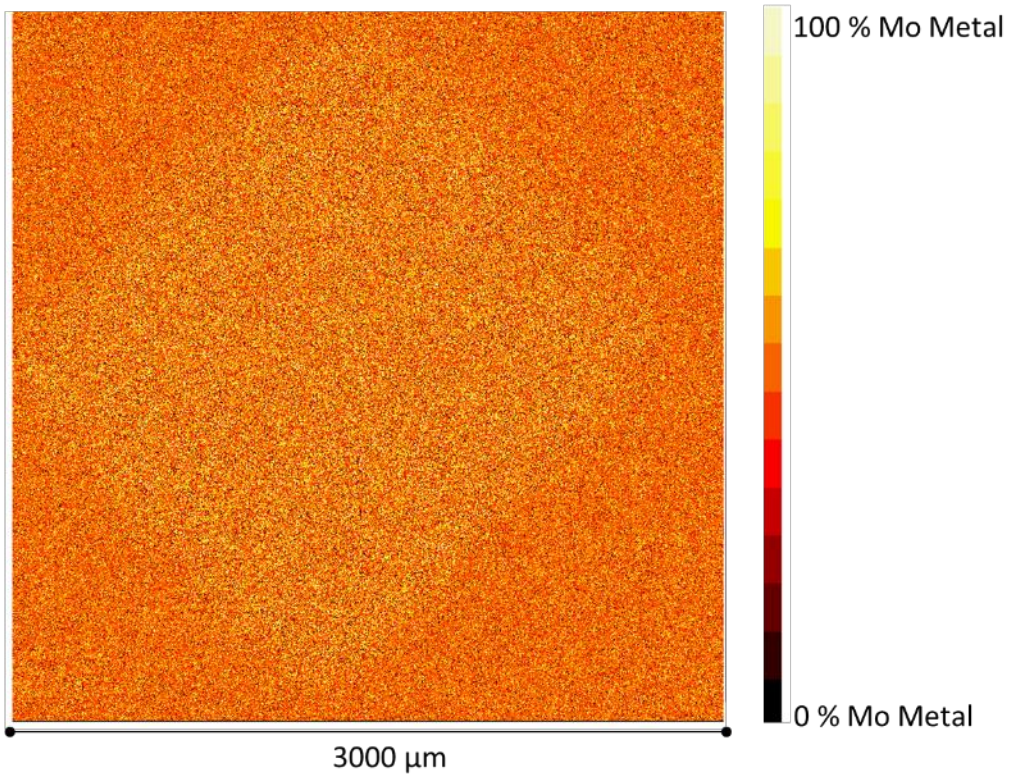

Figure 5.63 - Stitched XPS imaging of the etch crater. This image shows only the presence of metallic molybdenum.

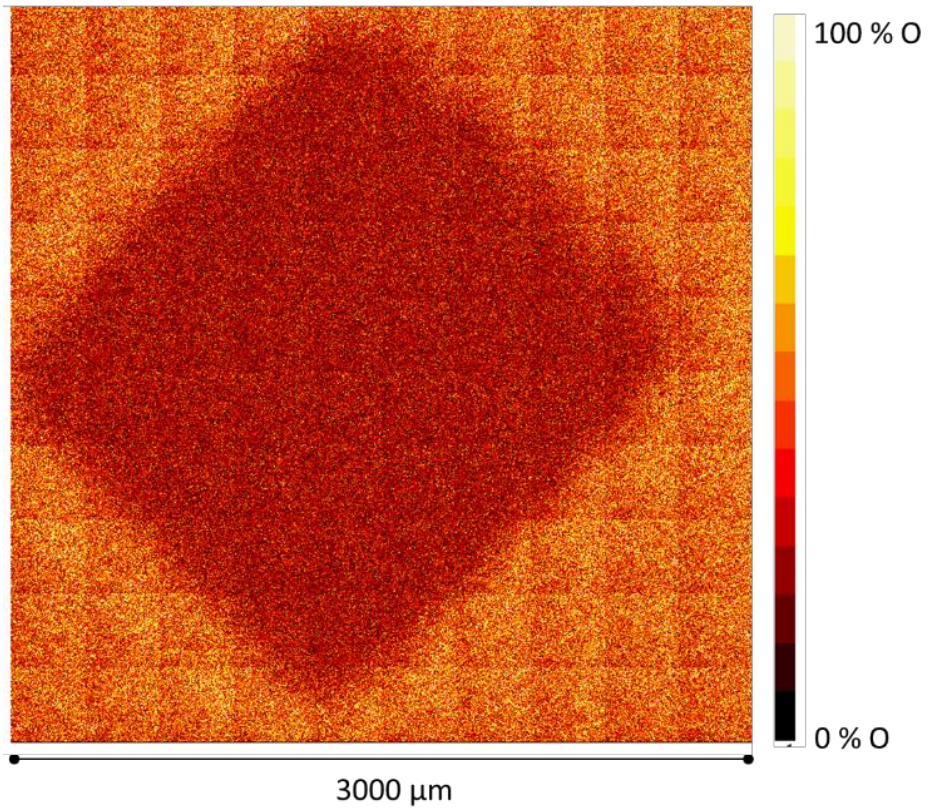

Figure 5.64 - Stitched XPS imaging of the etch crater. This image shows only the presence of oxygen, both as oxygen present in metal oxides and in organic contaminants.

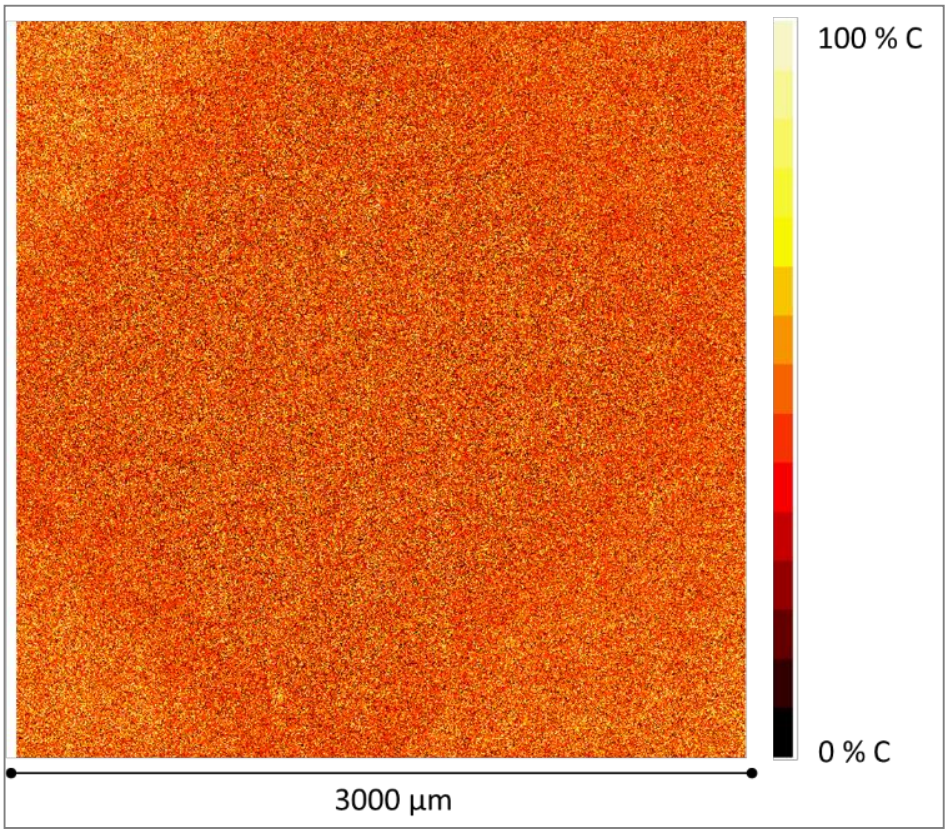

Figure 5.65 - Stitched XPS imaging of the etch crater. This image shows only the presence of carbon.

5.6 **Discussion of Section B**

The corrosion behaviour and rate of 316L stainless steel has been observed and measured by chemical descaling, SEM-EDX and XPS-AIM.

It has been shown that the gravimetric descale process is a reasonable method for determining the corrosion rates of 316L stainless steel, which appears to show both parabolic and logarithmic kinetics of corrosion. This is unusual, given that tests in the literature show the corrosion rate of 304L to follow purely parabolic type kinetics [28,31,121].

Logarithmic kinetics are generally used to describe the formation of very thin protective films, so it is not entirely unexpected that they should be observed in these circumstances. In fact, logarithmic kinetics often precede parabolic kinetics, as the formation of the protective film may, at first, be driven by ion migration responding to the strong electric field (set up by oxidisers adsorbed to the surface) which acts over very short range. With increasing film thickness the electric field becomes weaker, and the rate determining step becomes dominated by diffusion, which is described by parabolic kinetics. The change between the two regimes would not be discrete, but a gradual change from one to the other, which goes some way toward explaining why similar surfaces in similar conditions, studied by other researchers, have been observed to follow parabolic kinetics rather than logarithmic kinetics – their experiments have not observed the corrosion at regular enough intervals to observe the initial kinetics.

The fact that one set of results (those of the P120 ground sample data sets) exhibit parabolic corrosion kinetics, while the P1200 samples exhibit logarithmic kinetics, suggests that the role of the surface finish is to delay the onset of parabolic kinetics which in turn would appear as a reduction in the over corrosion rate of the material. This would mean that the oxide layer on the more highly finished surface would be a more compact and less defective layer, and rate control would reside in the adsorption of oxidising species and

the migration of ions across the oxide layer. The film will still grow, however and eventually the rate control will be governed by diffusion, no matter how compact the oxide layer is. With a carefully designed experiment, it might be possible to identify two distinct regions in the mass of alloy oxidised vs time profile, however this cannot be done with the currently available data, thus further work would be required to confirm this hypothesis; this will be discussed in section 9.1.2.

Calculation of the corrosion release rate of the material, defined as the mass of alloy transported away from the surface at which it originated, has been shown to be unreliable with the current method and rig set up. This is probably a result of the precipitation of non-indigenous metal oxides on the surface of the coupons due to super-saturation of the test fluid with corrosion products from the tubing of the rig. This could be addressed using an inert-material rig, however the concept of release rate should be treated with caution – the mass of metal oxidised that is not a part of the chromium rich protective layer is available to be released depending on the state of the test solution to which it is exposed. This is discussed further in section 9.1.2.

SEM-EDX imaging and analysis of cross-sections pieces of samples has been used to observe the oxide film directly and attempt to semi-quantitatively identify the sections of the double layer. The thickness of the inner oxide layer was found to vary between ~0.5 and 1 μm, however these estimates are based on the EDX composition line scans; this is problematic, as the interaction volume of the electron beam (~1 μm) is comparable to the thickness of the film making accurate analysis impossible by this technique.

The use of electron microscopy in this work would be greatly improved through the use of Focussed Ion Beam (FIB) micromachining of samples to be studied using TEM. While this was not pursued during this project due to time and training constraints, it will be included in suggestions for further work in

section 9.1.2. Examination of the surface oxides is critically important to the understanding of the mechanisms of initial surface corrosion.

XPS-AIM composition depth profiles and surface chemistry analysis has confirmed the presence of Fe^{2+} and Fe^{3+} in a ratio close to that of pure magnetite; the presence of Cr^{3+} was also detected, suggesting the presence of chromite. Interestingly, nickel oxides were not observed in the surface chemistry, suggesting that the outer layer was composed solely of magnetite and not nickel ferrite. This has been observed in the literature for 316L under similar conditions [122], though it is not fully understood why nickel ferrite does not form on 316L, and yet readily forms on 304 [28,31,150], though it is likely a consequence of the alloys position on potential vs pH diagram [120].

Composition depth profiles were produced using an argon ion milling gun, however the depth profiles did not fully remove the oxide layers and so could not be used for an independent calculation of corrosion rate. Due to time constraints and limited access to the spectrometer, it was not possible to continue sputtering to an extended depth; this would require an estimated additional 10 hours milling per sample. Post-depth profiling surface chemistry maps have been produced which show that the etching was insufficient to fully remove the oxide layers, as oxides are still clearly present inside the etch crater. XPS-AIM is a useful technique, and can provide data that is not available through other means, however its application should be considered carefully, as it is difficult to extract metrics such as film thickness due to the geometry of the surface.

5.7 **Conclusions for Section B**

This section of the programme has been focused on the measurement of the corrosion rate of 316L stainless steel in high temperature, mildly alkaline water. The purpose of this has been to provide fundamental corrosion constants to the

Rolls-Royce for use in modelling of primary coolant loops in PWRs, and as such this aim has been achieved. The corrosion rate of different surface finishes of stainless steel were measured across a range of temperatures and chemistries, and the behaviour of the material in these conditions has been studied using XPS-AIM, SEM and EDX, and chemical descaling.

XPS-AIM and SEM were able to show the presence of a double layer of magnetite and chromium oxides; magnetite is observed through the creation of a target factor analysis model for XPS results, and can be assumed to be large, iron rich crystals observed in SEM-EDX analysis.

Rates were most successfully determined using the gravimetric descaling of large surface area-to-volume ratio sample coupons, which were exposed to flowing solution for a period of 1,000 hours. The corrosion kinetics were found to be different depending on the surface finish applied to the coupon – rough surface finishes were found to exhibit parabolic corrosion kinetics, while more highly finished samples followed logarithmic kinetics more closely than parabolic kinetics. As logarithmic kinetics are observed to give way to parabolic kinetics with time [162], it is hypothesized that the role of the surface finish is to delay the change in kinetics through the formation of a compact and protective film.

The results generated in this work have provided the fundamental corrosion rate constants which were the goal of this section of the programme, however there is scope for further work to determine the true kinetics underlying the formation of the oxide film.

6 Section C - Metal Oxide Solubility in High Temperature Water

This section details the development of the Metal Oxide Solubility experimental program undertaken during this project. Preliminary experiments were carried out as a means to gather experience of operating high pressure high temperature equipment, and to assess the suitability of available analytical equipment while gathering the first sets of results. This work is described in section 6.1. The design, construction, and initial operation of the purpose-built metal oxide solubility rig is detailed in section 6.4. Results for the preliminary experimental programme are presented in section 6.2, and for the improved experimental programme in section 6.5.

6.1 Preliminary Experimental Work

6.1.1 Methodology

The autoclave used for the preliminary experiments is same as that described in section 5.1.1.1.

In this set up, a stainless steel cage containing magnetite powder was installed in the autoclave.

Test solution was made up by adjusting the pH of ~3 litres of high purity water using reagent grade LiOH. The solution was then degassed for a period of 1 hour using N_2 gas at a flow rate of 50 $ml.min^{-1}$. After degassing, the solution was charged to the autoclave and a blanket pressure of 10 bar nitrogen added.

The autoclave was brought to temperature and held for a period of 30 mins before a sample was extracted; samples were taken directly into a solution of 4% nitric acid. In cases where multiple samples were extracted at different temperatures, the temperature was increased by 40 °C after each sample.

Details of the experimental set up can be found in Appendix C, section C.1.

6.1.2 Analysis

6.1.2.1 GFAAS

All analysis for these experiments was performed using a Perkin-Elmer 3300 HGA 600 Graphite Furnace Atomic Absorption Spectroscopy, available through the University of Birmingham.

6.2 Results of Preliminary Experimental Work

6.2.1 GFAAS

All samples taken from the autoclave during the preliminary experiments were analysed by Graphite Furnace Atomic Absorption spectroscopy, and the results plotted in Figure 6.1.

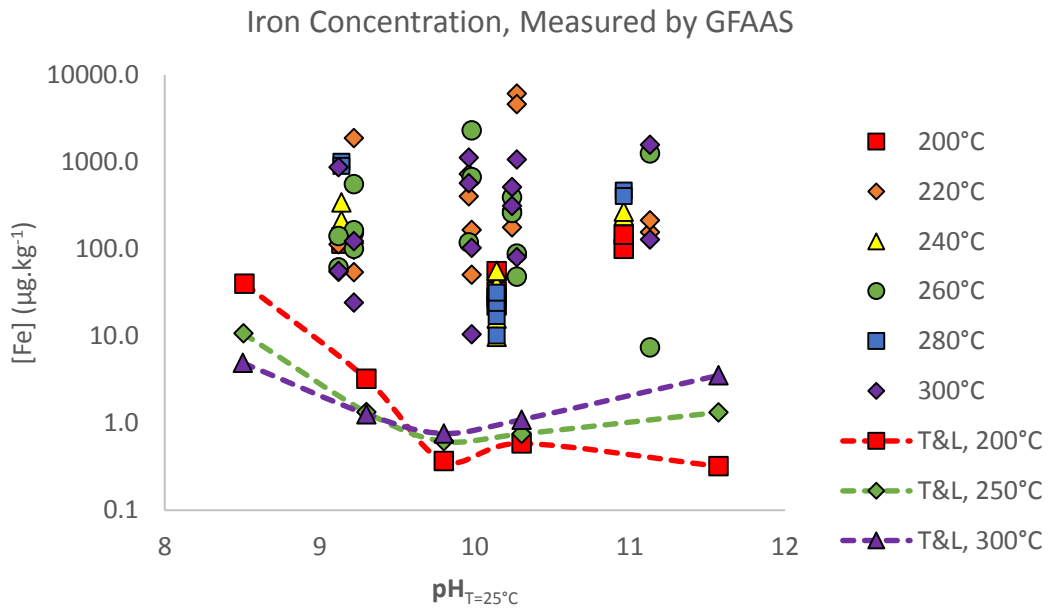

Figure 6.1 - Concentration of iron measured in samples taken from batch autoclave tests. Averaged data from Tremaine and LeBlanc [53] is shown as a base line for the solubility of pure crystalline magnetite.

6.3 Discussion of Preliminary Results

The data is extremely scattered and spreads across three orders of magnitude from highest to lowest measured point, lacking any type of clear trend. This as much as four orders of magnitude higher than literature data. It is likely that the quantity of iron in the samples was extremely high due to the presence of fine particulate matter or due to contamination once sampled. Contamination after sampling could be from unrefined handling protocols or through the use of standard reagent grade nitric acid which can contain 0.2 $mg.kg^{-1}$ of iron [200].

6.3.1 Preliminary Experimental Method Limitations

A number of issues were rapidly identified with the use of a stainless steel batch autoclave and instead a purpose built rig system was designed. Some of these issues were similar to those encountered in the corrosion work, described in section 5.3.1, including:

i. Small number of samples possible from any single run, due to limited volume of autoclave.
ii. Samples were vulnerable to contamination during the sampling procedure as it was not possible to adequately cover the collection vessel during the pressurised discharge.
iii. The chemistry of the solution changed during test, and with no analysis equipment to monitor the change, it was not possible to know for certain the condition of the liquid without extracting some.
iv. No control of dissolved hydrogen content.
v. The Graphite Furnace Atomic Absorption Spectrometer (GFAAS) was found to produce unreliable results, often giving significantly different readings for the same samples upon repeated analysis.

It was decided that a plug flow type system, seen regularly in the literature [42,48,53,57], would be a more reliable method of performing these tests. The use of the GFAAS was suspended and the use of the University's ICP-MS was started instead. The ICP-MS was found to give reliable and consistent results, and results from this spectrometer compared favourably to those produced by ICP-MS measurement by Intertek UK.

6.4 Bespoke Metal Oxide Solubility Rig

The design of the metal oxide solubility system is physically very simple, however, it must be understood that every stage of the system must be carefully considered to be aware of what a particular part of the rig will do when it is in contact with experimental solution.

6.4.1 Criteria and Experimental Requirements

6.4.1.1 Chemistry

The pH of the system was adjusted using reagent grade LiOH, purchased from Sigma Aldrich. Concentrations of 0.25, 2.5 and 25 ppm were chosen as these values equate closely to pH 9, 10 and 11 respectively.

In order to reduce interference from unexpected ions in the system, all wetted surfaces were made from 316L stainless steel, grade 2 titanium, an engineering plastic such as PTFE, or an inert metal oxide such as alumina.

6.4.1.2 Temperature

In order to simulate conditions within a nuclear reactor, the system needs to be able to reach temperatures of 300 °C and maintain that temperature with good stability for a long period of time.

The temperature of the air within the chamber also needs to be homogenous in order to avoid the appearance of hot spots, changing the expected conditions

of the experiment, therefore the oven should have a mechanical convection function.

6.4.1.3 Metal Oxide Specimens

Specimens of metal oxide could be placed in the cell and retained by Bekipor filters. For initial studies presented in this thesis, the materials of construction (316L stainless steel) was used to provide the metal oxide source. No additional metal oxide powders or granules were purchased of manufactured for this work.

6.4.1.4 Time

The length of time for which the experiment would be performed was not decided upon before the experiment was begun, instead the experiment was to be run for long enough to reach an equilibrium solubility level, which would be visible in the results gather by ICP-MS analysis of samples taken.

Tremaine & LeBlanc [53] described an issue encountered during their experiments where the magnetite bed being used as the solubility source was found to produce very high levels of iron which decayed over time to reach a consistent level which they took to be the equilibrium. In their experiments, iron samples were taken using ion exchange columns to capture all iron ions passing through them over a period of hours to days.

With the use of ICP-MS, the samples taken from a flowing rig would have a time resolution significantly greater than that of Tremaine & Leblanc's work – samples would be taken from the flowing system outlet and their time resolution would depend only on the period of time taken to gather the sample.

6.4.2 Design of Bespoke Metal Oxide Rig

An experimental rig was designed and built to address the stipulations of section 6.4.1. The rig consists of a tube into which samples of interest can be

installed and high pressure, high temperature water can be pumped through. A schematic of the rig can be seen in Figure 6.2.

Details of the design and contruction of the rig and its ancilliary components can be found in Appendix C, section C.2.

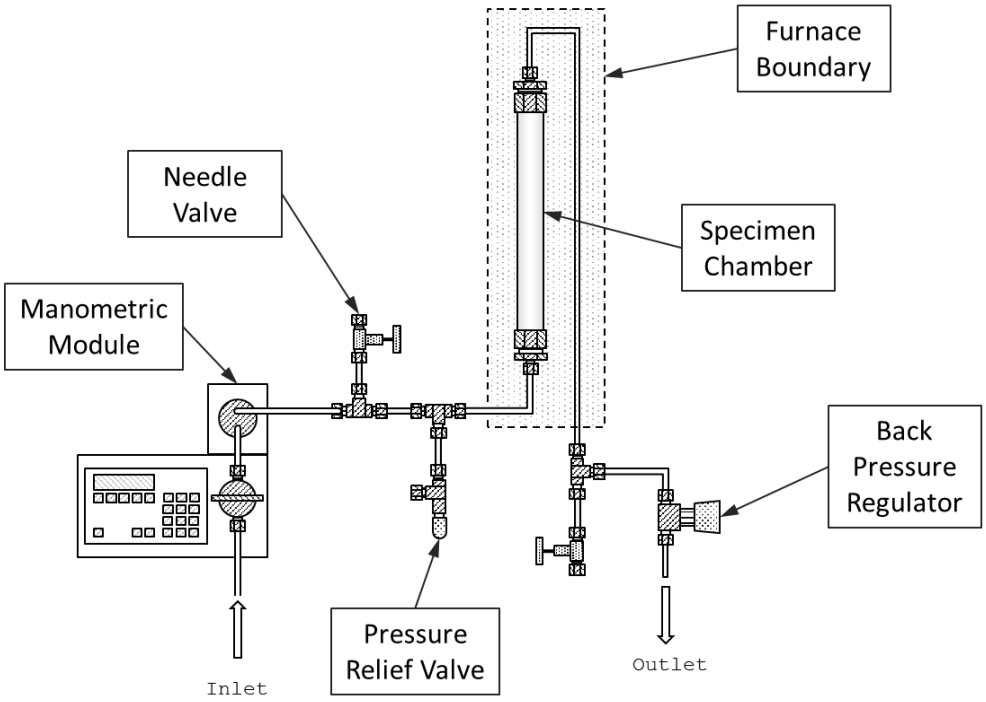

Figure 6.2 - The final implemented version of the Metal Oxide Solubility Rig.

6.4.3 Metal Oxide Solubility Experimental Methodology

6.4.3.1 Methodology

Feed water was preparated by adjusting the pH of ~50 litres of ultrahigh purity water using reagent grade LiOH. The feed water was sparged for a period for ~100 hours (2 hours per kilo).

The specimen cell was filled with a sample of interest before being reinstalled into the rig and pressure tested at 100 bar for a period of 24 hours.

When the test was begun, the rig was filled with water using the pump and pressurised to overcome the outlet BPR. Once a constant flow rate was established, the oven was brought up to the target temperature.

Samples of solution were taken directly from the outlet into clean plastic samping tubes before being stored in a fridge. Each sample were 4.00 ± 0.05 g and the mass of each sample was recorded.

Acidificaiton of the samples was done in batches to reduce error between each sample – any introduced error would be systematic across a whole batch rather than from sample to sample.

Further detail on the operation and sampling can be found in Appendix C, section C.2.3.

6.4.3.2 Analysis Methods

6.4.3.2.1 ICP-MS

All samples were analysed using an Agilent 7500ce Inductively Coupled Mass Spectrometer, operated by Dr. Steve Baker at the University of Birmingham. Samples were analysed for iron, nickel, chromium, molybdenum, and manganese, which constitute the main alloying components of 316L stainless steel. Results are presented in the next section.

6.5 Results of Metal Oxide Solubility Rig Work

Several experiments were run using the Metal Oxide Solubility rig in order to try to characterise the behaviour of the rig.

A difficulty discovered during these tests, which was not fully resolved until after test 7, was the irregular stalling of the pump. This was finally resolved by setting piston draw time to 1000 ms, and fitting a 1/8 in. stainless steel inlet tube, which ran from the feedwater tank to the pump inlet. The cause of this stalling appears to have been the accumulation of nitrogen bubbles in the inlet line; in smaller ID tubing, the bubbles were more easily entrained in the flow, rather than being allowed to accumulate and block flow.

A list of experiments and conditions carried out using the metal oxide solubility rig is shown in Table 6.1. Each new experiment followed on from the previous experiment, so cumulative time is shown as this is the total exposure time experienced by the test chamber that acted as the metal oxide source.

Table 6.1 - Experimental matrix for the Metal Oxide Solubility rig.

Test No.	[LiOH] (ppm)	T (°C)	Flow Rate (ml.min-1)	Time at Temperature (hrs)	Cumulative Time at Temperature (hrs)
1	25.00	300	2	29.25	29.3
2	25.00	300	0.5	90.63	119.9
3	0.25	300	2	221.1	341.0
4	0.25	300	0.5	64.15	405.1
5	0.25	300	0.1	40.75	445.9
6	0.25	250	1	18.88	464.8
7	0.25	200	1	46.28	511.0

6.5.1 Solubility of Major Alloying Elements

The first series of experiments performed using the Metal Oxide Solubility rig are presented here. In each plot, the average of each experiment is signified by a black filled marker, with error bars equal to the standard deviation of the data set. As two separate LiOH concentrations were used, each concentration has been presented on a separate plot. Average measured concentration of each condition is tabulated in Table 6.2 Table 6.3 and Table 6.4, and shown compared to literature data (where available) in section 6.6.1.

The solubility of iron data is tabulated in Table 6.2; results from pH 11 tests are plotted in Figure 6.3 and data from tests at pH 9 are plotted in Figure 6.4. Solubility data for nickel is tabulated in Table 6.3; pH 11 data are plotted in Figure 6.5 and pH 9 test data are plotted in Figure 6.6. Finally, chromium solubility data is tabulated in Table 6.4; pH 11 data is plotted in Figure 6.7 and pH 9 data is plotted in Figure 6.8. The data plotted in the graphs is the raw data from ICP-MS adjusted for isotopic abundance, as discussed below, and

corrected for concentration, as a small quantity of acid is added prior to the analysis changing the actual concentration. Averages of the concentration have been taken and are plotted at the average time for each data set, with error bars that show the standard deviation of the data set.

It should be noted that each element, measured by ICP-MS, is based on a single calibrated stable isotope. The actual concentration is then automatically calculated based on the abundance of that element. For example, nickel concentration is based on the concentration of Ni-60, a stable isotope which has an abundance of 26.223% [201]. In this specific case, Ni-60 was used instead of Ni-58 to avoid interference between the Ni-58 and the low abundance Fe-58 isotope; while the error from the Fe-58 interference would be small, the error from interference of Fe-60 is much smaller.

It should also be noted that in some of the plots, there is data which shows a negative solubility level, for example in Figure 6.5. Negative solubility's are the result of a disparity between blank samples of test solution, which show the background ion levels in the feed water, and the water used by the ICP-MS to perform calibrations. Negative values occur when the soluble ion concentration in the blanks is lower than in the background level in the calibration standard.

Table 6.2 - Average solubility of iron for tests 1 - 7.

Test No.	[LiOH] (ppm)	pHT	T (°C)	Flow Rate ($ml.min^{-1}$)		Average [Fe] ($\mu g.kg^{-1}$)	Standard Deviation
1	25.00	11.00	300	2		1.26	0.88
2	25.00	11.00	300	0.5		0.48	0.32
3	0.25	9.00	300	2		4.95	2.10
4	0.25	9.00	300	0.5		4.87	1.99
5	0.25	9.00	300	0.1		1.84	0.30
6	0.25	9.00	250	1		2.87	2.82
7	0.25	9.00	200	1		1.22	0.56

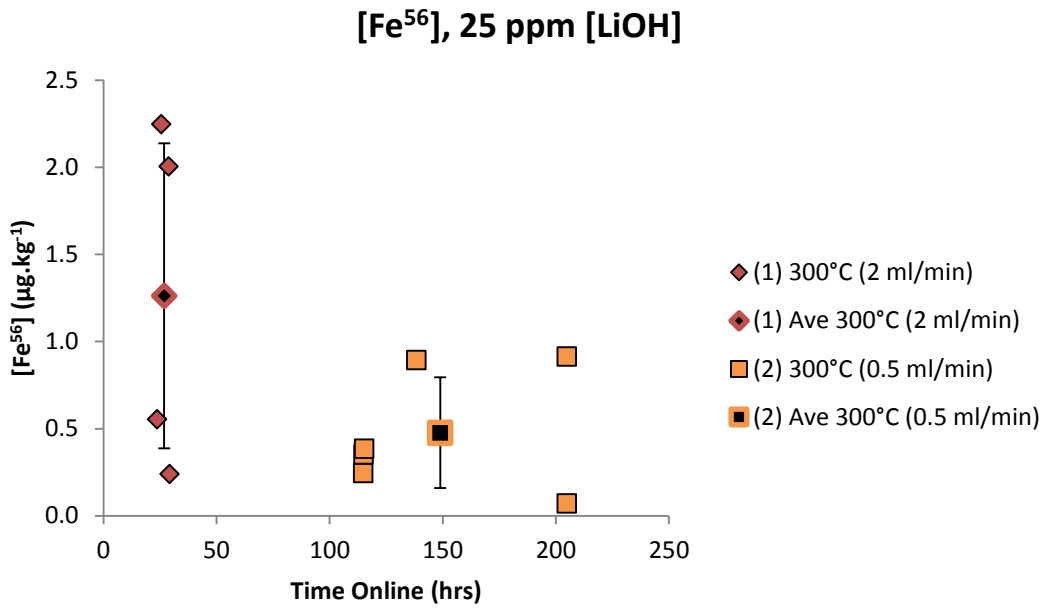

Figure 6.3 – The measured iron concentration, based on Fe-56, in rig outlet water at LiOH concentration of 25 ppm ($pH_{T=25\,°C}$ 11). The average concentration at each flow rate is represented by a black filled marker of the same shape and border colour as the raw data series. The error bars plotted on this point are the standard deviation of the data set.

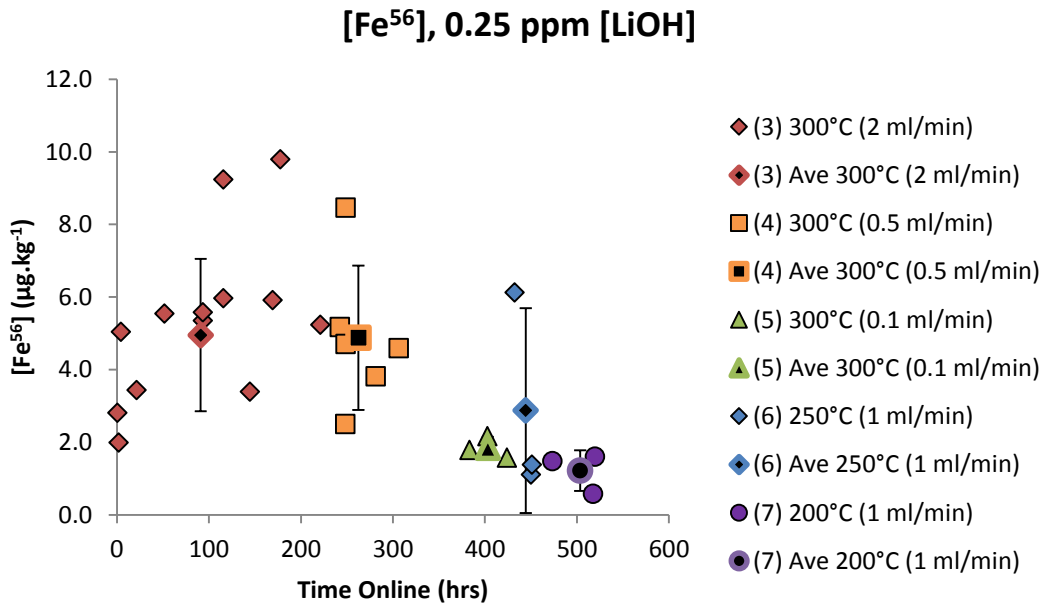

Figure 6.4 – The measured iron concentration, based on Fe-56, in rig outlet water at LiOH concentration of 0.25 ppm ($pH_{T=25\,°C}$ 9). The average concentration at each flow rate is represented by a black filled marker of the same shape and border colour as the raw data series. The error bars plotted on this point are the standard deviation of the data set.

Table 6.3 – Tabulated average solubility values of nickel for tests 1 - 7.

Test No.	[LiOH] (ppm)	pH_T	T (°C)	Flow Rate ($ml.min^{-1}$)		Average [Ni] ($\mu g.kg^{-1}$)	Standard Deviation
1	25.00	11.00	300	2		1.80	1.80
2	25.00	11.00	300	0.5		0.59	1.44
3	0.25	9.00	300	2		2.46	1.30
4	0.25	9.00	300	0.5		6.23	1.59
5	0.25	9.00	300	0.1		1.82	0.35
6	0.25	9.00	250	1		0.44	0.15
7	0.25	9.00	200	1		0.65	0.05

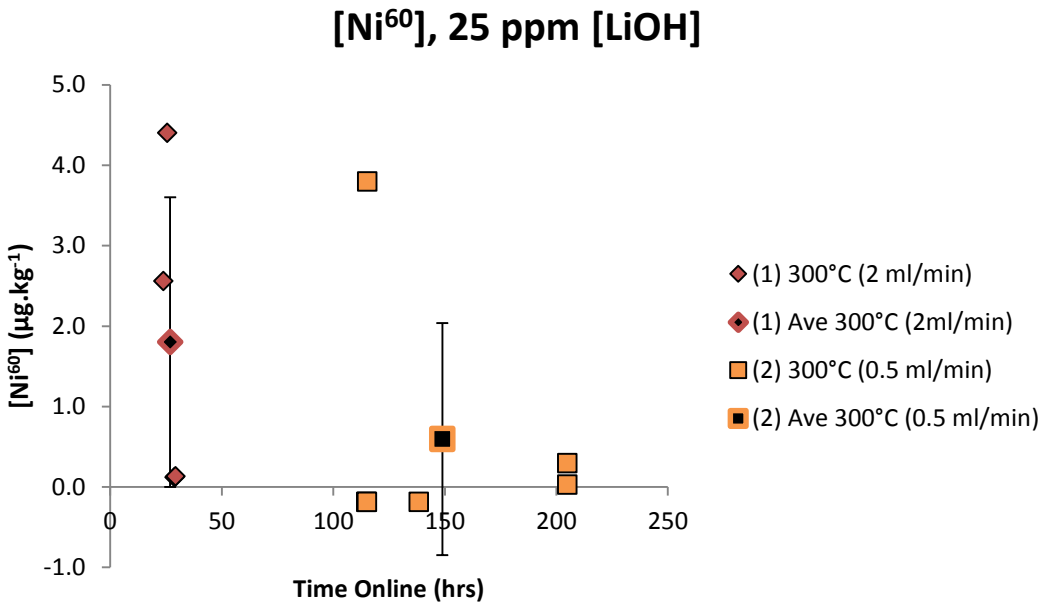

Figure 6.5 - The measured nickel concentration, based on Ni-60, in rig outlet water at LiOH concentration of 25.0 ppm ($pH_{T=25\,°C}$ 11). The average concentration at each flow rate is represented by a black filled marker of the same shape and border colour as the raw data series. The error bars plotted on this point are the standard deviation of the data set.

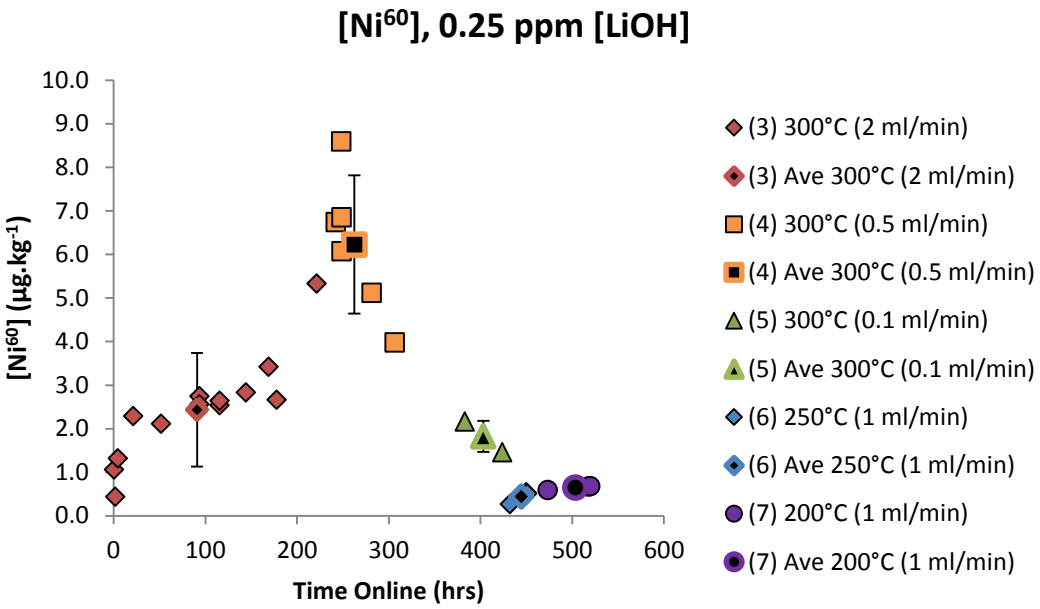

Figure 6.6 - The measured nickel concentration, based on Ni-60, in rig outlet water at LiOH concentration of 0.25 ppm ($pH_{T=25\,°C}$ 9). The average concentration at each flow rate is represented by a black filled marker of the same shape and border colour as the raw data series. The error bars plotted on this point are the standard deviation of the data set.

Table 6.4 – Tabulated average solubility values of chromium for tests 1 - 7.

Test No.	[LiOH] (ppm)	pH_T	T (°C)	Flow Rate ($ml.min^{-1}$)		Average [Fe] ($\mu g.kg^{-1}$)	Standard Deviation
1	25.00	11.00	300	2		0.88	0.34
2	25.00	11.00	300	0.5		2.04	1.97
3	0.25	9.00	300	2		0.28	0.36
4	0.25	9.00	300	0.5		0.37	0.67
5	0.25	9.00	300	0.1		0.13	0.03
6	0.25	9.00	250	1		0.00	0.00
7	0.25	9.00	200	1		0.00	0.01

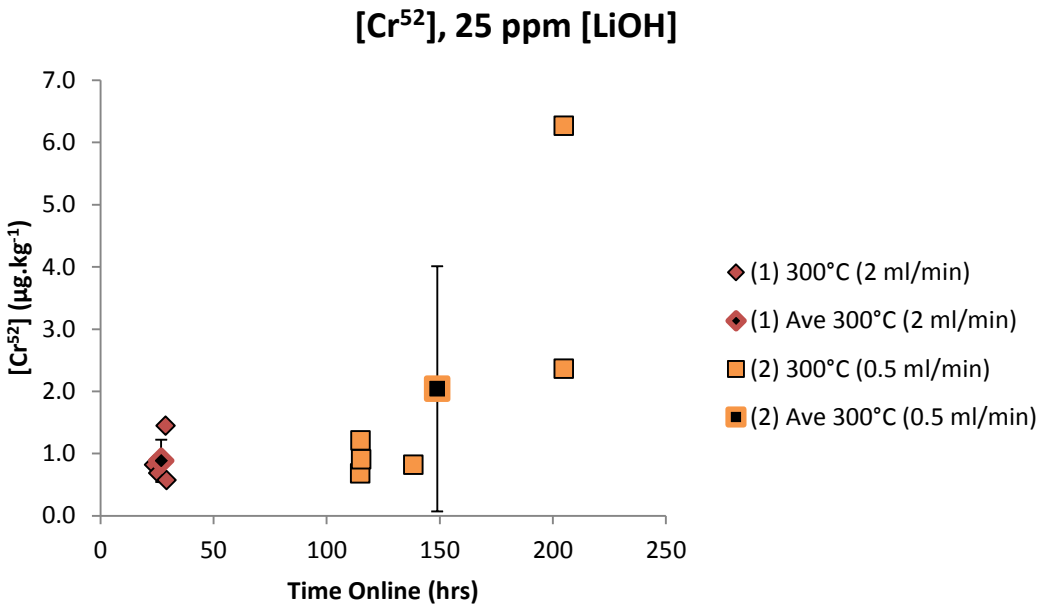

Figure 6.7 – The measured chromium concentration, based on Cr-52, in rig outlet water at LiOH concentration of 25.0 ppm ($pH_{T=25\,°C}$ 11). The average concentration at each flow rate is represented by a black filled marker of the same shape and border colour as the raw data series. The error bars plotted on this point are the standard deviation of the data set.

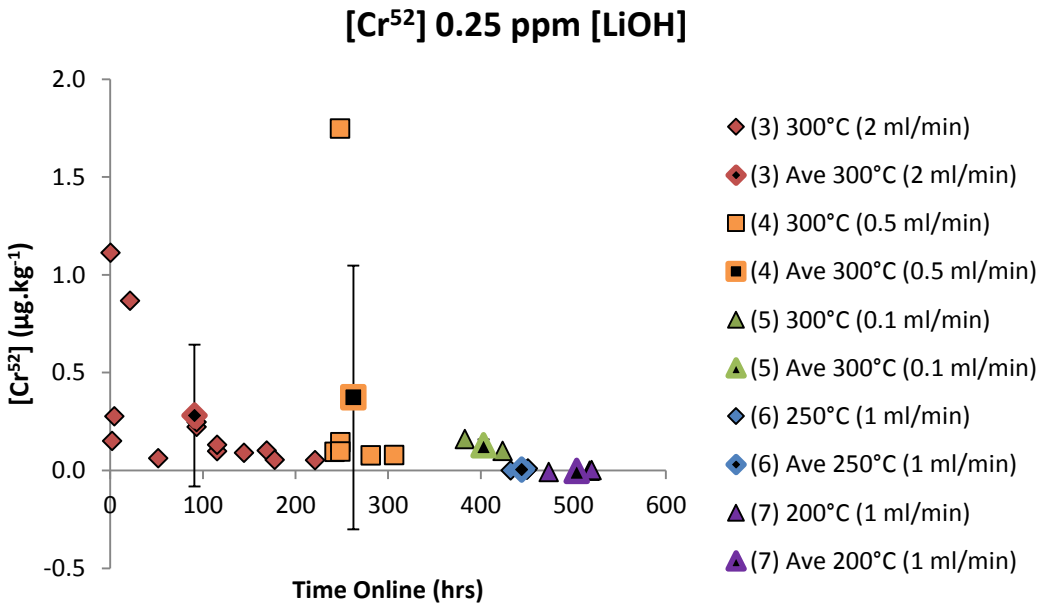

Figure 6.8 - The measured chromium concentration, based on Cr-52, in rig outlet water at LiOH concentration of 0.25 ppm ($pH_{T=25\,°C}$ 9). The average concentration at each flow rate is represented by a black filled marker of the same shape and border colour as the raw data series. The error bars plotted on this point are the standard deviation of the data set.

6.5.2 Solubility of Minor Alloying Elements

As an extension to the study of the solubility of iron, nickel and chromium from 316L stainless steel, the sub-saturation solubility of minor alloying elements, molybdenum and manganese, were also measured by ICP-MS and are presented here. These numbers do not represent a true solubility in the strictest sense; there is no solid oxide phase present, and thus no equilibrium solubility between solid and aqueous phase. Instead, the data here is a sub-saturation solubility for molybdenum and manganese, the equilibrium solubility of which may be significantly higher than shown.

Table 6.5 and Table 6.6 respectively show the tabulated data of molybdenum and manganese concentration in outlet water. The measured concentrations as a function of time are shown for molybdenum in Figure 6.9 and Figure 6.10, and for manganese in Figure 6.11 and Figure 6.12.

As has been discussed in section 6.5.1 for the major alloying elements, the average value for solubility of each data set is calculated and presented as a single data point at the average time of that experimental data set. The error bars represent the standard deviation of the data set.

Table 6.5 – Tabulated average solubility values of molybdenum for tests 1 - 7.

Test No.	[LiOH] (ppm)	pH_T	T (°C)	Flow Rate ($ml.min^{-1}$)		Average [Mo] ($\mu g.kg^{-1}$)	Standard Deviation
1	25.00	11.00	300	2		395.38	71.87
2	25.00	11.00	300	0.5		74.87	22.61
3	0.25	9.00	300	2		19.44	7.45
4	0.25	9.00	300	0.5		42.35	13.78
5	0.25	9.00	300	0.1		83.32	8.10
6	0.25	9.00	250	1		40.16	6.76
7	0.25	9.00	200	1		9.78	2.11

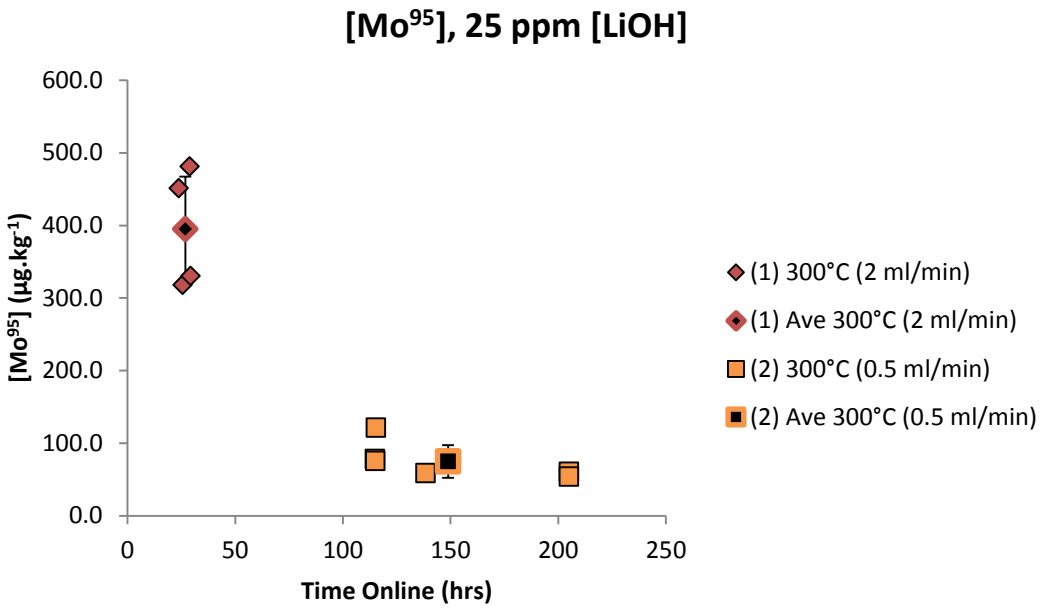

Figure 6.9 – The measured molybdenum concentration, based on Mo-95, in rig outlet water, at a LiOH concentration of 25.0 ppm ($pH_{T=25\,^{\circ}C}$ ~11). The average concentration at each flow rate is represented by a black filled marker of the same shape and border colour as the raw data series. The error bars plotted on this point are the standard deviation of the data set.

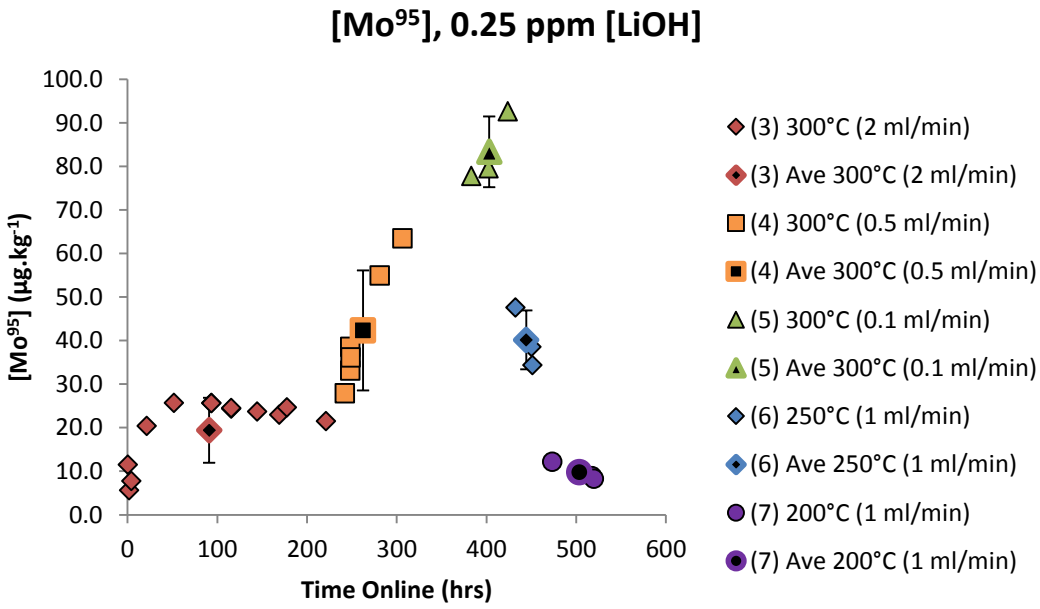

Figure 6.10 - The measured molybdenum concentration, based on Mo-95, in rig outlet water, at a LiOH concentration of 0.25ppm ($pH_{T=25\,^{\circ}C}$ ~9). The average concentration at each flow rate is represented by a black filled marker of the same shape and border colour as the raw data series. The error bars plotted on this point are the standard deviation of the data set.

Table 6.6 - Tabulated average solubility values of manganese for tests 1 - 7.

Test No.	[LiOH] (ppm)	pHT	T (°C)	Flow Rate (ml.min-1)		Average [Mn] (µg.kg-1)	Standard Deviation
1	25.00	11.00	300	2		0.42	0.24
2	25.00	11.00	300	0.5		-0.02	0.05
3	0.25	9.00	300	2		36.01	25.93
4	0.25	9.00	300	0.5		38.78	14.97
5	0.25	9.00	300	0.1		14.77	1.67
6	0.25	9.00	250	1		6.42	2.11
7	0.25	9.00	200	1		15.20	2.46

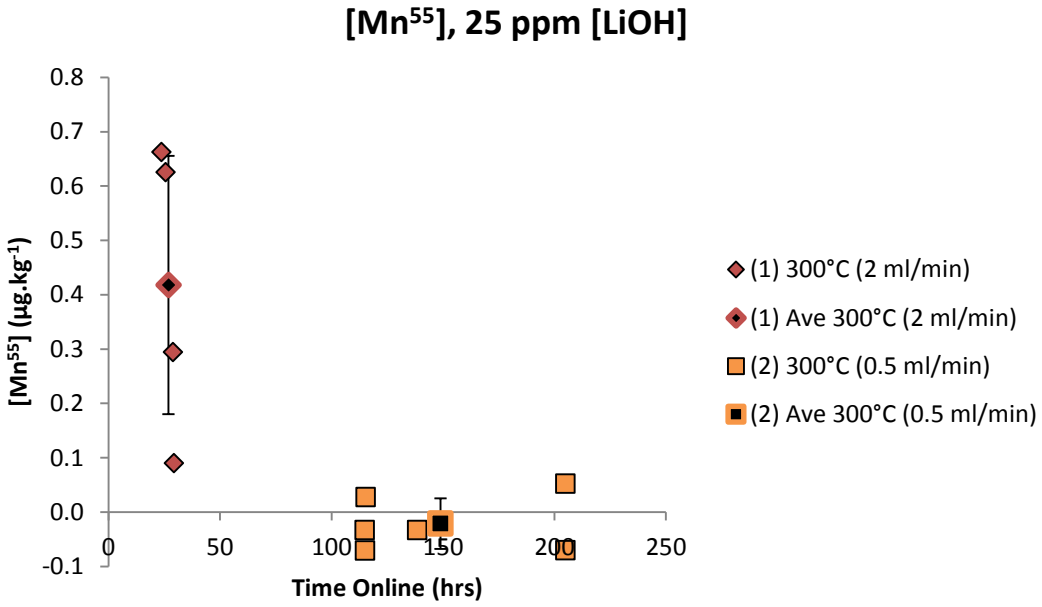

Figure 6.11 – The measured manganese concentration, based on Mn-55, in rig outlet water, at a LiOH concentration of 25.0 ppm ($pH_{T=25\,°C}$ ~11). The average concentration at each flow rate is represented by a black filled marker of the same shape and border colour as the raw data series. The error bars plotted on this point are the standard deviation of the data set.

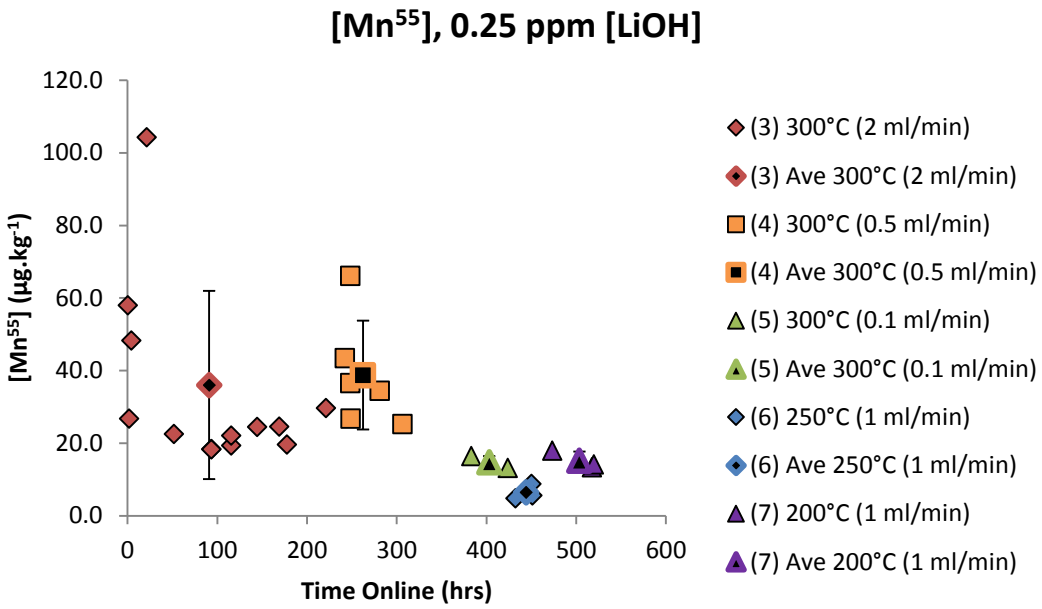

Figure 6.12 – The measured manganese concentration, based on Mn-55, in rig outlet water, at a LiOH concentration of 0.25ppm ($pH_{T=25\,^{\circ}C}$ ~9). The average concentration at each flow rate is represented by a black filled marker of the same shape and border colour as the raw data series. The error bars plotted on this point are the standard deviation of the data set.

6.5.3 SEM Imaging

SEM imaging of the internal surfaces of the tube was performed after the test series was complete. A section as cut from the centre of the tube and imaged using a Hitachi S4500-FEG SEM. All images were taken in secondary electron detection mode, at a beam energy of 20 kV and a working distance of 10 mm. Images of the surfaces are presented in Figure 6.13 and Figure 6.14.

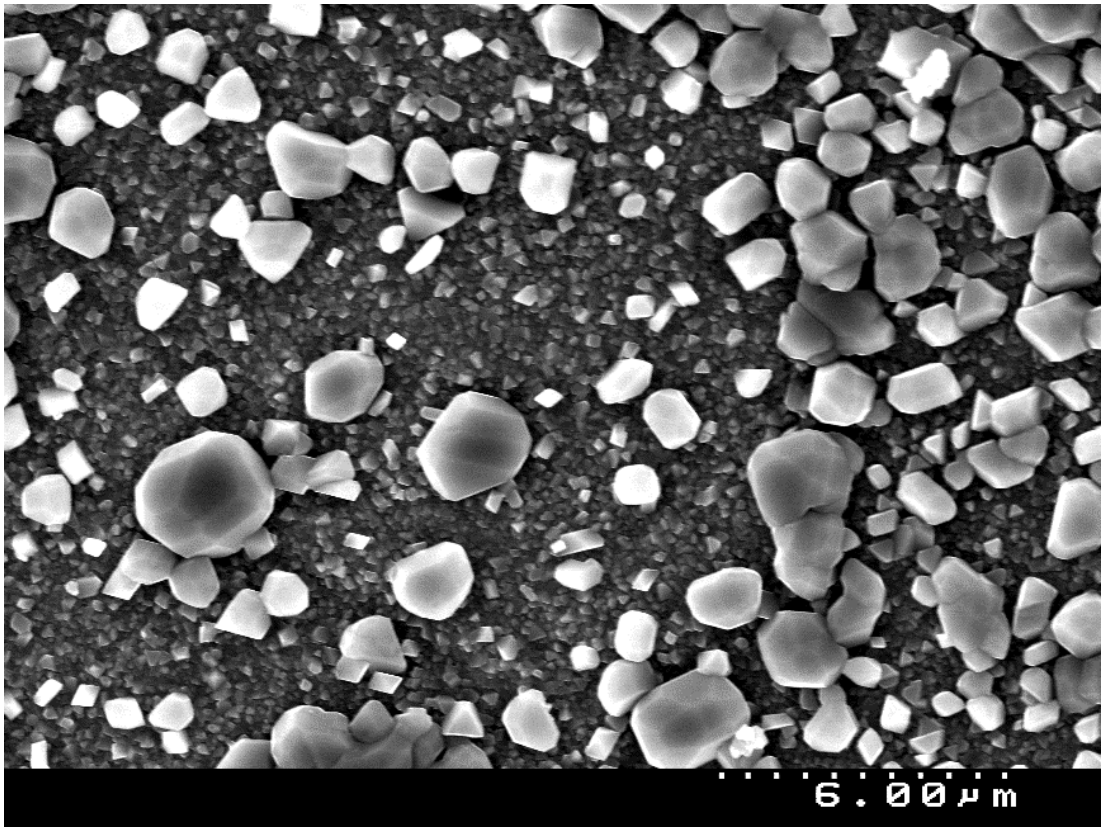

Figure 6.13 – SEM image of the internal surface of the specimen chamber after ~800 hours at temperatures between 200 and 300 °C, and $pH_{T=25\,°C}$ of 7 to 11. During the time online and the cycling of temperature, pH and flow rate, outer layer crystals, which normally present as truncated cubic shaped crystals, have swollen to a more irregular shape. Images taken in secondary electron detection mode, with a beam energy of 20 kV at a working distance of 10 mm.

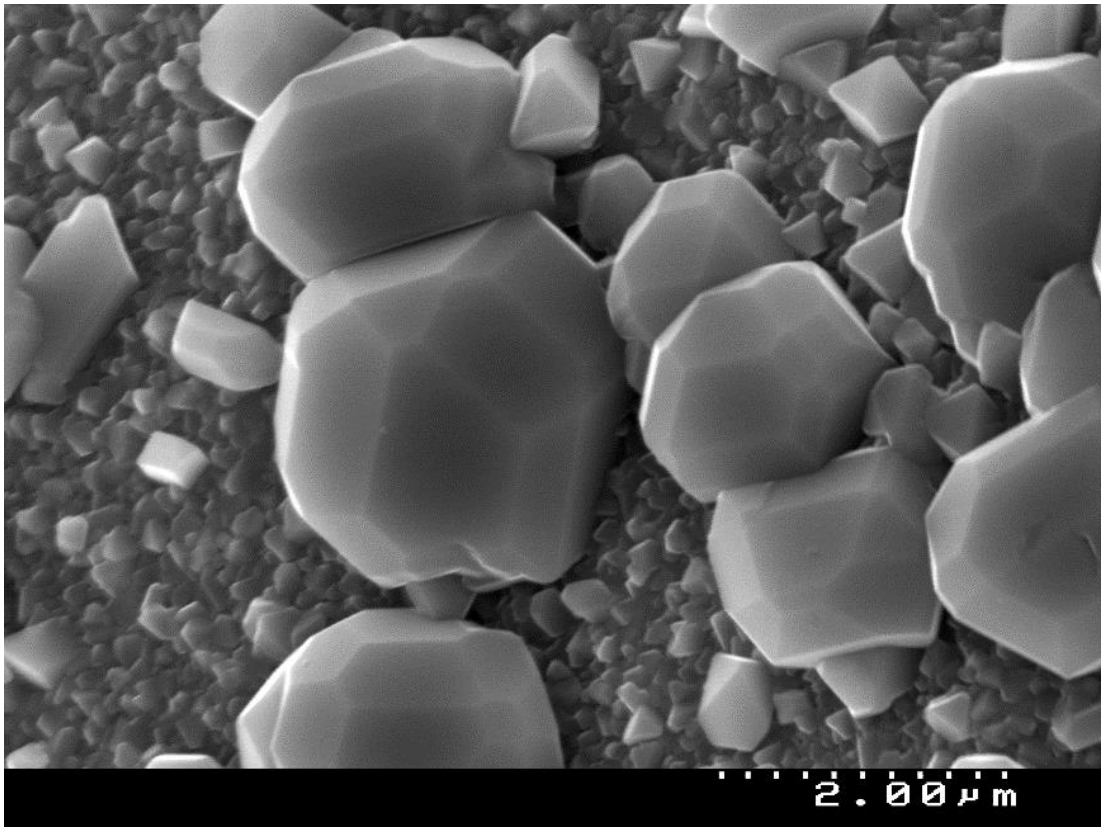

Figure 6.14 – The outer layer crystallites at higher magnification. Images taken in secondary electron detection mode, with a beam energy of 20 kV at a working distance of 10 mm.

A small piece of the same tube section was also cross sectioned with a slow speed diamond saw, without lubricant, mounted and polished to assess the oxide film. An image of the cross section, with line scans superimposed, can be seen in Figure 6.15. Imaging and analysis was performed using a Jeol 7000F SEM, using and Oxford Instruments INCA EDX Spectrometer. Imaging was performed with secondary electron detection at 20 kV and a working distance of 10 mm, and EDX was performed at a beam energy of 20 kV at a working distance of 10 mm.

The EDX results have been extracted and plotted in Figure 6.16, along with the ratio of chromium to iron across the spectra. The peak in the ratio at ~1.75 µm shows the location of the chromium rich inner oxide layer.

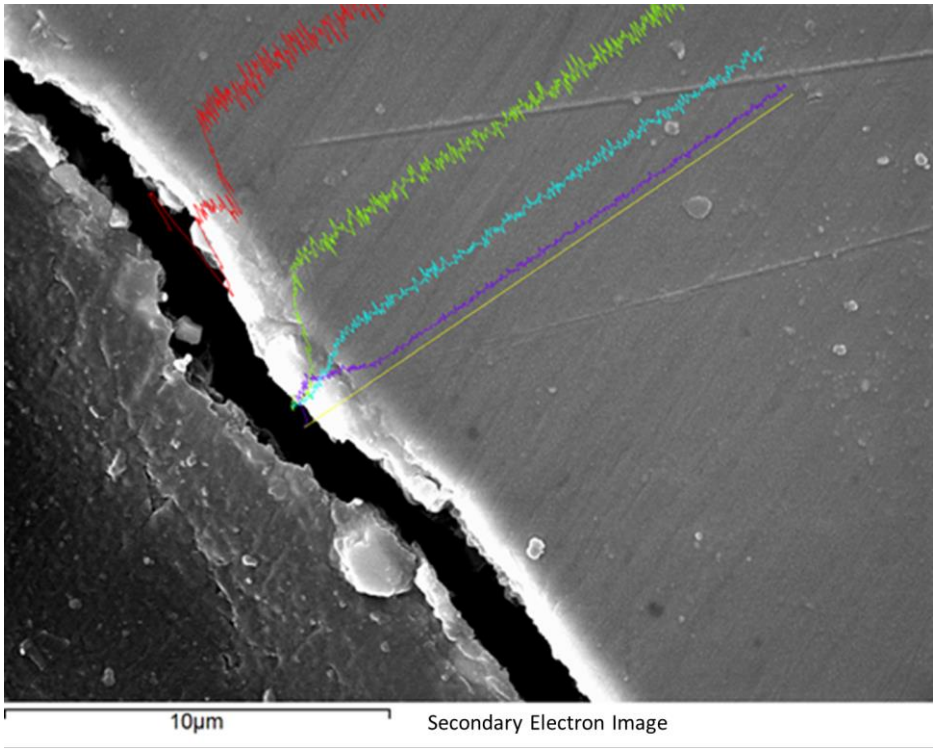

Figure 6.15 - Secondary electron image of the EDS line scan location, which is superimposed on the image. The sample and mounting resin had become de-laminated, possibly due to the curved shape of the sample. This location of the sample had not pulled the outer layer away from the surface with the resin, and was deemed suitable for this measurement. The coloured lines represent the number of counts for each element; red for ion, green for chromium, light blue for nickel and purple for oxygen. Images taken in secondary electron detection mode, with a beam energy of 20 kV at a working distance of 10 mm.

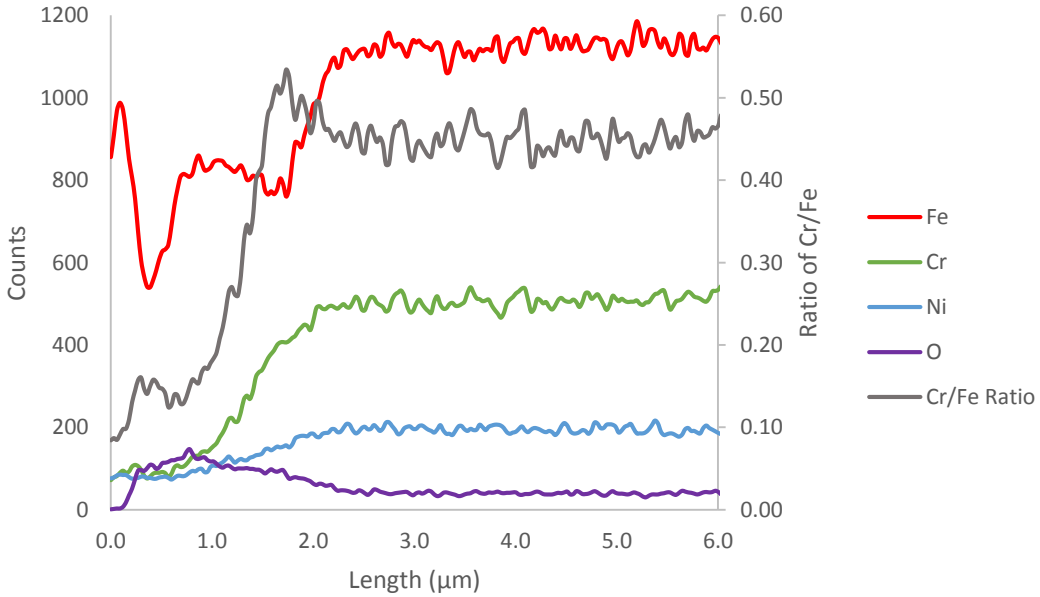

Figure 6.16 - EDX line scans showing compositional information through the depth of the oxide layer formed in the Metal Oxide Solubility rig sample chamber. The chromium/iron ratio is presented as the purple line; the peak ratio at ~1.75 µm can be interpreted as the centre of the chromium rich inner layer.

6.6 Discussions for Section C

6.6.1 Measurement of Dissolved Ion Concentrations by ICP-MS

As demonstrated by the results of the ICP-MS analysis, shown in section 6.5.1, the concentrations of major alloying elements iron, nickel and chromium are in the ppb range, as has been reported by other research groups (see section 2.5.4). This is also a vast improvement upon the experimental series detailed in section 6.1, the results of which were spread across several orders of magnitude (see section 6.2).

Even with these successful improvements, there are still some behaviour in the data that cannot be fully accounted for, given the present data. In the data shown in Figure 6.3 and Figure 6.5 (which show the measured iron and nickel concentrations at the beginning of the experimental series, where the tube surface had not yet been exposed), a general downward trend can be seen in the average concentration during experiments (1) and (2). This likely a result of the corrosion of the stainless steel being used as the ion source in the experiment, which was slowing with time, leading to a high ion concentrations while the oxide layers are forming. This is also similar to the trend observed by Lambert *et al.* [181] and Tremaine & LeBlanc [53], who saw that magnetite concentration in their experiments diminished with time, though this experimental work did not continue for the same timescale.

When the chemistry of the system was changed to 0.25 ppm LiOH from experiment (3) onward, the trend in concentration of iron (see Figure 6.4) and nickel (see Figure 6.6) ceased to match. The iron concentration continued to follow a general downward trend across the three different flow rates at 300 °C in experiments (3), (4) and (5), while nickel concentrations when through a period of relative stability during experiment (3), followed by a spike during experiment (4) when the flow rate was reduced to 0.5 $ml.min^{-1}$ and a rapid fall

when flow rate was reduced to 0.1 ml.min^{-1} in experiment (5). This spike is difficult to explain, as it appears to only involve the nickel, and not the iron as could be expected from a sudden release of particulate matter.

In the case of both iron and nickel, the solubility at lower temperatures (experiments (6) and (7)) was found to be lower than at 300 °C. This is surprising, given that the equilibrium solubility of both iron and nickel is higher at lower temperatures than at 300 °C [52,53]; this is demonstrated below where data from this experimental series is compared to literature data (see Figure 6.17, Figure 6.18 and Figure 6.19 for magnetite, and Figure 6.20, Figure 6.21 and Figure 6.22 for nickel). It is likely due to kinetics that the these values were significantly lower than the equilibrium solubility; at lower temperatures, the movement of ions from the walls to the bulk water is slower and given that the flow rate through the cell is laminar, there is limited convective mixing. Greater surface area and flow disturbance would help to achieve more accurate values at these temperatures.

Chromium concentration (plotted in Figure 6.7 and Figure 6.8) are consistently quite low, though on a few occasions the level is higher than would be expected [58], possibly due to contamination of the sample before analysis. The majority of samples reported values of ~1 ppb at 25 ppm LiOH (experiments (1) and (2)), and <0.5 ppb at 0.25 ppm LiOH concentrations (experiments (3) – (7)). Compared with the literature values for chromium concentration in high temperature high pressure water conditions [58], this level is still comparatively high (see Figure 6.23).

Measurement of the dissolved ion concentrations of minor alloying elements molybdenum and manganese showed that these elements are quite soluble in the aqueous phase, given the correct pH. During the first exposure experiment, at 25 ppm LiOH, molybdenum concentration in the water averages at ~395 ppb during experiment (1), before rapidly falling away to an average of 75 ppb

during experiment (2). This drop is probably the result of two processes; firstly, the formation of the protective oxide film is proceeding and is preventing the oxidation of the molybdenum into a soluble species, and secondly the quantity of molybdenum near the surface has been rapidly depleted by dissolution - from there on, molybdenum must diffuse through the solid phase before it can dissolve. These processes would result in a rapid drop in molybdenum concentration with time, as seen in Figure 6.9, however upon changing the LiOH concentration to 0.25 ppm in experiment (3), the molybdenum concentration undergoes a strange rise in concentration with time as the flow rate is reduced. The reduction in flow rate across experiments (3), (4) and (5) may be allowing the molybdenum ions more time to diffuse out of the solid phase and into the aqueous phase, resulting in the higher concentrations observed. The concentration drops with temperature and increasing flow rate in experiments (6) and (7), possibly due to the kinetics of diffusion from the solid phase and the shorter time afforded for diffusing into the bulk of the aqueous phase.

Contrary to the behaviour of molybdenum, manganese undergoes a minimum concentration during experiment (1), with an average concentration of ~0.4 ppb, falling to ~0 ppb during experiment (2). When the chemistry is changed to 0.25 ppm LiOH for experiment (3) onward, the concentration of manganese rises to ~36 - 39 ppb between experiments (3) and (4), though this falls to ~15 ppb with the reduced flow rate of experiment (5). Again, at 250 °C and 200 °C of experiments (6) and (7) respectively, the solubility is somewhat lower than seen at 300 °C. The behaviour of manganese in these experiments seem to suggest that its solubility is extremely sensitive to pH, though extensive further studies would need to be conducted to determine the true pH dependence.

To the best of the author's knowledge, there is no literature covering the equilibrium solubility of molybdenum or manganese under high temperature high pressure aqueous conditions, making comparison impossible.

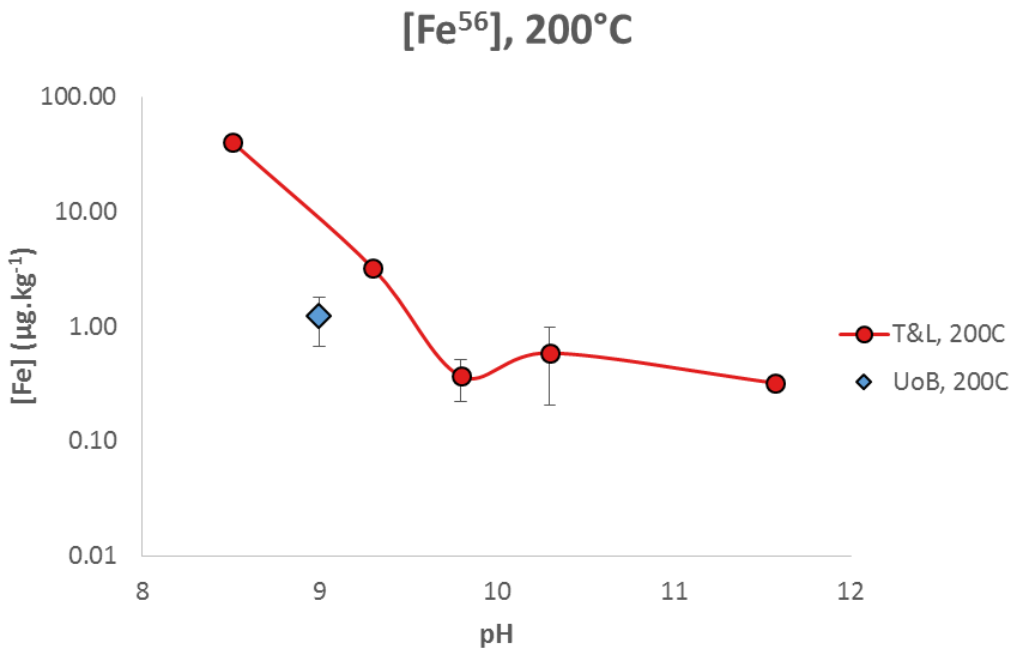

Figure 6.17 - Comparison of solubility of magnetite (as measured by Tremaine and Leblanc [53]) with the solubility iron from stainless steels corrosion product measured in this work, at T = 200 °C. The low concentration found in this project's work is surprising, as this represents a sub-saturation condition.

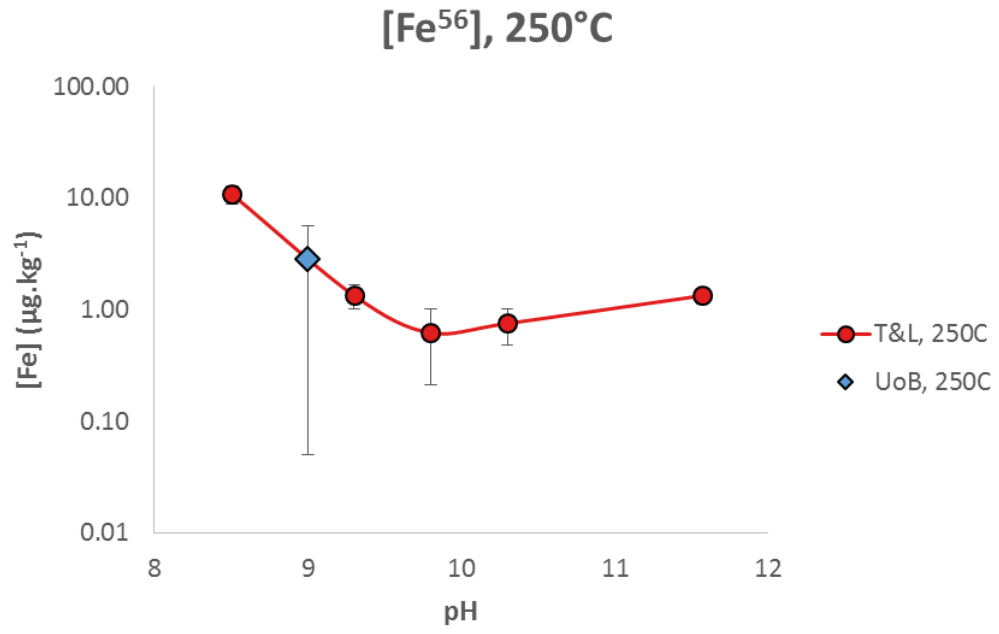

Figure 6.18 - Comparison of solubility of magnetite (as measured by Tremaine and Leblanc [53]) with the solubility iron from stainless steels corrosion product measured in this work, at T = 250 °C.

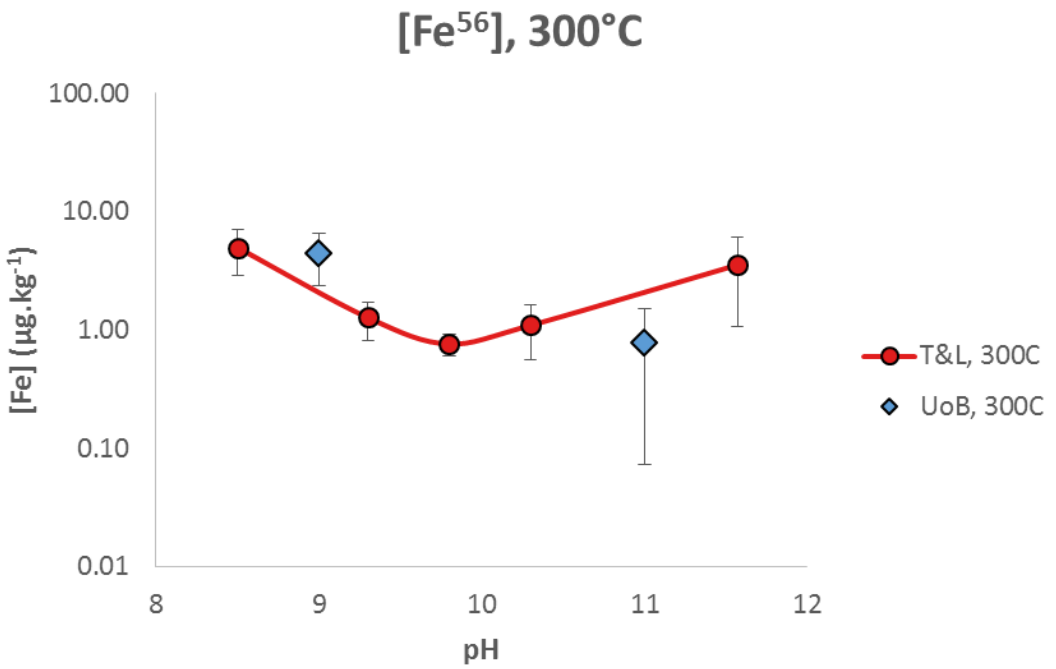

Figure 6.19 - Comparison of solubility of magnetite (as measured by Tremaine and Leblanc [53]) with the solubility iron from stainless steels corrosion product measured in this work, at T = 300 °C. The higher concentration of iron in the data from this project suggests the presence of particulate material which artificially inflates the total inventory of iron.

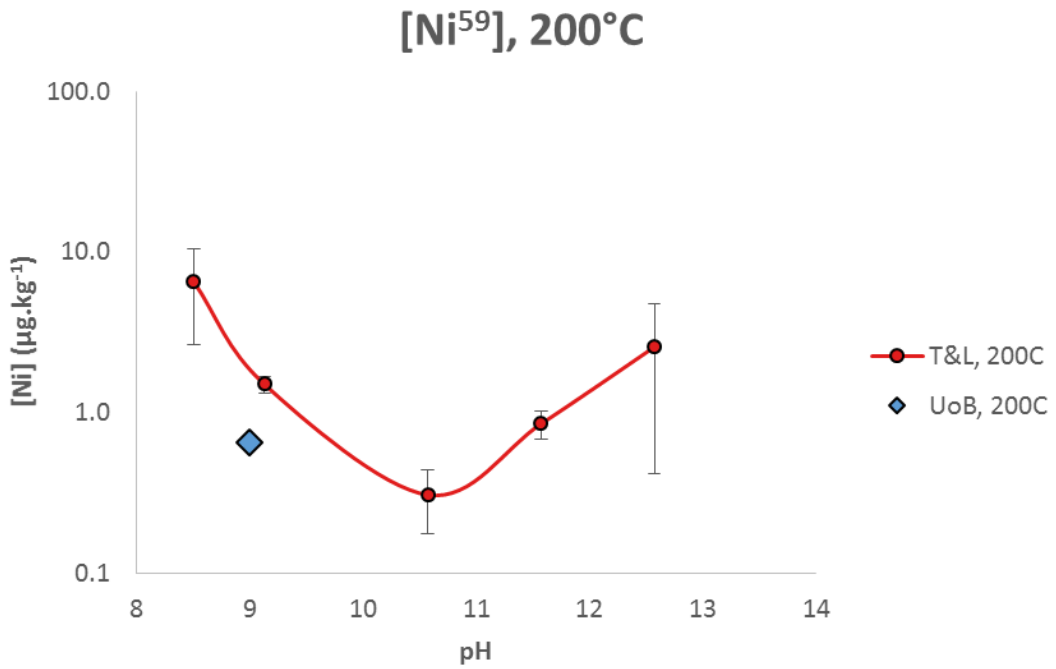

Figure 6.20 - Comparison of solubility of nickel (as measured by Tremaine and Leblanc [52]) with the solubility nickel from stainless steels corrosion product measured in this work, at T = 200 °C. Similarly to the data shown in Figure 6.17, the data from this project's work represents a state of sub-saturation compared to the equilibrium solubility.

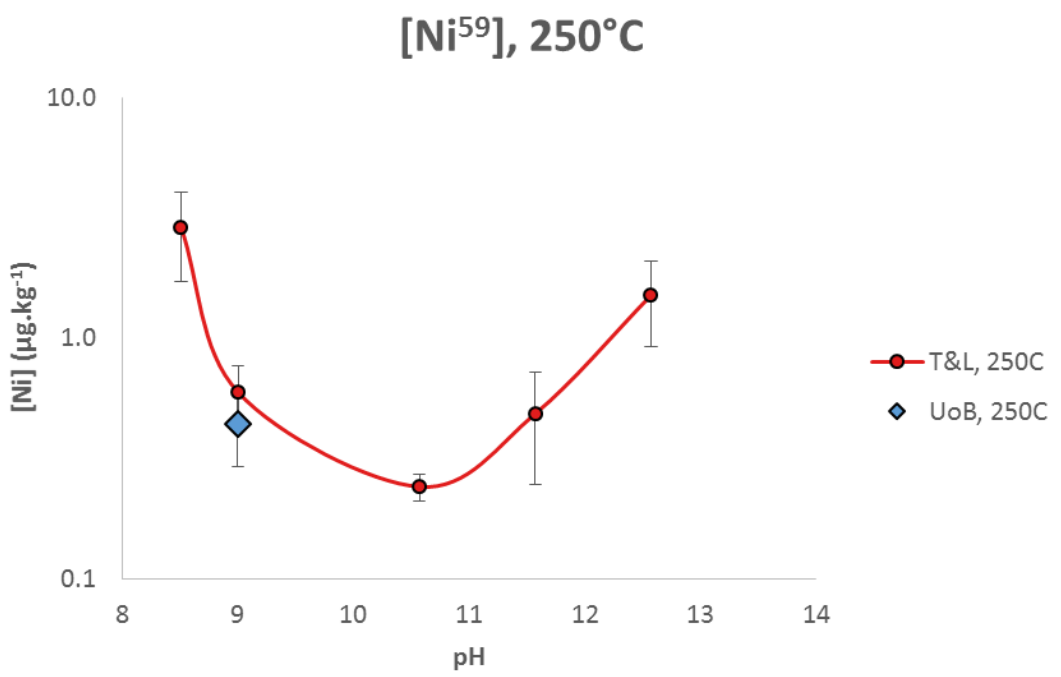

Figure 6.21 - Comparison of solubility of nickel (as measured by Tremaine and Leblanc [3]) with the solubility nickel from stainless steels corrosion product measured in this work, at T = 250 °C.

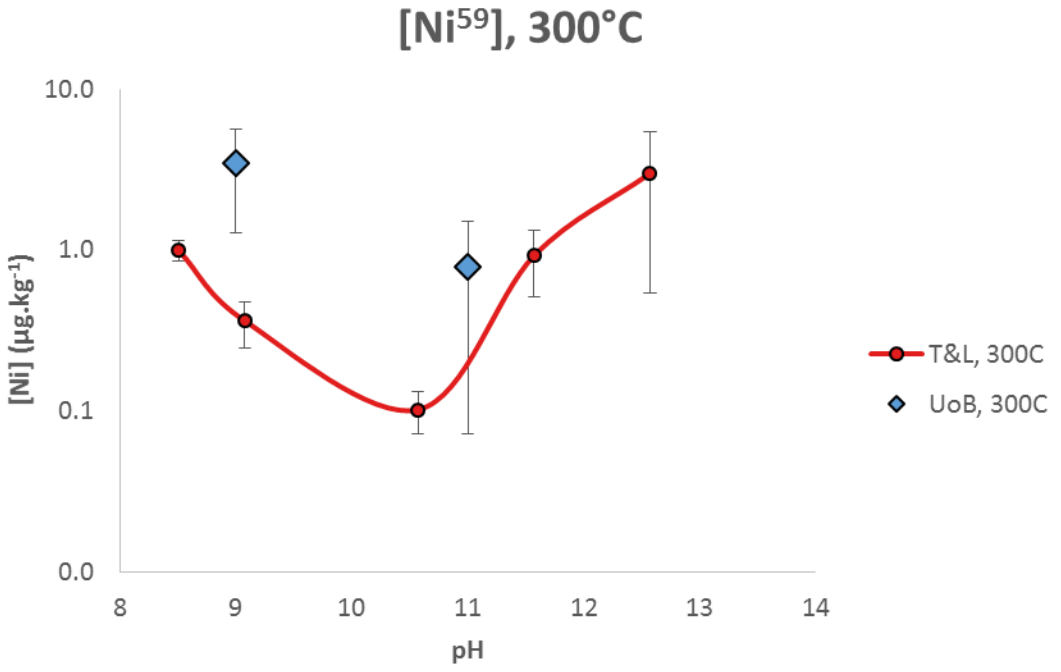

Figure 6.22 - Comparison of solubility of nickel (as measured by Tremaine and Leblanc [3]) with the solubility nickel from stainless steels corrosion product measured in this work, at T = 300 °C. In similar fashion to the data shown in Figure 6.19, the data from this projects work is higher than the equilibrium solubility, suggesting the presence of particulate contamination.

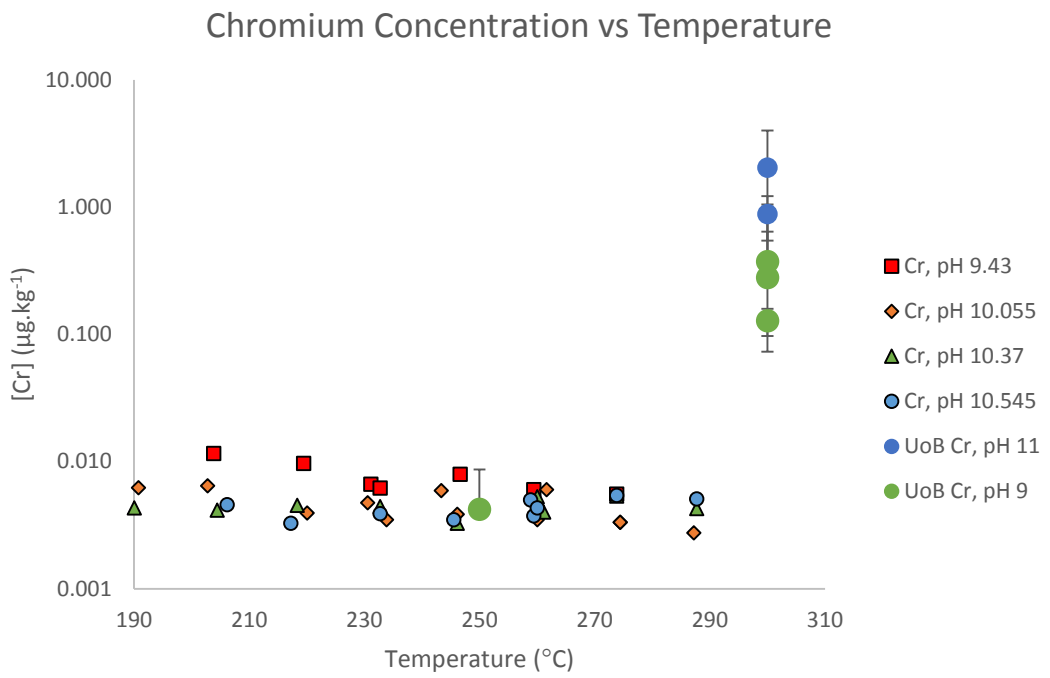

Figure 6.23 - Comparison of solubility of chromium (as measured by Ziemniak *et al.* [58]) with the solubility of chromium from stainless steels corrosion product measured in this work, identified by the large blue and green borderless circles.

6.6.2 SEM Analysis

SEM was used to perform a cursory analysis of the surface and attempt to characterise the metal oxides which were providing the source of metal ions for this experimental series.

Imaging of the surface revealed the expected surface structures; an outer layer of large crystals grown by re-deposition of material at the surface surrounded by smaller crystals (see Figure 6.13 and Figure 6.14) grown through either re-deposition or by solid state growth (see section 2.4.2).

Cross sectioning of the sample allowed for the observation of a proportional increase in chromium concentration, indicating the presence of the chromium-rich inner oxide layer (see Figure 6.15 and Figure 6.16). Unfortunately, the sample was sputter coated with gold to make it conductive, obscuring the molybdenum peak, which could have provide some interesting information about molybdenum concentration between the bulk and the near-surface

region. It is clear that more in-depth studies should be undertaken in any future work.

6.7 Conclusions for Section C

The solubility of oxidised alloying elements of 316L stainless steel in high temperature high pressure, mildly basic water have been measured by ICP-MS and a function of temperature, LiOH concentration and flow rate. The results of these experiments show that the purpose built rig is a vast improvement over the original method, where a metal oxide sample was suspended in a static batch type autoclave. Concentrations of metal ions, which had previously been spread across several orders of magnitude were now within a single order of magnitude, and in some cases close to the solubility reported in the literature for pure metal oxide samples in 'inert' rig environments; that is, where the materials of construction of the rig will not interfere with the solubility measurement.

The aim of this programme has been to provide inputs for a whole plant model to the sponsor company, Rolls-Royce plc; in this case, the solubility of metal oxides which form on plant surfaces. The work performed in this section has begun to provide values for expected metal ions in solution for a given material over a range of temperature and pH. The system is by no means perfect, and improvements could be made to both the system and to the experimental method which are discussed later in section 9.1.3.

7 Finite Element Modelling of Flow Assisted Deposition

The work presented in this section of the dissertation uses Finite Element Method (FEM) models of the fluid restrictions described in section 4.1.1 to extract fluid dynamics information required by the equations for electrokinetic deposition mechanism described in section 2.3.6. The equations provide the average shear rate of the system but cannot describe rapid change in shear rate during a sudden acceleration; for this, modelling provides an excellent assistive tool.

A more complex, proof-of-concept model was also developed, where deposit growth was simulated by the deformation of the model mesh. Mesh deformation would occur at a point calculated by the model, given set values of growth rate and shear rate.

The software package chosen for this work was the COMSOL Multiphysics package, a general purpose finite element modelling package capable of simulating coupled physics problems; central to its capability is computational fluid dynamics. The choice of this software was made on the basis that future work with more complex problems involving chemical species transport could easily be incorporated by the addition of modules which offer such functionality.

7.1 Basic Shear Rate Modelling

7.1.1 Development of Shear Rate Model

As a preliminary study, simple models of the geometry were developed with the intention of extracting shear rate data along the surface of the geometry. Initial models of the flow restriction were simple step geometries, moving from an 11 mm diameter cylindrical tubing to a 6 mm diameter tubing, which are the sample geometries described in section 4.1.1. Poorly made models are often

found to fail due to the software's inability to reach a convergence point, resulting in a great deal of wasted time and effort. This can be avoided by iterative improvement of a simplified model which is found to work.

For all models described herein, the Reynolds Averaged Navier-Stokes (RANS) based "Turbulent Flow, Low Re k-ε" physics package was employed. Unlike other turbulent flow packages, the low Reynolds number package does not use a "wall function", which is a simplifying assumption made by other packages to reduce computational load. Instead, this model package solves for flow everywhere, including the viscous sublayer at the wall. While the use of this physics package is more computationally intensive that other types, it is necessary to correctly describe flow in this work, as the streaming current behaviour is dependent upon the flow close to the wall.

In the case of these models, the geometry was first drafted in a two dimensional, axisymmetric domain. An axisymmetric model provides a central axis, which any geometry domain drawn by the user is wrapped around the axis in post-processing analysis. The assumption made by this model is that the three dimensional model is accurately described by the behaviour of elements within the two dimensional plane defined by the user. This model type is particularly well suited to simple cylindrical geometries, as the assumptions of the model are valid. This means that a geometry that would require a three dimensional cylinder can be cut down to a single rectangular plane in contact with the model's axis, and still return the same results. The reduction in the number of mesh elements in the model vastly reduces the computational requirements, meaning that a study can be completed in a matter hours, rather than days. For complex models the time required to reach completion may still be on the order of days, though this depends heavily on the computational capability of the computer. In this work, a high performance desktop computer was used, fitted with a quad core 3.4 GHz CPU (Intel i7-4770) and 16 GB of DDR3 RAM.

The geometry of these models was first drafted as a set of three rectangles, joined by a Boolean union and removing internal boundaries, creating a continuous step geometry (see Figure 7.1). A coarse mesh was then added using the software's physics controlled mesh option (see Figure 7.2). The domain of interest was defined as containing liquid water at room temperature, and the inlet and outlet boundary conditions were applied to the ends of the geometry. At this point, the draft model could be computed.

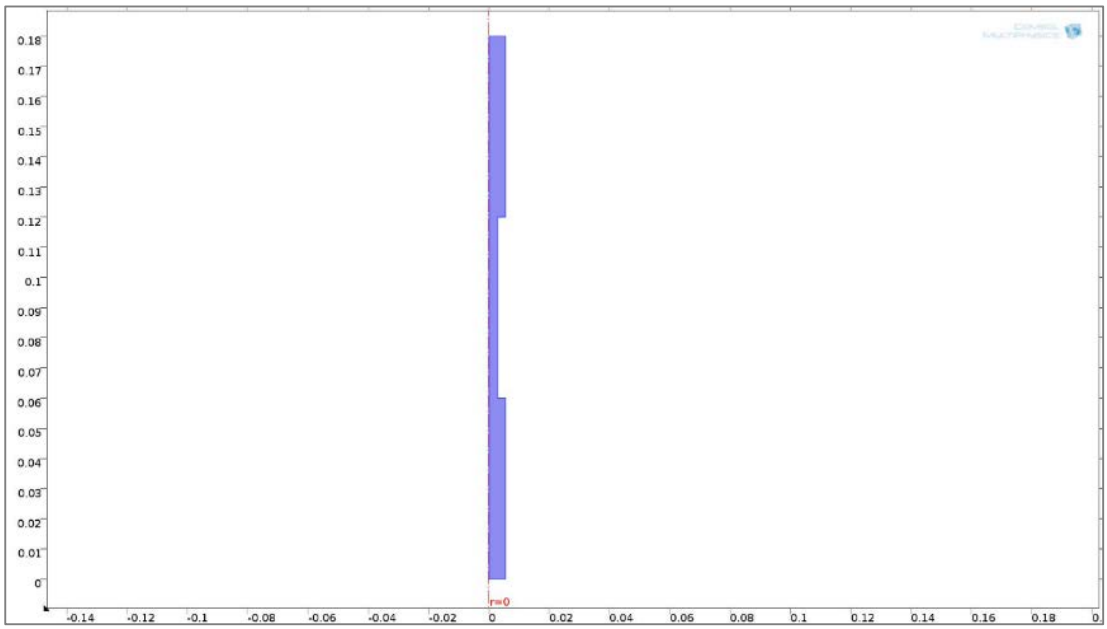

Figure 7.1 - The foundation geometry of the simple computer models used to extract shear rate information.

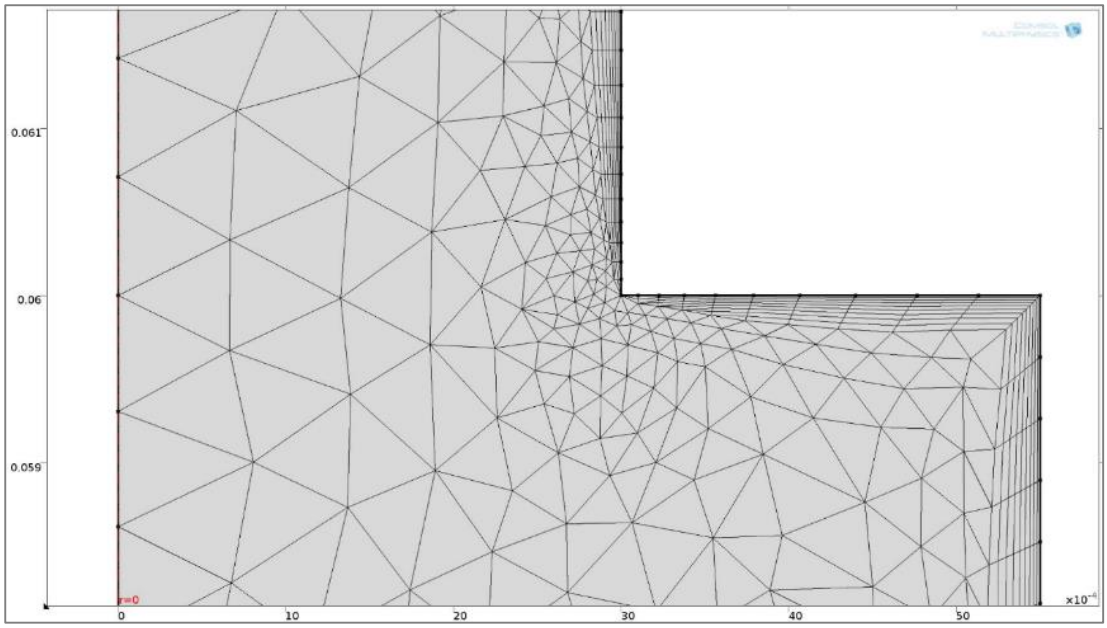

Figure 7.2 - Coarse mesh applied to the model. This mesh only provides 10 boundary elements along the restriction face.

Should the model be found to converge (that is, to reach a stationary solution across the geometry), complexity is added initially by improving the quality of the mesh. This is done by constructing a user controlled mesh, and applying finer meshes to the boundaries of interest. In the case of these models, the boundaries of interest include are in facing wall and the annulus of the restriction. As these models are built for extracting data for the electrokinetic deposition mechanism equations, the bulk liquid is of little concern and an appropriately coarse mesh can be applied to the rest of the domain. It is still advantageous to apply as high a resolution of mesh as possible to the remaining domain, as this improves the overall quality of the model results. An image of a model with improved meshing at the restriction can be seen in Figure 7.3

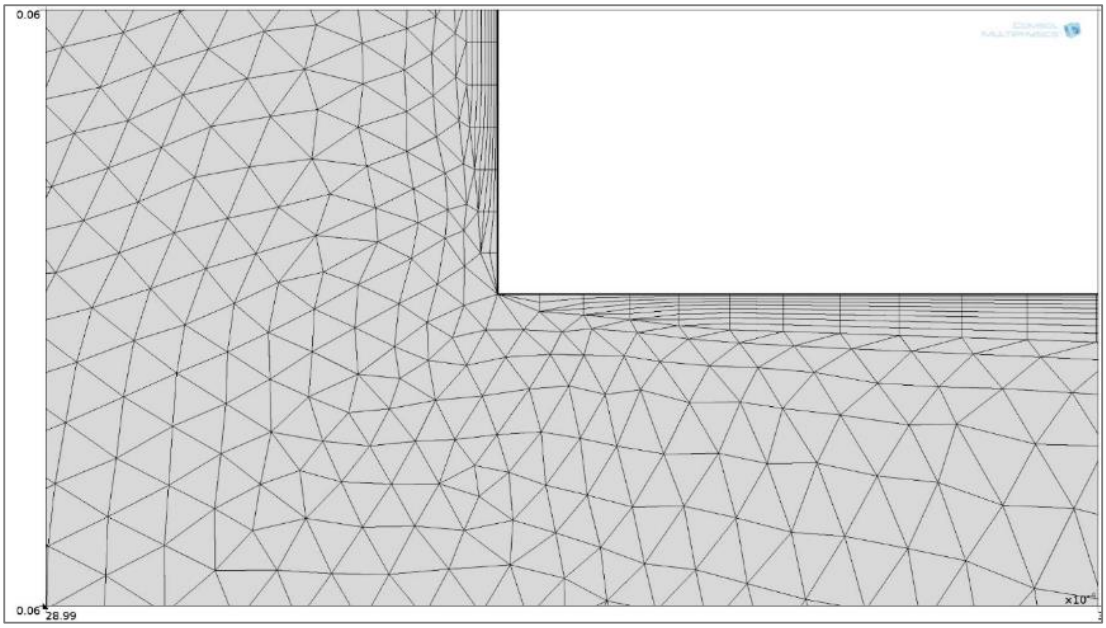

Figure 7.3 - A significantly finer mesh has been added to the model.

Minor changes to the geometry have been found to avoid computational difficulties, such as those seen at sharp corners which can cause the model to struggle to reach convergence. In these cases, a fillet of the sharp corner can solve the difficulty in addition to providing significantly greater mesh resolution at the corner (see Figure 7.4).

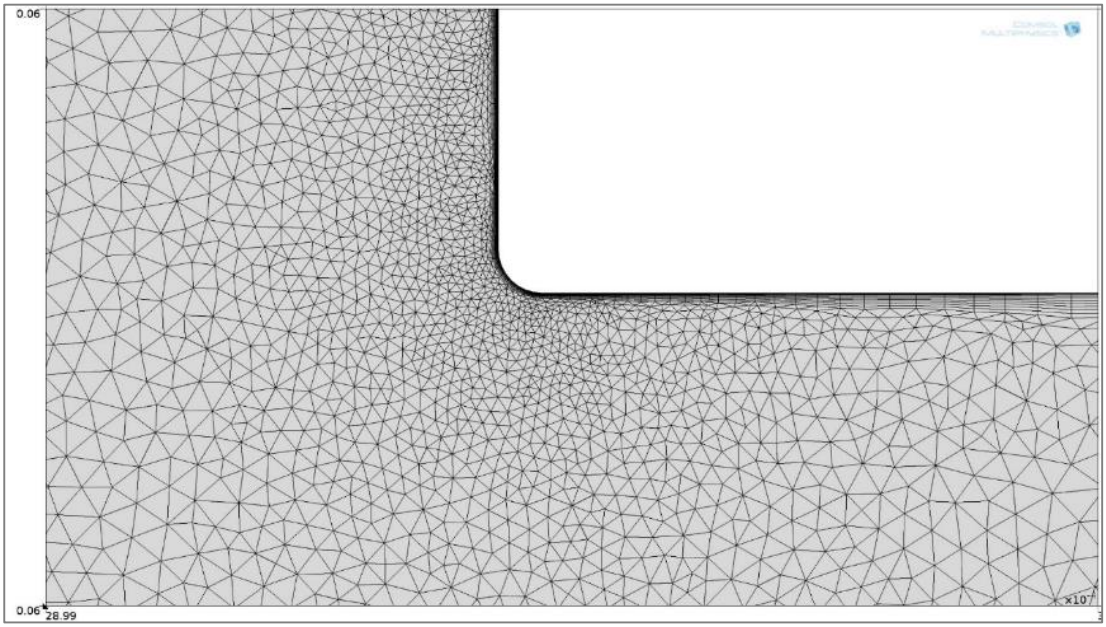

Figure 7.4 - The addition of a 10 μm radius fillet at the corner of the model significantly increases the number of boundary elements in the area of interest.

The final model used to extract shear rate as a function of various parameters consisted of a 60 mm inlet length of radius 5.5 mm, a 60 mm restriction length of radius 3 mm, and a 60 mm outlet length of radius 5.5 mm. These dimensions were based on the dimensions used for the test restriction used in the hot loop (see section 4.1.1), which is itself based on the restrictions used on AREVA's EMILIE loop [18–20,22,23]. In some models, the corners were refined using 10 µm radius fillets. A user defined mesh was applied to the model that produced mesh elements of various sizes along the length of the wall.

Several tests were run where flow rate was the primary variable. The size of the corner radius was also varied in order to study the effect of smoother geometry transitions. Attempts were made to simulate high temperature conditions as well, however these models were unable to reach convergence. Computational time for successful tests was approximately 8 hours. The tests performed are tabulated in Table 7.1.

Table 7.1 - Table of conditions run through the simple fluid dynamics model.

Test No.	Volume Flow ($m^3.s^{-1}$)	$V_{restriction}$ ($m.s^{-1}$)	Fillets Size (µm)	T (°C)	Density, ρ ($kg.m^{-3}$)	Dynamic Viscosity, η (Pa.s)
1	2.26E-04	8	0	20 °C	998.3	1.00E-03
2	3.39E-04	12	0			
3	4.52E-04	16	0			
4	5.65E-04	20	0			
5	2.26E-04	8	10			
6	3.39E-04	12	10			
7	4.52E-04	16	10			
8	5.65E-04	20	10			

7.1.2 Shear Rate Model Results

The simple fluid dynamics model, has been used to extract shear rate data and compare this to the equations developed by Robertson [89] and McGurk [17], which are discussed in section 2.3.6.

Shear rate data was extracted from the model along the outer boundaries of the geometry (see Figure 7.5); the data is plotted in Figure 7.6 and

Figure 7.7, against arc length, which is the total scalar distance along the boundary, originating at the beginning of the selected boundary closest to $z = r = 0$.

The expected shear rate (as calculated using Equation 2.18) inlet and the restriction radii were compared to the shear rate in the settled regions of the model, *i.e.*, the regions shear rate exhibited a stable value, between ~80 – 120 mm in Figure 7.6. The regions used for the averages are between 20 and 40 mm and 100 and 120 mm. These regions were selected to avoid the initial spike in shear rate (an artifact of the model), and the region of disturbed flow created by the rapid acceleration. The calculated shear rates and the averages derived from the model are presented in Table 7.2. On all occasions, the calculations and the averages from the model are closely matched; the data are plotted in Figure 7.8 for clarity. Note that all length scales are a function of 'arc length', which is the length along the outer boundary of the model.

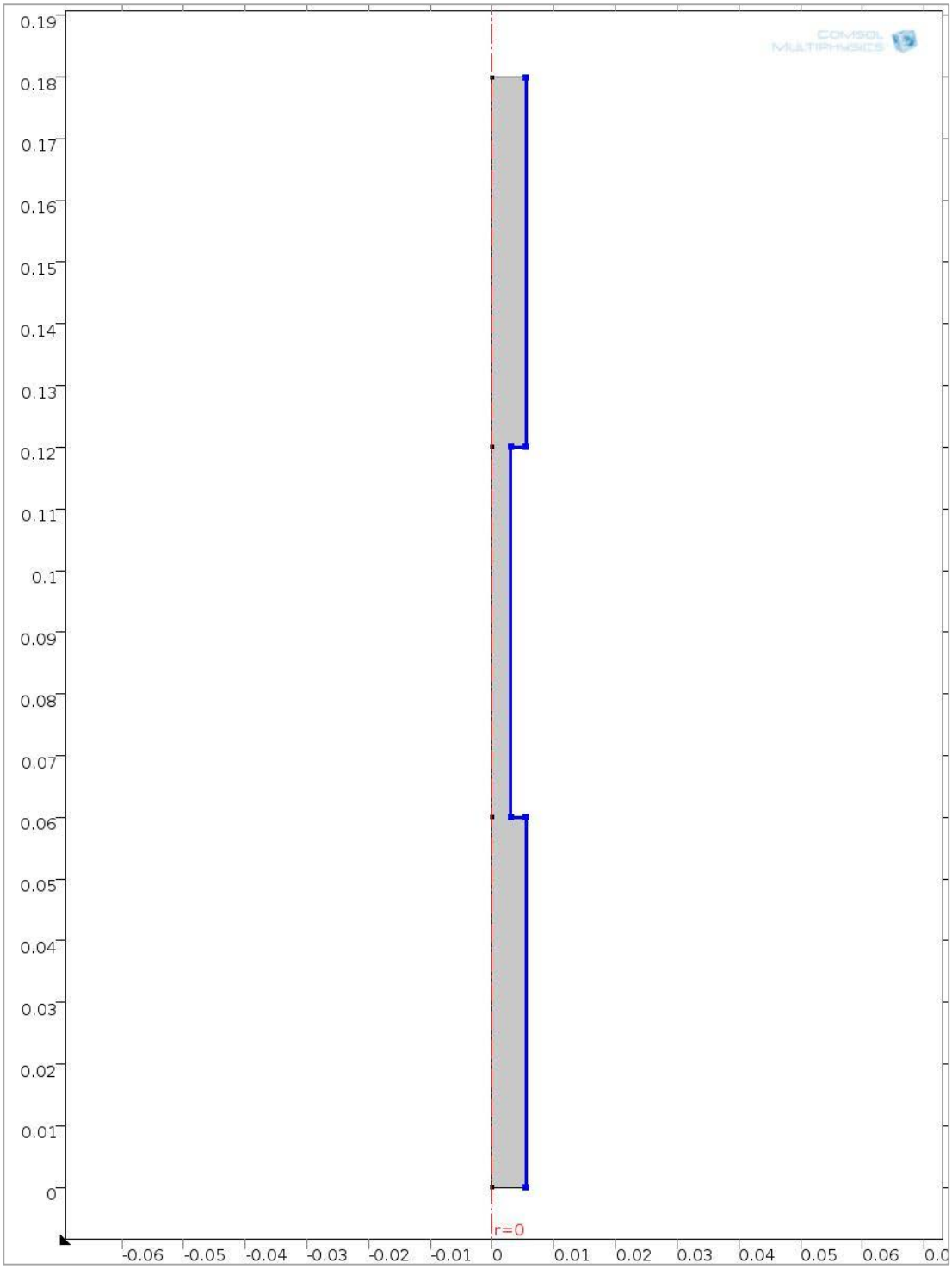

Figure 7.5 - The boundaries selected for shear rate data extraction; the arc length is the distance along these selected boundaries.

Table 7.2 – Tabulated stable shear rates (those between ~80 – 120 mm arc length, as in Figure 7.6), calculated using Equation 2.18 and averages derived from the COMSOL model.

		Shear Rate (s^{-1})			
		Velocity 8 $m.s^{-1}$	Velocity 12 $m.s^{-1}$	Velocity 16 $m.s^{-1}$	Velocity 20 $m.s^{-1}$
Inlet	**Equation 2.18**	1.70E+04	3.52E+04	5.91E+04	8.84E+04
	COMSOL Ave	1.60E+04	3.64E+04	6.30E+04	9.57E+04
Restriction	**Equation 2.18**	1.70E+05	3.53E+05	5.92E+05	8.84E+05
	COMSOL Ave	1.77E+05	3.62E+05	6.03E+05	8.99E+05

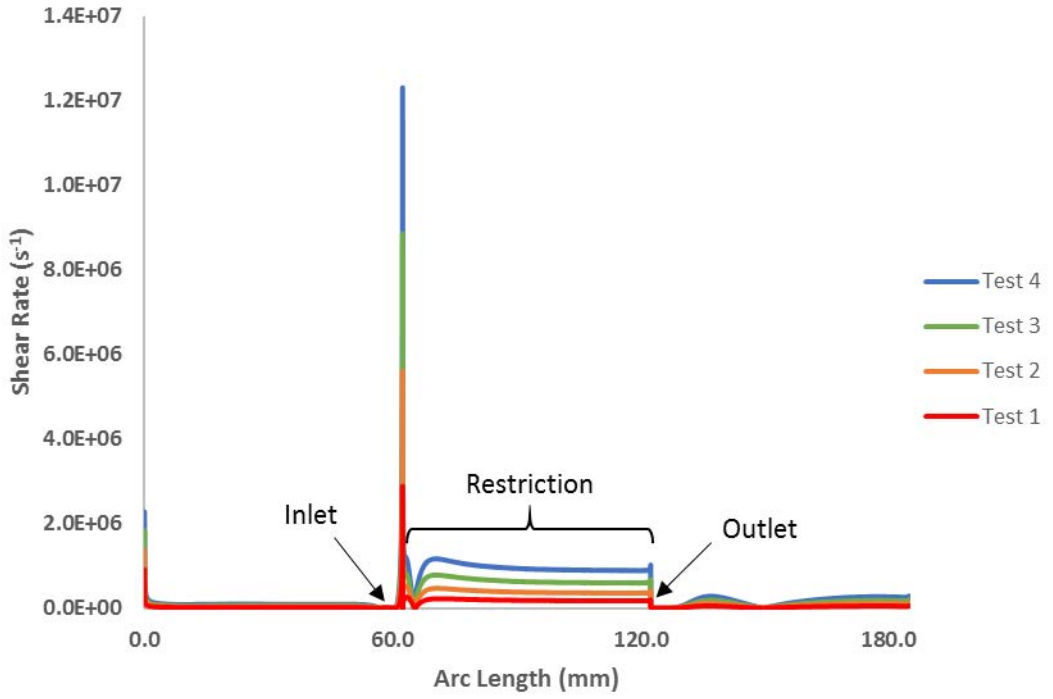

Figure 7.6 - Shear rate at the boundary wall as a function of arc length (the displacement distance along the boundary). Tests 1 – 4 have been plotted on the same axis.

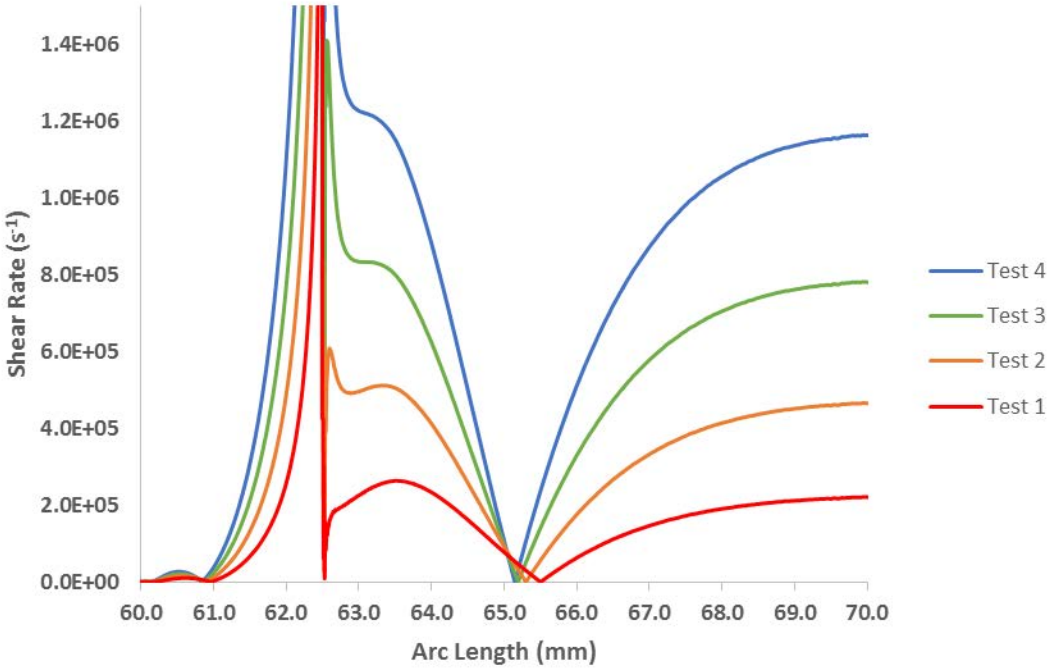

Figure 7.7 - Expanded view of the shear rate through the restriction, shown in complete form in Figure 7.6

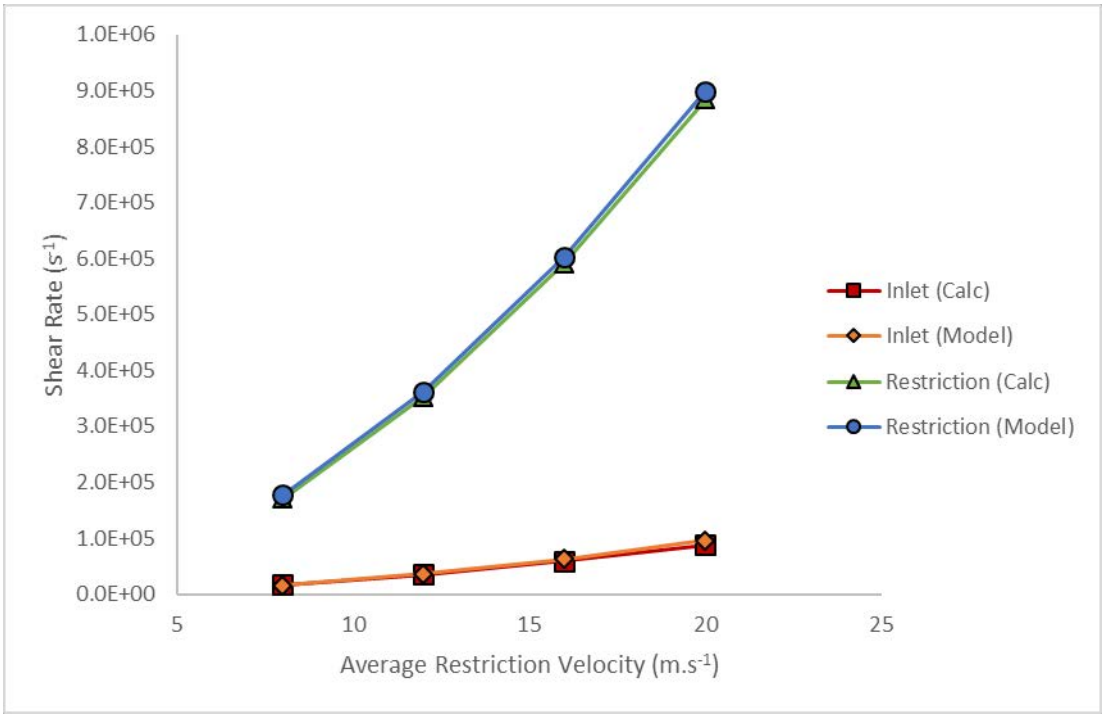

Figure 7.8 – Values of shear rate, as seen in Table 7.2, plotted against bulk fluid velocity.

The shear rate behaviour between arc length 60 and 66 mm can be attributed to the points of hydrodynamic attachment and separation – points of attachment exhibit high shear rates, while points of separation present as low shear rates. This can be seen in Figure 7.9, where the velocity profile shows the low velocity region close to the wall.

Given that streaming current is related to ζ-potential and shear rate (see Equation 2.17), it is clear that the peak streaming current will occur at the corner of the restriction.

Given an arbitrarily ζ-potential of -5 mV (a value based on the work of Jayaweera *et al.* [108,109]), the streaming current (I_s) and the wall current (i_w) have been calculated using equations 2.17 and 2.22 in section 2.3.6 and the shear rate calculated from the models. The streaming current has been plotted in Figure 7.10. The streaming current is then analytically differentiated with respect to distance, and multiplied by the reciprocal of circumference (see Equation 2.22), which yields the wall current density (see Figure 7.11).

The presence of this high current density spike is consistent with the formation of deposits at the entrance to the restriction. Another feature of interest is the presence of small regions of high and low current shortly after the spike, at approximately 62.52 mm in Figure 7.11 and Figure 7.12. The presence of these disturbances provides some basis for the rippled deposition seen by the AREVA group using the EMILIE loop [18–20,22,23].

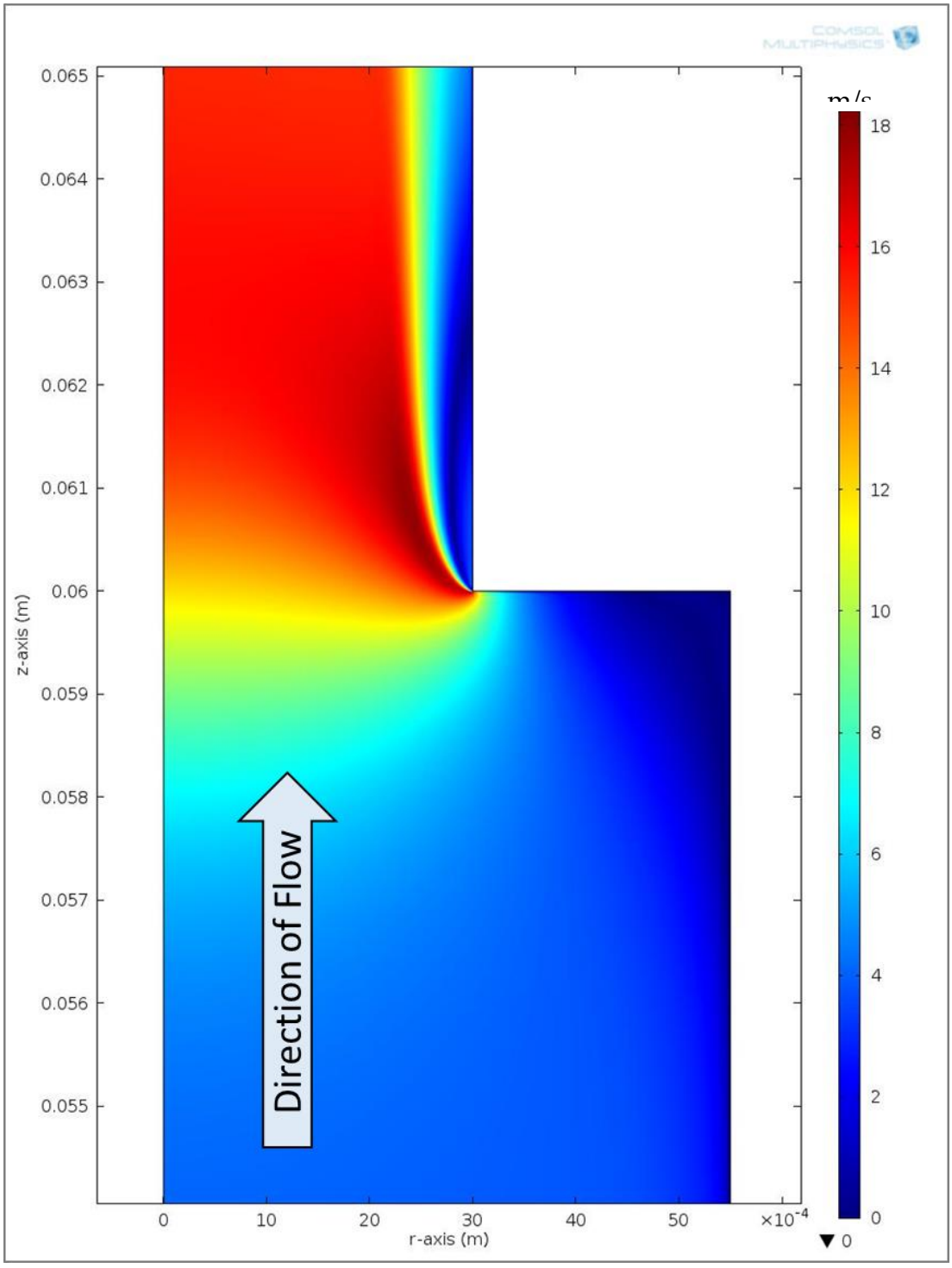

Figure 7.9 - The velocity profile for a 5.5 mm to 3 mm radius flow restriction, at a mean flow velocity of 3.5703 m.s-1 at the inlet and 12 m.s-1 in the restriction.

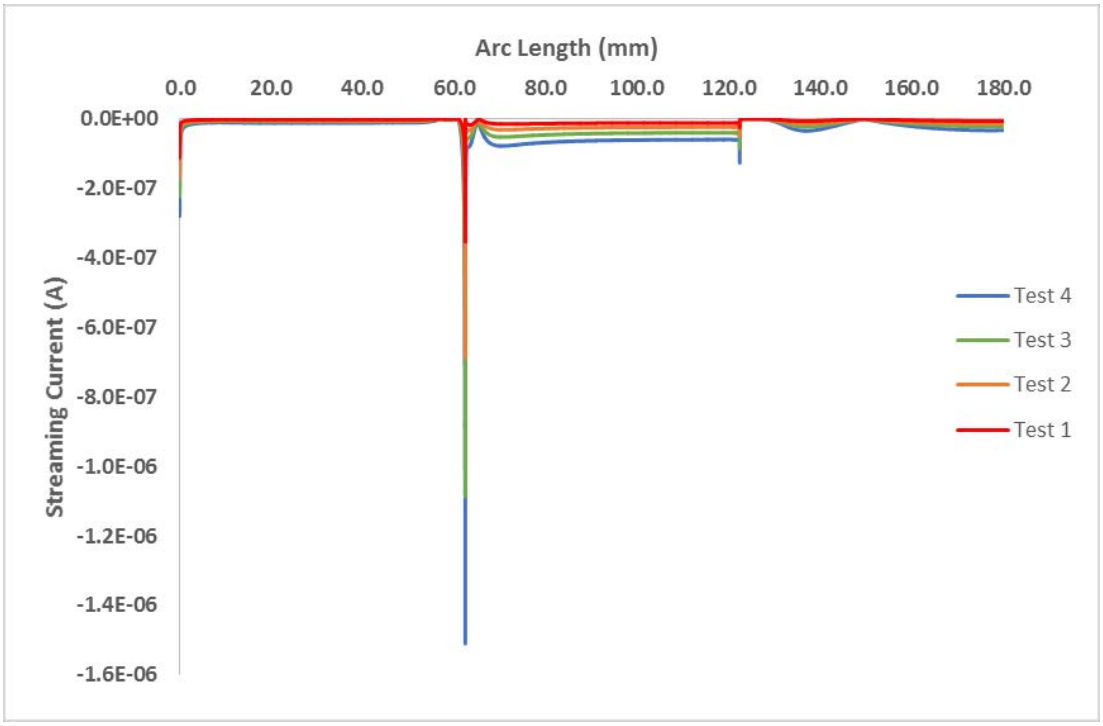

Figure 7.10 - Streaming current, based on a ζ-potential value of -5 mV. The curve is qualitatively, the inversion of the shear rate curves.

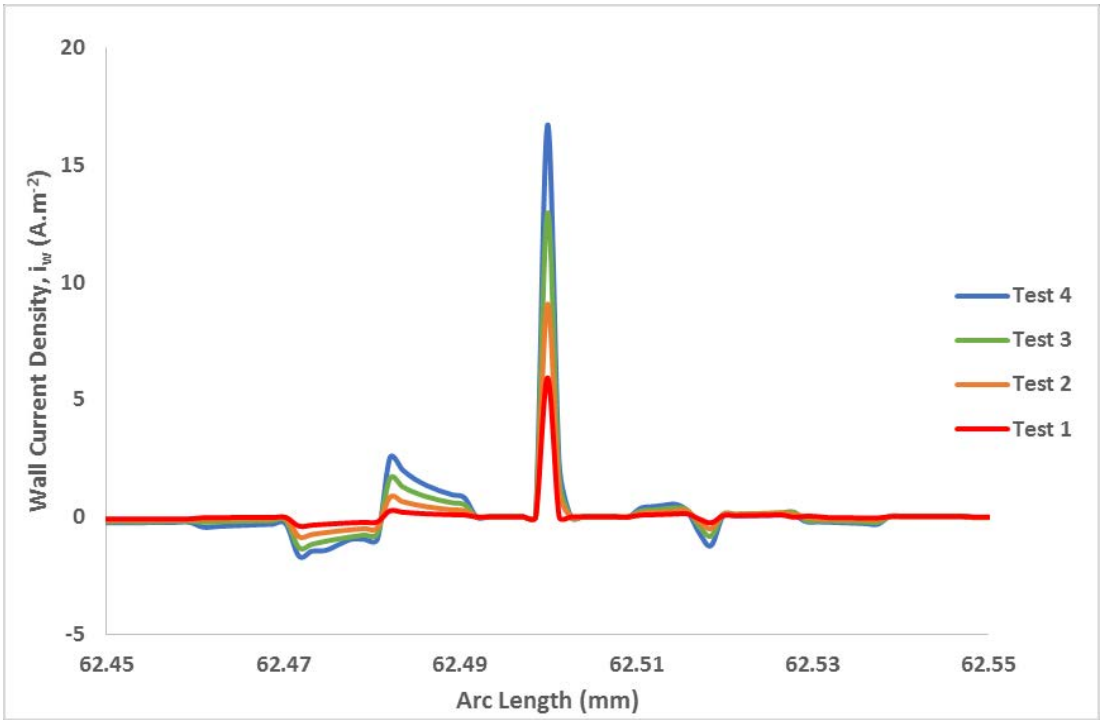

Figure 7.11 - Wall current density at the corner of the restriction (62.50 mm). A positive wall current density represents the flow of electrons into the wall.

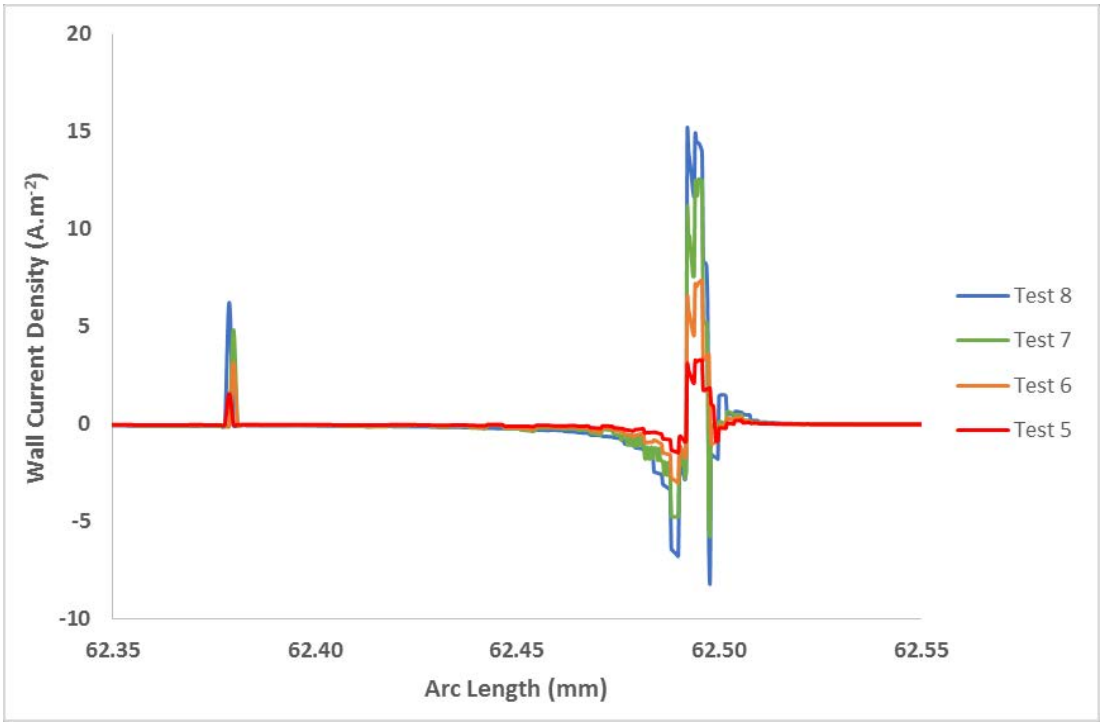

Figure 7.12 - Wall current density for flow across a curved corner into the restriction annulus. The non-smooth curve is a result of the increased resolution of the mesh for curved corners. An interesting spike occurs at ~62.38 mm which is not seen for sharp cornered geometries.

At room temperature, peak wall current densities for pure water have been presented in Table 7.3. Robertson [89] has reported that electrokinetic current densities on the order of 1 $A.m^{-2}$ have been estimated for water flowing at 10 $m.s^{-1}$ and a ζ-potential of 300 mV, however using a smaller ζ-potential (based on the ζ-potential of magnetite in mildly basic conditions [108,109]) the peak current density has be shown to have a significantly higher value.

Table 7.3 - Peak wall currents, calculated at the entrance and exit of a flow restriction, with sharp or curved corners (see Figure 7.3 and Figure 7.4). Inlet current density does not appear to be very sensitive to the filleted corner, but the outlet current density is, with values less than half those of the sharp cornered model.

Test	V_{bulk} ($m.s^{-1}$)	Flow Rate ($m^3.s^{-1}$)	Corner Radius (µm)	Peak Entrance i_w ($A.m^{-2}$)	Peak Exit i_w ($A.m^{-2}$)
1	8	2.26E-04	0	5.93	0.44
2	12	3.39E-04	0	9.07	0.96
3	16	4.52E-04	0	12.97	1.66
4	20	5.65E-04	0	16.71	2.47
5	8	2.26E-04	10	3.31	0.14
6	12	3.39E-04	10	7.38	0.37
7	16	4.52E-04	10	12.58	0.67
8	20	5.65E-04	10	15.13	1.14

7.2 Simulated Deposition Model

7.2.1 Geometry and Conditions

A more complex model which simulates the growth of a deposit through deformation of the mesh has also been built by the modelling consultancy Continuum Blue. The model is of similar geometry to the simpler model described in section 7.1, however the lengths of the inlet and outlet sections are different (an image of the geometry is seen in Figure 7.13)

This model is similar to the previous simpler models in that it uses the 2D axisymmetric modelling method, and is a RANS based k-ε turbulent flow model, however the particular physics packaged used here employs wall functions (discussed briefly in section 7.1). This is non-ideal, as the purpose of the models is to study the behaviour at the wall, but given that this model is extremely computationally intensive, it is a necessary approximation. Unlike previous simpler models, this model is time dependent rather than steady state, which means that the model will perform a series of set time iterations up to a specified limit.

The model was built to simulate the deposition of material at the entrance of the restriction based on variables known to affect the electrokinetically driven wall currents which are responsible for deposition. In section 2.3.6, it was shown that the wall currents are dependent upon the streaming current, which is dependent upon the velocity gradient at the wall (*i.e.*, the shear rate) which is a quantity that can be calculated by the model.

The model iterates through solving a given time step, determining local shear rate and comparing this to a preset value, above which the mesh will be deformed by a preset amount of 12.5 μm, a buildup rate estimated from the work of Brun *et al.* [18] and Guillodo *et al.* [19] by simply dividing the height of the deposits presented in their work by the experiment time. Once this iteration is solved and the mesh deformation applied, the model performs the next iteration based on the new geometry. Over time, the shift of shear rate maxima is expected to create the shape of deposition seen in the literature.

Several tests were run where the geometry of the corner radius was the primary variable at a flow rate of 2.376×10^{-5} $m^3.s^{-1}$ (1.426 $L.min^{-1}$). Attempts were made to simulate flow rates greater than this, however time to convergence was estimated at 50 days, and none of the runs were successful.

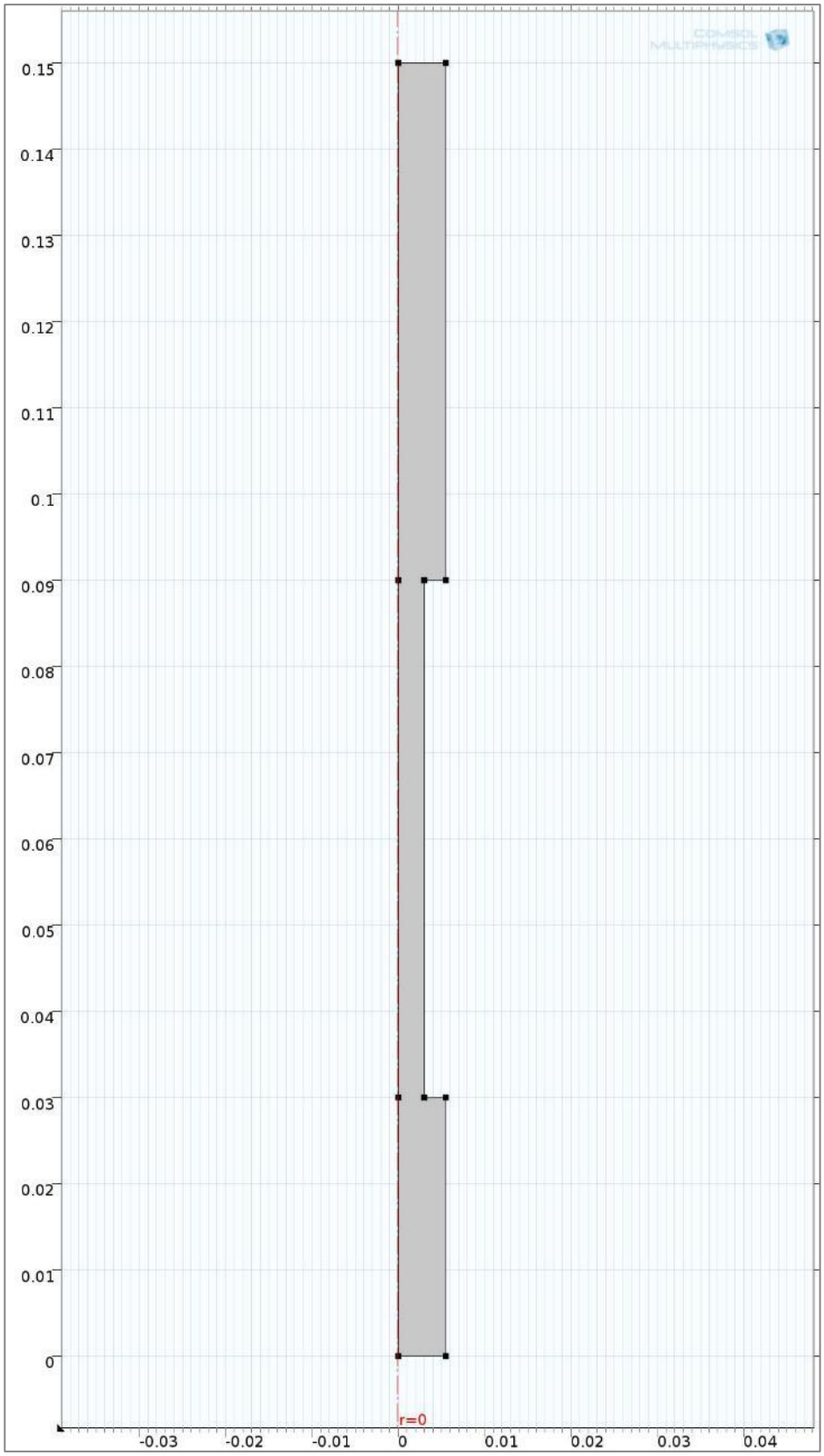

Figure 7.13 - The basic geometry of the deposition model, prior to mesh deformation during a test.

7.2.2 Results of the Simulated Deposit Model

The simulated deposition model was used to create estimates of the deposition shape based purely upon the shear rate and a deposition rate, derived from the work of Brun *et al.* [18], of 12.5 µm per day. A sweep of varying corner geometries was performed using sharp 90° corners (see Figure 7.14 and Figure 7.15), and filleted corners with radius between 50 and 250 µm (200 and 250 µm radius corners are shown in Figure 7.16 and Figure 7.17, Figure 7.18 and Figure 7.19).

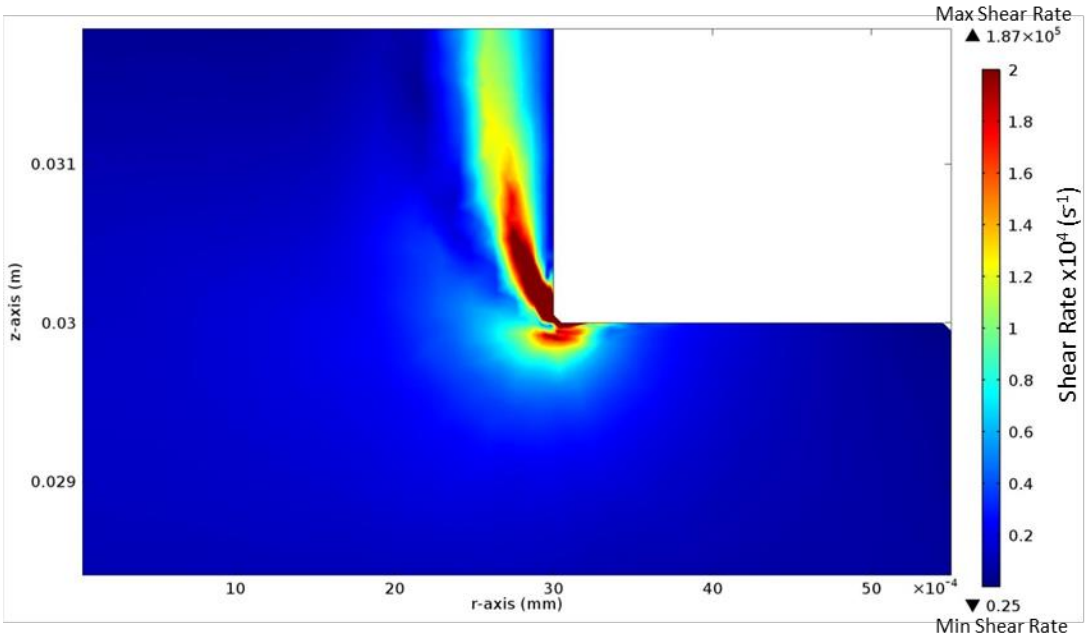

Figure 7.14 – Shear rate plotted on a two dimensional surface for a 50 µm rounded corner at t = 0 hrs. Due to the low resolution of the mesh (required to reach convergence within a reasonable time) the curve appears as a 45 ° angled chamfer.

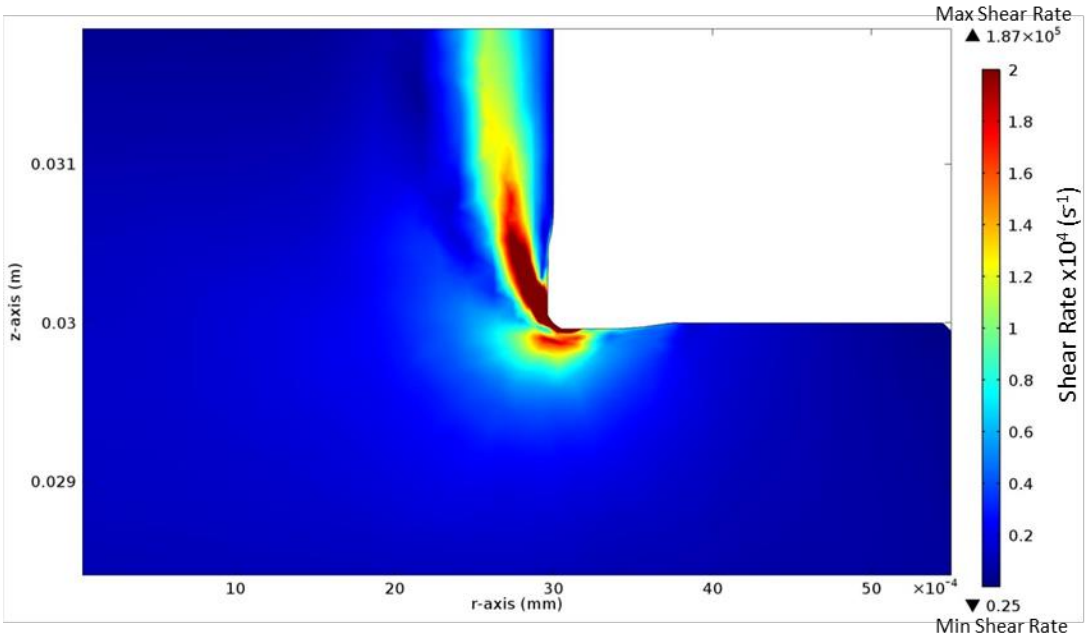

Figure 7.15 - Shear rate plotted on a two dimensional surface for a 50 µm rounded corner at t = 72 hrs. It can be seen that in the region of highest boundary shear rate, deposition has grown.

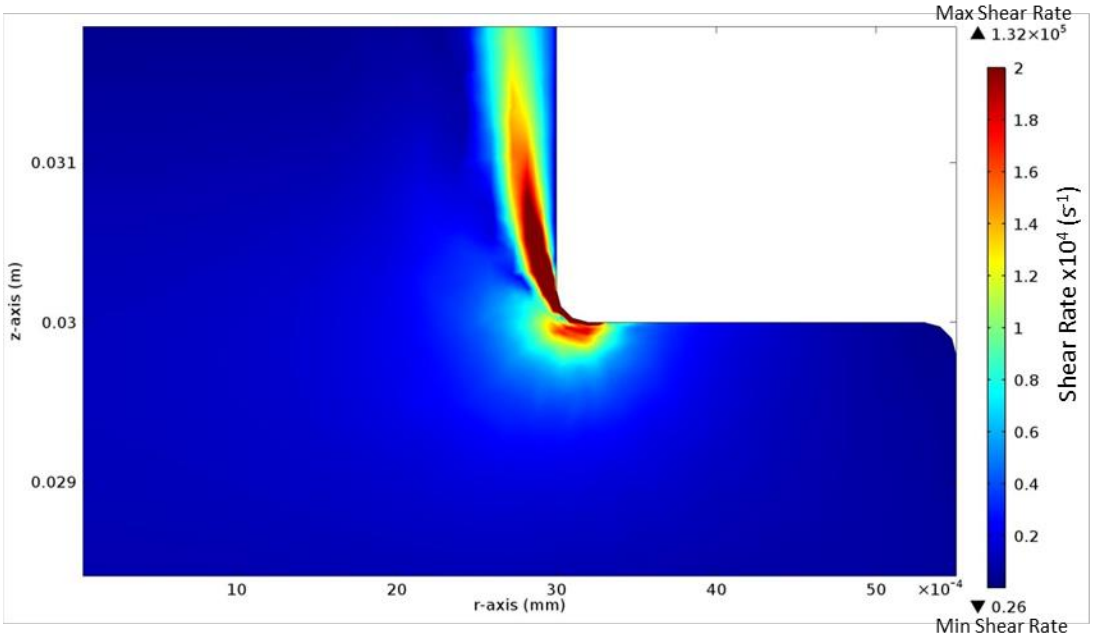

Figure 7.16 - Shear rate plotted on a two dimensional surface for a 200 µm rounded corner at t = 0 hrs. The size of the curvature is now great enough that the low mesh resolution does not obscure the curve.

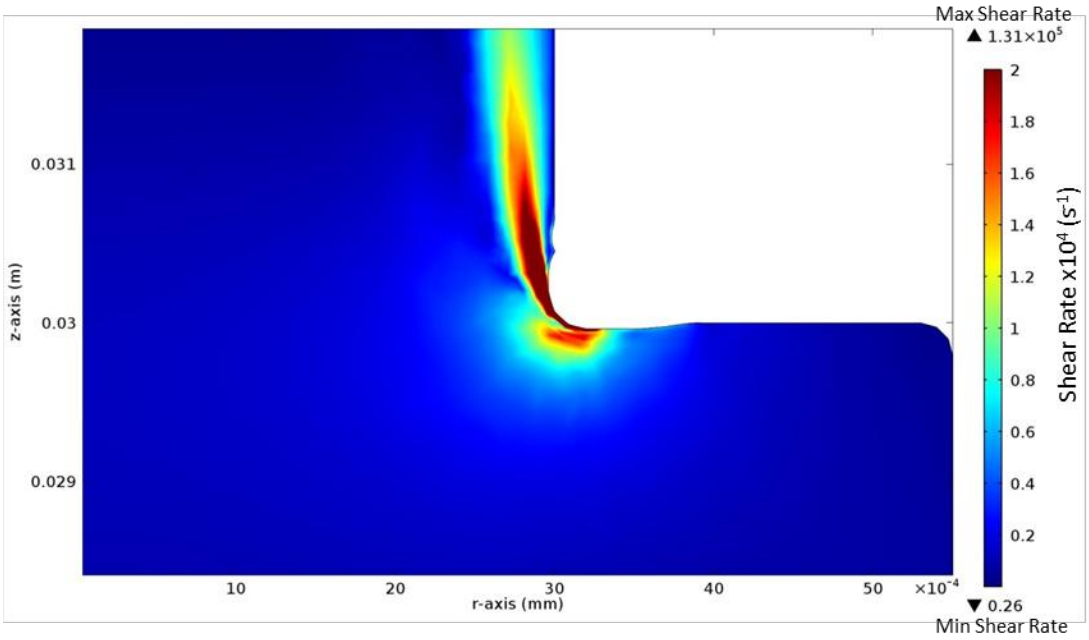

Figure 7.17 - Shear rate plotted on a two dimensional surface for a 200 µm rounded corner at t = 72 hrs. It can be seen that deposition has grown at the corner, and that shortly after the bulk of the desposit, a smaller bump has formed within the restriction annulus.

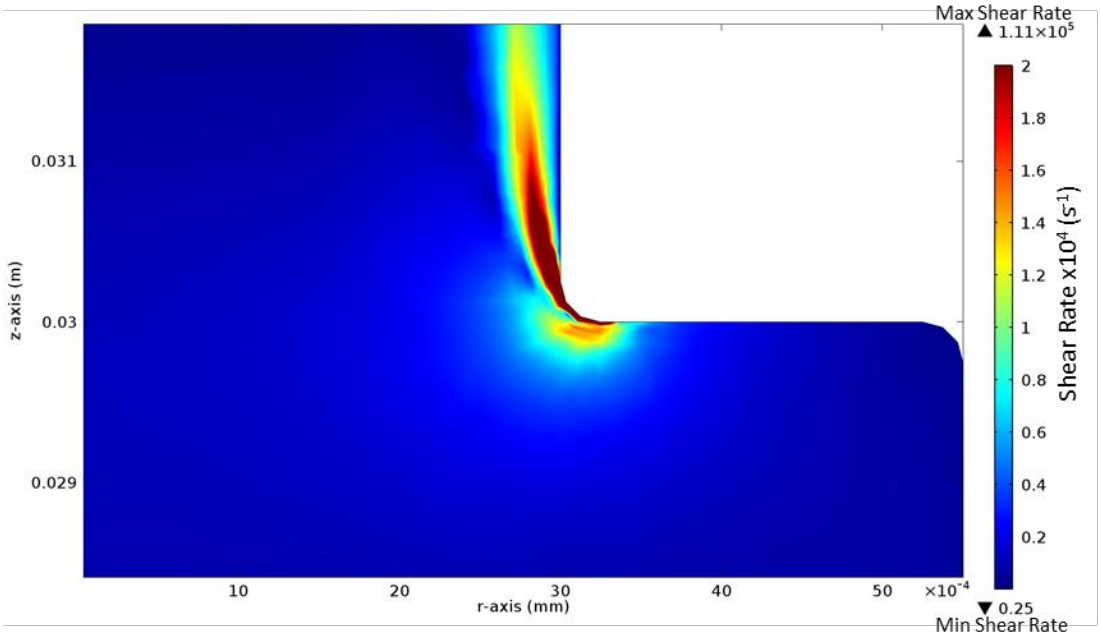

Figure 7.18 - Shear rate plotted on a two dimensional surface for a 250 µm rounded corner at t = 0 hrs.

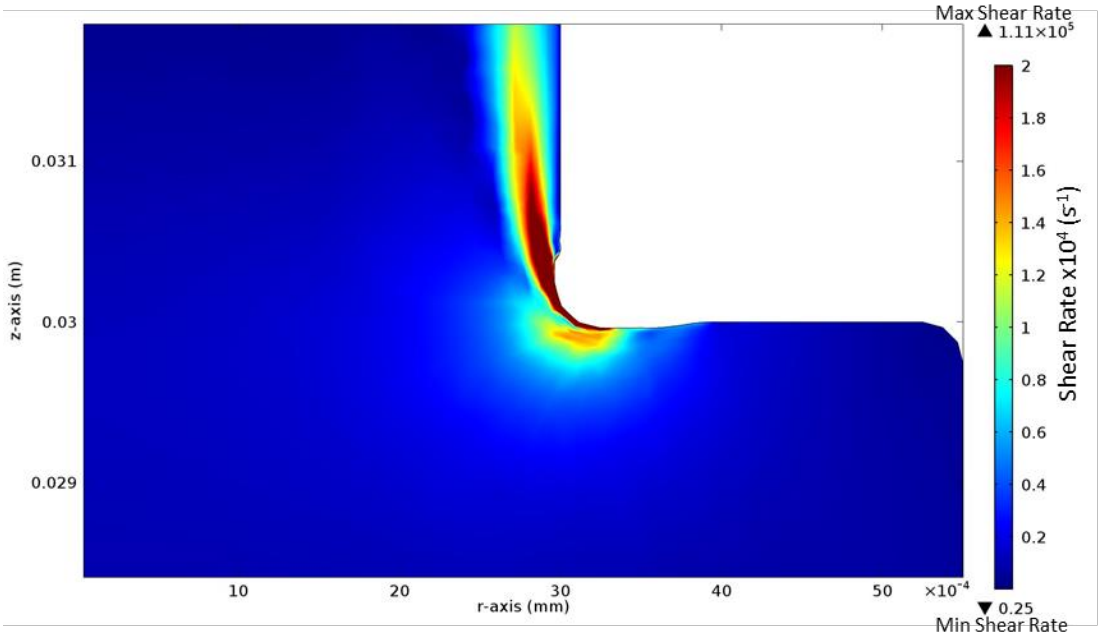

Figure 7.19 - Shear rate plotted on a two dimensional surface for a 250 µm rounded corner at t = 72 hrs. Deposition has grown at the corner, along with a small ripple just beyond the bulk of the deposition. Interestingly, the ripple size is smaller than that seen in Figure 7.17.

In each of the images, deposition has occurred at the location of greatest shear rate (*i.e.*, the corner of the restriction). There is an interesting change in the shape of deposition formed as the radius of the corner is increased. In the sharp cornered model, the deposition is simply an increase in the void volume (the domain outside of the meshed geometry) in all directions of the corner, while the 200 and 250 µm filleted corner models, the shape of the corner is visible but there is also a secondary bump shortly after the initial deposit. This rippled deposition is very similar to that suggested by the AREVA group's suggested mechanism of deposition propagation [19]. The absence of this rippled deposition effect in the sharp cornered model suggests that the model is not fully describing the deposition mechanism and will need further modification (see future work in section 8.2.4).

7.3 Discussion of Section D

Fluid dynamics models have been constructed to extract shear rate data at the boundary of a complicated geometry, which was used to calculate estimates of

streaming current and wall current density using the equations of Robertson [89] and McGurk [17] and a ζ-potential value of -5 mV, estimated from the work of Jayaweera [109]. It has been shown that the peak current density at the corner of the restriction can be on the order of in excess of 10 $A.m^{-2}$, though this depends directly on the actual system's ζ-potential and the shear rate.

Further, a time-dependent model to simulate deposition has been built. The model has been shown to produce the rippled deposit morphology seen in literature, however only does so where the radius of the corner is on the order of 200 μm, suggesting that the mechanism used by the model is incomplete. Were the model performing a perfect simulation of the electrokinetic deposition mechanism (and rippled deposits were a natural result of the simulation) the rippled deposition effect would be seen on all geometries rather than those with large corner curvatures. It is possible that this issue is an artifact of the manner in which the model had been built, *i.e.*, applying fixed rates and parameters rather that dynamic ones. It is also possible that the low resolution mesh simply did not allow for the appearance of the rippled deposition – a finer mesh can be run at the cost of increased time to completion.

These preliminary modeling studies outline the areas of interest which will be explored as part of an ongoing programme, which is discussed further in section 8.2.4.

7.4 **Conclusions for Section D**

The models designed and built here represent the first steps in the modelling of this phenomena. While previous work has attempted to model the deposition of material at the entrance of a fluid restriction, this has been largely based on the assumption that the deposition is particulate [23,202]. While this may be the case, a particulate deposition model does not account for any type

of electrochemical deposition, stimulated by the creation of a current by electrokinetic effects.

The models created in this work show were designed as a preliminary attempt to use available modelling software to calculate basic parameters that could be used in conjunction with the established theory of deposition, however it is clear that there is scope for a considerably more complex models to confirm or build upon the present theoretical basis.

Using a simple geometry allowed for the calculation of streaming rate based on the shear rate calculated for the geometry and on an idealized ζ-potential. Under the modelled conditions the peak current density was found to be between 5 and 20 $A.m^{-2}$, far in excess of the 1 $A.m^{-2}$ calculated by Robertson [89]. The difference between these values may be due to the improved resolution of the modelled values over the generalized equations used in Robertson's work to calculate shear rate.

The second part of this work involved solving a more complicated, yet still realistically simple model. The model was designed to change geometry after a fixed period of simulated time in response to a value of shear rate greater than a specified value. This simple method was shown to be able to grow a reasonable sized deposit after a simulated time of 72 hours, and in some cases was able to replicate the rippled deposition seen in some of the literature work [18]. The model is limited however, requiring enormous computing power to reach a solution for a simulated time of only 3 days, when real experiments could be run for a significantly longer period of time.

Further work to validate the results of calculations performed using the models output, and experimental work to confirm the basis in reality should be performed. Future work is discussed in section 8.2.4.

8 Summary and Conclusion

The central aim of this thesis has been to determine fundamental rate and equilibrium data which could be used for computational modelling of PWR primary coolant systems. In order to determine such parameters, equipment specifically designed for each study has been built for each of three main areas of study. Further, preliminary computer modelling has been undertaken, and the method shown to be valuable to the study of the deposition phenomena, though further work is required.

Overall discussion and conclusions from each part of this work is presented in section 8.1, and suggestions for future work are presented in section 8.2.

8.1 Overall Discussion and Conclusions of Present Work

The overall aims of this project were four fold:

i. Develop and test equipment for the replication of flow assisted, electrokinetically stimulated deposition.
ii. Develop and test equipment for the measurement of corrosion rate under high temperature and pressure water environments.
iii. Develop and test equipment for the measurement of the solubility of metal oxides.
iv. Test preliminary computer models for the simulation of the electrokinetic deposit phenomena.

Each of these areas of interest were selected for the specific purpose of developing the ability to provide various fundamental values on which computer models of a whole nuclear power plant could be based.

In section A, the study of electrokinetically stimulated deposition was not successful in demonstrating purely electrokinetic deposition, but did provide some initial information about an unexpected form of deposition, speculated

to be caused by cavitation at the entrance to the restriction. Section B focused on the corrosion of stainless steels in high temperature and pressure LiOH solutions, and demonstrated that the kinetics during the first 1,000 hours of exposure cannot be solely ascribed to parabolic corrosion kinetics, and instead that there is the potential to for the system to be a complex mix of kinetics. In section C, the solubility of metal oxides, primarily the metal oxides produced by corrosion of 316L stainless steel, were measured with success using once a purpose built system and cleanliness measures were instituted. Finally, section D detailed some preliminary work using the finite element modelling package COMSOL multiphysics to study the fluid dynamics of a modelling geometry identical to that of the section A test restriction, as well as novel model in which estimates of build-up rate from the literature were used to deform the mesh during simulated time steps.

This section seeks to draw together the final discussion and conclusions, along with suggestions for any future work derived from this project.

8.1.1 Section A: Flow Assisted Electrokinetically Stimulated Deposition

8.1.1.1 Discussion of Section A

In Section A: Chapter 4, the deposition of material at the entrance to a flow restriction was measured in a manner similar to that of the work published by Brun [18] and Guillodo [19–23]. In literature work, deposition of magnetite at restriction of various different materials was seen to occur under more highly oxidising conditions than would normally be found in a primary coolant circuit; addition of pH raisers and hydrogen were found to limit or prevent the deposition. In similar work performed by Scenini *et al.* [27] at the University of Manchester, depositions were seen to occur on micro-orifices in high purity

water solutions with added hydrogen, though the addition of 2 ppm LiOH led to no deposition being produced.

In this work, the most extensive depositions formed were found after conducting 'Run 5', during which feedwater had been prepared using high pressure nitrogen/hydrogen mix. The pressure used to prepare the water was equal to the back pressure of the system, which is thought to have led to a mechanism of deposition call 'flashing', where the pressure in the region of the restriction entrance is low enough that fluid becomes two phase. Dissolved or particulate matter passing through this region has deposited on the surface in wall-like structures. The differential pressure data gathered during this test (see Figure 4.26) shows unstable readings in both the differential pressure experienced across the test cell, and in the flow meter. The instability suggests that the flashing mechanism is rapid, causing deposits to appear quickly, but to become too large to support their size in the high velocity flow regime, at which point they are sheared from the surface and a new deposit begins to grow.

In tests 'Run 1' and 'Run 2' deposition was found to be very different from each other and from Run 5. In Run 1, the deposits appear as a dusting of material on the chamfered face at the edge of the restriction (see Figure 4.28) and a small deposit within the annulus itself (see Figure 4.31). The small size of this deposit explains the lack of any large change in the differential pressure measurement associated with the test (see Figure 4.19). In Run 2, the deposition is different again, and bears resemblance to the deposits seen in the work of the AREVA group [12] (see Figures 4.38 and 4.39). Again, the extent of the deposition was small, and there is no obvious change in differential pressure measurement associated with its presence (see Figure 4.20).

Perhaps most curious is the fact that none of the deposits were shown to be magnetite; instead the major components of all deposits was found to be

antimony (see Figures 4.30, 4.35, 4.44, and 4.45). Given that the deposit of Run 2 shows similarity in structure to that of the work done on the EMILIE loop, it is possible that the deposit was formed through the electrokinetic deposition mechanism, and that the mechanism does not discriminate between available ions.

The source of the antimony is unknown, though it is speculated that it is derived from flakes of graphite seals, which were used as gaskets for the autoclaves, valve packing, and the main seal of the pump. Time limitations did not allow for the determination of source, though this should be considered a crucial part of any future work using the equipment.

8.1.1.2 Conclusions of Section A

It is possible that the hot loop demonstrated electrokinetic deposition during the operation of Run 2, however with the present data sets it is not possible to make this statement with certainty. What can be stated with is that the hot loop has demonstrated that excessive gas concentrations will lead to deposition at flow restrictions, and that that mechanism of deposition will not be limited to iron-based oxides if there are other available ions in solution or suspended particles. While this is not the mechanism of deposition that was the primary area of interest for this project, it is nonetheless valuable to have identified this mechanism as a possible source of undesirable deposition in future testing.

8.1.2 Section B: Corrosion Kinetics of 316L Stainless Steel in High Temperature Water

8.1.2.1 Discussion of Section B

In Section B: Chapter 5, the corrosion behaviour of stainless steel was studied in high temperature and pressure aqueous solutions as a function of surface finish, temperature and chemistry.

Preliminary experiments (detailed in section 5.1 and 5.2) were performed by submerging small coupons of ground or electropolished 316L in pH 9.5 and 10.5 LiOH solutions, at temperatures of 200, 250 and 300 °C for approximately 300 hours. The mass of alloy oxidised during these tests was estimated from XPS-AIM and the use of confocal microscopy, and assuming parabolic kinetics (due to their wide spread use in the literature [28,31,90,119,133]), rate coefficients were calculated.

While this method provided some useful information about the rate of corrosion of the alloy under the given conditions, it was prone to enormous error (~38 %), and the assumed kinetics were later shown to not be necessarily correct. The quality of the XPS-AIM data used (see section 5.2.2) is also in question due to the prolonged presence of the oxygen peak throughout the composition depth profile, extending into the base metal passed the point where there are metal oxides for the oxygen to be associated with. It is postulated that the XPS-AIM may have contained oxygen due to either incomplete vacuum of the samples (and thus remnant adsorbed air/moisture still upon the surface), or perhaps the presence of deposited LiOH on the surface which could explain the lack of a metal signal to account for the oxygen (the Li1s peak is obscured by the iron peaks).

In the second part of the section, an improved method was conceived, and new equipment was designed and built to address the shortcomings of the preliminary experiment.

In this method, careful gravimetric descaling of samples from each of up to four time points was carried out, which provided a significantly improved estimate of the mass of alloy oxidised over that of the XPS-AIM method, resulting in significantly smaller errors, and a greater volume of data to work with.

The corrosion kinetics, originally assumed to be parabolic based on literature experience, were found to fit parabolic kinetics for rough surfaces, but

smoother surfaces were found to fit better with logarithmic kinetics. Literature suggests that oxidation of surfaces can proceed via logarithmic kinetics during the initial stages of corrosion (during which a protective oxide film less than 100 nm thick is formed) before becoming parabolic in nature once the film has become thick enough for diffusion to dominate the ion transfer kinetics. It is possible that the smoother surfaces in this experiment are acting to postpone the switchover point between logarithmic and parabolic kinetics. However it may also be that error in the data that has given a spuriously improved fit for the logarithmic kinetics – after all, it should be noted that each of the coupons was finished individually by hand which has very likely introduced a great deal of variation between the surfaces of each sample set. In order to deconvolution the true effect of surface finished on corrosion kinetics from the variation in surface introduce by manual grinding, it would be advisable to start with a sheet of material finished to a particular standard by machine.

Further to the gravimetric descaling analysis, SEM-EDX analysis of cross-section sectioned showed that the thickness of the inner oxide layer of the samples varied between 0.5 and 1 μm, however these estimates are based on the EDX data which is problematic due to the interaction volume of the electron beam being as large as the film is thick. Nonetheless, it was possible to see that there are clearly two distinctly different layers of composition; the iron rich outer layer and the comparatively chromium-rich inner layer. The oxidation states present in these layers were confirmed by XPS-AIM, and it can be seen that the outer layer is practically pure magnetite while the chromium is present as a Cr^{3+} species in the presence of magnetite-like binding energy peaks, suggesting the presence of non-stoichiometric iron chromite, as is predicted by the literature [28,29,31,35,36,90,119,121,122,136,137,140,150,151]. The thickness of the layer was not fully explored with XPS-AIM in the second set of experiments, as the film was significantly thicker than expected, and available

time on the spectrometer did not permit complete milling through to the base metal.

8.1.2.2 Conclusions for Section B

This section of the work was focused on determining a method for determination of corrosion rates of stainless steel in a PWR primary coolant-like environment. The technique was shown to be able to produce reasonably consistent corrosion rate data for 316L stainless steel in LiOH solutions at 300 °C, and the data has been provided to Rolls-Royce plc as fundamental constants computer modelling of a whole plant.

There still remain some questions about the validity of the parabolic or logarithmic corrosion kinetics, as the variation in oxidised alloy mass from sample to samples could be a result of the surface finish of the material. Further investigation of the kinetics is required to determine the true kinetics at any given time; section 8.2.2 details some suggestions for the improvement of the experimental method for future work.

8.1.3 Section C: Metal Oxide Solubility Measurements

8.1.3.1 Discussion of Section C

Section C: chapter 6 details the efforts made in this project to measure the solubility of metal oxides in high temperature LiOH solutions. Preliminary experiments were performed using an autoclave which contained samples of pure magnetite powder. Samples of water were extracted from the system once it has reached temperature, and analysed using GFAAS. This method was found to produce results scattered across a wide range of concentrations, and it was quickly determined that this was not an ideal method for this work.

In the second part of this work, a rig was designed and built specifically to provide a flowing environment where chemistry would be constantly

refreshed and samples could be taken without disturbing the metal oxide specimen within the rig. The metal oxide specimen in these experiments was simply the metal oxides produced by corrosion of the rig wetted components, and so the solubility of each of the various components of the alloy were measured using ICP-MS instead of GFAAS. Cleanliness procedures were also included in preparation of the tubes and handling of the samples to ensure that the tiny levels of metals in the samples was not masked by the introduction of contaminants.

As a result of these changes in operational procedure, the results produced by the rig were often close to the accepted values produced for the solubility of the pure metal oxides (see section 6.6.1). In addition, the sub-saturation solubility of the minor alloying components molybdenum and manganese were found to exhibit extreme sensitivity to pH; in the case of manganese, this manifest as a near zero concentration when exposed to $pH_{25\,^{\circ}C}$ 11 LiOH solution, but between 5 and 40 ppb when the chemistry was changed to $pH_{25\,^{\circ}C}$ 9. SEM-EDX analysis was also carried out on cross sections of the tubing, which confirmed the presence of the expected iron rich outer layer and chromium rich inner layer.

8.1.3.2 **Conclusions for Section C**

The method described has successfully demonstrated that the solubility of metal oxides in solution can be measured at the very low equilibrium concentration shown in literature using a reasonably simple stainless steel rig. The data has been provided to Rolls-Royce to provide additional data to for their modelling purposes.

While the use of a corroding alloy as the main material of construction will not allow for the measurement of solubility of any pure metal oxide, it does allow

for the measurement of concentrations of the mixed metal oxide's solubility in high temperature LiOH solution.

Further experiments using a larger mass and surface area of metal oxide source should be used to extend these studies and to study the effect of pH on the system more closely, though these suggestions for further work are discussed in greater detail in section 8.2.3.

8.1.4 Section D: Finite Element Modelling of Flow Assisted Deposition Mechanism

8.1.4.1 Discussion of Section D

In Section D: Chapter 7, some basic computer modelling work was started as a means to study its potential use for the modelling of the deposition phenomena. Two models were produced. First, a simple model based on the geometry of the hot loop test restriction, which was used to extract the shear rate for rudimentary estimation of the wall current density required by Robertson and McGurks theory of deposition (see section 2.3.6). The second model, produced by modelling consultancy Continuum Blue, was designed to simulate the deposition through the deformation of the mesh by a fixed amount in response to a shear rate above a critical value.

In the first model, the extraction of shear rate at different flow velocities and at varying resolutions showed that a shortcoming in the theory presented by McGurk [17], in that the shear rate was not correctly calculated in the region of the flow restriction entrance. McGurks theory suggests that the shear rate is a critical factor in the deposition behaviour, and computer modelling has provided the ability to determine this variable with reasonable accuracy and resolution. Using the global maximum value of shear rate (which was located at the entrance to the restriction), and an idealized ζ-potential based on the work of Jayaweera *et al.* [203], a wall current in excess of 10 $A.m^{-2}$ was estimated,

which is an order of magnitude greater than that estimated by Robertson [89]. The use of simple models to extract important fluid dynamic information for inclusion in the electrokinetic deposition theory could be of great value, and further work is recommended in section 8.2.4.

Further to the simple model, simulation of the deposition was performed using the model constructed by Continuum Blue. This model was able to simulate deposition over the course of 72 hours of simulated time, and predicted the build-up based on the value of shear rate at any given location. The corners of the restriction were filleted to improve the chances of the model reaching convergence, and it can be seen that at large fillet radii a small amount of secondary deposition occurs, reminiscent of the rippling seen in literature depositions [18].

8.1.4.2 Conclusions for Section D

The finite element modelling performed in this work is a very brief study of the potential for the use in further studies, however modelling has been shown to be a very rapid and powerful tool when used correctly and coupled with appropriate theory. There is a great deal of room for expansion on the work done in this thesis, and some suggestions are presented in section 8.2.4.

9 Future Work of Programme

The work described in this thesis is an ongoing program and development of all equipment is also a continuing process. While many improvements have been thought of, a selection have been presented here as they are of highest priority.

9.1.1 Electrokinetically Stimulated Deposition Programme

The Hot Loop is a complicated and challenging device to operate, and would benefit greatly from several improvements before the continuation of any experimental programme. Mundane repairs of currently out of service items – most notably the hot loop autoclave heaters - are essential, otherwise the maximum operating limits of the system are greatly reduced.

The substitution of all valve packing and seals which use graphite is highly recommended. These seals are most likely impregnated with antimony, which has been a major contaminant throughout this project. Any valve packing can be replaced with PTFE packing, however any valve exposed to fluid above 280 °C should be removed entirely if possible. Graphite gaskets can be replaced with compressible metal seals such as copper gaskets, however gold seals are recommended over copper, as they inert in high temperature water.

Leakage in the hot loop tube work is centered on the test cell, where the cell must be fitted manually into position, and the flanges sealed around the gasket by hand. It is exceptionally difficult to seal the cell reliably, due to the fact the cell must be perfectly in line with the connecting flanges which it often is not. The cell flanges should be substituted with a Swagelok fitting based system. This would require a section of tubing be replaced elsewhere to provide the necessary geometric clearance, however this method would be a significant improvement in reliability over the current method.

With these repairs and improvements, the hot loop would be well equipped to begin a new test series. Such a test series should be focused on determining the mechanism of deposition firstly, under ultrapure deoxygenated water using Alloy 600 (which is highly susceptible to deposition) as a reference against which other materials can be compared. This programme could then be extended to study the effects of LiOH addition and of dissolved hydrogen content.

The current method of chemistry control is limited in that there is only control of what goes into the system at the very beginning of the test, and no control of the chemistry while online. To remedy this, it is suggested that an online chemistry control system be developed and implemented to control the pH of system and the concentration of dissolved hydrogen. Such a system should have a constant feedback loop from pH and orbisphere probes which control metering pumps to inject LiOH stock solution and increase (or decrease) the quantity of hydrogen present in solution. Electrochemical potential and conductivity measurements would provide additional information regarding the chemical state of the system.

A further feedback control system which would be advantageous, would be one which controls the pump power in relation to flow rate. Instead of manually controlling the pump power, a feedback loop would ensure that the flow rate of the system remain constant throughout the experiment. The result of this would be that deposition behaviour would manifest as an increase in differential pressure across the cell, in same way such depositions have been measured in the literature.

Finally, as this test program seeks to show a direct relationship between electrokinetic streaming current and deposition, development of an electrochemically instrumented test cell is of great interest. Construction of

such a cell has been hampered in the past due to the challenge presented by operating at high temperatures and pressures.

9.1.2 Corrosion Rate Programme

The corrosion rate rigs have been shown to be successful in providing the required environment for high temperature aqueous corrosion. However, in order to accurately simulate primary coolant, a facility must be built to provide dissolved hydrogen.

Dissolved hydrogen gas is a dominant controlling factor in the system electrochemical potential, and as such it is a controlling parameter in the corrosion of materials under primary coolant chemistry conditions. Such a facility is presented in Figure 9.1, which has been named the 'hydrogen bubbler'. The device draws preconditioned (degassed of oxygen, chemically modified) water into the vessel via a metering pump, and bubbles hydrogen through the liquid. The pressure of the vessel is proportional to the concentration of gas in solution, so the vessel possess a variable backpressure regulator to control pressure between 0.5 and 1 bar. The hydrogen is safely disposed of using a catalytic burner to produce water as the byproduct.

With hydrogen control, the experimental program can be more confident in the validity of the data produced by testing. The experimental program such seek to continue to determine the effect of surface pre-treatment (particularly electropolishing) on corrosion rates for stainless steels, and perhaps extend to study other reactor relevant materials, such as nickel based alloys. An interesting effect noted during these tests, and the Metal Oxide Solubility tests, was the behaviour molybdenum in 316L stainless steel, which seemed to play no role in the passivation of the alloy. Surface chemistry analysis of the stainless steels in these tests has only been followed to very small extent; more extensive XPS-AIM studies are recommended, along with the use of other

techniques, such as Time of Flight-Secondary Ion Mass Spectrometry (ToF-SIMS).

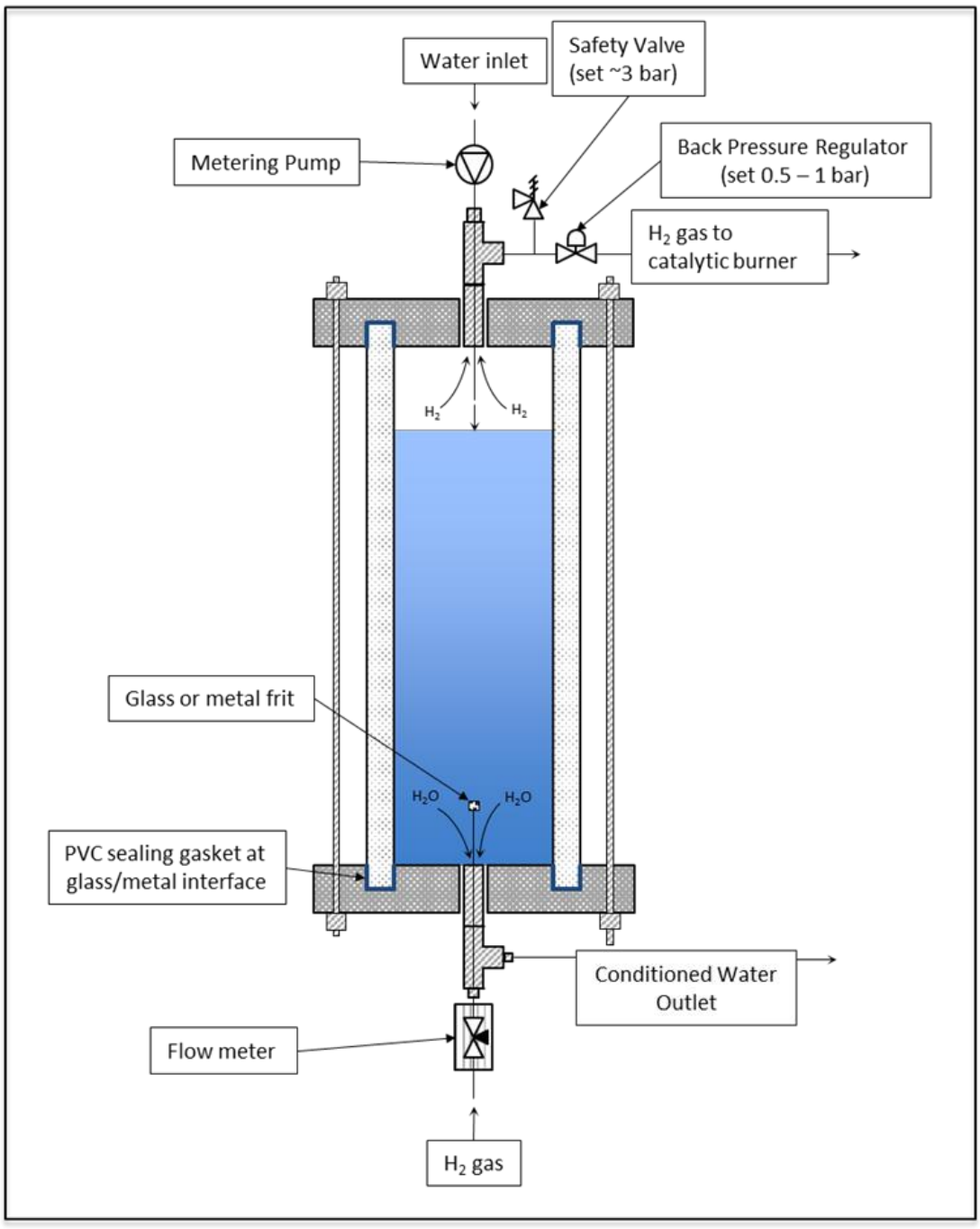

Figure 9.1 – Sketch of the 'hydrogen bubbler'.

As has been discussed previously, the kinetics of oxide film formation are not necessarily in line with the literatures assumption of parabolic corrosion kinetics. An improved fit was found for some of the data shown in section 5.5.1 using the logarithmic rate law, however the question of whether this is a true

effect or just the result of variation in surface finish due to manual grinding remains. This should be addressed using samples cut from a sheet which has been finished by machine to a standardized finish, and a study of different time scales (such as 0 – 100 hours and 0 – 2000 hours with four time points in each study) should be conducted to try to determine if logarithmic kinetics act at one time before switching over to parabolic.

Finally, during this project it was found that corrosion release mass (*i.e.*, the mass of corroded alloy dissolved into test solution), and thus release rate, could not be determined by the gravimetric descaling method developed to study corrosion rate. This was likely due to the precipitation of corrosion products from elsewhere in the system on the test coupons. Without substituting all rig materials for inert materials, such as titanium, this problem will persist and another method to determine release rates must be developed.

The construction of an inert surfaced rig for the Metal Oxide Solubility work (see section 9.1.3) provides an opportunity for accurate determination of corrosion release rate, as such a rig would have no extraneous dissolve ions in the water. Sample coupons of known surface area and mass could be exposed for long term experiments and released metal ions could be studied by ICP-MS analysis of the outlet water and by the suggested ion exchange column method. At the conclusion of the test, the samples could be gravimetrically descaled to determine retained corroded alloy, and one coupon could be examined by other methods, such as XPS, SEM, and possibly Laser Ablation ICP-MS.

9.1.3 Metal Oxide Solubility Programme

In a similar vein to the corrosion rate experiments, the solubility of corrosion products is dependent upon dissolved hydrogen concentration. It is highly recommended that the same hydrogen control system as that which should be

implemented on the corrosion rate rigs, also be fitted to the metal oxide solubility rigs.

It is also very apparent that the system current in place cannot be used to study the solubility of pure metal oxides, as the rig components are composed of stainless steel. The next logical step in this programme would be to eliminate all components with wetted surfaces that are not inert to high temperature aqueous corrosion. The use of titanium components for this new system is recommended, however care must be taken to condition the surfaces with a titania layer which would provide the inert surface. It would be prudent to perform studies of water content on this rig to ensure that background metal ion levels are well characterised prior to commencement of real testing.

An improvement in analytical efficiency could be provided by the introduction of an ion exchange column at the outlet of the rig. Currently, rig water is either collected for sampling or disposed of. The waste water could instead be run through an ion column where the dissolved ions would be extracted. At the end of the test, the column would be eluted and the concentration of dissolved ions from the total volume of waste water could be determined by ICP-MS, or potentially by atomic absorption spectroscopic methods. This would provide a secondary source of solubility information to supplement the current ICP-MS measurements.

9.1.4 **Computer Modelling**

Work on fluid dynamic modelling in this project represents the basis of a continuing programme of computer modelling of electrokinetically stimulated deposition, and other related phenomena.

It is advised that the time dependent deposition model (see section 7.3) be studied to find possible methods to streamline to the computation, as high flow rate models require significant periods of time to reach completion. It would

also be advised that models of this type be computed using a supercomputer cluster.

It is also advised that the work on simple fluid dynamic models be continued, however with a focus of improving the calculation of streaming current and wall current at the entrance to the flow restriction; validation of such models could be done should the hot loop test cell be instrumented to measure these variables.

Further to these models, it may be possible to construct ab initio atomistic models of the electrical double layer, which could provide a great deal of information regarding the mechanism of deposition that could not other be elucidated.

Bibliography

[1] N. I. Kolev, "10. Pipe Networks," in *Multiphase Flow Dynamics 5: Nuclear Thermal Hydraulics*, 2nd ed., New York, NY: Springer, 2011, pp. 852.

[2] B. Alexandreanu et al., "Stress Corrosion Cracking in Nickel-Base Alloys 690 and 152 Weld in Simulated PWR Environment.", U.S.NRC, Argonne, IL, NUREG/CR-7137, 2009

[3] International Atomic Energy Agency, *Nuclear Power Reactors in the World - Reference Data Series No. 2*, 2014 Edition, Vienna, Austria: IAEA, 2014, pp. 79.

[4] M. Schneider and A. Froggatt, *The World Nuclear Industry Status Report*, Paris, London, Washington D.C.: Mycle Schneider Consulting, 2014, pp. 159.

[5] J. Deshon, D. Hussey, and B. Kendrick, "Pressurized water reactor fuel crud and corrosion modeling," JOM J. Miner. Met. Mater. Soc., vol. 63, no. 8, p. 64, pp.64 – 72, 2011

[6] EPRI, "MULTEQ Version 4.0 Desktop Application." 2006.

[7] R. W. Staehle and J. A. Gorman, "Quantitative Assessment of Submodes of Stress Corrosion Cracking on the Secondary Side Steam Generator Tubing in Pressurised Water Reactors: Part 1," Corrosion, vol. 59, no. 11, pp. 931 – 993, 2003,

[8] United States Nuclear Regulatory Commission, "NRC File Photo".

[9] R. W. Staehle, "Anatomy of Proactivity," in Proceedings of the International Symposium of Aging Management of LWRs (The 15th Anniversary of INSS), Fukui, Japan, 2008, pp. 29 – 115

[10] B. J. Connolly, "Lecture Notes: Nuclear Materials Module, University of Birmingham." 2014.

[11] M. Guillodo *et al.* "Singular Deposit Formation in PWR due to Electrokinetic Phenomena - Application to SG Clogging," in Sixth CNS International Steam Generator Conference on "Management of Real-Life Equipment Conditions and Solutions for the Future,", Toronto, Ontario, Canada, 2009, p. 16.

[12] Private Communications with Dr. Pierre Combrade n.d.

[13] International Atomic Energy Agency, *Coolant technology of water cooled reactors*, vol. 3 Vienna, Austria: IAEA, 1992, pp. 72

[14] EPRI, *PWR Primary Water Chemistry Guildlines*, vol. 1, Palo Alto, CA: EPRI, 1999, pp. 208

[15] EPRI, Modeling the Axial Offset of Two Cycles of a 900-MW Pressurized, Palo Alto, CA: EPRI, 2006, pp. 66

[16] J. Robertson, "Modelling of Corrosion and Corrosion Release in PWR Primary Circuits," in *Water Chemistry of Nuclear Reactor Systems*, Bournemouth, UK 1989, pp. 1 – 7

[17] J. C. McGurk, "Oxide Deposition in High Temperature Water Orifices" NNL, Culham, UK RR04008/06/10/01, 2011.

[18] C. Brun *et al.*, "Investigation on the Relation Between Pressure Drops and Fluid Chemical Treatment," in *Water Chemistry of Nuclear Reactor Systems*, Avignon, France, 2002, pp. 1 – 7

[19] M. Guillodo *et al.,* "Formation of Deposits in HT Water under High Velocity Conditions: a Parametric Study," in *Water Chemistry of Nuclear Reactor Systems*, San Francisco, CA, 2004, pp. 1 – 7

[20] M. Barale *et al.*, "Preliminary Laboratory Tests of Investigation on the Blockage Phenomena Observed on TSP of French SGs," in *Water Chemistry of Nuclear Reactor Systems*, Berlin, Germany, 2008, pp. 1 – 9

[21] M. Guillodo *et al.,* "Steam Generator Fouling Assessment by HT Zeta Potential Measurements of Bundle Materials," in *Water Chemistry of Nuclear Reactor Systems*, Berlin, Germany, 2008, pp. 1 – 9

[22] M. Barale *et al.,* "Secondary Side TSP Deposit Build-up: Lab Test Investigation Focused on Electrokinetic Considerations," in *International Conference on Nuclear Plant Chemistry*, Quebec, Canada, 2010, pp. 1 – 28

[23] M. Guillodo *et al.*, "Experimental and Numerical Study of Deposit Formation in Secondary Side SG TSP by Electrokinetic Approach," in *International Conference on Nuclear Plant Chemistry*, Paris, France, 2012, pp. 1 – 14

[24] I. S. Woolsey *et al.,* "Occurrence and Prevention of Enhanced Oxide Deposition in Boiler Flow Control Orifices," in *Water Chemistry of Nuclear Reactor Systems 5*, Bournemouth, UK, 1989, pp. 219 – 228.

[25] D. J. Morris and I. S. Woolsey, "Studies of Oxide Deposition in Boiler Flow Control Orifices," in *Water Chemistry of Nuclear Reactor Systems 7*, Bournemouth, UK, 1996, pp. 243 – 246.

[26] G. Palumbo, F. Scenini, and N. Stevens, "Electrochemical Studies of CRUD", University of Manchester, Manchester, UK, MPC/R/097, 2011.

[27] F. Scenini *et al.*, "Electro deposition of CRUD", University of Manchester, Manchester, UK, R115529, 2014.

[28] S. E. Ziemniak, M. Hanson, and P. C. Sander, "Electropolishing effects on corrosion behavior of 304 stainless steel in high temperature, hydrogenated water," Corros. Sci., vol. 50, no. 9, pp. 2465–2477, Sep. 2008

[29] B. Stellwag, "The Mechanism of Oxide Film Formation on Austenitic Stainless Steels in High Temperature Water," Corros. Sci., vol. 40, no. 2/3, pp. 337 – 370, 1998,

[30] D. Féron, E. Herms, and B. Tanguy, "Behavior of stainless steels in pressurized water reactor primary circuits," J. Nucl. Mater., vol. 427, no. 1–3, pp. 364–377 Aug. 2012,

[31] S. E. Ziemniak and M. Hanson, "Corrosion behavior of 304 stainless steel in high temperature, hydrogenated water," Corros. Sci., vol. 44, no. 10, pp. 2209–2230, Oct. 2002,

[32] R. Castelli, *Nuclear Corrosion Modelling*, 1st ed., Oxford, UK: Butterworth-Heinemann, an imprint of Elsevier, 2009, pp. 195

[33] J. T. Orr et al., "Effect of Electropolishing and Thermal Annealing on the Corrosion/Release Behavior of UNS N 06690, Paper No. 10246" in *NACE 2010 Conference & Expo*, San Antonio, Texas, 2010, p. 1 – 20

[34] X. Liu, X. Wu, and E. H. Han, "Influence of Zn injection on characteristics of oxide film on 304 stainless steel in borated and lithiated high temperature water," Corros. Sci., vol. 53, no. 10, pp. 3337–3345, Oct. 2011,

[35] X. Cheng *et al.*, "Investigation of oxide film formation on 316L stainless steel in high-temperature aqueous environments," Electrochmica Acta, vol. 56, pp. 5860 – 5865, 2011,

[36] S. Cissé, *et al.*, "Effect of surface preparation on the corrosion of austenitic stainless steel 304L in high temperature steam and simulated PWR primary water," Corros. Sci., vol. 56, pp. 209–216, Mar. 2012,

[37] S. Odar, R. Cowan, and J. Kysela, LCC6 Special Topic Report: Effect of Zinc in BWR and PWR/VVER on Activity Build-up, IGSCC and Fuel Performance, Mölnlycke, Sweden: ANT International, 2010.

[38] R. Riess and S. Odar, LCC-8 Special Topic Report, PWR/VVER Primary Side Coolant Chemistry, Volume II - Water Chemistry Tool to Mitigate the Concerns, Mölnlycke, Sweden: ANT International, 2012.

[39] C. Gustafsson *et al.*, "The influence of Fe and Zn addition upon activity build-up in BWR system piping," in *International Conference on Nuclear Plant Chemistry*, Paris, France, 2012, pp. 1 – 11

[40] G. Bohnsack, The solubility of magnetite in water and in aqueous solutions of acid and alkali. Essen, Germany: Hemisphere Publishing Corporation, a subsidiary of Harper & Row, Publishers, Inc., 1987, pp. 161

[41] K. S. Venkateswarlu, *Water Chemistry: Industrial and Power Station Water Treatment*, New Dehli, India: New Age International Pvt Ltd Publishers, 1996, pp. 152

[42] D. J. Wesolowski, S. E. Ziemniak, and L. M. Anovitz, "Solubility and surface adsorption characteristics of metal oxides," in Aqueous Systems at Elevated Temperatures and Pressures; Physical Chemistry in Water, Steam and Hydrothermal Solutions, D. Palmer, R. Fernandez-Prini, and A. Harvey, Eds. London, UK: Elsevier Ltd, 2004, pp. 493 – 595.

[43] L. S. Darken and R. W. Gurry, "The System Iron-Oxygen: I. The Wustite Field and Related Equilibria," J. Am. Chem. Soc., vol. 67, no. 8, pp. 1398 – 1412, 1945.

[44] L. S. Darken and R. W. Gurry, "The System Iron-Oxygen: II. Equilibrium and Thermodynamics of Liquid Oxide and Other Phases," J. Am. Chem. Soc., vol. 68, no. 5, pp. 798 – 816, 1946.

[45] W. T. Holser and C. J. Schneer, "Hydrothermal Magnetite," Geol. Soc. Am. Bull., vol. 72, pp. 369 – 385, 1961.

[46] M. A. Styrikovich, O. I. Martynova, and I. S. Kurtova, Therm. Eng., vol. 13, no. 7, p. 61, 1966.

[47] F. H. Sweeton, C. F. Baes, and G. H. Jenks, "Solubility of Fe_3O_4 in Dilute Acid and Base Solution up to 300 °C," Trans. Am. Nucl. Soc., vol. 12, no. 1, pp. 82 – 83, 1969,

[48] F. H. Sweeton and C. F. Baes, "The solubility of magnetite and hydrolysis of ferrous ion in aqueous solutions at elevated temperatures," J. Chem. Thermodyn., vol. 2, no. 4, pp. 479 – 500, Jul. 1970,

[49] G. R. Helz, "Hydrothermal Solubility of Magnetite," Ph.D Thesis, Dept. of Geology, Pennsylvania State University, PA, 1971.

[50] M. A. Styrikovich *et al.*, "The Solubility of Magnetite in Water at High Temperature, in a Reducing Medium," Teploenergetika, vol. 19, no. 9, pp. 127 – 130, 1972,

[51] P. R. Tremaine, G. R. Shierma, and R. Von Masscowa, "A calculation of gibbs free energies for ferrous ions and the solubility of magnetite in H_2O and D_2O to 300 °C," Thermochim. Acta, vol. 19, no. 287, pp. 1 – 28, 1977,

[52] P. R. Tremaine and J. C. Leblanc, "The solubility of nickel oxide and hydrolysis of Ni 2+ in water to 573 K," J. Chem. Thermodyn., vol. 12, no. 6, pp. 521–538, 1980.

[53] P. Tremaine and J. LeBlanc, "The Solubility of Magnetite and the Hydrolysis and Oxidation of Fe 2+ in Water to 300 °C," J. Solution Chem., vol. 9, no. 6, pp. 415 – 442, 1980.

[54] S. E. Ziemniak, M. E. Jones, and K. E. S. Combs, "Solubility and phase behavior of nickel oxide in aqueous sodium phosphate solutions at elevated temperatures," J. Solution Chem., vol. 18, no. 12, pp. 1133, 1989.

[55] S. E. Ziemniak, "Metal Oxide Solubility Behavior in High Temperature Aqueous Solutions," J. Solution Chem., vol. 21, no. 8, pp. 745 – 760, 1992.

[56] K. Dinov *et al.,* "Solubility of magnetite in high temperature water and an approach to generalized solubility computations," J. Nucl. Mater., vol. 207, pp. 266–273, 1993.

[57] S. E. Ziemniak, M. E. Jones, and K. E. S. Combs, "Magnetite Solubility and Phase Stability in Alkaline Media at Elevated Temperatures," J. Solution Chem., vol. 24, no. 9, 1995.

[58] S. E. Ziemniak, M. E. Jones, and K. E. S. Combs, "Solubility and Phase Behavior of Cr (III) Oxides in Alkaline Media at Elevated Temperatures," J. Sol, vol. 27, no. 1, pp. 33 – 66, 1998.

[59] S. E. Ziemniak and M. A. Goyette, "Nickel (II) Oxide Solubility and Phase Stability in High Temperature Aqueous Solutions," J. Solution Chem., vol. 33, no. 9, 2004.

[60] S. Ziemniak *et al.,* "Oxidative dissolution of nickel metal in hydrogenated hydrothermal solutions," Corros. Sci., vol. 50, no. 2, pp. 449–462, Feb. 2008.

[61] S. Dickinson *et al.,* "Solubility of Chromium (III) Oxide and Metal Chromates: Development of MULTEQ Models," in *International Conference on Nuclear Plant Chemistry*, Paris, France, 2012

[62] O. C. Ralston, "Iron Oxide Reduction Equilibria," U. S. Bur. Mines, Washington D.C., 1929, pp. 296 – 326

[63] P. H. Emmett and J. F. Schultz, "Equilibria in the System Fe-Fe_3O_4-H_2O-H_2 at 400, 500 and 600 °C," J. Am. Chem. Soc., vol. 55, pp. 1376 – 1389, 1933.

[64] R. Fricke, K. Walter, and W. Lohrer, "Uber die Beeinflussung des Gleichwichtes Fe/Fe_3O_4 mit H_2O/H_2 durch den physikalischen Zustand der festen Reaktionsteilnehmer," Zeitschr. Elektrochem., vol. 47, pp. 487 – 500, 1941.

[65] R. Fricke and S. Rihl, "Zur Bestandigkeit des $Fe(OH)_2$," Naturwiss., vol. 31, pp. 326 – 327, 1943.

[66] EPRI, "MULTEQ: Equilibrium of an Electrolyic Solution with Vapor-Liquid Partitioning and Precipitation: The Database Version 7.0," Palo Alto, CA: EPRI, 2012.

[67] EPRI, "PWR Primary Water Chemistry Guidelines - Volume 2, Revision 4," Palo Alto, CA: EPRI, 1999.

[68] K. L. Murty and I. Charit, An Introduction to Nuclear Materials: Fundamentals and Applications, Oxford, UK: Wiley, 2012, pp. 398

[69] P. Beslu *et al.*, "Corrosion Ion Release from Stainless Steel and Higher Nickel Alloys Under PWR Conditions; Experimental and Theoretical Conditions," in *Water Chemistry of Nuclear Reactor Systems*, Bournemouth, UK, 1989.

[70] M. Tomlinson, "Transport of Corrosion Products," in *High Temperature High Pressure Electrochemistry in Aqueous Solutions*, NACE - 5, 1973, pp. 221 – 233.

[71] EPRI, "Update on Use of Enriched Boric Acid in Domestic Pressurized Water Reactors," Palo Alto, CA: EPRI, 2005.

[72] E. Michta, "Modeling of Subcooled Nucleate Boiling with OpenFOAM," M.S. thesis, KTH Royal Institute of Technology, Stockholm, Sweden, 2011.

[73] EPRI, "PWR Axial Offset Anomaly (AOA) Guidelines, Revision 1," Palo Alto, CA: EPRI, 2006.

[74] R. Castelli, *Nuclear Corrosion Modelling*, 2nd ed., Oxford, UK: Butterworth-Heinemann, an imprint of Elsevier, 2010, pp. 195

[75] IAEA, Current Trends in Nuclear Fuel for Power Reactors, Vienna, Austria: IAEA, 2006, pp. 1- 11

[76] D. H. Lister, "Nuclear Reactor Materials and Chemistry," in *Thermal Power Plants - Vol. II, Encyclopaedia of Life Support Systems (EOLSS)*, University of New Brunswick, Canada: United Nations Educational, Scientific and Cultural Organization, 2009, pp. 380

[77] EPRI, "PWR Primary Water Chemistry Guidelines," Palo Alto, CA; EPRI, 1986, pp. 198

[78] EPRI, "PWR Primary Water Chemistry Guidelines: Revision 1 (Research Project 2493)," Palo Alto, CA: EPRI, 1988, pp. 201

[79] EPRI, "PWR Water Chemistry Guidelines: Revision 2 (Research Project 2493)," Palo Alto, CA: EPRI, 1990, pp. 206

[80] EPRI, "PWR Primary Water Chemistry Guidelines: Revision 3 (Research Project 2493)," Palo Alto, CA: EPRI, 1995, pp. pp 206

[81] EPRI, "Multivariable Analysis of Effects of Li, Hydrogen and pH on PWR Primary Water Stress Corrosion Cracking," Palo Alto, CA: EPRI, 1996, pp. 76

[82] International Atomic Energy Agency, "Stress Corrosion Cracking in Light Water Reactors: Good Practises and Lessons Learned." Vienna, Austria: IAEA, Rep. NP-T-3.13, 2011

[83] A. Molander, "Comparison of PWSCC Initiation and Crack Growth Data for Alloy 600," in *International Conference of Nuclear Plant Chemistry*, Berlin, Germany, 2008.

[84] P. Andresen *et al.*, "Effect of H_2 on Migration of PWSCC in Nickel Alloys," in *International Workshop on Optimization of Dissolved Hydrogen*, Tohuku University, Sendai, Japan, 2007.

[85] A. Molander, "Online Electrochemical Monitoring in Light Water Reactor (LWR) Systems," in *Nuclear Corrosion Science and Engineering*, Oxford, UK: Woodhead, an Imprint of Elsevier, 2012, pp. 1072

[86] A. Molander, S. N. Ab, and S.- Nyköping, "Electrochemical Measurements in Nuclear Power Environments," in *IAPWS XV*, Berlin, Germany, 2008.

[87] H. Takiguchi, M. Ullberg, and S. Uchida, "Optimization of Dissolved Hydrogen Concentration for Control of Primary Coolant Radiolysis in Pressurized Water Reactors," J. Nucl. Sci. Technol., vol. 41, no. 5, pp. 601–609, May 2004.

[88] IAEA, "High temperature on-line monitoring of water chemistry and corrosion control in water cooled power reactors,", Vienna, Austria: IAEA, 2002, pp. 128

[89] J. Robertson, "Corrosion and Deposition due to Electrokinetic Currents," CEGB, Harwell, UK, Rep. TPRD/L/3030/R86, 1986.

[90] D. H. Lister, R. D. Davidson, and E. Mcalpine, "The Mechanism and Kinetics of Corrosion Product Release from Stainless Steel in Lithiated, High Temperature Water," Corros. Sci., vol. 27, no. 2, pp. 113 – 140, 1987.

[91] M. P. Unterweger, "Half-life measurements results at the National Institute of Standards and Technology," Appl. Radiat. Isot., vol. 56, pp. 125 – 130, 2002.

[92] R. A. Castelli, *Nuclear Corrosion Modelling*, 1st ed., Oxford, UK: Butterworth-Heinemann, an imprint of Elsevier, 2009, pp. 195

[93] F. Scenini, G. Palumbo, N. Stevens, A. Cook, and A. Banks, "Investigation of the role of electrokinetic effects in corrosion deposit formation," Corros. Sci., vol. 87, pp. 71–79, Oct. 2014.

[94] M. Vepsalainen, "Deposit formation in PWR steam generators," VTT, Espoo, Finland, Rep. VTT-R-00135-10, 2010.

[95] J. Bockris and A. Reddy, *Modern Electrochemistry 2*, New York, NY: Springer, 1973, pp. 623 – 1432

[96] A. J. Bard and L. R. Faulkner, *Electrochemical Methods: Fundementals and Applications*, Hoboken, NJ: Wiley & Sons, 2001, pp.833

[97] C. M. A. Brett and M. O. Brett, *Electrochemistry: Principles, Methods, and Applications*, Oxford, UK: Oxford University Press, 1993, pp. 464

[98] H. Helmholtz, "Studien über electrische," Grenzschichten. Ann Phys., vol. 7, pp. 337–82, 1879.

[99] D. Pletcher, A First Course in Electrode Processes, 2nd ed. London, UK: RSC, 2009, pp. 316

[100] D. C. Grahame, "The Electrical Double Layer and the Theory of Electrocapillarity," Chem. Rev., vol. 41, no. 3, pp. 441 – 501, 1947.

[101] M. J. Sparnaay, *The Electrical Double Layer*, Oxford, UK: Pergamon Press, 1972, pp. 658

[102] A. V. Delgado *et al.*, "Measurement and Interpretation of Electrokinetic Phenomena" Pure Appl. Chem., vol. 77, no. 10, pp. 1753–1805, 2005.

[103] C. Hamann, A. Hamnett, and W. Vielstich, *Electrochemistry*, Weinheim, Germany: Wiley VCH, 1998, pp. 423

[104] E. Dickinson, "Charge Transport Dynamics in Electrochemistry University of Oxford Charge Transport Dynamics in Electrochemistry," D.Phil Thesis, Dept. Chemistry, University of Oxford, UK, 2011, pp. 339

[105] J. Lyklema, "Fundamentals of Interface and Colloid Science, Vol I.," New York, NY: Academic Press, 1993, pp. 736

[106] R. J. Hunter, "Foundations of Colloid Science," Oxford, UK: Oxford University Press, 2001, pp. 820

[107] M. Smoluchowski, "Handbuch der Electrizität und des Magnetismus (Graetz), Vol II." Barth, Liepzig 1921, pp. 336

[108] P. Jayaweera and S. Hettiarachchi, "Determination of zeta potential and pH of zero charge of oxides at high temperatures," Rev. Sci. Instrum., vol. 64, no. 2, p. 524, 1993.

[109] P. Jayaweera, S. Hettiarachchi, and H. Ocken, "Determination of the high temperature zeta potential and pH of zero charge of some transition metal oxides," Colloids Surfaces A Physicochem. Eng. Asp., vol. 85, no. 1, pp. 19–27, Jun. 1994.

[110] J. C. McGurk, "Magnetite Deposition in High Temperature Water Orifices" NNL, Cullham, UK, Rep. RR05131/06/10/01, 2012.

[111] IUPAC, "Compendium of Chemical Terminology, 2nd ed. (the "Gold Book")," Oxford, UK: Blackwell Scientific Publications, 1997.

[112] J. C. McGurk, "Oxide Deposition in High Temperature Water Orifices," NNL, Cullham, UK, 2012.

[113] G. J. Bignold et al., "Erosion-corrosion in Nuclear Reactor Steam Generators," in *Water Chemistry of Nuclear Reactor System*, Bournemouth, UK, 1980.

[114] D. J. Finnigan, K. Garbett, and I. S. Woolsey, "The application of thin layer surface activation to the study of erosion-corrosion behaviour," Corros. Sci., vol. 22, no. 4, pp. 359–372, 1982.

[115] F. Scenini, J. Duff, N. Stevens, A. Cioncolini, A. Cook, and A. Banks, "Electrochemical and Microstructural Characterization of CRUD," in

International Conference on Nuclear Plant Chemistry, Sapporo, Japan, 2014, pp. 1–12.

[116] C. R. Clayton and I. Olefjord, "Passivity of Austenitic Stainless Steels," in *Corrosion Mechanisms in Theory and Practise,* London, UK: CRC Press, 2012, pp. 419 – 448.

[117] J. R. Davis, "ASM Speciality Handbook: Stainless Steel", Russell Township, OH: ASM International, 1994.

[118] C. P. Dillon, "Corrosion control in the chemical process industries", St. Louis, MO: Materials Technology Institute of Chemical Process Industries Inc., 1997, pp. 423

[119] J. Robertson, "The Mechanism of High Temperature Aqueous Corrosion of Stainless Steels," Corrosion, vol. 32, no. 4, pp. 443–465, 1991.

[120] B. Beverskog and I. Puigdomenech, "Pourbaix Diagrams for the Ternary System of Iron-Chromium-Nickel," Corrosion, vol. 55, no. 11, pp. 1077–1087, 1999.

[121] M. Warzee, J. Hennaut, M. Maurice, C. Sonnen, J. Waty, and P. Berge, "Effects of Surface Treatment on the Corrosion of Stainless Steels in High-Temperature Water and Steam," J. Electrochem. Soc., vol. 112, no. 7, pp. 670 – 674, 1965.

[122] R. Soulas, M. Cheynet, E. Rauch, T. Neisius, L. Legras, C. Domain, and Y. Brechet, "TEM investigations of the oxide layers formed on a 316L alloy in simulated PWR environment," J. Mater. Sci., vol. 48, no. 7, pp. 2861–2871, Nov. 2013.

[123] M. De Graff and M. E. McHenry, "Structure of Materials; an Introduction to Crystallography, Diffraction, and Symmetry" Cambridge, UK: Cambridge University Press, 2012, pp. 768

[124] J. F. Shackelford, "Introduction to Materials Science for Engineers" Upper Saddle River, New Jersey: Prentice Hall Inc., 1996, pp. 670

[125] J. R. Davis, "ASM Speciality Handbook: Stainless Steel", Materials Parks Campus, OH: ASM International, 1994.

[126] H. S. Khatak and R. Baldev, "Corrosion of Austenitic Stainless Steel", Cambridge, UK: Woodhead Publishing, 2002, pp. 385

[127] D. Talbot and J. Talbot, "Corrosion Science and Technology," 2nd Ed, London, UK: CRC Press 1998, pp. 552

[128] P. Marcus, Ed., "Corrosion Mechanisms in Theory and Practice", London, UK: CRC Press, 2012, 2002, pp. 941

[129] C. P. Dillon, "Corrosion control in the chemical process industries", St. Louis, MO: Materials Technology Institute of Chemical Process Industries Inc., 1997, pp. 423. 1997.

[130] H. H. Urlig, "Urlig's Corrosion Handbook", 2nd ed., Hoboken, NJ: John Wiley & Sons, Inc, 2000, pp. 1296

[131] V. Čihal, "Intergranular Corrosion of Steels and Alloys," New York, NY: Elsevier Science Ltd., 1984, pp. 378

[132] T. Thorvaldsson and A. Salwen, "Measurement of diffusion coefficients for Cr at low temperatures in a type 304 stainless steel," Scr. Metall., vol. 18, p. 739, 1984.

[133] J. Robertson, "The Mechanism of High Temperature Aqueous Corrosion of Steel," Corros. Sci., vol. 29, no. 11/12, pp. 1275 – 1291, 1989.

[134] T. Maekawa and M. Terada, "Infrared Study of Corrosion Products of Stainless Steel," J. Japanese Inst. Met., vol. 29, p. 421, 1965.

[135] J. M. Francis and W. H. Whitlow, "The Morphology of oxide film growth on AISI type 304 stainless steel in high temperature water at 300C and 350C," J. Nucl. Mater., vol. 20, p. 1, 1966.

[136] M. Warzee, C. Sonnen, and P. Berge, "Corrosion of Carbon Steels and Stainless Steels in Pressurized Water at High Temperatures," Eur. At. Energy Commission, 1967.

[137] T. Maekawa, M. Kagawa, and N. Nakajima, "Corrosion Behavior of Stainless Steels in High Temperature Water and Superheated Steam," Trans. Japanese Inst. Met., vol. 9, no. 130, 1968.

[138] T. Margulova *et al.*,, "Protective Oxide Film Formation on Mild Steel and High Temperature Magnetite Crystallization From Iron Chelate Solution," in *High Temperature High Pressure Electrochemistry In Aqueous Solutions*, Houston, TX, 1973, pp. 241 –244.

[139] A. J. Sedriks, "Corrosion of Stainless Steels" Oxford, UK: Wiley-Interscience, 1979, pp.464

[140] R. Bauch *et al.,* "Investigations on Oxide Formed In High-Temperature Water on Austenitic Steel," J. Nucl. Mater., vol. 92, pp. 334–344, 1980.

[141] D. Lister, E. Mcalpine, and W. Hocking, "The Release of Corrosion Products from Surfaces in the Primary Coolant and Systems of Light Water Reactors," in *Proceedings of the 43rd Meeting of the International Water Conference*, Pittsburg, PA, 1982.

[142] D. Lister, E. Mcalpine, and N. McIntyre, "The Release of Corrosion Products from Stainless Steel and Stellite to High-Temperature, Lithiated Water," in *Proceedings of the 3rd International Conference on Water Chemistry of Nuclear Reactor Systems*, Bournmouth, UK, 1983.

[143] R. C. Lobb and H. E. Evans, "An Evaluation of the Effect of Surface Chromium Concentration on the Oxidation of a Stainless Steel," Corros. Sci., vol. 23, no. 1, pp. 55 – 73, 1983.

[144] D. Lister *et al.*, "Corrosion Product Release in Light Water Reactors," Palo Alto, CA: EPRI, Rep. NP-6512, 1989.

[145] D. Lister, R. Davidson, and E. McAlpine, "The Compostion and morphology of Oxide Flims Formed on Type 304 Stainless Steel in Lithiated High Temperature Water," Corros. Sci., vol. 26, no. 8, pp. 563–576, 1986.

[146] H. Hanninen, M. Vulli, and W. H. Cullen, "Study of Corrosion Products on Fatigue Fracture Surfaces of Pressure Vessel Steels Tested in PWR Environments by Using X-Ray Photoelectron and Auger Electron Spectroscopies," in *Environmental Degradation of Materials in Nuclear Power Systems - Water Reactors*, Monterey, CA, 1988, pp. 289 – 299.

[147] G. O. Hayer *et al.*, "Examination of Tubes Removed From St. Lucie Unit 1 and Investigation of Causes of the Corrosion," in *Environmental Degradation of Materials in Nuclear Power Systems - Water Reactors*, Monterey, CA, 1988 pp. 449 – 456.

[148] E. Schuster, K. Neeb, W. Ahlanger, R. Henkelmann, and R. Jarnstrom, "Analysis of Primary Side Oxide Layers on Steam Generator Tubes from PWRs and Radiochemcial Issues on the Contamination of Primary Circuits," J. Nucl. Mater., vol. 152, pp. 1 – 8, 1988.

[149] P. Beslu *et al.*, "Corrosion ion release from stainless steel and higher nickel alloys under PWR conditions: experimental and theoretical conditions," in *Water Chemistry of Nuclear Reactor Systems 5*, Bournemouth, UK, 1989, pp. 77 – 80.

[150] Z. Szklarska-Smialowska, K. Chou, and Z. Xia, "The Composition and Properties of Oxide Films on Type 304 Stainless Steel on Exposure to Lithiated Water at 100-350C," Corrosion, vol. 32, no. 5, pp. 609–619, 1991.

[151] M. Da Cunha Belo, M. Walls, N. E. Hakiki, J. Corset, E. Picquenard, G. Sagonb, and D. Noel, "Composition, Structure and Properties of the Oxide Films Formed on the Stainless Steel 316L in a Primary Type PWR Environment," Corros. Sci., vol. 40, no. 2, pp. 447–463, 1998.

[152] F. P. Fehler, "Low Temperature Oxidation; the Role of Vitreous Oxides" New York, NY: J. Wiley & Sons, 1986, pp. 257

[153] J. Xu, X. Wu, and E.-H. Han, "The evolution of electrochemical behaviour and oxide film properties of 304 stainless steel in high temperature aqueous environments," Electrochimica Acta, vol. 71, pp. 219–226, 2012.

[154] M. Bojinov, P. Kinnunen, K. Lundgren, and G. Wikmark, "A Mixed-Conduction Model for the Oxidation of Stainless Steel in a High-Temperature Electrolyte," J. Electrochem. Soc., vol. 152, no. 7, p. B250, 2005.

[155] B. Beverskog, M. Bojinov, P. Kinnunen, T. Laitinen, K. Makela, and T. Saario, "A mixed-conduction model for oxide films on Fe, Cr and Fe-Cr alloys in high-temperature aqueous electrolytes - II. Adaptation and justification of the model," Corros. Sci., vol. 44, no. 9, pp. 1923–1940, 2002.

[156] I. Betova, M. Bojinov, P. Kinnunen, K. Lundgren, and T. Saario, "Mixed-Conduction Model for Stainless Steel in a High-Temperature Electrolyte: Estimation of Kinetic Parameters of Inner Layer Constituents," J. Electrochem. Soc., vol. 155, no. 2, pp. C81 – C92, 2008.

[157] L. F. Lin, C. Y. Chao, and D. D. Macdonald, "A Point Defect Model for Anodic Passive Films; II. Chemical Breakdown and Pit Initiation," J. Electrochem. Soc., vol. 128, no. 6, p. 1187, 1981.

[158] C. Y. Chao, L. F. Lin, and D. D. MacDonald, "A Point Defect Model for Anodic Passive Films; I. Film Growth Kinetics," J. Electrochem. Soc., vol. 128, no. 6, p. 1187, 1981.

[159] D. D. MacDonald, "The history of the Point Defect Model for the passive state: A brief review of film growth aspects," Electrochim. Acta, vol. 56, no. 4, pp. 1761–1772, 2011.

[160] D. D. Macdonald and M. Urquidi-Macdonald, "Theory of Steady-State Passive Films," J. Electrochem. Soc., vol. 137, no. 8, pp. 2395–2402, 1990.

[161] D. D. Macdonald, "The Point Defect Model for the Passive State," J. Electrochem. Soc., vol. 139, no. 12, p. 3434, 1992.

[162] N. Birks, G. H. Meier, and F. S. Pettit, "Introduction to the High-Temperature Oxidation of Metals," Cambridge, UK: Cambridge University Press, 2006, pp. 338

[163] A. S. Khanna, "Introduction to High Temperature Oxidation and Corrosion," Materials Park, OH: ASM International, 2002, pp. 325

[164] C. Wagner, "Beitrag zur Theorie des Anlaufvorgangs," Zeitschrift für Phys. Chemie, vol. B41, p. 42, 1933.

[165] N. Cabrera and N. F. Mott, "Theory of the Oxidation of Metals," Reports Oxid. Met., vol. 12, p. 163, 1949.

[166] E. Rau, "Corrosion of Type 304 Stainless Steel with Varying Carbon Content in Reference Primary Coolant Water," Bettis Atomic Power Laboratory, PA, Rep. WAPD-BT-3, 1957.

[167] M. C. Bloom, "A Survey of Steel Corrosion Mechanisms Pertinent to Steam Power Generation," in *Proceedings of the 21st Annual Meeting of the International Water Conference*, Pittsburgh, PA, 1960.

[168] Standard Guide for Electrolytic Polishing of Metallographic Specimens, ASTM E-1558 – 09, 2009.

[169] Standard Specification for the Passivation of Stainless Steels using Electropolishing, ASTM B912 – 02, 2002.

[170] S. E. Ziemniak and M. Hanson, "Corrosion behavior of NiCrFe Alloy 600 in high temperature, hydrogenated water," Corros. Sci., vol. 48, no. 2, pp. 498–521, Feb. 2006.

[171] S. Ziemniak and M. Hanson, "Corrosion behavior of NiCrFe Alloy 600 in high temperature, hydrogenated water," Corros. Sci., vol. 48, no. 2, pp. 498–521, Feb. 2006.

[172] J. R. Cooper and R. B. Dooley, "Release on the Ionization Constant of H_2O," Lucerne, Switzerland: IAPWS, 2007.

[173] C. E. Housecroft and A. G. Sharpe, *Inorganic Chemistry*, Edinburgh, UK: Pearson Education Limited, 2005.

[174] K. Mohajery, L. Deydier De Pierrfeu, and D. Lister, "The Dissolution Rate Constant of Magnetite in Water at Different Temperatures and pH Conditions," in *International Conference on Nuclear Plant Chemistry*, Paris, France, 2012

[175] G. Schikorr, "The iron (II) hydroxide and a ferromagnetic iron (III) hydroxide," Zeitschr. Anorg. Allg. Chemie., vol. 212, no. 1, pp. 33–39, 1933.

[176] M. A. Styrikovich, O. I. Martynova, I. F. Kobyakov, V. L. Men'Shikova, and M. I. Reznikov, "Solubility of Magnetite in Boiling Water of High Temperature," Teploenergetika, vol. 7, pp. 82–84, 1971.

[177] G. A. Kanert, G. W. Gray, and W. G. Baldwin, "The Solubility of Magnetite in Basic Solutions at Elevated Temperatures (AECL - 5528)," Pinawa, Manitoba, 1976.

[178] J. L. Mogollon, J. Ganor, J. M. Soler, and A. C. Lasaga, "Column experiments and full dissolution rate law of gibbsite," Am. J. Sci., vol. 296, pp. 729 – 765, 1996.

[179] T. Adschiri, K. Kanazawa, and K. Arai, "Rapid and Continuous Hydrothermal Crystalisation of Metal Oxide Particles in Supercritical Water," J. Am. Ceram. Soc., vol. 75, no. 4, pp. 1019 – 1022, 1992.

[180] T. Adschiri, K. Kanazawa, and K. Arai, "Rapid and Continuous Hydrothermal Synthesis of Boehmite Particles in Subcritical and Supercritical Water," J. Am. Ceram. Soc., vol. 75, no. 9, pp. 2615 – 2618, 1992.

[181] I. Lambert, P. Beslu, A. Lalet, and J. Montel, "Thermodynamique de Solubilisation de la Magnetite en Milieu Basique, Symposium Thermodynamics of Nuclear Materials," in Proceedings of International Atomic Energy Agency, 1979.

[182] G. Bohnsack, "Das Verhalten von Eisen(II)-hydroid bei höheren Temperaturen," VGB Mitt, vol. 4, pp. 328–338, 1971.

[183] C. E. Housecroft and E. C. Constable, *Chemistry*, Edinburgh: Pearson Education Limited, 2006.

[184] W. R. Busing and H. A. Levy, "Oak Ridge National Laboratory Report ORNL-TM-271,", Oak Ridge National Laboratory, Oak Ridge, TN, Rep. ORNL-TM_271, 1962.

[185] D. Bradbury, "The Chemical Dissolution of Fe(III) Oxide," in *International Conference on Water Chemistry of Nuclear Reactor Systems*, Bournemouth, UK, 1978, pp. 373 –376.

[186] X. Liu, "The solubility of iron hydroxide in sodium chloride solutions," Geochim. Cosmochim. Acta, vol. 63, no. 19–20, pp. 3487–3497, Oct. 1999.

[187] R. Levinson, *More Modern Chemical Techniques*, London, UK: RSC, 2001.

[188] C. Vandecasteele and C. B. Block, *Modern Methods for Trace Element Determination*, London, UK: Wiley, 1993

[189] Standard Test Method for Low-Level Dissolved Oxygen in Water, ASTM Standard D5543-09, 2009.

[190] G. N. Spokes, "Dissolved Oxygen in Water Measurements and Standardization," in EPRI PWR Plant Chemists' Meeting, 1992.

[191] F. Tuinstra and J. L. Koenig, "Raman Spectrum of Graphite," J. Chem. Phys., vol. 53, p. 1126, 1970.

[192] "Mechanical shaft seals for pumps," GRUNDFOS Management A/S, 2009.

[193] R. Harjula, A. Paajanen, R. Koivula, E. Tusa, and R. Kvarnström, "Removal of Antimony-124 from PWR Coolant Water," in *WM2009 Waste Management for the Nuclear Renaissance*, Pheonix, AZ, 2009, pp. 1–7.

[194] The University of Cambridge, "Slip in Single Crystals," DoITPoMS. [Online]. Available: http://www.doitpoms.ac.uk/tlplib/slip/intro.php.

[195] Standard Practice for Preparing, Cleaning, and Evaluating Corrosion Test Specimens," ASTM G1-03, 2011.

[196] Recommended Practice for Preparing, Cleaning and Evaluation of Corrosion Test Specimens, ASTM G1-67, 1971.

[197] D. Drouin, A. R. Courture, R. Gauvin, P. Hovington, P. Homy, and H. Demers, "CASINO." Université de Sherbrooke, Québec, Canada, 1999.

[198] "Private communications with Dr. Helen Brannon."

[199] T. Yamashita and P. Hayes, "Analysis of XPS Spectra of Fe^{2+} and Fe^{3+} Ions in Oxide Materials," Appl. Surf. Sci., vol. 254, no. 8, pp. 2441 – 2449, 2008.

[200] Sigma-Aldrich, "Nitric acid, ACS reagent, 70%." [Online]. Available: http://www.sigmaaldrich.com/catalog/product/sial/438073?lang=en&region=GB.

[201] J. Meija, "Isotopic compositions of the elements," Pure Appl. Chem., vol. in press, 2013.

[202] C. Henry, J.-P. Minier, and G. Lefèvre, "Towards a description of particulate fouling: from single particle deposition to clogging." Adv. Colloid Interface Sci., vol. 185–186, pp. 34–76, Dec. 2012.

[203] P. Jayaweera and S. Hettiarachchi, "Determination of zeta potential and pH of zero charge of oxides at high temperatures," Rev. Sci. Instrum., vol. 64, no. 2, p. 524, 1993.

[204]

Appendix A. Design, Construction and Operation of the University of Birmingham Hot Loop

A.1 Design

Using the work of AREVA [11,18–20] as a basis, there were several clear criteria, which needed to be filled:

- Fluid velocity must reach at least 12 ms^{-1} through a test restriction with an ID of 6 mm
- Temperature of the fluid must reach 300 °C
- Maintain a pressure significantly above the steam saturation pressure of water at temperature, to ensure the presence of one phase fluid and prevent localised cavitation.
- The system should be able to operate for times in excess of 1,000 hours
- Accurately measure differential pressure while system is online and at temperature and pressure.

The design of the system, based on these criteria, is detailed below.

A.1.1 Equipment and Materials

All wetted surfaces in the Hot Loop are constructed from type 316L stainless steel, excluding sections that could not be avoided (for example, pump components). Tubing for construction was all supplied with composition data to certify that it fell within the requirements for 316L stainless steel. Most tubing was purchased through Swagelok, who provided Sandvik tubing of the correct dimensions. Tubing above 1 in. OD was purchased from other supplier, as this diameter is not carried in stock by Swagelok. Flanges, valves and measurement apparatus were also supplied with certification of composition.

A.1.1.1 Flange and Gasket Requirements

Originally, it had been planned that the test cell would be electrically isolated from the rest of the system. This was attempted using vermiculite-covered flanges, washers, and bolt sheathes, which provide electrical insulation at temperatures up to 450 °C.

On installation, it was found that the internal diameter of the bolt sheathes was too small to accommodate the bolt, however it was decided that the flanges would be tested anyway; this testing revealed that the seals would leak excessively during cooling of the system. Upon removal after the test, the flanges were found to have disintegrated, leaving the graphite and metal of the flange internals exposed.

After observing such poor performance, it was decided that standard grafoil spiral gaskets with a stainless steel retaining ring on the inside and outside would be used until a suitable alternative was found. This meant that the test cell would not be electrically isolated, however it is reasonable to assume that the deposits formed on-plant are forming in locations which are not isolated from the rest of the RCS.

A.1.1.2 Bespoke Pump

The criteria for the pump was its ability to operate at high pressures, temperatures and still generate a flow velocity in the restriction of 12 $m.s^{-1}$; these requirements exceed the capability of most off-the-shelf pumps manufactured today. In order to fill the specification, a bespoke pump regenerative turbine pump head was constructed by Pump Engineering Ltd, attached to a standard 3 kW squirrel-cage electric motor.

A.1.1.3 Feed Water

The deposition mechanism under study only occurs in low conductivity water, so the highest quality water available must be used. For this purpose, a Direct-Q 8 Ultrapure Water System was used, producing water with a conductivity of 0.055 μS.cm.

Atmospheric gases will dissolve into water. Under standard conditions and atmospheric concentrations, water can be expected to contain approximately 13.4 ppm N_2, 8.7 ppm O_2, 0.5 ppm Ar, and 0.6 ppm CO_2. The presence of O_2 in the water is undesirable due to its effect on the redox potential of the system, and the presence of CO_2 will cause the formation of carbonic acid, which will increase water conductivity.

Conductivity after leaving the purifier and arriving in an atmosphere-controlled tank is generally in the range of 0.16 – 0.22 μS.cm. In order to ensure that the water quality is not diminished, careful handling of the fluid is essential.

A.1.2 Evolution of Design

A diagram of the EMILIE loop is shown in Figure 9.2. Initially, speculative line diagrams were drawn to explain the function of the system to the company hired to complete the design and build process. The line diagram shown in Figure 9.3 shows the overall concept of the loop.

The system comprises of two 2.6 L stainless steel autoclaves (vessels labelled 13534 and 15001 in Figure 9.3 – these are the serial numbers of the vessels) and two tubing loops, one large bore tube which carried water in a bypass loop from the pump outlet back to the pump inlet, and the second smaller bore tube loop carried water through the test cell and either through the autoclave (bypassing the large top-up heater) or back to the pump (bypassing the autoclave). The drawing was passed on to the contractor, who determined that connecting the autoclaves could be done very easily using flexible hoses, however the tube work would prove challenging to design and implement. Based on the drawing, the contractors drafted a computer aided design (CAD) diagram of the system, which can be seen in Figure 9.4.

Refinements were made at this point, as the size of the test cell was deemed insufficient to fit appropriately sized test pieces. The test cell design was more fully

developed at this stage, and the loop drawing was also modified to fit the newly designed test cell.

Two test cell designs were put forward, shown in Figure 9.5 and Figure 9.6, however due to expected difficulties machining the end cap shown in Figure 9.5, as well as the possibility of it seizing in place after a test, the second design, Figure 9.6, was chosen.

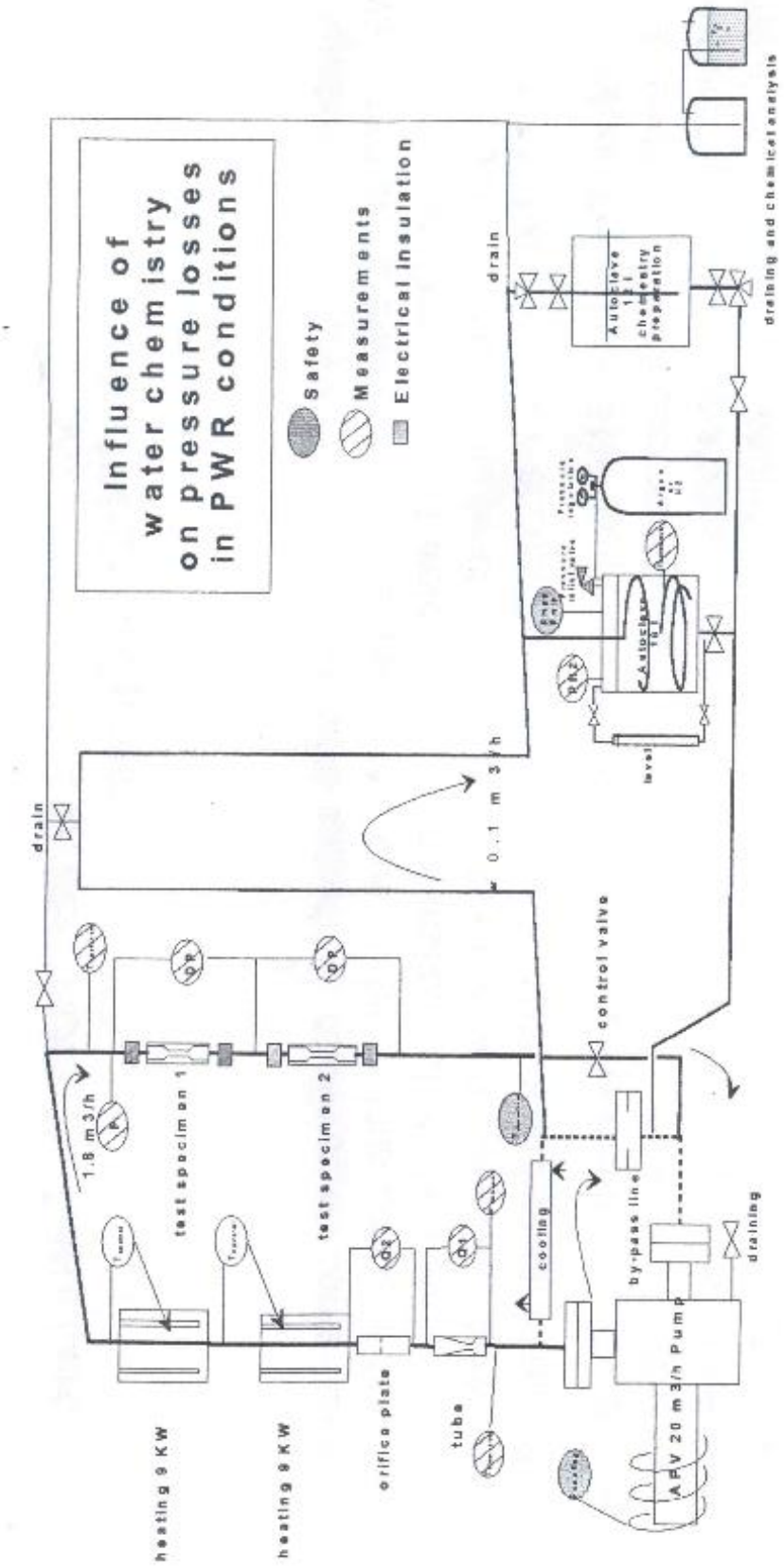

Figure 9.2 - The first instance of the EMILIE loop. Over several years this loop was modified in several ways, however the fundamental flow path, shown here, was always retained. Image taken from [18].

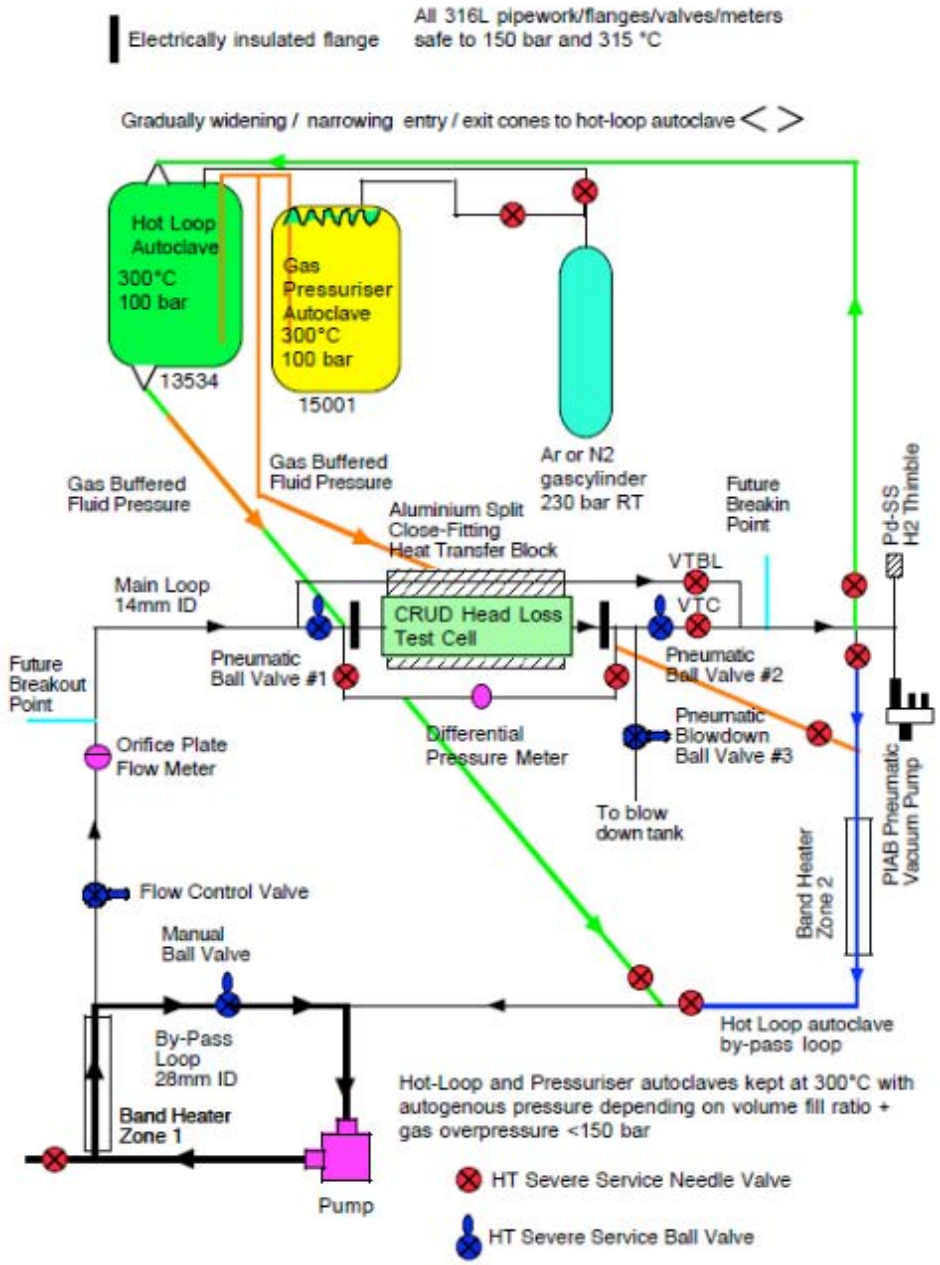

Figure 9.3 - Line diagram showing the concept of the hot loop. Drawing courtesy of Dr. Clive Ponton.

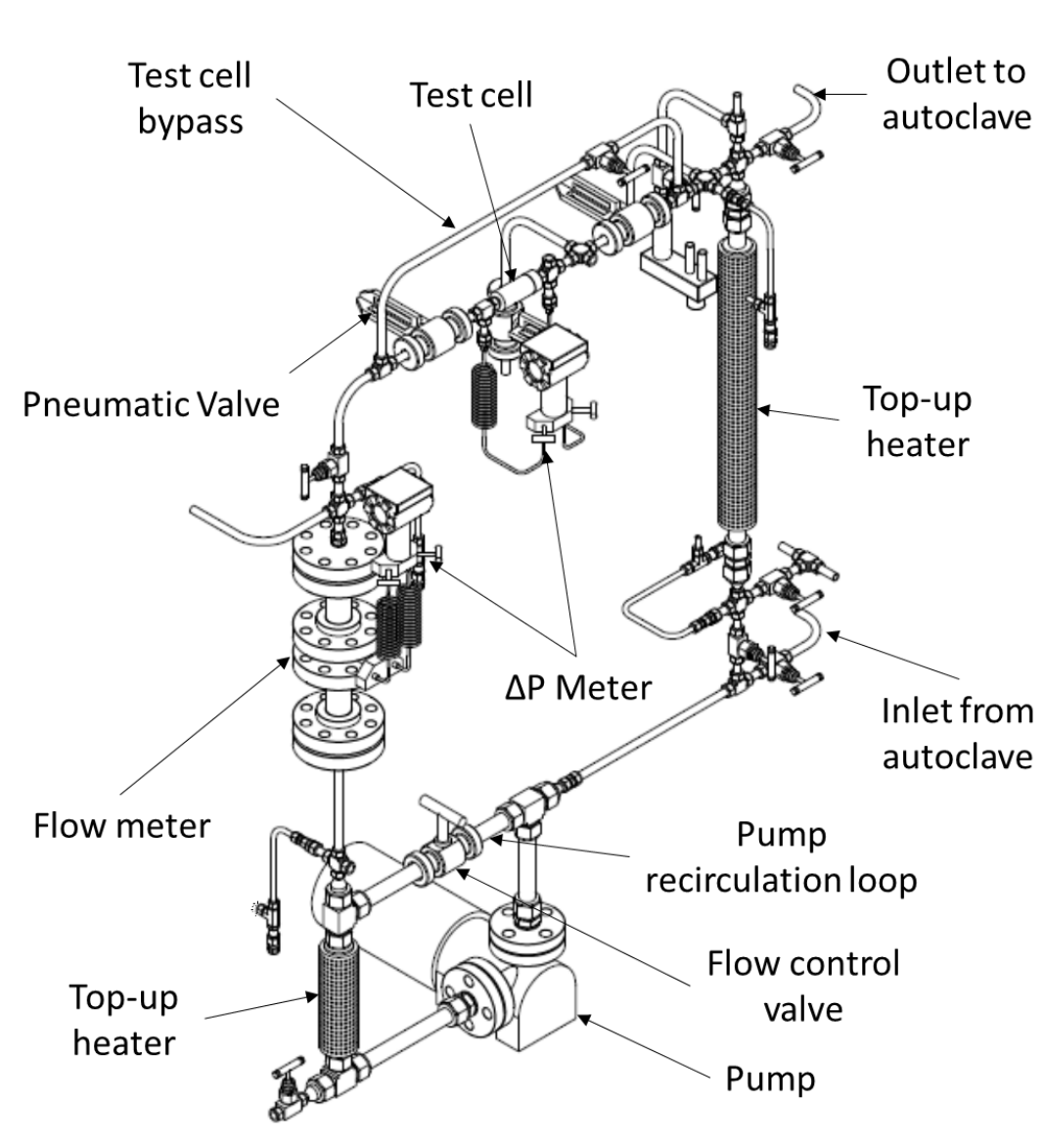

Figure 9.4 - CAD drawing of the first design for the hot loop. The core of this design was retained through to implementation, including the locations of the test cell, the pneumatic valves and flow meter.

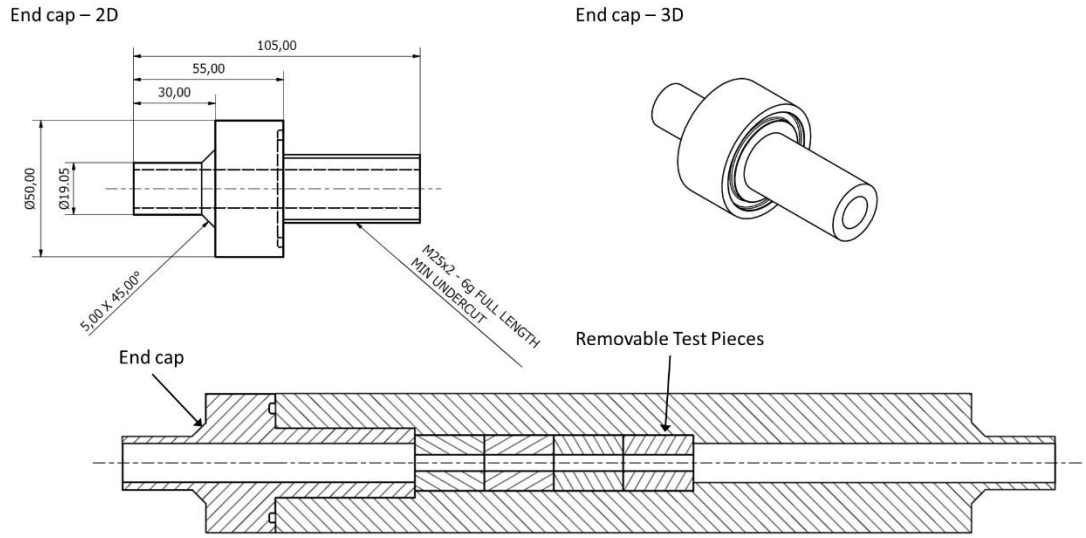

Figure 9.5 - First design of the test cell; this design was rejected due to prospective difficulties with machining of the end cap.

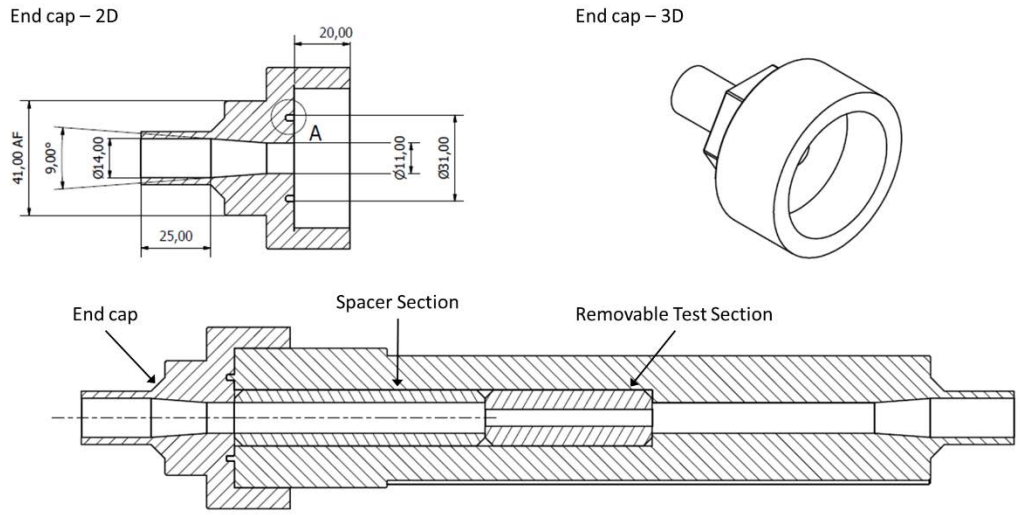

Figure 9.6 - The second design of the test cell. This design was implemented on the hot loop when it was built.

The OD of each end of the test cell was machined to 19.05 mm in order to be compatible with the ¾ in. OD Swagelok tube fitting to ¾ in. BSP fittings, which allowed the test cell to be connected to its flanges. In Figure 9.7 the second iteration of the hot loops design can be seen; the only major change at this stage from the design shown in Figure 9.4 the enlarging of the loop size to incorporate the larger test cell.

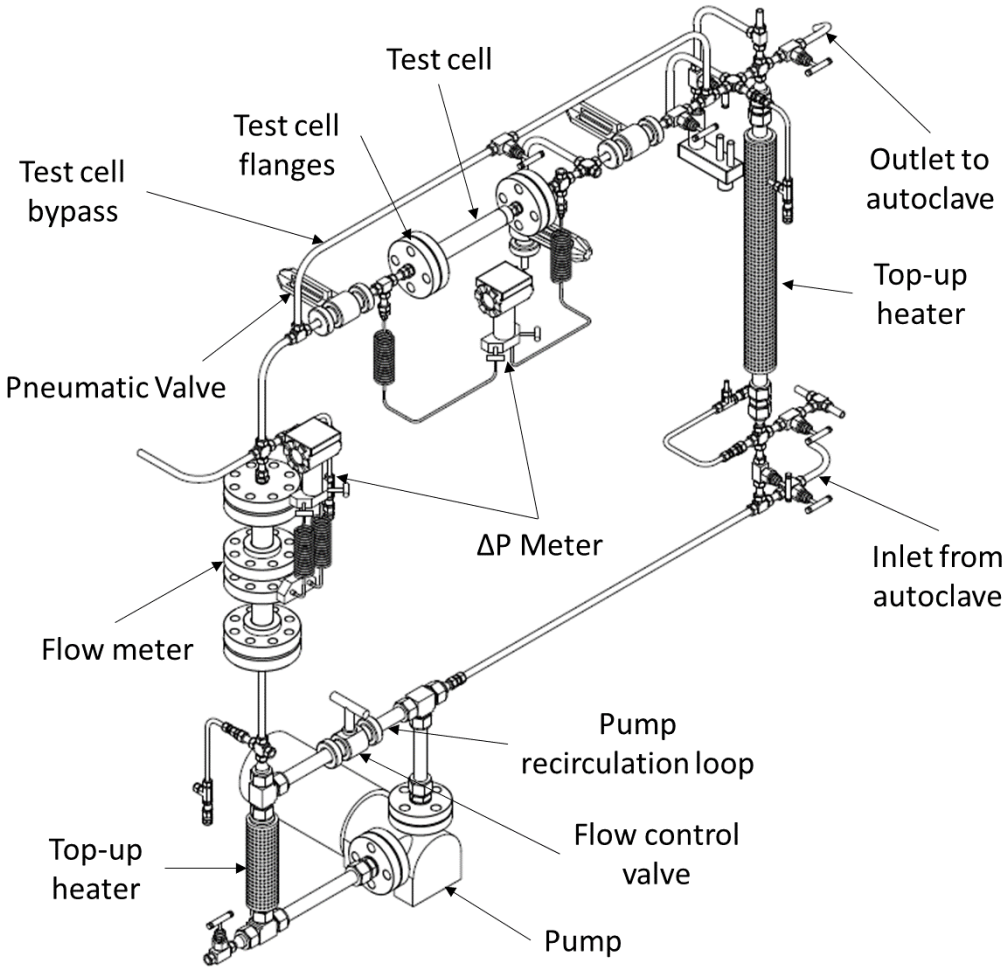

Figure 9.7 - Second design of the hot loop. In this drawing, the re-designed test cell has been incorporated and appropriate geometry changes to the tubing have been made.

Several shortcomings were identified in this design prior to construction. The CAD pneumatic valves (either side of the test cell in Figure 9.7) were smaller than the actual valves, and the flow path of the water around the loop would bypass the large top-up heater (shown on the right hand side of the loop in Figure 9.7).

The final iteration of design is shown in Figure 9.8. In this instance, the correct size of the pneumatic valve has been used and the large top up heater has been moved to a horizontal position. The pump recirculation loop has also been changed to smaller bore tubing as the specified pump was capable of variable output; this recirculation loop was designed in to act the flow rate control method, as it was originally thought that the pump would have a fixed output.

Flow direction has been drawn onto Figure 9.8 to demonstrate the flow path under normal operating configuration.

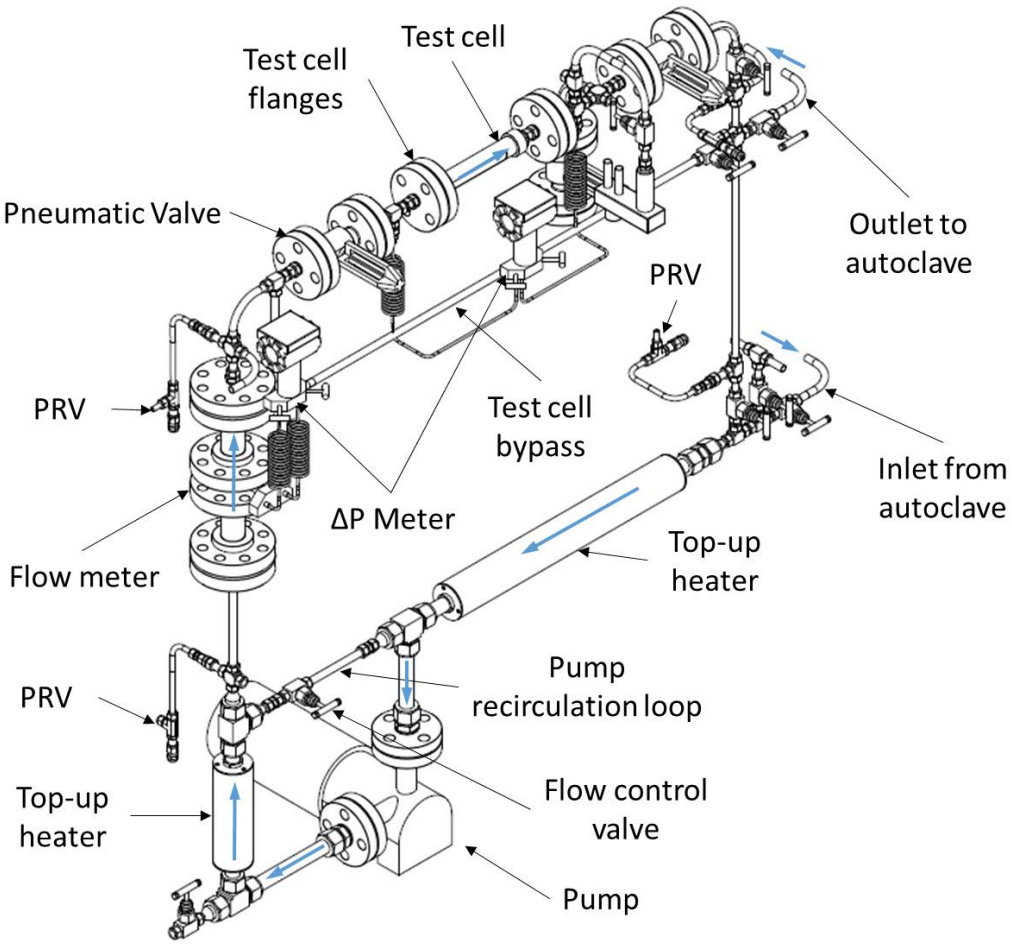

Figure 9.8 - The final design of the hot loop, drawn before final construction. The blue arrows indicate direction of flow. At the bottom right, flow is entering the loop from an external autoclave (not shown) which maintains the temperature of the system. At the top right of the image, the flow is directed back to this autoclave. Moving the top-up heater to the horizontal position shown ensured that it would always be in line with the flow.

The design shown in Figure 9.8 was the state of the hot loop when it was first installed at the University. Since installation, modifications have been made which are discussed in section A.1.2.1.

In addition to the loop and the autoclaves, three other safety systems were designed specifically for the hot loop. These were the blow down vessel, the dump manifold, and the emergency dump vessel.

The blow down vessel is a section of 1 ½ in. OD tubing, with a volume of approximately 1.4 L, which acted as a drain vessel for water present in the test cell during the blow down procedure (see Figure 9.9).

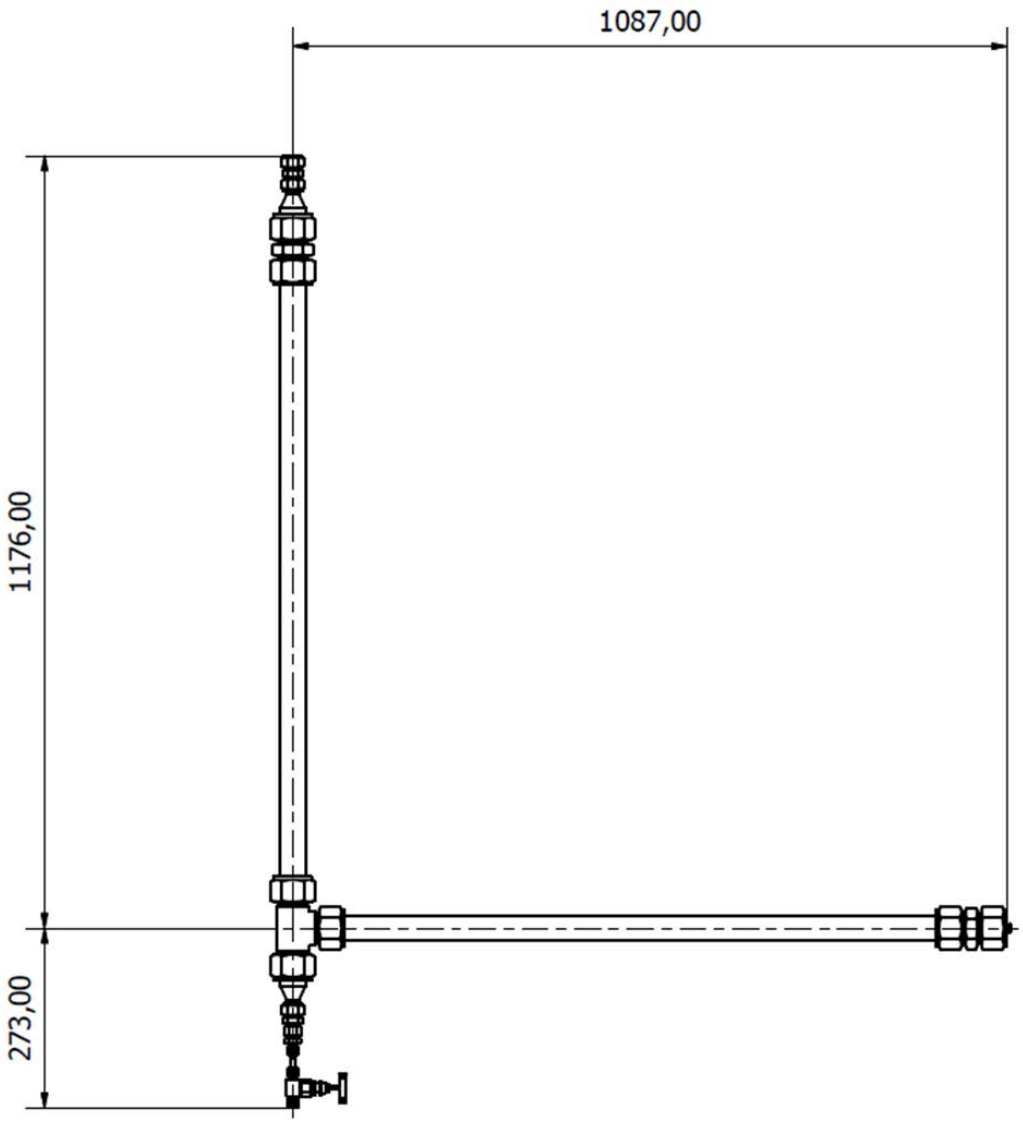

Figure 9.9 - The blow down dump vessel, shown with drain valve.

The dump manifold and emergency dump vessel are part of the same tubing system. In the event of an over pressure transient which results in the rupture of the burst discs (nickel foil disc, calibrated to rupture at 155 bar, the maximum working pressure of the autoclaves), the fluid must be discharged into a secondary pressure vessel, rather than into the lab. To ensure that this is the case, all relief valves and burst discs are connected to a central high pressure manifold, shown in Figure 9.10. The

secondary dump vessel, to which the fluid is redirected, was a flanged pipe, 8.625 in. OD with a 0.25 in WT. As shown in Figure 9.11 and Figure 9.12, the dump vessel was designed to be supported on a pair of stanchions approximately 2 m high.

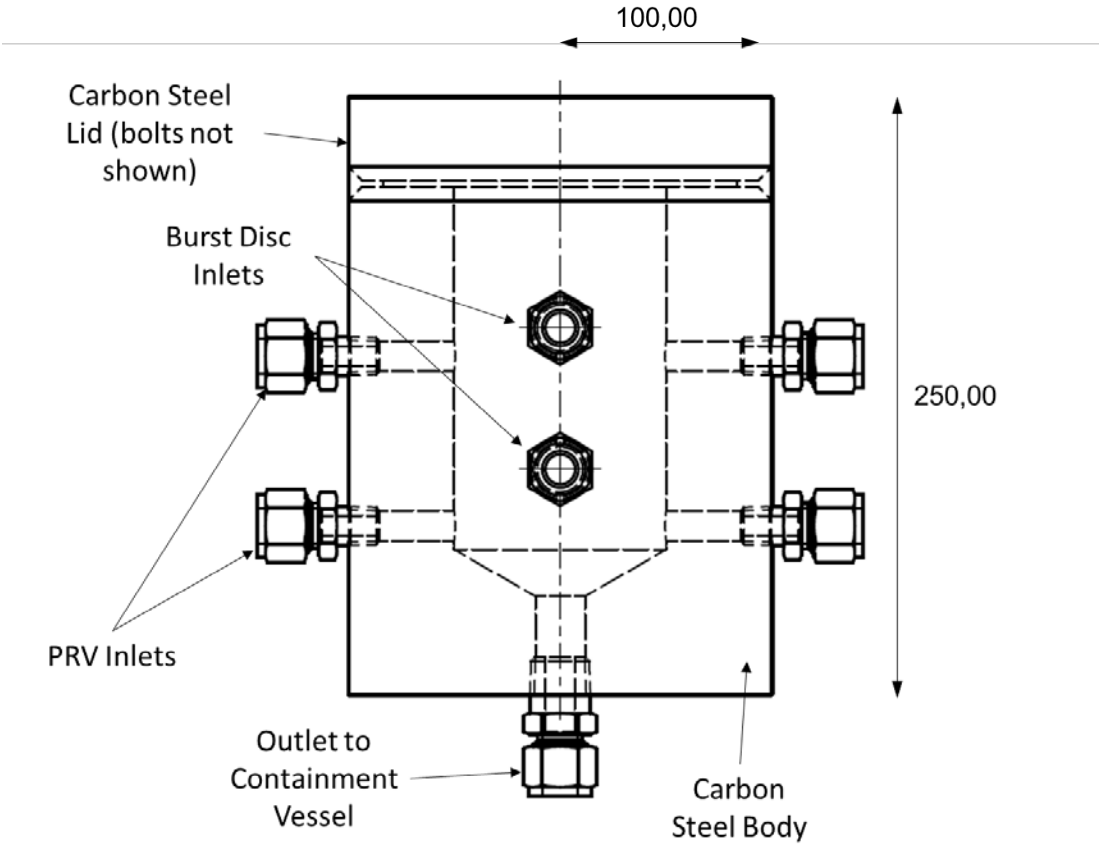

Figure 9.10 – The hot loop dump manifold.

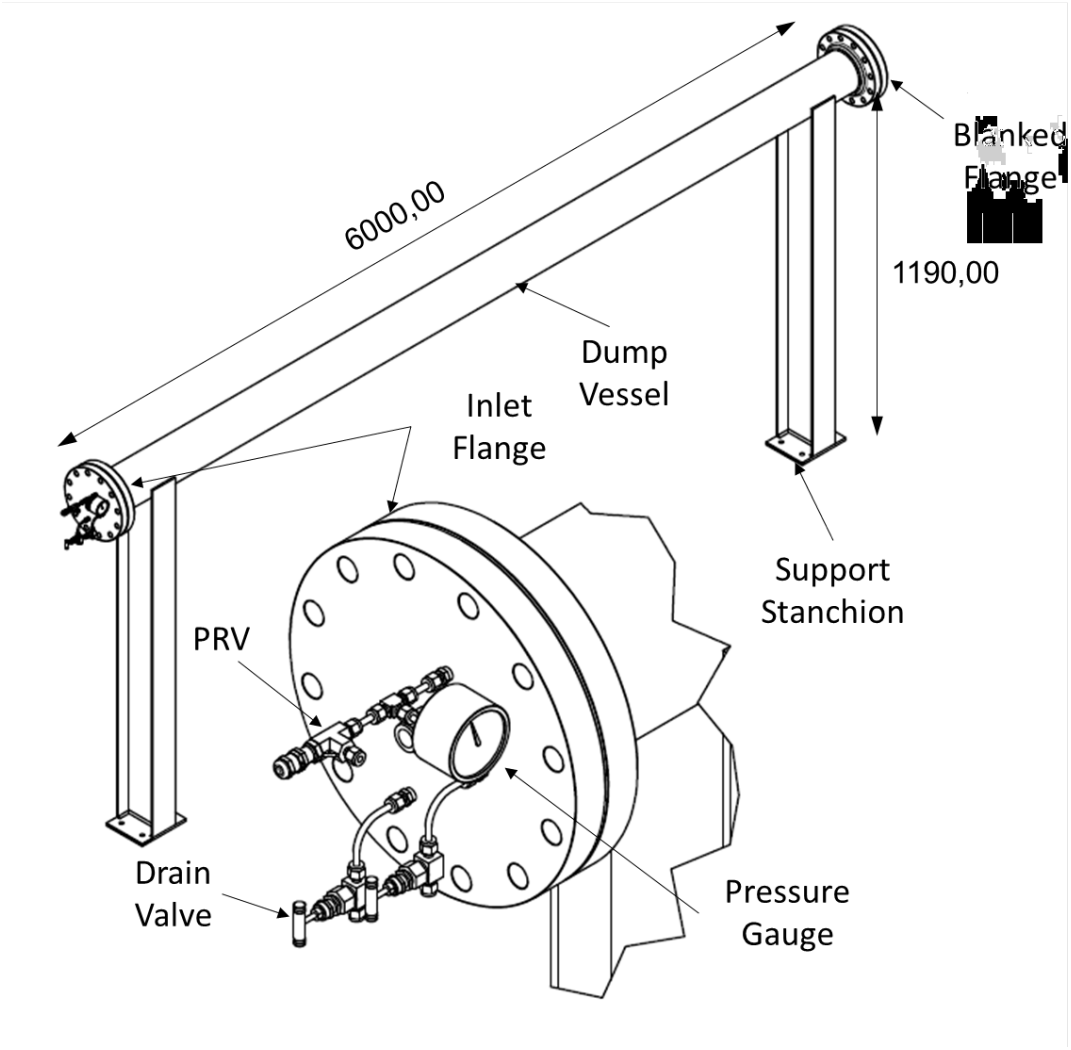

Figure 9.11 - The emergency dump vessel, shown on the support stanchions. The inlet flange was fitted with a final pressure relief valve (a requirement for any high pressure vessel), a pressure gauge and drain valves. In the event of a full system release, the dump vessel can be monitored for pressure before draining it.

Figure 9.12 - The final location placement of the emergency dump vessel.

A.1.2.1 Implementation

The hot loop was installed at the University by the contractors who had built it, however some preparatory work was performed by staff at the University prior to delivery of the loop. This involved the positioning of the autoclaves and associated control panels, and the installation of the emergency dump tank. The fully constructed and un-lagged hot loop can be seen in Figure 9.13.

Since delivery, some modifications have been made to the loop. These include the removal of the top-up heaters after they burnt out, and replacement with three mineral band heaters, and the removal of the pump recirculation loop entirely.

The band heaters were installed after the original top-up heaters burnt out during use. The band heaters were rated to higher temperatures, and also featured a split clamp for installation, where the original heaters did not – should the new heater fail, they could be quickly and easily replaced. The new heaters were now each powered by separate controllers, each with regulated by a separate thermocouple, which lead to more reliable heating – the original long band top-up heater contained three heating coils regulated by a single thermocouple which likely caused the heaters not in direct contact with the thermocouple to go above their maximum temperature, contributing to the heaters' failure.

The redundant pump recirculation loop was also removed because its presence made dismantling the loop during maintenance problematic.

Figure 9.13 - The hot loop, as delivered by the contractor.

Appendix B. Details of Design and Operation of Equipment for Corrosion Rate Measurements

B.1 Preliminary Corrosion Experimental Work

B.1.1 Autoclave Set-up

Cleanliness of the autoclave is vital to avoid the incorporation of ions known to accelerate corrosion, specifically chlorides. To this end, the autoclave must be meticulously cleaned before each experiment.

Cleaning was performed by hand, first by disassembling the autoclave head and winching it to a resting position, then sweeping debris from the disturbed graphite seal up and out of the vessel using compressed air and paper tissue, followed by numerous washes with high purity water and ethanol absolute and using paper tissue to wipe down the internals with whichever fluid was in use. Extreme care was taken to avoid skin contact with the autoclave internals to avoid inadvertent introduction of chloride ions to the system after cleaning.

The dip tube and thermocouple well which project downward from the autoclave head into the vessel must also be cleaned in a similar manner.

The coupons to be used in the test, along with all components associated with supporting them in place were cleaned using an ultrasonic bath before being clamped into place on the dip tube and thermocouple well. After positioning, the clamping framework and coupons were further rinsed with ultrahigh purity water.

Once all components had been assembled and cleaned to a satisfactory standard, the head was fitted back to the top of the autoclave.

The head nuts were then liberally coated with an anti-seize compound and screwed down onto the threaded bolts projecting through the head. The nuts were tightened

to 60 lbf.ft (~81 N.m), in a cross pattern; 60 lb.ft was found to produce a repeatable, reliable seal, while also improving the longevity of the gaskets operational life over the 100 lbf.ft initially used.

B.1.2 Operation

Prior to beginning the test, a gas pressure test was performed at 100 bar for 24 hours - if no leakage was observed, the vessel would be depressurised ready for test solution.

Approximately 3 litres of high purity water were placed in a plastic container, to which a measured quantity of reagent grade lithium hydroxide was added. The pH of the water was recorded, and corrected by addition of more LiOH or by dilution to reach the pH required for the test. Samples for pH testing were taken, and performed in isolation, from the bulk solution. These samples were discarded to prevent transfer of contaminants present on the pH meter electrode to the bulk solution.

Test solution was transferred from the container to the autoclave through clean nylon tubing connected to the dip tube, using a back pressure of ~0.1 bar nitrogen gas. The quantity of test solution used for each experiment was calculated, ensuring that there would still be gas head space in the vessel even after the water had expanded under the temperature. Once charged to the autoclave, the test solution was sparged with nitrogen gas for 1 hour at a flowrate of ~50 $ml.min^{-1}$. Dissolved oxygen levels in the water were measured using the ampoule method [189] (see section 4.2.3), this method was shown to consistently report oxygen concentrations between 0-2 $\mu g.L^{-1}$, though this method is prone to subjective error.

After sparging, a nitrogen over pressure of ~10 bar was added to the vessel to prevent boiling of the solution during the test and to decrease the partial pressure of oxygen in the atmosphere, thus reducing the concentration in solution. The nitrogen is expected to dissolve into solution, however experience showed that tests without additional gas pressure would be below the saturation point of water at temperature,

while those with additional gas pressure would be above the saturation point [206]. The heating controller was set to the target temperature; depending on the target temperature, this time taken to heat up could be between 1 hr 30 mins and 3 hrs.

Once at temperature, the test time was started. The equipment was monitored periodically to ensure that temperature and pressure were maintained throughout the test. After the test time had elapsed, the heating controllers were set to 0 °C and the system was left to cool for a period of about 18 hours.

B.2 Improved Experimental Rig

B.2.1 Evolution of Design

The design of the system has changed significantly from initial idea through to finalised build. This has largely been due to some obvious oversights, or to produce the most flexible system possible.

The most basic idea of the system is illustrated in Figure 9.14; the concept was simply to flow water through a series of heated cells containing sample coupons, with each cell being individually removable, however several short comings were quickly identified; the system used four back pressure regulators, which were originally intended to provide pressure relief to the system in case of a high pressure transient, however the final BPR would need to be set at a lower pressure than the first three. After the final cell was removed, the next-last BPR would need to be manually corrected to the outlet pressure. The first three BPRs cannot be set to the outlet pressure, as they would allow flow to pass directly to the outlet line without passing through the other cells. Additionally, no relief valves were designed in, meaning the cells could not be safely vented when they were ready for removal.

Iteration two of the design (see Figure 9.15) introduced a significantly safer method of flow redirection. This arrangement allows the user to close the valves around the cell

being removed, open those required to redirect flow from the next-to-last cell to the BPR, and vent to the cell being removed. An additional cell has been added to the design with the intention of running very long term tests, lasting for years at a time, on other alloys.

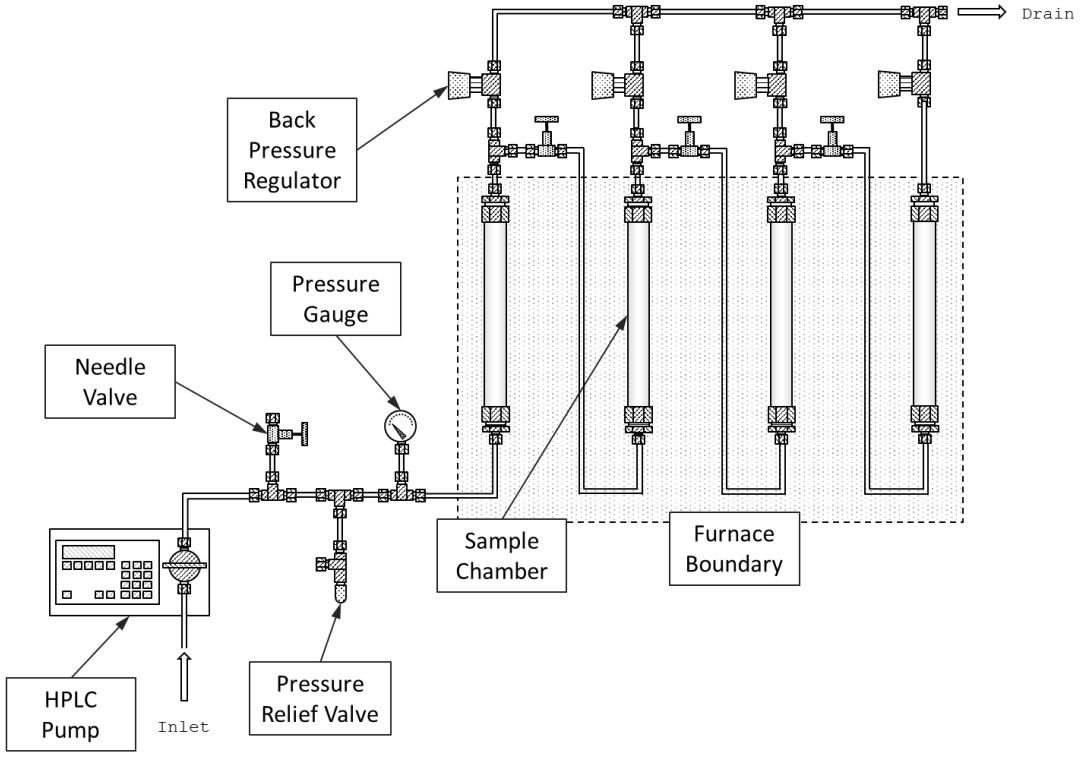

Figure 9.14 - The first design iteration of the corrosion rate rig system.

Iteration two needed only minor tweaking to ensure that the final design was the best possible. Iteration three, seen in Figure 9.16, shows perhaps the final change that was considered – the introduction of a gas pressuriser. It was eventually decided that this would not be included in the final design, based on experience gathered from the construction of the Metal Oxide Solubility Rig (see section **6.4**), as the system described here does not require a smooth flow, only a constant one - there was also some concern that should the system become blocked and the various safety valves not operate correctly, the pressure from the pump could force fluid into the gas bottle regulator, damaging a safety-critical component. Minor changes to the pump settings were still made to provide a smoothed flow – the pump piston draw rate, initially set at 125 ms, was increased to 1000 ms reducing the shock associated with the pump switching

from pushing fluid to pulling fluid. This was done in an effort to prevent pump stalling caused by the formation of small bubbles of N_2 in the feed line between the rig and the feedwater tanks, which obstructed the incoming flow; increasing the draw time eliminated this issue almost entirely. The finalised design can be seen in Figure 5.18. The only major changes to the system are the connections from the dump valves to the common drain line.

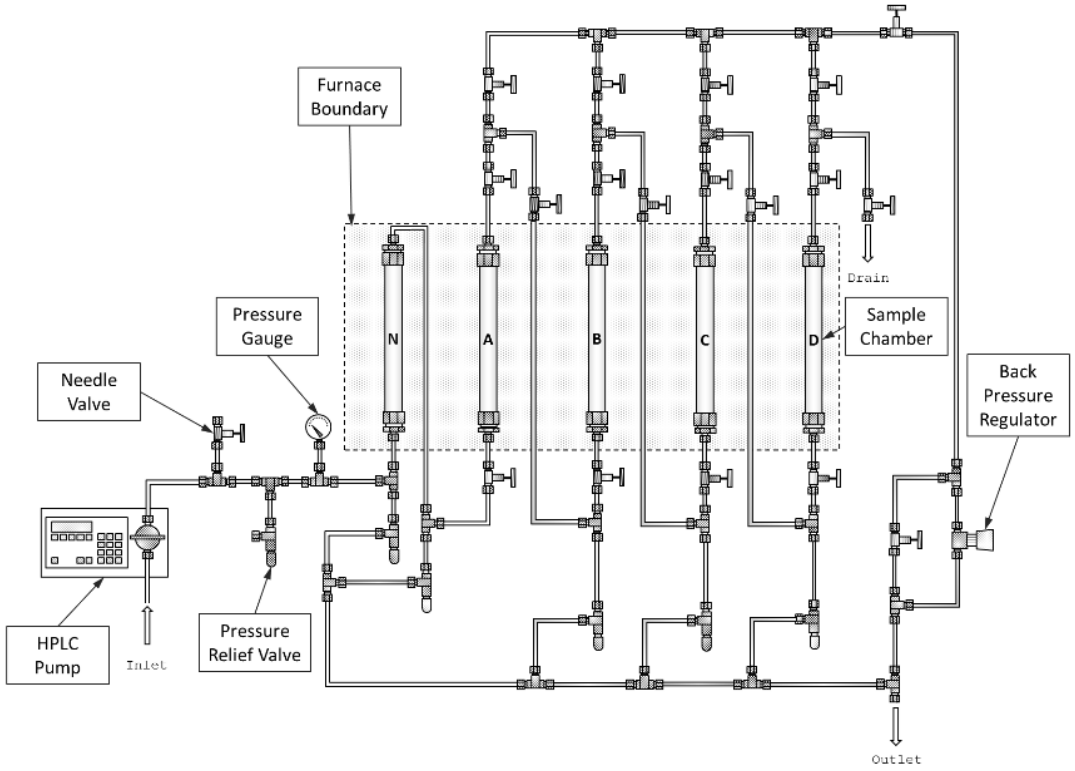

Figure 9.15 - Iteration two of the corrosion rig designs

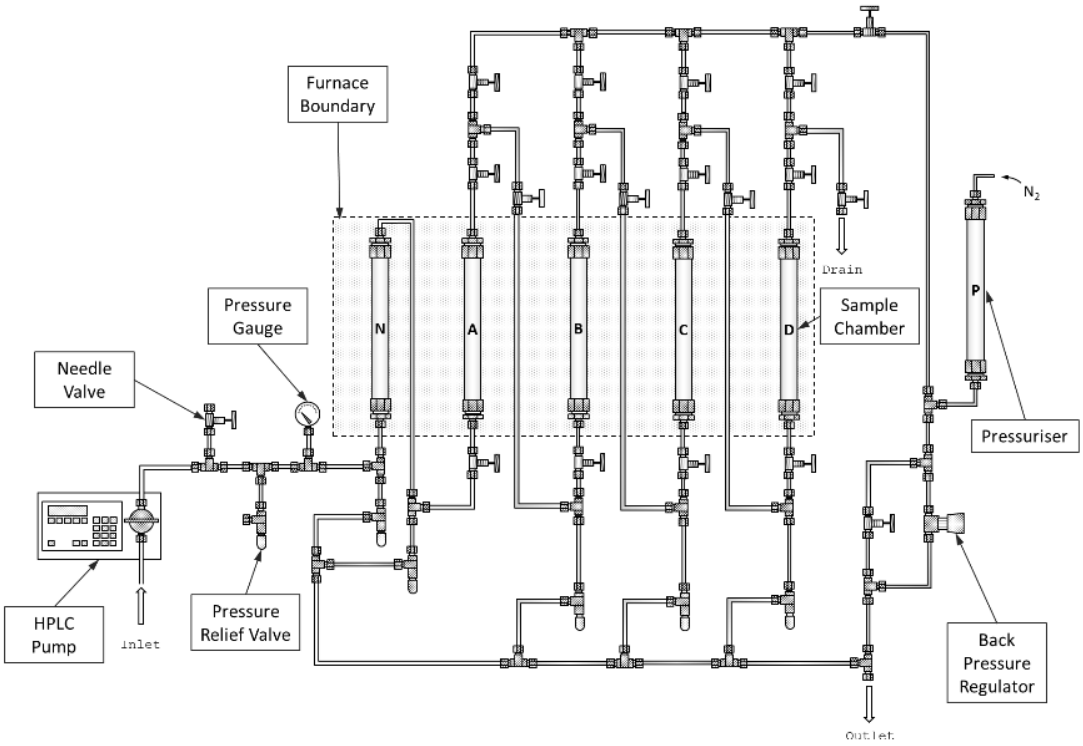

Figure 9.16 - Iteration three of the corrosion rig design.

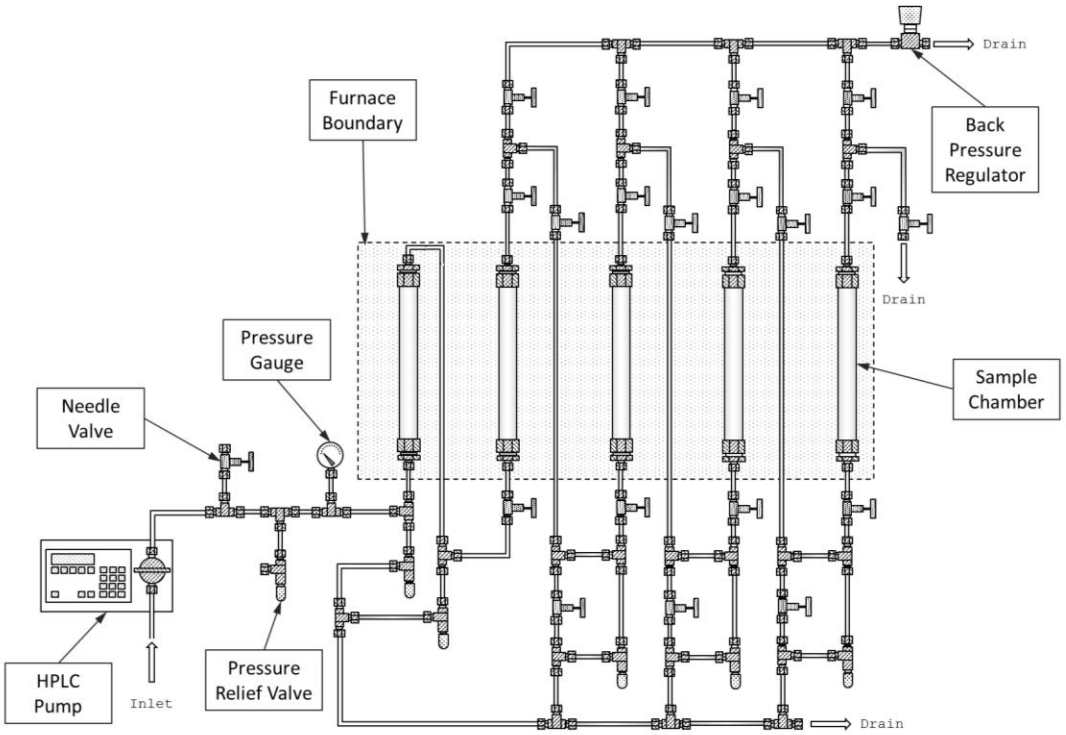

Figure 9.17 - Finalised design of the Corrosion Kinetic rig.

B.2.2 Implementation

B.2.2.1 Swagelok Tube Fitting System

The Swagelok tube fitting system was used extensively in this design; all tubing downstream of the pumps was sourced from Swagelok and fitted together using their fitting system.

The rig is simply a series of tubes of different diameter, the cells being the largest diameter tube easily available. The tubes were linked together by means of reducing unions, which allowed one diameter tube to be linked to a smaller diameter tubes by a single, pressure/temperature capable component.

B.2.2.2 Chamber Furnace

An air circulating chamber furnace capable of reaching 300 °C was selected with internal dimensions of 750 x 792 x 520 mm^3 (height/width/depth).

B.2.2.3 HPLC Pumping Apparatus

The pump type selected is normally used for HPLC and consists of a computer controlled motor body, and a replaceable piston-type pump head. Flow rates of 0.05 – 10.00 $ml.min^{-1}$ are common, however the flow rate is determined by the pump head in use and can be as high as 100 $ml.min^{-1}$.

The pumps can be operated in several different modes, however this work required the pump to operate in the constant flow mode, independent of pressure. This provides a continual renewal of chemistry within the rig. As the pumps were capable of operation at pressures far in excess of the components safe operating limits, PRVs were fitted to prevent component damage or failure.

B.2.2.4 Feed Water Storage Tanks

All of the feed water for each rig would be contained in a single 220 litre, stainless steel tank. The tank was machined with a G 2" hole, for which a custom made head was machined. Each head possessed 4x ¼ in. FNPT threaded holes, which were used to install a back pressure regulator to for the control of the tanks pressure, a dip tube to carry sparging gases, another dip tube to carry feed water to the rig pump, and the last for a three-way valve to allow for filling of the tank from the Millipore ultrahigh purity water reservoir (see Figure 9.18).

B.2.2.5 Gas Supply

The gas supply system is simply a gas manifold designed to provide the appropriate gases for feed water preparation (see Figure 9.19).

A feedback loop between the output of the platform balances and a controller was set up to control a pneumatically operated valve on the water outlet of the tank. This feedback loop was to prevent gas from reaching, and potentially damaging the pump.

Figure 9.18 - The finished feed water supply system. The two large tanks to the left and middle supply water to the corrosion kinetics rigs, while the smaller tank to the right supplies conditioned water to the metal oxide solubility rig. To the right hand side, the gas control panel can be seen fixed to the wall.

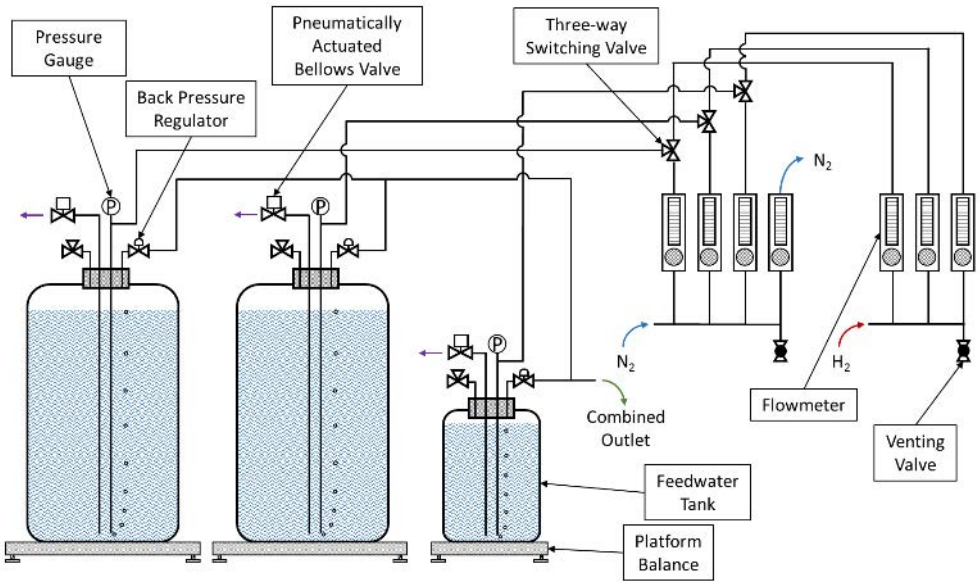

Figure 9.19 - Line diagram of the feed water storage tanks, along with associated gas conditioning setup.

B.2.2.6 Completion

The final of build of the corrosion system was to contain two identical rigs, both built into the same oven, using the same design and operating simultaneously to produce a large volume of data. The schematic of the rig shown in Figure 5.18 shows the system as it was finally implemented and a photograph of the rigs *in-situ* can be seen in Figure 9.20.

Figure 9.20 - A photograph of the Corrosion Kinetics Rigs.

B.2.3 Operation

B.2.3.1 Feed Water Preparation

Due to the volume of water required for the tests, it is necessary to fill the feed water tanks approximately 3 weeks in advance of an experiment to allow time for the displacement of oxygen from the water by nitrogen sparging.

High purity water was charged to the feed water tanks, the mass of which was reported by the platform balance. The total mass of water was used to calculate the volume of LiOH solution needed to achieve the pH of the test. After addition of the stock solution, the water within the tank would be sparged with nitrogen gas at ~20 $ml.min^{-1}$ for a period of at least 440 hours (2 hours sparging per kg of water). This degassing procedure produced an oxygen content of 0 – 2 ppb according to the ampoule test method, described in section 4.2.3 [189].

B.2.3.2 Preparation of Rig

The cells of each rig must be filled with the experimental coupons in a careful and precise manner in order to prevent the samples from contacting each other once sealed inside the cell.

Each sample has already been carefully cleaned and degreased using acetone and an ultrasonic bath, before being stored in a desiccator. The coupons are taken and placed in sets of three in the grooves of the alumina separating rings, described in section 5.4.2.1.1. The first set of coupons were sandwiched between a pair of separating rings, which were pushed into the bottom of the first cell in line (cell A). The second set of samples were aligned with grooves on the bottom of the first set's separating ring, and are pushed into the cell also. This process was repeated until the all coupons are in the cell; a maximum of twelve sample coupons can be fitted into each cell. The cell was tightened then and pressure tested, before being fitted into the rig.

The rig was then pressure tested, firstly using nitrogen gas at 100 bar for an hour at a time, and then with feed water pumped from the tanks; in this instance the pressure is provided by the action of the pump. The water was left pressurised in the rig for up to 2 hours to allow any small leaks to become visible, at which point the offending fitting would be tightened.

When the rig is known to be leak tight, the pumps were primed and set pumping at 2 $ml.min^{-1}$, and the chamber furnace is ramped up to temperature. The furnace can reach a maximum temperature of 300 °C in less than 2 hours. Once the furnace is at temperature, the time was recorded and time iterations calculated to determine when the various cells need to be extracted.

B.2.3.3 Cell Removal

The cells are designed to be removed from the rig at pre-determined times. In order to remove the cell, the pumps were first stopped, the cell isolated by the inlet and outlet line valves, and the flow path redirected to the BPR from the outlet of the next to last cell, as shown in Figure 9.21. The pump can be reactivated when this redirection is complete, as the cell being removed would be completely isolated from the rest of the rig.

While it is possible that a cell could be reinserted into the rig with fresh samples, it was considered to be hazardous to the operator and potentially disruptive to the test as a whole.

The cell to be removed was emptied by slowly releasing the water as steam through the drain line. The cell was removed then from the oven and left to cool, before opening and removing the samples. Samples were dried of any residual moisture, and stored in a desiccator prior to analysis.

B.2.3.4 Shutdown

Shutdown of the system occurs at the same time as the final cell is removed. For this step, the pump is stopped and the oven switched off, while the final cell is vented carefully via the drain line. Once the system is cold, the final cell (which is located at the back of the oven and is thus impossible extract without the other cells and tubing being removed first) can be taken out. The remaining tube work is purged of any residual test solution, and a small pressure of nitrogen is passed through to dry the wetted surfaces.

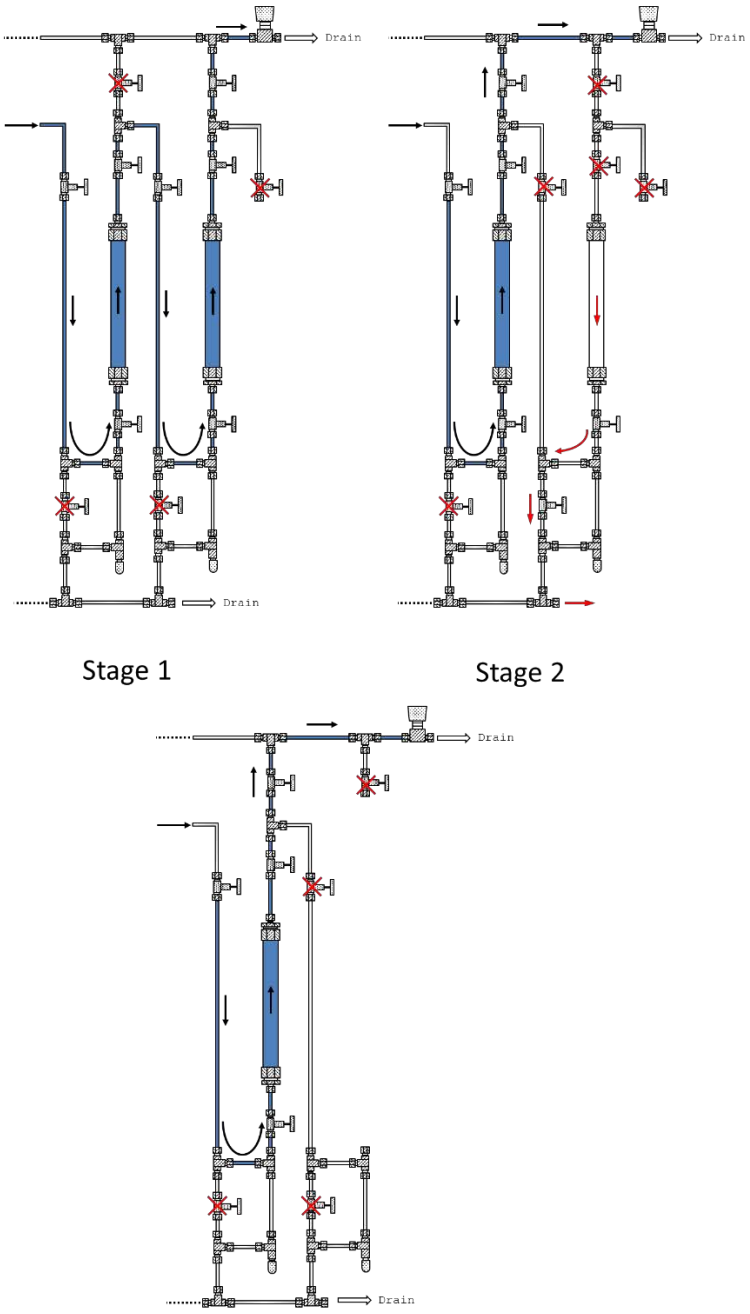

Figure 9.21 - Process of removing a cell from the Corrosion Kinetics Rig; red crosses over valves indicate the valve is closed, and black arrows indicate direction of flow. Blue colouring of cells and lines indicate which cells are in operation. In stage 1, normal flow is in action, and water is simply being pumped through the cells. In stage 2, the last cell in line in being vented through the lower drain line, with steam flow direction indicated by red arrows. In stage 3, the cell has been extracted from the rig, and normal flow conditions are in action again.

Appendix C. Details of Design and Operation for the Measurement of Oxide Solubility

C.1 Preliminary Experimental Details

C.1.1 Autoclave

The autoclave used for the preliminary experiments is same as that described in section 5.1.1.1

The premise of the experiment was to expose magnetite powder to high temperature high pressure water and extract samples of the liquid from the autoclave while at temperature. To do this, the autoclave was fitted with stainless steel powder cages (see Figure 9.22). The cage apparatus was attached to the dip tube and thermocouple well inside the autoclave by two split-bar clamps, each held together by four screws. The cages and all associated components were made from 316L stainless steel to ensure material compatibility. Photographs can be seen in Figure 9.23 and Figure 9.24.

The cages were cut from sheets of sintered 316L stainless steel fibrous mesh called "Bekipor", which had an average pore size of 3 μm, meaning that only the finest particles of magnetite could escape from the cages. The cages were isolated from the rest of the system with high purity alumina standoffs. The powder within the cell was purchased from Sigma-Aldrich and, alongside the powder, 3 mm balls of 99.9 % alumina were added to prevent the powder from becoming packed into a plug.

A small sampling cell of approximately 40 ml volume was fitted to the autoclave and with valves between the cell and the autoclave vessel, a cell leading to a "Christmas tree" valve arrangement (shown in Figure 9.25) and a release valve projecting radially out of the cell, from the bottom; this valve was used for extracting the sample from the cell while the system was still at temperature.

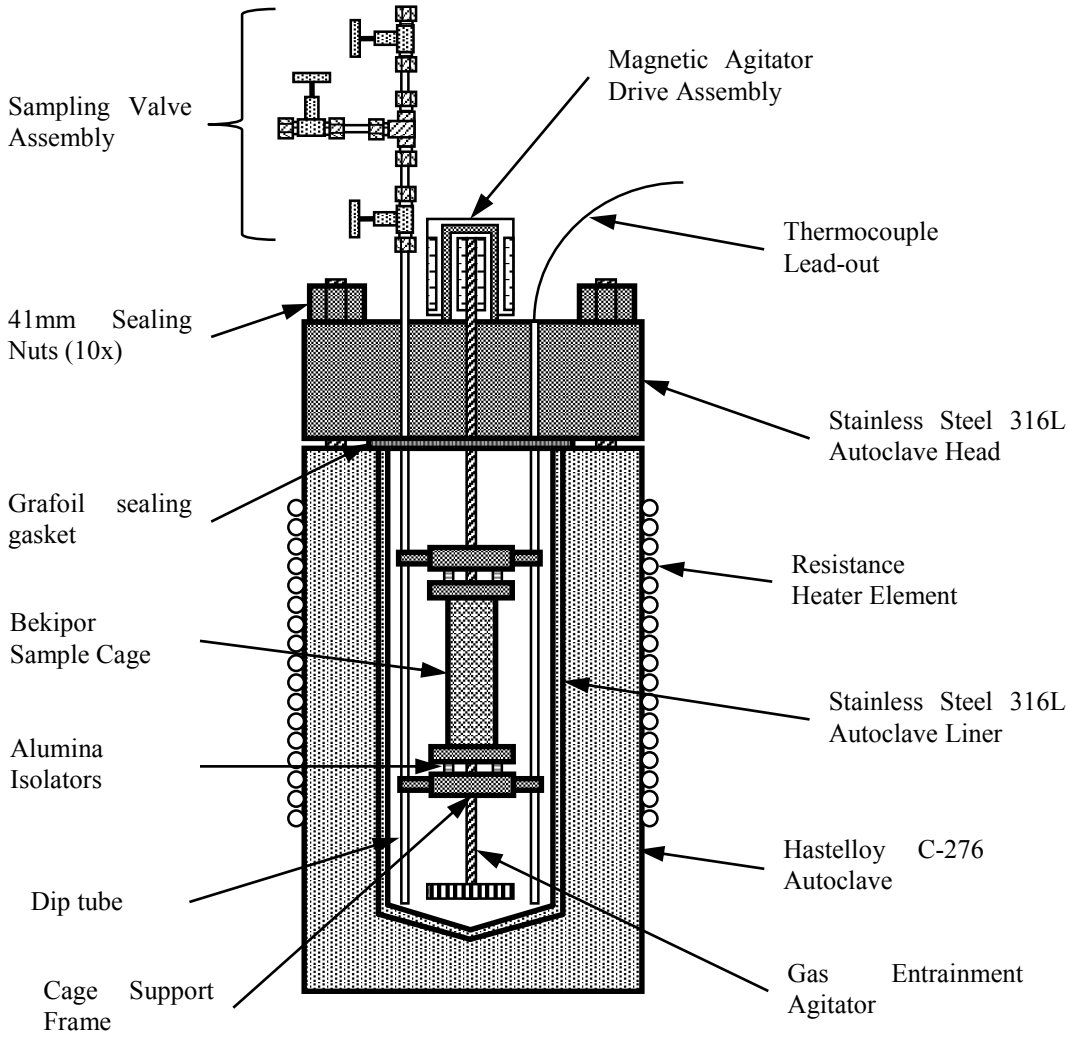

Figure 9.22 - A schematic of a batch type autoclave used for metal oxide solubility experiments.

Figure 9.23 - Photograph of the magnetite cages. The cages are mounted to the dip tube and thermocouple well which protrude from the autoclave head, into the pressure vessel.

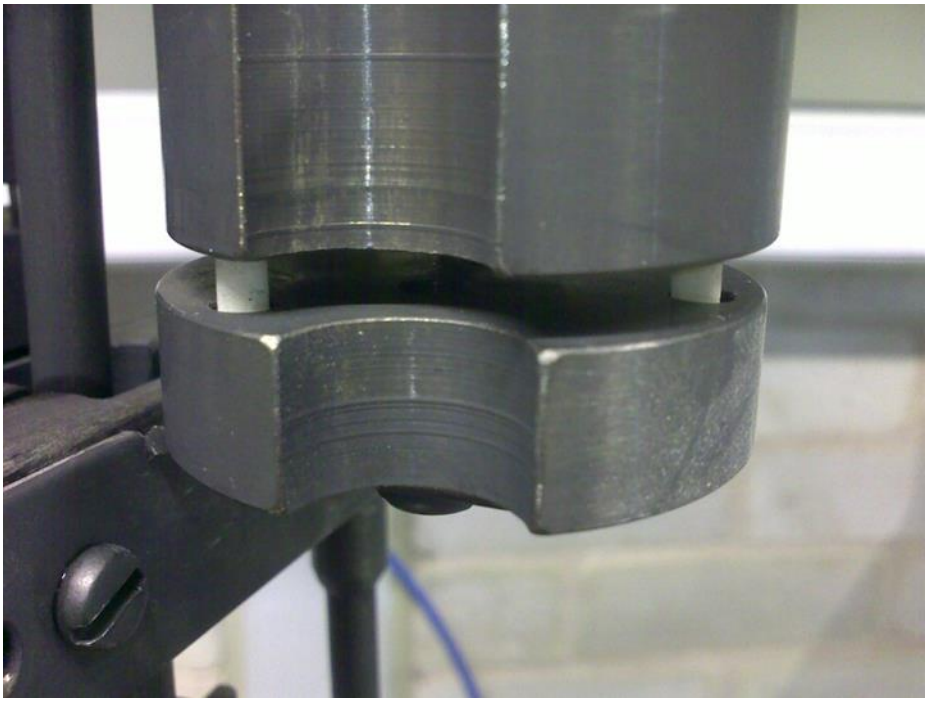

Figure 9.24 - Close-up photograph of the alumina spacers used to electrically isolate the cage from the rest of the autoclave.

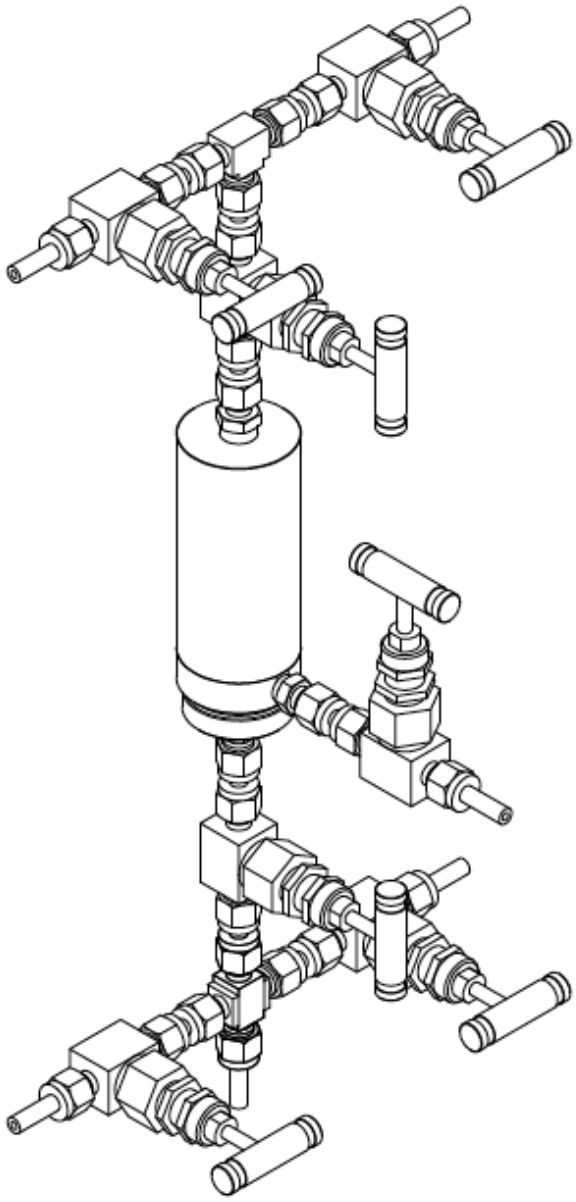

Figure 9.25 - The Christmas tree valve arrangement around a sample cell in the centre. The bottom vertical valve is connected to the dip tube of the autoclave (the two horizontal valves at the bottom are often removed and the port blanked off to reduce crowding around the autoclave head), while one of the two top valves connects the system to the hot loop via a flexible steel hose.

C.1.2 Experimental Set Up

C.1.2.1 Autoclave Set Up

The solubility of iron in water is known to be extremely low – on the order of low parts-per-billion [40,42,48,53,57]. With this in mind it is easy to understand how even tiny amounts of contamination (such as particulate iron adhered to the wall of the

autoclave during a previous test which could become mobile once fluid was reintroduced) could compromise the final result. Consequently, it is important to prepare the autoclave in as clean and careful a manner as possible.

The autoclave interior was cleaned manually between tests using compressed air to expel loose flakes of the grafoil gasket from the top and inside of the pressure vessel. The inside of the pressure vessel was washed with copious amounts of high purity water and ethanol absolute and wiped clean with paper towel. The autoclave head was treated in the same manner. The magnetite cages were washed down with water, though contact with ethanol wash avoided as it could not be guaranteed that the ethanol had been completely removed from within the cage prior to a test.

C.1.2.2 Operation

The autoclave was closed after cleaning and pressure tested with nitrogen gas at 100 bar for a period of one hour. Small leaks during this time were considered to be acceptable, as the tests would last for only ~6 – 8 hours, meaning a negligible loss of pressure during the test.

Solution was made up in a 5 L plastic container, which was modified to allow gas sparging. Nitrogen gas was connected to the inlet line of the container, and the outlet line was connected to the autoclave. The gas exited the autoclave via a water bubbler to prevent back flow of air into the vessel. This configuration allowed the solution was degassed and the autoclave purged of oxygen simultaneously. Degassing/purging was performed for one hour.

Solution was charged to the autoclave by reversing the gas flow through a manifold, meaning that none of the connected tubing needed to be disconnected and exposed to air.

A nitrogen gas blanket of ~10 bar was added to ensure that the pressure at temperature was greater than the saturation point. It was expected that some of this additional

nitrogen would dissolve into the water [206], but it was found that experiments were no additional gas pressure was added would express a pressure below the saturation point of water at a given temperature, while those with added gas pressure would be above the saturation point. The temperature controller was set to a point 5 °C below the target temperature and allowed to ramp up, after which the set point was changed to the target temperature, avoiding temperature overshoot. After each sampling procedure the temperature was raised by 20 °C, though at higher temperatures, the risk of temperature overshoot was considerably less so there was no need to ramp the temperature up in stages.

C.1.2.3 Sampling

Samples were taken via a sample cell, part of the "Christmas tree" arrangement above the autoclave (see Figure 9.25). The vessel was prepared by briefly rinsing it with high purity water before drying it with nitrogen gas flow. After this, the cell was evacuated with a small vacuum pump, and all valves around the cell closed off. The cell was connected to the autoclave vessel by a single isolation valve; to take a sample this valve was slowly and carefully opened, with the intention of allowing the cell to fill slowly and disturb the bulk of the system to the smallest extent possible. A hissing noise could be heard while the cell filled, which would subside once the cell had filled. The pressure of the system as a whole would fall while the cell filled, however it would stabilize once the cell was full.

The sample present in the cell was extracted directly into ~40 cm^3 of ~4 % nitric acid (in preparation of analysis). The total volume was recorded in order to make correct dilution calculations.

Multiple samples were taken from a single experiment, however it was important to be aware of the system pressure – a drop below the vapour pressure would cause a phase change of the test solution. In the case of multi-sample experiments, the temperature would initially be ramped up to the lower end of the temperature range,

either 200 or 220 °C, and allowed to reach equilibrium before sampling, after which the temperature would be ramped up by 40 °C, followed by the sampling procedure, and finally another 40 °C to the last sampling temperature. This produced two strings of experimental temperatures giving coverage of the entire range of interest with relatively good resolution; one experiment would produce samples for temperatures of 200, 240 and 280 °C, and the other for 220, 260 and 300 °C.

When sufficient samples had been taken, the heater controller was set to 0 °C and the system left to cool down, a process that could take as much as 18 hours.

C.2 Improved Metal Oxide Experimental

C.2.1 Evolution of Design

The design of the metal oxide solubility rig has been through several iterations of design. The overall design is based on the metal oxide solubility rig described by Wesolowski *et al.* [42] shown in Figure 2.48, which currently represents the state of the art in this field. The system described therein is composed entirely of inert materials such as platinum, titanium and zircalloy, however the system designed here is built primarily from stainless steel which is not inert under high temperature high pressure water. The rig described in the work is of a design and construction method that could easily be replicated with components of a different (inert) material.

Iteration one of the MOS rig, shown in Figure 9.26 is the most basic flow path required for these measurements. Water is introduced to the system via a high pressure piston pump, through the specimen chamber, and out through the back pressure regulator (BPR) which maintains the system pressure at a set value. The systems integrity is protected by a pressure relief valve (PRV), calibrated to a crack pressure of 120 bar. Pressure is monitored with a mechanical gauge and the entire system can be depressurised by one of two needle valves; one located shortly after the pump, and one in line with the BPR.

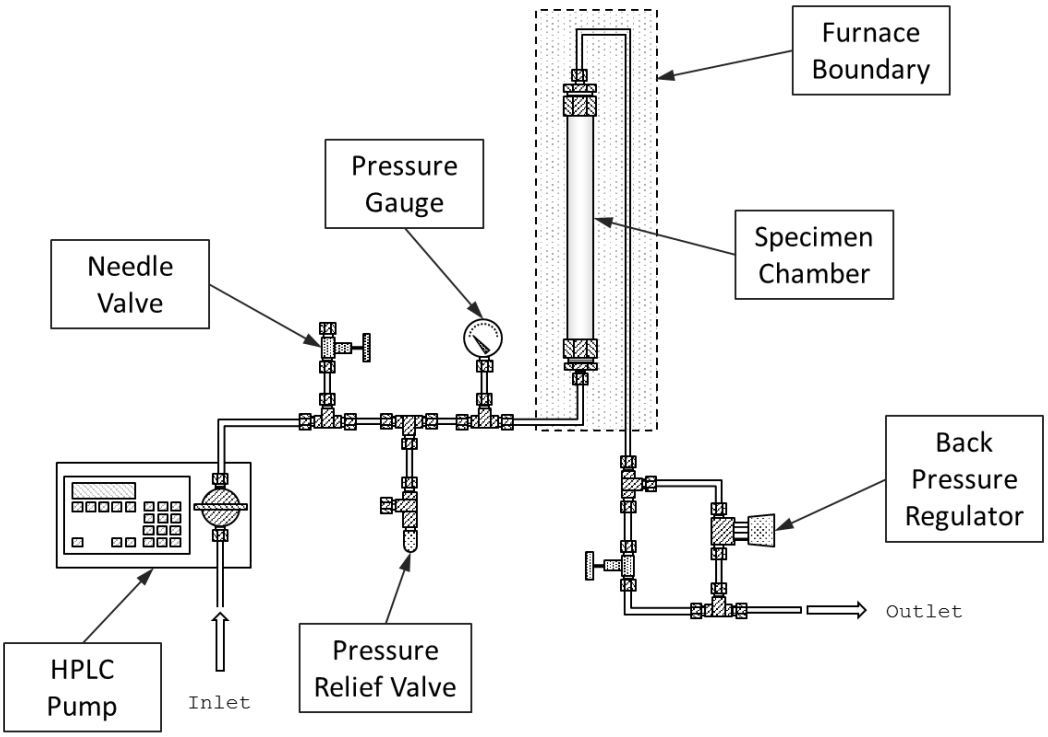

Figure 9.26 - The first design of the Metal Oxide Solubility Rig.

Iteration two, shown in Figure 9.27, built upon the first design by adding in a nitric acid delivery line similar to that seen on the ORNL rig, shown in Figure 2.48. The flow path remains the same, however a T-junction is drawn in directly after the specimen chamber where incoming dilute nitric acid would mix with the solution leaving the chamber, acidifying the solution ready for immediate analysis. In reality, the mixing tee would be held a distance from the specimen chamber to minimise the risk of backward diffusion of acid into the chamber when the system was running at low flow rates.

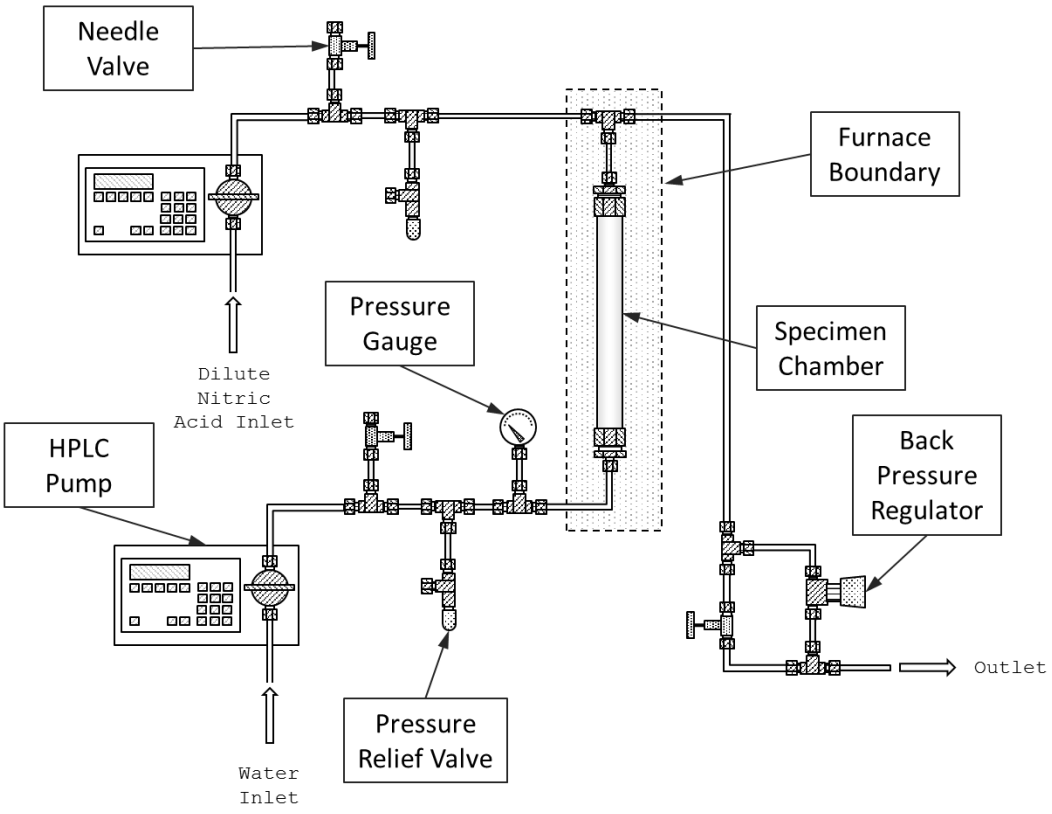

Figure 9.27 - The second design iteration of the Metal Oxide Solubility Rig. The basic flow path has been updated to include a second line carry dilute nitric acid directly to the outlet of the specimen chamber.

Iteration three built (see Figure 9.28) upon the previous design with the addition of a gas pressuriser. This was added to smooth flow pulsation, which can become a concern at higher flow rates when using powdered metal oxide samples. The flow pulsation could easily dislodge particles due to a sudden shearing flow, causing spurious readings for solubility due to particulate matter. The pressuriser would contain a volume of water, above which a volume of compressible gas would act as a shock absorber.

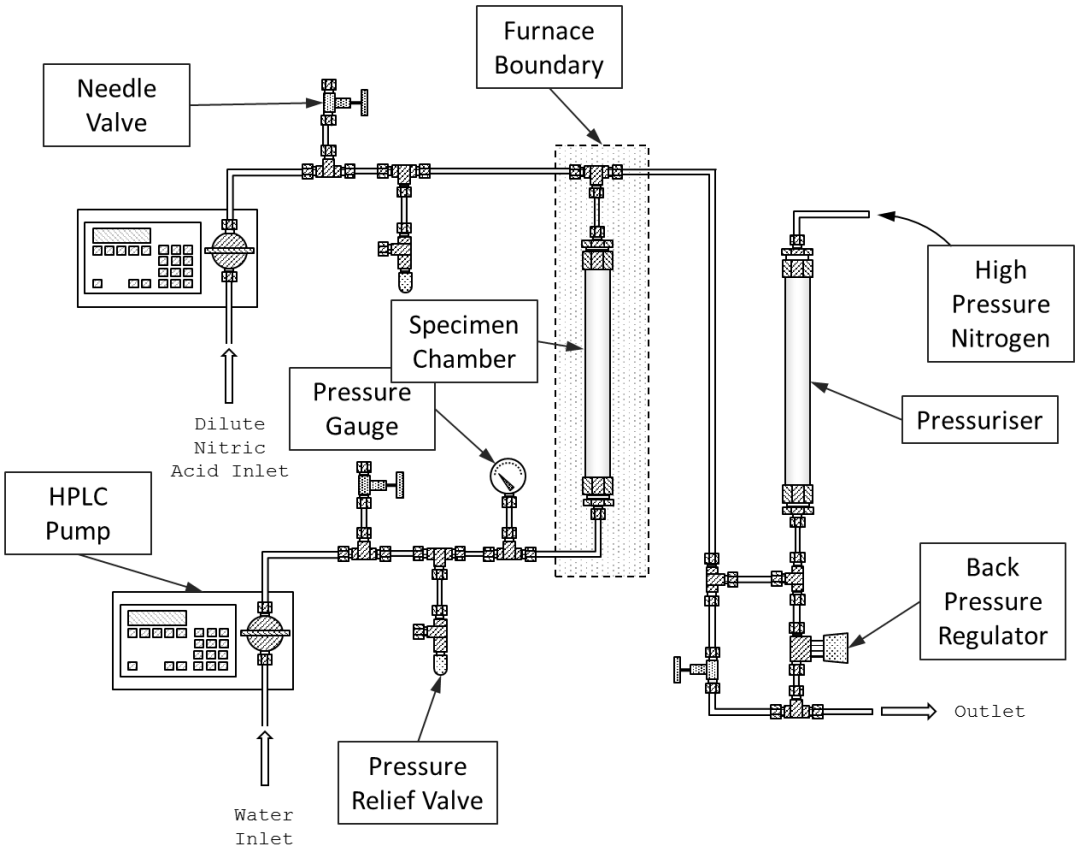

Figure 9.28 - The third design iteration of the Metal Oxide Solubility Rig. This design included a pressuriser tube, which would act as a compressible pocket to smooth flow pulsation through the rig.

The final design before construction began is shown in Figure 9.29. The system added only a sampling cell into the design, which could be used to extract volumes of material into a clean space, which had been carefully prepared to remove particulates and contaminants.

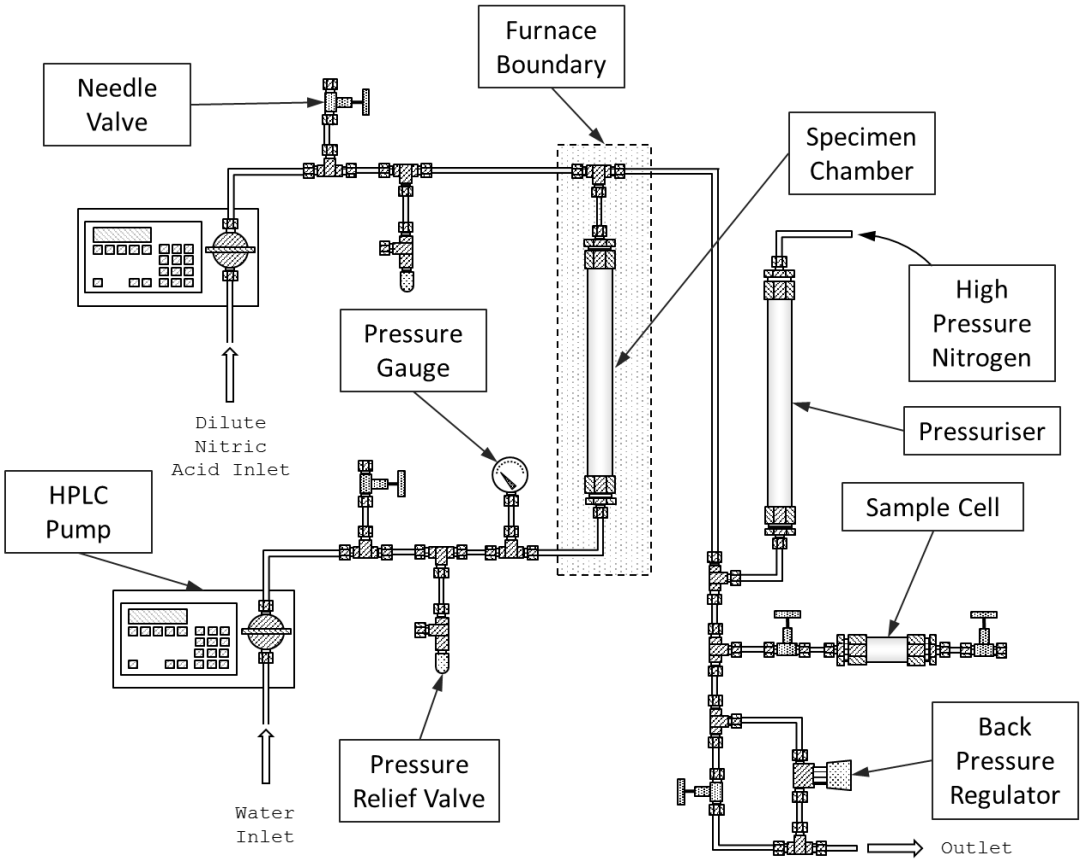

Figure 9.29 - The fourth, and penultimate, design included a sample cell which would be used to take samples of water directly from the rig rather than the drainline. Update to include the manometric modules.

C.2.1.1 Implementation

After the designs considered above, the design shown in Figure 9.29 was built using stainless steel components, however after several commissioning runs it was found that several modifications should be made.

Firstly, due to the materials incompatibility between high temperature nitric acid and stainless steel, the nitric acid supply line was removed; the dilute acid is not expected to cause component failure, but it is expected to give spurious readings for solubility.

Secondly, the sample cell was removed as this method of sampling cause very large and rapid pressure transients in the system, sometimes resulting in a pressure loss great enough to fall below the vapor pressure at the higher temperatures being tested.

Finally, the pressuriser tube was removed from the system. Its presence seemed to have an adverse effect on the flow pulsation, and so the flow smoothing was done using a combination of low flow rates, slowing down the motions of the pistons within the pump head, and use of the manometric modules.

The implemented system was simply a refined version of the very first design, the actual design can be seen in Figure 6.2. The only major design improvement included in the implemented design was the manometric module, which was a late addition to the designs. The module acts as a pulsation smoother and also an input/output device (I/O) to the HPLC pump's control computer, providing pressure information to the pump. This added an additional layer of protection for the systems integrity – the pumps could be set to stop should the pressure rise above a preset limit, in this case 110 bar.

C.2.2 Materials and Ancillary Apparatus

C.2.2.1 Swagelok Tube Fitting System

The Swagelok fitting system was used for the pressurised section of the metal oxide solubility rig. The tube was produced by Sandvik Materials Technology and distributed by Swagelok.

C.2.2.2 Materials of Construction

Due to its availability and pressure/temperature capability, stainless steel was the first material to be decided on for use in the metal oxide solubility rig and would be used as a proof of concept. Due to the simplicity of the design, a second rig, entirely in inert materials, could be built in an identical manner to the first as long as components were available in a particular material. For example, most components used for the proof-of-concept rig are available in grade 2 titanium.

In high temperature water, the passivation layer formed on the austenitic stainless steels will be largely magnetite with small amounts of non-stoichiometric nickel ferrite [28,31,36,90], as described in section 2.5.1. The passive layer will reach equilibrium with the solution in contact with it and diffusion will allow the transport of dissolved ions over a short distance, however reaching equilibrium with the bulk fluid is mass transport limited.

To some extend it is favourable to allow this layer to form and act as part of the experiment, however it must be borne in mind that stainless steel contains other soluble materials that may interfere with the measurement of soluble iron. Initial experiments were focused on studying the behaviour of the rig materials for this reason.

C.2.2.3 Chamber Furnace

To achieve and hold target temperatures with an acceptable margin, an air circulating chamber furnace was chosen in a similar manner to that chosen for the corrosion rate rigs, described in section B.2.2.2.

A chamber furnace was purchased from ThermoScientific, measuring 608 x 464 x 348 mm^3 (height/width/depth), capable of reaching 330 °C with an advertised temperature stability of ±0.3 °C.

C.2.2.4 HPLC Pumping Apparatus

Flow was provided to the system by a pair of Gilson 305 HPLC pump motors, identical to those described in section B.2.2.3, each fitted with a titanium pump head which was able to produce 0.05 – 10 ml/min.

The pumps described here differ from those of section B.2.2.3 in the use of manometric modules. These modules are fitted in the between the pumps outlet and the rig, and provide the system with a digital feedback system which can be set to stop the pumps

should the pressure pass a pre-set limit, providing a primary failsafe against a pressure spike due to flow blockage.

C.2.2.5 Feed Tanks

The feed water tank used was a 50 litre, 316L stainless steel barrel. The barrel and its associated apparatus is identical in every way except volume to those described in section B.2.2.4.

The barrel is included in part of the water supply system which provides water to both the metal oxide solubility system and to the corrosion rate rigs. A diagram of the system can be seen in Figure 5.26.

C.2.2.6 Gas Control System and Auto Shut-off

Gas control system used for the metal oxide solubility is identical in terms of operation to those described in section B.2.2.5, images of the system as a whole can be seen in Figures 5.25 and 5.26**.**

C.2.3 Methodology

C.2.3.1 Feedwater Preparation

The MOS rig uses a 50 L volume feedwater tank to store the feedwater, as shown in Figure 9.19. High purity water is charged to the tank and modified in pH using LiOH stock solution. Nitrogen gas is then sparged into the feed water tank at a rate of ~20 ml/min, and the BPR is tightened to maintain an internal positive pressure. The barrel is sparged for approximately 100 hours (2 $hr.kg^{-1}$) to remove dissolved oxygen and carbon dioxide. Measurements of dissolved oxygen are made using the ampoule method (see section 4.2.3) which returns a value of 0 – 2 ppb oxygen [189].

C.2.3.2 Rig Setup

The rig is connected together and purged with nitrogen gas for approximately 24 hours, to remove atmospheric gases. After this, a pressure of ~100 bar N_2 was charged to the rig and left for a period of 24 hours to test pressure integrity; any leakage could potentially damage equipment and must be dealt with prior to beginning of the test. Finally, the system was filled with conditioned water, pressurised by action of the pump, left at 100 bar for a further 24 hours.

C.2.3.3 Operation

With the system primed fully, the pump can be activated and set to the appropriate flow rate; in these experiments, the flow rate was restricted within the range of 0.1 – 2 ml/min. The system was allowed to reach 100 bar by hydraulic action of the pump and once at pressure, the oven temperature was ramped up; at the highest temperatures observed in this experiment series (~300 °C), the oven could reach the set point within 90 minutes of activation.

C.2.3.4 Sampling

Sampling was carried out by simply collecting the solution dripping from the exit port of the rigs BPR. The drops were collected directly into polypropylene ICP-MS autosampler tubes, purchased from Sarstedt, which were supported in place beneath the outlet on top of a 2 decimal place top loading balance. Samples of 4.00 ± 0.05 g, were collected with extreme care to avoid contamination by dust and other air borne debris, or through contact of the collect solution with rig components, skin or clothing.

Samples were prepared for analysis by acidification with 3 ml (3.17 ±0.05 g) of 10 % nitric acid solution prepared with ultrahigh purity water, producing a 15 ml sample of fluid held in a matrix of 2 % nitric acid as required for ICP-MS analysis. Samples were acidified in batches shortly before the analysis was due to take place.

Acidification in batches was done as a means to reduce error between individual samples; each sample was acidified with the same stock solution and the same pipettor, any contamination introduced by that acid would be consistent across all samples in that batch. In order to ensure quality control, blank samples were placed in the batch and could be used to estimate contamination levels should the concentrations appear excessively high. After acidification, samples were stored in a laboratory refrigerator at ~4 °C.

Surfaces in contact with the sample needed to be free from contamination and be stable during storage. Initially, glass sample vials were used for sampling and storage, but at the suggestion of the ICP-MS operator these were substituted with polypropylene (PP) test tubes, which had been shown to provide exceptional stability to chemical interaction with water samples. The sample tubes were soaked in a dilute nitric acid solution for 24 hours, before being rinsed and stored in ultrahigh purity water until they were required, at which point they were rinsed a further three times with fresh ultrahigh purity water; tube caps were treated at the same time in the same baths.

Similarly, the glass pipettes that were initially used for adding nitric acid stock solution to the water samples were replaced with an autopipette and disposable plastic nozzles, which were cleaned and stored in the same manner as described for the PP test tubes.

C.2.3.5 Shutdown

Shut down of the system was performed by first reducing the oven set point to 0 °C, and allowing the temperature to fall while a keeping the pump active. This was to prevent any type of damaging low-pressure balance, which could unseat the diaphragm within the BPR. Once temperature had been reduced to ambient, the pump was deactivated and the pressure relieved through a needle valve at the front end of the rig.